

Solid-State NMR Spectroscopy of Inorganic Materials

August 1, 2012 | <http://pubs.acs.org>
Publication Date: March 18, 1999 | doi: 10.1021/bk-1999-0717.fw001

ACS SYMPOSIUM SERIES **717**

Solid-State NMR Spectroscopy of Inorganic Materials

John J. Fitzgerald, EDITOR
South Dakota State University



American Chemical Society, Washington, DC

In Solid-State NMR Spectroscopy of Inorganic Materials; Fitzgerald, J.;
ACS Symposium Series; American Chemical Society: Washington, DC, 1999.



Solid-state NMR spectroscopy of inorganic materials

Library of Congress Cataloging-in-Publication Data

Solid-state NMR spectroscopy of inorganic materials / John J. Fitzgerald, editor.

p. cm.—(ACS symposium series , ISSN 0097-6156 ; 717)

“Developed from a symposium sponsored by the Division of Industrial and Engineering Chemistry at the 212nd National Meeting of the American Chemical Society, Orlando, Florida, August 25-29, 1996.”—T.p. verso.

Includes bibliographical references and index.

ISBN 0-8412-3602-X (alk. paper)

1. Nuclear magnetic resonance spectroscopy—Congresses. 2. Inorganic compounds—Analysis—Congresses.

I. Fitzgerald, John J. II. American Chemical Society. Division of Industrial and Engineering Chemistry. III. American Chemical Society. Meeting (212nd : 1996 : Orlando, Fla.) IV. Series.

QD96.N8S65 1999

543'.0877—dc21

98-38894

CIP

The paper used in this publication meets the minimum requirements of American National Standard for Information Sciences—Permanence of Paper for Printed Library Materials, ANSI Z39.48-1984.

Copyright © 1999 American Chemical Society

Distributed by Oxford University Press

All Rights Reserved. Reprographic copying beyond that permitted by Sections 107 or 108 of the U.S. Copyright Act is allowed for internal use only, provided that a per-chapter fee of \$20.00 plus \$0.25 per page is paid to the Copyright Clearance Center, Inc., 222 Rosewood Drive, Danvers, MA 01923, USA. Republication or reproduction for sale of pages in this book is permitted only under license from ACS. Direct these and other permissions requests to ACS Copyright Office, Publications Division, 1155 16th Street, N.W., Washington, DC 20036.

The citation of trade names and/or names of manufacturers in this publication is not to be construed as an endorsement or as approval by ACS of the commercial products or services referenced herein; nor should the mere reference herein to any drawing, specification, chemical process, or other data be regarded as a license or as a conveyance of any right or permission to the holder, reader, or any other person or corporation, to manufacture, reproduce, use, or sell any patented invention or copyrighted work that may in any way be related thereto. Registered names, trademarks, etc., used in this publication, even without specific indication thereof, are not to be considered unprotected by law.

PRINTED IN THE UNITED STATES OF AMERICA

**American Chemical Society
Library**

1155 16th St., N.W.
Washington, D.C. 20036

In Solid-State NMR Spectroscopy of Inorganic Materials: Fitzgerald, J.; ACS Symposium Series; American Chemical Society: Washington, DC, 1999.

Advisory Board

ACS Symposium Series

Mary E. Castellion
ChemEdit Company

Arthur B. Ellis
University of Wisconsin at Madison

Jeffrey S. Gaffney
Argonne National Laboratory

Gunda I. Georg
University of Kansas

Lawrence P. Klemann
Nabisco Foods Group

Richard N. Loepky
University of Missouri

Cynthia A. Maryanoff
R. W. Johnson Pharmaceutical
Research Institute

Roger A. Minear
University of Illinois
at Urbana-Champaign

Omkaram Nalamasu
AT&T Bell Laboratories

Kinam Park
Purdue University

Katherine R. Porter
Duke University

Douglas A. Smith
The DAS Group, Inc.

Martin R. Tant
Eastman Chemical Co.

Michael D. Taylor
Parke-Davis Pharmaceutical
Research

Leroy B. Townsend
University of Michigan

William C. Walker
DuPont Company

Foreword

THE ACS SYMPOSIUM SERIES was first published in 1974 to provide a mechanism for publishing symposia quickly in book form. The purpose of the series is to publish timely, comprehensive books developed from ACS-sponsored symposia based on current scientific research. Occasionally, books are developed from symposia sponsored by other organizations when the topic is of keen interest to the chemistry audience.

Before agreeing to publish a book, the proposed table of contents is reviewed for appropriate and comprehensive coverage and for interest to the audience. Some papers may be excluded in order to better focus the book; others may be added to provide comprehensiveness. When appropriate, overview or introductory chapters are added. Drafts of chapters are peer-reviewed prior to final acceptance or rejection, and manuscripts are prepared in camera-ready format.

As a rule, only original research papers and original review papers are included in the volumes. Verbatim reproductions of previously published papers are not accepted.

ACS BOOKS DEPARTMENT

Preface

During the past two decades, solid-state NMR spectroscopy has become firmly established as one of the premier approaches to examine the structure and dynamics of complex organic, inorganic, and biological solid materials. Recent advances in solid-state NMR of inorganic materials have flourished as a result of important developments in solid-state NMR techniques (including MAS, CP/MAS, DAS, MQMAS, and 2D NMR methods) that have occurred in parallel with the worldwide revolution in materials science of technologically important inorganic materials such as metal oxide catalysts and supports, zeolites, ceramics, glasses, thin films, semiconductors, superconductors, and inorganic composites.

This volume summarizes some of the important recent developments in the use of solid-state NMR to investigate inorganic materials. The book includes a thorough and comprehensive introductory chapter that provides an Overview of Solid-State NMR of Inorganic Materials, including a survey of recent advances in solid-state NMR approaches and the applications of these techniques to studies of a diverse range of inorganic materials. The section on NMR of Metal Oxide Systems includes an important contribution that discusses the salient features of multiple-quantum MAS (MQMAS) NMR of half-integer quadrupolar nuclei. Significant contributions are also included on solid-state NMR of oxygen in simple and complex oxides, the NMR study of fluoridated hydroxyapatites, and the use of multinuclear NMR to study the surface and “interfacial” chemistry of alumina. The section on Solid-State NMR of Amorphous Glasses and Gels includes a contribution on 2D heteronuclear correlation NMR studies of phosphate glasses. Recent advances in studies of borate glasses by dynamic-angle spinning (DAS) NMR, and the use of ^{17}O NMR to examine sol–gel precursors to electronic materials are also presented. The continued intense exploration of Silica-Containing Materials by Solid-State NMR is discussed in the next section, including contributions on guest–host interactions in Sodalites by multinuclear NMR, and the use of 1D- and 2D-NMR methods to investigate guest–host relationships in molecular sieves. An important contribution that focuses on the recent use of 2D and double resonance ^{29}Si NMR studies of minerals is also summarized. An equally significant overview is then presented on solid-state NMR studies of siloxane-based solid networks, including materials spanning silicas to silicones. The section on NMR Studies of Inorganic Nitro-

gen-Containing Materials, includes two contributions involving wide-line ^{14}N NMR in inorganic solids, and an overview of solid-state NMR studies of important nitride and oxynitride ceramic materials.

This volume was developed as a result of the recent intense advances occurring in the use of solid-state NMR spectroscopy to study important scientific questions regarding inorganic materials. These advances stimulated the successful symposium on this topic presented at the National American Chemical Society Meeting in Orlando, Florida, August 25–29, 1996. While contributions in this book represent some of the important ongoing research related to this subject, several of the other symposium contributors and numerous national and international researchers have made important contributions to the study of inorganic materials using solid-state NMR techniques. Much of their significant work up to 1997 is discussed in the introductory overview chapter or cited in the other contributions in this book. It is hoped that this volume will provide important insights into the many scientific issues and problems being addressed by research involving solid-state NMR studies of inorganic materials, thus motivating future research and symposia on these topics and important new contributions to this active multidisciplinary field of research.

The author is indebted to the commitment and scientific ideas expressed by the contributors to this volume on Solid-State NMR Spectroscopy of Inorganic Materials. Appreciation to Connie Granbois for her assistance in the preparation of materials for this book is gratefully acknowledged.

As a creative scientist, chemist and humanist has noted: “A great deal of information about the structure of molecules”...(and crystalline and amorphous materials)...“has been obtained by analysis of their spectra.”... (Linus Pauling, *The Nature of the Chemical Bond*, Cornell University Press, 1939).

JOHN J. FITZGERALD
Department of Chemistry and Biochemistry
South Dakota State University
Brookings, SD 57007

Chapter 1

Solid-State NMR Spectroscopy of Inorganic Materials: An Overview

John J. Fitzgerald¹ and Susan M. DePaul^{2,3}

¹Department of Chemistry and Biochemistry, South Dakota State University,
Brookings, SD 57007

²Materials Sciences Division, E. O. Lawrence Berkeley National Laboratory and
Department of Chemistry, University of California, Berkeley, CA 94720

Advances in solid-state nuclear magnetic resonance (NMR) investigations of a diverse range of important inorganic materials are reviewed. Fundamental and new solid-state NMR methods including magic-angle spinning, cross-polarization, multiple-quantum and various two-dimensional techniques that are applicable to both spin-1/2 and quadrupolar nuclides are discussed. An overview of the successful applications of these solid-state NMR methods to obtain new information about the salient chemical, structural and dynamical features of several important classes of inorganic materials is given. Key literature pertaining to selected solid-state NMR studies of refractory metal oxides, catalysts, zeolites and layered materials, ceramics and glasses, biomaterials, semiconductors, ion conductors, superconductors and inorganic composites is discussed. Various chemical issues that have been addressed by these investigations suggest that in the future solid-state NMR will play an important role in expanding our detailed atomic-level understanding of the chemical behavior of these and other advanced inorganic materials.

Solid-State NMR of Inorganic Materials

During the past five decades, nuclear magnetic resonance (NMR) spectroscopy has been one of the most important spectroscopic approaches for obtaining physical and chemical information about a diverse range of complex chemical systems (1-7). The last two decades, in particular, have experienced significant advances in the study of the atomic-level structure and dynamics of both organic and inorganic materials using solid-state nuclear magnetic resonance spectroscopy (8-13). In the case of inorganic materials, such studies have often provided crucial insight into the chemistry of complicated systems. The complexity of inorganic materials has its origins in their

³Current address: Max-Planck-Institut für Polymerforschung, Postfach 3148, D-55021 Mainz, Germany.

diverse three-dimensional structures and in the presence in many cases of multiple solid phases, interfaces, surface sites or impurities. Advanced inorganic materials exhibit a wide range of functional dynamics and structural features that underlie properties such as catalytic activity, electronic and ionic conductivity, superconductivity and dielectric behavior. Applications of modern inorganic materials includes uses such as specialized industrial catalysts, molecular sieves and adsorbents, high-temperature structural ceramics, electrooptic and laser materials, electronic ceramics, semiconductors, specialized glasses and amorphous fibers, cements, and, most notably, high-temperature superconductors.

The emerging demands for inorganic composite materials and multilayered electronic devices requires a new atomic-level understanding of interfacial interactions at organic-inorganic and inorganic-inorganic interfaces. Other interesting inorganic materials, such as those arising from biomineralization, have also stimulated study of processes at the atomic-level by solid-state NMR. In geochemistry and mineralogy, important geological problems involving the high-temperature structural chemistry of mineral phases, mineral surface adsorption and ion exchange reactions in natural geochemical processes, and the migration and deposition chemistry of inorganic ion (e.g., Pb^{2+} , Cd^{2+}) and organic (e.g., pesticides) pollutants are presently the subject of intense solid-state NMR study.

Recent advances in the development and understanding of inorganic materials have occurred in parallel with major advances in solid-state NMR methods and approaches. Increased resolution in NMR spectra of solids has resulted from the use of line-narrowing techniques such as magic-angle spinning (MAS) NMR for most NMR-active spin-1/2 nuclei in the Periodic Table. In addition, methods such as Double Rotation (DOR) and Dynamic Angle Spinning (DAS) have allowed high-resolution spectra of many quadrupolar (spin $I > 1/2$) nuclides to be obtained. The use of DOR and DAS for improved NMR spectral resolution of quadrupolar broadened signals has recently been augmented by major developments in multiple-quantum MAS (MQMAS) NMR to obtain detailed descriptions of atomic sites in a variety of inorganic materials.

Research investigations of inorganic solids have also benefited from the selectivity and signal enhancement characteristics of cross-polarization MAS (CP/MAS), which in the last decade led to major advances in understanding organic polymers and biomass materials. Multidimensional NMR techniques (e.g., isotropic/anisotropic correlations, heteronuclear shift correlations, COSY and INADEQUATE experiments) are being used to extract new information about local metal and oxygen atom environments in metal oxides and zeolites. Recent solid-state NMR experiments such as REDOR, TEDOR, SEDOR, TRAPDOR and REAPDOR reveal internuclear distances, while two-dimensional exchange experiments provide insight into molecular mobility.

This introductory chapter will review the major classes of inorganic materials and their NMR nuclide compositions, including the most significant spin-1/2 and quadrupolar nuclides currently being used to study solid inorganic materials. The important interactions in solid-state NMR will then be discussed, followed by a review of NMR approaches that can be used to provide detailed, site-specific structural and dynamical information about inorganic materials. Finally, this chapter will give an overview of important past and current solid-state NMR studies of various classes of inorganic materials, focusing on the types of information obtainable and using selected

examples from the literature. These NMR investigations have provided a major impetus for the organization of the recent ACS symposium on "Solid-State NMR Spectroscopy of Inorganic Materials".

I. COMPOSITION OF INORGANIC MATERIALS

Inorganic materials exhibit a enormously diverse range of functional properties due to their complex catalytic, adsorptive, ion exchange, magnetic, electronic, optical, thermal, photochemical, and structural behavior. Several categories of inorganic materials are summarized in Table I. The use of solid-state NMR spectroscopy to examine the structural nature, reactivity and physico-chemical properties of these materials is based on the ability of NMR to obtain nuclide-specific information about these solids. The most important criterion is the presence of a nucleus that possesses a non-zero nuclear magnetic moment since only such nuclei are observable by NMR spectroscopy. Because nearly all of the stable elements of the Periodic Table have at least one isotope with a non-zero magnetic moment, NMR can be used to study a wide variety of inorganic substances. In particular, diamagnetic materials containing the nuclides such as ^1H , ^{11}B , ^{13}C , ^{15}N , ^{19}F , ^{23}Na , ^{27}Al , ^{29}Si and ^{31}P (Tables II and III) have been extensively studied in systems such as silicon and aluminum oxides; silicon carbides and nitrides; zeolites; alkali silicate, borosilicate and fluoride-containing glasses; and aluminum phosphates. Recent interest in the study of metal oxide catalysts, geomaterials, ceramics, electronic materials, semiconductors and superconductors has motivated solid-state NMR studies of both low abundance nuclides (^{17}O , ^{25}Mg , $^{47,49}\text{Ti}$ and ^{95}Mo) and high abundance nuclides (^{51}V , ^{69}Ga and ^{93}Nb) with more complex NMR characteristics. For the low-abundant nuclei, isotopic-labelling approaches are increasingly being used both for signal enhancement and for site selectivity.

The solid-state NMR spectra of many of these less-studied nuclides, however, can be extremely complex due to their NMR relaxation processes, to chemical shift anisotropy and quadrupolar effects, and to the possible presence of paramagnetic oxidation states in many materials that contain these nuclides. Although only elements in diamagnetic states are typically studied by NMR, the presence of paramagnetic species (e.g., due to free radicals, oxygen defect sites, or intermediate or minor species containing paramagnetic metal ions) in copper, vanadium and molybdenum systems has provided significant solid-state NMR challenges. Systems where these situations occur include metal oxide catalysts, high- T_c copper oxide superconductors, complex perovskite-type ion conductors, and high-temperature ceramics.

In many systems, however, paramagnetic effects are negligible, and the NMR spectra are dominated by the interactions of a given nucleus with its neighboring nuclei and electrons. The following section describes a few of these interactions, the information they provide, and how they are manifested in solid-state NMR spectra.

II. NMR INTERACTIONS IN INORGANIC SOLIDS

A. Spin-1/2 Nuclei.

Nuclei with a spin quantum number, I , equal to 1/2 have been extensively studied by NMR spectroscopy. Some of the most widely examined spin-1/2 nuclides in inorganic

Table I. Several major categories of inorganic materials

Metal Oxides (Catalysts/Supports/Reagents)

SiO₂, SiO₂·nH₂O
 Al₂O₃·nH₂O
 Na₂O·SiO₂ (Sodium Silicates)
 Na₂O·Al₂O₃ (Sodium Aluminates)
 SiO₂/Al₂O₃ (Silica/Alumina)
 TiO₂, ZrO₂ (Titania, Zirconia)
 V₂O₅, Nb₂O₅, MoO₃

Open Framework and Layered Materials

Zeolites (Si/Al-Containing)
 AlPO (Zeolitic Al/P-Containing)
 SAPO (Zeolitic Si/Al/P-Containing)
 Si/Al Minerals (Kaolin, Pyrophyllite, Montmorillonite)
 Ti/Si Layered Materials
 Zr(HPO₄)₂, ZrHPO₄·nH₂O

Glasses

SiO₂
 Al₂O₃·SiO₂
 SiO₂·B₂O₃
 (Na₂)(K₂O)·2SiO₂
 Li₂O·Al₂O₃·SiO₂

Cements/Adhesives

CaO·Al₂O₃·SiO₂ (Portland Cements)
 AlPO₄ (Aluminophosphates)
 Ca₃(PO₄)₂·nH₂O

Structural Ceramics

TiB₂, ZrB₂
 SiC, TiC, ZrC
 BN, Si₃N₄, TiN
 ZrO₂, ZrO₂/Al₂O₃
 SiAlON
 BaSiAlON

Electronic/Magnetic Materials

BaTiO ₃	PMN	Fe ₂ O ₃
PbTiO ₃	PZN	CoFe ₂ O ₄
PZT	PMN/PT	LiFeO ₂
PLZT	TiO ₂	LaMnO ₃
		YMnO ₃

Ion Conductors

LaCrO₃
 MgCr₂O₄
 Ba₂In₂O₅
 β-Al₂O₃

Semiconductors

AlN, GaN
 AlP, GaP, InP
 Ga_xAl_yP
 GaAs

Superconductors

Bi₂Sr₂CaCu₂O_{8+x}
 YBa₂Cu₃O_{7-x}
 Tl₂Ba₂CaCu₂O_{8+x}
 La_{1.85}Sr_{0.15}CuO_{4-x}

Table II. Properties of selected spin-1/2 nuclei.

Nucleus	% Abundance	Receptivity (Relative to ^1H)	Frequency (MHz) at 11.7 T	Examples of Inorganic Materials
^1H	99.985	1.000	500.0	Hydrates, Sol-gel Intermediates
^{13}C	1.10	1.76×10^{-4}	125.7	Metal Carbides Chelated Metal Oxides
^{15}N	0.37	3.85×10^{-6}	50.7	Nitride Ceramics
^{19}F	100	0.834	470.4	Fluoridated Hydroxyapatites
^{29}Si	4.70	3.69×10^{-4}	99.3	Glasses, Zeolites Silicon Nitride Silicon Carbide
^{31}P	100	0.0665	202.4	Glasses, Catalysts Semiconductors
^{77}Se	7.6	5.30×10^{-4}	95.3	Semiconductors
^{89}Y	100	1.19×10^{-4}	24.5	Laser Materials, Ceramics Superconductors
^{113}Cd	12.26	1.35×10^{-3}	110.9	Semiconductors Photovoltaic Oxides
^{119}Sn	8.58	4.51×10^{-3}	186.4	Oxides, Ion Conductors Photovoltaics
^{125}Te	6.99	2.24×10^{-3}	158.0	Semiconductors
^{195}Pt	33.8	3.39×10^{-3}	107.5	Catalysts
^{207}Pb	22.60	2.10×10^{-3}	104.6	Oxides, Sulfides Electronic Materials

Receptivity equals $|\gamma|^3 \cdot (\% \text{ abundance}) \cdot I(I+1)$

Table III. Properties of selected quadrupolar nuclei.

Nucleus	Spin	% Abundance	Receptivity (Relative to ^1H)	Frequency (MHz) at 11.7 T
^2H	1	0.015	1.45×10^{-6}	76.8
^6Li	1	7.42	6.31×10^{-4}	72.6
^7Li	3/2	92.58	0.272	194.3
^{10}B	3	19.58	3.89×10^{-3}	53.7
^{11}B	3/2	80.42	0.133	160.4
^{14}N	1	99.63	1.00×10^{-3}	36.1
^{17}O	5/2	0.037	1.08×10^{-5}	67.8
^{23}Na	3/2	100	1.3×10^{-2}	132.3
^{25}Mg	5/2	10.1	2.72×10^{-4}	30.6
^{27}Al	5/2	100	0.207	130.3
^{39}K	3/2	93.1	4.75×10^{-4}	23.3
^{47}Ti	5/2	7.3	1.53×10^{-4}	28.2
^{49}Ti	7/2	5.5	2.08×10^{-4}	28.2
^{51}V	7/2	99.76	0.383	131.4
^{63}Cu	3/2	69.09	6.45×10^{-2}	137.6
^{65}Cu	3/2	30.91	3.54×10^{-2}	142.0
^{69}Ga	3/2	60.4	4.19×10^{-2}	120.2
^{71}Ga	3/2	39.6	60.4	152.5
^{75}As	3/2	100	0.11	85.9
^{85}Rb	5/2	72.14	2.3×10^{-2}	48.4
^{87}Rb	3/2	27.85	4.92×10^{-2}	164.1
^{91}Zr	5/2	11.2	1.06×10^{-3}	46.7
^{93}Nb	9/2	100	0.487	122.2
^{95}Mo	5/2	15.7	5.14×10^{-4}	32.6
^{113}In	9/2	4.28	1.48×10^{-2}	109.3
^{115}In	9/2	95.72	0.337	109.6
^{133}Cs	7/2	100	4.82×10^{-2}	65.6
^{137}Ba	3/2	11.3	7.89×10^{-4}	55.6

Receptivity equals $|\gamma|^3 \cdot (\% \text{ abundance}) \cdot I(I+1)$

materials are listed in Table II together with some of their relevant parameters, including natural abundances, receptivities (relative to ^1H), Larmor frequencies at 11.7 T (corresponding to 500 MHz for ^1H), and examples of important inorganic systems containing these nuclides. The most important interactions for spin-1/2 nuclei in solids include the Zeeman interaction, the chemical shift interaction, and the dipolar interaction.

1. Zeeman Interaction. By the laws of angular momentum, a nucleus with spin-quantum number I has $2I+1$ states. These states are labeled by the quantum number m where m has one of the following values: $\{-I, -I+1, \dots, I-1, I\}$. Thus, a spin- 1/2 nucleus is a two-level system with states $m = +1/2$ and $m = -1/2$. In the presence of an externally applied magnetic field, these states become non-degenerate due to the Zeeman interaction, and the application of electromagnetic radiation (in the form of radio waves) of the appropriate frequency can induce transitions between them. The splitting between successive levels is given by the Larmor frequency $\omega_0 = \gamma B_0$, where γ is the gyromagnetic ratio, which is nuclide dependent (cf. the fourth column of Table II), and B_0 is the strength of the applied magnetic field. Note the wide variation in the Larmor frequencies of different nuclides (see Tables II and III). Since pulsed NMR techniques typically excite spectral ranges on the order of tens to hundreds of kilohertz, signals due to a single isotope can (in most cases) be selectively observed, making NMR a powerful technique for obtaining site-specific information. For spin-1/2 nuclei and magnetic field strengths of several Tesla (typical for NMR spectrometers), the Zeeman interaction dominates the NMR Hamiltonian, and all other interactions can be considered as small perturbations relative to it.

2. Chemical-Shift Interaction. The chemical shift (δ) reflects the magnetic shielding of a nucleus by neighboring electron clouds and is the most commonly used NMR parameter. Like the Zeeman interaction, the chemical shift is proportional to the strength of the applied magnetic field. Both diamagnetic and paramagnetic effects contribute to the chemical shift, which is an orientation-dependent (tensor) quantity. In solution-state NMR spectroscopy, rapid molecular tumbling averages out this orientation-dependence and produces a narrow line at a position known as the isotropic chemical shift (δ_{iso}), which reflects the average electronic environment of the nucleus. In spectra of powdered solid samples, however, all orientations of a given site with respect to the B_0 field are present. When the local symmetry is less than cubic, most of these orientations have slightly different resonance frequencies. This leads to a broad lineshape known as a "powder pattern" (cf. Figures 1A and 1B) from which the eigenvalues of the chemical-shielding tensor in its diagonal representation ($\sigma_{11}, \sigma_{22}, \sigma_{33}$) can be extracted. The eigenvalues are referred to as the principal values of the chemical-shielding anisotropy (CSA), and they can often be correlated with site symmetry, chemical bonding and next-nearest neighbor effects. An equivalent set of linear combinations of these parameters is also frequently used and consists of the previously mentioned isotropic chemical shift (δ_{iso}), the anisotropy parameter ($\Delta\delta$), and an asymmetry parameter (η^{CS}).

3. Direct Magnetic Dipolar Interaction. Another important interaction in solid-state NMR is the through-space interaction between the magnetic moments of two nuclei. The strength of this interaction is directly proportional to the product of the gyromagnetic ratios of each nucleus and inversely proportional to the cube of the

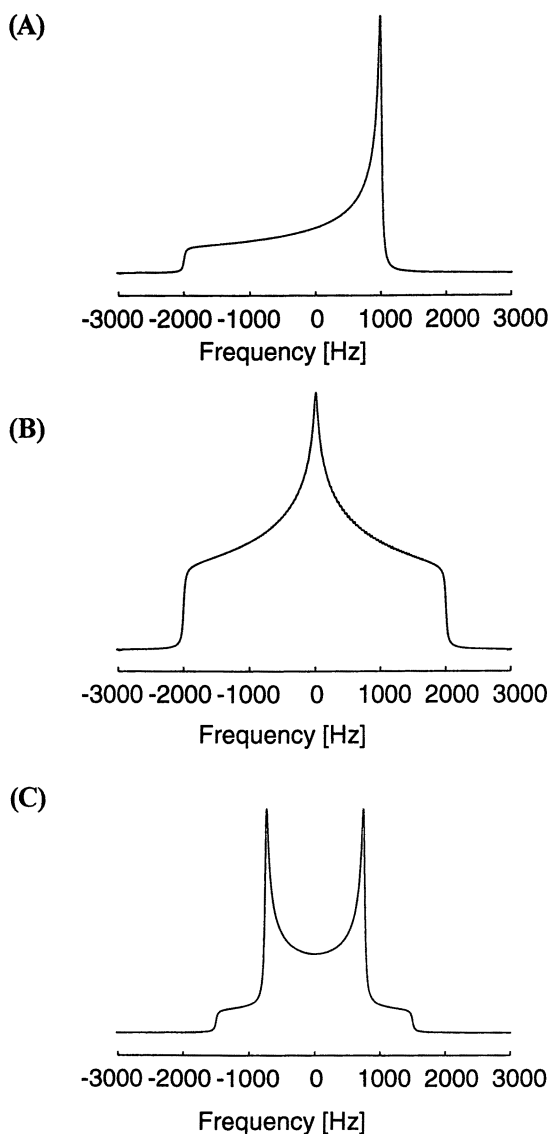


Figure 1. Simulated static powder patterns due to various NMR interactions for a spin-1/2 nucleus. (A) Axially symmetric chemical-shielding powder pattern. (B) Asymmetric chemical-shielding powder pattern. (C) Dipolar Pake pattern for an isolated spin pair. Note that the principle values of CSA ($\sigma_{11}, \sigma_{22}, \sigma_{33}$) correspond to the "singularities" in the powder spectra while the separation between the horns in the dipolar powder pattern is related to the internuclear distance.

distance between them. As in the case of the chemical shift interaction, the direct dipolar interaction is anisotropic; it depends on the orientation of the internuclear vector with respect to the static B_0 field. Thus, for a powder sample, a broad lineshape will be generated. However, this pattern can contain singularities which allow the average internuclear distance to be directly determined. Figure 1C shows a powder (Pake) pattern for an isolated pair of spins. In this idealized case, the chemical shielding anisotropy is negligible, and since the separation between the peaks in Hz is given by $(\mu_0/4\pi)\gamma_I\gamma_S r_{IS}^{-3}(h/2\pi)$ for a pair of unlike spins, the internuclear distance can be extracted directly from the peak separation. In larger spin systems, the spectra become more complicated and the distance information correspondingly harder to extract.

4. Other Interactions. A few other interactions can also potentially affect the solid-state NMR spectra of spin-1/2 nuclei. In addition to the direct dipolar interaction mentioned above, there is also an indirect dipolar-coupling mechanism which involves bonding electrons. This through-bond interaction, also known as the scalar interaction, is characterized by a coupling constant J . It is an important interaction in solution-state spectroscopy where motional averaging removes the effects of the direct dipolar interaction on the positions of the resonances. In solids the J -coupling is often neglected since it is typically much smaller than the direct dipolar coupling, but it can be significant in highly crystalline samples.

Another interaction which can influence the spectra of spin-1/2 nuclei is the hyperfine coupling between nuclear magnetic moments and the magnetic moments of conduction electrons in a metal. This produces a shift of the NMR resonance frequency which is known as the Knight shift. Although the Knight shift has the same functional form as the chemical shift, it arises from a different physical mechanism, and the two effects can be distinguished using a combination of experiment and theory. Measurements of the temperature-dependence of the Knight shift have been used to test theories of high- T_c superconductivity (14).

While the above interactions contain a wealth of structural and dynamical information, the presence of more than one of them in a sample (as is generally the case) can lead to spectra too complex to interpret. Fortunately, a wide range of NMR experiments (see Section III) have been developed to selectively enhance or suppress given interactions and thus permit the extraction of chemically relevant information.

B. Quadrupolar Nuclei.

Nuclei with a spin-quantum number I greater than 1/2 are known as quadrupolar nuclei. Over two-thirds of the NMR-active nuclei in the Periodic Table are quadrupolar nuclei (15,16), but many of them have not yet been widely utilized. Several quadrupolar nuclides used for studies of inorganic materials are listed in Table III, together with relevant NMR parameters, including nuclear spin (I), natural abundance, Larmor frequencies at 11.7 Tesla and receptivities relative to ^1H . In this overview, we will focus on quadrupolar nuclei with odd half-integer spin quantum numbers ($I = 3/2, 5/2, 7/2 \dots$ etc.) since they are abundant in inorganic materials and have been the focus of much technique development during the past decade.

As in the case of spin-1/2 nuclei, the levels of a quadrupolar nucleus undergo

Zeeman splitting when placed in a large external magnetic field (see Figure 2A), and the presence of the chemical shift, direct dipolar coupling, scalar coupling, or Knight shift interaction will further perturb them. Since there are now more than two energy levels, multiple transitions (and hence multiple resonances for a single nucleus) are possible (see Figures 2A and 2B).

A nucleus with $I > 1/2$ also has a non-spherically symmetric charge distribution and hence a non-zero nuclear electric quadrupole moment, eQ . Such a moment will interact with an electric field gradient (EFG) present in the sample due to an asymmetric distribution of electrons around the nucleus. This interaction is known as the quadrupolar interaction; like the chemical shift and direct dipolar interactions, it is anisotropic (orientation-dependent) and leads to powder patterns in polycrystalline samples. The widths and shapes of these powder patterns are strongly influenced by two parameters, respectively: (1) the quadrupolar coupling constant, $C_q = e^2qQ/h$, which is proportional to the product of the nuclear electric quadrupole moment, eQ , and the magnitude of the electric field gradient along its principal axis, eq [note that there are alternative definitions of the quadrupolar coupling constant in the literature which involve scaling factors that are functions of the spin-quantum number I]; and (2) the asymmetry parameter, η^Q , which reflects the deviation of the electric field gradient from cylindrical symmetry.

The quadrupolar coupling constant can have a wide range of values. When C_q is very small relative to the Zeeman splitting, the quadrupolar interaction can be treated by first-order perturbation theory. Figure 2B shows an example of a static powder pattern for a spin-5/2 nucleus subject to the first-order quadrupolar interaction. This pattern is a superposition of the powder patterns for the five allowed transitions. The narrowest peak in the center of the spectrum corresponds to the central transition ($m = +1/2 \leftrightarrow m = -1/2$) which is unaffected by the quadrupolar interaction to first order, while the wings on the side correspond to anisotropic powder patterns for the four satellite transitions ($m = +5/2 \leftrightarrow m = +3/2$), ($m = +3/2 \leftrightarrow m = +1/2$), ($m = -1/2 \leftrightarrow m = -3/2$), and ($m = -3/2 \leftrightarrow m = -5/2$).

Often, however, the quadrupolar interaction is strong enough that second-order perturbation theory must be invoked to accurately describe the observed spectrum. In such a case, the center of mass of the central transition resonance will be shifted from the isotropic shift position; this additional shift is often termed the isotropic second-order quadrupolar shift. Along with the width and shape of the central transition anisotropic powder pattern, it is sensitive to values of γB_0 , C_q , η^Q and I . Figure 3A shows a simulation of a second-order powder pattern for the central ($m = +1/2 \leftrightarrow m = -1/2$) transition of a spin-5/2 nucleus with $\eta^Q = 0.5$ under static conditions. (Figure 3B shows a simulation of the same second-order powder pattern under fast MAS conditions.) Static powder patterns can also be calculated for satellite transitions, but in practice these transitions are often spread out over such a wide range of resonance frequencies that they are difficult to detect and measure accurately.

Sometimes the quadrupolar interaction is so strong that it cannot be treated as a perturbation to the energy. In such cases, high-field NMR is not done at all; instead, the quadrupolar interaction is used as the axis of quantization, and a very small B_0 field is applied as a perturbation to it. This method, known as Nuclear

(A)

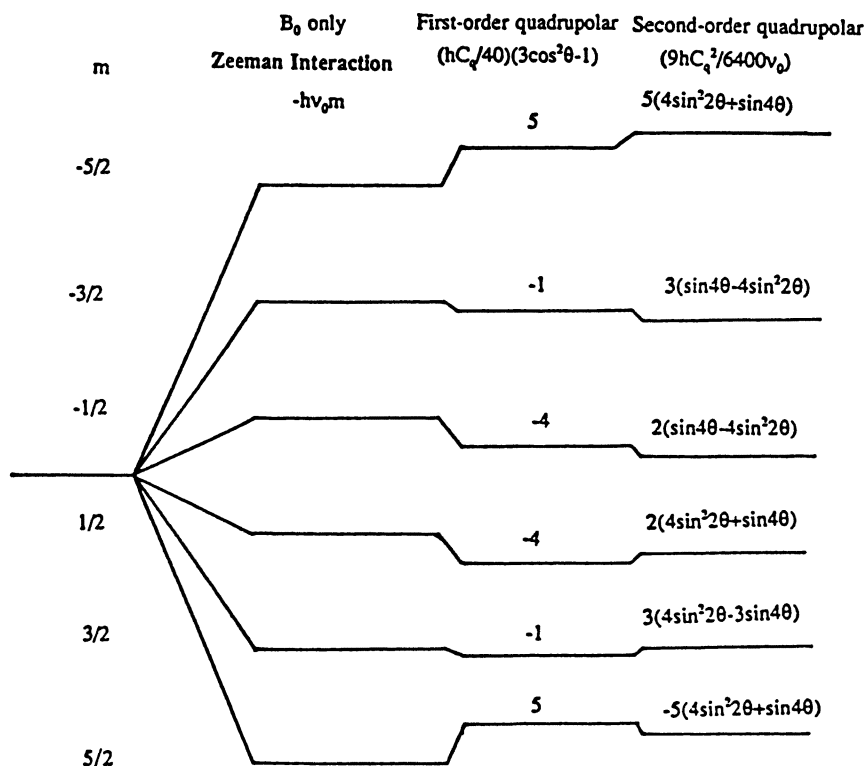


Figure 2. (A) Energy level diagram for a single crystallite of a spin- 5/2 nuclei such as ¹⁷O and ²⁷Al under only the Zeeman interaction and the first-order quadrupolar perturbation, and under the Zeeman interaction and both the first-order and second-order quadrupolar perturbations. (B) A simulated static NMR powder pattern subject to first-order perturbations showing the five allowed transitions, including the central 1/2 ↔ -1/2 transition and the four satellite transitions. The dotted line represents pure first-order quadrupolar broadening while the solid line includes additional Gaussian broadening as is typically observed in measured spectra. The symbol θ is the angle of a given crystallite with respect to the applied magnetic field B₀, C_q is the quadrupolar coupling constant, ν₀ is the Larmor frequency, and ν_Q equals the quadrupolar frequency (165).

(B)

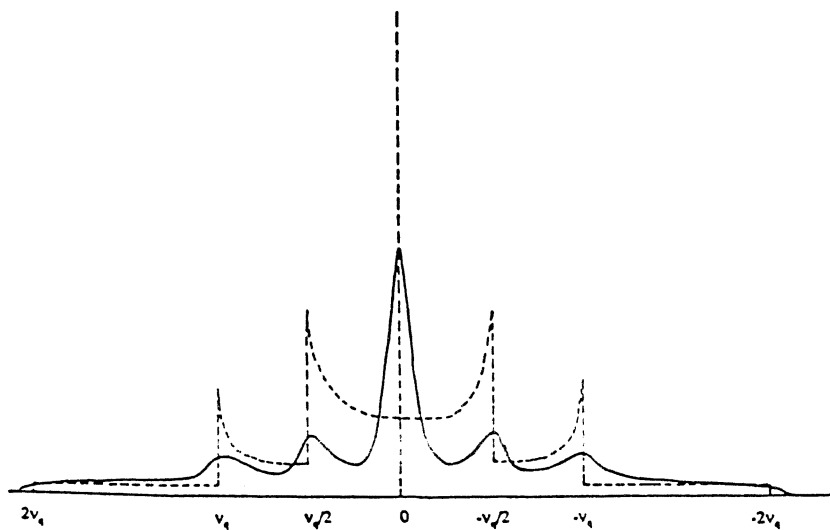
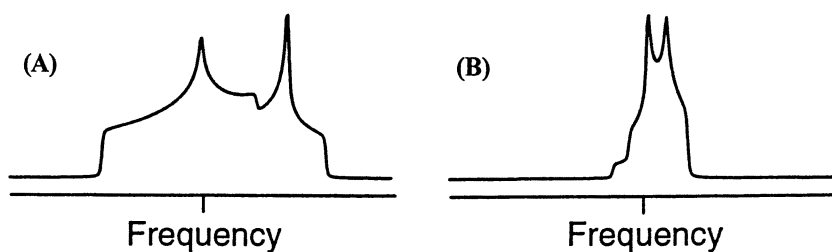
Figure 2. *Continued.*

Figure 3. Simulated spectra of (A) the static powder pattern for the central transition of a quadrupolar nucleus ($\eta^Q = 0.5$), and (B) the MAS powder pattern spectrum in the fast spinning speed limit. Note that even at fast spinning speeds, MAS alone cannot fully eliminate the second-order quadrupolar anisotropy.

Quadrupole Resonance (NQR), can be used to obtain values of C_q and η^Q but is outside of the scope of this review (17).

The quadrupolar interaction provides information about bond strengths, bond angles and site symmetry in the vicinity of the quadrupolar nucleus. However, like the other anisotropic interactions, it also further complicates the solid-state NMR spectrum, and special techniques must be used to isolate its effects.

III. FUNDAMENTAL APPROACHES TO STUDY INORGANIC SOLIDS

If a nuclear spin is subject to a variety of interactions simultaneously, its solid-state NMR spectrum will be very complicated. The powder patterns corresponding to each interaction (cf. Figures 1 through 3) will be convolved with each other leading to a broad line that is often uninterpretable. The presence of multiple sites further compounds the situation. Fortunately, solid-state NMR spectra can be considerably simplified by techniques which involve mechanical manipulation of the sample and/or specific sequences of radio-frequency irradiation. Such techniques can suppress some interactions so that others can be isolated and the relevant chemical information extracted.

Over the past fifty years, many such techniques have been developed, and no introductory chapter can do justice to all of them. What follows is a brief overview of some, but by no means all, of the techniques that have been applied to the study of inorganic materials in recent years. All of the techniques mentioned here are based on pulsed Fourier transform spectroscopy. That is, a sequence of rf-pulses (of μ s to ms length) is applied to the sample to manipulate the spins in the desired manner. The response of the spin system as a function of time is then recorded. This time-domain signal is known as a free-induction decay (FID) with the decay being caused by the relaxation of the perturbed spin-system back toward equilibrium (3-5). In NMR, relaxation of magnetization can be described by two parameters: the spin-lattice relaxation time constant, T_1 , which is a measure of the rate of recovery of magnetization back to its equilibrium state (parallel to the B_0 field), and the spin-spin relaxation time constant, T_2 , which is a measure of the decay of magnetization in the plane perpendicular to the B_0 field. For most solids, T_2 is significantly shorter than T_1 . Studies of NMR relaxation rates (2) can provide much physical insight and are a rich subject in their own right, but they are outside the scope of this review. However, relaxation time constants will often constrain the type of experiments that can be performed on a given sample, as will be shown below. Performing a Fourier transformation on the free-induction decay leads to a frequency spectrum (3-5).

The examples presented in this chapter have been chosen to give the reader a perspective of the types of scientific questions that can be addressed by solid-state NMR studies of materials; the selection is neither comprehensive nor do the cited examples necessarily reflect the full scope of applications of a given technique.

A. General Techniques in High-Resolution Solid-State NMR.

While solid-state NMR is a powerful tool for answering questions about local

structure and dynamics, it suffers from the drawbacks of poor resolution and low sensitivity. Techniques of varying complexity have been developed to solve these problems; some of the most routinely used ones include magic-angle spinning, decoupling, and cross polarization.

1. ***Magic-Angle Spinning (MAS)***. Although static spectra of powdered samples are poorly resolved, considerable line narrowing can occur if the sample is rapidly rotated (18,19). In particular, if the sample is spun about an axis that makes an angle θ of 54.74° (the magic angle) with respect to the static B_0 field and if the rate of rotation is significantly faster than the width of the powder pattern (in Hz), the anisotropic portions of the chemical-shift and dipolar interactions will disappear, leaving a narrow line at the isotropic chemical shift position. Even if the sample is not spun that rapidly, the resolution can still be improved because the powder pattern will break up into relatively narrow lines spaced at integer multiples of the rotation frequency (spinning sidebands). Figures 4A through 4D show simulations of the effects of MAS on a chemical shift "powder pattern" for a spin-1/2 nucleus. Note that CSA parameters can be determined either from "singularities" in a static powder pattern (Figure 4A) or from the relative intensities of sidebands in an MAS spectrum acquired at a moderate spinning speed (Figure 4C) (20).

Rapid sample spinning at the magic-angle also eliminates the first-order quadrupolar anisotropy. However, even at fast speeds, magic-angle spinning alone does not average out the second-order quadrupolar effects. Comparison of Figures 3A and 3B shows that MAS leads to a partial averaging of the quadrupolar anisotropy, but there is still a strong orientation-dependence. In Section III.B., various techniques for obtaining high-resolution spectra of quadrupolar nuclei will be discussed.

While the well-resolved spectra obtainable by MAS may seem reminiscent of solution-state spectra, there are important differences. Unlike the molecular tumbling that occurs in solution, magic-angle spinning is a *coherent*, rather than a random, averaging process; therefore, it can be described at all times by a well-defined Hamiltonian. This provides the NMR spectroscopist with the opportunity to use rotor-synchronized pulse sequences to selectively reintroduce certain anisotropic interactions -- a practice common in experiments designed to measure internuclear distances. Another difference is that linewidths resulting from MAS, even in the limit of fast rotation, are typically larger than the corresponding solution-state linewidths due to distributions of the isotropic chemical shifts (termed chemical-shift dispersion) in solid samples.

Magic-angle spinning has been applied to a wide variety of materials to yield information about chemical composition. For instance, the MAS NMR spectrum of ^{29}Si in the zeolite analcite shows separate peaks for silicon atoms with zero, one, two, three, and four aluminum next-nearest neighbors (Figure 5A). Since peak intensity is directly proportional to the number of atoms contributing to the signal, the relative intensities of the peaks due to different $\text{Si}(\text{OSi})_{4-x}(\text{OAl})_x$ structural units (Figure 5B) allow one to derive the Si/Al ratio of the zeolite from experimental NMR results (22,131,132,137). For many materials, MAS NMR spectra can also be acquired as a function of temperature to permit one to follow phase transitions and solid-state chemical reactions by monitoring the changes in the intensities of NMR resonances and, therefore, changes in the populations of chemical species. For example, the ^{27}Al

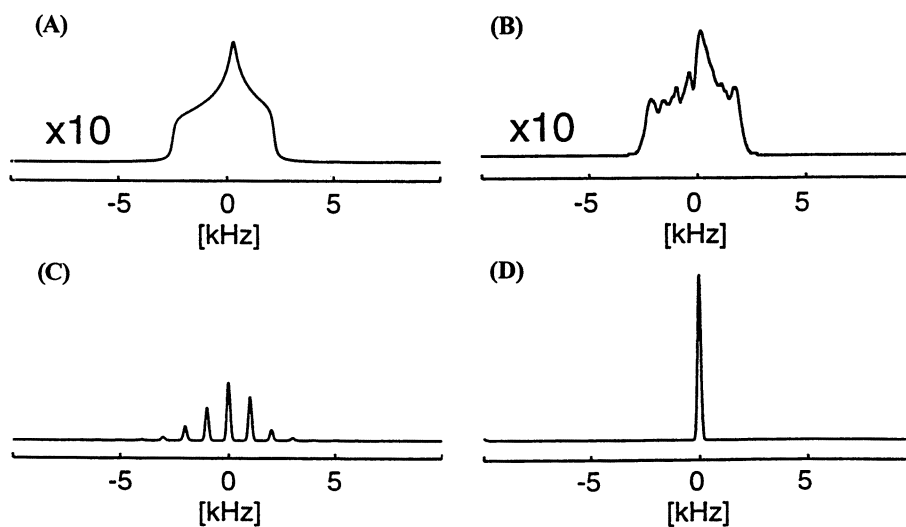


Figure 4. Effects of magic-angle spinning on the chemical-shielding anisotropy interactions for a spin-1/2 nucleus. Spectra (A) through (D) show simulations of the effect of MAS on a chemical-shielding powder pattern for spinning rates of (A) 0 Hz, (B) 100 Hz, (C) 1 kHz, and (D) 10 kHz. The vertical scale in (A) and (B) has been magnified by a factor of ten for easier viewing.

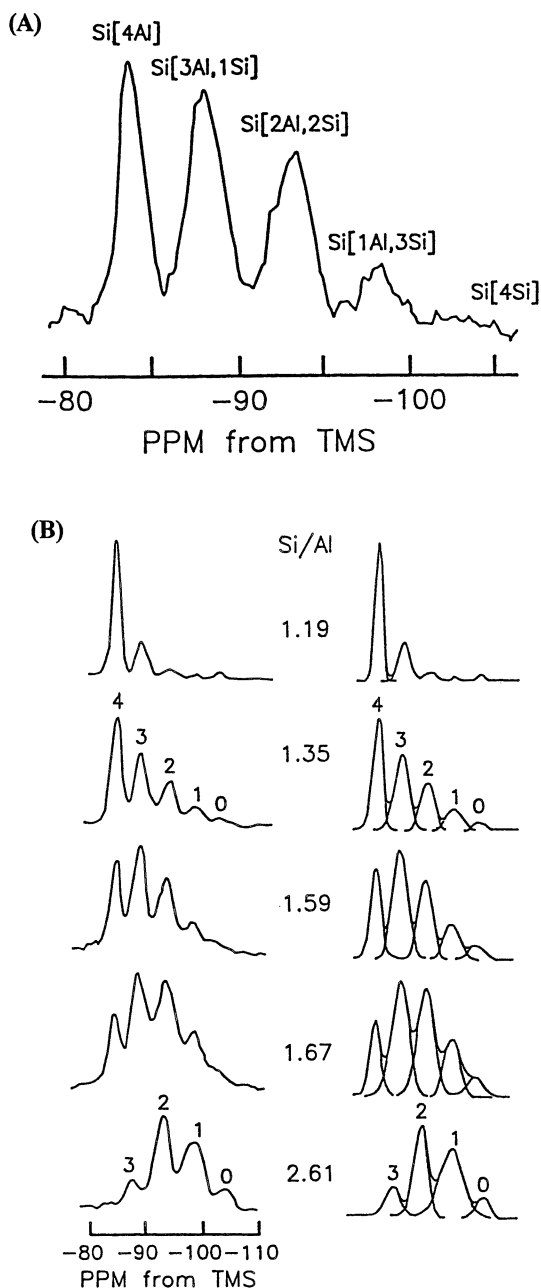


Figure 5. ^{29}Si MAS NMR spectrum of (A) analcite showing separate resonances for silicon atoms with different numbers of aluminum next-nearest neighbors (11,137,142). The relative intensities of the ^{29}Si peaks for spectra of various faujasites (B) with different Si/Al ratios allows one to determine the Si/Al ratio of the sample from NMR experimental results (22).

MAS NMR spectra given in Figure 6A for kaolinite (a 1:1 layered clay mineral depicted in Figure 6B) show primarily six-coordinate aluminums prior to thermal conversion to the intermediate metakaolinite. The ^{27}Al MAS NMR spectrum of metakaolinite at 650°C shows three overlapping resonances due to the formation of this Si/Al intermediate phase which contains 4-, 5- and 6-coordinate aluminums (23). At higher temperatures such as 950°C to 1050°C , the ^{27}Al NMR spectra show only two peaks due to 4- and 6-coordinate aluminums in a transition alumina phase formed following separation of the silica and alumina phases. In addition, ^{29}Si NMR measurements (not shown) of samples heated from 950°C to 1050°C indicate that a silica phase and a minor mullite phase are formed from the separated silica components at these intermediate temperatures (23). Similar types of studies have also been reported for numerous materials, including Si/Al catalysts and the related mineral pyrophyllite (24). The ease and versatility of solid-state MAS NMR have made this technique an important spectroscopic approach in many research laboratories and analytical facilities devoted to materials.

2. Decoupling. Although in principle sample spinning at the magic angle can eliminate the direct dipolar anisotropy, in many cases this is not practical. This is because nuclei with high gyromagnetic ratios (such as ^1H , ^{19}F , and ^{31}P) have correspondingly large dipolar coupling constants. When these coupling constants are of greater magnitude than the technically achievable MAS rotation rates, MAS fails to fully average out the dipolar anisotropy. Furthermore, even if the dipolar coupling is small enough to be averaged out, there are still many instances in which it is desirable to spin at slower rates (i.e., to determine the principal values of the CSA from sideband intensities) and yet still remove the effects of dipolar couplings from the spectra (19).

To eliminate dipolar coupling effects in such cases (as well as in static samples), rf irradiation can be used. A variety of pulse sequences have been designed to efficiently suppress dipole-dipole couplings between like nuclei (homonuclear decoupling) or unlike nuclei (heteronuclear decoupling). The simplest of the heteronuclear techniques is continuous-wave (CW) decoupling in which a long rf pulse of constant phase is applied to one of the spin species. If this pulse is of sufficiently high power, it has the effect of averaging out the heteronuclear dipolar coupling so that it does not contribute to the spectrum of the other spin species. Other more-sophisticated heteronuclear decoupling sequences also exist, but CW decoupling is sufficient for many cases.

Decoupling of like spins can be significantly more challenging, requiring precisely timed, high-power pulses and a well-tuned spectrometer. A variety of specialized homonuclear decoupling techniques have been developed for solids, yet, in general, they have found more applications in studies of organic compounds than in studies of inorganic materials. This is due to the fact that many interesting inorganic materials only contain nuclei with relatively low gyromagnetic ratios (see Tables II and III). In such cases, the dipolar couplings may be only a few hundred Hertz, and, therefore, both homonuclear and heteronuclear couplings are easily averaged out by magic-angle spinning alone. Even when protons are present in a sample, if they are found only on highly mobile species (82) (such as water molecules

diffusing through microporous media), motional averaging can reduce the effective dipolar coupling strength.

For ^1H or ^{19}F spectra of relatively rigid solids, however, multipulse homonuclear decoupling becomes important (25-31). In general, ^1H (or ^{19}F) NMR experiments on solid samples are encumbered by severe line broadening effects due to strong ^1H - ^1H (or ^{19}F - ^{19}F) magnetic dipolar interactions. If these effects are not too large, because of large ^1H - ^1H (or ^{19}F - ^{19}F) internuclear distances and/or fast motional averaging, then sharp ^1H or ^{19}F NMR resonances can be observed by MAS alone. For ^1H NMR on systems in which the ^1H - ^1H dipolar broadening is significant, e.g., > 20 kHz, either extremely fast MAS or multiple-pulse line-narrowing is necessary. Signals from different proton sites in a silica gel, for example, cannot easily be resolved at moderate (less than 10 kHz) spinning speeds. However, a series of ^1H CRAMPS (Combined Rotation And Multiple Pulse Spectroscopy) spectra of silica gels of different degrees of hydration (Figure 7), permits resolution of the peaks assigned to protons of "physisorbed water" and the various types of silanols (26-28). In the CRAMPS experiment, the proton signal is acquired during the multiple-pulse sequence (e.g., BR-24 (29)). A sufficiently long delay between successive applications of the multipulse sequence is required to allow the system to return to thermal equilibrium. The two-dimensional version of the CRAMPS experiment (see Section III.C.3) has also been used to obtain well-resolved spectra as in the case of ^1H - ^{31}P HETCOR (32) experiments for calcium phosphate systems.

Decoupling techniques not only improve spectral resolution but also can provide structural information. A comparison of linewidths in decoupled and non-decoupled spectra can reveal which sites are close to the type of nucleus that is being decoupled. For instance, some of the resonances in the ^{77}Se MAS NMR spectra of the ionic conductor $\text{Ag}_7\text{Se}_6\text{P}$ narrow dramatically when ^{31}P decoupling is applied. This permits the assignment of these resonances to the selenium sites that are near phosphorus atoms (33).

3. Cross Polarization(CP). While magic-angle spinning and decoupling lead to line-narrowing and thus increase sensitivity as well as resolution, cross polarization can be used to further enhance the sensitivity of a nucleus with a low gyromagnetic ratio (34-43).

The cross-polarization process begins with the generation of transverse magnetization from the more sensitive spin species. This magnetization can then be "spin-locked" along an rf-field, B_1 , that precesses in phase with it in the transverse plane. Because the B_1 field is much smaller than the B_0 field under which the original magnetization was established, the spin-locked magnetization is in a non-equilibrium state. If an rf-field of the appropriate amplitude (determined by the "Hartmann-Hahn match condition" (34,35,38)) is simultaneously applied to the other spin species, energy-conserving magnetization transfer can occur between the two types of spins, leading to enhancement of the signal of the less-sensitive spins. The duration that the matched pulses are applied is known as the contact time. Additional enhancement can occur if the more-sensitive spin species has a shorter relaxation time than the less-sensitive species since this permits more scans to be accumulated in a given time.

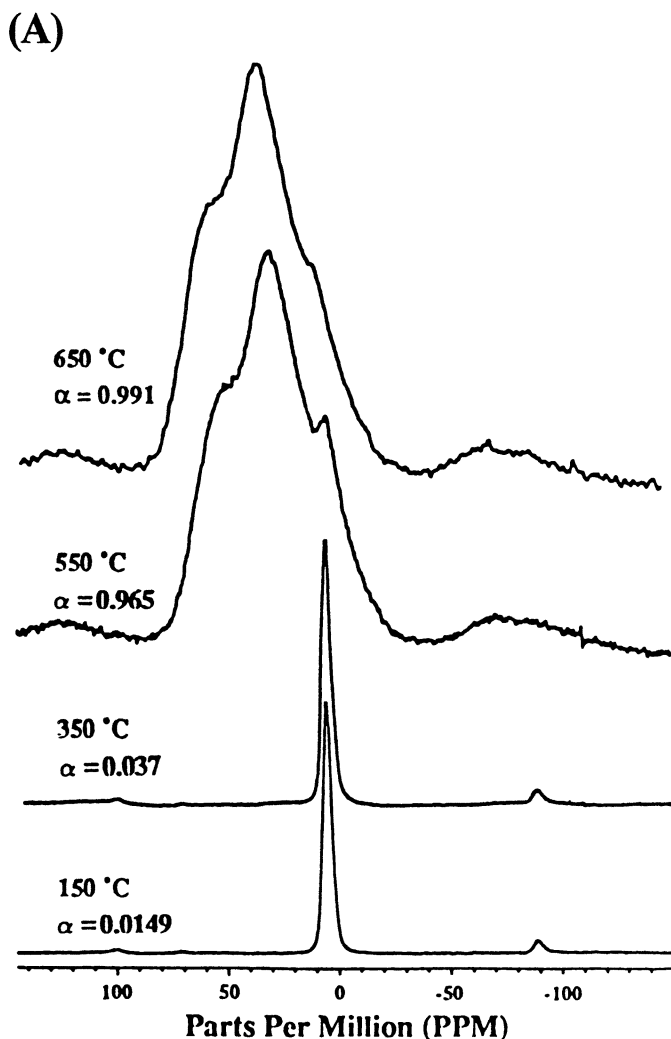
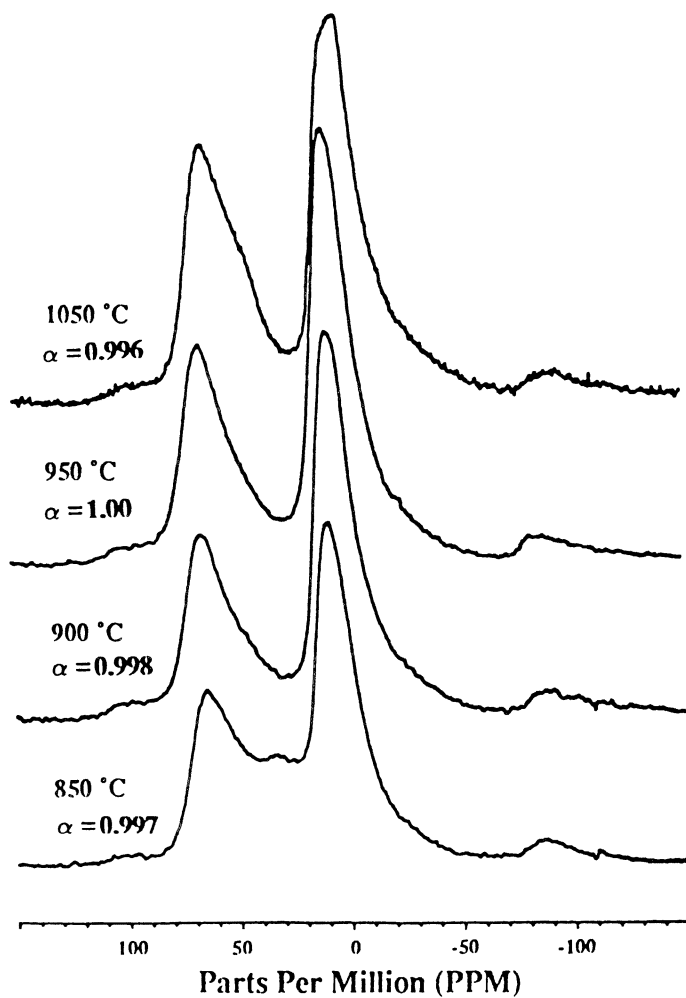


Figure 6. Solid-state MAS ^{27}Al NMR spectra (A) obtained at 14 Tesla showing the dehydroxylation and solid-state thermal conversion following thermal treatment for the 1:1 Si/Al layered clay mineral kaolinite, $\text{Si}_4\text{Al}_8\text{O}_8(\text{OH})_{12}$, where α = the degree of dehydration. At 650°C, metakaolinite, an important metastable phase, consisting of a mixture of 4-, 5- and 6-coordinate aluminums is formed, while at 1050°C a transition alumina-like phase containing both 4- and 6-coordinate aluminum forms, together with an amorphous silica phase and minor mullite component based on MAS ^{29}Si NMR (not shown) is formed. A schematic diagram of the structure of kaolinite (B) is also depicted (23).

Figure 6A. *Continued.*

Continued on next page.

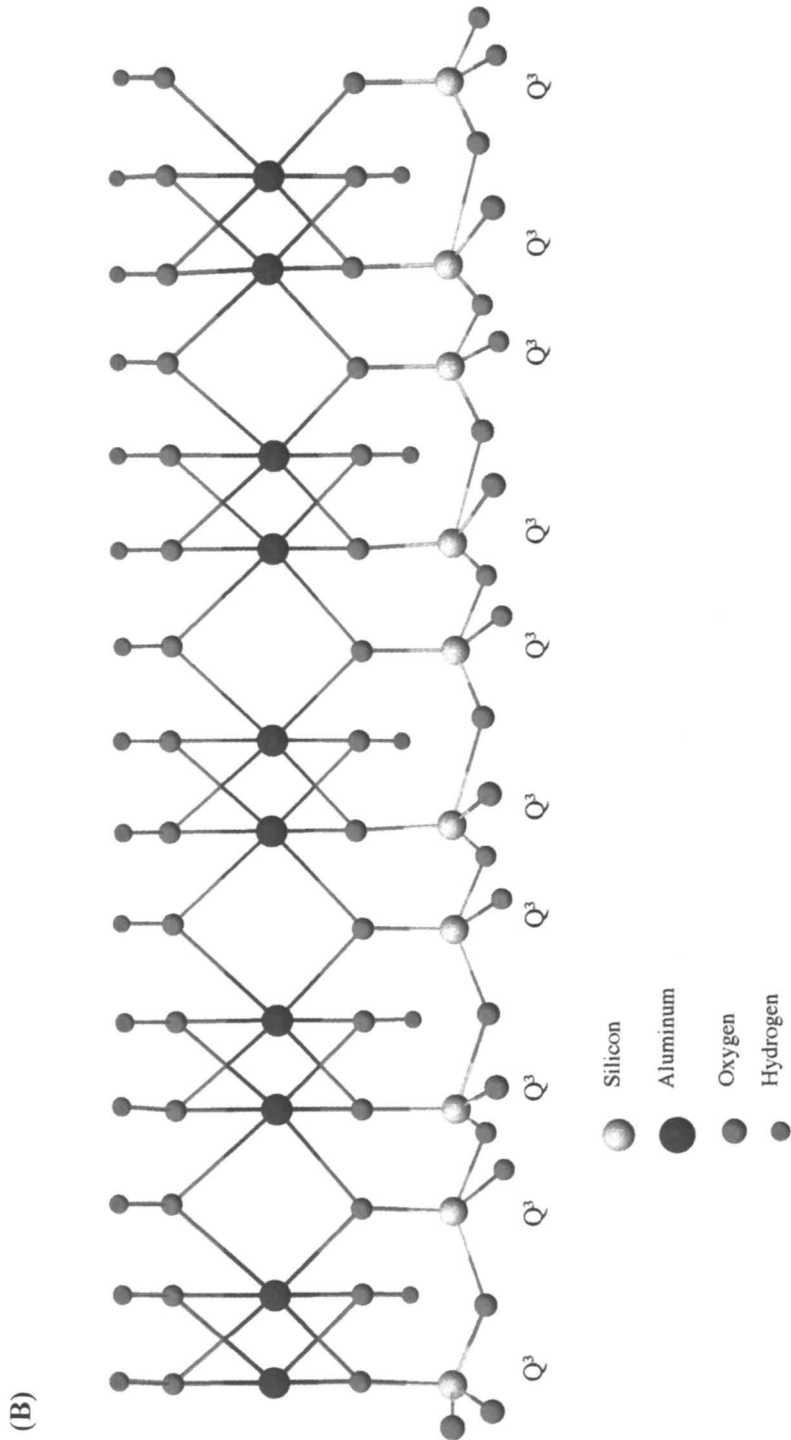


Figure 6B. See caption on page 20.

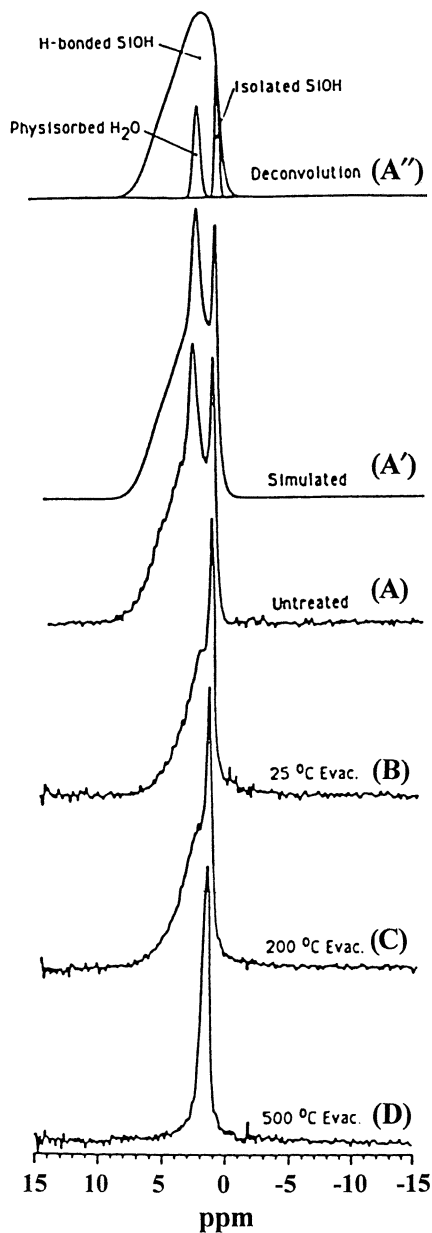


Figure 7. ^1H CRAMPS spectra of Fisher S-679 silica gel at 187 MHz. The simulated spectral components (A'') and the simulation spectrum (A') of "as received" material shows the spectral assignments of the three proton resonances associated with isolated silanols, hydrogen-bonded silanols and "physisorbed water". Spectra (A) thru (D) show ^1H CRAMPS spectra acquired after various treatments. After 24 hours of evaluation at 500°C, only the isolated silanols remain (26,28).

The energy transfer process in cross polarization is generally mediated through the direct dipolar interaction, and therefore, the initial rate with which magnetization is transferred can often be related to distances between spins. For instance, a comparison of ^1H to ^{13}C cross polarization intensity buildup rates has been used to describe the location of dimethylsulphoxide in the layered aluminosilicate clay mineral, kaolinite (46). The general distance-dependence of cross polarization rates can also be used as a tool for spectral editing, leading to selective enhancement of certain resonances (38,39,41,42).

Cross-polarization has been widely applied to many inorganic materials and is frequently combined with MAS to yield well-resolved spectra with a good signal-to-noise ratio. It is particularly useful for enhancing the spectra of nuclei with a low natural abundance, which otherwise would be difficult to observe. For example, the ^1H - ^{29}Si CP/MAS NMR spectrum of silica gel given in Figure 8A shows three different ^{29}Si peaks, including peaks due to two different surface silanol groups (Si-OH): single silanols (Q^3) and geminal silanols (Q^2). The dynamics of cross-polarization, which depend on the strength of the ^1H - ^{29}Si and ^1H - ^1H dipolar couplings associated with these two silanols, have been extensively measured. The rate of cross-polarization, $1/T_{\text{HSi}}$, can be considered to be proportional to $1/r_{\text{HSi}}^6$ and is strongly influenced by hydrogen bonding interactions with "physisorbed water" and by the location of the silanols (internal versus external) (41-43,47-51). Figure 8B shows ^1H - ^{29}Si CP/MAS peak intensities as a function of cross-polarization contact time for the three different silicon sites in a silica gel (including the non-protonated Q^4 siloxane moieties). Relaxation parameters relating to the polarization transfer process can be extracted from such results and the proximity of different ^{29}Si nuclei to nearby protons can be qualitatively determined.

Although CP/MAS has most commonly been used with spin-1/2 nuclei, it has recently, with slight modifications, been applied to quadrupolar nuclei as well. For example, CP/MAS experiments reported between spin-1/2 and quadrupolar nuclei, e.g., ^1H - ^{27}Al (54,55), ^1H - ^{23}Na (45,56,57), ^{29}Si - ^{27}Al (53,58), ^{19}F - ^{27}Al (64), ^{31}P - ^{27}Al (59-61) and ^{31}P - ^{23}Na (84), as well as between two quadrupolar nuclei, e.g., ^{11}B - ^{27}Al (63), suggest the potential of CP/MAS NMR to study a variety of complex inorganic systems (44-46,52-64). A CP/MAS contact time study of ^{23}Na ($I = 3/2$) in borax ($\text{Na}_2\text{B}_4\text{O}_7 \cdot 10\text{H}_2\text{O}$) is shown in Figure 9. The ^{23}Na NMR signals due to different sodium atoms show signal intensity variations as a function of both dipolar decoupling (DD) and contact time (CT) that can be related to the relative distances of these different sodium atoms from nearby protons (56). Recent studies of ^{27}Al - ^{29}Si CP/MAS NMR of zeolite NaA (58) and the mineral low albite (53) suggest the types of heteronuclear proximity questions that might be able to be addressed in more complex aluminosilicate materials.

Cross polarization is not the only technique for transferring magnetization. If the transverse relaxation times (T_2) are sufficiently long, polarization can also be transferred through scalar couplings by using the INEPT (Insensitive Nuclei Enhanced by Polarization Transfer) sequence (65) adapted from solution-state NMR. This technique is less technically demanding than cross polarization since it does not require precise amplitude matching, but it has not yet been widely applied since it

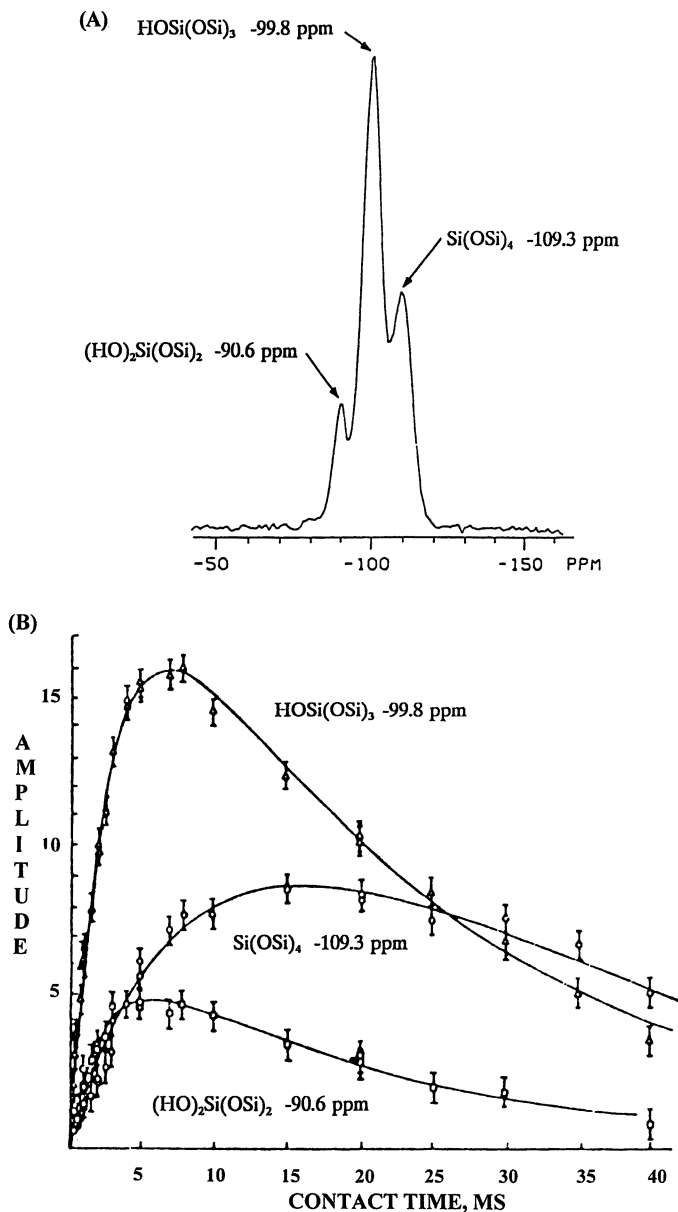


Figure 8. CP/MAS ^{29}Si NMR spectrum (A) of a silica gel (hydrated silica) showing three different types of surface and internal silicon sites, including ^2Q -type geminal silanols, ^3Q -type single silanols and ^4Q -type siloxane sites; and (B) plot of ^{29}Si signal intensity versus contact time (msec) for the three different silicon sites (41). The solid-lines represent fits of the cross-polarization dynamics (7), parameterized by ^1H and ^{29}Si rotating-frame relaxation times ($T_{1\rho}$) and the rate of cross-polarization (T_{HSi}). From these fits, $T_{1\rho}$ equalled 20.3, 22.1 and 21 msec., and T_{HSi} equalled 2.3, 2.9 and 12.7 msec., for the ^{29}Si peaks at -90.6, -99.8 and -109.3, respectively.

requires approximate knowledge of the J-couplings, which are often difficult to measure in solids. Since the scalar coupling interaction is a through-bond interaction, sequences incorporating INEPT-type transfer will yield information about connectivities rather than distances.

B. Special Techniques for High-Resolution of Quadrupolar Nuclei.

As Figure 3B shows, magic-angle spinning alone does not fully eliminate the quadrupolar anisotropy which can make resolution of multiple sites in the spectrum of a quadrupolar nucleus difficult. Fortunately, several techniques have been developed to produce high-resolution spectra of odd half-integer quadrupolar nuclei (66-76).

The $(+m \leftrightarrow -m)$ transitions of a quadrupolar nucleus can be shown to be unaffected to first order by the quadrupolar Hamiltonian (see Figure 2A). When second-order perturbation theory is applied, however, the frequencies of these transitions are affected in an orientation-dependent manner. For a sample spun at an angle θ with respect to the static field, the $(+m \leftrightarrow -m)$ transition frequency of an individual crystallite is given (66) by

$$\omega_{+m \leftrightarrow -m}^{(2Q)} = \frac{C_q^2}{\omega_0} [A_0 C_0(I, m) + A_2(\alpha, \beta) C_2(I, m) P_2(\cos\theta) + A_4(\alpha, \beta) C_4(I, m) P_4(\cos\theta)] \quad (1)$$

where $\omega_0 = \gamma B_0$ is the Larmor frequency; the angles α and β define the orientation of the crystallite with respect to the axis of rotation; P_2 and P_4 are Legendre polynomials; and the $\{C_n\}$ are coefficients that depend on which transition is excited. To obtain narrow resonances from quadrupolar nuclei in powder samples, the second and third terms on the right hand side of Equation (1) must be made to vanish for all values of α and β , leaving only the isotropic second-order quadrupolar shift. This can be accomplished by Double Rotation, Dynamic-Angle Spinning, or Multiple-Quantum Magic-Angle Spinning as will be discussed in Sections 1-3 below.

An alternative way to study quadrupolar nuclei at high field is to observe the MAS spectra of the $(m \leftrightarrow m - 1; m \neq 1/2)$ satellite transitions rather than the central transition. The orientation-dependence of the satellite transitions has a different functional form than that of the central transition, and this can be advantageous in certain cases. This forms the basis of Satellite Transition Spectroscopy which will be discussed in Section III.B.4.

1. Double Rotation (DOR). The technique of DOuble Rotation (DOR) eliminates the second-order quadrupolar anisotropy of the central transition by spinning the sample about two axes simultaneously (71,72). The $(+m \leftrightarrow -m)$ transition in such a case is

$$\omega_{\pm m \leftrightarrow -m}^{(2Q)}(\theta_1, \theta_2) = \frac{C_q^2}{\omega_0} [A_0 C_0(I, m) + A_2(\alpha, \beta) C_2(I, m) P_2(\cos\theta_1) P_2(\cos\theta_2) + A_4(\alpha, \beta) C_4(I, m) P_4(\cos\theta_1) P_4(\cos\theta_2)] \quad (2)$$

where θ_1 is the angle of the axis of the outer rotor with respect to the static magnetic field B_0 and θ_2 is the angle between the axes of the inner and outer rotors (Figure 10A). For sufficiently rapid spinning rates, the choice $\theta_1 = 54.74^\circ$ (the magic angle) and $\theta_2 = 30.56^\circ$ will lead to the elimination of the quadrupolar anisotropy for all crystallite orientations since both $P_2(\cos(54.74^\circ))$ and $P_4(\cos(30.56^\circ))$ equal zero. In addition, since θ_1 is the magic angle, both dipolar couplings and chemical-shielding anisotropies will also be averaged. As in the case of MAS, slower spinning speeds lead to partial averaging of the anisotropies and produce spinning sideband patterns (see Section III.A.1).

DOR is a technically demanding technique which requires special equipment. Because high spinning speeds are not achievable with the double rotor configuration, DOR spectra tend to have a large number of spinning sidebands that can complicate spectral interpretation. However, since the technique at least partially averages out dipolar couplings, it works well for highly abundant quadrupolar nuclei. It also works well for samples with short T_1 times (in contrast to DAS) because the averaging process is continuous. The high-resolution obtained by DOR, for instance, permitted a study of the different aluminum sites present in both the dehydrated and hydrated forms of the aluminophosphate molecular sieve VPI-5 (73). While the ^{27}Al MAS NMR (Figure 11A) shows only a single, broad, slightly asymmetric line due to the two tetrahedral sites, Al-1 and Al-2 in dehydrated VPI-5, the ^{27}Al DOR NMR spectrum (Figure 11B) shows two peaks (d and e) assigned to these two different tetrahedral structural aluminums. VPI-5 at various stages of rehydration was also shown by ^{27}Al DOR NMR spectra (Figures 11C or 11D) to exhibit eight different partially overlapping ^{27}Al sites due to a range of various 4-, 5- and 6-coordinate aluminums. The 5-coordinate (peak f) and 6-coordinate Al sites (peak c) likely contain coordinated waters (s) following rehydration of the two original tetrahedral Al sites (see Figure 11C or 11D). In addition, original peaks d and e are partially converted to peaks a, b, g and h during rehydration.

2. *Dynamic-Angle Spinning (DAS).* Dynamic Angle Spinning (DAS) also involves spatial manipulation of the sample to eliminate the quadrupolar anisotropy of the central transition (74,75). In the DAS technique, the sample is spun about one axis for part of the evolution period and then the sample is quickly reoriented and spun about a second axis relative to the static magnetic field (Figure 10B). The angles of the two axes and the amount of time spent at each angle are chosen such that the anisotropic evolution at the first angle (see last two terms in Equation (1)) is canceled out by the evolution at the second angle, leaving only the isotropic signal at the end (plus sidebands, if the spinning rate is not sufficiently rapid). Although many sets of angles could be used for this experiment, the most commonly used pairs are 37.38° and 79.19° (as depicted in Figure 10B), with equal time spent at each angle, and the pair 0.00° and 63.43° , with the time spent at the second angle being five times as long as that at the first angle (74,75).

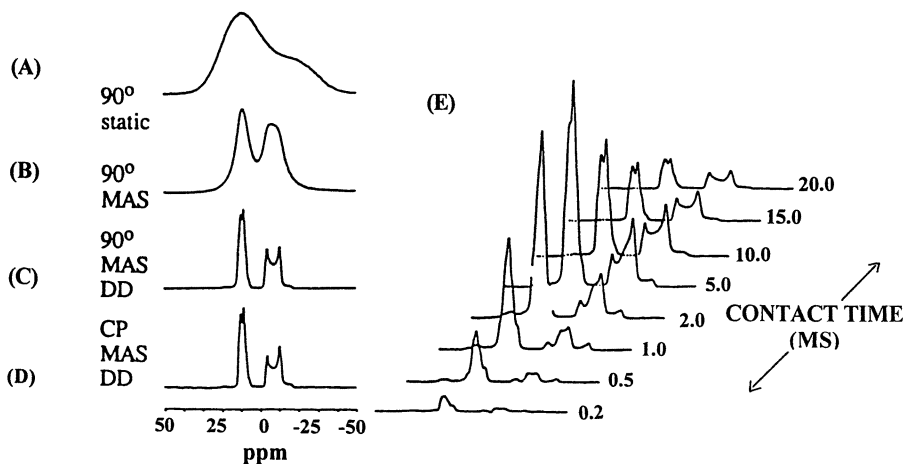
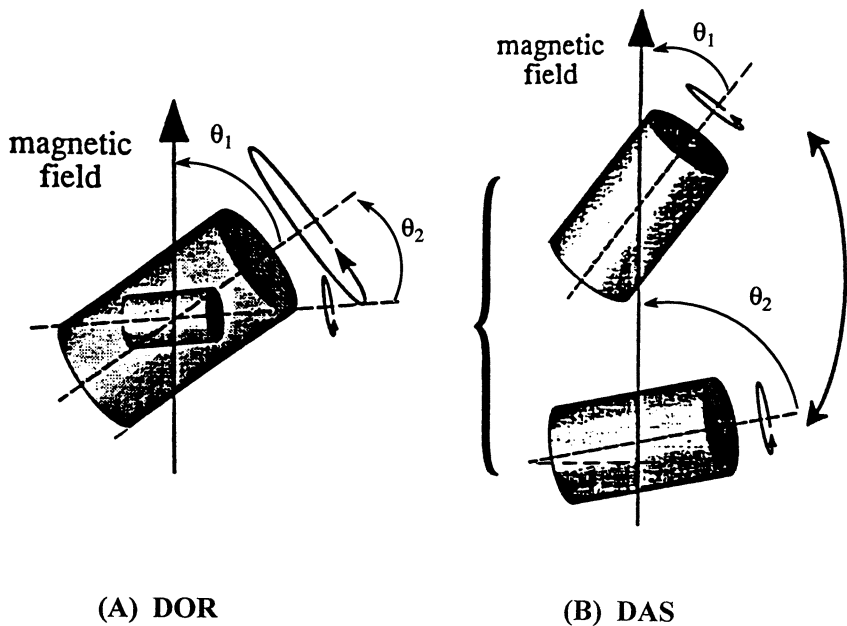


Figure 9. ^1H - ^{23}Na CP/MAS NMR spectra of borax $\text{Na}_2\text{B}_4\text{O}_7 \cdot 10\text{H}_2\text{O}$ showing: (A) static, (B) MAS, (C) MAS with decoupling, (D) CP/MAS with decoupling and (E) CP/MAS variable contact time study (56).



(A) DOR

(B) DAS

Figure 10. Schematic diagram depicting (A) DOR ($\theta_1 = 54.74^\circ$ and $\theta_2 = 30.56^\circ$) and (B) DAS ($\theta_1 = 37.38^\circ$ and $\theta_2 = 79.19^\circ$) spinner systems, showing the relationship of the spinning axis to B_0 (71,72, modified from 136,137).

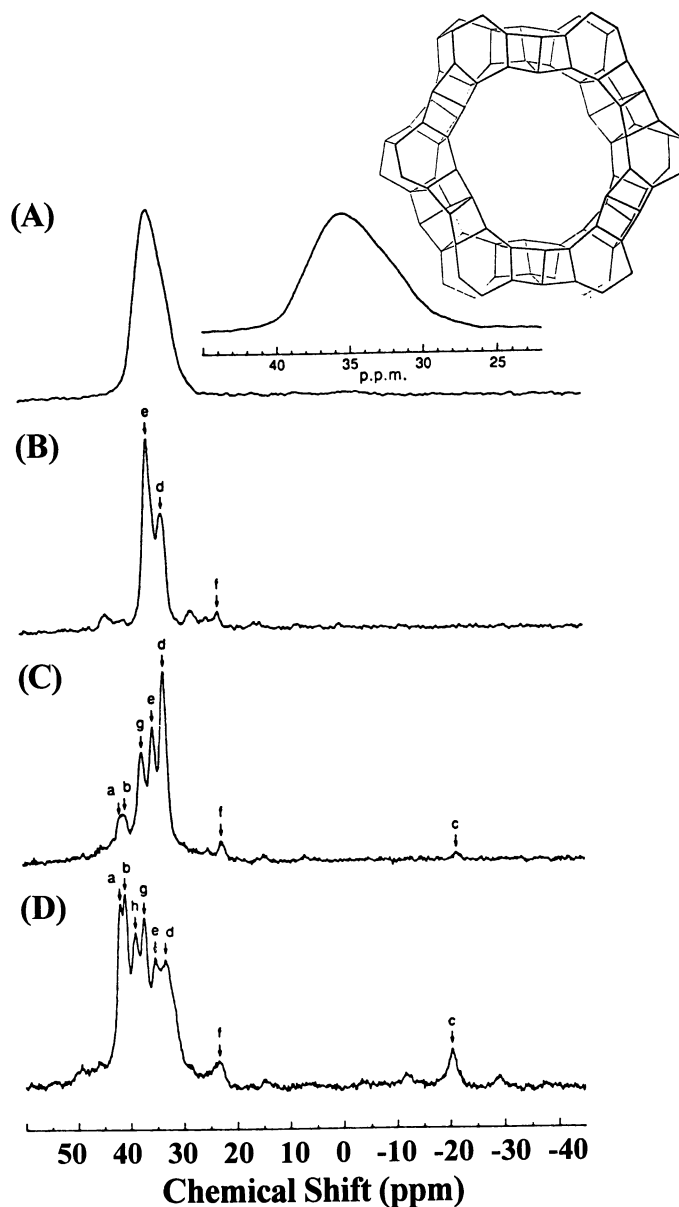


Figure 11. ^{27}Al NMR of the microporous aluminophosphate VPI-5. (A) MAS spectrum of dehydrated VPI-5 (note expansion of spectrum in inset). (B) DOR of dehydrated VPI-5. (C and D) DOR of partially rehydrated VPI-5. The various ^{27}Al NMR peaks discussed in text are identified by lower case, i.e., a, b, g. The framework structure of VPI-5 is given in the inset. (73).

The DAS experiment does not fully average out homonuclear dipolar couplings which restricts its utility to dilute spin systems (77). DAS also can only be performed on samples with T_1 relaxation times that exceed the time it takes to reorient the sample (typically 30-50 ms). However, many quadrupolar nuclei (such as ^{17}O and ^{87}Rb) do have sufficiently long T_1 's to permit DAS experiments to be performed. Furthermore, unlike DOR, DAS is an inherently two-dimensional technique (see Section III.D.7), and the narrow isotropic lines can be correlated with the C_q and η^Q parameters to provide site-specific structural information. ^{17}O DAS NMR (113) has been successfully applied to study the five different oxygen sites in the mineral coesite (Figure 16), as well as selected glasses and zeolites. In addition, this approach has recently been applied to identify two of the three different oxygens in the ion conductor $\text{Ba}_2\text{In}_2\text{O}_5$ (382) of the perovskite lattice structure (Figure 45D).

3. Multiple-Quantum Magic-Angle Spinning (MQMAS). While DOR and DAS use spatial manipulation of the sample to achieve high-resolution spectra of quadrupolar nuclei, the Multiple-Quantum Magic-Angle Spinning (MQMAS) technique (66,67,70,76) achieves high resolution by manipulation of the spins through the $C_n(I,m)$ terms in Equation (1) while spinning only at the magic angle. Like DAS, MQMAS does its averaging sequentially. First, a rf-pulse (or series of pulses) is used to excite a ($+m \leftrightarrow -m$) multiple-quantum coherence, such as the triple-quantum (3Q) coherence that connects the $m = +3/2$ and $m = -3/2$ states. (A coherence may loosely be thought of as a correlation between two states; a more precise quantum mechanical definition can be found elsewhere (5).) This multiple-quantum coherence cannot be directly detected, but it is allowed to evolve for a period of time and is subsequently converted into an observable single-quantum coherence between the $m = +1/2$ and $m = -1/2$ states. As in the DAS experiment, a careful choice of the evolution periods permits the anisotropic signal from one time period (here, the multiple-quantum evolution period) to cancel that from the other period (the single-quantum evolution period), producing narrow lines. These lines will be somewhat shifted in frequency from the DAS and DOR positions because the $C_n(I,m)$ term in Equation (1) is also affected; depending on the values of I and m , this can lead to better or worse resolution relative to the other techniques. Since MQMAS is performed at the magic angle, the dipolar couplings can be averaged out by sufficiently fast spinning, and there is no restriction on the T_1 relaxation times. In addition, the experiment can be performed on conventional MAS equipment. However, the efficiency of the multiple quantum excitation and conversion is strongly dependent on C_q , which makes obtaining signals with quantitative intensities difficult. MQMAS is, like DAS, a two-dimensional technique (see Section III.D.7) which allows the quadrupolar parameters for individual sites to be determined. For example, the use of both 3Q- and 5Q-MQMAS ^{27}Al ($I = 5/2$) NMR has been applied to the examination of various AIPO zeolitic-like molecular sieve catalysts such as VPI-5 and AIPO-11 (204,205) (see Figure 24). Additionally, a comparison between the MAS and MQMAS ^{23}Na ($I = 3/2$) NMR for complex aluminum phosphate oxynitride materials (303) as shown in Figure 38 also provides an exemplary demonstration of some of the benefits of simultaneously using MAS and MQMAS.

4. Satellite Transition Spectroscopy (SATRAS). Another approach for

obtaining high-resolution spectra of quadrupolar nuclei is the SATellite TRAnsition Spectroscopy (SATRAS) technique (78). SATRAS does not eliminate the quadrupolar anisotropy but, instead, takes advantage of the fact that in certain cases the quadrupolar broadening of the satellite transitions is not as great as for the central transition. This technique has permitted resonances which overlap in an MAS NMR spectrum, such as 4-, 5-, and 6- coordinate ^{27}Al resonances in aluminoborate glasses (79) and in a χ -transition alumina (see Figure 26), to be resolved by SATRAS (189).

SATRAS is a somewhat technically demanding technique. Although the sample only needs to be spun at a single angle, fast (10-15 kHz) and stable spinning, precise setting of the magic angle, exact tuning, and high-power rf pulses are required. The measured spinning sideband patterns for the satellite transitions can then be compared with simulations to extract the quadrupolar parameters such as discussed for the ^{27}Al SATRAS results obtained for a χ -transition alumina (Figure 26). SATRAS has likewise been applied to other important glass and ceramic systems, particularly using ^{11}B and ^{27}Al NMR (79,80).

5. Sensitivity Enhancement for the Central Transition of Quadrupolar Nuclei. Techniques which are based on detecting only the central transition of a quadrupolar nucleus (such as DOR, DAS, and MQMAS) suffer from an inherent loss in sensitivity since only a fraction of the quadrupolar nuclei in the sample are observed. While SATRAS often detects magnetization from a larger fraction of the nuclei in the sample, the signal is spread out over a wide range of frequencies, and, therefore, the sensitivity of this technique is also sub-optimal. However, it is possible to enhance the signal of the central transition of a quadrupolar nucleus by using adiabatic frequency sweeps to transfer the populations of the outermost energy levels to the central transition (81). This results in a potential sensitivity enhancement of up to $2I$ (where I is the spin quantum number of the quadrupolar nucleus). Such enhancement experiments require special equipment and so far have only been performed on static samples; in theory, however, they could be combined with DAS or other high-resolution techniques to obtain spectra of quadrupolar nuclei that are both sensitive and well resolved.

C. Multidimensional NMR Techniques.

One-dimensional, high-resolution spectra of spin-1/2 and quadrupolar nuclei are routinely used to characterize inorganic materials, but even more can be learned if the information is spread into two or more dimensions. Pulse sequences used for two-dimensional NMR experiments can typically be described by four stages: (1) a preparation period in which pulses are applied to place the spin system in the desired initial state, (2) an evolution or frequency-labeling period (t_1) which will correspond to one of the dimensions in the 2D experiment, (3) a mixing period during which the spins may be subjected to further interactions, and (4) a detection period (t_2) during which the signal is acquired (5). To obtain a two-dimensional data set, an array of one-dimensional spectra is collected with the evolution period (t_1 time) incremented from experiment to experiment. These data can then be Fourier transformed along each time dimension to obtain a two-dimensional spectrum which is a function of the

frequencies ω_1 and ω_2 that characterize each time period. Two-dimensional spectra can give information about the proximities of different sites (e.g. - HETCOR, COSY, INADEQUATE, double-quantum MAS spectroscopy, SEDOR, REDOR, TEDOR, TRAPDOR, REAPDOR), the local environments of specific sites (e.g. - VACSYS, MAT, DAS, MQMAS), or the dynamics of the system (e.g. - 2D exchange). In the following sections, a few of the two-dimensional NMR experiments that have been used to study inorganic materials will be discussed.

1. Heteronuclear Correlation. The most basic type of heteronuclear correlation (or HETCOR) experiment in solids is simply a two-dimensional extension of cross polarization in which the pulse that generates the initial transverse magnetization is separated from the Hartmann-Hahn matching pulses by a time period t_1 (82). The resulting two-dimensional spectrum will then correlate specific sites in the MAS spectrum of the first nucleus with the sites of the second nucleus that are near enough for polarization transfer to occur between them. The peak intensities are typically not quantitative, but HETCOR experiments can provide qualitative information about spatial proximity. More complicated pulse sequences exist for cases in which homonuclear decoupling is necessary (89) or for cases in which a high-resolution quadrupolar dimension is desired (83,84). In addition, there are variants of the experiment which utilize TEDOR-type transfer (see Section III.C.3 below) through dipolar coherences (58,60) in place of the Hartmann-Hahn cross polarization step (59,62,136,137). HETCOR experiments have been used to characterize surface-adsorbate interactions and to assign peaks in complicated spectra. One of the earliest uses of HETCOR for inorganic materials was the use of ^1H - ^{29}Si HETCOR to study the surface silanols in zeolites and silicas (82). A recent report of ^1H - ^{31}P HETCOR studies of the calcium phosphate precursors of bone and native bone materials (Figure 12) also demonstrates the utility of this technique (32). In this latter work, the narrow ^{31}P chemical shift range observed for these systems would severely limit solid-state NMR investigations of the structurally related phosphate species found in these different calcium phosphate-containing materials without the additional advantage of the ^1H NMR dimension afforded by this two-dimensional approach.

2. Homonuclear Correlation. Homonuclear correlation experiments can also be applied to inorganic materials. The solution-state techniques (5) of CORrelation Spectroscopy (COSY) and Incredible Natural Abundance Double QUAntum Transfer Experiment (INADEQUATE) can be performed on solids under MAS conditions to reveal which NMR signals correspond to sites that are connected through one or more covalent bonds. In these experiments, non-selective rf-pulses are used to create magnetization during the t_1 time period. A pulse (or pulses) during the mixing period transfers magnetization between spins which are scalar-coupled, and the signal is recorded. A pattern of cross peaks will appear which indicates which sites are connected. The INADEQUATE experiment is particularly simple to interpret since it does not contain any signal from nuclei that are not coupled to other nuclei. Such experiments facilitate spectral assignment in complex samples. For instance, resonances corresponding to twenty-one of the twenty-four crystallographically distinct ^{29}Si sites in a completely siliceous form of the zeolite ZSM-5 have been resolved by ^{29}Si MAS NMR, and the pattern of cross-peaks in the INADEQUATE spectrum

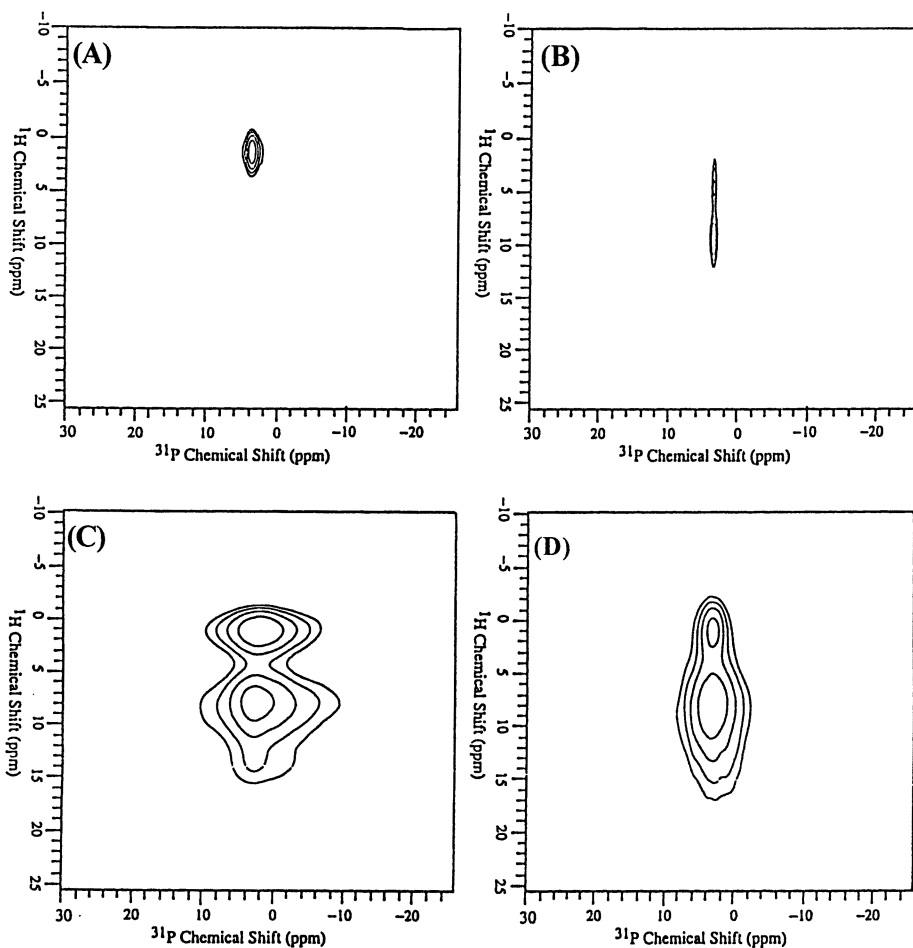


Figure 12. ^1H - ^{31}P HETCOR experimental results for (A) hydroxyapatite, and the calcium phosphate bone precursors: (B) octacalcium phosphate and (C) brushite, and (D) a bone material (32).

combined with X-ray diffraction data allowed them to be unambiguously assigned (85). Similarly, detailed COSY results for ZSM-12 shown in Figure 13 also demonstrate the application of such connectivity experiments for these types of materials (136,137,138).

Other types of homonuclear correlation experiments rely on dipolar rather than scalar couplings. In one such experiment, rotor-synchronized multiple pulse sequences are used to excite double-quantum coherences between spatially proximate spins. As in the INADEQUATE experiment, the resulting pattern of crosspeaks is easy to interpret. This experiment has been used to provide information concerning phase separation (86) and Q-species connectivities (87) in phosphate glasses.

3. Spin Diffusion. Another way to obtain qualitative structural information about a material is by monitoring the spin diffusion (88,89). The phenomenon of "spin diffusion" is actually a coherent process rather than a diffusive one. It is a spatial spreading out of magnetization through mutual spin-flips between pairs of nuclei. Since the rate of spin diffusion is distance-dependent, nuclei which are physically near each other are the first to exchange magnetization; thus, experiments which probe the spin diffusion process can provide information about domain sizes in disordered samples.

A variety of pulse sequences have been developed to measure spin diffusion. A simple, two-dimensional experiment consists of three pulses and works well for nuclei with low gyromagnetic ratios. In this experiment, the first 90° pulse creates magnetization which evolves for a time period t_1 . This magnetization is flipped along the z-axis for a mixing period, τ_m , during which time spin diffusion occurs. Another 90° pulse is then applied and the signal recorded. If spin diffusion occurs, a two-dimensional pattern of peaks will result with off-diagonal peaks indicating which sites have exchanged magnetization during a given mixing time. More complicated CRAMPS sequences incorporating multipulse homonuclear decoupling during the evolution and detection periods are typically used for ^1H or ^{19}F spectra (26,32,89). Series of one-dimensional experiments involving selective inversion or saturation of part of the spectrum and subsequent monitoring of changes in peak intensities as a function of mixing time can also be performed and allow one to determine the rate of spin diffusion from a given site. In addition, the rate of spin diffusion among nuclei with low gyromagnetic ratios can be increased by using rf-irradiation during the mixing time or by matching the rotor frequency to the chemical shift differences between a pair of spins.

4. Techniques for Distance Measurement between Heteronuclei (SEDOR, REDOR, TEDOR). As mentioned in Section II.A.3, the strength of the heteronuclear dipolar coupling between two nuclei is given by $(\mu_J/4\pi)\gamma_I\gamma_S r_{IS}^{-3}(h/2\pi)$. Thus, in systems which effectively contain isolated spin pairs, a measurement of the dipolar coupling constant translates into a direct determination of the internuclear distance. The Spin-Echo DOuble Resonance (SEDOR) technique (6) is the simplest method for measuring internuclear distances between a pair of unlike nuclei. The pulse sequence in Figure 14A depicts a "spin echo" on a spin species I . In this sequence, the 90° pulse generates transverse magnetization which subsequently dephases due to a variety of NMR interactions. Application of a 180° pulse to the I spins at time τ will reverse

the effects of the heteronuclear dipolar couplings, rf-inhomogeneities, and the chemical-shift interactions so that they rephase, leading to the formation of an echo at the time 2τ . However, if 180° pulses are applied to the I and S spins simultaneously, the heteronuclear dipolar coupling continues to dephase during the second half of the experiment. Taking the difference between the spectra with and without the 180° pulse on the S spins gives a residual signal that is due to the heteronuclear dipolar interaction. Typically, the SEDOR experiment is performed by collecting a series of spectra in which the placement of the 180° pulse on the S spins is varied (see Figure 14A). In essence, this is a two-dimensional technique even though a Fourier transform of the t_1 dimension is generally not performed. Instead, the set of difference-signal intensities can be fit to determine the strength of the heteronuclear dipolar coupling. SEDOR can only be applied to static samples, but it has successfully been applied to a variety of systems. Even when isolated pairs of nuclei are not present, it can be used to obtain qualitative information. For instance, SEDOR has been used to study the chemisorption of CO on dispersed Pt (90). SEDOR results have also been applied to test atomic distribution models in P-Se glasses (91), and in complex P-Cd semiconducting glasses as shown in Figure 44 (92-94).

In many cases the high resolution associated with magic-angle spinning is desirable, thus a technique has been developed for measuring heteronuclear distances in rotating samples. This technique is known as Rotational-Echo Double Resonance (REDOR) (95,96). Conceptually, it is similar to SEDOR, but since sample spinning itself averages out the heteronuclear dipolar interactions, a series of rotor-synchronized 180° pulses is required to produce the appropriate dephasing and rephasing behavior. One version of the REDOR experiment is depicted in Figure 14B. Here, two series of spectra with and without 180° pulses on the S -spins are acquired with the number of rotor cycles over which the experiment is performed being incremented in steps of two. As in the case of SEDOR, the intensities of the difference spectra provide a measure of the internuclear distance. Both SEDOR and REDOR are sensitive to pulse imperfections, but the phases of the pulses can be cycled to minimize artifacts. As with all forms of difference spectroscopy, long-term spectrometer stability is necessary.

Another useful experiment for measuring internuclear distances is the Transferred-Echo Double Resonance (TEDOR) experiment (97); one version of this experiment is depicted in Figure 14C. TEDOR is also a rotor-synchronized technique, and the first part of the pulse sequence is similar to REDOR with a series of 180° pulses being used to maintain the dipolar coupling as the sample undergoes MAS. Simultaneous 90° pulses are then applied to transfer the dipolar coherence to the S spins. The coherence transfer step ensures that no background signal from uncoupled spins will contribute to the spectrum; this greatly simplifies analysis of the signal intensities. Further evolution of the dipolar coupling occurs after the coherence transfer, and the S spin signal is then acquired. The number of rotor cycles after the coherence transfer step is incremented from experiment to experiment, and the signal intensities can be fit to extract the internuclear distance. REDOR and TEDOR have been applied to materials with well-resolved MAS spectra including

(B)

T-site	Occupancy	Connectivities
T ₁	1	2T ₂ : 2T ₃
T ₂	1	2T ₁ : 2T ₄
T ₃	1	2T ₁ : 2T ₅ : 1T ₇
T ₄	1	2T ₂ : 1T ₅ : 1T ₆
T ₅	1	1T ₃ : 1T ₄ : 2T ₆
T ₆	1	1T ₄ : 2T ₅ : 1T ₇
T ₇	1	1T ₃ : 1T ₆ : 2T ₇

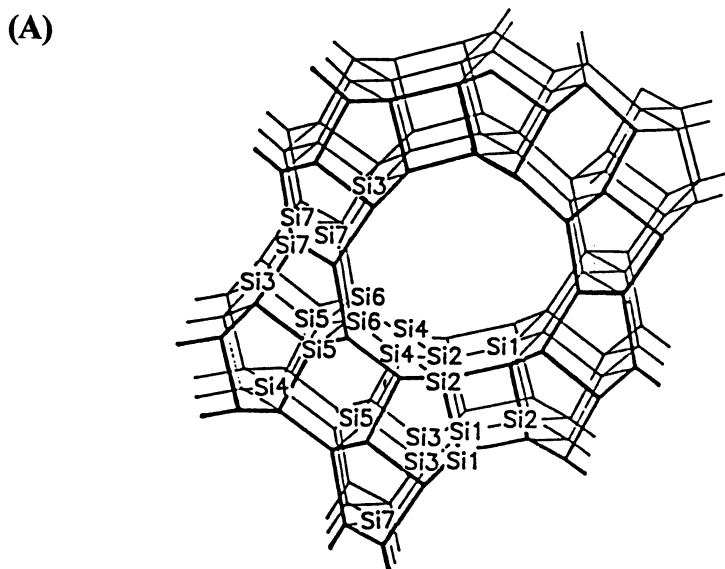
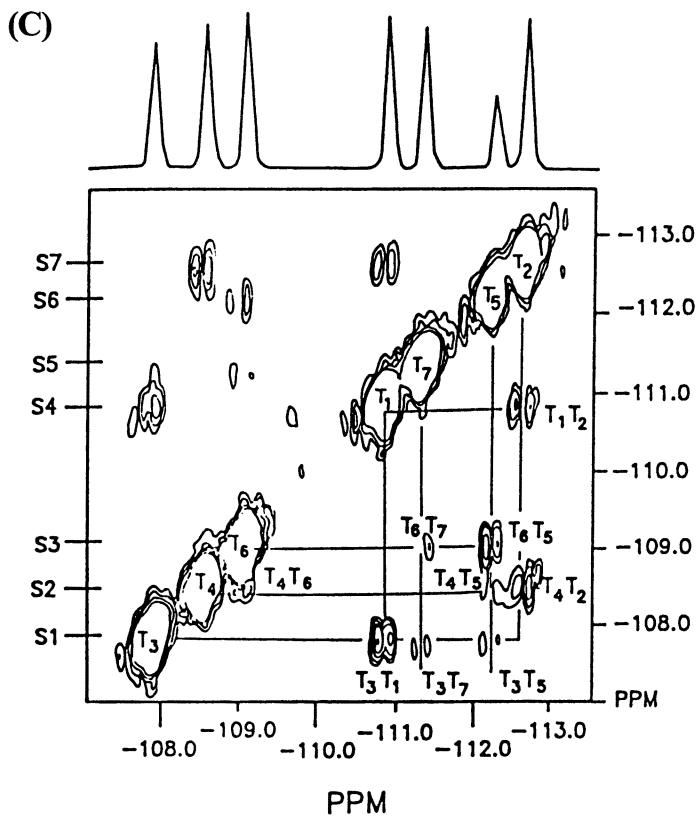


Figure 13. Schematic of the structural representation of the zeolite ZSM-12 lattice framework (A), where the seven crystallographically inequivalent lattice sites are depicted by the notation T1....T7. Summary table (B) of the T-silicon sites, their occupancies and their connectivities (B); Contour plot of a COSY experiment on ZSM-12 (C) with projection in the F2 dimension. The connectivities of the various T1 through T7 silicon sites are shown (136-140).



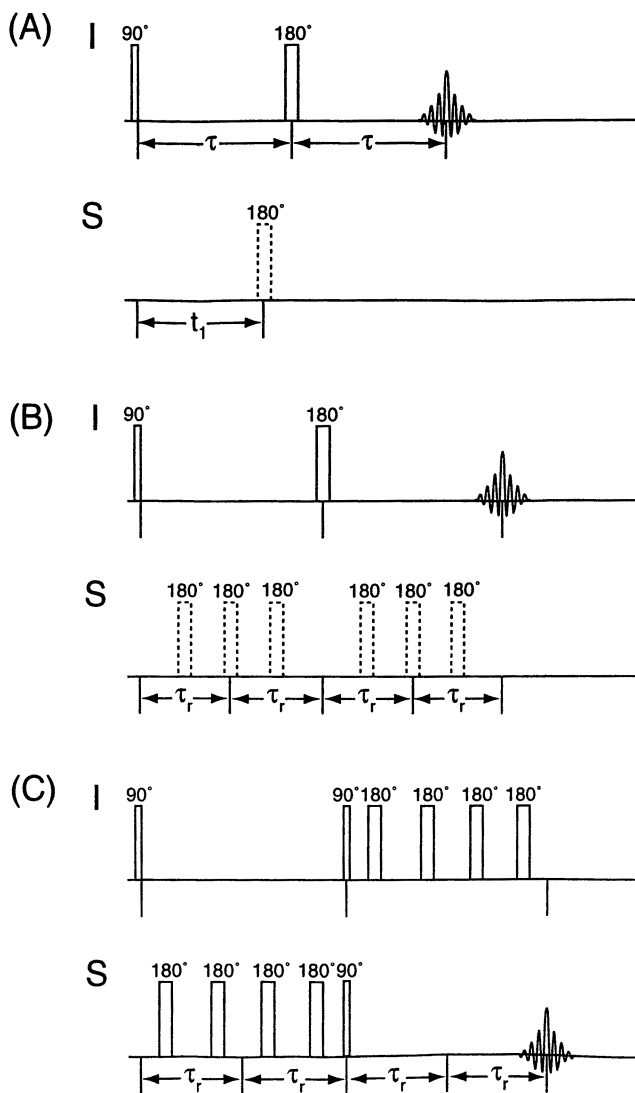


Figure 14. Pulse sequences for heteronuclear distance measurement experiments. (A) The SEDOR experiment. A simple spin-echo experiment is performed on the *I*-spins and a 180° pulse is applied to the *S*-spins after a time t_1 . The time t_1 is varied from experiment to experiment, and taking the difference of experiments performed with and without the 180° pulse on the *S* spins permits the strength of the coupling between an *I* spin and a *S* spin to be determined. (B) A version of the REDOR experiment used to measure internuclear distances in spinning samples. The pulses must be synchronized with the rotation period as shown, and again the difference between two experiments with and without a 180° pulse on the *S* spins is taken. (C) The TEDOR experiment is similar to REDOR but incorporates a coherence-transfer step to eliminate background signal from uncoupled spins. For a given number of rotor cycles only a single experiment is performed.

aluminophosphates (60,61), zeolites (58), amorphous aluminas (98), aluminoborate glasses (63), and zirconium phosphate vanadate solid solutions (99). In most studies of inorganic materials, multiple spin pairs are present; the information obtained in those cases does not reflect individual distances but rather averaged distances.

The coherence-transfer property of TEDOR also permits it to be used as an alternative to cross polarization in heteronuclear correlation experiments (58,60). Since TEDOR does not require precise and stable amplitude matching, it may be more robust than cross polarization. In some cases, however, it can be significantly less efficient.

Solid-state NMR techniques for measuring precise distances between like nuclei (e.g. - the rotational resonance technique (R^2) (100), Dipolar Recovery At the Magic Angle (DRAMA) (101)) have also been developed. Such methods have so far primarily been applied to organic compounds where isolated spin pairs can easily be introduced by site-specific isotopic labeling. In typical inorganic materials, such labeling is not possible, and these methods have not yet been widely exploited.

5. Techniques for Distance Measurement between Spin-1/2 and Quadrupolar Nuclei (TRAPDOR, REAPDOR). Although SEDOR, REDOR, and TEDOR have been applied to quadrupolar nuclei, the presence of the quadrupolar interaction can complicate the interpretation of the results. Recently, two techniques have been developed specifically to address the issue of dipolar couplings to quadrupolar nuclei.

The TRAnsfer of Populations in DOuble Resonance (TRAPDOR) technique (102) was designed to detect dipolar couplings to quadrupolar nuclei even when the quadrupolar coupling constant is large. The experiment is based on the behavior of quadrupolar nuclei under high-power rf-irradiation in a spinning sample. When sufficiently high rf-fields are applied during the spinning process, the first-order quadrupolar coupling of a crystallite can change sign adiabatically, and the populations of different quantum states will then be interchanged. This, in turn, means that a spin-1/2 nucleus that was coupled to a quadrupolar nucleus in a given state will now be coupled to a nucleus that has a different state. Figure 15A shows the TRAPDOR sequence. In the first experiment, a conventional spin echo is applied to the spin-1/2 nuclei (I): the echo refocuses the chemical shift interaction, the heteronuclear dipolar coupling, and the magnetic field inhomogeneity. A second experiment is identical to the first except that high-power rf-irradiation is applied to the quadrupolar (S) species during the first half of the sequence. In this second experiment, the heteronuclear dipolar coupling between an I spin and an S spin which has changed its state will not be refocused by the 180° pulse on the I spins. Thus, taking the difference between the spectra from the two experiments provides an indication of the dipolar coupling. TRAPDOR can also be used to estimate the strength of the quadrupolar coupling constant. This is done by performing the experiment with the high-power irradiation applied at a range of frequency offsets from the S -spin Larmor frequency. TRAPDOR-type dephasing will only occur if the frequency offset falls within the width of the first-order quadrupolar line. The extent of dephasing for different offsets can be compared with semi-quantitative calculations, and an approximate value for the quadrupolar coupling constant can be extracted. This technique is particularly useful in cases where the quadrupolar broadening is so

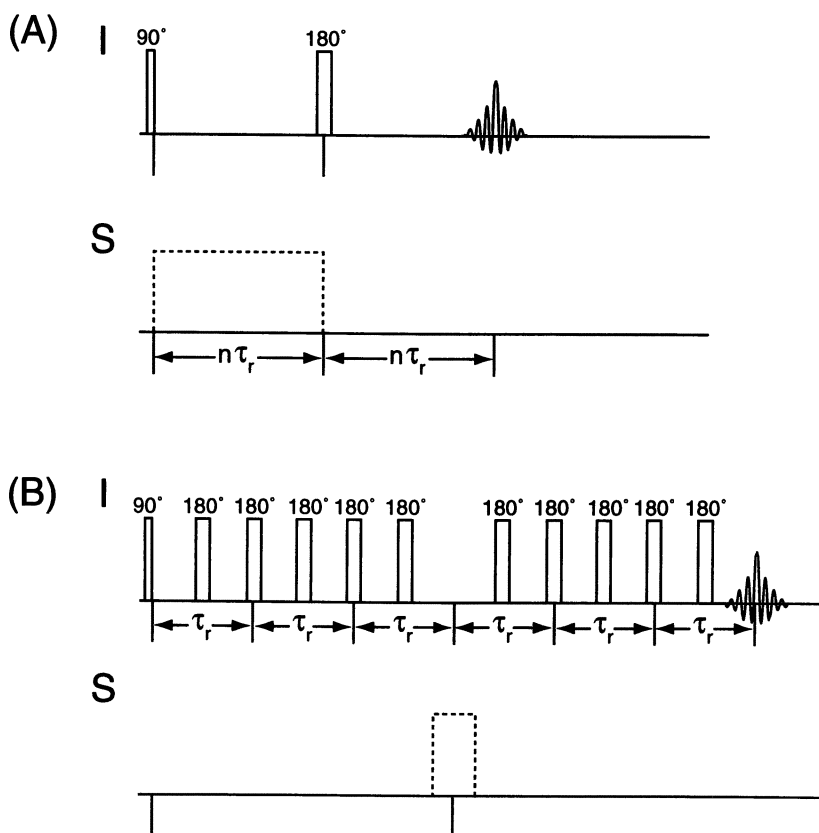


Figure 15. Pulse sequences for heteronuclear distance measurement experiments involving quadrupolar nuclei. (A) The TRAPDOR pulse sequence. Taking the difference of spectra with and without high-power irradiation on the quadrupolar species provides an indication of dipolar couplings. (B) The REAPDOR pulse sequence. Features of TRAPDOR and REDOR are combined to measure weak dipolar couplings to quadrupolar nuclei. For a given number of rotor cycles, only a single experiment is performed.

large that direct detection of the quadrupolar resonance is impractical. For instance, it has been used to study the aluminum atoms at the Brønsted acid sites in dehydrated (102) and calcined samples of zeolite H-Y (103) and in an AlPO_4 glass (104).

The TRAPDOR experiment requires high rf-fields and a stable spinning speed, and it is sensitive to probe tuning. It also has complicated phase behavior which, in practice, necessitates performing a phase correction before taking the difference between the two spectra. Furthermore, a unique determination of the quadrupolar coupling constant is not always possible because, in some cases, several combinations of C_q and η correspond to the same dephasing vs. offset behavior. However, even in such cases, the TRAPDOR experiment can provide useful constraints on the range of possible quadrupolar coupling constants, and such information can aid in the interpretation of other experimental results.

The Rotational-Echo Adiabatic Passage DOuble Resonance (REAPDOR) experiment (105) combines features of REDOR and TRAPDOR to measure distances between a quadrupolar nucleus and a spin-1/2 nucleus in cases where the dipolar coupling is weak and the quadrupolar spectrum is broad. The REAPDOR experiment is shown in Figure 15B. A train of rotor-synchronized 180° pulses is applied to the spin-1/2 nuclei (I) to refocus the heteronuclear dipolar interaction during MAS. A second experiment is identical except for the application of strong rf-irradiation on the quadrupolar spins. As in the TRAPDOR experiment, this rf-irradiation causes heteronuclear dephasing since it alters the quantum states of the quadrupolar nuclei, preventing dipolar refocusing. In REAPDOR, the rf-irradiation period is kept short to simplify the theoretical analysis of the experiment and to reduce the rf demands on the probe; the pulse train can be made arbitrarily long, however, so that weak couplings can be measured. Difference spectra are acquired for various numbers of rotor periods and can be fit to a model with two adjustable parameters: (1) the dipolar coupling constant and (2) the fraction of nuclei with quadrupolar coupling constants that undergo an odd number of sign changes during the irradiation period (since only these nuclei will cause dephasing). This fraction can be estimated from theory and the dipolar coupling extracted for the case of isolated spin pairs.

REAPDOR requires high rf-fields, stable spinning, and precise 180° pulses. Phase distortions due to the strong rf-irradiation are inevitable, although predictable. This new technique has recently been used to locate cations in molecular sieves (107) and should be applicable to a wide range of distance problems associated with various inorganic materials.

6. Isotropic-Anisotropic Correlation of Chemical Shifts. While two-dimensional NMR can be used to probe the connectivities between different sites in a sample, multidimensional experiments can also be used to provide information about the local environments of individual sites. In such experiments, the spectral resolution is improved since the information content is spread over more than one dimension. The techniques of Variable-Angle Correlation Spectroscopy (VACSYS), Magic-Angle Hopping (MAH), and Magic-Angle Turning (MAT) among others produce two-dimensional spectra in which broad anisotropic chemical shift powder patterns (such as shown in Figures 1A-B) in one dimension are correlated with narrow, well-resolved isotropic chemical shifts in the other dimension.

Variable-Angle Correlation Spectroscopy (VACS)Y (106) involves acquiring a series of one-dimensional spectra for different angles of the sample rotation axis with respect to the magnetic field. Since the width of the anisotropic part of the chemical shielding interaction is scaled by the angle of rotation, this set of data contains enough information to separate the isotropic and anisotropic portions of the chemical shift. Interpolation procedures are used to produce a conventional two-dimensional time-domain data set which can then be Fourier transformed. Although the angle adjustment must be precise, the pulse sequence is simple (only an excitation pulse is required). Therefore, the technique is particularly useful for samples with short relaxation times.

In the Magic-Angle Hopping (MAH) experiment (108), the sample is mechanically reoriented about the magic-angle axis in discrete "hops" of 120° . Pulses are applied in such a way that equal amounts of t_1 evolution occur at each of these orientations, and, due to the symmetry of the chemical shift interaction, the anisotropy is refocused at the end of the evolution period. During the detection period, the sample remains static, permitting the collection of the full anisotropic powder patterns. While this experiment requires special equipment, a very similar experiment can be performed on conventional MAS equipment provided slow spinning speeds are used. In this experiment, which is known as Magic-Angle Turning (MAT) (109), rotor-synchronized pulses permit t_1 evolution every third of a rotor period, and slow-spinning anisotropic spectra are recorded during the time t_2 . The chemical shielding tensor components for each site can be extracted from the ω_2 dimension by comparison with simulations.

Other pulse sequences can also be used for isotropic-anisotropic correlation. One is based on the TOtal Suppression of Sidebands (TOSS) experiment (110) which uses a series of 180° pulses to create destructive interference among the MAS sidebands so that only the centerband remains. In the TOSS-deTOSS experiment (111), a TOSS sequence precedes the t_1 evolution to create a high-resolution dimension. Then, a time-reversed TOSS sequence is applied to reintroduce the anisotropy, and the signal is acquired.

Isotropic-anisotropic correlation spectra have been used for ^{31}P spectral assignment in silver iodide-silver phosphate conducting glasses (112). The different geometries of phosphorous sites with different numbers of bridging oxygens (Q^0 , Q^1 , Q^2 , etc.) are reflected in the shapes of the anisotropic powder patterns; thus, isotropic-anisotropic chemical shift correlation spectra allow the resonances to be unambiguously assigned. Such spectra also assist in the interpretation of isotropic lines that are broadened due to the presence of multiple sites since the extent of variation of the chemical-shielding anisotropy over such a broad line provides a measure of local disorder. Furthermore, the principal values of the chemical-shielding tensor can be correlated with bond lengths and bond angles. Similar studies are possible for ^{29}Si NMR measurements in glasses and minerals (229).

7. Isotropic-Anisotropic Correlation of the Quadrupolar Interaction. In Sections III.B.2 and III.B.3, the techniques of DAS and MQMAS were introduced as ways of removing the second-order quadrupolar broadening to produce high-resolution, one-dimensional spectra. However, the quadrupolar parameters, C_q

and η^Q , reflect the electric field gradient surrounding the quadrupolar nucleus, and, thus, can be directly related to local conformations, bond angles, and bond strengths. To obtain high-resolution while at the same time retaining this structural information, the two-dimensional nature of DAS and MQMAS can be exploited. In such experiments, a series of spectra which refocus the quadrupolar interaction at different times (t_1) is collected. Two-dimensional Fourier transformation of this data set leads to a spectrum in which narrow resonances are correlated with anisotropic quadrupolar patterns.

Figure 16 shows an example of such a two-dimensional DAS spectrum for ^{17}O in the SiO_2 polymorph coesite (113). Separate quadrupolar powder patterns were obtained for each of the five oxygen environments, and by fitting simulated spectra to these patterns, the quadrupolar parameters (C_q in the range of 5.16 to 6.05 MHz, and η^Q in the range 0.000 to 0.292) for the five oxygen sites were obtained. These parameters were then directly correlated with Si-O-Si bond angles that varied from 137.22° to 180° . Similar two-dimensional ^{17}O DAS experiments were performed on a $\text{K}_2\text{Si}_4\text{O}_9$ glass and revealed the distribution of bond angles present in this material (114). Even in cases in which the presence of degenerate isotropic shifts prevents individual pairs of quadrupolar parameters from being extracted, two-dimensional separation of the quadrupolar interaction can provide useful information about a sample. For instance, when the MQMAS technique is applied to ^{27}Al in glasses, the two-dimensional spectra can reveal distinct peaks corresponding to 4-, 5-, and 6-coordinate aluminum sites (115). Five-coordinate aluminum is often not detected in one-dimensional spectra of glasses; thus, the two-dimensional MQMAS method is a good technique for determining if such species are present.

8. Two-dimensional Exchange. NMR can be used not only to determine the structure of a material but also to characterize its dynamics. One way this is done is through two-dimensional EXchange SpectroscopY (2D-EXSY) (5). The simplest form of 2D-EXSY is a three-pulse sequence identical with the one described in Section III.C.3 for measuring spin-diffusion. For sufficiently short mixing times, a dynamic process will often dominate over spin diffusion, and the pattern of off-diagonal intensity can indicate what types of atomic rearrangements occurred during the mixing time. Performing the experiment over a range of temperatures allows the Arrhenius parameters for the motion to be determined.

2D-EXSY has been applied to a variety of materials. Figure 17 shows a two-dimensional ^6Li NMR exchange spectra for the diffusion of lithium ions in lithium orthosilicate (Li_4SiO_4), a ceramic conductor (116) at two different mixing times of (A) 47 ms, and (B) 188 ms. The off-diagonal peaks indicate that "hopping" occurs among lithium ions in LiO_3 , LiO_4 , LiO_5 , and LiO_6 oxide lattice site with exchange rates that vary from 0.35 Hz ($K_{3,4}$) to 0.85 Hz ($K_{4,6}$) for different lithium ion site pairs. The activation energies for the pairwise lithium ion "site hopping" ranged from 54 to 74 kcal/mol. Exchange spectroscopy was also applied to study Q-species exchange in potassium tetrasilicate at temperatures just above the glass transition (117).

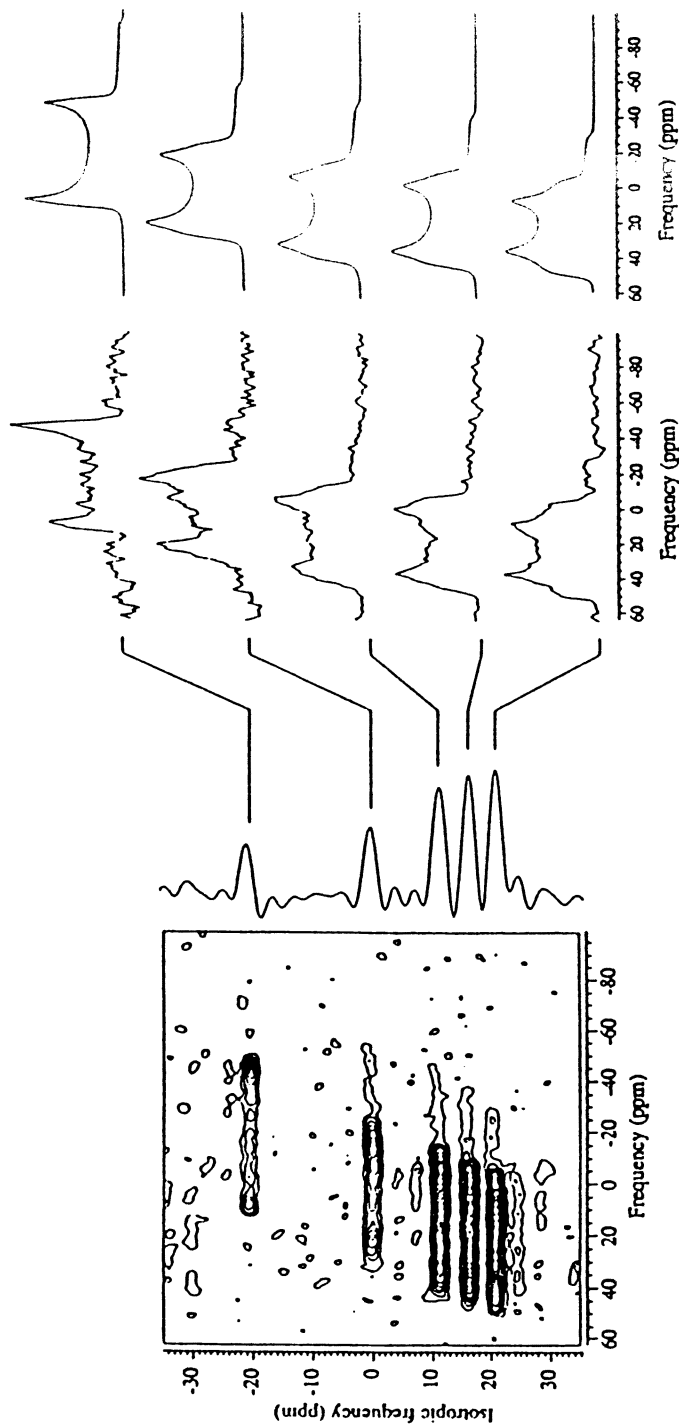


Figure 16. A two-dimensional ^{17}O DAS spectrum of mineral coesite SiO_2 , showing individual anisotropic quadrupolar powder patterns and corresponding simulations for each oxygen site (173). The C_q values obtained for the five sites are in the range of 5.16 to 6.05 MHz, and η^o is in the range 0.000 to 0.292. These parameters were directly correlated with Si-O-Si bond angles that varied from 137.22° to 180° .

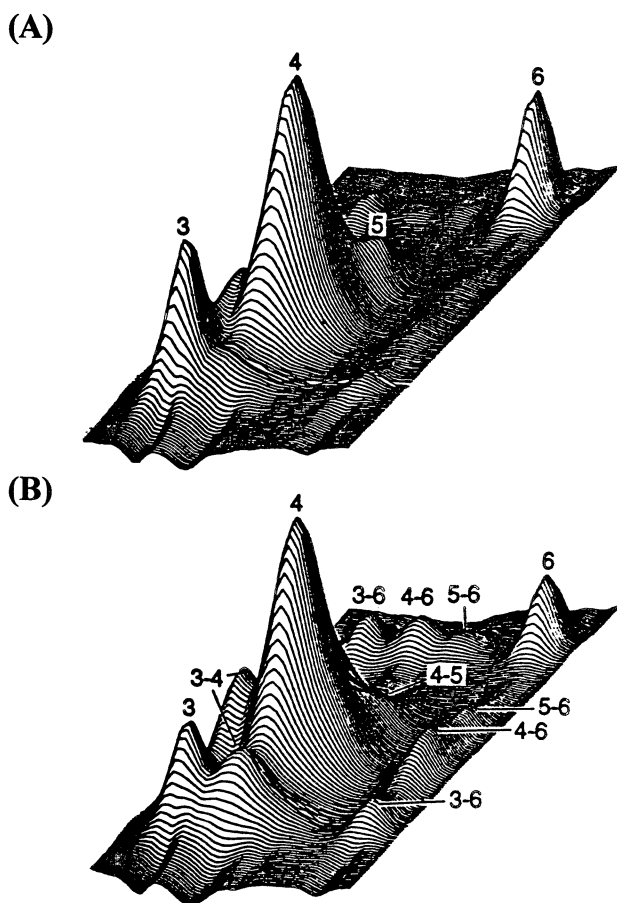


Figure 17. Two-dimensional exchange ${}^6\text{Li}$ NMR spectra of the ${}^6\text{Li}$ sites in Li_4SiO_4 at 33°C with mixing times (A) 47 ms and (B) 188 ms. The labels indicate exchange between selected pairs of LiO_3 , LiO_4 , LiO_5 , and LiO_6 sites. The ${}^6\text{Li}^+$ ion "hopping" rates are in the range from 4.7 to 6.1 Hz between different pairs of ions at 33°C (116)

IV. SOLID-STATE NMR OF INORGANIC SOLID MATERIALS

A. Types of Chemical Information.

Solid-state NMR studies have shown enormous potential to obtain both structural and dynamical information about: 1) the chemical environments in specific structural sites, 2) the inter-site correlations, including distances between different atoms and relative bond orientations, and 3) the chemical dynamics (on the NMR time scale) as related to reaction chemistry, structural reorganization and various chemical diffusion and/or cation and anion exchange processes. The relationship between these important types of information and the elementary NMR parameters discussed previously (in Section II) is summarized in Table IV.

The next section focuses on how the primary NMR parameters are used to obtain an understanding of the chemistry and, to a lesser extent, the physics of inorganic materials. Important materials science issues that have been addressed by NMR include:

- 1) structural and bonding information, including short- and intermediate-range order, atomic-level chemical environments and site symmetry, the presence and concentration of impurities and defect sites, bonding and through-space connectivity between atoms, and the temperature dependence of structural and phase transformations,
- 2) knowledge of the effects of synthesis and processing on the structural nature of these materials, including the kinetics and solid-state reaction pathways that modify or alter structural units or substructures, as well as those processes leading to the formation of impurities or minor amorphous and crystalline solid phases,
- 3) quantitative measurements of the rates of solid-state chemical reactions, cation and anion exchange, and atomic rearrangements occurring during thermal transformations at various temperatures and pressures,
- 4) understanding of the surface and "interfacial interactions" important in inorganic materials, including interphase bonding in composites, interlayer interactions in layered and complex mesophases, identification of crystalline and amorphous grain boundary materials, and interfacial processes important in gas/solid and solution/solid interfacial chemistry.

An understanding of such chemical questions is obviously specific to the inorganic material of interest. In this overview, chemical issues will be addressed in light of selected examples of solid-state NMR research carried out in the past decade.

Table IV. Relationship between NMR parameters and chemical information

NMR PARAMETER	CHEMICAL INFORMATION
Isotropic chemical shift (δ_{iso})* chemical-shift anisotropy parameter ($\Delta\delta$), and chemical- shift asymmetry parameter (η^{CS})	Bond angles, bond lengths, coordination number, and related local influences of neighboring atoms (also related to electronegativity and bonding type)
OR	
Principle values of the chemical- shielding anisotropy (σ_{11} , σ_{22} , σ_{33})	
Scalar coupling constant (J)	Through-bond connectivities between nuclei
Dipolar coupling constant (d_{ij})	Through-space distances between nuclei
Quadrupolar coupling constant (C_q)	Symmetry of electronic environment around an atomic site (large C_q values indicate significant distortions from cubic symmetry), including bond angles and bond lengths
Quadrupolar asymmetry parameter (η^{Q})	Deviation of local electronic environ- ment from cylindrical symmetry, bond angles and bond lengths

* For quadrupolar nuclides, e.g., ^{17}O , ^{23}Na , ^{27}Al , the notation δ_{iso} is used throughout the text to denote purely chemical shift interactions, whereas, the notation δ_{obs} represents the center-of-mass of a resonance peak (containing both chemical shift and quadrupolar contributions).

**American Chemical
Society Library
1155 16th St. N. W.**

In Solid-State NMR Spectroscopy of Inorganic Materials, Fitzgerald, J.;
ACS Symposium Series; American Chemical Society: Washington, DC, 1999.

B. Types of Inorganic Materials.

Current and future advances in the understanding of inorganic materials by solid-state NMR methods are expected to benefit primarily several distinct, but not mutually exclusive classes of inorganic materials as summarized in Table I: 1) metal oxide catalysts and supports, 2) open framework and layered materials, including zeolites, 3) glasses, ceramics and cements, including electronic, optic and electrooptic materials, 4) semiconductor, ion conducting and superconducting materials, and 5) composite materials containing inorganic substances.

1. ***Metal Oxides, Metal Oxide Catalysts and Supports.*** Metal oxides are one of the largest groups of inorganic materials, exhibiting a diverse range of physical and chemical properties (118-123). The structure of several common metal oxides of the corundum, spinel, zinc blende, wurtzite and perovskite lattices show coordination numbers of 4, 6, 8, and 12 for the metal ions and coordination numbers of 2, 3 and 4 for the oxide (and also chalcogen) sites in these classic lattice structures (121). Metal oxides generally exist as microporous solids, powders of variable surface areas or densified ceramic forms. Their synthesis can be performed using gas phase approaches; metal oxide sintering and densification processes; controlled dehydration of hydroxide, hydrous oxides and sol-gel precursors; and, recently, pyrolysis of chelated and polymer precursors. Metal oxides of silica, alumina, vanadia, titania, zirconia and molybdena have been most extensively studied by solid-state NMR since the oxides of these metal ions are diamagnetic in their highest oxidation state. Some of their important industrial uses are summarized in Table V.

a) ***Silica Materials.*** The most abundant and extensively studied metal oxide solids include hydrous silicon dioxides, organic and sol-gel precursors of silicon dioxides, chemically-modified silicon dioxides and mineral and synthetic forms containing both aluminum and silicon (11-13,123-133). Amorphous, crystalline, hydrated and dehydrated variants (e.g., SiO_2 , $\text{SiO}_2 \cdot n\text{H}_2\text{O}$) exist with a wide range of surface areas and porosities. Hydrated silica materials, termed silica gels, are often used as supports for bonded phase chromatography in separation science (48,122,124,129). These materials are synthesized by either low-temperature sol-gel or high-temperature (fumed) methods. Besides their use in chromatography and separation processes, silica materials find widespread utility in microelectronic fabrication technologies and as fillers and components of inorganic composites. Chemically-modified silicas, colloidal silicas and sodium silicates are of major significance in flocculation and dispersion technologies (124). Colloidal silicas and hydrated alkali silicates are also important in the geochemistry of silicas and aluminosilicates (11,124,129). Silica materials are major reagent components used to prepare glasses, cements, zeolites and related molecular sieves (133-135).

Because of the extensive use of ^{29}Si MAS NMR (spin-1/2 nucleus), solid-state NMR studies of silica-containing gels, minerals, glasses and zeolites have been the subject of numerous reviews (10,12,125,136,137), including an extensive book reviewing early investigations of these systems (11). The solid-state MAS NMR results obtained for silica materials provide a striking demonstration of the utility of this spectroscopic approach to obtain both structural and dynamical information not

accessible by other methods. Pioneering studies in the early 1980s (140,142,157) showed that the ^{29}Si chemical shift (δ) could be related directly to the chemical environment around 4-coordinate tetrahedral silicon in crystalline silicates, aluminosilicates and zeolites as summarized in Table VI. This work has been extended to a myriad of structurally more complex zeolites, silicate and aluminosilicate glasses, minerals and clays to obtain chemical information about nearest neighbor (NN) and next-nearest neighbor (NNN) atoms (e.g., Si-N-Si, Si-O-Si, Si-O-Al), as well as bond angles, bond lengths and other bonding parameters (11,12,125,136,140-142). Recently, the effects of other NNN atoms such as titanium on the observed ^{29}Si NMR chemical shifts have been reported (148).

One of the major advances in silica surface chemistry of the past decade has been the use of ^1H CRAMPS and ^{29}Si CP/MAS NMR (see Figures 7 and 8) to obtain structural information about surface silanol groups (both geminal and vicinal) for silica gel materials (26-28,41-44,47-51). Fundamental information about hydration mechanisms, hydrogen-bonding, motional dynamics and the interactions of "physiosorbed" water have been detailed. In addition, these approaches have been extended to surface reactions important in the formation of derivatized silicas (51,122,129,147,153,154) as well as to studies of the hydrolysis of alkali silicate glasses (162).

While the majority of the published literature related to the structural and surface chemistry of silicate materials has used ^{29}Si MAS, ^1H - ^{29}Si CP/MAS NMR, ^1H MAS NMR and ^1H CRAMPS techniques (26-28,41-43,47-51,125,136,137,140-147,149-152,160-162) several two-dimensional solid-state NMR approaches including isotropic/anisotropic correlation, ^1H - ^{29}Si HETCOR, INADEQUATE and COSY (see Figures 13 and 41B) have recently been applied to more complex silicate systems (79,113,136,137,154-156). Two-dimensional NMR approaches are now being used to study complex silicates, zeolites and silicate glasses, thus providing important details regarding connectivity and structural information for specific sites in these systems. Fundamental solid-state ^1H , ^{17}O and ^{29}Si MAS NMR studies of the surface and "interfacial" chemistry of complex silica-containing fibers, the role of siloxane coupling agents in composites and advanced materials (153,154), and the reactivity and chemical dynamics of silica sol-gel chemistry (127,128,156,288) are needed.

Besides the use of ^1H and ^{29}Si MAS NMR to study various silica materials, NMR studies of quadrupolar nuclides such as ^{17}O , ^{23}Na , ^{25}Mg and ^{39}K can provide an atomic-level understanding of complex silicates such as sodium silicates (including hydrates), and various alkali (e.g., K^+) and alkaline earth (Mg^{2+}) silicates of relevance to materials science and geochemistry. Recently, for example, ^{23}Na MAS NMR studies of several model sodium silicate hydrates and sodium phosphate hydrates were reported (306,307). Sodium silicate hydrates of the formula $\text{Na}_2\text{SiO}_2(\text{OH})_2 \cdot n\text{H}_2\text{O}$, where n is the number of lattice waters (e.g., $n = 8, 7, 5$ and 4), represent relevant model complexes where sodium ions are coordinated to both water and the monomeric silicate anions. Several of the known local sodium ion coordination environments are depicted in Figures 18A through 18C. These well-defined crystalline solids are highly useful for obtaining a fundamental understanding of the important interactions of various cations with silicate species in concentrated aqueous solution, e.g., water glass

Table V. Summary of various metal oxide materials

Functional Properties	Substance	Uses/Applications
Biological	Alumina (Al_2O_3)	Artificial Joints
	Hydroxyapatite/Bioglass	Tooth, Bone and Facial Implants
Chemical	Titanates	Photochemical and Redox Electrodes
	Zeolites and Si/Al (e.g., ZSM-5)	Chemical Catalysts
	$2 \text{MgO} \cdot 2\text{Al}_2\text{O}_3 \cdot 5 \text{SiO}_2$ (Cordierite)	Catalysts for Emission Control
	$\text{SiO}_2, \text{SiO}_2 \cdot n\text{H}_2\text{O}$	Fillers, Supports Composite Fibers
	$\text{Al}_2\text{O}_3, \text{Al(O) OH}$ Transition Aluminas	Hydrocarbon Cracking and Reformation Isomerization Catalysts
	K-V-O, V-P-O, V_2O_5 , Bi-V-O	Oxidation Catalysts (SO_2 , acrolein, and CH_3OH)
	Bi-Mo-O, MoO_3 , V-Mo-O	Oxidation Catalysts (Propene, Acrolein)
$\text{Ln}_2\text{Sn}_2\text{O}_7$, Pyrochlores	Methane Catalysts	
Mechanical	$\text{Al}_2\text{O}_3, \text{ZrO}_2$	Wear Resistant Seals, Bearings, Sensors, Engine Ceramics, Tools
	$\text{SiC}/\text{Al}_2\text{O}_3$ Composites	High Temperature Composites
	$\text{Si}_3\text{N}_4/\text{Al}_2\text{O}_3, \text{SiAlON}$	High Temperature Oxidative Resistant Materials

Table V. Continued.

Functional Properties	Substance	Uses/Applications
Optical	$Y_2O_3 - ThO_2$	Laser Materials
	$LaAlO_3, MgAl_2O_4$	Optical Components
	PLZTs	Light Memory Elements, Video Display/Storage
Electrical	$ZnO, Fe_2O_3, SnO_2, ZrO_2$	Gas Measurement Devices and Monitors
	$MgCr_2O_4 - TiO_2$	Cooling Elements
	$BaTiO_3, SrTiO_3, TiO_2$	Capacitors, Electronics
	PZTs, PMNs	Acoustic Transducers Ultrasound Devices
Magnetic	$Fe_2O_3, LiFeO_2, CoFe_2O_4, LaMnO_3, YMnO_3$	Magnetic Tapes
Nuclear	UO_2	Nuclear Fuel Pellets
	Al_2O_3/ZrO_2	Shielding
	Translucent Al_2O_3	Na Vapor Lamps
	Mullite ($3 Al_2O_3 \cdot 2SiO_2$)	IR Windows
	Titanosilicates	Cesium/Strontium Ion Exchangers

Table VI. Relationship between solid-state NMR chemical shift δ (^{29}Si) and local chemical environments in silicates, aluminosilicates and zeolites (125,140,142,157).

Tetrahedral Silicates¹⁴⁰

Notation	$\delta^{29}\text{Si}$ (ppm)	Local Site
Q^0	-66 to -74	SiO_4
Q^1	-78 to -83	$\text{SiO}_3(\text{OSi})$
Q^2	-86 to -88	$\text{SiO}_2(\text{OSi})_2$
Q^3	-91 to -99	$\text{SiO}(\text{OSi})_3$
Q^4	-107 to -110	$\text{Si}(\text{OSi})_4$

Tetrahedral Aluminosilicates¹³⁶

Notation	$\delta^{29}\text{Si}$ (ppm)		Local Site
	Zeolites ¹⁴²	Other Aluminosilicates ¹⁴⁰	
Q^4 (OA1)	-107 to -110	-103 to -112	$\text{Si}(\text{OSi})_4$
Q^4 (1A1)	-97 to -104	-99 to -105	$\text{SiO}_3(\text{OA1})$
Q^4 (2A1)	-93 to -96	-94 to -99	$\text{SiO}_2(\text{OA1})_2$
Q^4 (3A1)	-88 to -89	-88 to -94	$\text{SiO}(\text{OA1})_3$
Q^4 (4A1)	-83 to -84	-83 to -85	$\text{SiO}(\text{OA1})_4$
Q^3 (OA1)	---	-91 to -95	$\text{HOSi}(\text{OSi})_3$
Q^3 (1A1)	---	-84 to -87	$\text{HOSi}(\text{OSi})_2(\text{OA1})$
Lippmaa et al. ¹⁴⁰ Lippmaa et al. ¹⁴² See Smith et al. ¹⁵⁷ for other ^{29}Si NMR parameters for framework and layered aluminosilicate Q^3 and Q^4 silicon environments.			

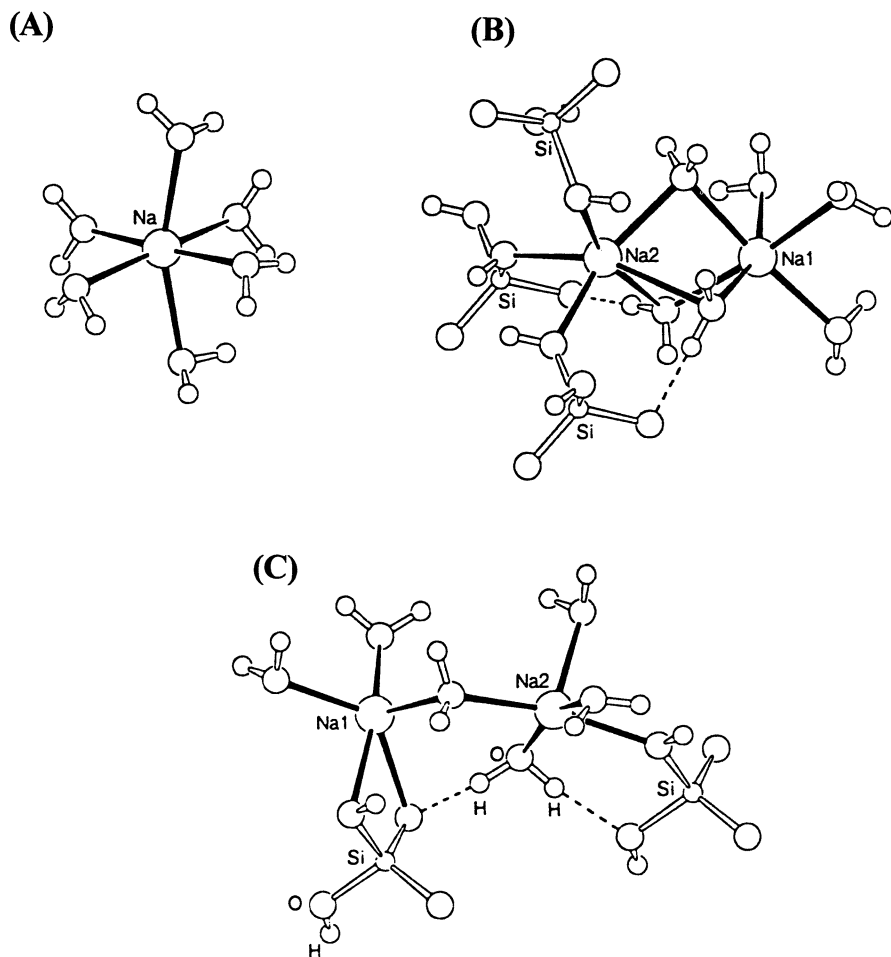


Figure 18. Local sodium coordination environments of five or six for various crystalline sodium silicate hydrates (n = number of waters), $\text{Na}_2\text{SiO}_2(\text{OH})_2 \cdot n\text{H}_2\text{O}$, where hydrates of the n values are depicted in (A) $n = 8$, (B) $n = 5$ and (C) $n = 4$ (306,307).

systems, cements containing sodium and calcium silicates, commercial sodium silicates (used in zeolite synthesis), and aqueous geochemical and biochemical systems.

The experimental and simulated ^{23}Na MAS NMR spectra for these various sodium silicate hydrates are given in Figure 19. The MAS NMR spectra show residual second-order powder patterns for the different ^{23}Na sites that have local sodium-oxygen coordination numbers of five or six. The variations in the ^{23}Na MAS NMR spectral parameters, including isotropic chemical shifts and C_q values indicate that NMR is sensitive to different sodium ion/ligand (waters or silicate ions) interactions, although attempts to definitively relate these parameters to the local sodium coordination number have so far been inconclusive. Correlations were obtained using a valence bond model for the relationship between the ^{23}Na isotropic chemical shifts and the average Na-O bond distances within 3.4\AA of the sodium ions. The quadrupolar coupling constants were related by different models to the covalencies of the oxygens within 3.4\AA of the sodium ions and to the oxygen atomic charges (and, thus, electronegativity). ^1H , ^{23}Na and ^{29}Si MAS NMR studies of these sodium silicate hydrate crystals, their melts and glasses (307), and hydrous sodium silicate glasses (162) have also provided important information about the variable temperature behavior of these crystalline and amorphous materials.

b) Alumina and Alumina Supports. Alumina materials encompass a wide range of crystalline hydrous oxides ($\text{Al}_2\text{O}_3 \cdot n\text{H}_2\text{O}$), hydroxides (e.g., gibbsite or bayerite, $\text{Al}(\text{OH})_3$), oxyhydroxides (pseudo-boehmite or boehmite), metal aluminates, and transition aluminas derived from specific dehydration treatments of various hydrous aluminum oxide materials (130-133). The transition aluminas, γ - and η -alumina, are widely used catalysts and catalytic supports due to their highly reactive Lewis and Brønsted acid sites. The hydrophilic surface of alumina, unlike the hydrophobic silica surface, has a propensity for H-D exchange, dissociative chemisorption of water, and other surface reactions where bond strain involving the reduced coordination of the aluminum site leads to energetics favorable for catalysis. The two most important catalysts are transition aluminas for hydrocarbon reformation reactions involving carbonium ion and γ -alumina supported noble metal catalysts for hydrocarbon cracking and hydrodesulfurization. In addition, aluminas have found extensive use as drying agents, sorption materials, chromatographic supports, abrasives with excellent strength and hardness properties, coatings, thin films and electrical insulators. They are also key reactants in zeolite, glass and cement synthesis and processing.

A large number of early solid-state ^{27}Al MAS NMR studies (149-151, 155-157, 159, 165-171) were of paramount importance in establishing an experimental correlation between $\delta(^{27}\text{Al})$ and the local chemical environment of aluminum in a diverse range of aluminum oxides, aluminates and related aluminum-oxygen compounds, including zeolites, Si/Al minerals and clays. These empirical studies of known aluminum-oxygen systems showed that $\delta(^{27}\text{Al})$ is highly dependent on the aluminum coordination number with different chemical shift regions being observed for 4-, 5- and 6-coordinate aluminums (see Figure 20) (165, 170, 172, 173, 176, 187-190, 194, 195, 216, 217). The $\delta(^{27}\text{Al})$ and C_q values for different aluminum resonances have been related to Al-O-Al and Al-O-Si bond angles and bond lengths in aluminates

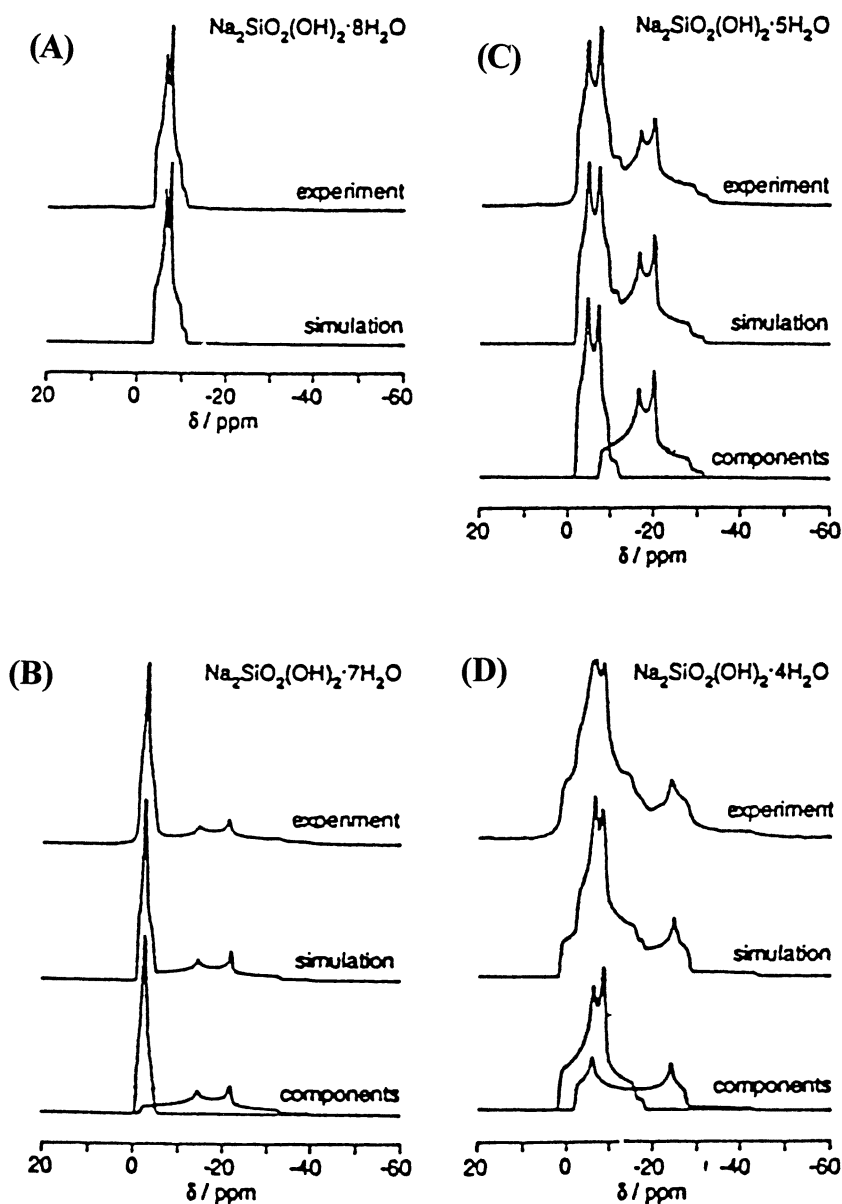


Figure 19. Experimental and simulated ^{23}Na MAS NMR spectra at 9.4 Tesla (A through D, corresponding to $n = 8, 7, 5$ and 4 , respectively), showing sodium sites with different coordination environments for a series of sodium silicate hydrates of the general formula $\text{Na}_2\text{SiO}_2(\text{OH})_2 \cdot n\text{H}_2\text{O}$, where n is the number of lattice waters (i.e., $n = 8, 7, 5$ and 4) (306,307).

and aluminosilicates (168,169,172,173). Additional relationships between $\delta(^{27}\text{Al})$ and the local environment of 4- and 6- coordinate AlO_x , AlN_4 and $\text{AlO}_{4-x}\text{N}_x$ chemical environments (see also Figure 20) in aluminum oxynitride systems have been obtained (174,341,347-349,353).

The quadrupolar nature of the ^{27}Al nucleus ($I = 5/2$) has presented significant solid-state NMR challenges due to line broadening caused by second-order contributions that are not removed under MAS conditions (see Section III.B) (149,150,164-166,172,173). Figure 2A (cf. Section II.B) shows the energy level diagram for $I = 5/2$ nuclei such as ^{27}Al and ^{17}O . The static and MAS ^{27}Al NMR spectra of $\text{KAl}(\text{SO}_4)_2 \cdot 12\text{H}_2\text{O}$ (alum), a common aluminum reference compound with negligible second-order quadrupolar broadening of the ^{27}Al resonance, are shown in Figure 21A and 21B, respectively. More representative ^{27}Al MAS NMR spectra which show significant second-order quadrupolar line broadening can be seen in Figures 22 and 23. Experimental factors that generally lead to the most meaningful ^{27}Al MAS spectra include fast spinning (11 kHz to 20 kHz), high magnetic fields (14 T) for aluminum sites with C_q values up to 14 MHz, and short excitation pulses, particularly to obtain quantitative results (173,179-182). In these cases, significant information regarding the chemical environment around the aluminum in specific sites can be obtained from quadrupolar coupling constants, C_q , and η^Q values that are derived from MAS spectral results (173,180). For example, the ^{27}Al MAS NMR for the Si/Al mineral sillimanite (Si_2AlO_5) shown in Figure 22, exhibits two second-order powder pattern resonances due to the different 4- and 6-coordinate aluminum sites in this Si_2AlO_5 mineral (183). By contrast, kyanite, another Si_2AlO_5 polymorph, shows a more complex, only partially resolved ^{27}Al MAS NMR powder pattern spectrum (Figure 23) that has been deconvolved and assigned to four different 6-coordinate aluminum sites with a range of C_q values, i.e., 3.7 MHz (A2), 6.53 MHz (A3), 9.37 MHz (A4) and 10.03 MHz (A1) (173). However, deconvolution of MAS spectra is not always possible in other complicated systems, necessitating the use of techniques such as DAS or DOR. For example, ^{27}Al MAS and DOR NMR studies of various Al-O systems have shown that overlapping aluminum resonances can be separated (or deconvolved), thereby providing more accurate isotropic $\delta(^{27}\text{Al})$ values for distinct 4-, 5- and 6-coordinate aluminum sites. Similarly, ^{27}Al MQMAS NMR has recently shown that the two-dimensional results obtained from these experiments can provide independent information about the different contributions of quadrupolar line broadening effects, and chemical shift dispersion to the overall MAS resonance linewidths and shapes (see Figure 24) as discussed subsequently for important AlPO systems such as AlPO-11 and VPI-5 (199,200). However, the issues of quantitation of aluminum NMR resonances have still not been completely overcome by either DOR, DAS or MQMAS NMR techniques.

The understanding of alumina surface chemistry has been significantly advanced through the use of ^1H CRAMPS and ^{17}O and ^{27}Al MAS NMR studies (55,171-176,190-196). Numerous different proton, oxygen and aluminum surface sites have been spectroscopically observed by MAS NMR for these systems (190-196). An example of how a series of different NMR experiments can be used to characterize the surface chemistry of aluminas is shown in Figure 25 (196). Normally, two peaks

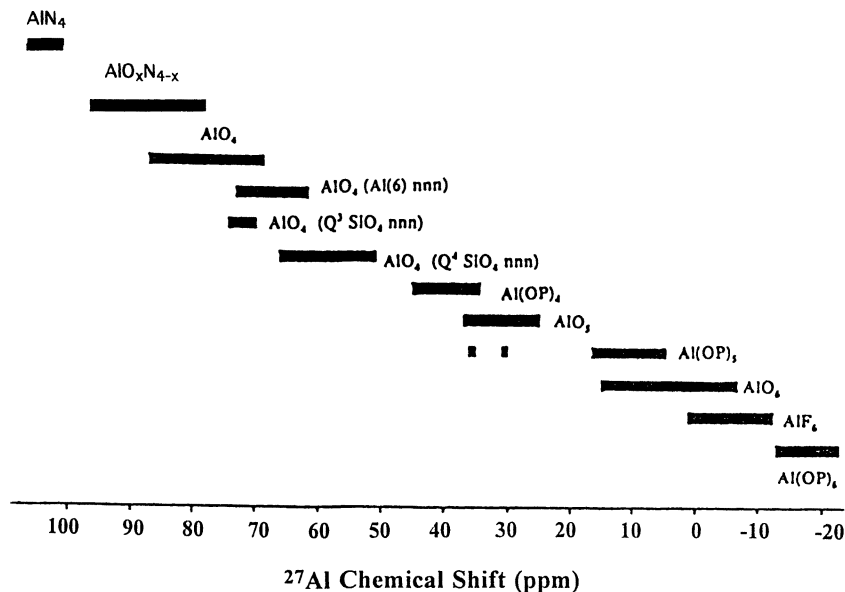


Figure 20. Relationship between solid-state NMR chemical shift δ (^{27}Al) and local chemical environments in aluminum-oxygen compounds, including aluminum oxides, aluminates, aluminosilicates, nitrides and oxynitrides (165, 171, 173; modified from Ref. 173).

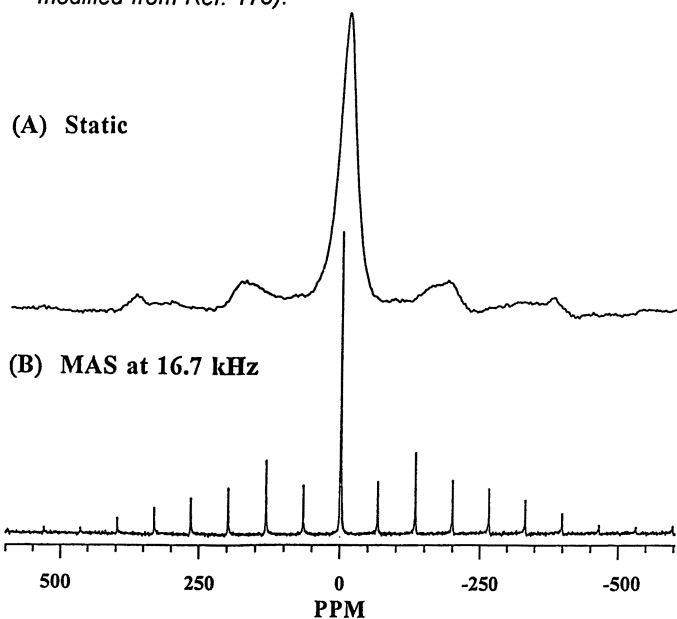


Figure 21. Experimental ^{27}Al NMR spectra of $\text{KAl}(\text{SO}_4)_2 \cdot 12\text{H}_2\text{O}$ ($C_7 = 0.4$ MHz, $\eta^a = 0.0$), under (A) static and (B) MAS at 16.7 kHz, showing the central transition and satellite transitions. Note under MAS conditions, the envelope of spinning sidebands maps out the satellite transitions and that individual lineshapes are symmetric. (J.J.Fitzgerald, unpublished results).

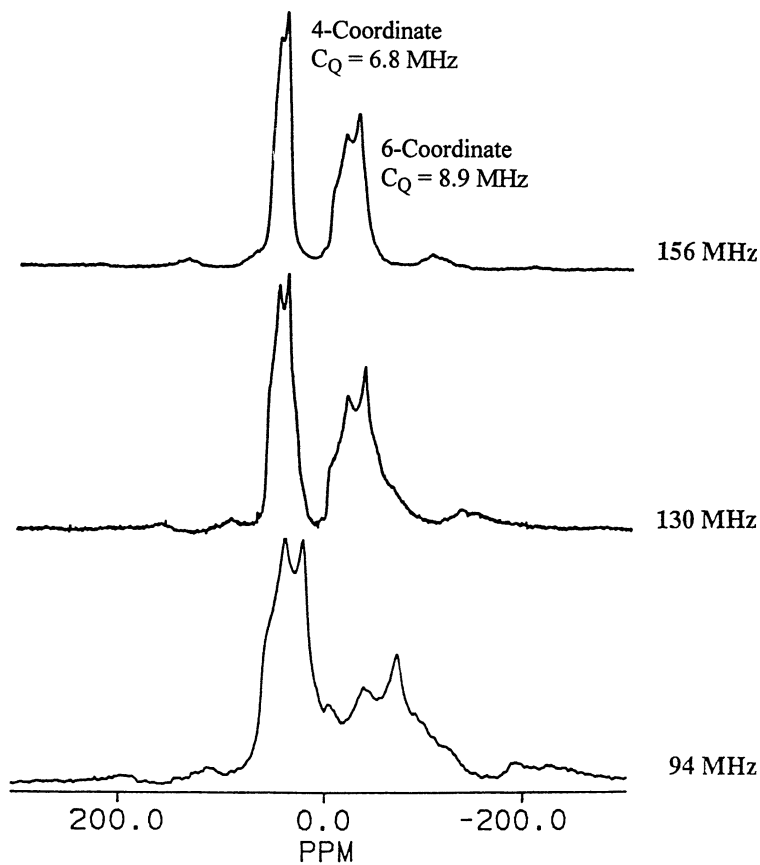


Figure 22. ^{27}Al MAS NMR spectra of the aluminosilicate Al_2SiO_5 polymorph, sillimanite, showing resolved 4- and 6-coordinate aluminum sites with different C_q values of 6.8 MHz and 8.9 MHz, respectively. (S.F. Dec and G.E. Maciel, unpublished results).

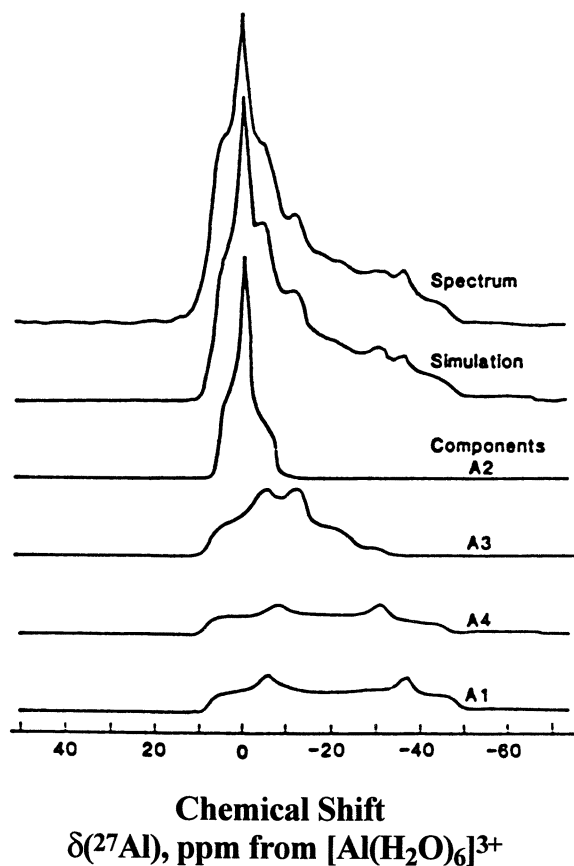
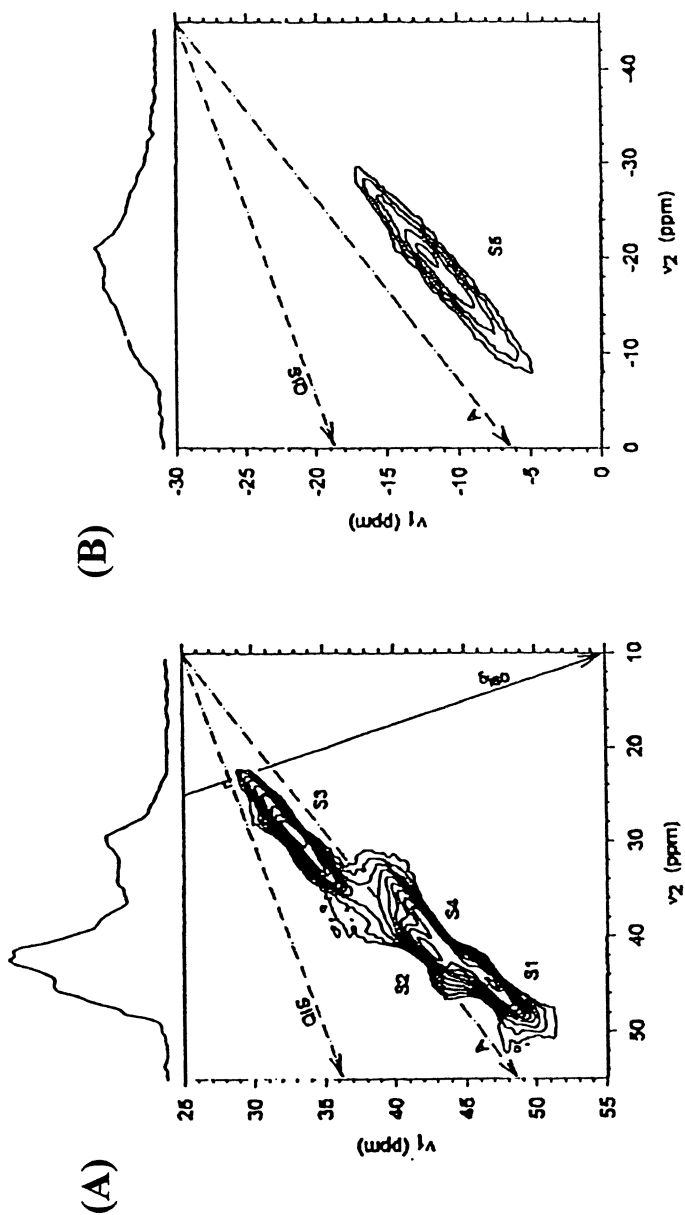


Figure 23. Experimental and simulated ^{27}Al MAS NMR spectrum obtained at 11.7 Tesla and 11.3 kHz sample spinning for the mineral kyanite (Al_2SiO_5), showing the presence of four powder patterns due to four unique aluminum sites with different C_q values (3.7 MHz (A2), 6.53 MHz (A3), 9.37 MHz (A4) and 10.03 MHz (A1)) (173).



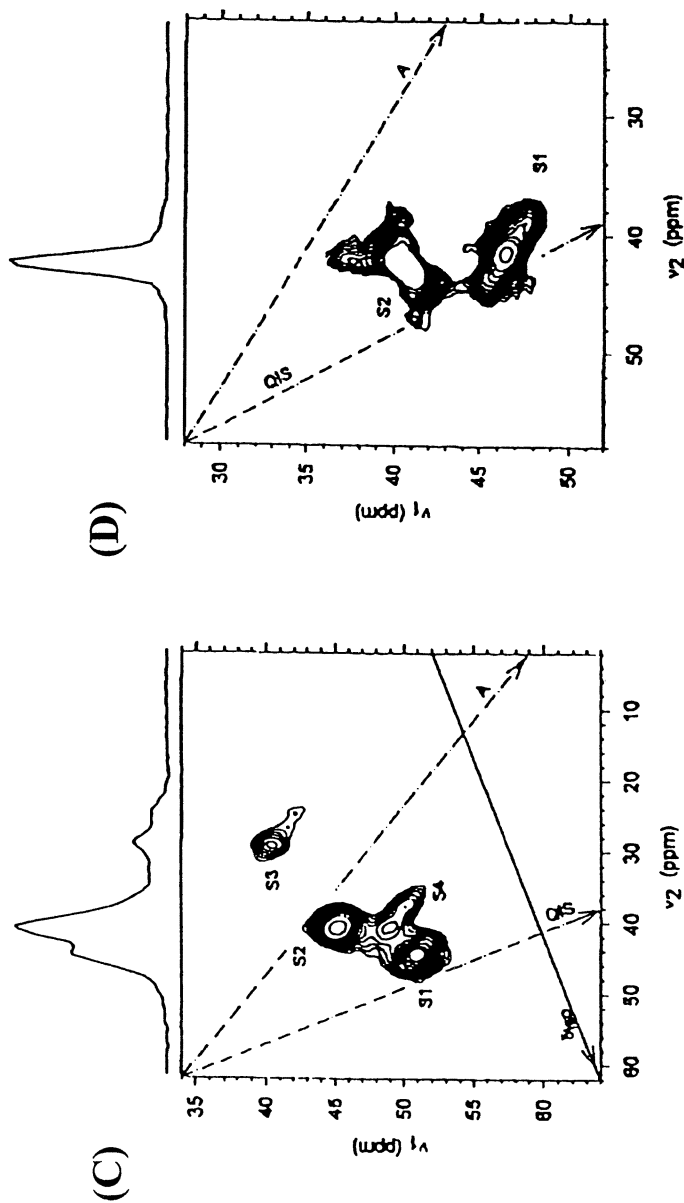


Figure 24. Two-dimensional triple quantum (2D-3Q) MAS ^{27}Al NMR spectra of AlPO-11 at 104.3 MHz: (A) region from 0 ppm to 55 ppm corresponding to four 4-coordinate (S1-S4) Al sites, and (B) region below 10 ppm corresponding to one 6-coordinate (S5) site. Quintuple quantum (2D-5Q) MAS ^{27}Al NMR spectra of AlPO-11 and VPI-5 at 104.3 MHz: (C) region of 4-coordinate (S1-S4) Al sites for AlPO-11 and (D) 4-coordinate sites (S1 and S2) for VPI-5. In all figures, the anisotropic dimension is parallel to the line labelled A (199). The structure of VPI-5 is shown in Figure 11.

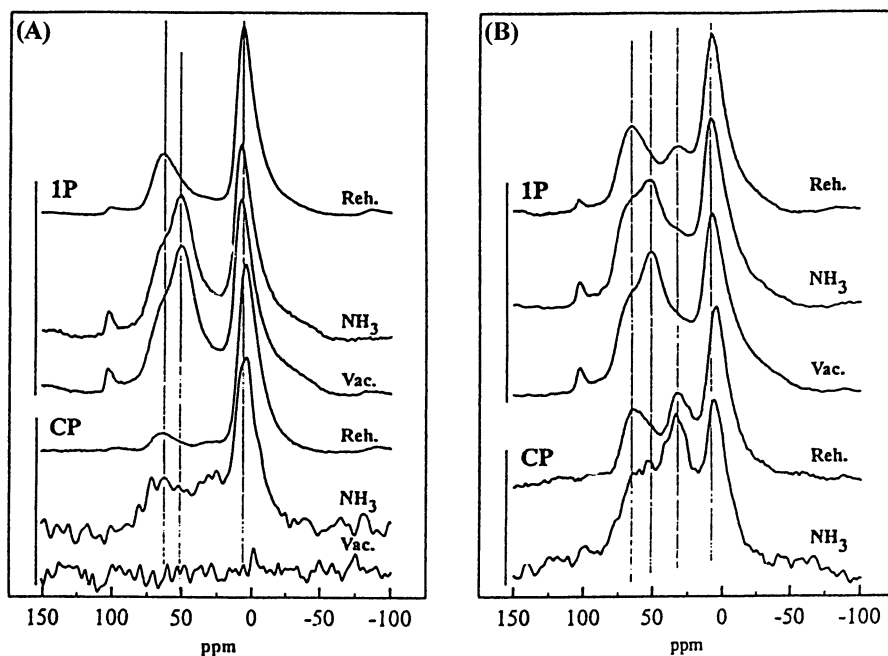


Figure 25. ^{27}Al MAS NMR spectra of (A) γ -alumina, and (B) Super5 transition alumina (2). Definitions according to Coster, Blumenfeld and Fripiat (196). The following notation is used in the figure: 1P indicates a one-pulse experiment, CP indicates for ^1H - ^{27}Al cross-polarization, Reh. represents rehydrated sample, NH_3 indicates that ammonia was adsorbed on the sample, and Vac. indicates that the sample was evacuated. A spinning sideband is also noted at 100 ppm in nearly all spectra.

are observed by single-pulse ^{27}Al MAS NMR for transition aluminas at 12 and 67 ppm and are assigned to the structural (bulk internal) six-coordinate and four-coordinate aluminums, respectively (194). For high-surface area γ -aluminas, however, ^1H - ^{27}Al CP/MAS NMR previously showed two low intensity resonances due to both surface $\text{Al}_{\text{OH}}\text{-OH}$ and $\text{Al}_{\text{Ta}}\text{-OH}$ sites (195). Recent ^1H - ^{27}Al CP/MAS NMR, however, for a high-surface area γ -alumina and a Super5 alumina containing significant amounts of 5-coordinate aluminums (196) have demonstrated that the different surface 4-, 5- and 6-coordinate Lewis acid sites (Figure 25) may be distinguished. In this work, $^{15}\text{NH}_3$ (which avoids the presence of ^{14}N quadrupolar effects) adsorbed onto the Lewis acid surface sites was used as a probe molecule to enhance the CP intensities of the surface aluminums through magnetization transfer from the ammonia protons. This work showed that dehydrated γ -alumina without adsorbed ammonia shows no ^{27}Al CP/MAS peaks, while the single pulse spectrum shows three peaks due to two four-coordinate Lewis acid sites, and one six-coordinate Lewis acid site. The sample with adsorbed ammonia also shows a fourth peak due to one five-coordinate Lewis acid site. Different C_q and η^Q values and isotropic ^{27}Al chemical shifts were determined for the four sites observed on γ -alumina and also the high 5-coordinate aluminum (Super 5) transition alumina. Single-pulse and ^{27}Al CP/MAS NMR of the γ -alumina sample following rehydration by water, however, showed three peaks due to three Lewis acid sites of different intensities, with the four-coordinate ^{27}Al peak at 50 ppm disappearing. Two types of new surface Lewis acid sites were also observed for Super 5 alumina following chemisorption of ammonia, a 4-coordinate (58 ppm) and a 5-coordinate site (40 ppm). Chemisorption of water by rehydration was also shown to convert these two sites to new 5-coordinate and 6-coordinate aluminum sites, respectively. This water readsorption process was proposed to occur by a surface reconstruction process involving rearrangement of highly distorted, aluminum-oxygen sites following chemisorption of water.

For the transition alumina, χ -alumina, formed from gibbsite, ^{27}Al MAS NMR spectra obtained using SATRAS (189) have also permitted the resolution and quantification of the relative site content and C_q and η^Q values for 4-, 5- and 6-coordinate aluminums. This work showed that while the three C_q values for the 4-, 5- and 6-coordinate aluminum sites varied from 2.7 to 5.0 MHz, three somewhat featureless resonances in the ^{27}Al MAS NMR spectra (Figures 26A through E) due to 4-, 5- and 6-coordinate aluminums could be better resolved in the satellite transition region (Figure 26F through J). Analysis of the sideband patterns allowed the following parameters to be determined: (AlO_6 , 70.0 \pm 2% content, $C_q = 3.96\pm 0.20$ MHz, $\eta^Q = 0.3$, $\delta_{\text{iso}} = 11.5\pm 0.5$ ppm; AlO_5 , 7.5 \pm 1% content, $C_q = 2.33\pm 0.23$ MHz, $\eta^Q = 0.3$, $\delta_{\text{iso}} = 38.0\pm 1.0$ ppm; and AlO_4 , 22.5 \pm 1.5% content, $C_q = 4.37\pm 0.32$ MHz, $\eta^Q = 0.3$, $\delta_{\text{iso}} = 71.5\pm 1.0$ ppm). These results, as well as those obtained from recent ^{27}Al MQMAS NMR studies (198), suggest the importance of these more advanced NMR approaches for obtaining significantly new information regarding both the internal (bulk) and surface aluminum sites in these materials. Knowledge of these surface aluminum site distributions is of critical importance for understanding the catalytic activity and catalytic support properties of transition alumina materials.

Several of the most important questions that still persist in alumina surface

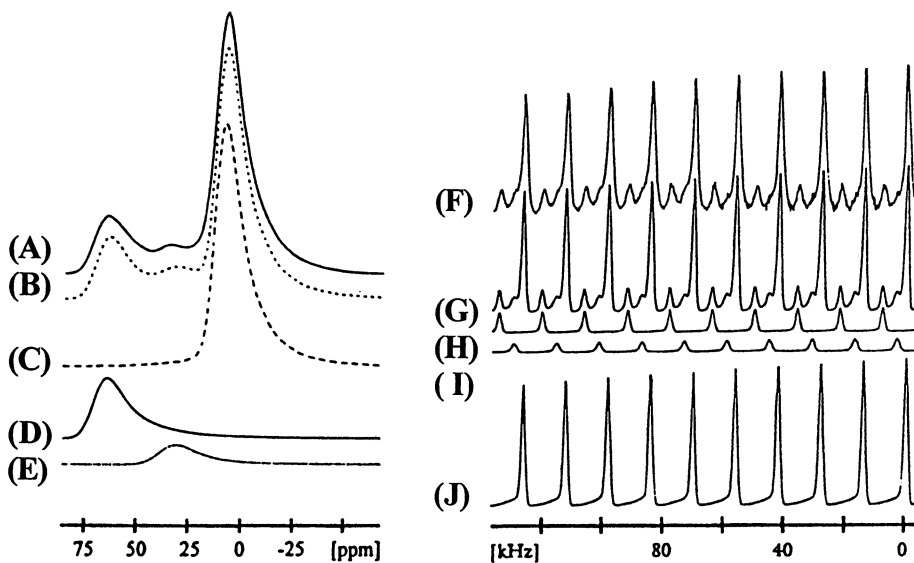


Figure 26. Satellite transition spectroscopy (SATRAS) for ^{27}Al NMR of the transition alumina, χ -alumina, showing 4-, 5- and 6-coordinate aluminum sites. Left: (A) Experimental ^{27}Al MAS spectrum of the central transition, (B) total simulated central transition MAS spectrum, and (C/D/E) simulations of various AlO_6 , AlO_4 and AlO_5 components. Right: (F) Experimental ^{27}Al MAS SATRAS spectrum, (G) simulated satellite transition SATRAS spectra, and (H/I/J) simulated spectra for various AlO_4 , AlO_5 and AlO_6 components, respectively (189).

chemistry are related to the structural and dynamical nature of the heterogeneity of the surface sites, the domain structures of 4-, 5- and 6-coordinate aluminums (190,196), and the nature of different defect sites in high-surface area aluminas. The development of more quantitative approaches to examine the "interfacial" chemistry of alumina materials in such systems and related studies of alumina composites and multilayered alumina-containing materials are needed.

Metal aluminate systems are also of technological significance and several important systems have been studied by solid-state NMR: sodium aluminate, an important intermediate formed from bauxite during the Bayer process, and the series of calcium aluminates that exist as complex and related phases found in Portland-type cements (169,185,186,188). These solid-state NMR studies have emphasized ^{27}Al MAS NMR although the use of the metal NMR nuclides such as ^{23}Na and ^{43}Ca is currently under investigation. Studies of the dehydration of a hydrated sodium aluminate, $\text{Na}_2\text{O}\cdot\text{Al}_2\text{O}_3\cdot 2\text{H}_2\text{O}$ from 100°C to 151°C using ^{23}Na and ^{27}Al MAS NMR have been reported (308). The ^{27}Al MAS NMR results indicated that sodium aluminate hydrate consists of polymeric chains of 4-coordinate aluminum-containing polyaluminate -Al-O-Al-O-Al-O- chains (with two non-bridging oxygens on Q^2 -type Al units) based on the C_q , η^q and δ_{iso} parameters ($C_q = 4.12$ MHz, $\eta^q = 0.85$ and $\delta_{\text{iso}} = 76$ ppm) obtained from the observed residual second-order quadrupolar powder pattern. The ^{27}Al NMR spectra further showed that the structural units in these linear -Al-O-Al-O-Al-O- chains are converted to the highly symmetrical, monomeric aluminate containing Q^0 -type AlO_4 sites ($C_q = 2.0$ MHz and $\delta_{\text{iso}} = 81$ ppm) following dehydration. The corresponding ^{23}Na MAS NMR spectra showed that at least three different six-coordinate sodium ion sites ($C_q = 1.30$ MHz, $\eta^q = 0.75$ and $\delta_{\text{iso}} = 14.2$ ppm; $\delta_{\text{iso}} = 7.7$ ppm; and $C_q = 1.91$ MHz, $\eta^q = 0.76$ and $\delta_{\text{iso}} = 1.9$ ppm) are associated with the non-bridging oxygens of the linear polyaluminate chains, thereby crosslinking these chains in the solid hydrate. Upon dehydration of the polyaluminate system, the three types of sodium ions are converted into a new 6-coordinate sodium ion ($C_q = 2.19$ MHz, $\eta^q = 0.65$ and $\delta_{\text{iso}} = 26.3$ ppm), which associates with the aluminate ion. In addition, a minor sodium oxide component, due to surface 5- or 6-coordinate sodiums, is also observed.

c) ***Amorphous Alumina-Silicas.*** High-surface area alumina-silica solids have extensive use as non-selective catalysts, as support and filler materials, and as reactants in the preparation of zeolitic precursors and solids. One of the earliest wide-line ^1H NMR studies of alumina-silicas (202) involved the examination of the protons associated with surface Si-OH and Al-OH Lewis and Brønsted acid sites, in addition to physisorbed and chemisorbed water. The use of ^1H , ^{27}Al and ^{29}Si MAS NMR to study the various surface and internal (including bulk) 4-coordinate silicon and 4-,5- and 6-coordinate aluminum sites in these materials has been reported (26,48,51,149,150,152,160,161,173). The catalytic surface sites of most significance are the $\text{Al}(\text{OH})^+-\text{Si}$ sites that have been assigned using ^1H CRAMPS techniques (26,48). Both Lewis acid and Brønsted acid sites have been identified and quantified by ^1H , ^{13}C and ^{15}N MAS NMR measurements with probe molecules such as ammonia, pyridine, n-butylamine, triphenylphosphine, CO, N_2O and $\text{CH}_3^{13}\text{CN}$ (51,152,203,204). Recently, ^1H - ^{29}Si HETCOR has expanded the types of NMR experiments available to

study the surface chemistry of silicas, alumina-silicas and zeolites (82). Since numerous methods of preparation are used to obtain alumina-silica materials with varying surface areas, porosities and catalytic activities, the study of both the short-range order of the bulk (internal) structural arrangements and the surface chemistry of silicas and silica-aluminas will continue.

d) Zirconium and Titanium Silicate and Phosphate Catalysts and Supports.

The potential of titania and zirconia materials as chromatographic and catalytic supports, as catalysts for hydrocarbon reactions, as components in refractory metal oxide ceramics and glasses, and as component ions in molecular sieves is currently being examined (158,246-250). Due to the high acidity of the ZrO_2 and TiO_2 surface Brønsted and Lewis acid sites, their refractory nature and their ranges of coordination numbers (four to six for titanium, and six to eight for zirconium), materials derived from these metal oxide systems are likely to provide improved selectivity, facile catalytic activities and applications in more stereochemically diverse reactions. Various titania and zirconia systems of interest include: metal oxides, surface-derivatized metal oxides, Ti-containing zeolites, zirconia/titania phosphates, and the recently discovered titanasilicate layered materials (158,238,244-250). High surface-area TiO_2 and ZrO_2 solids obtained from both sol-gel and high-temperature (fused) methods of preparation are of current interest since they can be used to obtain fine powdered nanomaterials (176,177).

The use of solid-state NMR to examine Si-O-Ti/Si-O-Zr systems, and Ti- and Zr-containing molecular sieves has been recently reported (244-250). For Si-O-Ti systems such as TiO_2 - SiO_2 gels (354), solid-state ^{17}O and ^{29}Si MAS NMR have been used to distinguish different Si- ^{17}O -Si, Si- ^{17}O -Ti and Ti- ^{17}O -Ti linkages containing oxygen and silicon atoms with different numbers and types of neighboring (actually next-nearest neighboring in the case of silicon) titanium atoms (292-294,299,300,359).

The ^{17}O MAS NMR spectra of various titania/silica gels including an immediately formed TiO_2 - SiO_2 gel (41% TiO_2), the same gel evacuated at RT, and that same SiO_2 - TiO_2 gel dehydrated at 100°C and 200°C, are shown in Figure 27. These spectra show peaks all reported as δ_{obs} values due to polymeric titanasilicate species. The ^{17}O peak at -10 ppm exhibits a residual second-order ^{17}O powder pattern and is assigned to Si- ^{17}O -Si (Q^1 silicons) groups (due to Si_2O_7 units), while the lower intensity ^{17}O resonance at 280 ppm is assigned to Si- ^{17}O -Ti linkages containing four-coordinate titanium. Several broader signals at 370 and 560 ppm are assigned to oxygens of OTi_3 and OTi_4 groups indicating more highly organized titania gel moieties that may contain poorly ordered domains of crystalline anatase, which normally crystallizes from TiO_2 gels from 300 to 350°C. The ^{17}O MAS NMR spectra of gels dehydrated at temperatures above 350°C (not shown) show increases in the intensities of the 370 and 560 ppm resonances assigned to the OTi_3 and OTi_4 moieties resulting from the initial formation of crystalline anatase. The decrease in the intensity of the Ti- ^{17}O -Si signal observed is a consequence of titanasilicate gel reorganization processes that occur during the higher temperature gel-crystallization. While more detailed investigations are needed, these studies provide important direction for future studies of the use of titanasilicate (and zircosilicate) sol-gel systems as precursors of

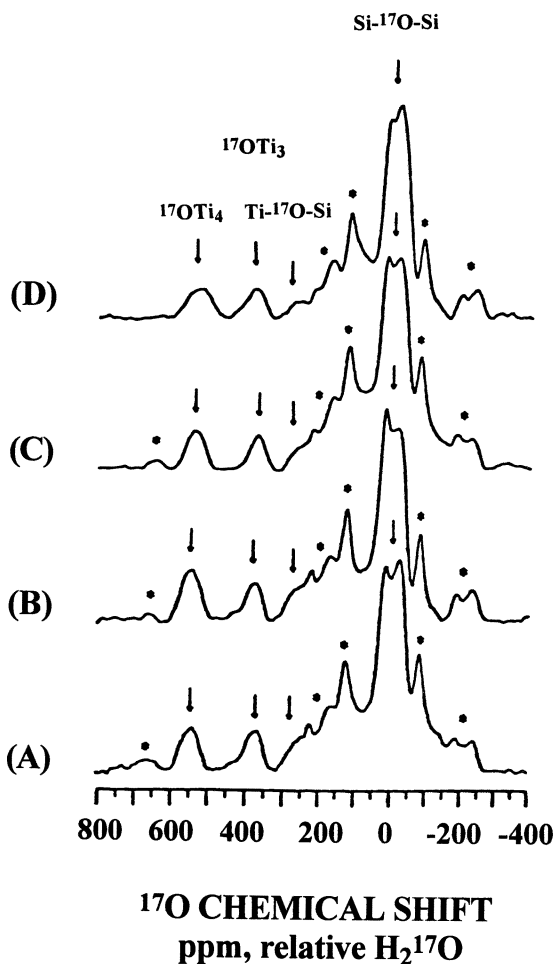


Figure 27. ¹⁷O MAS NMR of titania-silica gel (41 wt% TiO₂) following (A) immediate reaction, (B) dehydration under vacuum, (C) heating at 100°C and (D) heating at 200°C. ¹⁷O NMR resonances due to Si-¹⁷O-Si, Si-¹⁷O-Ti, ¹⁷OTi₃ and ¹⁷OTi₄ moieties are observed. Above 350°C, the intensity of the ¹⁷OTi₃ and the ¹⁷OTi₄ resonances increases as anatase crystallization is initiated (359).

titanosilicate crystalline catalytic materials and numerous complex titania-based ceramic and thin film electronic materials (244,245,248,256).

The recently discovered layered titanosilicates, which contain 5-coordinate titanium-oxygen sites involved in Ti-O-Si linkages to silicate chains (248), are important new catalytic oxidation materials that are readily amenable to both ^{17}O and ^{29}Si MAS NMR studies. The newest developments in the preparation of high-surface area titania and zirconia materials will also require substantial development of selective and quantitative ^1H and ^{17}O MAS NMR approaches to examine their complex surface chemistry. Similar NMR studies of surface-derivatized titanium and zirconium oxides used as chromatographic supports for enzyme separations and other biological separations are also needed.

e) **Vanadia-Containing Catalysts.** Vanadia is a common component of multicomponent metal oxide catalysts that are prepared by the deposition of layers of metal oxides on supports such as silica, alumina and titania. Vanadium oxides supported on titania, for example, are superior catalysts to unsupported V_2O_5 for the selective oxidation of hydrocarbons. Examples of such catalytic systems include: 1) the use of potassium vanadium (V) oxides on silica to oxidize SO_2 to sulfuric acid, 2) vanadia phosphate catalysts used for the conversion of butane to maleic anhydride, and 3) $\text{Bi}_2\text{O}_3\text{-V}_2\text{O}_5$ catalysts used for the oxidation of methanol to formaldehyde. Because these vanadia catalytic materials are redox catalysts, NMR investigations can be severely limited or at least complicated by the occurrence of paramagnetic vanadium oxidation states. Solid-state MAS NMR spectroscopic studies of these vanadia materials have been investigated to some extent (207-212), and have been recently reviewed (207,211).

Such solid-state NMR investigations often require multidisciplinary materials characterization techniques that address and complement NMR information. For example, the determination of the composition and phases present is usually obtained by XRD analysis. The site specific characterization of the local coordination number and chemical environment of the metal ion and oxide sites, the oxidation states of the metal ion, and their internal (bulk) sites often requires both solid-state NMR and EPR spectroscopy. The identification of the content and nature of defect sites, the presence of dopant ions and the structural characteristics of highly-distorted surface sites benefits from a combination of NMR, EPR, high-vacuum surface XPS and EXAFS, x-ray fluorescence, and elemental chemical analyses.

Solid-state MAS NMR, however, offers unique capabilities to obtain information relevant to many of these questions, since various NMR parameters may be related to local site connectivities, coordination numbers, bond lengths and angles, and various intermolecular chemical bonding modes. Most importantly, the NMR signal intensity is generally proportional to the concentration of observable metal oxide species under appropriate NMR experimental conditions. For example, to obtain structural information about V(V) sites in vanadia catalysts, static ^{51}V NMR has been used to study various V(V) compounds (Figure 28) as models for vanadia catalytic sites where the vanadium coordination number and site geometry were related to the measured anisotropic chemical shift parameter $\Delta\delta(^{51}\text{V})$ (207,210,212) and to some extent, the calculated quadrupolar C_q and η^Q values of the ^{51}V sites (207-212).

A detailed chemical understanding of vanadium catalysts, including the SO_2 -

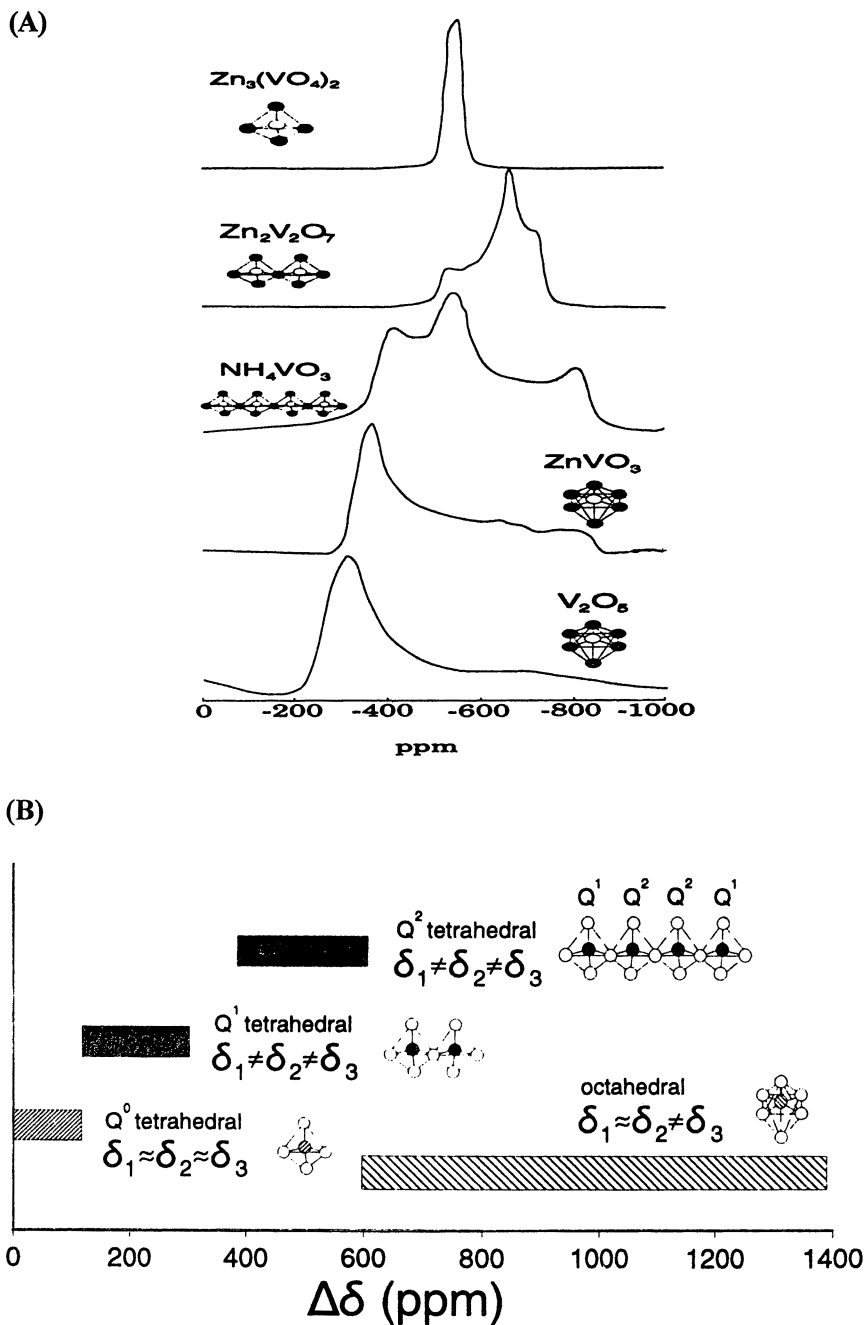


Figure 28. Static ^{51}V NMR spectra (A) of various vanadium systems with different coordination numbers of four, five and six, and the related VO_x structural connectivities. The observed range of $\Delta\delta$ values (B) shows that different anisotropic chemical shifts are observed for different geometries of the vanadium (V) sites (212).

vanadia catalysts used to oxidize sulfur dioxide to sulfuric acid, has recently been obtained using ^{51}V MAS NMR (210,211). For example, the potassium vanadate catalysts of the K/V mole ratio 3/1 are a typical example of catalytic materials that are deposited on surfaces such as SiO_2 , followed by drying and calcination at 500°C to form thin films of metal oxide surfaces. While evidence from wide-line ^{51}V NMR for square planar 5-coordinate vanadium in these materials has been obtained (207-212), the complicated NMR lineshapes observed for these systems are likely due to unpaired electron effects.

Another interesting vanadium (IV/V) oxide system is the $\text{V}(\text{PO}_4)$ catalysts of P/V mole ratios from 0.9 to 1.1 that have been shown by ^{51}V MAS NMR and EPR to contain both +4 and +5 vanadium internal sites (207). Species of structural formulas such as $(\text{VO})_2\text{P}_2\text{O}_7$ and $\text{VO}(\text{PO}_4)$ have been implicated in these catalytic reactions.

For Bi/V catalysts of Bi/V mole ratios from 60/1 to 1/1, ^{51}V MAS NMR has also been used to identify various surface vanadate species (209). The presence of several bismuth/vanadium-oxygen phases including BiVO_4 (monoclinic), $\text{Bi}_4\text{V}_2\text{O}_{11}$ (orthorhombic), $\text{Bi}_{12}\text{V}_2\text{O}_{23}$ (triclinic), $\text{Bi}_{20}\text{V}_2\text{O}_{35}$ (fcc) and $\text{Bi}_{23}\text{VO}_{40}$ (bcc) containing four-coordinate vanadium has been proposed based on ^{51}V MAS NMR results. Each of these five bismuth vanadate phases was found to exhibit a characteristic NMR spectrum indicating a possible 4-coordinate vanadium site. The local vanadium coordination environment (coordination number and symmetry) in these different phases was found to affect the isotropic ^{51}V chemical shifts and residual second-order quadrupolar broadening observed for the ^{51}V NMR resonances.

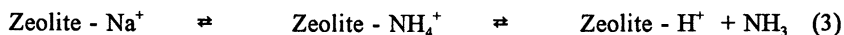
Related ^{51}V NMR studies have also proved useful to distinguish differences in the vanadium surface species formed following deposition of V_2O_5 on various metal oxide supports such as alumina, silica and titania (208). The existence of two types of four-coordinate V(V) surface sites were proposed to form from V_2O_5 following surface deposition and thermal dehydration reactions of the initial six-coordinate V(V) surface species associated with the deposited V_2O_5 catalysts.

f) Molybdena-Containing Catalysts. Several molybdena-containing catalysts have been recently studied using solid-state ^{95}Mo NMR, including V/Mo mixed oxides supported on silica that are used to oxidize acrolein to acrylic acid. In these systems, the catalytic activity depends on the variable oxidation states of both the V and Mo sites, as well as their local coordination environments (both 4- and 6-coordinate Mo). Bi_2O_3 - MoO_3 catalysts are used for ammonia oxidation, and MoO_3 supported on alumina is used for the hydrodesulfurization of organics such as thiophene. For the latter system, a range of mixed $\text{MoO}_x\text{S}_{4-x}$ species containing molybdenum in both Mo(VI) and Mo(IV) oxidation states has been identified by ^{95}Mo NMR using both static-echo and MAS-echo NMR techniques (213). To aid in the interpretation of ^{95}Mo MAS NMR of these catalysts, various four-coordinate MO_4 sites and six-coordinate MoO_6 sites in model complexes such as dimolybdate(VI) and heptamolybdate(VI) anionic species have been characterized in detail (214). These studies have been used to obtain a correlation between the ^{95}Mo chemical shifts and the local molybdenum (VI) chemical environments for surface and internal (bulk) sites in several reduced sulfided catalysts.

2. Open Framework and Layered Materials. The inorganic materials most

widely studied by solid-state NMR are open framework zeolites, the related aluminophosphate (AlPO) systems, layered clays and pillared clays (11,62,125,136-140,144,149-152,160-163,223,236-240). The predominant use of solid-state NMR to examine these systems is due to the widespread applicability of ^{27}Al , ^{29}Si and ^{31}P MAS NMR to obtain detailed structural information not achievable by techniques such as powder x-ray diffraction.

a) Zeolites. Zeolites comprise an enormous class of complex three-dimensional aluminosilicate materials that consist of a range of variable-sized void spaces or cavities (4Å to 12Å). The cavities confer steric exclusion capabilities on these materials, in addition to providing sites for acidic catalysis when aluminums are substituted for silicons in the lattice framework of these materials. Zeolites are three-dimensional materials of the general formula, $\text{M}^{\text{x}+}_{y/x}[(\text{AlO}_2)_y(\text{SiO}_2)_{1-y}] \cdot n\text{H}_2\text{O}$, where the differences in charge between the Al and Si requires the presence of extra-lattice metal ions ($\text{M}^{\text{x}+}$) to obtain electroneutrality (133-139). A single positive charge is required for every aluminum atom that is substituted for a silicon atom. Normally, water is also present, but not as a framework lattice component. The acid form of most zeolites is the catalytic form, and is usually prepared by a two-step exchange reaction of the cationic form of the zeolites,



The shape and size selectivity of zeolites is derived from their unique framework structures. The three most important zeolites, Zeolite A, X and Y, are shown in Figure 29, together with the truncated octahedron or sodalite cage subunit, sodalite, and a more complex zeolite, ZSM-5, that is an important catalyst for the commercial conversion of methanol to gasoline. The structure of zeolites formed from sodalite subunits illustrates many of the important structural features common to zeolites, including both small (4.1Å for Zeolite A) and large cavities as shown in Figure 29 (11-13,133-139,141,163,223). Zeolites such as ZSM-5 and ZSM-11, comprising pentasil structural units, by contrast, are more complex in structure and have additional selected catalytic features.

Solid-state ^{29}Si MAS NMR studies of the silicon sites in zeolites have provided detailed information about their second-nearest neighbor atoms (Table VI and Figure 5), and together with ^{27}Al NMR allow the determination of the silicon/aluminum ratios and non-network aluminums in these materials. Solid-state MAS NMR approaches have also been used to aid in detailing the catalytic surface and cavity sites, to elucidate the mechanisms of dealumination, and to describe both reaction dynamics and proximity information related to important zeolite-substrate interactions (136-138,152,160,161,163,223). Extensive reviews of the use of solid-state NMR techniques and approaches to examine important structural and dynamical questions in zeolite research have been published (11-13,137,152,163,223), and the recent use of two-dimensional solid-state NMR to provide detailed information regarding the atomic connectivities in these complex zeolite materials has also been reviewed (67,136-139). For example, COSY experiments on ZSM-12 (Figure 13) show the connectivity interrelationships between the seven unique tetrahedral silicon sites in this

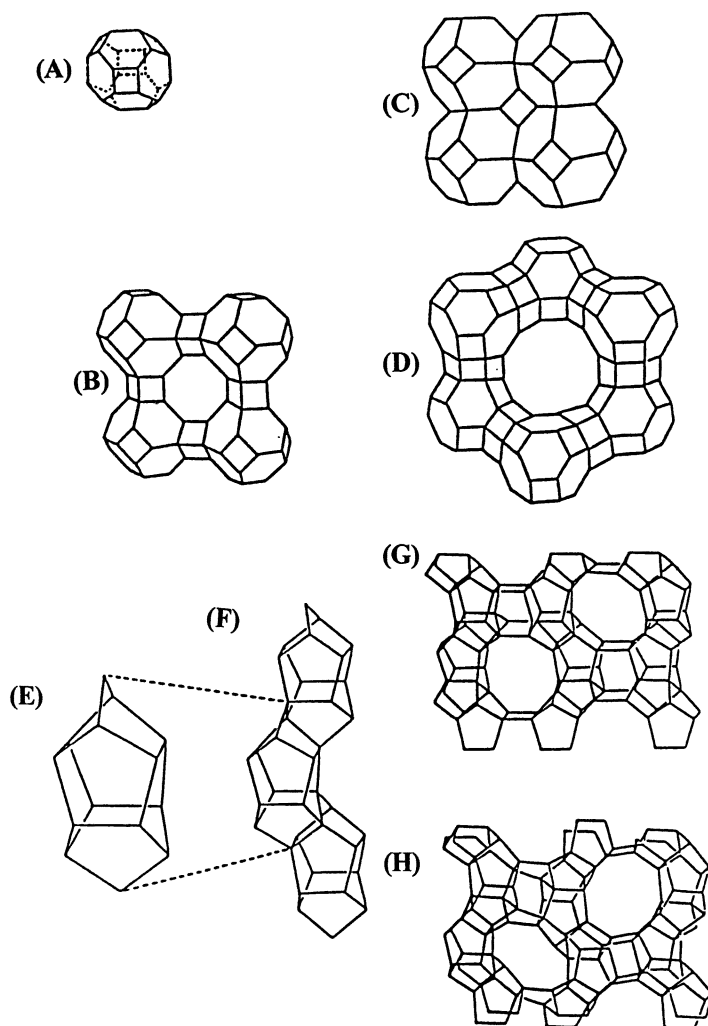


Figure 29. Structural depiction of important zeolite materials, showing (A) truncated octahedron or sodalite subunit cage with faces of four- and six-membered Si rings, (B) joining of four sodalite units to form basic structure of Zeolite A (8-membered ring openings are 4.1 Å for Na⁺, with the size being dependent on counter cation), (C) sodalite lattice structure with four truncated octahedrons, (D) Zeolites X and Y (faujasitic zeolites of different Si/Al ratios), with a large central cavity. The pentasil unit (E) containing five-membered Si rings can be joined together to form interlocking chains (F). Zeolites ZSM-11 (G) and ZSM-5 (H) consist of pentasil units (10-membered rings of 5.6 Å) (13,133-137).

asymmetric zeolite (87,137), while INADEQUATE results have been obtained for ZSM-5 (136-139,223) to support the silicon atom connectivities for this system.

b) Clays and Alumina-Silica Minerals. Solid-state ^{27}Al and ^{29}Si MAS NMR of numerous clay minerals and other model alumina/silica minerals with known crystal structures have been prevalent in the literature (140-142,149-151,155-159,172,175,218-222,232-235). These investigations have not only helped to establish important relationships between molecular structure and the NMR chemical shifts for aluminum and silicon sites but have also provided a basis for more detailed NMR studies of layered materials of unknown structure. The study of clay minerals has been particularly intriguing due to their complex three-dimensional nature. (215). Several solid-state ^{29}Si MAS NMR studies of layered Si/Al minerals have shown correlations between the $\delta(^{29}\text{Si})$ and the structural parameters (mean secant (Si-O-Si bond angles), sum of cation-oxygen bond strengths, and mean Si-O bond lengths) (155,159). Recent solid-state NMR studies, however, have examined chemical modifications of clay minerals and high temperature thermally-induced transformation processes (158,219-223,234).

Solid-state ^1H , ^{27}Al and ^{29}Si MAS NMR studies of layered kaolinite (Figure 6B), montmorillonite, pyrophyllite and mica, for example, illustrate some of the relevant chemical and structural issues that have been addressed using multinuclear NMR approaches (23,24,155-159,172,173,175,216,217,219-221,234). For example, both kaolinite and pyrophyllite represent 1:1 and 2:1 Si/Al layered materials with the silicate layer(s) containing 4-coordinate Si sites that are attached by Si-O-Al linkages to the aluminum hydroxide layers containing 6-coordinate aluminums. The solid-state thermally-induced conversions of these two clays have been extensively examined by solid-state ^1H CRAMPS, ^{27}Al and ^{29}Si MAS NMR (23,24,158,172,175,219-222), with the ^{27}Al MAS NMR measurements requiring the highest available field to minimize second-order quadrupolar line broadening (see Eq. 1). Recent studies (167,207-211) have suggested that five-coordinate aluminums are formed in the intermediate temperature regions for these clays as illustrated in Figure 6A for kaolinite (23,24). Extensive ^1H , ^{27}Al and ^{29}Si MAS NMR studies have also been reported for high temperature formation of refractory mixtures of transition aluminas, amorphous silicas and mullite obtained from layered clays and for acid dealumination used to form kaolinite-derived acidic catalysts (23,172,220,221).

In addition to these ^{27}Al and ^{29}Si MAS NMR studies of layered Si/Al clays, static ^{17}O MAS NMR measurements (305) of ^{17}O -labelled crystalline talc ($\text{Mg}_3\text{Si}_4\text{O}_{10}(\text{OH})_2$) have shown the usefulness of ^{17}O NMR to probe important structural issues for layered materials. Talc is a 2:1 Si/Mg layered material (similar to the 2:1 Si/Al-containing pyrophyllite) that consists of a six-coordinate magnesium in a brucite-like $\text{Mg}(\text{OH})_2$ layer sandwiched between two 4-coordinate silicon-containing silicate layers. The Si-O-Mg, Si-O-Si and Mg-O-H units exist in a 2:3:1 ratio. The ^{17}O MAS NMR spectrum and its corresponding simulated spectral components shown in Figure 30 indicate the presence of three ^{17}O signals due to Si- ^{17}O -Mg units ($C_q = 3.2$ MHz and $\delta_{\text{iso}} = 40$ ppm), Si- ^{17}O -Si units ($C_q = 5.8$ MHz and $\delta_{\text{iso}} = 50$ ppm) and Mg- ^{17}O -H units ($C_q = 7.3$ MHz and $\delta_{\text{iso}} = 0$ ppm) in the appropriate 2:3:1 ratio. For montmorillonite and kaolinite, both ^{113}Cd and ^{207}Pb NMR are likely to be highly useful to study heavy

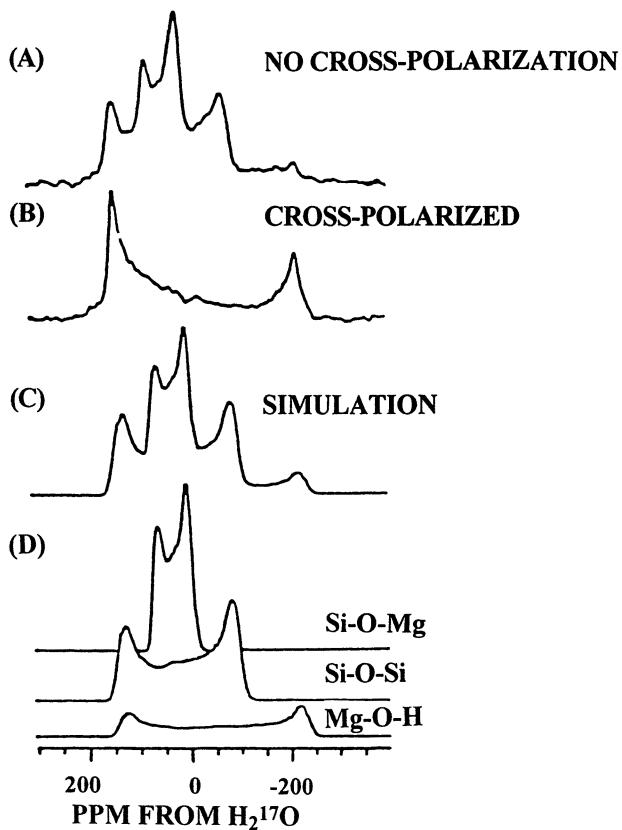


Figure 30. Static ^{17}O NMR spectra of isotopically labeled polycrystalline talc, $\text{Mg}_3\text{Si}_4\text{O}_{10}(\text{OH})_2$: (A) ^{17}O direct excitation, (B) ^1H - ^{17}O CP, (C) total simulation spectrum, and (D) simulations of spectral components for Si-O-Si, Si-O-Mg and Mg-O-H groups (305).

metal pollutant ions (Cd^{2+} and Pb^{2+}) adsorbed onto clays and clay-containing soils (158,231-234,302,313,314). ^{113}Cd NMR investigations (231,234) have been reported for Cd^{2+} ion adsorbed onto several clays and show the presence of two types of adsorbed cadmium species. Additionally, ^{13}C CP/MAS NMR (57,158,233) has been particularly useful to examine the sorption and/or intercalation of various organics onto or within the interlayer region of various geochemically important clay materials found in polluted soils. The binding of cesium ion to montmorillonite and other layered minerals has also been examined by ^{133}Cs NMR (234,235), thus providing information on the dynamics of metal ion binding and the nature of the interlayer and surface adsorbed Cs^+ ion species. Such species are of significance in understanding $^{133}\text{Cs}^+$ and $^{90}\text{Sr}^{2+}$ ion radionuclides in contaminated soils. Pillared kaolinite and montmorillonite-derived materials, where the pillared species are formed by intercalation of aqueous metal ion hydrolysis species followed by calcination of adsorbed metal oxides of titanium, aluminum and zirconium, are also important layered clay materials of catalytic interest that have been studied by solid-state NMR approaches (158,242,243).

c) *Aluminum Phosphates (AIPO)* AIPOs represent a unique class of molecular sieve analogs of zeolites, where both 4-coordinate and 6-coordinate aluminum atoms are present together with 4-coordinate phosphate lattice units (236-241). These molecular sieves can have very large cavities (12Å to 15Å) compared to many zeolites, and have unique catalytic activities. ^{27}Al and ^{31}P MAS NMR have been particularly useful to study these systems because of the high NMR receptivities of these nuclides (Tables II and III). Recent ^{27}Al - ^{31}P CP/MAS NMR experiments (60,61) have been used to obtain atomic connectivity information for materials such as VPI-5 (see structure in Figure 11E). Detailed triple- and quintuple-quantum MAS (3Q-MAS and 5Q-MAS) studies of the zeolitic materials AIPO-11 and VPI-5, have also been reported (199,200). These MQMAS studies (199,200) reported several different aluminum sites that were undetected or only partially resolved by either MAS or DOR NMR measurements (see Figures 24A thru 24D). In the case of AIPO-11, which contains four different 4-coordinate and one 6-coordinate aluminum site, only three of the 4-coordinate sites had been observed by ^{27}Al MAS and DOR NMR. The 3Q-MAS ^{27}Al NMR spectrum of AIPO-11 given in Figure 24A shows complete resolution of all four 4-coordinate Al sites and the 6-coordinate Al site (Figure 24B), as does the related 5Q-MAS spectrum of the AIPO-11 (Figure 24C). For VPI-5, which contains two different 4-coordinate (Al-1 and Al-2) sites that are located between the two four-membered rings and the six-membered ring (see Figure 11E), both the 3Q-MAS and DOR ^{27}Al NMR spectra provide complete resolution (Figure 11E).

In addition to these MQMAS studies, ^{27}Al MQMAS NMR has been recently used to identify quite similar four-coordinate AlO_4 sites that differ to only a minor extent in both their isotropic chemical shifts and quadrupole coupling constants for the microporous AIPO-like inorganic-organic composite aluminum methylphosphonate ($\text{Al}(\text{MepO}-\beta)$) (201). In $\text{Al}(\text{MepO}-\beta)$, the three-dimensional structure is made up of fused 4-membered rings composed of 4-coordinate aluminums and phosphonate groups that form unidimensional 18-membered ring openings similar to several AIPOs. The 3Q-MAS ^{27}Al NMR spectrum of $\text{Al}(\text{MepO}-\beta)$ shows resolution of three structurally

similar 4-coordinate Al sites designated S1, S2 and S3, with their calculated isotropic chemical shifts and quadrupolar coupling constants being quite similar: S3, $\delta_{\text{iso}} = 42.3$ ppm, $C_q = 1.6\text{-}1.9$ MHz; S2, $\delta_{\text{iso}} = 42.8$ ppm, $C_q = 1.7\text{-}2.0$ MHz; and S1, $\delta_{\text{iso}} = 45$ ppm, $C_q = 2.2\text{-}2.5$ MHz.

d) Zirconium Phosphates. Zirconium phosphates and titanium phosphates form three-dimensional layered materials of the formula $M(\text{HPO}_4)_2 \cdot n\text{H}_2\text{O}$ with different metal ion-phosphate configurations (158). These materials exist in both amorphous and crystalline forms, the latter having layered structures with heterogeneous catalytic activity. The catalytic properties of these materials are determined by their methods of synthesis, structures, crystallinity and surface areas. Three forms of zirconium phosphates with different structures and degrees of hydration exist, including: $\text{Zr}(\text{HPO}_4)_2 \cdot 2\text{H}_2\text{O}$, $\text{Zr}(\text{HPO}_4)_2 \cdot \text{H}_2\text{O}$ and anhydrous $\text{Zr}(\text{HPO}_4)_2$. The structure of $\alpha\text{-Zr}(\text{HPO}_4)_2 \cdot 2\text{H}_2\text{O}$, for example, includes hydrogen bonding between P-OH groups of different layers, with these groups also being coordinated to the zirconium (IV) ion. Several of these phases exhibit ion exchange capabilities and show similar structural features to those of the 2:1 layered clays (244,245). Structural studies of the thermal stability of these materials by ^{31}P MAS NMR have been used to obtain information regarding the identity and content of the phosphate structural units in the $\alpha\text{-}$ and $\epsilon\text{-}$ forms of crystalline zirconium phosphates and zirconium phosphate gel phases (205,206). For example, the ^{31}P chemical shifts observed for all three systems indicate that the structurally different phosphate groups in each of these systems coordinate in various configurations with the zirconium (IV) ion. $^1\text{H}\text{-}^{31}\text{P}$ CP/MAS and ^{31}P MAS NMR show that heating of these materials at 773 K leads to condensation of acidic P-OH groups that comprise the zirconium hydrogen phosphate layers. This condensation process at intermediate temperatures is accompanied by an increase in the interlayer separation of the resulting zirconium phosphate layers. At 1323 K, these different intermediate zirconium phosphates are converted by further dehydration to ZrP materials containing linear or bent pyrophosphate (P-O-P containing Q^1) units with observed ^{31}P chemical shifts of -35, -37, -40 and -43 ppm, similar to the ^{31}P chemical shifts observed for the high temperature ZrP_2O_7 phase. This latter material consists of multiple pyrophosphate units due to different *cis* and *trans* forms of linear or bent P-O-P moieties. These stereochemically different pyrophosphate groups found in the high temperature ZrP_2O_7 phase are useful models for the catalytically active surface species formed on the high-temperature ZrP-materials obtained from the three precursor zirconium phosphate materials studied.

In addition to these studies of the dehydration of layered zirconium phosphate catalytic precursors, ^{31}P MAS NMR of zirconium phosphates containing phosphonates as well as amine intercalated $\text{Zr}(\text{PO}_4)_2$ systems have also been reported (158,237,238). The NMR results were consistent with the presence of $\text{P}(\text{OZr})_4$ groups and $\text{P}(\text{OZr})_2(\text{OH})_2$ units in the zirconium phosphate phase of these phosphonate and amine intercalated materials.

3. Ceramics and Glass Materials. Ceramics are a diverse group of technologically important inorganic materials that include traditional materials such as amorphous glasses, cements and structural clay materials, and newer, modern ceramics used as high performance thermal insulating refractories, structural

composites, cutting tools and electronic and optical materials (235-251,265,266). These materials are currently synthesized, processed and fabricated by complex high temperature or pressure reactions, including sol-gel or precursor syntheses, sintering, high-temperature reaction bonding, hot-pressing, hot-isostatic pressing (HIPing), and sintered reaction-bonding (SRB) processes. The surface and interfacial chemistry of ceramics is of importance during their synthesis and processing and also contributes to their stability under extreme (e.g., oxidizing, high-temperature) environments. Recent developments in ceramics require a multidisciplinary approach to study their synthesis, structural features, and processing as these relate to their mechanical, thermal and other functional properties.

Solid-state NMR studies of six major classes of modern inorganic ceramics are considered here in relationship to the types of chemical and structural information obtained (263-267,331,339):

1. oxide ceramics of silica, alumina, beryllia, magnesia, phosphates and borates,
2. oxide ceramics of the transition metals including vanadates, titanates, zirconates, niobates, tantalates and stannates,
3. borides, carbides and nitrides, including the complex SiAlON ceramics,
4. semiconductors, including silicon doped with phosphorus, arsenic, etc.,
5. superconductors such as the Y-Ba-Cu oxides and related Hg-based high-T_c materials, and
6. amorphous glasses of phosphates, silicates, borates and aluminosilicates.

In addition, recent aspects of NMR studies of various Si/Al cements, Al/P adhesives and biomaterials will be discussed in a subsequent section.

The nature of the "ceramic bond" is often partially ionic and typical anions include boride, carbide and nitride. Cations that are significant components of modern ceramics include: 1) the main group elements of phosphorus, silicon and aluminum, 2) the early transition metal elements yttrium, titanium, zirconium, vanadium, niobium, and tantalum, and 3) the later transition metal elements chromium, iron, nickel and copper. Alkali and alkaline earth metals such as lithium, sodium, potassium, beryllium, calcium and magnesium play significant roles as cations in the oxide-type crystalline ceramic lattices and in amorphous, glassy materials. All of these anionic and cationic elements have NMR observable nuclei, although many are quadrupolar (²⁷Al, ^{47,49}Ti, ⁶³Cu, ⁹¹Zr, ⁹³Nb) and others have multiple oxidation states, some of which are paramagnetic. Both these factors lead to significant line broadening as well as other complications in the NMR spectra.

Three strategies have emerged in solid-state NMR studies of ceramics, 1) solid-state static, MAS and CP/MAS NMR studies of the NMR behavior and structural chemistry of model systems and a broad range of ceramics, 2) development of new

NMR techniques to examine the dynamics and connectivities of these materials during synthesis and after various reactions, and 3) development of novel NMR techniques to explore impurities, defect sites, phase boundaries, and surface and interfacial interactions in multiphase systems.

a) **Refractory Metal Oxides.** Metal oxides and refractory mixed metal oxide ceramics such as aluminas and silicas, various Si/Al crystalline materials, aluminum phosphates, and various borates generally contain one or several NMR observable nuclides such as $^{10,11}\text{B}$, ^{27}Al , ^{29}Si and ^{31}P . Solid-state MAS NMR studies have been performed on many of these systems, including gamma-alumina (a spinel structure), corundum, boron oxide, various SiO_2 polymorphs, aluminum phosphates (berlinite), high temperature silicates, yttrium and magnesium aluminates, and various titanium and zirconium oxide phases.

The use of ^{17}O -labelling for ^{17}O MAS and DAS NMR has been particularly illuminating for obtaining information about the important structural features of many refractory metal oxides (193,282,290,291,293,382). Isotopic ^{17}O enrichment is normally carried out using solid-state reactions with gaseous $^{17}\text{O}_2$, or by aqueous solution metal hydrolysis reactions with H_2^{17}O , followed by a higher temperature dehydration (182,261,282,291,301,305). The wide range of chemical shifts ($\delta(^{17}\text{O})$) observed for binary and ternary metal oxides, plus the larger chemical shift regions observed for oxygens in copper oxides and superconductors, are summarized in Table VII. The nearly 700 ppm chemical shift range (excluding the chemical shifts for the paramagnetically shifted CuO(II) and $\text{Cu}_2\text{O(I)}$ oxygen resonances) reported to date suggests that ^{17}O NMR has enormous potential to study important structural questions and also to address important issues relating to chemical reactivities, solid-state rearrangements and exchange processes for complex metal oxide systems.

^{17}O MAS NMR studies of binary metal oxides have shown several general correlations: 1) the ^{17}O NMR chemical shifts increase with decreasing ionic radius for isoelectronic metal oxides of Groups 5-8 and selected oxyanions (282,291), 2) the isotropic ^{17}O chemical shifts increase with increasing oxygen coordination numbers for oxygens in aluminum oxides (193,382), and 3) the ^{17}O NMR quadrupolar parameter C_q decreases as the percentage of ionic bonding increases, with covalent X-O systems (C-O, P-O) having large C_q values (10 to 15 MHz), intermediate bonding systems (Si-O, B-O) having C_q values from 4 to 6 MHz, and ionic metal ion systems (Mg-O, Al-O, Zn-O) having very small C_q values (1 to 3.5 MHz) (291). For more complex metal oxides of ABO_3 stoichiometry and various oxyanions, few correlations have been established due to the diversity of next-nearest neighbor metal ions (A/B), significant variations in next-nearest neighbor M-O bond lengths, and variations in bond angles and site symmetry, particularly for the more complex lattice structures (358). In general, low C_q values (1-3 MHz) and large chemical shifts in the 300 ppm to 600 ppm range are observed for oxides associated with highly ionic metal ions such titanium (IV) and zirconium (IV). Highly symmetric oxide sites in perovskite lattices have low C_q values, but structural distortions around the oxygens lead to increases in the quadrupolar coupling and thus to residual second-order quadrupolar line broadening contributions under MAS conditions. In addition, a large CSA is observed for ^{17}O resonances ($\Delta\delta = -300$ to -500 ppm) in many perovskite systems. The

Table VII. Summary of δ (^{17}O) values from ^{17}O NMR spectra of various metal oxide systems (193,290-294,382,383).

Compound	Chemical Shift (ppm)	Compound	Chemical Shift (ppm)
H_2O	0	LiNbO_3	504
BeO	26	LaAlO_3	170
ZnO	-18	Li_2TiO_3	406/372
MgO	47	CaTiO_3	448/443
SiO_2	46	SrTiO_3	465
Al_2O_3	72-79	BaTiO_3	564/523
		Li_2ZrO_3	298/280
		Na_2ZrO_3	309/286
CaO	294	CaZrO_3	336/329
SrO	390	SrZrO_3	343/340
BaO	629	BaZrO_3	376
Y_2O_3	356		
TiO_2	591	$\text{Cu}_2\text{O(I)}$	-181
CeO_2	877	CuO(II)	4500
ZrO_2	383	$\text{KCuO}_2\text{(III)}$	30
HfO_2	267/335		
$\text{YBa}_2\text{Cu}_3\text{O}_{7-x}$			
Chain Oxygens 300		Plane Oxygens 1800	

diversity of the metal-oxygen bond and large effects of local site symmetries on C_q values make such correlations ambiguous at present for a wide range of metal oxide systems. Studies of these correlations in the context of various bonding models and theoretical approaches are thus needed.

Extensive solid-state ^{17}O MAS NMR studies of only a few metal oxide systems have been reported to date, excluding the continued use of static ^{17}O NMR in relaxation studies of superconductors. For γ -alumina, for example, both MAS and static ^{17}O NMR show two peaks due to trigonal Al_3O sites and tetrahedral Al_4O sites, with ^{27}Al MAS NMR showing two resonances at 12 and 67 ppm due to both 4- and 6-coordinate aluminums (see Figure 25) (193). Recent use of ^{17}O MAS NMR to examine ternary metal oxides of the ABO_3 perovskite lattice structure has also been reported (358). Solid-state ^{17}O and ^{27}Al MAS NMR have been used to address important structural and dynamical questions regarding the cation disorder of Mg^{2+} and Al^{3+} ions in 4-coordinate and 6-coordinate cation sites in MgAl_2O_4 spinels prepared by quenching at 700°C and 1400°C (230). The normal spinel lattice structure has the site occupancy $^{[4]}\text{A}^{[6]}\text{B}_2\text{O}_4$, while an inverse spinel is $^{[4]}\text{B}^{[6]}\text{[AB]O}_4$. The ^{27}Al MAS NMR spectra of MgAl_2O_4 quenched at 700°C and 1400°C (shown in Figure 31A) indicate changes in the Al^{3+} site occupancy. Complete resolution of the 4- and 6-coordinate Al sites and quantitation measurements using short excitation pulses permitted the determination of the relative Al content for these two sites. Temperature-dependent increases in the disorder parameter x (degree of spinel inversion) were observed, where $^{[4]}(\text{A}_{1-x}\text{B}_x)^{[6]}(\text{B}_{2-x}\text{A}_x)\text{O}_4$. From the ^{27}Al MAS NMR data, $x = 0.22 \pm 0.03$ at 700°C , and $x = 0.29 \pm 0.03$ at 1400°C . The ^{17}O MAS NMR results for these quenched MgAl_2O_4 spinels are also shown in Figure 31B, where the two ^{17}O peaks observed are assigned to oxygens where either Al or Mg is located in the 4-coordinate sites. Ideally, five different oxygen sites should exist for these spinels; however, several of the resonances are overlapping. The ^{17}O NMR peak at $\delta_{\text{obs}} = 66$ ppm is assigned to oxygen sites associated with the normal spinel configuration involving ^{17}O - $^{[4]}\text{Mg}$ units, and the peak at $\delta_{\text{obs}} = 54$ ppm is assigned to oxygens associated with the inverted spinel ^{17}O - $^{[4]}\text{Al}$ units. Analysis of the temperature-dependent ^{17}O data showed that the disorder parameter was $x = 0.16$ at 700°C and $x = 0.24$ at 1400°C . Although the exact values for the disorder parameters do not agree, the trend is the same for the ^{17}O and ^{27}Al NMR results.

^{25}Mg MAS NMR studies of the refractory mineral forsterite, Mg_2SiO_4 , have been used to examine the temperature-dependent cation exchange of Mg^{2+} ions in the two different 6-coordinate magnesium-oxygen lattice sites (224). The room temperature ^{25}Mg MAS NMR spectrum of single crystal Mg_2SiO_4 shows four separate ^{25}Mg signals; two signals are due to M1 sites in chains of Mg^{2+} -oxygen octahedra, and two signals are due to M2 sites in adjacent corner-sharing Mg^{2+} -oxygen octahedra (Figure 32). At high temperatures the M2 resonances coalesce into a single resonance due to Mg^{2+} ion site hopping between adjacent (0.38 nm) M2 sites. An exchange frequency of 800 Hz was calculated for the M2 sites at 1314°C and 1800 Hz at 1344°C . The Mg^{2+} ion exchange process for M1 sites was also observed, but NMR simulation limitations precluded reliable estimates of exchange rates for these M1 sites.

Studies of other binary and ternary refractory metal oxides by metal nuclide NMR approaches have also been reported (286,293-298,300). The TiO_2 polymorphs

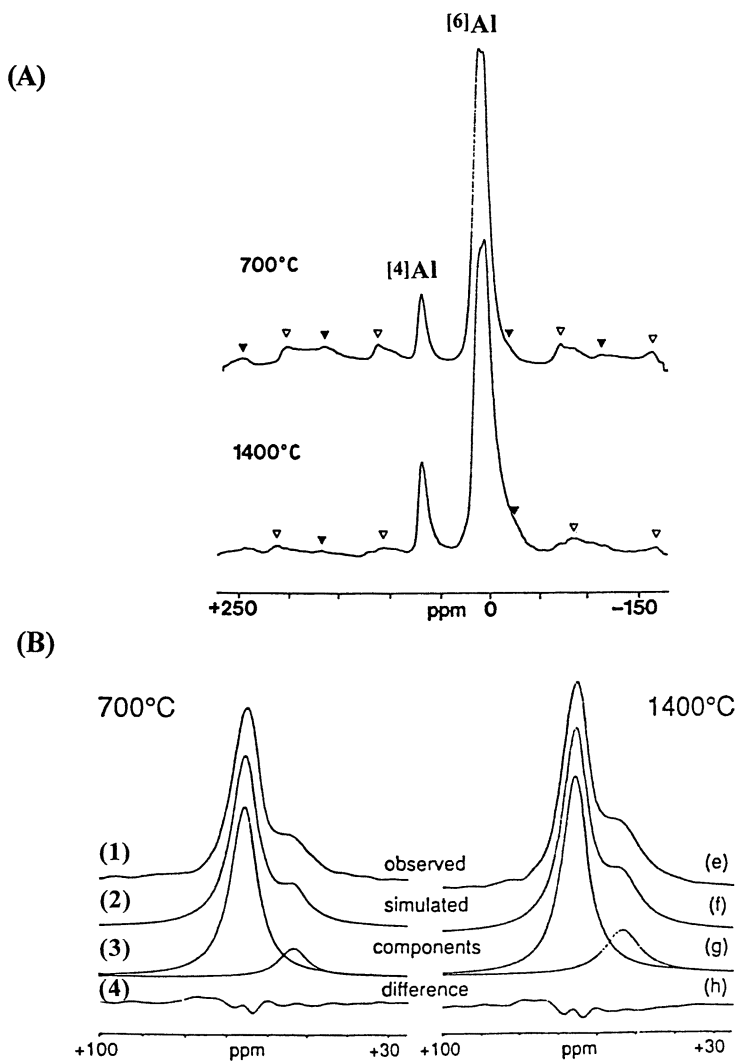


Figure 31. ^{27}Al and ^{17}O MAS NMR spectra of MgAl_2O_4 following quenching at various temperatures. (A) ^{27}Al MAS NMR spectra for synthetic magnesium aluminate spinel quenched at 700°C and 1400°C , showing two peaks of different intensities corresponding to $^{[4]}\text{Al}$ and $^{[6]}\text{Al}$ sites. Note increases in intensity of $^{[4]}\text{Al}$ peak with increase in quenching temperature. (B) ^{17}O MAS NMR spectra of MgAl_2O_4 samples quenched 700°C (left) and 1400°C (right). The smaller peak is due to oxygens in a disordered inverse spinel lattice (with $^{[4]}\text{Al}$ - ^{17}O structural features) and the larger peak is due to oxygens in an ordered spinel (with $^{[4]}\text{Mg}$ - ^{17}O features). The spectral components following deconvolution show increases in cation disorder (smaller peak) due to inverse spinel lattice structure following quenching at higher temperatures (230).

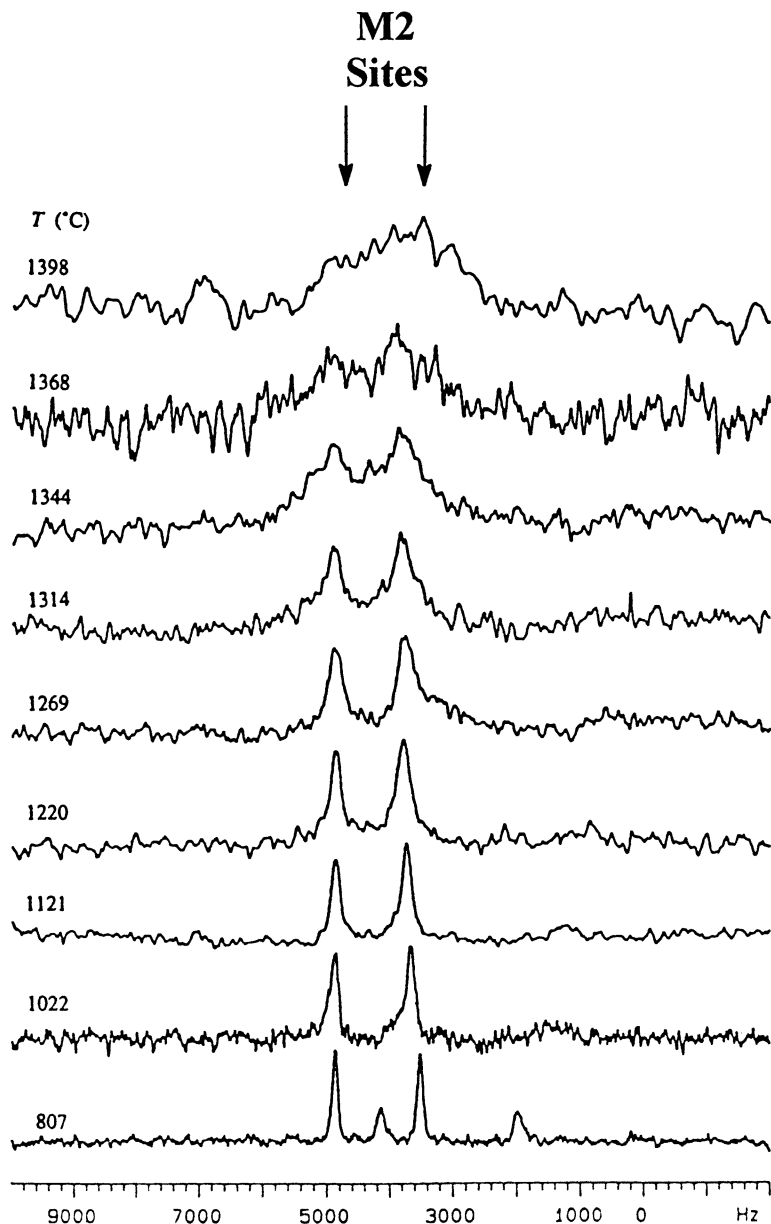


Figure 32. ^{25}Mg MAS NMR spectra for forsterite Mg_2SiO_4 at different temperatures. At room temperature, four magnesium sites, two due to related M1-a and M1-b sites on adjacent chains and two due to M2-a and M2-b corner-shared sites are observed. Exchange averaging is observed due to cation exchange or hopping (e.g., 140 Hz at 1200 $^{\circ}\text{C}$, 800 Hz at 1314 $^{\circ}\text{C}$ and 1800 Hz at 1344 $^{\circ}\text{C}$ between Mg^{2+} ions) between different M2 sites at elevated temperature leading to the coalescence of the two resonances into a single ^{25}Mg peak (224).

and BaTiO₃ have been examined by static and ^{47,49}Ti MAS NMR (285,293,295,296) while static and ⁹¹Zr MAS NMR have been used to study barium zirconate, the pure phases of ZrO₂ (monoclinic, tetragonal and cubic), and MgO- and Y₂O₃-stabilized phases of zirconia ceramics (295-298). Recently, MAS and 3Q-MAS ²³Na NMR measurements of Na₂HfO₃, which is isostructural with Na₂ZrO₃, have been reported (294). This system contains three well-defined 6-coordinate sodium sites in a 2:1:1 ratio. The ²³Na MAS NMR shows three overlapping ²³Na powder patterns for these three sites, with C_q values of 2.64 MHz, 2.05 MHz and 4.25 MHz, and δ_{iso} values of 15.75 ppm, 28.75 ppm and 19.0 ppm, respectively. In addition, 3Q-MAS ²³Na NMR was used to completely resolve these three sodium sites, whereas ¹⁷O MAS NMR was able to resolve only two of the three oxygen sites corresponding to local ON₄Hf₂ metal ion environments.

b) **Titanium, Zirconium, Niobium and Tantalum Oxides.** Titanium, zirconium, niobium and tantalum oxides are widely used in specialized electronic ceramics with piezoelectric and electrooptic properties as summarized in Table VIII (253-255). In addition, titanium oxide and zirconium oxide ceramics are used as photovoltaic materials and oxygen sensors, respectively. Zirconia ceramics exist in several forms, monoclinic, tetragonal and cubic, in addition to the yttria and magnesium-stabilized phase materials, while several crystallographic forms of titania (rutile and anatase) exist. Perovskite lattice structures of the formula ABO₃ (A = Li⁺, Na⁺, K⁺ and B = Nb⁵⁺, Ta⁵⁺ or A = Ca²⁺, Ba²⁺, Sr²⁺, Pb²⁺ and B = Zr⁴⁺, Ti⁴⁺) are common for many of the electronic ceramics of titanium, zirconium, niobium and tantalum (253-255,310,311). PZT (lead zirconium titanate) and PMN (lead magnesium niobate) are two technologically significant piezoelectric materials with perovskite lattice structures that contain two different B site metal ions (311). Oxide ceramics of this class have found important use as components of piezoelectric and ferroelectric ceramic thin films, electronic dielectric materials and ultrasound transducers.

Solid-state static and MAS ¹⁷O, ^{47,49}Ti and ⁹¹Zr NMR studies have been reported for several simple TiO₂ and ZrO₂ phases and several perovskites such as BaTiO₃, PbTiO₃ and BaZrO₃ (253-255,285,312,355). The ^{47,49}Ti MAS NMR spectra of the TiO₂ polymorph anatase obtained at 11.7 T and 14.1 T (as shown in Figure 33) indicate that the two NMR signals for the single distorted TiO₆ site in anatase are due to the two different titanium nuclides (with nearly identical Larmor frequencies) that have nearly overlapping powder pattern resonances (312). The quadrupolar parameters (C_q = 4.6 MHz; η^Q = 0) indicate that the titanium has axial symmetry. Static and MAS ⁹¹Zr NMR spectra of highly symmetric 6-coordinate zirconium sites such as found in cubic BaZrO₃, show sharp resonances, while SrZrO₃ has a broadened signal due to non-cubic zirconium-oxygen sites in the orthorhombic lattice (312). More highly distorted zirconium sites with higher coordination number (seven or eight) such as found in the ZrO₂ polymorphic phases and metal oxide-stabilized zirconia ceramics have required wide-line point-by-point NMR measurements due to the very large residual second-order quadrupolar (C_q range 15-20 MHz) line broadening effects observed (298).

For many electronic materials of the perovskite and tetragonal bronze lattice structures, lead and barium are important A site cation constituents. Static and MAS

Table VIII. Summary of various titanium, zirconium, niobium and tantalum electronic ceramics and various applications (253,254,255).

BaTiO ₃ , SrTiO ₃ , PbTiO	Capacitors, Electronic Devices Piezoelectric Materials
LiNbO ₃ , KNbO ₃ , PbNb ₂ O ₆	Dielectric/Ferroelectric Materials (Films, Ceramics, Single Crystals)
Pb(Zr _x Ti _{1-x})O ₃ (PZT)	Microelectronic, Electromechanical and Electrooptic Ceramics and Thin Films RAM Access Devices
(Pb _y La _{1-y})(Zr _x Ti _{1-x})O ₃ (PLZT)	Optical Image Storage, Electrooptical Devices
Pb(Mg _{1/3} Nb _{2/3})O ₃ (PMN) Pb(Sc _{1/2} Ta _{1/2})O ₃ (PST)	Relaxor Ferroelectrics, Piezoelectric Ceramics
(1-x)Pb(Mg _{1/3} Nb _{2/3})O ₃ /xPbTiO ₃ (PMN/PT)	Ultrasound Transducers, Sonar Multilayer Capacitors, Electrostrictive Devices and Micropositioners

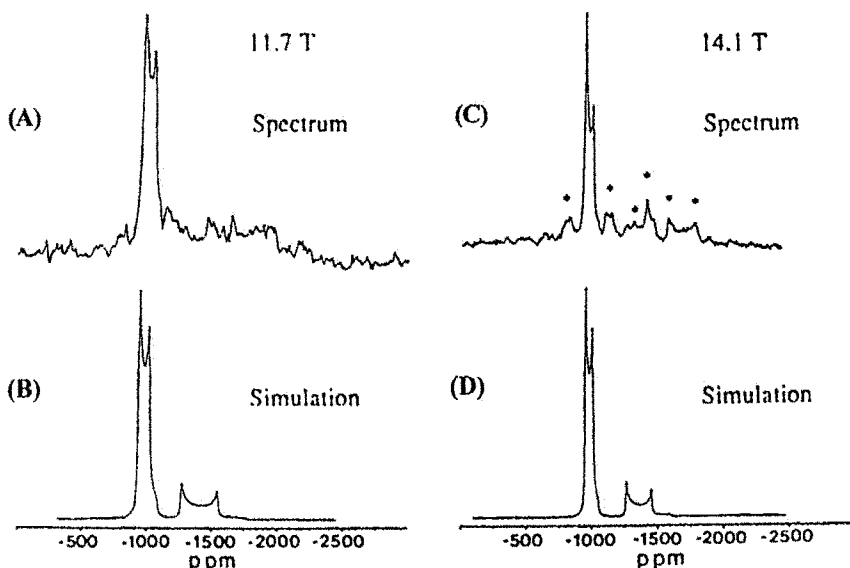


Figure 33. Experimental and simulated ^{47}Ti and ^{49}Ti MAS NMR experimental (A,C) and simulated (B,D) spectra of the TiO₂ polymorph anatase at 11.7 T and 14.1 T (312). Note that there are two powder pattern resonances ($C_q = 4.6$ MHz, $\eta^{\text{Q}} = 0.0$) for the single six-coordinate titanium (IV) site in anatase due to both the ^{47}Ti and ^{49}Ti nuclei, which have nearly identical Larmor frequencies.

²⁰⁷Pb NMR studies on various lead-oxygen compounds (302,313,314) and several important electronic materials such as lead niobate, PZT and PMN (302) have been recently reported. ¹³⁷Ba MAS NMR spectra obtained at 14 Tesla have also been reported for several barium oxide compounds, including the perovskites barium zirconate and barium titanate, both containing BaO₁₂ sites (312). A narrow peak is seen for the cubic barium site in the zirconate, and a second-order quadrupolar broadened resonance is seen for the distorted barium sites in tetragonal barium titanate. In addition, for barium oxide containing cubic BaO₆ sites in the NaCl lattice structure, a sharp NMR signal with no residual second-order line broadening is observed (312). In addition to these studies of BaTiO₃, studies using ^{47,49}Ti and ¹³⁷Ba MAS NMR to examine the tetragonal to cubic conversion (T_c = 400 K) as a function of temperature for single crystal BaTiO₃ have been reported (285,286,295,296). Using temperature-dependent ^{47,49}Ti and ¹³⁷Ba linewidth and relaxation studies for the polymorphic phases of barium titanate, information regarding the mechanism of relaxation over a wide temperature range was obtained. In addition to these metal nuclide NMR studies, ¹⁷O static and MAS NMR studies have been also been reported for both rutile and anatase forms of TiO₂ and a range of metal titanates and zirconates of the perovskite lattice structure (358).

Recent attention has focused on structural studies of niobium(V)-containing piezoelectrics such as lead niobate and lead magnesium niobate using solid-state ⁹³Nb NMR. The static ⁹³Nb NMR spectra of PbNb₂O₆ at different magnetic field strengths, including experimental and simulated spectra, are given in Figure 34. The anisotropic chemical-shielding parameters ($\Delta\delta = 454$ ppm and $\eta^{CS} = 0.67$) and the quadrupolar parameters ($C_q = 22.5$ MHz and $\eta^Q = 0.82$) calculated from simulations for the single ⁹³Nb site indicate the complexity of the NMR behavior of this nuclide, similar to that observed for the ⁵¹V nuclide in many materials (316). Related static and MAS ⁹³Nb NMR of the model niobium oxide systems, Nb₂O₅, LiNbO₃, KNbO₃ and NaNbO₃, and two-dimensional ⁹³Nb nutation NMR measurements of lead magnesium niobate (PMN) and lead niobate have also been reported (316). While investigations of these electronic materials of the perovskite structure have used primarily single-pulse NMR measurements, multiple-axis (DOR and DAS) and multiple-quantum (MQMAS) techniques are likely to increase the types of structural information obtainable by separating the effects of second-order quadrupolar line broadening, chemical shift anisotropy, and chemical shift dispersion for the ⁹³Nb nuclide in complex multiple A- and B-site perovskite ceramics such as PMN (311).

c) **Borides, Carbides and Nitrides.** Borides, carbides and nitrides, including nitrides and carbides of boron, aluminum, silicon, titanium and zirconium (also oxynitrides and oxycarbides) (251-253,259-264,276), encompass one of the largest classes of structural high-temperature ceramics, containing readily accessible NMR nuclei. The silicon carbides and nitrides, in particular, have received interest as components in composite materials. Silicon carbide and nitride are prepared by reactions of their metallic elements with methane and ammonia or nitrogen, respectively, followed by pressure or pressureless sintering in the presence or absence of sintering aids. These systems are readily amenable to study by solid-state MAS NMR methods although ¹⁵N labelling is required for NMR studies of the anion nitride sites in metal nitrides (339). In addition, extensive studies of the synthesis and

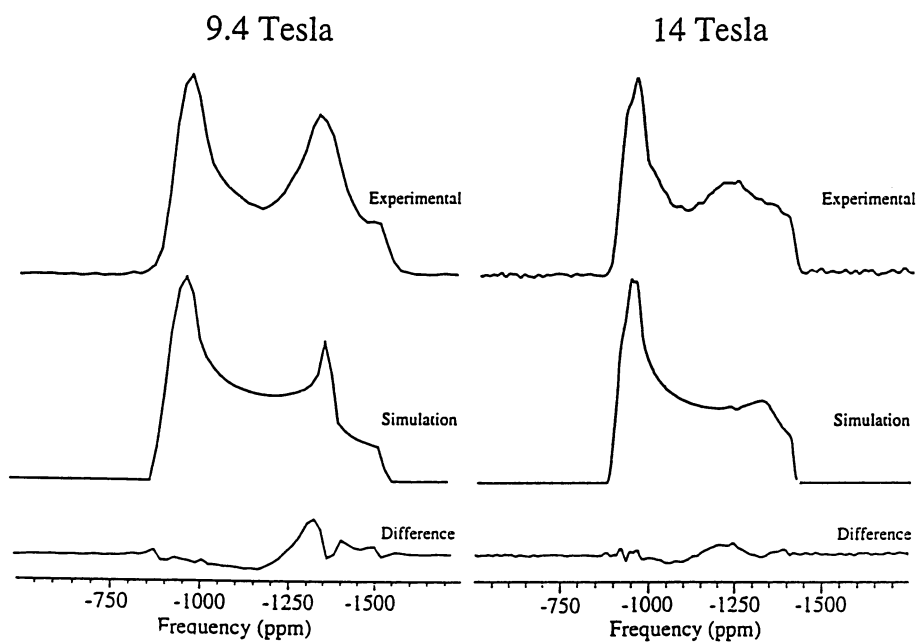


Figure 34. Static ^{93}Nb NMR spectra of the low-temperature form of PbNb_2O_6 at different magnetic fields, including experimental and simulated spectra. The various anisotropic chemical-shielding and quadrupolar parameters for this electronic material are: $C_Q = 20 \pm 1$ MHz, $\eta^Q = 0.6 \pm 0.2$, $\delta_{\text{iso}} = -1010 \pm 10$ ppm, $\Delta\delta = 420 \pm 50$ ppm, $\eta^{\text{CS}} = 0.85 \pm 0.2$, $\alpha = 42^\circ \pm 5^\circ$, $\beta = 42^\circ \pm 10^\circ$ and $\gamma = 42^\circ \pm 5^\circ$ (316).

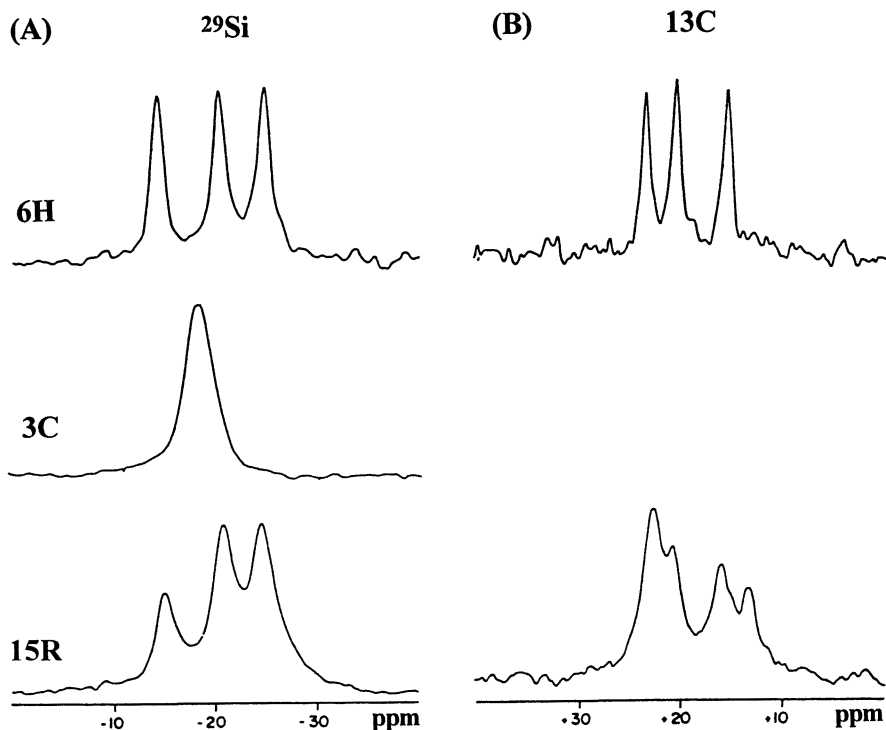
characterization of these materials from organosilicon, aluminum or boron precursors, followed by pyrolysis, has been explored. Another class of related materials, the SiAlONs (containing Si, Al, O, and N), are synthesized by high temperature (>1800°C) reactions of silicon nitride, silica, alumina and aluminum nitride under reducing conditions or by pyrolysis of polymeric precursors at 600-800°C.

Solid-state MAS NMR is of significant utility in studies of the formation, structure and surface chemistry of SiC- and Si₃N₄-based ceramics. Numerous ²⁹Si and/or ¹³C MAS NMR studies have been reported for Si₃N₄ and SiC (318,320-342,344-353). The ²⁹Si and ¹³C MAS NMR of various SiC ceramics as shown in Figure 35 provide examples of the utility of solid-state NMR to define the number and type of both carbon and silicon lattice sites in SiC polymorphs and polytypes. The ²⁹Si and ¹³C MAS NMR spectra shown in Figure 35A and 35B for three different silicon carbide polytypes exhibit different resonances due to stereochemically different silicon and carbon sites designated as Type A, B and C (320). The ²⁹Si and ¹³C MAS NMR chemical shifts for the A, B and C sites found in the important silicon carbide polytypes 6H, 3C and 15R, where H = hexagonal, C = cubic and R = rhombohedral lattices, are summarized in Figure 35C. (320). A fundamental limitation of ²⁹Si NMR is the long relaxation times (e.g., 129 seconds for the β-SiC resonance, 307, 313 and 362 seconds for the three resonances from α-SiC), necessitating very long delay times between successive scans to avoid signal saturation (318,320-322).

The utility of solid-state NMR to characterize bulk silicon nitride materials has also been extensively examined. Silicon nitride exhibits a ²⁹Si MAS NMR spectrum consisting of two distinct ²⁹Si NMR resonances assigned to α-Si₃N₄ and β-Si₃N₄ (331-334,351). ²⁹Si MAS NMR spectra of Si₃N₄/Si₂O₂N mixtures and various commercial silicon nitrides show distinct resonances for the silicon site environments in both the α- and β-polymorphs of silicon nitride, in silicon oxynitride, and in unreacted elemental silicon (331). Analytical ²⁹Si NMR approaches to identify and quantify the three types of Si₃N₄ (crystalline α-, β- and amorphous phases), have been reported; however very large relaxation times necessitate NMR pulse delay times of 500 seconds for the pure phase materials (289). Nevertheless, ²⁹Si MAS NMR studies of SiC and Si₃N₄ indicate that NMR often provides structural details unobtainable by XRD and other techniques.

In addition to ²⁹Si MAS NMR studies of Si₃N₄ powders, whiskers and thin films, ¹⁵N MAS NMR studies can provide further information when isotopically-enriched ¹⁵N-Si₃N₄ ceramics are used (263,338). In ¹⁵N NMR investigations of the oxidation of silicon nitride, differences in the local nitride environments, e.g., nitride (69-52 ppm) versus oxynitride (40 ppm), could be observed (263). The use of both ¹⁵N and ¹⁷O MAS NMR for isotopically-labelled silicon nitride materials, including SiAlONs and other oxynitrides, has been reviewed (338).

Recently, ²⁹Si MAS NMR has also been used to identify and quantify Si-O, Si-N and Si-C groups in both amorphous (e.g., Nicalon fibers) and crystalline materials derived from polymeric organosilicon precursors (323-327,345). Four-coordinate silicon moieties ranging in stoichiometry from SiC₄ to SiO₄, including the intermediate structural units C₃SiO, C₂SiO₂, and CSiO₃, have been distinguished and assigned based on chemical shift relationships of organosilicons (Table IX), together with related chemical shift correlations for different oxynitride and carbonitride



(C) Table I. Chemical Shifts of Silicon Carbide Polytypes^a

	site type	6H	3C	15R
²⁹ Si	A	-13.9	-18.3	-14.9
	B or C	-20.2		-20.8
	B or C	-24.5		-24.4
¹³ C				+13.3
	A ^b	+15.2	^c	+16.0
	B or C ^b	+20.2		+20.7
	B or C ^b	+23.2		+22.7

^appm to low field of tetramethylsilane. ^bTentative assignment. ^cNot detected under a wide range of acquisition conditions.

Figure 35. ²⁹Si NMR (A) and ¹³C MAS NMR (B) spectra of different silicon carbide polytypes 6H, 3C and 15R), that contain three stereochemically different types of silicon and carbon sites designated Type A, B and C. Summary of chemical shifts (C) for the A,B and C sites for the important silicon carbide polytypes 6H, 3C and 15R, where H = hexagonal, C = cubic and R = rhombohedral lattices, is shown (322).

Table IX. Summary of various ^{29}Si chemical shifts ranges for silicon carbide, nitride, oxynitride, oxycarbide and carbonitride materials (275,318,320-323,332,334,339).

Structural Unit	Compound	δ (^{29}Si), ppm
SiC_4	α -SiC(2H)	-14
	α -SiC(6H)	-20
	α -SiC(15R)	-24
	β -SiC (3C)	-18
	SiC_3N	+5.9
	SiC_2N_2	-1.7
	SiCN_3	-17.5
	SiN_4	-28.1
SiN_4	α - Si_3N_4	-46.8, -48.9
	β - Si_3N_4	-48.7
	a- Si_3N_4 (amorphous)	-46.7
	SiN_3O	-63
	SiN_2O_2	-75
	SiNO_3	-88
SiO_4	SiO_2 (quartz)	-106.6
	SiO_3C	-71.5
	SiO_2C_2	-32.8
	SiOC_3	-0.7
SiC_4	SiC_4	-12.2

structural units (323,348). These correlations have also been used to obtain structural information regarding SiC and Si₃N₄ ceramic fibers prepared from polymeric methylpolysilane precursors and SiC/Si₃N₄ composites prepared from alkylpolysilane precursors (324-328,343-345,356,357).

The use of ²⁹Si MAS NMR to examine the silicon coordination environments in Si₃N₄ and silicon oxynitride materials obtained from alkylaminosilane precursors (356,357), as well as SiAlON materials such as β'-SiAlON and β'-MgSiAlON, has also been reported (337,338,346,349). Although only limited NMR results have been obtained, ²⁹Si resonances for SiN₄, SiN₃O, Si₂N₂O₂, SiNO₃ and SiO₄ units were assigned (see Table IX). Some of the most significant uses of solid-state ²⁹Si and ⁸⁹Y MAS NMR are the investigations of YSiON and YSiAlON materials where yttrium oxide is used as a sintering aid. ²⁹Si MAS NMR, in particular, has been used to study the Y-Si-O-N grain boundary phases of densified Si₃N₄ ceramics prepared by sintering powders with Y₂O₃. These investigations have identified a range of mixed oxynitride grain boundary phases based on interpretation of significant differences in the chemical shifts for both the ²⁹Si and ⁸⁹Y oxynitride chemical environments (337,338,346,349). The conversion of α-Si₃N₄ to β-Si₃N₄ was monitored and the α/β silicon nitride ratios were determined. The ²⁹Si MAS NMR spectra of various pure Y-Si-O-N compounds and two sintered Si₃N₄ materials containing specific yttrium silicon oxynitride intergranular phases (denoted K and H) are shown in Figure 36 (323). Various impurities and grain boundary materials, e.g., H phase (Y₁₀Si₆O₂₄N₂) and K phase (YSiO₂N), were detected, identified and quantified. Assignments for many of these complex oxynitride phases have been used to establish a relationship between the NMR chemical shift δ (²⁹Si) and the local silicon chemical environments in (Y,La)SiAlON materials containing SiO_xN_{4-x} (0<x<4) tetrahedra as summarized in Figure 37 (349).

Several ²⁷Al MAS NMR studies of the aluminum sites in AlN, AlONs and the 15R SiAlON polytype have been reported (338,339,353). The ²⁷Al NMR spectrum of SiAlON exhibits both tetrahedral and octahedral Al resonances (3:1 ratio compared with 4:1 theoretical), although incomplete resolution was obtained at 7.05 T and 9.4 T magnetic fields due to spinning sidebands and second-order quadrupolar broadening effects. The use of ²⁷Al MAS NMR to study AlN, AlONs and SiAlONs has been particularly useful from the viewpoint of resolution only at very high magnetic fields (≥ 11.7). Recent high field ²⁷Al MAS NMR studies at 14 Tesla for AlON ceramics, for example, have shown that various four-coordinate AlO₄, AlO₃N, AlO₂N₂ and AlON₃ and AlN₄ structural units can be identified (see Figure 20) and resolved in an AlON material prepared from a 35.7 mole% AlN/Al₂O₃ reaction mixture at 1850°C (353). In addition to these studies of aluminum nitrides and oxynitrides, titanium nitrides, carbides and carbonitrides have also been examined by ¹³C and ^{47,49}Ti MAS NMR measurements (276).

Numerous investigations of the pyrolysis of carbide and nitride precursor systems have made use of both solid-state ²⁷Al and ²⁹Si NMR (326-328,343-345). Similarly, boron nitrides have also been explored using ^{10,11}B static and MAS NMR to examine cubic and hexagonal BN phases and the pyrolysis products derived from polymeric borane precursors (317). In addition to investigations of nitride and oxynitride ceramics of boron, silicon and aluminum, studies of newer nitride materials

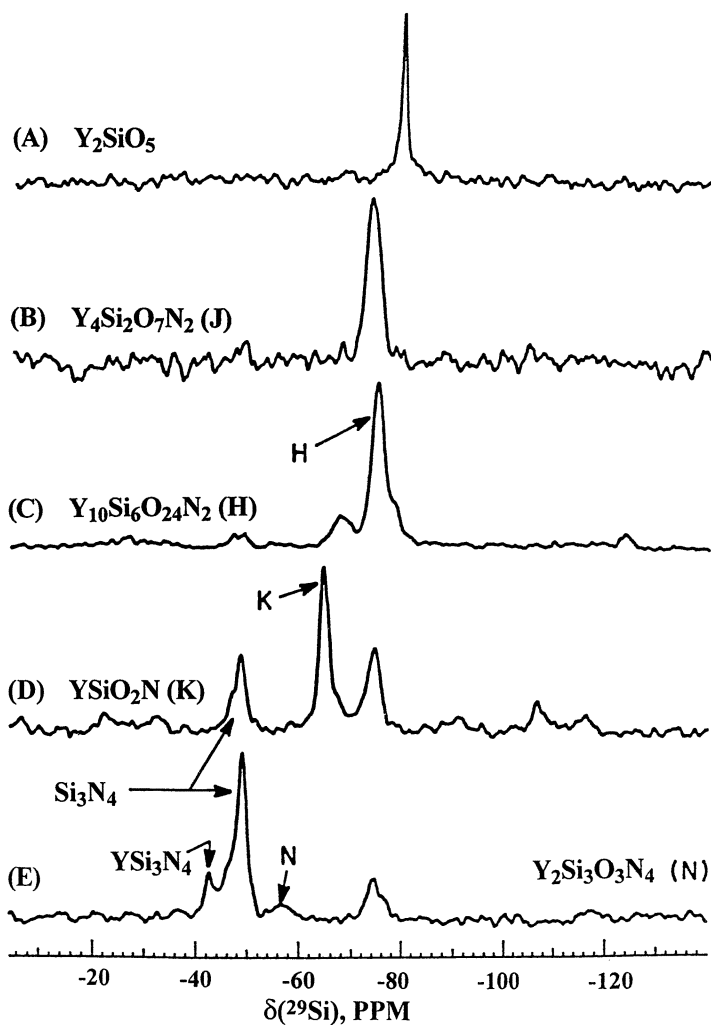
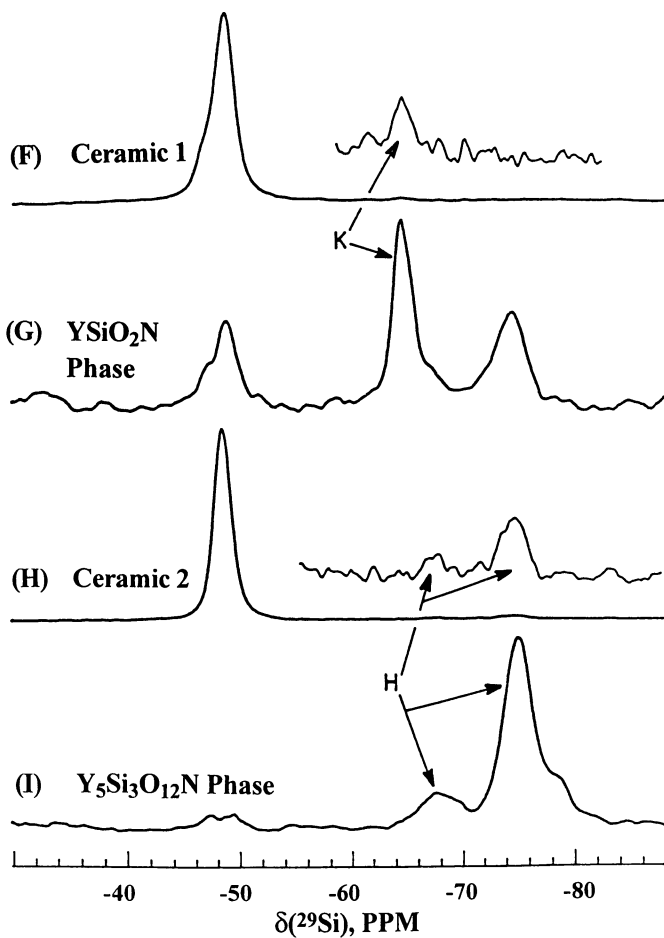


Figure 36. ^{29}Si MAS NMR spectra of various Y-Si-O-N phases and sintered Si_3N_4 materials containing intergranular phases. Spectra of various reference Y-Si-O-N phases, including intergranular phases H, J, K and N, are shown in A through E. Spectra of several Si_3N_4 ceramics sintered with Y_2O_3 are shown in F and H, with resonances being observed for the intergranular phases K and H (spectra for reference compounds) given in (C) and (D) (332).

Continued on next page.

Figure 36. *Continued.*

such as crystalline sodium aluminum phosphorus oxynitrides have also been reported. The experimental and simulated ^{23}Na MAS NMR spectra (top) and ^3Q -MAS spectra (bottom) of different sodium sites in two crystalline sodium aluminum nitridophosphate materials, $\text{Na}_3\text{AlP}_3\text{O}_9\text{N}$ and $\text{Na}_2\text{Mg}_2\text{P}_3\text{O}_9\text{N}$, are given in Figure 38 (303). The MQMAS spectra are plotted such that isotropic lines in one frequency dimension are correlated with anisotropic lines in the other frequency dimension. The improved resolution of the 2D experiment is apparent when one compares it to the one-dimensional spectra.

d) *Amorphous Glasses.* Amorphous glasses have major applications as insulating and optical materials, as adhesives, and as matrix substances in ceramics (11,125,256,263-268). These materials are also important model systems for high-temperature geomaterial transformations. The application of solid-state NMR has had a major impact on the fundamental knowledge of the short- and intermediate-range ordering in these materials, as well as the reaction processes of significance in the formation of amorphous and crystalline materials during the various melt stages. Single-pulse ^{29}Si MAS NMR studies of silica glasses containing alkali and alkaline earth metal ions have been previously reviewed (11,125,265-267).

The effects on the silicate network structure of adding modifier ions such as sodium and calcium have also been examined using ^{23}Na and ^{29}Si MAS NMR (11,269,270,273,277-280,284,285). The addition of modifier cations has been shown to influence the Q^n distributions by facilitating disproportionation reactions, e.g., $2\text{Q}^3 \rightleftharpoons \text{Q}^2 + \text{Q}^4$ and $2\text{Q}^2 \rightleftharpoons \text{Q}^1 + \text{Q}^3$. While one-dimensional ^{29}Si MAS NMR has been widely used (11,134,229), recent two-dimensional isotropic/anisotropic correlation studies of the calcium silicate glass (CaSiO_3) have shown increased resolution and improved quantification of the Q^n species based on the separated anisotropic lineshapes obtained from the two-dimensional data (229). From these studies, the measured Q^n distributions were used to calculate the following equilibrium constants for the disproportionation reactions $\text{Q}^n \rightleftharpoons \text{Q}^{n-1} + \text{Q}^{n+1}$: 0.105 ± 0.019 , 0.156 ± 0.005 and 0.106 ± 0.022 for $n = 1, 2$ and 3 , respectively. While the alkali silicate melts appear to obey the binary model of Q^n species disproportionation reactions, the behavior of the alkaline earth silicate melts deviates significantly from this model. A proposed explanation for this effect is calcium association by clustering near the non-bridging oxygens of different Q^n species.

Variable temperature NMR studies of glasses, including those under high pressure, have begun to provide important information about silicate glasses (278,285,307). The recent ^1H , ^{23}Na and ^{29}Si MAS NMR studies of sodium silicate hydrates suggest the importance of solid-state NMR for understanding transformations between crystalline precursor materials, melts and glasses (306,307). The ^{29}Si MAS NMR spectrum of crystalline $\text{Na}_2\text{SiO}_2(\text{OH})_2 \cdot 8\text{H}_2\text{O}$ at 298 K shown in Figure 39A consists of a single sharp resonance at -68.3 ppm due to the monomeric ion $\text{SiO}_2(\text{OH})_2^{2-}$ that is associated with a hexahydrated $\text{Na}(\text{H}_2\text{O})_6^+$ ion in the crystalline state. Melting of this solid at 323 K leads to liquid-state condensations to form mobile anionic silicate species containing Q^0 , Q^1 , Q^2 and Q^3 units (Figure 39B) associated with peaks at -70.3 ppm (monomer, Q^0), -77.4 ppm (dimer, Q^1), -79.9 ppm (cyclotrimer, Q^2), -85.3 ppm (cyclotetramer, Q^2) and -87.8 ppm (prismatic hexamer, Q^3), similar to species found in aqueous sodium silicates. The ^{29}Si MAS NMR spectra

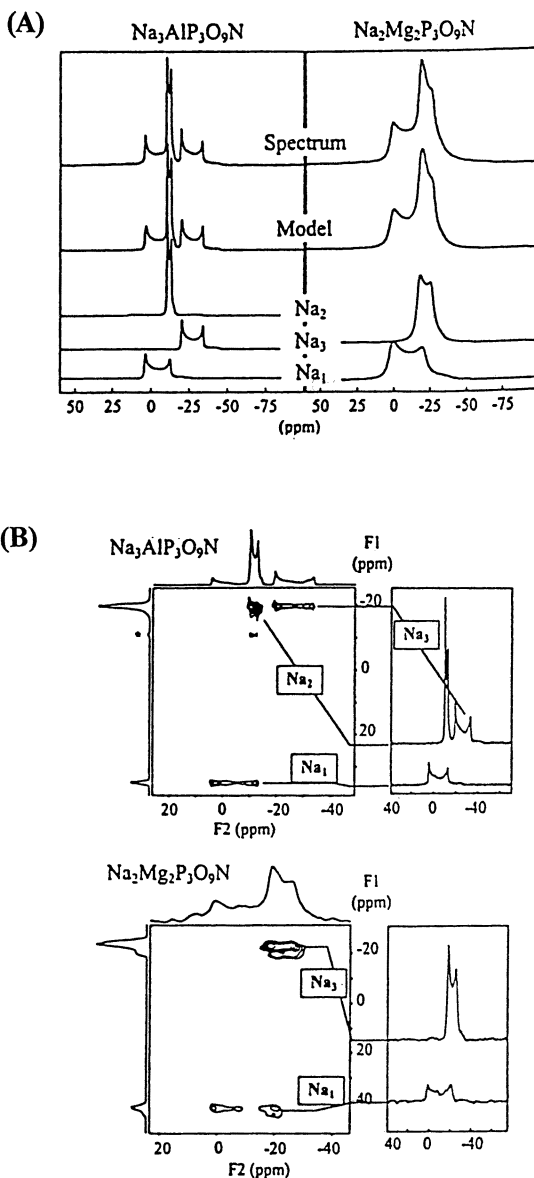


Figure 38. Solid-state experimental and simulated ^{23}Na MAS NMR spectra (A, top) and 3Q-MQMAS spectra (B, bottom) of different sodium sites in two crystalline sodium aluminum nitridophosphate materials, $\text{Na}_3\text{AlP}_3\text{O}_9\text{N}$ and $\text{Na}_2\text{Mg}_2\text{P}_3\text{O}_9\text{N}$. The MQMAS spectra are plotted such that isotropic lines in one frequency dimension are correlated with anisotropic lines in the other frequency dimension. The improved resolution of the 2D experiment is apparent when one compares it to the anisotropic dimension. The MAS spectra were simulated using the quadrupolar parameters obtained from the higher resolution MQMAS experiments (303).

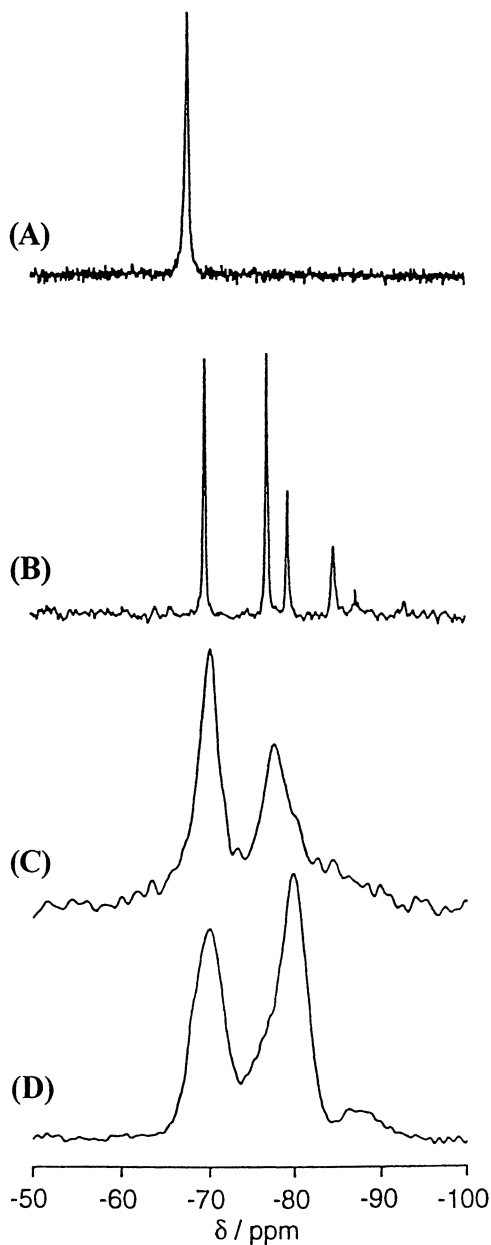


Figure 39. Variable temperature ^{29}Si MAS NMR spectra of crystalline $\text{Na}_2\text{SiO}_2(\text{OH})_2 \cdot 8\text{H}_2\text{O}$ at: (A) 298 K, (B) its melt at 330 K, (C) its supercooled melt at 240 K, and (D) its glass at 200 K. Spectra (A) and (B) were measured using ^1H - ^{29}Si cross-polarization (307).

of the supercooled melt formed at 240 K (Figure 39C) and the glass formed at 200 K (Figures 39D) show two broad Q^2 and Q^3 resonances due to decreases in the mobility of the species as noted by the linewidths. The glass formed at 200 K has a lower content of the cyclootrimer (Q^2), with the system Q^n composition being consistent with the expected species distribution for this glass stoichiometry. Conversion by heating of either the supercooled or quenched glass to the liquid state, followed by resolidification, was found by ^{29}Si NMR to be reversible with respect to the silicate species distributions.

The possibility of using ^{17}O MAS and DAS NMR to study the distribution of bridging and non-bridging oxygens in silicate glasses has also been explored. Correlation of ^{17}O NMR parameters and the local oxygen chemical environments have been reported for metal silicate glasses, including high-pressure glasses that also contain 5- and 6-coordinate silicons (265,278,285). A number of important correlations have been established for bridging oxygens (BO) in $\text{Si-}^{17}\text{O-Si}$ units, and non-bridging oxygens (NBO) in metal ion- $^{17}\text{O-Si}$ units as summarized in Table X for silicate glasses and crystalline metal silicates (362, and Table X references). The ^{17}O resonances of the bridging oxygens often give powder patterns due to larger C_q values (4 to 6 MHz), while NBO sites give sharper signals for smaller C_q values from 1.5 to 3.0 MHz (for sodium silicate glasses the C_q of BOs varies from 5.0 to 5.7 MHz and the C_q of NBOs from 2.3 to 3.0 MHz). The isotropic ^{17}O chemical shifts of NBO resonances are also sensitive to network-modifying cations with the chemical shifts of NBOs associated with potassium ions being greater than those with sodium ions. In addition, the ^{17}O chemical shifts of BOs increase as the sodium content increases.

The issues of deconvolution of broad ^{17}O NMR signals from single-pulse NMR measurements have been recently approached by 2D DAS ^{17}O NMR measurements for a series of mixed alkali (Na,K) silicate glasses as shown in Figure 40 (288). The 2D DAS ^{17}O NMR spectra for a series of mixed cation glasses show partial resolution of the BO (chemical shift range from 11.8 to 16.3 ppm) and NBO (chemical shift range from 27.0 to 68.7 ppm) ^{17}O resonances. Deconvolution of the isotropic lineshapes is shown in Figure 40 for the five disilicate glasses studied, including a pure potassium silicate glass, three mixed cation silicate glasses, and a pure sodium silicate glass. The various local chemical environments for the non-bridging oxygens have been simulated by component peaks assuming a binomial distribution of four - coordinate ONa_4 through OK_4 structural units.

In addition to providing structural information, solid-state NMR can also be used to examine the motion in glasses. This is exemplified by the ^6Li MAS two-dimensional exchange NMR spectra shown in Figure 17 for lithium orthosilicate, Li_2SiO_4 (116). By analysis of the cross-peak intensities in such spectra over a range of temperatures, information regarding the diffusion of lithium ions between 4-, 5- and 6-coordinate silicate sites and related activation energy barriers were obtained. The application of DAS and DOR techniques to examine the short-range and intermediate-range order in borate glasses was also recently reported (315). Besides these important glasses, solid-state NMR studies have also been reported on sodium phosphate glasses using two-dimensional NMR approaches, as well as $^{23}\text{Na} \leftrightarrow ^{31}\text{P}$ CP NMR methods (319).

Future investigations of other widely used glass systems such as aluminum

Table X. Summary of δ (^{17}O), C_q and η^a values from various ^{17}O NMR spectra of glassy and crystalline silicate systems (114,216,217,228,264,284,286-288,290,293,309,340,355,360,361,367,382).

Silica/Metal Oxides ^{216,217,264,284,288-290,293,355,382}			
	$\delta(^{17}\text{O})^\dagger$	e^2qQ/h (MHz)	η
CaO	294	<0.005	--
SiO ₂ (Cristobalite), BO	46*	5.3	0.125
SiO ₂ (Coesite)			
BO1	-19.24*	6.05	0.000
BO2	1.54*	5.52	0.169
BO3	17.92*	5.54	.0168
BO4	1.54*	5.43	0.166
BO5	21.93*	5.16	0.292
SiO ₂ (Stishovite) ¹³ O	109*	6.5	0.125
SiO ₂ (amorphous)	37*	5.0	--
SiOSi	44-52	5.8	0
SiOH	20*	4.0	0.3
SiOH (Silica Gel)	37*	4.4	0.0
Crystalline Metal Silicates ^{228,286-288,340,360,361}			
α -Na ₂ Si ₂ O ₅			
BO(O1)	52*	5.74	0.2
BO(O2)	74/55*	4.67	0.3
NBO(O3)	36*	2.40	0.2
ϵ -Na ₂ Si ₂ O ₅ , NBO	45*		
α -CaSiO ₃			
NBO1	94*	2.1	0.1
NBO2	91*	2.3	0.1
BO	75*	3.8	0.2

Table X. Continued.

Calcium Silicate Hydrate^{360,361}

Si-O-Si	36.7-75*	3.8-5.3	0.0-0.5
Si-O-Ca	88-112*	3/3.15/2.4	0.1-0.8
Ca-OH	70-71*	6.2-6.5	0.1-0.3
SiOH	10*	4.1	0.6
H ₂ O	-10-16	0	0

Sodium Silicate Glasses^{114,286-288,309,340}**Na₂O•2SiO₂**

BO	11.8	--	--
NBO	27.0	--	--

Na₂Si₂O₅

BO	69/65*	4.9	0.1
NBO	37/40*	2.35	0.2

Na₂Si₃O₇

BO	60*	5	0
NBO	39*	2.3	0

Na₂Si₄O₉

BO	50*	5	0
NBO	36*	2.3	0

Calcium Silicate Glasses (Ca/Si = 0.7)^{360,361}

BO	66*	4.6	0
NBO	110*	2.1	0.2

† All $\delta(^{17}\text{O})$ values are δ_{obs} values (center-of-mass of peak) except for δ_{iso} (purely chemical shift) values that are denoted by *.

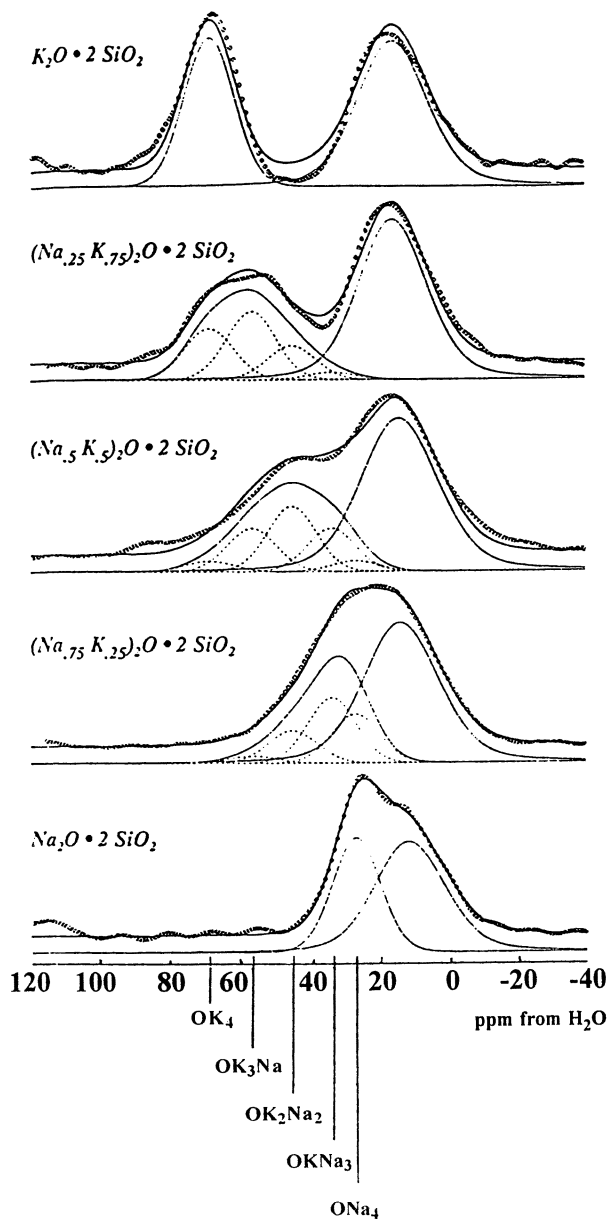


Figure 40. One-dimensional isotropic ^{17}O DAS spectra at 9.4 T of various mixed alkali (Na,K) silicate glasses, showing nearly complete resolution of bridging oxygens (BO) from 11.8 to 16.3 ppm, and non-bridging oxygens (NBO) from 27.0 to 68.7 ppm for the high K-content glasses. Deconvolution corresponding to a binomial distribution of four-coordinate oxygens with different nearest neighbor sodium and potassium ions is also depicted (288).

phosphates, aluminosilicates, and alkali and alkaline earth aluminosilicates using 1D and 2D NMR techniques are likely. Other refractory glasses (256) that have been studied by ^{17}O , ^{23}Na , ^{29}Si and ^{91}Zr MAS NMR, such as sodium zirconium silicates, could benefit from MQMAS and other two-dimensional NMR approaches. More elaborate 2D NMR studies of amorphous SiO_2 materials are also needed to discriminate between crystalline and noncrystalline silica domain regions in semiconductor materials (370). In addition to the many structural issues associated with both short-range and intermediate-range order, 2D NMR methods may increase our understanding of "sol-gel" phases used to prepare precursors of many technologically important, specialized glassy materials (126,128) and the complex physical-chemical processes important in the quenching and vitrification of glass preparations (264-268).

e) **Cements and Adhesives.** Cements and adhesives represent a fruitful area for the application of solid-state NMR studies since these materials are normally prepared as pastes, and require various setting and dehydration processing steps (289). $\text{CaO}\cdot\text{Al}_2\text{O}_3\cdot\text{SiO}_2$ cements, including low-iron content Portland and high alumina content cements, represent some of the oldest known commodity inorganic materials where detailed chemical knowledge about the hydration and setting reactions and related structures is severely lacking. The use of ^1H , ^{27}Al and ^{29}Si MAS NMR to examine these systems has led to significant progress (169,185-188,289,360,361). In particular, ^1H MAS NMR, ^1H CRAMPS and ^{29}Si MAS and CP/MAS NMR have been successfully used to study various hydrated calcium silicate crystalline phases formed during the setting and dehydration of calcium silicate cements. Recently, both ^{17}O and ^{29}Si MAS NMR approaches have been used to examine the curing of several hydrated calcium silicate phases over a range of cement compositions (360,361). ^{17}O MAS NMR spectra of calcium silicate hydrates formed from calcium silicates with different Ca/Si ratios have provided structural information about six different ^{17}O resonances in these materials. The relative amounts of the Ca- ^{17}O -H (NBO), Si- ^{17}O -H (NBO), Si- ^{17}O -Si (BO), two Si- ^{17}O -Ca (NBO) moieties (the latter having two or three associated calciums) and H_2^{17}O were obtained, thus providing information about the different ^{17}O -containing structural units during the formation of calcium silicate hydrates from $\beta\text{-}2\text{CaO}\cdot\text{SiO}_2$. While the quadrupolar parameter C_q could only be estimated for the oxygen sites due to the presence of overlapping resonances with unknown chemical shift dispersion, more definitive two-dimensional ^{17}O DAS and ^{29}Si isotropic/anisotropic NMR experiments may prove useful for obtaining a detailed understanding of these complex hydration processes.

Static and MAS ^{27}Al NMR at high spinning speeds and magnetic field strengths have also been useful for obtaining a more detailed understanding of various calcium aluminate phases containing 4-, 5- and 6-coordinate aluminum sites in cement systems (169,185-188). The hydration scheme for many of the important calcium aluminates (CA) involved in both high alumina content and Portland cements is quite complex and the details of interconversions between these CA species have not been fully delineated. Recently, important ^{27}Al MAS NMR studies of the structural features of many of these CA intermediates have been reported. For example, the ^{27}Al MAS NMR spectrum of one of the more complex calcium aluminate phases, $\text{CaO}\cdot 2\text{Al}_2\text{O}_3$ (CA_2), has been fit to six different 6-coordinate

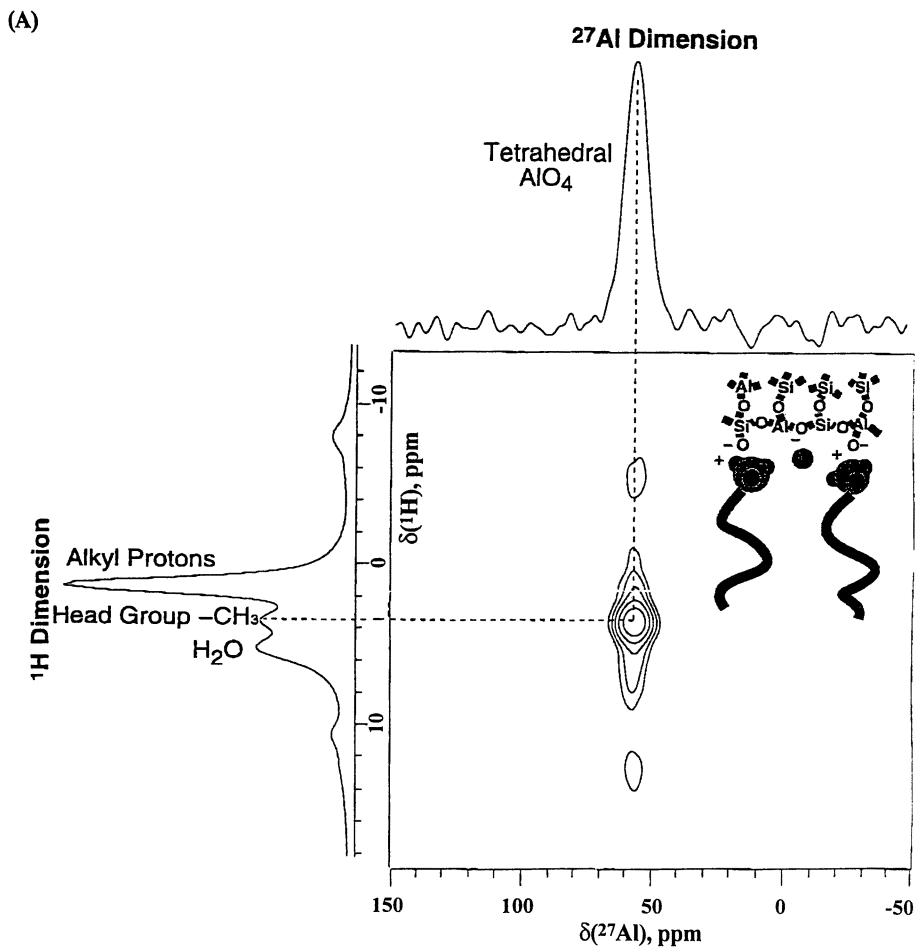
aluminum resonances (169,188). The quadrupolar parameters for these six different 6-coordinate aluminum sites in CA_2 are summarized in Table XI, together with related parameters for various aluminum sites found in other calcium aluminates (and hydrates). These results suggest that further solid-state NMR studies using 1H - ^{27}Al CP/MAS, ^{27}Al MQMAS NMR and other two-dimensional NMR approaches are likely to more fully expand our understanding of the structural features and hydration reactions of these complex materials found in cements.

Besides these silica/alumina and alumina-type cements, other potentially important cement-related materials such as aluminum phosphates and lithium aluminosilicates are also in need of thorough study by solid-state NMR methods.

f) *Bioceramics and Biomaterials.* Recent developments in the preparation and processing of biomaterials including Bioglasses[®], alumina, hydroxyapatite and calcium phosphate bioceramics suggest a new area for in-depth solid-state NMR investigations. ^{31}P MAS and CP/MAS NMR studies of hydroxyapatites (HA) and their calcium phosphate precursors have been reported (362-368). These studies have been directed toward providing an understanding of the relationship between the structures of the various calcium phosphates and the intricate biomineralization processes leading to hydroxyapatite (HA) formation in bone. Numerous P-OH and P-O-P sites in these different Ca/P-containing bone precursors have been identified by ^{31}P CP/MAS NMR (364-368). However, 1H - ^{31}P HETCOR (Figure 12) and other two-dimensional NMR experiments seem most likely to successfully unravel the complex crystallization and reorganization processes leading to hydroxyapatite crystallization and maturation in bone materials.

Bioglass[®] materials that are currently used surgically to replace soft tissues and bone have also been examined by ^{23}Na , ^{29}Si and ^{31}P MAS NMR (362,363,367), and recently by ^{17}O MAS NMR for ^{17}O -labelled materials (367). These complex bioactive glasses are sodium calcium silicate glasses, containing 6% P_2O_5 , and primarily consist of Q^2 and Q^3 silicate glass networks with associated modifying sodium and calcium ions. They undergo extensive surface chemistry involving silicate network reorganization and the formation of hydroxyapatite, a major constituent of bone, from unknown calcium phosphate precursors. Recent use of CP/MAS ^{29}Si and ^{31}P CP/MAS NMR to study the early stages of the surface and interfacial chemistry of these bioimplant materials has been reported (367).

The study of silicon biomineralization has recently been approached using solid-state heteronuclear correlation techniques and ^{13}C - ^{29}Si REDOR (369). In addition, 1H - ^{27}Al HETCOR and 1H - ^{29}Si HETCOR experiments have also been used to explore the interactions of the complex mesophase composite material MCM-41 (373). These materials represent technically important three-dimensional inorganic materials, but also provide model systems for the supramolecular assembly of organosilicates relevant to the biomineralization of silicon at inorganic/organic interfaces. The solid-state two-dimensional HETCOR NMR spectra shown in Figure 41 provide evidence for inorganic-organic interfacial interactions in aluminosilicate-containing MCM-41 mesophases on which trimethylammonium is adsorbed. The 2D 1H - ^{27}Al HETCOR spectrum (Figure 41A) of the aluminosilicate MCM-41 shows that short-range (< 1 nm) 1H - ^{27}Al dipolar coupling is observed between the framework 4-coordinate aluminums and the trimethylammonium head group of the cationic CTMA⁺



F Figure 41. Solid-state two-dimensional NMR studies of inorganic-organic interfacial interactions in aluminosilicate containing MCM-41 mesophases. 2D- ^1H - ^{27}Al HETCOR spectrum (A) of aluminosilicate MCM-41 showing in addition the corresponding 1D ^{27}Al CP/MAS and ^1H MAS NMR spectra plotted along their corresponding axes. 2D- ^1H - ^{29}Si HETCOR spectrum (B) of aluminosilicate MCM-41 showing in addition the corresponding 1D ^{29}Si CP/MAS and ^1H MAS NMR spectra plotted along their corresponding axes. The various cross peaks in each 2D HETCOR spectrum indicate dipole-dipole couplings between the nearby protons of the cationic trimethylammonium head and specific framework silicon and aluminums in the MCM-41 mesophases.(373).

Continued on next page.

(B)

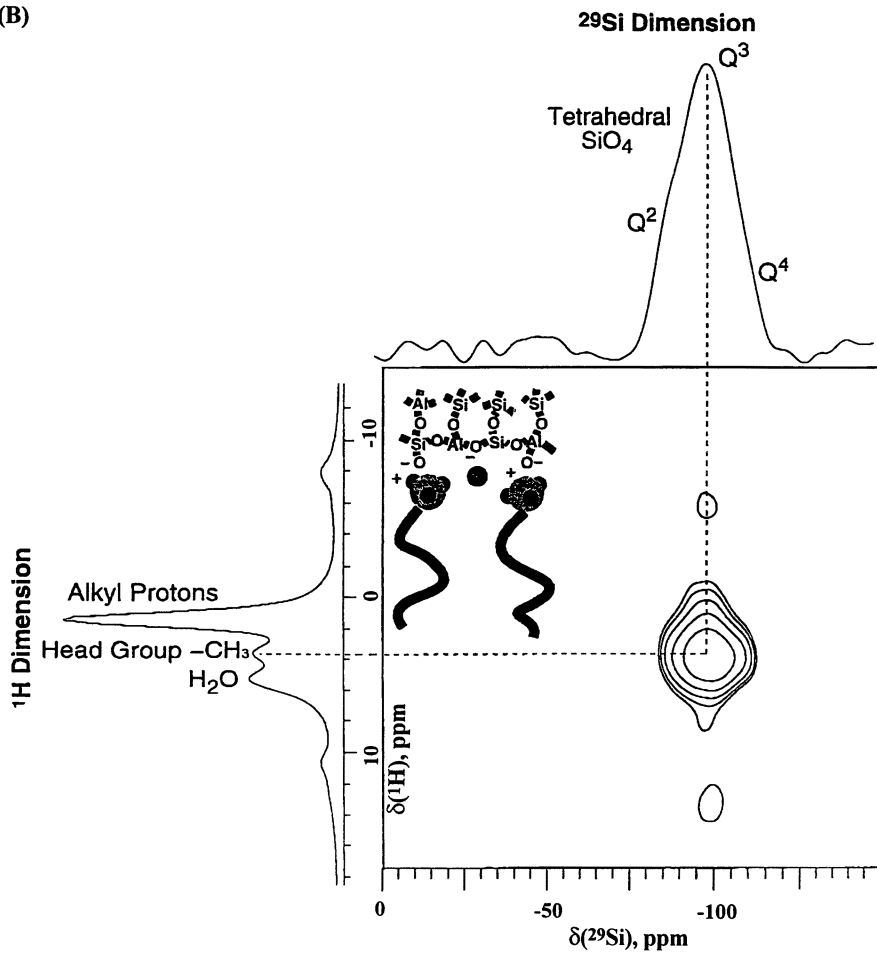
Figure 41. *Continued.*

Table XI. Summary of ^{27}Al quadrupolar coupling constants (C_Q), asymmetry parameters (η^Q) and isotropic chemical shifts (δ) for synthetic calcium aluminates of importance in high alumina and Portland cements (169, 173, 188).

Compound		C_Q (MHz)	η^Q	δ (ppm)
CA	Al(1)	6.25±0.05	0.88±0.02	75.5±0.5
	Al(2)	9.55±0.05	0.82±0.02	69.5±0.5
CA_2	Al(1)	2.50	0.20	81.9
	Al(2)	2.60	0.75	83.8
	Al(3)	2.60	0.95	86.2
	Al(4)	3.32	0.53	82.7
	Al(5)	3.37	0.39	81.6
	Al(6)	4.30	0.47	81.2
C_{12}A_7	Al(1)	9.7±0.2	0.40±0.10	85.9±1.0
	Al(2)	3.8±0.2	0.70±0.10	80.2±0.3
C_3A	Al(1)	8.69±0.05	0.32±0.02	79.5±0.5
	Al(2)	9.30±0.05	0.54±0.02	78.3±0.5
CAH_{10}		2.4±0.2 ^b		10.2±0.3
C_3AH_6		0.705±0.010	0.09±0.02	12.36±0.06
C_4AH_{13}		1.8±0.2 ^b		10.2±0.2
$\gamma\text{-AH}_3$	Al(1)	1.91±0.07	0.73±0.04	10.4±0.3
	Al(2)	4.45±0.05	0.44±0.03	11.5±0.3
$\text{C}_6\text{AS}_3\text{H}_{32}$		0.360±0.010	0.19±0.03	13.1±0.1
$\text{C}_4\text{ASH}_{12}$		1.7±0.2 ^b		11.8±0.2

(cetyltrimethylammonium) surfactant. The corresponding 1D ^{27}Al CP/MAS and ^1H MAS NMR spectra are plotted along the axes. The related 2D ^1H - ^{29}Si HETCOR spectrum (Figure 41B) of MCM-41 shows that the framework silanol of MCM-41 is also in close proximity to the trimethylammonium head group leading to strong ^1H - ^{29}Si dipolar interactions between the surfactant head group protons and the 4-coordinate framework silicons in MCM-41. Again, the corresponding 1D ^{29}Si CP/MAS and ^1H MAS NMR are plotted along their corresponding axes. The various cross peaks in each 2D HETCOR spectrum thus indicate dipole-dipole couplings between the nearby protons of the cationic trimethylammonium head group and specific framework silicon and aluminums in the MCM-41 mesophases. (373). These two-dimensional NMR results suggest new research avenues where NMR experiments may be used to examine weak interfacial interactions in mesoporous and micellar type systems.

4. Semiconductors, Ion Conductors and Superconductors. Solid-state NMR techniques have become increasingly important for studying inorganic semiconductors, ion conductors and superconductors due to the need to understand their short-range order and complex temperature-dependent behaviors. Studies of various superconductors using both static and MAS NMR as well as relaxation measurements have contributed significantly to our understanding of the complex behavior of high- T_c materials.

a) Semiconductors. Binary alloys of nonmetals (GaAs , GaP and GaN), pseudobinary $\text{A}_x\text{B}_{1-x}\text{C}$ alloys (where AC and BC are GaAs , GaP and InP) of isovalent semiconductors such as $\text{Ga}_x\text{In}_{1-x}\text{P}$, and pseudobinary alloys such as in $\text{Cd}_x\text{Hg}_{1-x}\text{Te}$ and $\text{InAs}_x\text{P}_{1-x}$ are widely used in a variety of electronic devices (370-378). Many of the simple binary and pseudobinary semiconductors exhibit variable material properties (such as band gaps) that are dependent on the composition, the presence of dopants and impurities, and the crystal growth conditions. Understanding such relationships can provide a means of fine tuning their electronic properties. While the macroscopic structures of these pseudobinary materials are related to their parent compounds, the microscopic structures of atomic level domains are quite variable. The degree of structural ordering found in these materials, the effects of subtle changes in A-C and B-C bond lengths in pseudobinary alloys, and variations in local chemical bonding are affected by compositional variations in semiconductors, often due to low concentration doping.

Solid-state NMR studies of semiconductors are in an early stage of development in terms of spectral resolution, sensitivity and assignment of various structural units based on NMR chemical shifts for nuclides such as ^{31}P , $^{69,71}\text{Ga}$, ^{115}In , ^{119}Sn and ^{125}Te , despite the fact that most of these nuclides have favorable natural abundances and receptivities. However, extensive quadrupolar line broadening for $^{69,71}\text{Ga}$, ^{75}As and ^{115}In makes all but the most symmetric sites difficult to observe, except possibly by using very high magnetic field strengths.

One of the earliest NMR studies of semiconductors involved ^{27}Al , ^{69}Ga , ^{71}Ga , ^{113}In and ^{115}In MAS NMR studies of binary semiconductors (374). These MAS NMR studies showed that the central transition resonance of these quadrupolar nuclides in binary semiconductors of the cubic zinc blende structure (AlP , AlAs , GaP , GaAs , InP and InAs) was primarily broadened by exchange interactions, whereas for the nitrides GaN and AlN of the hexagonal wurtzite lattice structure, the second-order quadrupolar

interaction ($C_q = 2.8$ MHz for ^{69}GaN , $C_q = 1.7$ MHz for ^{71}GaN and $C_q = 2.2$ MHz for ^{27}AlN) was the dominant line-broadening mechanism. More detailed studies of gallium phosphide (374) by ^{69}Ga MAS NMR showed that lineshape analysis, spin counting and quadrupolar nutation NMR for ^{69}Ga were useful for quantifying the semiconductor crystal quality for various GaP materials prepared from solid-state metathesis reactions involving gallium halides and sodium phosphide.

The importance of atomic cation ordering in Group III-V semiconductor alloys is of significance for the band gap properties of both bulk and thin film materials and can be controlled by growth conditions (375,376). The Group V semiconductor system, $\text{Ga}_x\text{In}_{1-x}\text{P}$, which contains the cations Ga and In has been shown by ^{31}P MAS NMR to exist in neither a random nor an ordered structure as depicted in Figure 42A for $\text{Ga}_{0.5}\text{I}_{0.5}\text{P}$. Rather, these systems exhibit some degree of order designated S, where $0 < S < 1$. The ^{31}P MAS NMR spectra of crystalline and thin films of the $\text{Ga}_x\text{In}_{1-x}\text{P}$ system, where five possible phosphorus clusters with $\text{Ga}_n\text{In}_{4-n}\text{P}$ sites may exist, have been examined. The ^{31}P MAS NMR spectrum of the polycrystalline $\text{Ga}_{0.14}\text{In}_{0.86}\text{P}$ material, obtained at various sample spinning speeds (see Figure 42B), exhibits three resonances assigned to $\text{Ga}_n\text{In}_{4-n}\text{P}$ clusters with $n = 0, 1$ and 2 . The predicted random distribution of $n = 0, 1$ and 2 is expected to be 0.547/0.356/0.087 and the MAS NMR spectrum indicates a cluster distribution of 0.53/0.38/0.09. The ^{31}P MAS NMR spectrum for $\text{Ga}_{0.5}\text{I}_{0.5}\text{P}$ thin films prepared under different growth conditions as shown in Figure 42C exhibit all five types of local phosphorus clusters in a 0.055/0.235/0.374/0.265/0.070 ratio, indicating an intermediate order with $S > 0.6$ (376). Such determinations of cation ordering in these types of semiconductors make it possible to begin relating this type of structural information to band gap properties and effects of semiconductor growth conditions on the quality of semiconductors.

Recent studies of more complex ternary and quaternary semiconductors such as ZnCd chalcogenides, ZnSe/GaP materials, and cadmium germanium arsenic phosphides of the formula $\text{CdGeAs}_{2-x}\text{P}_x$ have been reported (377,378). Typically, the cation (^{113}Cd) resonances are dominated by nonlocal effects due to charge delocalization and lattice contractions, while the anion (^{31}P) resonances are influenced by both second-nearest-neighbor effects and these nonlocal effects. Single-pulse ^{113}Cd and ^{31}P MAS NMR (Figure 43), however, were both found to be highly sensitive to the composition of the $\text{CdGeAs}_{2-x}\text{P}_x$ alloys in the range $x = 0.00$ to 0.875 , with the ^{113}Cd NMR resonances varying over 93 ppm and the ^{31}P NMR peaks over a narrower chemical shift range (378). The changes in the ^{113}Cd chemical shifts were interpreted in terms of next-nearest-neighbor effects in the second coordination sphere of the cadmiums which consists of eight germaniums, n cadmiums and $4-n$ zincs, where n varies from zero to four. The ^{31}P MAS NMR spectra were not as informative from a local chemical environment viewpoint since there is only a 28 ppm chemical range between the pure end-members CdGeP_2 and ZnGeP_2 of these solid-solutions. The use of experiments that depend on the ^{31}P - ^{113}Cd heteronuclear dipolar coupling, however, has provided a means to distinguish between different phosphorous units such as the $\text{PGe}_2\text{Zn}_n\text{Cd}_{2-n}$ sites and non-Cd-bonded PGe_2Zn_2 sites.

Besides these MAS NMR investigations, related studies of $\text{CdGeAs}_{2-x}\text{P}_x$ materials have been reported using both spin-echo ^{31}P and ^{113}Cd measurements, and ^{31}P - ^{113}Cd SEDOR (378). The results of ^{31}P - ^{113}Cd SEDOR measurements are given in

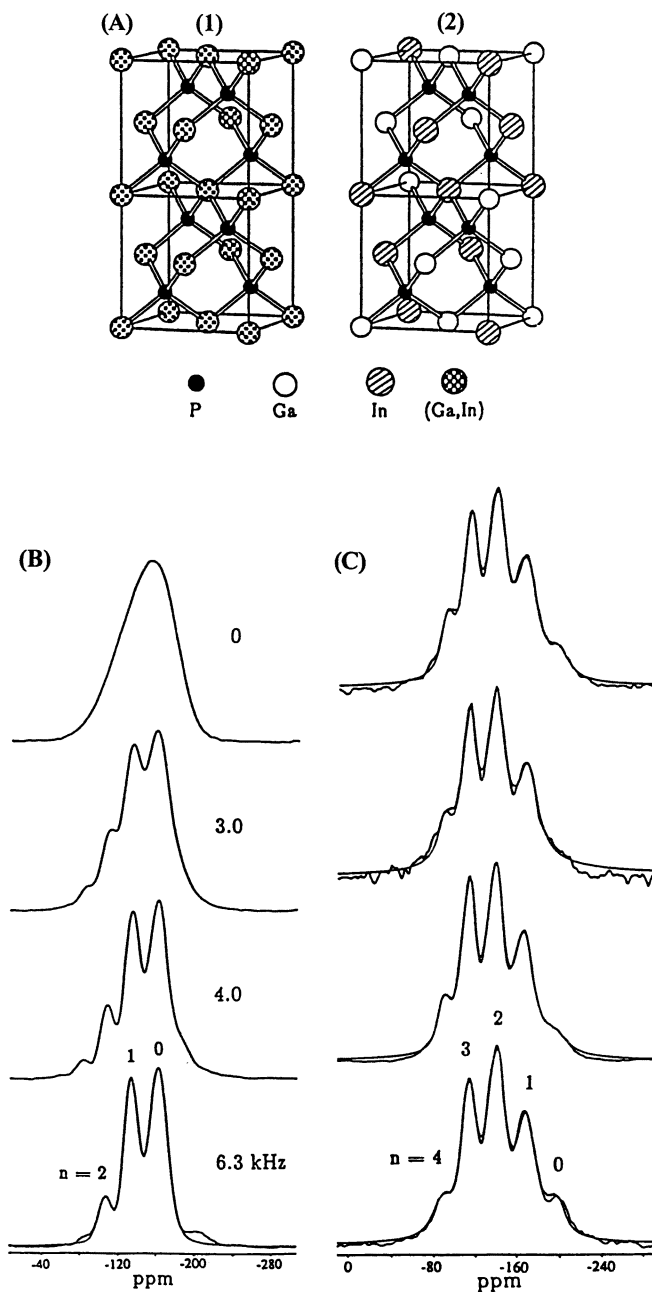


Figure 42. A structural diagram of both ideal random and fully ordered $\text{Ga}_{0.5}\text{In}_{0.5}\text{P}$ materials is shown in (A). ^{31}P MAS NMR spectra of (B) bulk, polycrystalline $\text{Ga}_{0.14}\text{In}_{0.86}\text{P}$ semiconductor, and (C) thin film $\text{Ga}_{0.14}\text{In}_{0.86}\text{P}$ material, obtained at various sample spinning speeds. The various ^{31}P resonances denoted by $n = 0, 1$ and 2 are assigned to $\text{Ga}_n\text{In}_{4-n}\text{P}$ clusters for partially ordered materials. (376).

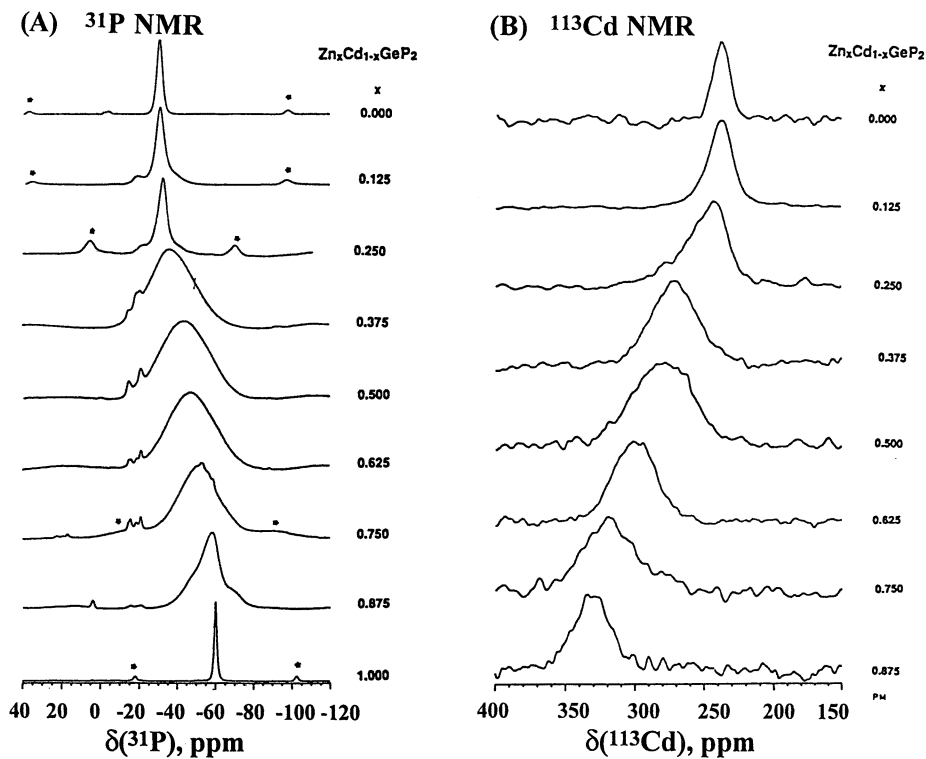


Figure 43. Solid-state NMR showing the compositional variation of the phosphorus and cadmium sites in the $\text{Zn}_x\text{Cd}_{1-x}\text{P}_2$ semiconductor glass system: (A) ^{31}P spectra and (B) ^{113}Cd spectra (377).

Figure 44 for both $\text{CdGeAs}_{2-n}\text{P}_x$ glasses, where $x = 0.5, 1.0$ and 2.0 , and for the crystalline $\text{CdGeAs}_{1.0}\text{P}_{1.0}$ material. These results show that for the glassy materials, the strength of the ^{31}P - ^{113}Cd dipolar interactions increase as the phosphorus content of the glasses increases (Figure 44A) and that the ^{31}P - ^{113}Cd dipolar strengths are comparable for both the glassy and crystalline material with a $\text{CdGeAs}_{1.0}\text{P}_{1.0}$ composition (Figure 44B). Based on these measurements, various atomic distribution models, including both random zinc blende and ordered chalcopyrite lattice arrangements of the P and As atoms, were evaluated as structural models for these amorphous semiconductor materials.

While these results indicate the applicability of solid-state NMR to study more complex quaternary semiconducting alloys, many of the more advanced CP/MAS and 2D NMR methods are likely to greatly expand our understanding of the structure, bonding and domain regions of these materials.

b) Ion Conductors. Inorganic ion conductors are attractive candidates for solid-state electrolytes, electrodes, electrocatalysts and many other materials where ion or vacancy migration are important (118-121). Nonstoichiometric mixed metal oxides of the perovskite structure, in particular, have attracted interest, although many of these systems contain paramagnetic metal ions. The $\text{Ba}_2\text{In}_2\text{O}_5$ material of the perovskite lattice structure exemplifies an ion conducting system where oxygen migration has been examined by solid-state ^{17}O NMR over the temperature range of room temperature to 1200°C (381). The lattice structure consists of two-dimensional layers of corner-sharing InO_6 octahedra and distorted, corner-sharing InO_4 tetrahedra, with a fixed concentration of oxygen ion vacancies that are ordered in the two-dimensional planes as shown in Figure 45A. This structure has three distinct oxygen sites: O(1) in the equatorial plane of the indium octahedra, O(2) in the apical sites of indium octahedra and tetrahedra, and O(3) in the equatorial plane of the indium tetrahedra (Figure 45B). The solid-state static ^{17}O NMR spectra of this material at various magnetic field strengths at room temperature (Figure 45C) are poorly resolved but can be fit to a sum of two quadrupolar powder patterns (assigned to O(1) and O(2) sites) and a narrower Gaussian (assigned to the O(3) sites). MAS narrows this O(3) peak, but the O(1) and O(2) site resonances remain broad. However, the broad resonances can be narrowed by performing a DAS experiments, displaying the two sharp resonances seen in Figure 45D, with isotropic second-order quadrupolar shifts between 150 and 200 ppm. Higher temperature ^{17}O MAS NMR spectra (Figure 45E) reveal dramatic changes in the NMR spectra characterized by coalescence to a single motional averaged sharp peak at 210 ppm that is 10-15 times more intense than at RT. This peak is a consequence of both structural changes in symmetry in the materials as well as rapid motion (>36 MHz) of all the oxygens at elevated temperature. These results suggest the usefulness of solid-state NMR approaches to examine ion mobility as a function of temperature and to study the oxygen-site vacancy equilibria in mixed metal oxides such as these ion conductors.

c) Superconductors. Solid-state NMR techniques, including both static relaxation studies (385), and MAS approaches, have been used to probe both the chemical and electronic structures of high- T_c superconductors such as $\text{YBa}_2\text{Cu}_3\text{O}_{7-x}$ (274,382-387,407-409). Early studies of superconductors involved both ^{63}Cu and ^{17}O MAS NMR of powdered and magnetically aligned $\text{YBa}_2\text{Cu}_3\text{O}_{7-x}$ (1-2-3) at 8.45 T and

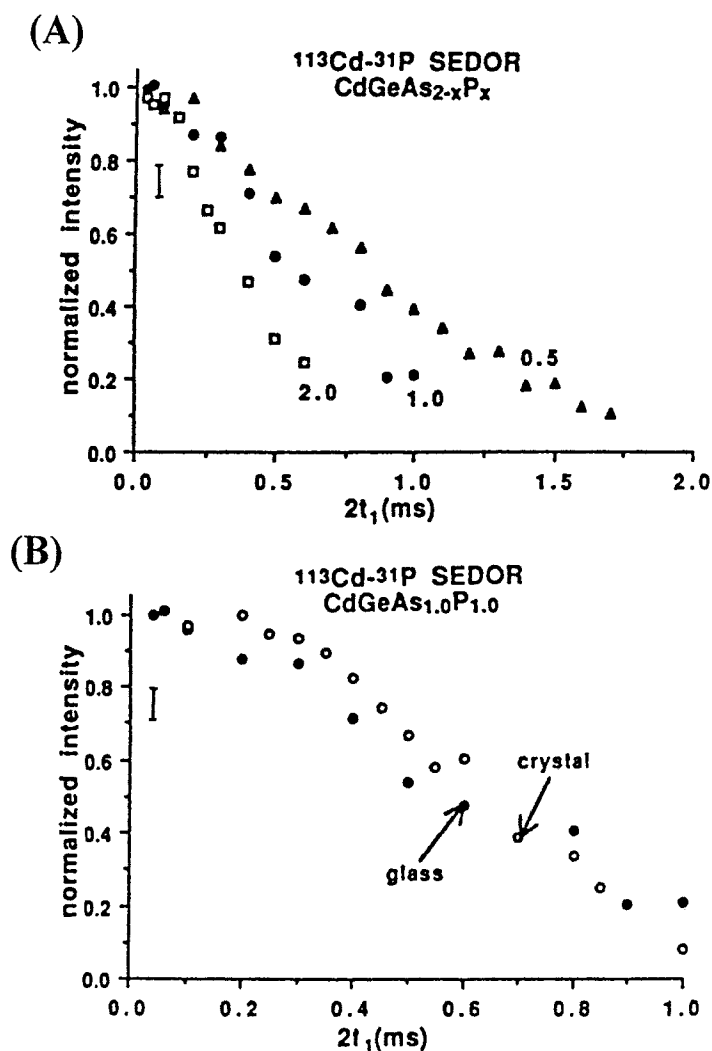


Figure 44. (A) ^{113}Cd - ^{31}P SEDOR results (normalized intensity versus $2t_1$ in ms) for several $\text{Zn}_x\text{Cd}_{1-x}\text{P}_2$ semiconductor glass systems at different values of x : $x = 0.5$ (closed triangles), 1.0 (closed circles) and 2.0 (open squares); and (B) comparison between the ^{113}Cd - ^{31}P SEDOR decays for crystalline (open circles) and glassy (closed circles) $\text{CdGeAs}_{1.0}\text{P}_{1.0}$ materials (378).

11.7 T (382,383). Detailed ^{17}O NMR results at 8.45 T for isotopically O-17 labelled $\text{YBa}_2\text{Cu}_3\text{O}_{7-x}$ show two major features at 300K, an intense paramagnetically shifted peak at ca. 1800 ppm assigned to the two CuO_2 planar oxygens O(2) and O(3) and a weaker signal near 400 ppm assigned to the column oxygens O(1) (Figure 46) (382). The intense peak was observed to undergo a 800 ppm diamagnetic shift when the temperature was lowered to 77K. Further work also revealed a weak signal at ca. 3000 ppm with a very large (100 kHz) linewidth assigned to the chain oxygen O(4). Enhanced resolution of the ^{17}O NMR of magnetically aligned isotopically O-17 labelled $\text{YBa}_2\text{Cu}_3\text{O}_{7-x}$ shown in Figure 47, reveals a remarkable spectrum where the 19 of the 20 possible transitions (central and satellite) are observed for the four different oxygens of this material: O(1), peaks 2,4,12,18,19; O(2,3), peaks 5-8, (10,11), 13-16; O(4), peaks 1,3,9,17,20. For the O(2) and O(3) planar oxygens, a C_q value of 6.5 MHz and near axial symmetry ($\eta^Q = 0.20-0.25$) were obtained by fitting the peak positions. For the column (bridging) oxygen O(1), a C_q of 7.7 MHz and $\eta^Q = 0$ were observed, and the chain oxygen O(4) was found to have a C_q of 0.9 MHz and $\eta^Q = 0.38$. The large chemical shift of the planar oxygens O(2,3) is due to an anisotropic Knight frequency shift caused by the metallic nature of the CuO_2 planes, while the large breadth and large chemical shift of the O(4) oxygen resonances is likely due to antiferromagnetic spin fluctuations in the CuO chains. The variable temperature ^{17}O NMR spectra of various $\text{YBa}_2\text{Cu}_3\text{O}_{7-x}$ materials over a range of oxygen compositions (from $x = 0.0$ to 1.0) are shown in Figure 48. Changes in the composition of oxygen for $\text{YBa}_2\text{Cu}_3\text{O}_{7-x}$ from O_7 stoichiometry to values as low as $\text{O}_{6.5}$ were shown to decrease the intensity of the O(4) peak due to preferential removal of these oxygens in the non-stoichiometric materials.

Similar ^{17}O NMR measurements of $\text{YBa}_2\text{Cu}_3\text{O}_{7-x}$, and other high- T_c superconductors including $\text{Bi}_2\text{Sr}_2\text{CaCu}_2\text{O}_{8+x}$ and $\text{Tl}_2\text{Ba}_2\text{CaCu}_2\text{O}_{8+x}$ have also been reported (383,384,386) as shown in Figure 49. In each of the CuO -materials, two major resonances were observed, a broad, paramagnetically shifted resonance between 1500 and 2000 ppm due to oxygens in the conducting CuO_2 planes and a narrower, diamagnetically shifted peak between 0 to 500 ppm due to BaO , SrO or BiO planar oxygens in the insulating planes. A recent ^{17}O NMR study of the high T_c (125 K) triple-layered material $\text{Tl}_2\text{Ba}_2\text{Ca}_2\text{Cu}_2\text{O}_{8+x}$ also shows these two characteristic ^{17}O resonances at room temperature. However, detailed lower temperature measurements of the paramagnetically shifted peak at 1400 ppm shows that this resonance assigned to the conducting CuO_2 planar oxygens shifts dramatically at its T_c value of 125 K for samples before and after annealing as shown in Figure 50. The relationship between the shift in the $\delta_{\text{obs}}(^{17}\text{O})$ values and the ac-susceptibility measurements shown in the inset of Figure 50 indicates that the temperature dependence of this shift is due to changes in the spin susceptibility and hole density of the material (386,387).

In addition to the extensive studies of various superconducting systems, both ^{89}Y MAS NMR and static ^{17}O NMR have also been performed on metal-substituted and related high- T_c superconductors (274,407-409). Temperature-dependent relaxation studies using ^{17}O , ^{63}Cu and ^{89}Y MAS NMR have also related NMR behavior to superconducting properties (407-409), but are beyond the scope of this discussion. However, these investigations together with the static temperature-dependent relaxation studies of high- T_c superconductors over the last decade (385) have added

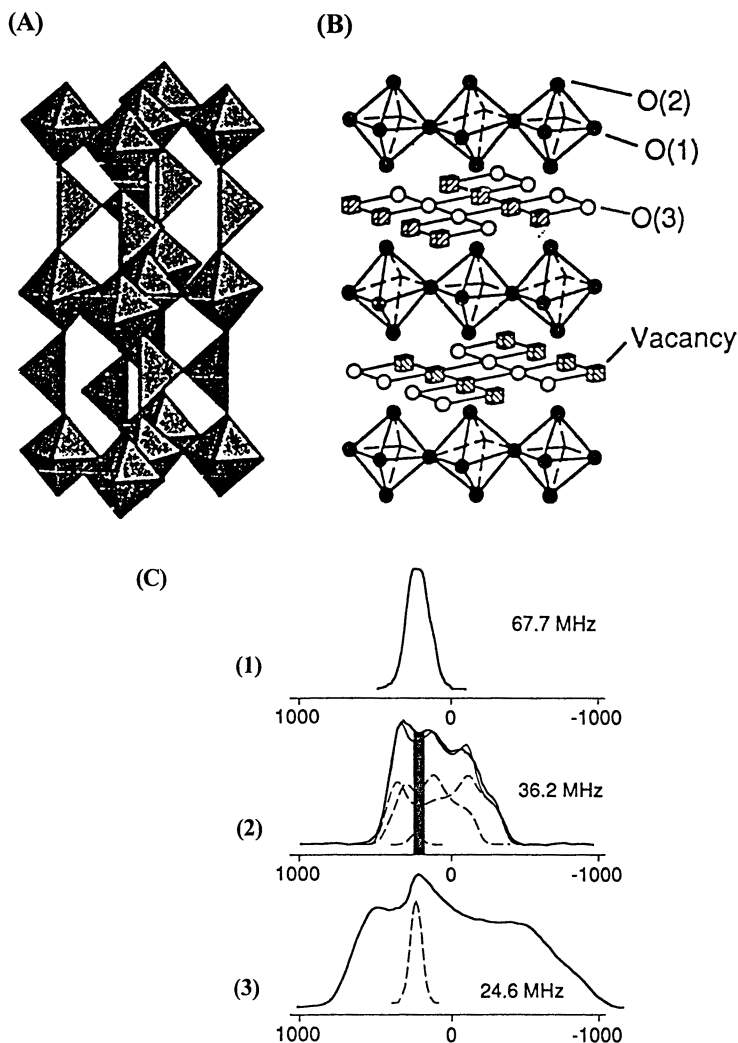
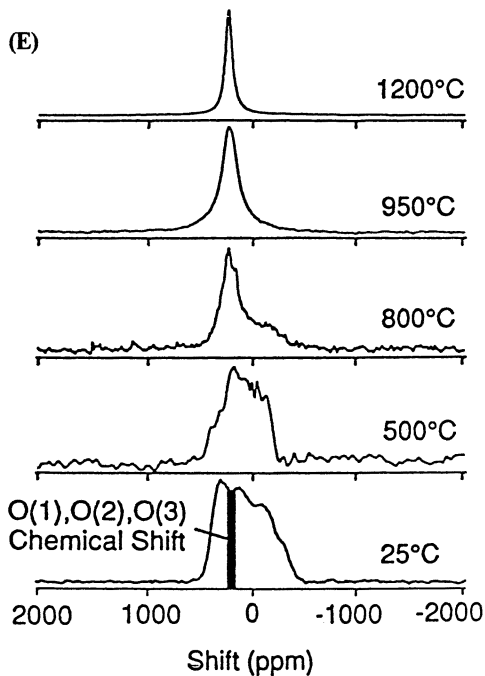
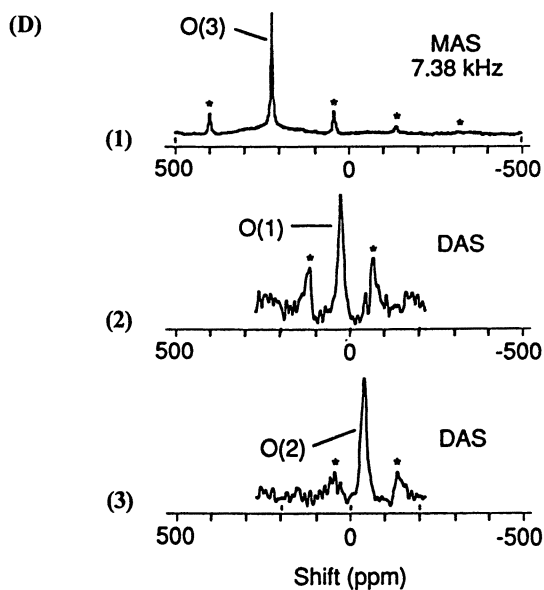


Figure 45. (A) The proposed structure of $\text{Ba}_2\text{In}_2\text{O}_5$ showing the tilting arrangement of the InO_4 and InO_6 structural units. (B) The ordering of oxygen vacancies in the layers of four-coordinate indiums is also shown. (C) ^{17}O MAS NMR spectra at RT for $\text{Ba}_2\text{In}_2\text{O}_5$ at various magnetic fields. The spectra consist of three components: two quadrupolar powder patterns ($C_q = 7.8$ MHz, $\eta^{\text{O}} = 0.3$, $\delta_{\text{iso}} = 160$ ppm; $C_q = 6.9$ MHz, $\eta^{\text{O}} = 0.3$, $\delta_{\text{iso}} = -160$ ppm) and a Gaussian peak corresponding to O(1), O(2) and O(3), respectively. (D) The ^{17}O MAS spectrum denoted (a) and ^{17}O DAS spectral resonances denoted (b) and (c), the latter taken from slices of the 2D DAS experiment, show peaks corresponding to the O(1), O(2) and O(3) sites. (E) Variable temperature ^{17}O MAS NMR spectra from RT to 1200°C show rapid (>36 MHz) oxygen ion movement between oxide sites (381).

Continued on next page.

Figure 45. *Continued.*

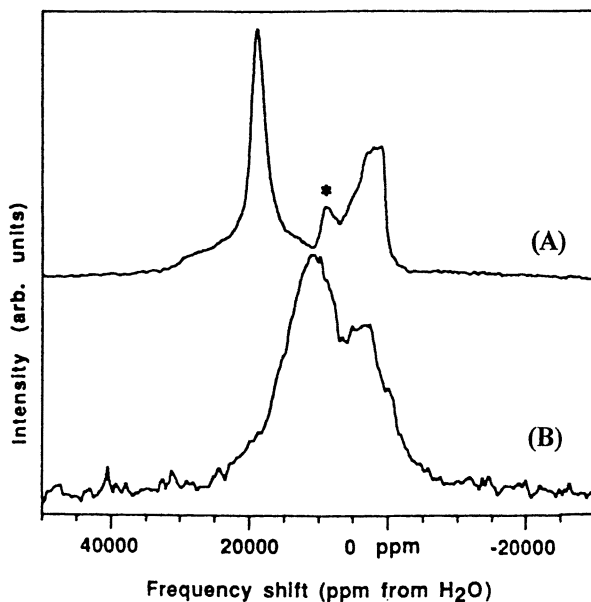


Figure 46. Static spin-echo ^{17}O NMR spectra at 8.45 T of a random powder of $\text{YBa}_2\text{Cu}_3\text{O}_{7-x}$ at (a) 300 K and (b) 77 K. The * indicates the resonance from O(1) in aligned crystallites (382,383). Inset shows a schematic partial structure of the 1-2-3 Y-Ba-Cu oxide superconductor material.

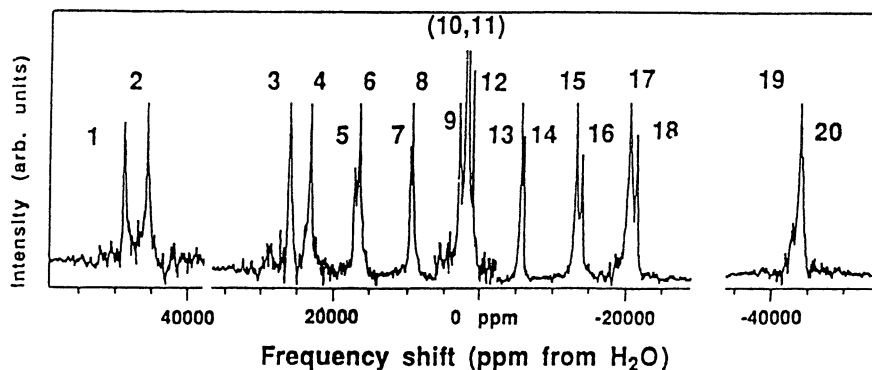


Figure 47. ^{17}O MAS NMR spectra at 8.45 T and 300 K of magnetically aligned $\text{YBa}_2\text{Cu}_3\text{O}_{7-x}$ ($B_0 \parallel c$). The intensities of the five transitions (central and satellite transitions) have a 5:8:9:8:5 ratio. Nineteen of the twenty possible resonances (for the four different oxygens each with five transitions) are observed for the four different oxygen sites: O(1), peaks 2,4,12,18,19; O(2,3) peaks 5-8, (10,11 are degenerate), 13-16; and O(4), peaks 1,3,9,17,20 (382).

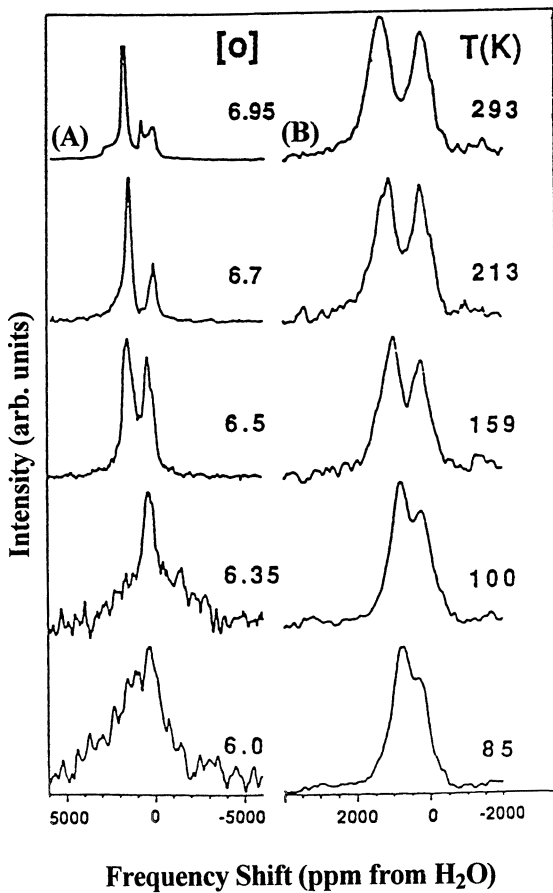


Figure 48. ^{17}O MAS NMR at 11.7 T of various $\text{YBa}_2\text{Cu}_3\text{O}_{7-x}$ materials with oxygen compositions (from $x = 0.05$ to 1.0), taken at various temperatures in K (382).

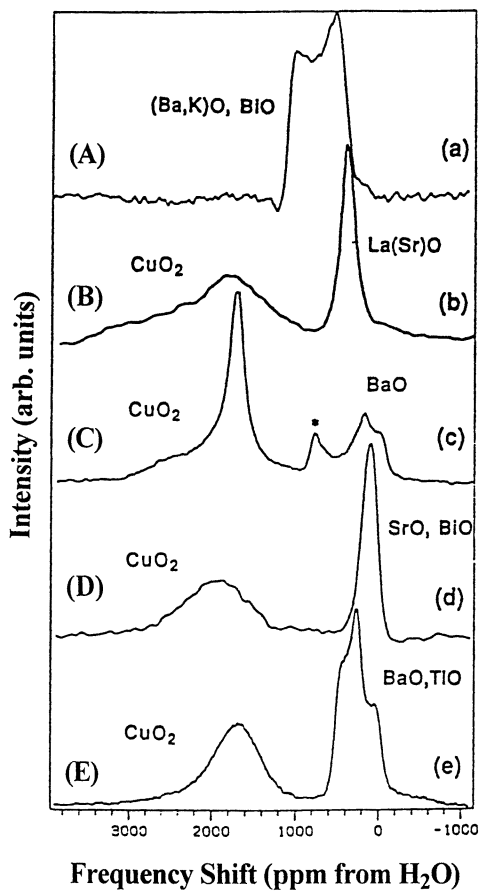


Figure 49. MAS ^{17}O NMR at 11.7 T and 300 K of various superconductors: (A) $\text{Ba}_{0.6}\text{K}_{0.4}\text{BiO}_3$, (B) $\text{La}_{1.85}\text{Sr}_{0.15}\text{CuO}_4$, (C) $\text{YBa}_2\text{Cu}_3\text{O}_{7-x}$, (D) $\text{Bi}_2\text{Sr}_2\text{CaCu}_2\text{O}_{8+x}$, and (E) $\text{Tl}_2\text{Ba}_2\text{CaCu}_2\text{O}_{8+x}$ (382).

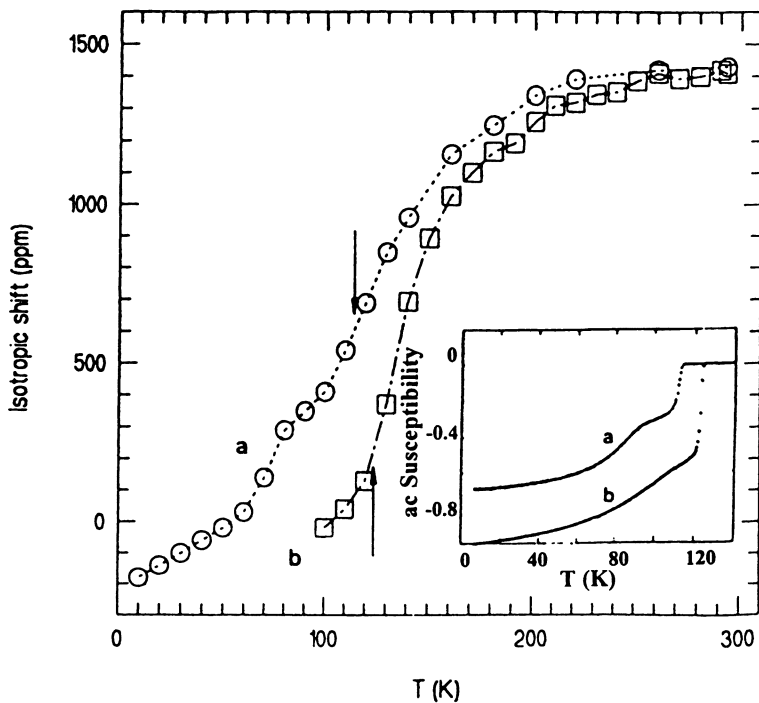


Figure 50. Temperature dependence of the isotropic chemical shift of ^{17}O NMR resonance for conducting CuO_2 oxygen sites in $\text{Tl}_2\text{Ba}_2\text{CaCu}_2\text{O}_{8+x}$ before (o) or after (□) annealing. Inset shows the corresponding ac susceptibility of these samples (386).

enormously to our current understanding of the structural nature and mechanisms of these important inorganic materials.

5. *Composites Containing Inorganic Particles/Fibers and Matrix Materials.*

Composite materials represent a class of technologically important inorganic materials which generally have unique mechanical properties (388,406). Composites are complex chemical substances that contain two major components: a reinforcing material and a matrix material. In addition, fabrication processes commonly involve the use of a third reactive component to improve the "interfacial bonding" between the matrix and the reinforcement material (153,154,256,362,403). The adhesion at the interface between the matrix and reinforcing element (e.g., fiber) ultimately dictates the mechanical performance and thermal stability of the composite. This is particularly important since many composites such as glass and carbon fiber-based composites are made using specific silane coupling agents to promote adhesion (122).

Excluding metal-containing composites, most inorganic composites consist of either inorganic/organic or inorganic/inorganic matrix/reinforcement material compositions. Glass fiber/epoxy resin and carbon fiber/inorganic glass or ceramic composites are examples of the former, while silicon nitride-based composites, ceramic matrix composites, fiber-reinforced ceramics and SiC fiber/SiAlON ceramic combinations are in the latter category (388-392).

Important problems in the solid-state NMR study of composite materials relate to three fundamental areas: 1) development of sensitive characterization techniques to understand the reinforcement and matrix components themselves, including the pre-fabrication surfaces and reactions, 2) examination of matrix/reinforcement material following fabrication and various treatments, and 3) examination of the adhesion and/or bonding at the "interface" of the reinforcement material and the matrix substance. ^{13}C and ^{29}Si CP/MAS NMR techniques, in particular, have been highly useful for probing the "interfacial region" in epoxy/glass composites and epoxy/carbon fiber composites (404-406). In addition, ^{13}C and ^{29}Si MAS NMR studies of the interfacial chemistry of silane coupling agents at the surface of silica particles have also been reported (153,154,404-406). An improved understanding of the functional groups that anchor these coupling agents to the composite material interfaces is critical to determining the ultimate functional properties of both carbon and silica composites. Therefore, molecular level descriptions of "bonding" between the coupling agents and the composite components as derived from nondestructive solid-state NMR measurements could provide direction necessary to chemically engineer interfaces in these and newer composite materials. Of particular importance is the selectivity of solid-state NMR to discriminate the interfacial species from the other fiber/matrix components, to provide information regarding the modes of interfacial binding, and to obtain quantitative information relevant to interfacial interactions, void spaces and domain regions (397-402).

The study of silicon carbide or alumina fiber/glass and silicon carbide or alumina/ceramic glass composites is another area of interest due to the ability of reinforcement fibers of silicon carbide, silicon nitride or alumina to improve toughness of glasses and ceramics. Other interesting materials include silicon carbide fiber/barium silicate, silicon carbide/silicon nitride, and silicon carbide/lithium silicate ceramic/glass composites (258,389). These systems are well suited for both 1D and 2D ^{13}C , ^{27}Al and ^{29}Si MAS NMR studies (5,12,13,53,62,76-87,95-97).

V. CONCLUSIONS

Atomic-level studies of the structure and dynamics of inorganic materials by solid-state NMR spectroscopy have made significant advances in the past decade. Both fundamental and new solid-state NMR methods and approaches have been utilized to obtain important structural and dynamical information pertaining to metal oxides, catalysts, zeolites, ceramics and glasses. These approaches have contributed significantly to advancing our understanding of the chemical and physical properties of inorganic semiconductors, ion conductors, superconductors and electronic materials. Novel solid-state NMR methods for both spin-1/2 and quadrupolar nuclides contained in traditional and advanced inorganic solid materials, are currently being utilized to address chemical issues of relevance to these materials. The use of cross-polarization methods and two-dimensional approaches has been particularly helpful for obtaining connectivity information and structural details for many inorganic systems that were previously inaccessible. The recent development of high-resolution techniques is expected to greatly expand our understanding of quadrupolar nuclides contained in metal oxide catalysts, ternary metal oxide ion conductors, electronic materials and electrochemical systems. The success of solid-state NMR approaches in addressing complex structural and reactivity questions suggests an important role for solid-state NMR in future research and development of advanced inorganic materials.

REFERENCES

- (1) Pople, J.A.; Schneider, W.G.; Bernstein, H.J. *High-Resolution Nuclear Magnetic Resonance*, McGraw-Hill, New York, 1959.
- (2) Abragam, A. *Principles of Nuclear Magnetism*, Clarendon Press, Oxford, England, 1961.
- (3) Becker, E.D. *High Resolution NMR. Theory and Chemical Applications*, 2nd Edition, Academic Press, New York, 1959.
- (4) Farrar, T.C.; Becker, E.D. *Pulse and Fourier Transform NMR. Introduction to Theory and Methods*, Academic Press, New York, 1971.
- (5) Ernst, R.R.; Bodenhausen, G.; Wokaun, A. *Principles of Nuclear Magnetic Resonance in One and Two Dimensions*, Clarendon Press, Oxford, England, 1987.
- (6) Slichter, C.P. *Principles of Magnetic Resonance*, Springer-Verlag, Berlin, Germany, 1990.
- (7) Mehring, M. *Principles of High-Resolution NMR in Solids*, Springer-Verlag, Berlin, Germany, 1976.
- (8) Haeberlen, H. *High Resolution NMR in Solids - Selective Averaging*, Academic Press, New York, 1976.
- (9) Gerstein, B.C.; Dybowski, C.R. *Transient Techniques in NMR of Solids*, Academic Press, Inc. Orlando, Florida, 1985.
- (10) Fyfe, C.A. *Solid-State NMR for Chemists*, C.F.C. Press, Guelph, Ontario, 1983.
- (11) Engelhardt, G.; Michel, D. *High-Resolution Solid-State NMR of Silicates and Zeolites*, John Wiley and Sons, Chichester, England, 1987.
- (12) Maciel, G.E. ed., *Nuclear Magnetic Resonance in Modern Technology*, NATO ASI Series, Vol. 447, Kluwer Academic Publishers, Dordrecht, The Netherlands, 1994.
- (13) Bell, A.T.; Pines, A. eds., *NMR Techniques in Catalysis*, Marcel Dekkar, Inc., New York, 1994.

- (14) Brinkmann, D.; Mali, M. *NMR Basic Principles and Progress* **1994**, *31*, 171.
- (15) Freude, D.; Haase, J. *NMR Basic Principles and Progress* **1993**, *29*, 1.
- (16) Cohen, M.H.; Reif, F. In *Solid State Physics*, Volume 5, Seitz, F.; Turnbull, D. eds., Academic Press, New York, 1957.
- (17) Das, T.P.; Hahn, E.L. *Nuclear Quadrupole Resonance Spectroscopy*, Academic Press, New York, 1958.
- (18) Andrew, E.R. *Prog. NMR Spect.* **1971**, *8*, 1.
- (19) Lowe, I. *J. Phys. Rev. Lett.* **1959**, *2*, 285.
- (20) Herzfeld, J.; Berger, A.E. *J. Chem. Phys.* **1980**, *73*, 6021.
- (21) Fyfe, C.A.; Gobbi, G.C.; Hartmann, J.S.; Klinowski, J.; Thomas, J.M. *J. Phys. Chem.* **1982**, *86*, 1247.
- (22) Klinowski, J.; Ramdas, S.; Thomas, J.M.; Fyfe, C.A.; Hartman, J.S. *J. Chem. Soc. Faraday Trans. II* **1983**, *78*, 1025.
- (23) Fitzgerald, J.J.; Dec, S.F., unpublished results, 1998.
- (24) Fitzgerald, J.J.; Hamza, A.I.; Dec, S.F.; Bronnimann, C.E. *J. Phys. Chem.* **1996**, *100*, 17351.
- (25) Gerstein, B.C.; Pembleton, R.G.; Wilson, R.C.; Ryan, L. *J. Chem. Phys.* **1977**, *66*, 361.
- (26) Bronnimann, C.E.; Chuang, I.; Hawkins, B.L.; Maciel, G.E. *J. Am. Chem. Soc.* **1987**, *109*, 1562.
- (27) Bronnimann, C.E.; Hawkins, B.L.; Zhang, M.; Maciel, M.E. *Anal. Chem.* **1988**, *60*, 1743.
- (28) Bronnimann, C.E.; Ziegler, R.C.; Maciel, G.E. *J. Am. Chem. Soc.* **1988**, *110*, 2023.
- (29) Burum, D.P.; Rhim, W.K. *J. Chem. Phys.* **1979**, *71*, 944.
- (30) Burum, D.P. *Concepts in Magn. Reson.* **1990**, *2*, 213.
- (31) Dec, S.F.; Maciel, G.E. *J. Magn. Reson.* **1990**, *87*, 153.
- (32) Santos, R.A.; Wind, R.A.; Bronnimann, C.E. *J. Magn. Reson. B* **1994**, *105*, 183.
- (33) Maxwell, R.; Lathrop, D.; Franke, D.; Eckert, H. *Angew. Chem. Int. Ed. Engl.* **1990**, *29*, 882.
- (34) Hartmann, S.R.; Hahn, E.L. *Phys. Rev.* **1962**, *128*, 2042.
- (35) Pines, A.; Gibby, M.G.; Waugh, J.S. *J. Chem. Phys.* **1973**, *59*, 569.
- (36) Yannoni, C.S. *Acct. Chem. Res.* **1982**, *15*, 201.
- (37) Yannoni, C.S. "Basic Cross-Polarization Magic-Angle Spinning" in *Nuclear Magnetic Resonance in Modern Technology*, Maciel, G.E., ed., NATO ASI Series, Vol. 447, Kluwer Academic Publishers, Dordrecht, The Netherlands, 1994.
- (38) Schaefer, J.; Stejskal, E.O. *J. Am. Chem. Soc.* **1976**, *98*, 1031.
- (39) Schaefer, J.; Stejskal, E.O.; Garbow, J.R.; McKay, R.A. *J. Magn. Reson.* **1984**, *59*, 150.
- (40) Roberts, J.E.; Vega, A.; Griffin, R.G. *J. Am. Chem. Soc.*, **1984**, *106*, 2506.
- (41) Sindorf, D.; Maciel, G.E. *J. Am. Chem. Soc.* **1980**, *102*, 7606.
- (42) Sindorf, D.; Maciel, G.E. *J. Phys. Chem.* **1982**, *86*, 5208.
- (43) Sindorf, D.; Maciel, G.E. *J. Am. Chem. Soc.* **1983**, *105*, 1487.
- (44) Vega, A.J. *J. Magn. Reson.* **1992**, *96*, 50.
- (45) Vega, A.J. *Solid State NMR* **1992**, *1*, 17.
- (46) Hayashi, S.; Akiba, E. *Chem. Phys. Lett.* **1994**, *226*, 495.
- (47) Chuang, I.S.; Kinney, D.R.; Bronnimann, C.E.; Maciel, G.E. *J. Phys. Chem.* **1988**, *92*, 5569.
- (48) Kinney, D.R.; Chuang, I.S.; Maciel, G.E. *J. Am. Chem. Soc.* **1993**, *115*, 6786.
- (49) Chuang, I.S.; Kinney, D.R.; Maciel, G.E. *J. Am. Chem. Soc.* **1993**, *115*, 8695.
- (50) Chuang, I.S.; Maciel, G.E. *J. Am. Chem. Soc.* **1996**, *118*, 401.

- (51) Maciel, G.E.; Ellis, P.D. "NMR Characterization of Silica and Alumina Surfaces", in *NMR Techniques in Catalysis*, Bell, A.T.; Pines, A., eds., Marcel Dekkar, Inc. New York, 1994.
- (52) Wu, Y.; Lewis, D.; Frye, J. S.; Palmer, A.R.; Wind, R.A. *J. Magn. Reson.* **1992**, *100*, 425.
- (53) De Paul, S.M.; Ernst, M.; Shore, J.S.; Stebins, J.F.; Pines, A. *J. Phys. Chem. B* **1997**, *101*, 3240.
- (54) Blackwell, C.S.; Patton, R.L. *J. Phys. Chem.* **1984**, *88*, 6135.
- (55) Morris, H.D.; Ellis, P.D. *J. Am. Chem. Soc.* **1989**, *111*, 6045.
- (56) Harris, R.K.; Nesbitt, G. *J. Magn. Reson.* **1988**, *78*, 245.
- (57) Hayashi, S. *Solid State NMR* **1994**, *3*, 93.
- (58) Fyfe, C.A.; Wong-Moon, K.C.; Huang, Y.; Grondey, H.; Mueller, K.T. *J. Phys. Chem.* **1995**, *99*, 8707.
- (59) Fyfe, C.A.; Grondey, H.; Mueller, K.T.; Wong-Moon, K.C.; Markus, T. *J. Am. Chem. Soc.* **1992**, *114*, 5876.
- (60) Fyfe, C.A.; Mueller, K.T.; Grondey, H.; Wong-Moon, K.C. *Chem. Phys. Lett.* **1992**, *199*, 198.
- (61) Fyfe, C.A.; Mueller, K.T.; Grondey, H.; Wong-Moon, K.C. *J. Phys. Chem.* **1993**, *97*, 13484.
- (62) Fyfe, C.S.; Mueller, K.T.; Wong-Moon, K.C. "Cross-Polarization Process to Less Common Pairs", in *Nuclear Magnetic Resonance in Modern Technology*, Maciel, G.E. ed., NATO ASI Series, Vol. 447, Kluwer Academic Publishers, Dordrecht, The Netherlands, 1994.
- (63) van Wüllen, L.; Züchner, L.; Müller-Warmuth, W.; Eckert, H. *Solid-State NMR* **1996**, *6*, 203.
- (64) Grey, C.P.; Corbin, D.R. *J. Phys. Chem.* **1995**, *99*, 16821.
- (65) Fyfe, C. A.; Wong-Moon, K. C.; Huang, Y.; Grondey, H. *J. Am. Chem. Soc.* **1995**, *117*, 10397.
- (66) Frydman, L.; Harwood, J. S. *J. Am. Chem. Soc.* **1995**, *117*, 5367.
- (67) Fernandez, C.; Amoureux, J.P. *Chem. Phys. Lett.* **1995**, *242*, 449.
- (68) Fernandez, C.; Amoureux, J.P.; Chezeau, J.M.; Delmotte, L.; Kessler, H. *Microporous Mater.* **1996**, *6*, 331.
- (69) Vega, S. *Phys. Rev., A* **1981**, *23*, 3152.
- (70) Massiot, D.; Touzs, B.; Trumeau, D.; Coutures, J. P.; Virlet, J.; Florian, P.; Grandinetti, P. *J. Solid-State NMR*, **1996**, *6*, 73.
- (71) Samoson, A.; Lippmaa, E.; Pines, A. *Mol. Phys.* **1988**, *65*, 1013.
- (72) Samoson, A. "Introduction to DOR NMR", in *Nuclear Magnetic Resonance in Modern Technology*, Maciel, G.E. ed., NATO ASI Series, Vol. 447, Kluwer Academic Publishers, Dordrecht, The Netherlands, 1994.
- (73) Wu, Y.; Chmelka, B.F.; Pines, A.; Davis, M.E.; Grobet, P.J.; Jacobs, P.A. *Nature* **1990**, *346*, 550.
- (74) Llor, A.; Virlet, J. *Chem. Phys. Lett.* **1988**, *152*, 248.
- (75) Mueller, K.T.; Sun, B.Q.; Chingas, G.C.; Zwanziger, J.W.; Terao, T.; Pines, A. *J. Magn. Reson.* **1990**, *86*, 470.
- (76) Medek, A.; Harwood, J.S.; Frydman, L. *J. Am. Chem. Soc.* **1995**, *117*, 12779.
- (77) Baltisberger, J.H.; Gann, S.L.; Grandinetti, P.J.; Pines, A. *Mol. Phys.* **1994**, *81*, 1109.
- (78) Jäger, C. *NMR Basic Principles and Progress* **1994**, *31*, 133.

- (79) Jäger, C. *J. Magn. Reson.* **1992**, *99*, 353.
- (80) Jäger, C.; Herzog, K.; Thomas, B.; Feike, M.; Kunath-Fandrei, G. *Solid State NMR* **1995**, *5*, 51.
- (81) Haase, J.; Conradi, M.S. *Chem. Phys. Lett.* **1993**, *209*, 287.
- (82) Vega, A.J. *J. Am. Chem. Soc.* **1988**, *110*, 1049.
- (83) Jarvie, T.P.; Wenslow, R.M.; Mueller, K.T. *J. Am. Chem. Soc.* **1995**, *117*, 570.
- (84) Wang, S.H.; De Paul, S.M.; Bull, L.M. *J. Magn. Reson.* **1997**, *125*, 364.
- (85) Fyfe, C.A.; Grondey, H.; Feng, Y.; Kokotailo, G.T. *Chem. Phys. Lett.* **1990**, *173*, 211.
- (86) Feike, M.; Graf, R.; Schnell, I.; Jäger, C.; Spiess, H.W. *J. Am. Chem. Soc.* **1996**, *118*, 9631.
- (87) Feike, M.; Jäger, C.; Spiess, H.W. *J. Non-Cryst. Solids* **1998**, *223*, 200.
- (88) Schmidt-Rohr, K.; Spiess, H.W. *Multidimensional Solid-State NMR and Polymers*, Academic Press Inc. San Diego, California, 1994.
- (89) Caravatti, P.; Neuenschwander, P.; Ernst, R.R. *Macromol.* **1985**, *18*, 119.
- (90) Makowka, C.D.; Slichter, C.P.; Sinfelt, J.H. *Phys. Rev. B* **1985**, *31*, 5663.
- (91) Lathrop, D.; Eckert, H. *J. Am. Chem. Soc.* **1990**, *112*, 9017.
- (92) Franke, D.; Maxwell, R.; Lathrop, D.; Eckert, H. *J. Am. Chem. Soc.* **1991**, *113*, 4822.
- (93) Franke, D.; Maxwell, R.; Lathrop, D.; Banks, K.; Eckert, H. *Phys. Rev. B* **1992**, *46*, 8109.
- (94) Franke, D.; Banks, K.; Maxwell, R.; Eckert, H. *J. Phys. Chem.* **1992**, *96*, 1906.
- (95) Gullion, T.; Schaefer, J. *J. Magn. Reson.* **1989**, *81*, 196.
- (96) Gullion, T.; Schaefer, J. *Adv. in Magn. Reson.* **1989**, *13*, 57.
- (97) Hing, A.W.; Vega, S.; Schaefer, J. *J. Magn. Reson. Series A* **1993**, *103*, 151.
- (98) Blumenfeld, A.L.; Coster, D.J.; Fripiat, J.J. *Chem. Phys. Lett.* **1994**, *231*, 491.
- (99) Hudalla, C.; Eckert, H. *J. Phys. Chem.* **1996**, *100*, 15986.
- (100) Raleigh, D.P.; Levitt, M.H.; Griffin, R.G. *Chem. Phys. Lett.* **1988**, *146*, 71.
- (101) Tycko, R.; Dabbagh, G. *Chem. Phys. Lett.* **1990**, *173*, 461.
- (102) Grey, C.P.; Vega, A.J.; *J. Am. Chem. Soc.* **1995**, *117*, 8232.
- (103) Kao, H.M.; Grey, C.P. *J. Phys. Chem.* **1996**, *100*, 5105.
- (104) Harmer, M.A.; Vega, A. *J. Solid State NMR* **1995**, *5*, 35.
- (105) Gullion, T. *J. Magn. Reson, Series A* **1995**, *117*, 326.
- (106) Frydman, L.; Chingas, G.C.; Lee, Y.K.; Grandinetti, P.J.; Eastman, M.A.; Barrall, G.A.; Pines, A. *J. Chem. Phys.* **1992**, *97*, 4800.
- (107) Ganapathy, S.; Vega, S. *J. Am. Chem. Soc.* **1998**, *120*, 1078.
- (108) Bax, A.; Szeverenyi, N.M.; Maciel, G.E. *J. Magn. Reson.* **1983**, *52*, 147.
- (109) Gan, Z. *J. Am. Chem. Soc.* **1992**, *114*, 8307.
- (110) Dixon, W.T.; Schaefer, J.; Sefcik, M.D.; Stejskal, E.O.; McKay, R.A. *J. Magn. Reson.* **1982**, *49*, 341.
- (111) Kolbert, A.C.; Griffin, R.G. *Chem. Phys. Lett.* **1990**, *166*, 87.
- (112) Olsen, K.K.; Zwanziger, J.W. *Solid State NMR* **1995**, *5*, 123.
- (113) Grandinetti, P.J.; Baltisberger, J.H.; Farnan, I.; Stebbins, J.F.; Werner, U.; Pines, A. *J. Phys. Chem.* **1995**, *99*, 12341.
- (114) Farnan, I.; Grandinetti, P.J.; Baltisberger, J.H.; Stebbins, J.F.; Werner, U.; Eastman, M. A.; Pines, A. *Nature* **1992**, *358*, 31.
- (115) Baltisberger, J.H.; Xu, Z.; Stebbins, J.F.; Wang, S.H.; Pines, A. *J. Am. Chem. Soc.* **1996**, *118*, 7209.
- (116) Xu, Z.; Stebbins, J.F. *Science* **1995**, *270*, 1332.
- (117) Farnan, I.; Stebbins, J.F. *J. Non-Cryst. Sol.* **1995**, *124*, 207.

- (118) Kung, H.H. *Transition Metal Oxides, Surface Chemistry and Catalysis*, Elsevier, New York, 1989.
- (119) Rao, C.N.R.; Raveau, B. *Transition Metal Oxides*, VCH Publishers, New York, 1995.
- (120) Rao, C.N.R.; Rao, G.V.S. *Transition Metal Oxides, Crystal Chemistry and Phase Transitions*, National Bureau of Standards, Washington, DC., 1974.
- (121) Wells, A.F. *Structural Inorganic Chemistry*, Fifth Edition, Clarendon Press, Oxford, 1984.
- (122) D.E. Leyden, ed. *Silanes, Surfaces and Interfaces*, D.E. Leyden, ed., Gordon Breach New York, 1986.
- (123) Grasselli, R.K.; Brodzil, J.F. eds., *Solid-State Chemistry in Catalysis*, American Chemical Society Series, ACS Publishing, New York, 1985.
- (124) Iler, R.K. *The Chemistry of Silica, Solubility, Polymerization, Colloid, Surface Properties, and Biochemistry*, Wiley-Interscience, Inc. New York, 1979.
- (125) Engelhardt, G.; Koller, H. *NMR Basic Principles and Progress* 1994, 31, 1.
- (126) Brinker, C.J.; Scherer, G.W. *Sol-Gel Science: The Physics and Chemistry of Sol-Gel Processing*, Academic Press, Inc. New York, 1990.
- (127) Jones, K.; Davies, T.J.; Emblem, H.G.; Parkes, P. *Mater. Res. Soc. Symp. Proc.* 1986, 73,111.
- (128) Klemperer, W.G.; Mainz, V.V.; Millar, D.M. *Mater. Res. Soc. Symp. Proc.* 1986, 73, 15.
- (129) Akapo, S.O.; Simpson, C.F. *J. Chromatogr. Sci.* 1990, 28, 186.
- (130) Lippens, B.C.; Steggerda, J.J. in *Physical and Chemical Aspects of Adsorbents and Catalysts*, Linsen, B. G., Fortuin, J. M. H., Okkerse, C., Steggerda, J.J. eds., Academic Press, New York, 1970.
- (131) Wefers, K.; Misra, C. *Oxides and Hydroxides of Aluminum*, Alcoa Technical Paper No. 19, Alcoa Laboratories, 1987.
- (132) Gitzen, W.H. *Alumina as a Ceramic Material*, The American Ceramic Society, Columbus, OH, 1971.
- (133) Meier, W.M.; Smith, J.V. *Zeolite Chemistry and Catalysis*, Rabo, J.A., ed., ACS Monograph 171, ACS Books, New York, 1976.
- (134) Barrer, R.M. *Zeolites and Clay Minerals as Sorbents and Molecular Sieves*, Academic Press, Inc. New York, 1978.
- (135) Meier, W.M.; Olson, D.H. *Atlas of Zeolite Structure Types*, Butterworth-Heinemann, London, 1992.
- (136) Fyfe, C.A.; Kokotailo, G.T. "Solid-State NMR Investigations of Zeolites and Related Materials", in *Nuclear Magnetic Resonance in Modern Technology*, Maciel, G.E., ed., NATO ASI Series, Vol. 447, Kluwer Academic Publishers, Dordrecht, The Netherlands, 1994.
- (137) Fyfe, C.A.; Mueller, K.T.; Kokotailo, G.T. "Solid-State NMR Studies of Zeolites and Related Systems", in *NMR Techniques in Catalysis*, Bell, A.T.; Pines, A. eds., Marcel Dekkar, Inc., New York, 1994.
- (138) Fyfe, C.A.; Feng, Y.; Gies, H.; Grondey, H.; Kokotailo, G.T. *J. Am. Chem. Soc.* 1990, 112, 3264.
- (139) LaPierre, R.B. *Zeolites*, 1985, 5, 346.
- (140) Lippmaa, E.; Magi, M.; Samoson, A.; Engelhardt, G.; Grimmer, A.R. *J. Am. Chem. Soc.* 1980, 102, 4889.
- (141) Magi, M.; Lippmaa, E.; Samoson, A.; Engelhardt, G.; Grimmer, A.R. *J. Phys. Chem.* 1984, 88, 1518.
- (142) Lippmaa, E.; Magi, M.; Samoson, A.; Tarmak, M.; Engelhardt, G. *J. Am. Chem. Soc.* 1981, 103, 4992.

- (143) Hater, W.; Muller-Warmuth, W.; Frischat, G.H. *Glastech* **1989**, *62*, 328.
- (144) Smith, J.V.; Blackwell, C.S.; Hovis, G.L. *Nature* **1984**, *309*, 140.
- (145) Haukka, S.; Roat, A. *J. Phys. Chem.* **1993**, *98*, 1695.
- (146) Haukka, S.; Lakomaa, E.L.; Root, E.L. *J. Phys. Chem.* **1994**, *97*, 5085.
- (147) Caravajal, G.S.; Leyden, D.E.; Quinting, G.R.; Maciel, G.E. *Anal. Chem.* **1988**, *60*, 1776.
- (148) Dirken, P.J.; Smith, M.E.; Whitfield, H.J. *J. Phys. Chem.* **1995**, *99*, 395.
- (149) Klinowski, J. *Prog. Nucl. Magn. Reson. Spectrosc.* **1984**, *16*, 237.
- (150) Thomas, J.M.; Klinowski, J. *Adv. In Catal.* **1985**, *33*, 199.
- (151) Thomas, J.M., Klinowski, J.; Wright, P.A.; Roy, R. *Angew. Chem. Int. Ed. Engl.* **1983**, *22*, 614.
- (152) Pfeifer, H. "Applications of NMR Spectroscopy to Surfaces and Catalysts: Acidic Sites and Absorbed Species", in *Nuclear Magnetic Resonance in Modern Technology*, Maciel, G.E. ed., NATO ASI Series, Vol. 447, Kluwer Academic Publisher, Dordrecht, Netherlands, 1994.
- (153) Hoh, K.P.; Ishida, H. Koenig, J.L. *Polym. Compos.* **1990**, *11*, 192.
- (154) Bhagawan, S.S.; Tripathy, D.K.; De, S.K. *J. Appl. Polym. Sci.* **1987**, *34*, 1581.
- (155) Kirkpatrick, R.J.; Smith, K.A.; Schramm, S.; Turner, G.; Yang, W.H. *Annu. Rev. Earth and Planet. Sci.* **1985**, *13*, 29.
- (156) Kirkpatrick, R.J.; Kinsey, R.A.; Smith, K.A.; Henderson, D.M., Oldfield, E. *Am. Mineral.* **1985**, *70*, 106.
- (157) Smith, K.A.; Kirkpatrick, R.H.; Oldfield, E.; Henderson, D.M. *Am. Mineral.* **1983**, *68*, 1206.
- (158) Haddix, G.W.; Narayana, M. "NMR of Layered Materials for Heterogeneous Catalysis", in *NMR Techniques in Catalysis*, Bell, A.T.; Pines, A., eds. Marcel Dekkar, Inc. New York, 1994.
- (159) Smith, K.A.; Kirkpatrick, R.J.; Oldfield, E.; Henderson, D.M. *Am. Mineral.* **1985**, *70*, 106.
- (160) Pfeifer, H. *Colloids and Surfaces* **1989**, *36*, 169.
- (161) Hunger, M.; Freude, D.; Pfeifer, H. *J. Chem. Soc. Faraday Trans.* **1991**, *87*, 657.
- (162) Kummerlien, J.; Merwin, L.H.; Sebal, A.; Keppler, H. *J. Phys. Chem.* **1992**, *96*, 6405.
- (163) Haw, J.F. "In Situ NMR", in *NMR Techniques in Catalysis*, Bell, A.T.; Pines, A. eds., Marcel Dekkar, Inc., New York, 1994.
- (164) Peeters, M.P.J.; Wahelkamp, W.J.J.; Kentgens, A.P.M. *J. Non-Cryst. Solids* **1995**, *189*, 77.
- (165) Muller, D.; Gessner, W.; Behrens, H.J.; Scheler, G. *Chem Phys. Lett.* **1981**, *79*, 59.
- (166) Mueller, D.; Hoebbel, D.; Gessner, W. *Chem. Phys. Lett.* **1982**, *84*, 25.
- (167) Mueller, D.; Rettel, A.; Gessner, W.; Scheler, G. *J. Magn. Reson.* **1984**, *57*, 152.
- (168) Muller, D.; Gessner, W.; Samoson, A.; Lippmaa, E.; Scheler, G. *J. Chem. Soc. Dalton Trans.* **1986**, 1277.
- (169) Muller, D.; Gessner, W.; Samoson, S.; Lippmaa, E., Scheler, G. *Polyhedron* **1986**, *5*, 779.
- (170) Samoson, A.; Kundla, E.; Lippmaa, E. *J. Magn. Reson.* **1982**, *49*, 350.
- (171) Kundla, E.; Samoson, A.; Lippmaa, E. *Chem. Phys. Lett.* **1981**, *83*, 229.
- (172) Sanz, J.; Serratos, J.M. *J. Am. Chem. Soc.* **1984**, *106*, 4790.
- (173) Smith, M.E. *Appl. Magn. Reson.* **1993**, *4*, 1.
- (174) Smith, M.E. *Solid-State NMR* **1994**, *3*, 111.
- (175) Lambert, S.F.; Millman, W.S.; Fripiat, J.J. *J. Am. Chem. Soc.* **1989**, *111*, 3517.
- (176) Alemany, L.B.; Kirker, G.W. *J. Am. Chem. Soc.* **1986**, *108*, 6158.
- (177) Gilson, J.P.; Edward, G.C.; Peters, A.W.; Rajagopalan, K.; Worsbecker, R.F.; Roberie, T.G.; Shatlock, M.P. *J. Chem. Soc. Chem. Comm.* **1987**, 91.

- (178) Ganapathy, S.; Schramm, S.; Oldfield, E. *J. Phys. Chem.* **1982**, *77*, 4360.
- (179) Dec, S.F.; Maciel, G.E. *J. Magn. Reson.* **1990**, *87*, 153.
- (180) Alemany, L.B.; Massiot, D.; Sheriff, B.L.; Smith, M.E.; Taulelle, F. *Chem. Phys. Lett.* **1991**, *177*, 301.
- (181) Samoson, A.; Lippmaa, E. *Phys. Rev. B*, **1983**, *28*, 6567.
- (182) Alemany, L.B. *Appl. Magn. Reson.* **1993**, *4*, 170.
- (183) Alma, N.C.M.; Hayes, R.G.; Samoson, A.; Lippmaa, E. *Anal. Chem.* **1984**, *56*, 729.
- (184) Alemany, L.B. *Appl. Magn. Reson.* **1993**, *4*, 172.
- (185) Clayden, N.J.; Dobson, C.M.; Groves, G.W.; Hayes, C.J.; Rodger, S.A. *Brit. Ceram. Proc.* **1984**, *35*, 55.
- (186) Clayden, N.J. *J. Chem. Soc.* **1987**, 1877.
- (187) Skibsted, J.; Jakobsen, H.J.; Hall, C. *J. Chem. Soc. Faraday Trans.* **1994**, *90*, 2095.
- (188) Skibsted, J.; Henderson, E.; Jakobsen, H.J. *Inorg. Chem.* **1993**, *32*, 1013.
- (189) Kunath-Fandrei, G.; Bastow, T.J.; Hall, J.S.; Jäger, C.; Smith, M.E. *J. Phys. Chem.* **1995**, *99*, 15138.
- (190) Fitzgerald, J. J.; Piedra, G.; Dec, S. F.; Seger, M.; Maciel, G. E. *J. Am. Chem. Soc.* **1997**, *33*, 7832.
- (191) Piedra, G.; Fitzgerald, J.J.; Ridenour, C.F.; Maciel, G.E. *Langmuir* **1996**, *2*, 1958.
- (192) Piedra, G.; Fitzgerald, J.J.; Dando, N.; Dec, S.F.; Maciel, G.E. *Inorg. Chem.* **1996**, *35*, 3474.
- (193) Walter, T.H.; Oldfield, E. *J. Phys. Chem.* **1989**, *93*, 6744.
- (194) John, C.S.; Alma, N.C.M.; Hays, G.R. *Appl. Catal.* **1983**, *6*, 341.
- (195) Huggins, B.A.; Ellis, P.D. *J. Am. Chem. Soc.* **1992**, *114*, 2098.
- (196) Coster, D.; Blumenfeld, A.L.; Fripiat, J.J. *J. Phys. Chem.* **1994**, *98*, 6201.
- (197) Kunath, G.; Losso, P.; Schneider, H.; Steuermagel, S.; J.S.; Jager, C. *Solid-State NMR* **1992**, *1*, 261.
- (198) Kraus, H.; Prins, R.; Kentgens, A.P.M. *J. Phys. Chem.* **1996**, *100*, 16336.
- (199) Fernandez, C.; Amoureux, J.P. *Chem. Phys. Lett.* **1995**, *242*, 449.
- (200) Rocha, J.; Esculcas, A.P.; Fernandez, C.; Amoureux, J.P. *J. Phys. Chem.* **1996**, *100*, 17889.
- (201) Rocha, J.; Lin, Z.; Fernandez, C.; Amoureux, J.P. *Chem. Comm.* **1996**, 251.
- (202) Schreiber, L.B.; Vaughan, R.W. *J. Catal.* **1975**, *40*, 226.
- (203) Batusis, L.; Fyre, J.S.; Maciel, G.E. *J. Am. Chem. Soc.* **1987**, *109*, 40.
- (204) Batusis, L.; Fyre, J.S.; Maciel, G.E. *J. Am. Chem. Soc.* **1986**, *108*, 7119.
- (205) Segawa, K.; Kurusu, Y.; Nakajima, Y.; Kinoshita, M. *J. Catal.* **1985**, *94*, 491.
- (206) Segawa, K.; Nakajima, Y.; Nakata, S.; Asaaka, S.; Takahashi, T. *J. Catal.* **1985**, *101*, 81.
- (207) Eckert, H. "NMR Spectroscopy of Bulk Oxide Catalysts" in *NMR Techniques in Catalysis*, Bell, A.T.; Pines, A., eds. Marcel Dekkar, Inc. New York, 1994.
- (208) Eckert, H.; Wachs, I.E. *J. Phys. Chem.* **1989**, *93*, 6796
- (209) Hardcastle, F.D.; Wachs, I.E.; Eckert, H.; Jefferson, D.A. *J. Solid-State Chem.* **1991**, *90*, 194.
- (210) Mastikhin, V.M.; Lapina, O.B.; Krasilnikov, V.N.; Ivakin, A.A. *React. Kinet. Catal. Lett.*, **1984**, *24*, 119.
- (211) Mastikhin, V.M.; Mudrakovsky, I.L.; Nasov, A.V. *Prog. NMR Spectrosc.* **1991**, *23*, 259.
- (212) Smits, R.H.H.; Seshan, K.; Ross, J.R.H.; Kentgens, A.P.M. *J. Phys. Chem.* **1995**, *99*, 169.
- (213) Edwards, J.C.; Adams, R.D.; Ellis, P.D. *J. Am. Chem. Soc.* **1990**, *112*, 8349.

- (214) Edwards, J.C.; Zubieta, J.; Shaikh, S.N.; Chen, Q.; Bank, S.; Ellis, P.D. *Inorg. Chem.* **1990**, *29*, 3381.
- (215) Weaver, C.E.; Pollard, L.D. *The Chemistry of Clay Minerals*, Elsevier Science Publishers, Inc. Netherlands, 1993.
- (216) Schramm, S.; Kirkpatrick, R.J.; Oldfield, E. *J. Am. Chem. Soc.* **1983**, *105*, 2483.
- (217) Schramm, S.; Oldfield, E. *J. Am. Chem. Soc.* **1984**, *106*, 2502.
- (218) Dec, S.F.; Fitzgerald, J.J.; Frye, J.S.; Shatlock, M.P.; Maciel, G.E. *J. Magn. Reson.* **1989**, *93*, 403.
- (219) Fitzgerald, J.J.; Hamza, A.I.; Dec, S.F. *Am. Mineral.* **1989**, *74*, 1405.
- (220) Fitzgerald, J.J.; Hamza, A.I.; Bronnimann, C.E.; Dec, S.F. *Solid-State Ionics* **1989**, *32/33*, 368.
- (221) Fitzgerald, J.J.; Bronnimann, C.E.; Dec, S.F.; Hamza, A.I. *J. Am. Chem. Soc.* **1997**, *119*, 7105.
- (222) Fitzgerald, J.J.; Hamza, A.I.; Dec, S.F.; Bronnimann, C.E. *J. Phys. Chem.* **1996**, *100*, 17351.
- (223) Kolodziejewski, W.; Klinowski, J. "New Techniques for the Study of Catalysis", in *NMR Techniques in Catalysis*, Bell, A.T.; Pines, A. eds., Marcel Dekker, Inc. New York, 1994.
- (224) Stebbins, J.F. *Am. Mineral.* **1996**, *9*, 1315.
- (225) Xue, X.; Stebbins, J.F.; Kanzaki, M. *Am. Mineral.* **1994**, *79*, 31.
- (226) Xue, X.; Stebbins, J.F. *Phys. Chem. Min.* **1993**, *20*, 297.
- (227) Jager, C.; Dupree, R.; Kohn, S.C.; Mortuza, M.G. *J. Non-Cryst. Sol.* **1993**, *155*, 95.
- (228) Timken H.K.C.; Schramm, S.E.; Kirkpatrick, R.J. Oldfield, E. *J. Phys. Chem.* **1987**, *91*, 1054.
- (229) Zhang, P.; Grandinetti, P.J.; Stebbins, J.F. *J. Phys. Chem. B* **1997**, *101*, 4004.
- (230) Millard, R.L.; Peterson, R.C.; Hunter, B.K. *Am. Mineral.* **1992**, *77*, 44.
- (231) Bank, S.; Bank, J.F.; Ellis, P. *J. Phys. Chem.* **1989**, *93*, 4847.
- (232) Liang, J.J.; Sherrif, B.L. *Geochim. et. Cosmochimica.* **1993**, *57*, 3885.
- (233) Bank, J.F.; Ofori-Okai, G.; Bank, S. *Clay and Clay Minerals*, **1993**, *41*, 95.
- (234) Laperche, V.; Lambert, J.F.; Frost, R.; Fripiat, J.J. *J. Phys. Chem.* **1990**, *94*, 8821.
- (235) Weiss, C.A.; Kirkpatrick, R.J.; Altaner, S.P. *Geochim. Cosmochim. Acta.* **1990**, *54*, 1655.
- (236) Wilson, S.T.; Lok, B.M.; Messina, C.A.; Cannan, T.R.; Flanigen, E.M. *J. Am. Chem. Soc.* **1982**, *104*, 1146.
- (237) MacLachlan, D.J.; Morgan, K.R. *J. Phys. Chem.* **1990**, *94*, 7656.
- (238) Davies, M.E.; Murray, B.D.; Narayana, M. in *Novel Materials in Heterogeneous Catalysis*, ACS Symposium, Series 437, Baker, R.T.K.; Murrell, L.L., eds. ACS Books, New York, 1990.
- (239) Barrie, P.J.; Klinowski, J. *J. Phys. Chem.* **1989**, *93*, 5972.
- (240) Szostak, R. *Molecular Sieves*, Van Nostrand, Reinhold, New York, 1989.
- (241) Grobet, P.J.; Martens, J.A.; Balakrishnan, I.; Mertens, M.; Jacobs, P.A. *Appl. Catal.* **1989**, *56*, L21.
- (242) Tanev, P.T.; Chibwe, M; Pinnavaia, T.J. *Nature* **1994**, *368*, 321.
- (243) Zhang, W.; Froba, M.; Wang, J.; Tanev, P.T.; Wong, J.; Pinnavaia, T.J. *J. Am. Chem. Soc.* **1996**, *118*, 9164.
- (244) Bortun, A.I.; Bortun, L.N.; Clearfield, A. *Chem. Mater.* **1997**, *9*, 1854.
- (245) Poojary, D.M.; Bortun, A.I.; Bortun, L.N.; Clearfield, A. *Inorg. Chem.* **1996**, *35*, 6131.

- (246) Clerici, M.G.; Bellussi, G.; Romano, U. *J. Catal.* **1991**, *129*, 159.
- (247) Huybrechts, D.R.C.; DeBruycker, L.; Jacobs, P.A. *Nature* **1990**, *345*, 240.
- (248) Sankar, G.; Rey, F.; Thomas, J.M.; Greaves, G.N.; Corma, A.C.; Dobson, B.R.; Dent, A.J. *J. Chem. Soc. Chem. Comm.* **1994**, 2279.
- (249) Serrano, O.P.; Uguina, M.A.; Ovejero, G.; Van Grieken, R.; Camacho, M. *Chem. Comm.* **1996**, 1097.
- (250) Anderson, M.W.; Terasaki, O.; Ohsuna, T.; Phillippou, A.; MacKay, S.P.; Ferreira, A.; Jocha, J.; Lidin, S. *Nature* **1994**, *367*, 347.
- (251) Kingery, W.D.; Bowen, K.H.; Wholman, D.R. *Introduction to Ceramics*, 2nd Ed., John Wiley, New York, 1975.
- (252) Ichinose, N. *Introduction to Fine Ceramics*, John Wiley and Sons, New York, 1987.
- (253) Buchanan, R. ed., *Ceramic Materials for Electronics*, Marcel Dekkar, Inc. New York, 1986.
- (254) Lines, M.E.; Glass, A.M. *Principles and Applications of Ferroelectric and Related Materials*, Clarendon Press, Oxford, 1977.
- (255) Jona, F.; Shirane, G. *Ferroelectric Crystals*, Dover Publishers, Inc. New York, 1993.
- (256) Hench, L.L.; Ulrich, D.R., eds. *Ultrastructure Processing of Ceramics, Glasses, and Composites*, Wiley-Interscience, New York, 1984.
- (257) Hench, L.L.; Ulrich, D.R., eds. *Science of Ceramic Chemical Processing*, Wiley-Interscience, New York, 1986.
- (258) Pask, J.; Evans, A., eds. *Surfaces and Interfaces in Ceramics*, Materials Science Research, Volume 14, Plenum Press, New York, 1980.
- (259) Thompson, D.P. *Nitrogen Ceramics*, Riley, F.L. ed., Noordhoff, Leyden, 1977.
- (260) Jack, K.H. *Progress in Nitrogen Ceramics*, Riley, F.L. ed., Martinus, Nijhoff, 1983.
- (261) Jack, K.H. *Mat. Sci.* **1976**, *11*, 1135.
- (262) Thompson, D.P. "Nitride Ceramics," in *Tailoring Multiphase and Composite Ceramics*, Tressler, R.E.; Messing, G.L.; Pantono, C.G.; Newnham, R.G. eds., Plenum, New York, 1986.
- (263) Turner, G. L.; Kirkpatrick, R. T.; Risbud, S. H.; Oldfield, E. *Am. Ceram. Soc. Bull.* **1987**, *66*, 656.
- (264) Bray, P.J.; Gravine, J.S. "NMR of Ceramics", in *Ultrastruct. Pro. Ceram.Glasses*, (Proc. Internatl. Conf.), Hench, L.L.; Ulrich, D.R. eds., Wiley-Interscience, New York, 1984.
- (265) Dupree, R. "NMR Studies of Glasses and Ceramics", in *Nuclear Magnetic Resonance in Modern Technology*, Maciel, G.E. ed., NATO ASI Series, Vol. 447, Kluwer Academic Publishers, Dordrecht, Netherlands, 1994.
- (266) Kemiya, K. *Preparation of Oxide Glasses From Metal Alkoxides By Sol-Gel Method*, NASA, Washington, D.C. 1987.
- (267) Kirkpatrick, R.J.; Dunn, T.; Schramm, S.; Sinter, K.A.; Oestrike, R. Turner, G. "Magic-Angle Sample Spinning NMR Spectroscopy of Silicate Glasses", in *Structure and Bonding Noncrystalline Solids*, Walrafer, G.E.; Revesz, A.G. eds., Plenum Press, New York, 1986.
- (268) Pye, L.D.; Frechette, V.D.; Kreidl, N.J. eds., *Boron in Glass and Glass Ceramics*, Materials Science Research, Volume 12, Plenum Press, New York, 1978.

- (269) Dupree, R.; Holland, D.; Mortuza, M.G.; Collin, J.A.; Lockyer, M.W.G. *J. Non-Cryst. Sol.* **1989**, *112*, 111.
- (270) Dupree, R.; Holland, D.; Mortuza, M.G.; Collin, J.A.; Lockyer, M.W.G. *J. Non-Cryst. Sol.* **1988**, *106*, 403.
- (271) Dupree, R.; Holland, D.; Williams, D. S. J. *De Physique* **1985**, *46*, 119.
- (272) Dupree, R.; Holland, D.; McMillan, P.W.; Pettifer, R.F. *J. Non-Cryst. Sol.* **1984**, *68*, 399.
- (273) Dupree, R.; Holland, D.; Mortuza, M.G. *Phys. Chem. Glasses* **1988**, *29*, 18.
- (274) Dupree, R.; Gencten, A.; Paul, D.M. *Physica C.* **1992**, *193*, 81.
- (275) Carduner, K.R.; Shinozaki, S.S.; Rokosz, M.J.; Peters, C.R.; Whalen, T.J. *J. Am. Ceram. Soc.* **1990**, *73*, 2281.
- (276) MacKenzie, K.J.D.; Meinhold, R.H.; McGavin, D.G.; Ripmeester, J.A.; Moudrakovski, I. *Solid-State NMR* **1995**, *4*, 193.
- (277) Brow, R.K.; Kirkpatrick, R.J.; Turner, G.L. *J. Non-Cryst. Sol.* **1990**, *116*, 39.
- (278) Xue, X.; Stebbins, J.F. *Phys. Chem. Min.* **1993**, *20*, 297.
- (279) Sato, R.K.; McMillan, P.F.; Denison, P.; Dupree, R. *J. Phys. Chem.* **1991**, *95*, 4483.
- (280) Dupree, R.; Holland, D.; Mortuza, M.G. *Nature* **1987**, *328*, 416.
- (281) Schramm, C.M.; de Jong, B.H.W.S.; Parziale, V.E. *J. Am. Chem. Soc.* **1984**, *106*, 4396.
- (282) Schramm, S.; Oldfield, E. *J. Am. Chem. Soc.* **1984**, *106*, 2502.
- (283) Turner, G.L.; Chung, S.E.; Oldfield, E. *J. Magn. Reson.* **1985**, *64*, 316.
- (284) Jager, C.; Dupree, R.; Kohn, S.C.; Mortuza, M.G. *J. Non-Cryst. Sol.* **1993**, *155*, 95.
- (285) Forbes, C.E.; Hammond, W.B.; Cipollina, N.E.; Lynch, J.F. *J. Chem. Soc. Chem. Comm.* **1987**, *6*, 433.
- (286) Xue, X.; Stebbins, Kanzaki. M. *Am. Mineral.* **1994**, *79*, 31.
- (287) Maekawa, H.; Florian, P.; Massiot, D.; Kiyono, H.; Nakamura, M.E. *J. Phys. Chem.* **1996**, *100*, 5525.
- (288) Florian, P.; Vermillion, K.E.; Grandinetti, P.J.; Farnan, I.; Stebbins, J.F. *J. Am. Chem. Soc.* **1996**, *118*, 3493.
- (289) Soroka, I. *Portland Cement Paste and Concrete*, Chemical Publishing Co., Inc. New York, 1980.
- (290) Turner, G.L.; Chung, S.E.; Oldfield, E. *J. Magn. Reson.* **1985**, *64*, 316.
- (291) Yang, S.; Park, K.D.; Oldfield, E. *J. Am. Chem. Soc.* **1985**, *111*, 7278.
- (292) Dirken, P.J.; Dupree, R.; Smith, M.E. *Mater. J. Chem.* **1995**, *5*, 1261.
- (293) Bastow, T.J.; Stuart, S.N. *Chem. Phys.* **1990**, *143*, 459.
- (294) Bastow, T.J.; Hobday, M.E.; Smith, M.E.; Whitfield, H.J. *Solid-State NMR* **1996**, *5*, 293.
- (295) Bastow, T.J. *J. Phys. Condens. Mat.* **1989**, *1*, 4985.
- (296) Kanert, O.; Schulz, H.; Albers, J. *J. Solid State Comm.* **1994**, *91*, 464.
- (297) Bastow, T.J.; Smith, M.E. *Solid-State NMR* **1992**, *1*, 165.
- (298) Ali, F.; Smith, M.E.; Steuernagel, S.; Whitfield, H.J. *J. Mater. Chem.* **1996**, *6*, 216.
- (299) Bastow, T.J.; Smith, M.E.; Whitfield, H.J. *J. Mater.* **1996**, *6*, 1951.
- (300) Bastow, T.J.; Hobday, H.E.; Smith, M.E.; Whitfield, H.J. *Solid-State NMR.* **1996**, *5*, 293.
- (301) Geissberger, A.E.; Bray, P.J. *J. Non-Cryst. Sol.* **1983**, *54*, 121.
- (302) Zhao, P.; Prasad, S.; Benjamin, M.; Huang, J.; Fitzgerald, J.J.; Shore, J. "Lead-207 NMR Spectroscopic Study of Piezoelectric Lead Magnesium Niobate and Related Materials." Rocky Mountain Conference on Analytical Chemistry, Aug., 1997.

- (303) Massiot, D.; Conanec, R.; Feldman, W.; Marchand, R.; Laurent, Y. *Inorg. Chem.* **1996**, *35*, 4957.
- (304) Hanna, J.V.; Smith, M.E.; Whitfield, H.J. *J. Am. Chem. Soc.* **1996**, *118*, 5772.
- (305) Walter, T.H.; Turner, G.L.; Oldfield, E. *J. Magn. Reson.* **1988**, *76*, 106.
- (306) Koller, H.; Engelhardt, G.; Kentgens, A.P.M.; Sauer, J. *J. Phys. Chem.* **1994**, *98*, 1544.
- (307) Koller, H.; Engelhardt, G.; Felsche, J. *Z. Anorg. Allg. Chem.* **1995**, *621*, 301.
- (308) Dec, S.F.; Maciel, G.E.; Fitzgerald, J.J. *J. Am. Chem. Soc.* **1990**, *112*, 9069.
- (309) Maekawa, H.; Florian, P.; Massiot, D.; Kiyono, H.; Nakamura, M. *J. Phys. Chem.* **1996**, *100*, 5 525.
- (310) Newnham, R.E. "Tunable Transducers: Nonlinear Phenomena in Electroceramics", in *Chemistry of Electronic Materials* (NIST Special Publication 804), **1990**, p. 39.
- (311) Cross, L.E. *Ferroelectrics* **1987**, *76*, 241.
- (312) Dec, S.F.; Davis, M.F.; Maciel, G.E.; Bronnimann, C.E.; Fitzgerald, J.J.; Han, S. *Inorg. Chem.* **1993**, *32*, 955.
- (313) Fayon, F.; Farnon, I.; Bessada, C.; Coutures, J.; Massiot, D.; Coutures, J.P. *J. Am. Chem. Soc.* **1997**, *119*, 6837.
- (314) Neue, G.; Dybowski, C.; Smith, M.L.; Hepp, M.A.; Perry, D.L. *Solid-State NMR*, **1996**, *6*, 241.
- (315) Youngman, R.E.; Hanbrick, S.T.; Zwanziger, J.W.; Janicke, M.T.; Chmelka, B.F. *Science*, **1995**, *269*, 1416.
- (316) Prasad, S.; Zhao, P.; Huang, J.; Fitzgerald, J.J.; Shore, J. "Niobium-93 Nutation Spectroscopic Study of Piezoelectric Lead Magnesium Niobate and Related Materials" Rocky Mountain Conference on Analytical Chemistry, Aug., 1997.
- (317) Marchetti, P.S.; Kwon, D.; Schmidt, W.R.; Interrante, L.V.; Maciel, G.E. *Chem. Mater.* **1990**, *3*, 482.
- (318) Finlay, G.R.; Hartman, J.S.; Richardson, M.F.; Williams, B.L. *J. Chem. Soc. Chem. Commun.* **1985**, 159.
- (319) Wenslow, R.M.; Mueller, K.T. In press, 1998.
- (320) Hartman, J.S.; Richardson, M.F.; Sherriff, B.L.; Winsbarrow, B.G. *J. Am. Chem. Soc.* **1987**, *109*, 6059.
- (321) Inkrott, K.E.; Wharry, S.M.; O'Donnell, D.J. *Mater. Res. Soc. Symp. Proc.* **1986**, *23*, 165.
- (322) Marshall, G.L.; Harris, R.K.; Apperly, D.; Yeung, R. *Sci. Ceram.* **1988**, *14*, 347.
- (323) Lipowitz, J.; Turner, G.L. *Polym. Prepr.* **1989**, *29*, 74.
- (324) Seyferth, J.; Strohmann, C.; Dando, N.R.; Perrotta, A.J. *Chem. Mater.* **1995**, *7*, 2058.
- (325) Seitz, J.; Bill, J.; Egger, N.; Aldinger, F. *J. Eur. Ceram. Soc.* **1996**, *16*, 885.
- (326) Schmidt, W.R.; Interrante, L.V.; Doremus, R.H.; Trout, T.K.; Marchetti, P.S.; Maciel, G.E. *Chem. Mater.* **1991**, *3*, 257.
- (327) Narsavage, D.M.; Interrante, L.V.; Marchetti, P.S.; Maciel, G.E. *Chem. Mater.* **1991**, *3*, 721.
- (328) Dybowski, C.; Gaffney, E.J.; Sayir, A.; Rabinowitz, M.R. *Colloids and Surf.* **1996**, *118*, 171.
- (329) Shinozak, S.S.; Carduner, K.R. *Trans. Mater. Res. Soc. Jpn. A* **1994**, *14*, 857.
- (330) McKenzie, K.J.D.; Meinhold, R.H.; Brown, I.W.; White, G.V. *J. Mater. Sci.* **1994**, *29*, 5631.
- (331) Carduner, K.R.; Carter, R.O.; Milberg, M.E.; Crosbie, G.M. *Anal. Chem.* **1987**, *59*, 2794.
- (332) Carduner, K.R.; Carter, R.O.; Rokosz, M.R.; Peters, C.; Crosbie, G.M.; Stiles, E.D. *Chem. Mater.* **1989**, *1*, 302.

- (333) Hatfield, G.; Li, B.; Hammond, W.B.; Reidinger, F.; Yamanis, J. *J. Mater. Sci.* **1992**, *25*, 4032.
- (334) Carduner, K.R.; Blackwell, C.S.; Hammond, W.B.; Reidinger, F.; Hatfield, G.R. *J. Am. Chem. Soc.* **1990**, *112*, 4676.
- (335) Zhang, M.; Maciel, G. *Anal. Chem.* **1990**, *62*, 633.
- (336) Olivieri, A.; Hatfield, G. *J. Magn. Reson.* **1991**, *94*, 535.
- (337) Harris, R.K.; Leach, M.; Thompson, D.P. *Chem. Mater.* **1989**, *1*, 336.
- (338) Harris, R.K.; Leach, M.J.; Thompson, D.P. *Chem. Mater.* **1990**, *2*, 320.
- (339) Harris, R.K.; Leach, M.J. *Chem. Mater.* **1992**, *4*, 261.
- (340) Harris, R.K.; Leach, M. *J. Am. Chem. Soc.* **1992**, *4*, 2, 260.
- (341) Smith, M.E. *J. Phys. Chem.* **1992**, *96*, 1444.
- (342) Dupree, R.; Lewis, M.H.; Smith, M.E. *J. Amer. Chem. Soc.* **1989**, *111*, 5125.
- (343) Kwon, D.; Schmidt, W.R.; Interrante, L.V.; Maciel, G.E. *Chem. Mater.* **1991**, *3*, 482.
- (344) Interrante, L.V.; Schmidt, W.R.; Marchetti, P.; Maciel, G.E. *Proc. Symp. Inorg. Polym.* Montreal, Canada, 1990.
- (345) Schmidt, W.R.; Interrante, L.V.; Doremus, R.H.; Trout, T.K.; Marchetti, P.; Maciel, G.E. *Chem. Mater.* **1991**, *3*, 257.
- (346) Dupree, R.; Lewis, M.H.; Smith, M.E. *J. Am. Chem. Soc.* **1988**, *110*, 1083.
- (347) Butler, D.; Dupree, R.; Lewis, M.H. *J. Mater. Sci. Lett.* **1984**, *3*, 469.
- (348) Li, H.; Butler, I.S.; Denis, F.R.; Harrod, J.F.; Morin, F.G. *J. Phys. Chem.* **1995**, *99*, 8490.
- (349) Carduner, K.R.; Blackwell, C.S.; Hammond, W.B.; Reidinger, F.; Hatfield, G.R. *J. Am. Chem. Soc.* **1990**, *112*(12), 4676.
- (350) Sjoeborg, J.; Harris, R.K.; Apperly, D.C. *J. Mater. Chem.* **1992**, *2*, 433.
- (351) Nordmann, A.; Cheng, Y.B.; Smith, M.E. *Chem. Mater.* **1996**, *8*, 2516.
- (352) MacKenzie, K.J.D.; Meinhold, R.H. *J. Mater. Chem.* **1994**, *4*, 1595.
- (353) Fitzgerald, J.J.; Kohl, S.D.; Piedra, G.; Dec, S.F.; Maciel, G.E. *Chem. Mater.* **1994**, *6*, 1915.
- (354) Massiot, D.; Conanec, R.; Feldman, W.; Marchand R.; Laurent, Y. *Inorg. Chem.* **1996**, *35*, 4957.
- (355) Bastow, T.J.; Dirken, P.J.; Smith, M.E. *J. Phys. Chem.* **1996**, *100*, 18539.
- (356) Whitmarsh, C.W.; Sherwood, W.; Wu, H.J.; Lewis, R.; Maciel, G.E. *Mater. Res. Soc. Symp. Proc.* **1994**, *346*, 593.
- (357) Weller, M.T.; Brenchley, M.E.; Apperly, D.C.; Davies, N.A. *Solid-State NMR* **1994**, *3*, 103.
- (358) Bastow, T.J.; Dirken, P.J.; Smith, M.E.; Whitfield, H.J. *J. Phys. Chem.* **1996**, *100*, 18539.
- (359) Dirken, P. J.; Smith, M. E.; Whitfield, H. J. *J. Phys. Chem.* **1995**, *99*, 395.
- (360) Cong, X.; Kirkpatrick, R.J. *Cement and Concrete Res.* **1993**, *23*, 1065.
- (361) Cong, X.; Kirkpatrick, R.J. *J. Am. Ceram. Soc.* **1996**, *79*, 158.
- (362) Holland, D.; Lockyer, M.W.G.; Dupree, R. *Br. Ceram. Proc.* **1996**, *55*, 145.
- (363) Lockyer, M.W.G.; Holland, D.; Dupree, R. *J. Non-Crys. Sol.* **1995**, *188*, 207.
- (364) Aue, W.P.; Roufosse, A.H.; Glimcher, M.J.; Griffin, R.G. *Biochem.* **1984**, *23*, 6110.
- (365) Rothwell, W.P.; Waugh, J.S.; Yesinowski, J.P. *J. Am. Chem. Soc.* **1980**, *102*, 2637.
- (366) Hinedi, Z.R.; Goldberg, S.; Chang, A.C.; Yesinowski, J.P. *J. Coll. Interf. Sci.* **1992**, *152*, 141.
- (367) Sarkar, G.; Fitzgerald, J.J. "²⁹Si and ³¹P CP/MAS NMR Studies of the Interfacial Interactions of Bioglass Materials", Rocky Mountain Conference on Analytical Chemistry, Aug., 1997.

- (368) Wu, Y.; Glimcher, M.J.; Rey, C.; Ackerman, J.L. *J. Mol. Biol.* **1994**, *244*, 423.
- (369) Janicke, M.T.; Landry, C.C.; Christianson, S.C.; Kumar, D.; Stucky, G.D.; Chemlka, B. *F. J. Am. Chem. Soc.* **1998**, *120*, 6940.
- (370) Knights, J.C., in *The Physics of Hydrogenated Amorphous Silicon. I. Structure, Preparation and Devices*, Joannopoulos, J.D.; Lucovsky, G. eds. Springer-Verlag, New York, 1984.
- (371) Taylor, P.C., "Semiconductors and Semimetals", Vol. 21, Part C, in *Hydrogenated Amorphous Silicon. Electronic and Transport Properties*, Pankove, J.I., ed. Academic Press, New York, 1984, and references therein.
- (372) Boshah, K.; Zamir, D.; Becla, P.; Wolff, P.A.; Griffin, R.G. *Phys. Rev. B.* **1987**, *36*, 6420.
- (373) Tolbert, S.H.; Firouz, A.; Stucky, G.D.; Chmelka, B.F. In press, 1998.
- (374) Han, O.H.; Timken, H.K.C.; Oldfield, E. *J. Chem. Phys.* **1988**, *89*, 6046.
- (375) Ryan, M.A.; Peterson, M.W.; Williamson, D.L.; Frye, J.S.; Maciel, G.E.; Parkinson, B. *A. Mater. J. Res.* **1987**, *2*, 528.
- (376) Tycko, R.; Dabbagh, G.; Kurtz, S.R.; Goral, J.P. *Phys. Rev. B.* **1992**, *54*, 13452.
- (377) Franke, D.; Banks, K.; Eckert, H. *J. Phys. Chem.* **1992**, *96*, 11048.
- (378) Franke, D.; Maxwell, R.; Lathrop, D.; Banks, K.; Eckert, H. *Phys. Rev. B* **1992**, *46*, 8109.
- (379) Williams, G.V.; Tallon, J.L.; Michalak, R.; Dupree, R. *Phys. Rev. B. Condens. Mat.* **1996**, *54*, R6909.
- (380) Franke, D.; Hudalla, C.; Maxwell, R.; Eckert, H. *J. Phys. Chem.* **1996**, *19*, 7506.
- (381) Adler, S.B.; Reimer, J.A.; Baltisberger, J.; Werner, U. *J. Am. Chem. Soc.* **1994**, *116*, 675.
- (382) Oldfield, E.; Coretsopoulos, C.; Yang, S.; Reven, L.; Shore, J.; Han, O. H.; Ramli, E.; Hinks, D.G. *Phys. Rev. B.* **1989**, *40*, 6832.
- (383) Coretsopoulos, C.; Lee, H.C.; Ramli, E.; Reven, L.; Rauchfuss, T.B.; Oldfield, E. *Phys. Rev. B.* **1989**, *39*, 781.
- (384) Reven, L.; Shore, J.; Yang, S.; Duncan, T.; Schwartz, D.; Chung, J.; Oldfield, E. *Phys. Rev. B.* **1991**, *43*, 10466.
- (385) Pennington, C.H.; Slichter, C.P. "Nuclear Resonance Studies of $\text{YBa}_2\text{Cu}_3\text{O}_{7-x}$ ", in *Physical Properties of High-Temperature Superconductors II*, Ginsberg, D.M. ed., World Scientific, Singapore, 1990.
- (386) Howes, A.P.; Dupree, R.; Han, Z.P.; Liu, R.S.; Edwards, P.P. *Phys. Rev. B.* **1993**, *47*, 11529.
- (387) G.P.; Martins, J.L.; Zunger, A. *Phys. Rev. B.* **1985**, *31*, 2561.
- (388) Hull, D. in *Introduction to Composite Materials*, Cambridge University Press, Cambridge, England, 1981.
- (389) "Ceramic Matrix Composites" in *Composites* **1987**, *18*, 88.
- (390) Peters, P.W.M.; Chou, T.W. *Composites* **1987**, *18*, 40.
- (391) Bergstrom, L.; Pugh, R.J. *J. Am. Ceram. Soc.* **1989**, *72*, 103.
- (392) Rice, R.W. *Ceram. Eng. and Sci. Proc.* **1981**, *7-8*, 661.
- (393) Buljan, S.T.; Sarin, V.K. *Composites* **1987**, *18*, 92.
- (394) Lundberg, R.; Nyberg, B.; Willander, K.; Persson, M.; Carlsson, R. *Composites* **1987**, *18*, 125.
- (395) Sarin, V.K.; Ruhle, M. *Composites* **1987**, *18*, 129.
- (396) Crimp, M.J.; Johnson, Jr., R.E.; Halloran, J.W.; Feke, D.L. "Colloidal Behavior of Silicon Carbide and Silicon Nitride," in *Science of Ceramic Chemical Processing*, Hench, L.L.; Ulrich, D.R. eds., Wiley, New York, 1986.

- (397) Turan, S.; Knowles, K. *J. Am Ceram. Soc.*, **1996**, *79*, 2892.
- (398) Xu, X.; Holmes, J.W.; Hilmas, G.E. *Handb. Contin. Fiber-Reinf. Ceram. Matrix Compos.* **1995**, 431.
- (399) Vicens, J.; Doreau, F.; Chermant, J.L. *J. Microsc.* **1995**, *177*, 242.
- (400) Huang, C.M.; Zhu, D.; Xu, Y.; Kriven, W.M.; Chao, C.Y. *Mater. Sci. Eng. A* **1996**, *220*, 176.
- (401) Bronsveld, P.M.; Gideonse, I.; Van der Heide, A.; Guder, S.; De Hosson, J.H.M.; Sabouret, E.; Xu, X.; Holmes, J.M.; Hilmas, G.E. *Handb. Contin. Fiber-Reinf. Ceram. Matrix Compos.* **1995**, 431.
- (402) Razzell, A.G.; Lewis, M.H. *J. Microsc.* **1993**, *169*, 215.
- (403) Lee, K.N.; Jacobson, N.S.; Miller, R.A. *Refractory Oxide Coatings on Silicon Carbide Ceramics*, NASA, Washington, D.C., 1994.
- (404) Roychem, J.; Zhang, S.; For, W.T. *Macromol.* **1996**, *29*, 1305.
- (405) Koeniz, J.L. *Polym. Compos.* **1990**, *11*, 121.
- (406) Weeding, T.L.; Veeman, W.S.; Jennekens, L.W.; Gaur, H.A.; Schuurs, H.E.C.; Huysmans, W.G. B. *Macromol.* **1989**, *22*, 206.
- (407) Corey, R.L.; Curro, N.J.; O'Hara, K.; Imai, T.; Slichter, C.C.; Yashimura, K.; Katoh, M.; Kosuge, K. *Phys. Rev. B Condens. Mat.* **1996**, *53*, 5907.
- (408) Han, Z.P.; Dupree, R.; Gencten, A.; Lui, R.S.; Edwards, P.P. *Phys. Rev. Lett.* **1992**, *69*, 1256.
- (409) Imai, T.; Slichter, C.P.; Cobb, J.L.; Markert, J.T. *J. Phys. Chem.* **1995**, *56*, 1921.

Chapter 2

Multiple-Quantum Magic-Angle Spinning NMR of Half-Integer Quadrupolar Nuclei

Ales Medek, Laura Marinelli, and Lucio Frydman¹

Department of Chemistry (M/C 111), University of Illinois at Chicago, 845 West Taylor Street, Chicago, IL 60607-7061

The present report reviews some of the principles and practical details involved in multiple-quantum magic-angle spinning (MQMAS) NMR, a technique that we have recently introduced for the acquisition of high-resolution solid phase spectra from half-integer quadrupolar spins. The way in which MQMAS achieves the simultaneous averaging of all solid state spin anisotropies is discussed and placed in perspective with respect to previous procedures involving spatial averaging. The new chemical information that in a high resolution format can become available using MQMAS is described and illustrated, as are a number of experimental hints useful for its practical implementation. Challenges currently faced by the MQMAS procedure are discussed and potential solutions to these problems presented.

The NMR of Half-Integer Quadrupolar Spins

Quadrupolar nuclei with half-integer spin numbers ($S = 3/2, 5/2, 7/2, 9/2$) constitute the single largest group of magnetically active nuclides in the Periodic Table (Figure 1) (1). The elements associated with these isotopes play fundamental roles in a variety of technologically important materials including ceramics, glasses, catalysts and semi-conductors, as well as in numerous bioorganic processes and biological structures. The inconvenience and sometimes even impossibility of characterizing the structure and dynamics of many of these systems using conventional liquid phase spectroscopy has stimulated a continued interest in the development of methods that will allow their study in the solid phase. Particularly promising appears the study of these mostly inorganic structures by way of nuclear magnetic resonance (NMR) (2-4), a method which has already proven decisive in the study of organic and bioorganic systems using spin-1/2 probes (5). An important difference that from the NMR point of view arises between the spectroscopy of half-integer quadrupoles and that of spin-1/2 nuclei, is that the former interact not only with the external magnetic field but also with local electric field gradients (6). The resulting quadrupolar interaction can give origin to considerably large coupling constants (e^2qQ/h) capable of reaching into the hundreds or even thousands of MHz; in such extreme cases quadrupole and Larmor frequencies become comparable and the

observation of signals from powdered samples may actually become easier to achieve under zero-field operation (6,7).

The scenario that we will be considering here is one where although large, the e^2qQ/h coupling constant is still small compared to the Larmor frequency ν_L . It is then possible to describe the effects introduced by the quadrupolar couplings on a spin energy spectrum using a perturbative approach like the one illustrated in Figure 2 for a spin-3/2. As shown in this hierarchical diagram quadrupole effects are to first order proportional to the square of the z angular momentum of the S spin ($m = 3/2, 1/2, \dots$), thus shifting the satellite $+3/2 \leftrightarrow +1/2$ and $-3/2 \leftrightarrow -1/2$ transitions but leaving unaffected the central $-1/2 \leftrightarrow +1/2$ spectral line. Since these first order effects $\Delta_1(\theta, \varphi)$ are proportional to e^2qQ/h and anisotropic, they will complicate or even preclude the detection in powdered solids of all single-quantum transitions other than the central one. For small enough values of e^2qQ/h this remaining $-1/2 \leftrightarrow +1/2$ transition will be essentially devoid from quadrupolar broadening, and high-resolution solid state NMR spectra can simply be recorded by its observation (8,9). This situation does occasionally arise when dealing with chemical sites possessing a sufficiently high degree of local symmetry; in a majority of cases, however, quadrupolar effects will not be sufficiently small to allow this first-order description of the events to be appropriate. In these cases the $e^2qQ/h \ll \nu_L$ condition is violated, and even central transition signals will show anisotropic broadenings due to the onset of second-order effects $\Delta_2(\theta, \varphi)$ (Figure 2, right-hand column). We will be concerned with this kind of situation throughout the present treatment.

An important distinction between second-order effects and the more familiar first-order ones like the shielding or dipolar couplings occurring in spin-1/2 spectroscopy, is that instead of being linearly dependent on the spin interaction they are proportional to the interaction *squared* (6,8-10). A consequence of this is that even though the quadrupolar interaction itself is a traceless second-rank tensor with a $(3\cos^2\theta - 1)/2$ angular dependence, the second-order effects that it originates will involve a more complex behavior. Symmetry considerations allow one to conveniently decompose the orientation dependence of $\Delta_2(\theta, \varphi)$ into three frequency terms $\{\delta_q^{(i)}\}_{i=0,2,4}$, according to (11,12)

$$\Delta_2(\theta, \varphi) = \frac{(e^2qQ/h)^2}{\nu_L} [\delta_q^{(0)} + \delta_q^{(2)}(\theta, \varphi) + \delta_q^{(4)}(\theta, \varphi)] \quad (1)$$

Each of these terms possesses a characteristic behavior upon sample reorientation. $\delta_q^{(0)}$ is an orientation independent contribution of quadrupolar origin that behaves very similarly to the isotropic chemical shift ν_{CS} ; $\delta_q^{(2)}(\theta, \varphi)$ is a second-rank anisotropic frequency term that transforms in the same manner as shielding or dipolar anisotropies; $\delta_q^{(4)}$ is a new fourth-rank anisotropy that arises due to the fact that we are dealing with the square of the quadrupolar interaction. Notice that in spite of their different angular dependence all these terms will affect an NMR spectrum in direct proportion to the quadrupole coupling squared, and inversely proportional to the strength of the applied field B_0 .

																		Spin-1																							
																		Half-Integer Quadrupolar Spins																							
																		Spin-1/2																							
																		No Spin																							
H																	He	B	C	N	O	F	Ne																		
Li	Be															Al	Si	P	S	Cl	Ar																				
Na	Mg															K	Ca	Sc	Ti	V	Cr	Mn	Fe	Co	Ni	Cu	Zn	Ga	Ge	As	Se	Br	Kr								
Rb	Sr	Y	Zr	Nb	Mo	Tc	Ru	Rh	Pd	Ag	Cd	In	Sn	Sb	Te	I	Xe																								
Cs	Ba	La	Hf	Ta	W	Re	Os	Ir	Pt	Au	Hg	Tl	Pb	Bi	Po	At	Rn																								
Fr	Ra	Ac															Ce	Pr	Nd	Pm	Sm	Eu	Gd	Tb	Dy	Ho	Er	Tm	Yb	Lu											
			Th	Pa	U	Np	Pu	Am	Cm	Bk	Cf	Es	Fm	Md	No	Lr																									

Figure 1. Periodic Table of the Elements indicating the nature of the most abundant NMR-active isotopes.

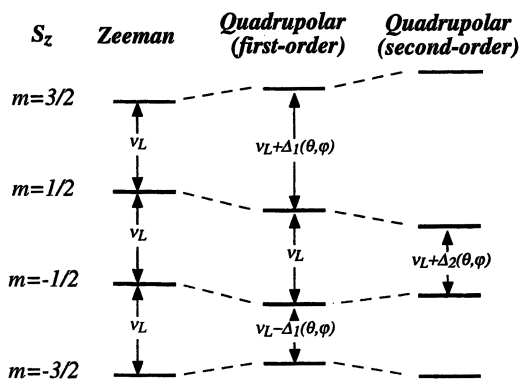


Figure 2. Perturbative description of the effects introduced by Zeeman and quadrupolar interactions on the energy levels of a spin-3/2.

Although the presence of an isotropic quadrupolar shift opens up the attractive possibility of distinguishing chemical sites according to the symmetry of their ground-state electronic environments, $\delta_q^{(2)}$ and $\delta_q^{(4)}$ will usually broaden the central transition signals arising from $\Delta_2(\theta, \varphi)$ and thus prevent the resolution or analysis of inequivalent sites. The resolution of these quadrupolar spectra can be improved by rapid spinning of the powdered sample at an angle β with respect to the external magnetic field (5). Under the effect of this process each term in equation 1 will transform differently, leading in the fast-spinning regime to an average time evolution given by (13,14)

$$\phi(\beta, t) = (v_{cs} + v_q^{(0)})P_0(\cos\beta)t + v_q^{(2)}(\theta, \varphi)P_2(\cos\beta)t + v_q^{(4)}(\theta, \varphi)P_4(\cos\beta)t \quad (2)$$

where ϕ corresponds to the usual rotating frame phase evolved by the spins a time t after excitation. In this equation the $\{v_q^{(l)}\}_{l=0,2,4}$ represent l^{th} -rank quadrupolar frequencies arising from the $\{\delta_q^{(l)}\}_{l=0,2,4}$ terms,

$$P_0(\cos\beta) = 1 \quad (3)$$

$$P_2(\cos\beta) = (3\cos^2\beta - 1)/2 \quad (4)$$

$$P_4(\cos\beta) = (35\cos^4\beta - 30\cos^2\beta + 3)/8 \quad (5)$$

are zero-, second- and fourth-order Legendre polynomials of the cosine of the spinning angle β , and for the sake of completeness we have included the possibility of having a distinct isotropic chemical shift v_{cs} .

Averaging Out the Second-Order Quadrupolar Anisotropies

The simultaneous presence of anisotropies proportional to $P_2(\cos\beta)$ and $P_4(\cos\beta)$ in equation 2 confronts solid state quadrupolar NMR with a serious resolution limitation. Even though first-order effects can be bypassed by monitoring the central transition and second-order effects can be scaled down by sample spinning, equations 2-5 imply that no rotation angle β can be found for which all anisotropic contributions will simultaneously vanish. This can be more clearly appreciated from the diagrams of $P_2(\cos\beta)$ and $P_4(\cos\beta)$ in Figure 3, which show that even though these function can be individually nulled they do not share a common root. Solutions to this important and long-standing challenge in solid state NMR were put forward in the late eighties and crystallized in the development of two new techniques, dynamic-angle spinning (DAS) and double rotation (DOR), of important practical consequences (11,12,15-17). A common characteristic that distinguishes these novel high-resolution techniques from conventional spatial averaging methods such as MAS is the introduction of an additional spatial degree of freedom in the manipulations that define the spin evolution. Indeed both DOR and DAS involve *changing* the values taken by $P_2(x)$ and $P_4(x)$ throughout the course of the experiment, a time modulation which occurs continuously in DOR by virtue of simultaneous sample spinning about two different axes, and in a stepwise fashion in DAS via the implementation of a 2D NMR experiment. Specifically, this latter approach involves two different evolution times (t_1 and t_2) associated with

independent spinning angles (β_1 and β_2), all chosen so as to simultaneously cancel second- and fourth-rank anisotropies by fulfilling the conditions

$$P_2(\cos\beta_1)t_1 + P_2(\cos\beta_2)t_2 = 0 \quad (6)$$

$$P_4(\cos\beta_1)t_1 + P_4(\cos\beta_2)t_2 = 0 \quad (7)$$

In spite of the promising applications opened up by these new high-resolution methods, the question arises of whether it is possible to achieve a similar averaging of second-order anisotropies *without* employing complex mechanical manipulations. We have recently shown that such goal is indeed possible, based on a re-consideration of the energy level diagram presented in Figure 2 (18,19). According to this diagram, the quadratic dependence of $\Delta_1(\theta,\varphi)$ on the quantum number m implies that not only the central but in fact *any* $-m \leftrightarrow +m$ transition within a half-integer spin manifold will be devoid from first-order effects. These additional multiple-quantum transitions (of which there is always at least a triple-quantum one for any quadrupolar spin) will consequently be affected only by second-order effects $\Delta'_2(\theta,\varphi)$, which by symmetry considerations will in turn be composed by a sum of zero- through fourth-rank terms such as the one described in equation 1. The resulting "proportionality" between the anisotropic components affecting central and multi-quantum transitions provides the possibility of employing the quantum number m —rather than the spinning angle β —in order to achieve the elimination of quadrupolar broadenings. In order to clarify this possibility it becomes necessary to include the quantum number m defining a particular $-m \leftrightarrow +m$ transition into the full description of the spin coherence evolution. Appropriate transformations then lead to a generalized version of equation 2 applicable to all symmetric transitions within the spin manifold, of the form

$$\begin{aligned} \phi(m, \beta, t) = & 2m\nu_{cs}t + C_s^{(0)}(m)P_0(\cos\beta)v_q^{(0)}t + C_s^{(2)}(m)P_2(\cos\beta)v_q^{(2)}(\theta, \varphi)t \\ & + C_s^{(4)}(m)P_4(\cos\beta)v_q^{(4)}(\theta, \varphi)t \end{aligned} \quad (8)$$

The $\{C_s^{(l)}\}_{l=0-4}$ polynomials appearing in this expression

$$C_s^{(0)}(m) = 2m[S(S+1) - 3m^2] \quad (9)$$

$$C_s^{(2)}(m) = 2m[8S(S+1) - 12m^2 - 3] \quad (10)$$

$$C_s^{(4)}(m) = 2m[18S(S+1) - 34m^2 - 5] \quad (11)$$

include now all the effects resulting by a change in the coherence number m for a given spin S .

As apparent from equation 8, the $\{C_s^{(l)}(m)\}_{l=0-4}$ polynomials play on the phase evolved by the spins a role that is formally analogous to that of the Legendre polynomials $\{P_l(\cos\beta)\}_{l=0-4}$. This in turn suggests two different alternatives to the stepwise refocusing of the quadrupolar anisotropies: the DAS route, where evolution is confined to a constant quantum number value ($m = 1/2$) while spinning angles are made time dependent, and the multiple-quantum (MQ) route, in which

spinning angles are now kept fixed while m quantum numbers and their associated evolution times are chosen to fulfill the refocusing conditions

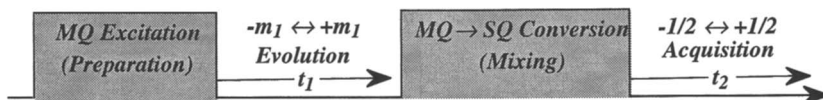
$$C_2(m_1)t_1 + C_2(m_2)t_2 = 0 \quad (12)$$

$$C_4(m_1)t_1 + C_4(m_2)t_2 = 0 \quad (13)$$

There is a clear analogy between this "spin-space" refocusing of the anisotropies, and the "spatial-space" DAS refocusing implied by equations 6 and 7. Moreover in the same manner as DAS echoes could be devised for different spin transitions, multiple quantum refocusing does not in principle specify the spinning angle β to be employed. A particularly convenient spinning axis that allows second-order quadrupole anisotropies to be refocused is the magic angle, as then the time average $\langle P_2(\cos 54.7^\circ) \rangle$ becomes effectively nulled and all remaining anisotropies (shielding and dipolar) are removed. The combined spin and spatial averaging processes involved in this multiple-quantum/magic-angle-spinning (MQMAS) procedure enable the acquisition of high-resolution solid state NMR spectra from half-integer quadrupolar spins devoid of chemical shift, dipolar or quadrupolar anisotropies.

MQMAS NMR: Spectral Features

When these considerations are translated into a practical 2D NMR experiment the value of m_2 becomes confined to $1/2$, as central single-quantum transitions are the only ones that can be easily detected by NMR. This leads to an overall experiment of the form:



The evolution phases (ϕ_1, ϕ_2) that will be correlated during such MAS experiment can be computed from equation 8 as

$$\phi_1(t_1) = sg \cdot [2m_1\nu_{cs} + C_s^{(0)}(m_1)\nu_q^{(0)} + C_s^{(4)}(m_1)\left(\frac{-7}{18}\right)\nu_q^{(4)}(\theta, \varphi)]t_1 = sg \cdot \nu_1 t_1 \quad (14)$$

$$\phi_2(t_2) = [\nu_{cs} + C_s^{(0)}(1/2)\nu_q^{(0)} + C_s^{(4)}(1/2)\left(\frac{-7}{18}\right)\nu_q^{(4)}(\theta, \varphi)]t_2 = \nu_2 t_2 \quad (15)$$

where the sign factor $sg = \pm 1$ denotes the apparent sense of precession of the spins during the indirectly detected evolution time t_1 . This sign can be selected by manipulating the relative phases of radiofrequency (rf) excitation and demodulation according to the conventional rules of 2D NMR phase cycling (20). This freedom to choose the apparent sense of spin precession plays an important role in the acquisition of the high-resolution quadrupolar NMR spectra, since it means that signals fulfilling the refocusing condition

$$sg \cdot C_s^{(4)}(m_1)t_1 + C_s^{(4)}(1/2)t_2 = 0 \quad (16)$$

can always be generated. For this particular choice of sg equations 14 and 15 predict the formation of an isotropic echo devoid from anisotropic contributions at times

$$t_2 = \left[\left| C_s^{(4)}(m_1) \right| / C_s^{(4)}(1/2) \right] \cdot t_1 \quad , \quad (17)$$

whose signal will be solely dictated by a combination of $v_q^{(0)}$ and v_{cs} .

The verification of this prediction is probably the most basic test of the performance of an MQMAS NMR experiment. Its realization will result in a slowly decaying ridge of echoes appearing in the (t_1, t_2) time-domain with a slope $\left| C_s^{(4)}(m_1) / C_s^{(4)}(1/2) \right|$. Examples of this behavior for $S = 3/2$, $S = 5/2$ and $m_1 = 3/2$ are illustrated by the 2D contour plots in Figure 4 (top) and compared with the slope predicted by the coefficient in equation 11; agreement between this theory and the experiment is excellent. The signals that are observed in these 2D plots for the $t_1 = 0$ slice correspond to the ones that would result from conventional MAS acquisitions; their fast decay reflects the presence of second-order quadrupolar anisotropies, which result in broad powder line shapes in the frequency domain (Figure 4, center). The slower decay occurring along the time-domain ridge described by equation 17 is indicative of much sharper frequency-domain signals free from anisotropic contributions, which lead to high resolution NMR spectra by Fourier transformation (Figure 4, bottom).

It is of course unnecessary to extract a time-domain slice at a particular slope in order to calculate the high-resolution MQMAS NMR spectra. A similar goal can be achieved by carrying out conventional Fourier processing of the whole 2D time-domain data set (weighting, zero-filling, phasing), in combination with a shearing transformation of the form

$$I(v_1, v_2) \rightarrow I\left(v_1 + v_2 \left| C_s^{(4)}(m_1) \right| / C_s^{(4)}(1/2), v_2\right) \quad . \quad (18)$$

This linear manipulation of the 2D spectrum exploits the fact that anisotropic quadrupolar contributions along the two frequency axes are proportional to one another (equations 14 and 15), in order to remove the broadening from one of the spectral axes and yield a purely isotropic-anisotropic correlation spectrum (Figure 5). A convenient way of carrying out such shearing of the data without resorting to interpolations is by implementing it in the mixed time-frequency domain (t_1, v_2) using a time-proportional phase correction (19,20). It should be kept in mind, however, that this shearing may complicate the referencing of the resulting peaks, particularly if an external reference placed at a frequency other than the transmitter carrier is employed.

Besides their high resolution, an interesting feature of the 2D NMR spectra resulting from this procedure is that the centers of mass characterizing resonances along the two spectral axes are different. These centers of mass are solely determined by isotropic chemical and quadrupolar shift contributions, and their non-coincident values are a reflection of the different strengths with which these shifts influence the evolution of multiple- and single-quantum coherences. The weighting coefficients (a_{cs}^i, a_q^i) that define the isotropic chemical and quadrupolar contributions to peaks in sheared MQMAS NMR spectra can be calculated from equations 9 and 11, and they are summarized for different S and m_1 numbers in Table I. These coefficients allow one to discriminate the relative contributions of

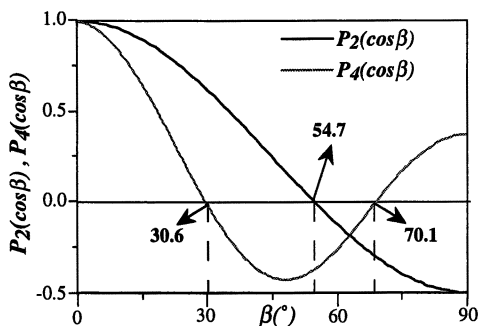


Figure 3. Orientation dependence of Legendre polynomials $\{P_l(\cos\beta)\}_{l=2,4}$ on the spinning angle β , indicating the positions of their non-coincident roots ($\beta = 54.7^\circ$: magic angle).

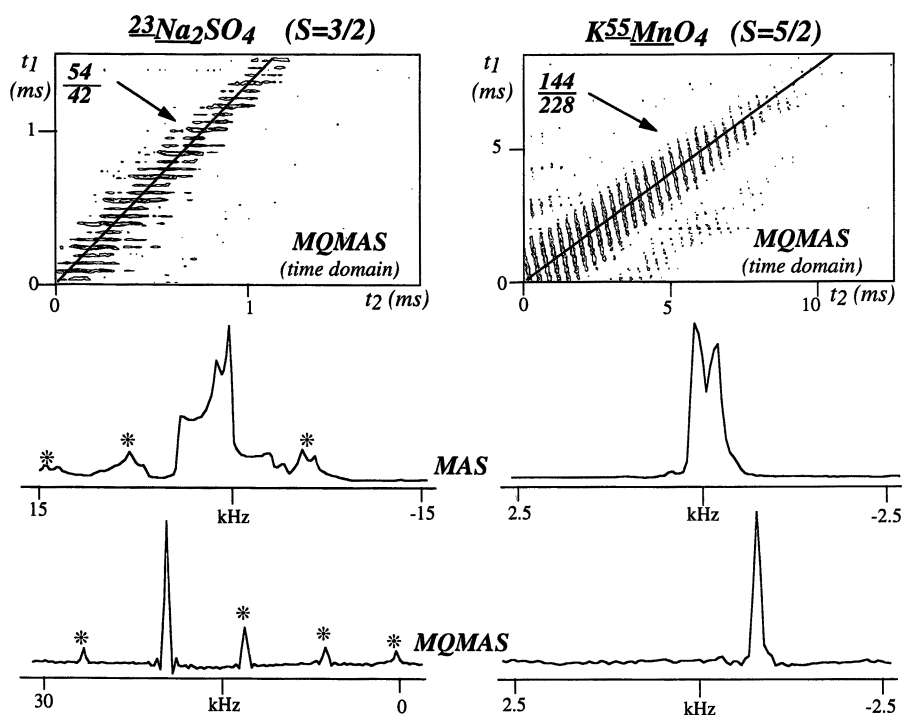


Figure 4. MAS and MQMAS experiments on $S = 3/2$, $S = 5/2$ samples. Top: 2D triple-/single-quantum MAS data sets showing the ridges of anisotropy-free data, and their comparison with the expected t_1/t_2 ratios. Center: MAS powder NMR spectra originated by second-order quadrupole effects. Bottom: Isotropic spectra afforded by the MQMAS experiment. All data were acquired at 4.7 T using a home-built spectrometer and probe while doing MAS at ca. 7 kHz; asterisks indicate spinning sidebands.

v_{cs} and $v_q^{(0)}$ by a simple center of mass calculation of a peak's position in the 2D NMR spectra; it is worth noting that until now similar model-free determination of these parameters required measurements at two or more magnetic field strengths (9,21).

Table I. Coefficients (a_{cs}^1, a_q^1), (a_{cs}^2, a_q^2) determining a peak's center of mass $\langle v_1 \rangle, \langle v_2 \rangle$ in a sheared MQMAS spectrum in terms of isotropic chemical and quadrupolar shifts.^{a,b}

Spin	Transition	a_{cs}^1	a_q^1	a_{cs}^2	a_q^2
<i>S</i>	$-m_1 \leftrightarrow +m_1$				
3/2	$-3/2 \leftrightarrow +3/2$	34/9	-20/3	1	3
5/2	$-3/2 \leftrightarrow +3/2$	-17/12	20/3	1	8
7/2	$-3/2 \leftrightarrow +3/2$	-34/45	20/3	1	15
9/2	$-3/2 \leftrightarrow +3/2$	-17/36	20/3	1	24
5/2	$-5/2 \leftrightarrow +5/2$	85/12	-100/3	1	8
7/2	$-5/2 \leftrightarrow +5/2$	-34/9	100/3	1	15
9/2	$-5/2 \leftrightarrow +5/2$	-85/36	100/3	1	24

^aAssuming v_1 = isotropic axis; v_2 = isotropic + anisotropic axis.

^b $\langle v_1 \rangle = a_{cs}^1 v_{cs} + a_q^1 v_q^{(0)}$; $\langle v_2 \rangle = a_{cs}^2 v_{cs} + a_q^2 v_q^{(0)}$; v_{cs} in Hz, $v_q^{(0)}$ in Hz as defined by equation 19.

Although this simple analytical procedure can be used to estimate the quadrupole coupling constant from the isotropic quadrupolar shift

$$v_q^{(0)} = -\frac{(e^2qQ/h)^2(3 + \eta_q^2)}{10\nu_L[2S(2S-1)]^2}, \quad (19)$$

an exact value for e^2qQ/h cannot be retrieved due to the unknown value of the quadrupole asymmetry parameter η_q . Discrimination among the exact contributions of e^2qQ/h and η_q to $v_q^{(0)}$ can be carried out by analyzing the powder line shapes that for each chemical site can be resolved from the 2D MQMAS spectra. This analysis can usually be performed without paying attention to details of the multiple-quantum excitation or conversion processes, and only requires integration of the ideal MAS frequency expression

$$v_2 = v_{cs} + C_s^{(0)}(1/2)v_q^{(0)} + C_s^{(4)}(1/2)\left\{-\frac{(e^2qQ/h)^2}{720\nu_L[2S(2S-1)]^2}[(18 + \eta_q^2)(1 - 5\sin^2\theta) + 45\eta_q\sin^2\theta\cos 2\varphi + \frac{35}{4}\sin^4\theta(3 - \eta_q\cos 2\varphi)]\right\} \quad (20)$$

over a solid sphere. The only precaution required by this line shape fitting procedure is to remember to consider the signal intensity that may be distributed among the strong spinning sidebands usually appearing along the multiple-quantum frequency domain (22). Simple solutions to this problem involve adding up the spinning sideband manifold of a particular site in the frequency domain prior to the line shape fitting, using rotor-synchronized t_1 increments throughout the 2D acquisition or, if possible, increasing the sample spinning rate until sideband intensities become negligible. When these precautions are taken into account the full analysis of the MQMAS data allows one to extract all the spectroscopic constants that determine conventional MAS NMR spectra in a high-resolution fashion. An illustration of this analytical capability is presented in Figure 6 with the ^{23}Na NMR characterization of Na_2TeO_3 .

MQMAS can also provide valuable information regarding the distribution of chemical shift and quadrupole couplings in a complex solid. Such distributions are of common occurrence in partially disordered materials (e.g., glasses), and their NMR quantification offers detailed insight about their behavior at a localized atomic level. Whereas distributions of this type are usually difficult to analyze using unidimensional NMR methods due to insufficient spectral resolution, 2D MQMAS offers the benefit of enhanced site separation. The method also offers the possibility of discriminating between the onset of chemical shift and of quadrupolar coupling distributions, owing to the different contributions that these two effects will have on the 2D spectral line shapes (coefficients in Table I). For certain spin numbers such as $S = 3/2$, quadrupolar and chemical shift dispersions will actually broaden the peaks along almost orthogonal spectral directions (Figure 7). Furthermore, MQMAS spectra will retain in most cases enough resolution to discriminate among inequivalent sites even when a direction along which a sharp isotropic-like projection does no longer exist; ^{27}Al and ^{11}B NMR examples of this interesting phenomenon have recently been reported (23,24).

Having discussed the high resolution aspects and new spectral information that can be retrieved using MQMAS it is worth mentioning an important piece of information that this experiment *does not* provide, namely, the quantitative characterization of relative site abundances in the sample. Lack of quantitiveness arises in MQMAS due to the dependence of the multiple-quantum excitation and conversion efficiencies on the quadrupolar and shielding parameters, and even though pulse sequences capable of alleviating this problem have been proposed (25), none is currently available to completely solve it. A general solution, however, can be worked out by incorporating into the MQMAS line shape evaluation an analysis of a quantitative set of conventional MAS data collected using short excitation pulse widths (19,26). Since as discussed earlier MQMAS will afford in a resolved format all the shielding and quadrupolar parameters that define the MAS spectrum, relative site abundances can be obtained by a line shape analysis of the latter based on these *a priori* known spectral parameters. Although this proposal sounds like a reversal to numerically challenging multi-site MAS line shape analyses, the knowledge provided by MQMAS on the number and NMR parameters of the various sites makes this quantification process numerically trivial. An example of results afforded by this procedure when applied to the analysis of the Na_2TeO_3 data is presented in Figure 8.

MQMAS NMR: Pulse Sequence Considerations

In order to retrieve the valuable information that was described in the last paragraphs, strategies capable of supplying MQMAS data with sufficient signal-to-noise ratio (S/N) need to be devised. It is consequently not surprising that a number of different approaches have already been proposed for collecting

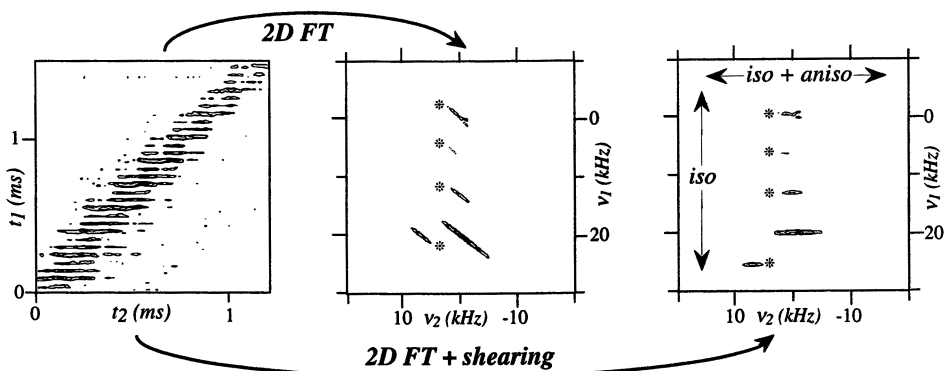


Figure 5. Alternative processing approaches in 2D MQMAS NMR. Center: conventional Fourier transformation. Right: Fourier processing including a shearing transformation. Processing is exemplified using the Na_2SO_4 time-domain data shown in Figure 4 (left); asterisks denote spinning sidebands.

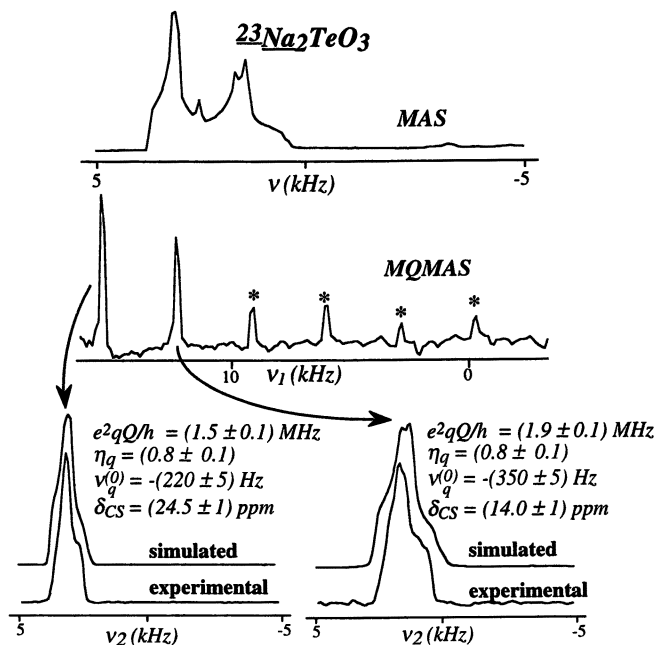


Figure 6. MAS (top) and MQMAS ^{23}Na NMR analyses of polycrystalline Na_2TeO_3 . The MQMAS trace corresponds to the isotropic projection of the 2D spectrum and clearly shows two inequivalent sites that overlap under regular MAS. Anisotropic line shapes extracted at the indicated isotropic MQMAS frequencies can be used to obtain the quadrupolar parameters involved in each case (bottom).

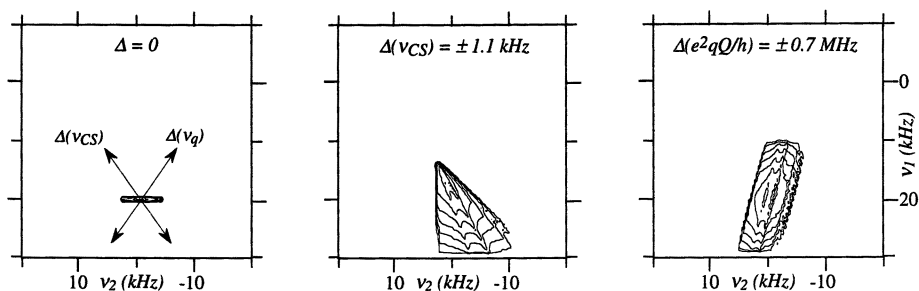


Figure 7. Effects introduced by distributions Δ of the quadrupolar (center) and chemical shift (right) parameters on the shape of an $S = 3/2$ MQMAS resonance. The unperturbed spectrum (left) corresponds to Na_2SO_4 NMR parameters at 4.7 T and shows the directions along which quadrupolar and chemical shift distributions will distort the signal.

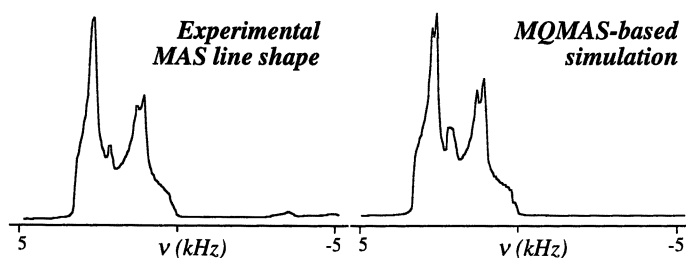


Figure 8. Extraction of quantitative information by a combination of MAS and MQMAS data. The simulation on the right is based on the parameters listed in Figure 6 and assumes a 1:1 relative abundance of the two sites.

MQMAS data (18,19,25,27-29), and these efforts are likely to continue as the applications of the technique expand. Rather than trying to be comprehensive we will describe here a few basic approaches that enable the acquisition of MQMAS spectra with sufficient S/N within reasonable averaging periods, as well as briefly discuss some of their current limitations.

The simplest procedure capable of affording MQMAS data is probably the two-pulse sequence

$$(\theta_1)\phi_1 - t_1 - (\theta_2)\phi_2 - t_2(\phi_{Rx}) \quad , \quad (21)$$

originally developed within the framework of ^2H NMR (an $S = 1$ nucleus) and subsequently extended to half-integer quadrupolar spins (30-34). The first pulse in this sequence (θ_1) is capable of exciting, in addition to conventional single-quantum transitions, $-m \leftrightarrow +m$ multiple quantum coherences, due to the perturbing effects of the quadrupolar interaction which lifts the usual $\Delta m = \pm 1$ NMR selection rule. The second pulse (θ_2) will convert these multiple-quantum coherences into, among other, observable single-quantum magnetizations. The signal corresponding to a particular order of multiple-quantum coherence (e.g., triple-quantum) can be distinguished from single-quantum signals excited by θ_1 by virtue of its peculiar behavior upon rf phase shifts (30,35). Indeed one of the characteristics of n -quantum coherences is that upon shifting their excitation pulse by $\Delta\phi$ degrees, their resulting signals will undergo a phase shift $n \cdot \Delta\phi$. A six scan phase cycle involving the sequence in equation 21 with

$$\phi_1 = 0^\circ, 60^\circ, 120^\circ, 180^\circ, 240^\circ, 300^\circ \quad (22)$$

$$\phi_2 = 0^\circ, 0^\circ, 0^\circ, 0^\circ, 0^\circ, 0^\circ \quad (23)$$

$$\phi_{Rx} = 0^\circ, 180^\circ, 0^\circ, 180^\circ, 0^\circ, 180^\circ \quad (24)$$

will therefore succeed in selecting signals from the coherence pathway involved in the triple-/single-quantum correlation, while filtering out the stronger single-/single-quantum correlation signal. Similar multi-quantum filtration procedures are implemented in a variety of solution 2D NMR experiments by phase cycling or by field gradients (35,36); other common 2D solution NMR strategies such as TPPI, hypercomplex acquisition, echo and anti-echo pathway selection, etc. (20,37), are also directly applicable to the pulse sequence represented by equations 21-24.

Although this approach may enable the acquisition of MQMAS data, strong NMR signals will only be retrieved provided that the values for the nutation angles θ_1, θ_2 are properly set. Measurable factors such as the rf nutation frequency ν_{rf} and the Larmor frequency will influence these values, as will *a priori* unknown parameters including e^2qQ/h and ν_{cs} . In spite of these indeterminations suitable models can be devised and exploited for predicting the pulse angles that under common conditions will result in optimized S/N spectra. An important simplification results by restricting the consideration of quadrupolar effects to first order while disregarding the effects of chemical shifts and sample spinning, as this allows one to describe the rf manipulations of multiple quantum coherences solely in terms of the $(e^2qQ/h)/\nu_{rf}$ ratio (19,27,28,38). Figure 9 presents a series of triple-quantum excitation and conversion profiles that for $S = 3/2$ are predicted by

this model as a function of θ_1, θ_2 . These plots reveal that even though the settings that maximize S/N conditions vary with the $(e^2qQ/h)/\nu_{rf}$ ratio, suitable values for excitation and conversion pulses can be established for a considerable range of experimental conditions. Additional results arising from such simplified calculations concerning the θ_1, θ_2 values that will maximize S/N for different spins are summarized in Table II (38). It should be kept in mind, however, that these parameters are only idealized pulse values obtained after neglecting potentially important factors such as offsets and the rate of sample spinning, and should consequently be viewed only as initial approximations susceptible to improvement by additional fine tuning. A simple procedure for achieving this optimization

Table II. Approximate nutation pulses for optimized S/N in MQMAS correlation experiments.^a

Spin	Transition	θ_1 (cycles)	θ_2 (cycles)
<i>S</i>	$-m_1 \leftrightarrow +m_1$		
3/2	$-3/2 \leftrightarrow +3/2$	0.76	0.18
5/2	$-3/2 \leftrightarrow +3/2$	0.48	0.17
7/2	$-3/2 \leftrightarrow +3/2$	0.34	0.13
9/2	$-3/2 \leftrightarrow +3/2$	0.25	0.10
5/2	$-5/2 \leftrightarrow +5/2$	0.5	0.2

^aCalculated disregarding second-order quadrupolar, chemical shift and spinning effects, and considering only the magnitude of the signal.

involves monitoring the MQMAS signal as a function of initial and final pulse widths for a fixed t_1 value (e.g., the first rotor period) until a maximum is observed; this is usually a short and highly beneficial procedure worth carrying out before embarking on a definitive 2D NMR acquisition.

In addition to their excitation by a single pulse θ_1 , multiple-quantum coherences can be generated using a two-pulse sequence analogous to the one involved in solution INADEQUATE experiments (39,40). The overall MQMAS sequence would then take the form

$$(\theta_1)\phi_1 - \Delta - (\theta_2)\phi_2 - t_1 - (\theta_3)\phi_3 - t_2(\phi_{Rx}) \quad (25)$$

where Δ is a usually fixed period chosen for maximum multiple-quantum excitation. Since the orientation dependence of the coupling constants makes the selection of Δ in powdered solids a non-trivial procedure, we decided to investigate numerically the optimized conditions ($\theta_1, \theta_2, \phi_1, \phi_2, \Delta$) that will for different $(e^2qQ/h)/\nu_{rf}$ ratios maximize the excitation of multiple-quantum coherences (41). In the absence of substantial chemical shift or second-order quadrupole effects, these multidimensional searches consistently revealed that pulse sequences with $\Delta = 0$, $\phi_2 = \phi_1 + 90^\circ$ give the largest amounts of triple-quantum excitation. In the $e^2qQ/h = 2-4$ MHz region for instance, calculations show that composite $(\theta_1)_x(\theta_2)_y$ pluses with $\theta_2 \approx 1.7 \theta_1$ can afford $S = 3/2$ MQMAS spectra whose signal exceeds by

between 30 and 50% (per unit time) the signal resulting from single-pulse excitation experiments at similar rf field strengths. An experimental verification of this behavior is presented in Figure 10.

Although under such optimized conditions an MQMAS experiment can yield close to 30% of the conventional MAS signal intensity, its performance will be significantly reduced by the introduction of frequency offsets. These effects may originate in isotropic chemical shifts, shielding anisotropies or second-order quadrupolar dispersions, and their consequences will be significant even when their sizes are moderate ($\approx 0.2 \cdot \nu_{rf}$). This attenuation can be traced to a reduction in the efficiency of the multiple-quantum coherence excitation, as can be appreciated from the single-pulse excitation plots presented in Figure 11. Offset effects can become particularly serious when dealing with low- γ nuclei due to the usually large magnitudes of their second-order shifts, combined with the difficulty of achieving on these spins large rf nutation fields. Excitation problems may also arise in the case of heavy metals, which tend to be affected by large isotropic and anisotropic chemical shift dispersions. If not taken care of by a suitable change in the Larmor frequency of observation or by sufficient increases in ν_{rf} —which will eventually be limited by the duration of phase transients—these offset phenomena may attenuate the MQMAS signal until making it altogether unobservable. A drastic example of this behavior is presented in Figure 12, which compares ^{59}Co MAS and MQMAS NMR data for two species possessing cobalts in octahedrally-coordinated sites characterized by similar quadrupole coupling constant values ($\approx 2\text{--}4$ MHz). Due to strong electronic conjugation with the tetraphenylporphyrin (TPP) and N-methylimidazole (MeIm) rings, the cobalt site in one of these complexes has a much larger shielding anisotropy than in the other one (42). This in turn prevents the observation of its MQMAS signal via the single-pulse excitation sequence even after extensive signal averaging. A substantial improvement in S/N can be achieved by resorting again to composite pulse excitation; for this particular case calculations reveal that a $(\theta_1)_x(\theta_2)_x$ excitation yields the most efficient triple-quantum coherence generation, and indeed its use enables the emergence of ^{59}Co signals from the background noise in reasonable acquisition times (Figure 12, right). Still, even when employing such numerically-optimized conditions, current pulse sequences may still have problems in yielding routine MQMAS spectra with appropriate S/N when dealing with large offset dispersions. Further progress is needed in order to bypass these restrictions and enable a more general application of MQMAS.

Conclusions and Outlook

The present account described some of the opportunities and challenges opened up by MQMAS, an approach that we have recently proposed for the high-resolution NMR analysis of half-integer quadrupolar nuclei in solids. The most important characteristic of this simple experiment is that it can yield highly resolved resonances from either dilute or abundant spin systems using conventional spectrometers and probeheads. For doing so it relies on the complete averaging of chemical shift as well as of homo- and hetero-nuclear dipolar anisotropies by fast magic angle spinning, combined with the multiple-quantum refocusing of second-order quadrupole effects. For each inequivalent chemical site that can be resolved in this manner MQMAS will then provide the isotropic chemical and quadrupolar shift parameters from a model-free fixed-field analysis, and the individual e^2qQ/h and η_q values with the aid of 1D simulation procedures. Distribution of NMR parameters in disordered glassy systems can also be extracted

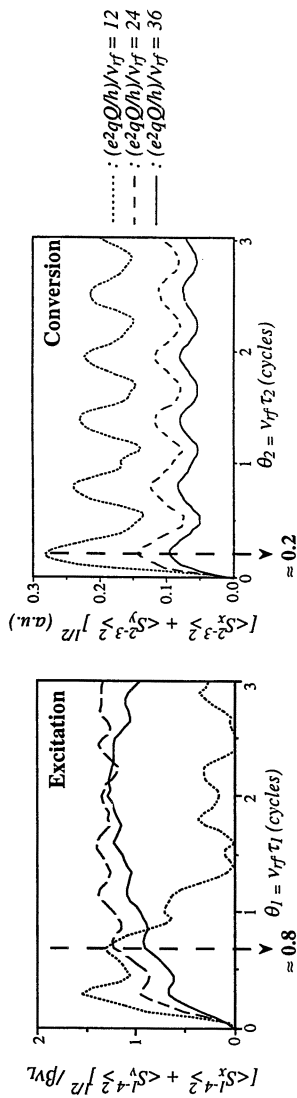


Figure 9. Idealized magnitude dependence for the excitation of triple-quantum coherences for $S = 3/2$, and their subsequent conversion to single-quantum observables. Dashed vertical lines indicate regions of efficient (although not necessarily optimal) pulse widths.

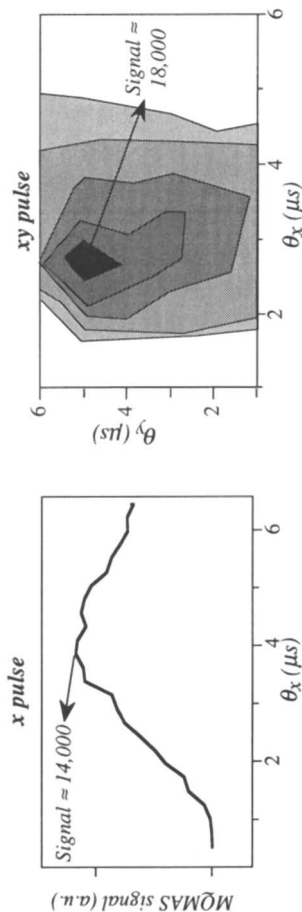


Figure 10. Triple-quantum ^{23}Na excitation profiles afforded by a single pulse (left) and a composite pulse (right) sequence on a Na_2SO_4 sample. Experimental conditions were as described in Figure 4, with $\nu_{rf} \approx 120$ kHz and t_1 fixed at one rotor period.

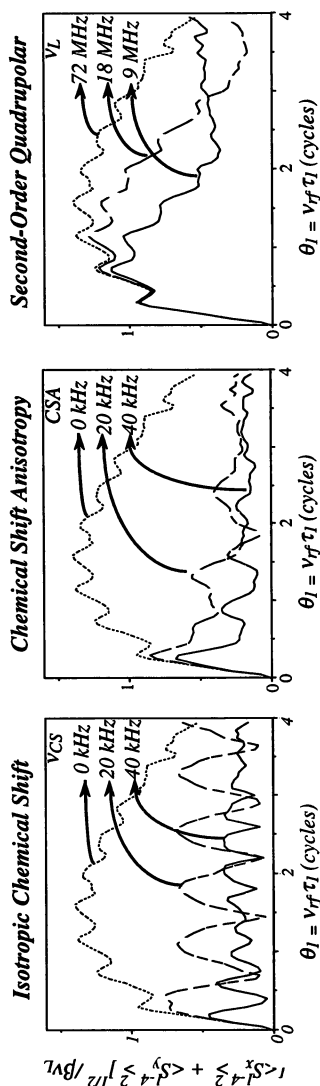


Figure 11. Dependence of the triple-quantum excitation profiles afforded by a single-pulse excitation sequence (equation 21) on isotropic and anisotropic offsets. These calculations assumed $S = 3/2$, $e^2qQ/h = 2.4$ MHz, $\eta_q = 0$ and $\nu_f = 100$ kHz, and only considered one effect at a time. Notice that not only intensities change with offsets but also the maxima shift their positions.

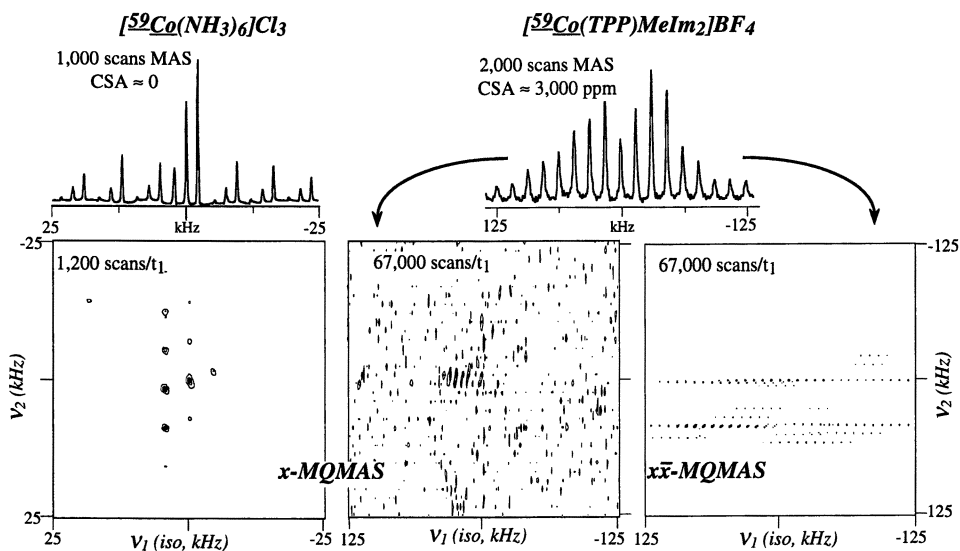


Figure 12. Illustration of the effects introduced by the chemical shielding anisotropy (CSA) on the efficiency of MQMAS, and of the improvement achievable by composite pulse excitation. Cobalt sites in both complexes have similar quadrupole coupling constants, although the porphyrin compound yields little MQMAS signal after 4 days of acquisition due to its large CSA (center). The situation can be improved using composite $x\bar{x}$ pulses (right). All data were collected at 4.7 T using MAS at 10 kHz and $\nu_{rf} \approx 100$ kHz.

by line shape analyses of the 2D data, while the relative abundance of different sites in the sample can be computed by a combined analysis of single-pulse MAS and MQMAS data.

In spite of these valuable characteristics, it should be noted that MQMAS is not a signal averaging technique in the classical sense of involving the collapse of a broad powder line shape into a single sharp resonance. Instead it is a 2D NMR experiment that by correlating scaled but otherwise identical powder line shapes along different spectral axes, manages to separate the isotropic and anisotropic frequency contributions to the total spin evolution along independent frequency dimensions. Consequently MQMAS should *not* be considered as a signal enhancement procedure of the MAS type; in fact, as was discussed earlier, S/N in the 2D NMR experiment is usually inferior to the one afforded by standard 1D NMR acquisitions. This state of affairs may change in the future as research on the optimized excitation of multiple quantum coherences in quadrupole nuclei and their subsequent conversion into observable magnetization continues; a number of alternatives involving single- and composite-pulse excitation procedures were discussed in the present work. Among the problems that remain to be addressed regarding the implementation of this experiment we have noted a particularly serious one, involving the generation of significant amounts of signal in the presence of shielding and quadrupolar offsets and anisotropies. In view of the potential that the MQMAS method appears to hold for the study of a wide variety of inorganic and bioinorganic systems, pulse sequences capable of dealing with these limitations are likely to materialize in the coming future. Even in its current form, MQMAS has already proved to be a powerful aid in the characterization of catalytic, glassy and mineral structures (23,24,43-45).

Acknowledgment. This work was supported by the National Science Foundation through grants DMR-9420458 and CHE-9502644 (CAREER Award). AM is a UIC Dean Awardee (1996-1997); LF is a Camille Dreyfus Teacher-Scholar (1996-2001), Beckman Young Investigator (1996-1998), University of Illinois Scholar (1997-2000).

Literature Cited

- (1) *Handbook of Chemistry and Physics, Section 9*; Lide, D. R., Ed.; CRC Press: Boston, 1991.
- (2) Maciel, G. E. *Science* **1984**, 226, 282.
- (3) Oldfield, E.; Kirkpatrick, R. J. *Science* **1985**, 227, 1537.
- (4) Turner, G. L.; Kirkpatrick, R. J.; Risbud, S. H.; Oldfield, E. *Am. Ceram. Soc. Bull.* **1987**, 66, 656.
- (5) Fyfe, C. A. *Solid State NMR for Chemists*; CFC Press: Ontario, 1983.
- (6) Abragam, A. *The Principles of Nuclear Magnetism*; Oxford University Press: Oxford, 1985.
- (7) Slichter, C. P. *Principles of Nuclear Magnetic Resonance*; Springer-Verlag: New York, 1990.
- (8) Kundla, E.; Samoson, A.; Lippmaa, E. *Chem. Phys. Lett.* **1981**, 83, 229.
- (9) Ganapathy, S.; Schramm, S.; Oldfield, E. *J. Chem. Phys.* **1982**, 77, 4360.
- (10) Goldman, M.; Grandinetti, P. J.; Llor, A.; Olejniczak, Z.; Sachleben, J. R.; Zwanziger, J. W. *J. Phys. Chem.* **1992**, 97, 8947.
- (11) Llor, A.; Virlet, J. *Chem. Phys. Lett.* **1988**, 152, 248.
- (12) Samoson, A.; Lippmaa, E.; Pines, A. *Mol. Phys.* **1988**, 65, 1013.
- (13) Chmelka, B. F.; Zwanziger, J. W. *NMR Basic Principles. and Progress* **1994**, 33, 79.

- (14) Medek, A.; Sachleben, J. R.; Beverwyk, P.; Frydman, L. *J. Chem. Phys.* **1996**, *104*, 5374.
- (15) Chmelka, B. F.; Mueller, K. T.; Pines, A.; Stebbins, J.; Wu, Y.; Zwanziger, J. W. *Nature* **1989**, *339*, 42.
- (16) Mueller, K. T.; Sun, B. Q.; Chingas, G. C.; Zwanziger, J. W.; Terao, T.; Pines, A. *J. Magn. Reson.* **1990**, *86*, 470.
- (17) Wooten, E. W.; Muller, K. T.; Pines, A. *Acc. Chem. Res.* **1992**, *25*, 209.
- (18) Frydman, L.; Harwood, J. S. *J. Am. Chem. Soc.* **1995**, *117*, 5367.
- (19) Medek, A.; Harwood, J. S.; Frydman, L. *J. Am. Chem. Soc.* **1995**, *117*, 12779.
- (20) Ernst, R. R.; Bodenhausen, G.; Wokaun, A. *Principles of Nuclear Magnetic Resonance in One and Two Dimensions*; Clarendon: Oxford, 1987.
- (21) Baltisberger, J. H.; Gann, S. L.; Wooten, E. W.; Chang, T. H.; Mueller, K. T.; Pines, A. *J. Am. Chem. Soc.* **1992**, *114*, 7489.
- (22) Massiot, D. *J. Magn. Reson. A* **1996**, *122*, 240.
- (23) Kraus, H.; Prins, R.; Kentgents, A. P. N. *J. Phys. Chem.* **1996**, *100*, 16336.
- (24) Hwang, S.-J.; Fernandez, C.; Amoureux, J. P.; Cho, J.; Martin, S. W.; Pruski, M. *Solid State NMR*; in press.
- (25) Wu, G.; Rovnyak, D.; Griffin, R. G. *J. Am. Chem. Soc.* **1996**, *118*, 9326.
- (26) Eenzke, D.; Freude, F.; Frohlich, T.; Haase, J. *Chem. Phys. Lett.* **1984**, *111*, 171.
- (27) Fernandez, C.; Amoureux, J. P. *Chem. Phys. Lett.* **1995**, *242*, 449.
- (28) Wu, G.; Rovnyak, D.; Sun, B.; Griffin, R. G. *Chem. Phys. Lett.* **1995**, *249*, 210.
- (29) Massiot, D.; Tonzon, B.; Trumeau, D.; Coutures, J. P.; Virlet, J.; Florian, P.; Grandinetti, P. *J. Solid State NMR* **1996**, *6*, 73.
- (30) Vega, S.; Pines, A. *J. Chem. Phys.* **1977**, *66*, 5624.
- (31) Wokaun, A.; Ernst, R. R. *J. Chem. Phys.* **1977**, *67*, 1752.
- (32) Vega, S. *J. Chem. Phys.* **1978**, *68*, 5518.
- (33) Vega, S.; Naor, Y. *J. Chem. Phys.* **1981**, *75*, 75.
- (34) Nielsen, N. C.; Bildsøe, H.; Jakobsen, H. J. *Chem. Phys. Lett.* **1992**, *191*, 205.
- (35) Wokaun, A.; Ernst, R. R. *Chem. Phys. Lett.* **1977**, *52*, 407.
- (36) Keeler, J. in *Multinuclear Magnetic Resonance in Liquids and Solids*; P. Granger and R. K. Harris, Eds.; Kluwer: Dordrecht, 1990; pp 103.
- (37) Derome, A. E. *Modern NMR Techniques for Chemistry Research*; Pergamon Press: Oxford, 1987.
- (38) Amoureux, J. P.; Fernandez, C.; Frydman, L. *Chem. Phys. Lett.* **1996**, *259*, 347.
- (39) Drobny, G.; Pines, A.; Sinton, S.; Weitekamp, D. P.; Wemmer, D. *Faraday Disc. Chem. Soc.* **1979**, *13*, 49.
- (40) Bodenhausen, G. *Prog. Nucl. Magn. Reson. Spectrosc.* **1981**, *14*, 137.
- (41) Marinelli, L.; Medek, A.; Frydman, L.; in preparation.
- (42) Medek, A.; Frydman, V.; Beverwyk, P.; Frydman, L.; submitted for publication.
- (43) Fernandez, C.; Amoureux, J. P.; Delmotte, L.; Kessler, H. *Microporous Materials* **1996**, *6*, 125.
- (44) Massiot, D.; Conanec, R.; Feldman, W.; Marchand, R. *Inorg. Chem.* **1996**, *35*, 4957.
- (45) Baltisberger, J. H.; Xu, Z.; Stebbins, J. F.; Wang, S. H.; Pines, A. *J. Am. Chem. Soc.* **1996**, *118*, 7209.

Chapter 3

Oxygen Motion in Simple and Complex Oxides

Jeffrey A. Reimer¹ and Stuart B. Adler²

¹Lawrence Berkeley National Laboratory and the University of California,
Berkeley, CA 94720

²Cermatec, Inc., 2425 South 900W Salt Lake City, UT 84119

We summarize here our computational and experimental studies of ¹⁷O NMR phenomena in simple and complex oxides, such as yttria-doped ceria and transition metal perovskites. We illustrate how simulation, theory, and experiment are needed to fully relate NMR structural and kinetic parameters to macroscopic rates of oxygen motion.

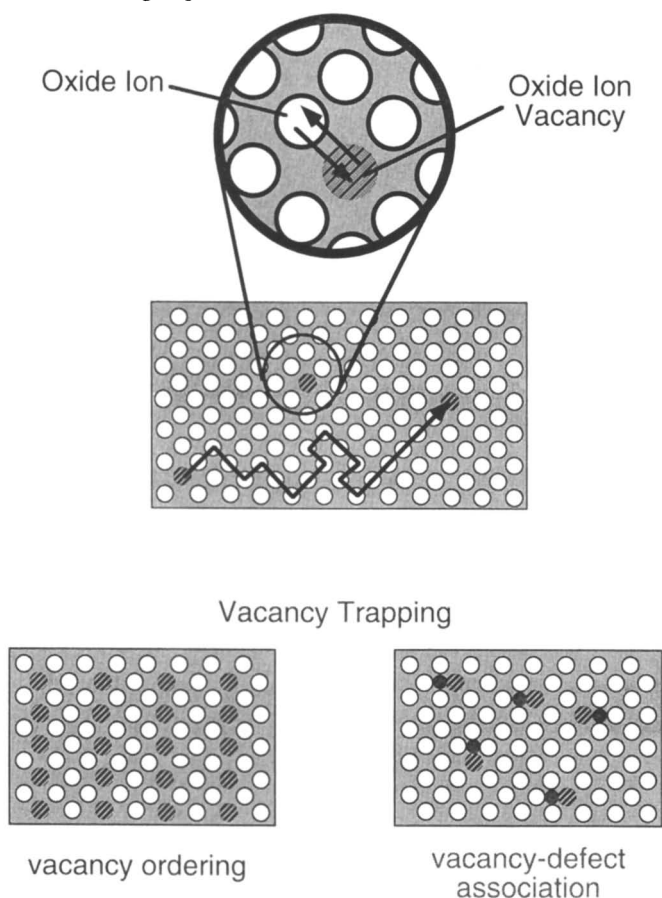
Electrochemical ceramics exhibiting high ionic and/or electronic transport show promise in a wide spectrum of applications, from sensors and fuel cells to large-scale separation and chemical processing. Although much progress has been made in developing these materials for practical applications, fundamental understanding remains limited. Of particular interest is the relationship between structure/composition and thermodynamic and transport properties. Elucidation of this relationship is challenging since properties are influenced equally by long-range crystalline order as well as local atomic interactions. Thus classic paradigms of semiconductor physics and solution electrochemistry are inadequate by themselves. Systematic understanding requires addressing disparate length scales.

Oxide-ion transport is particularly sensitive to interactions over disparate length scales. It has been shown that transport usually occurs by diffusion or migration of oxygen-ion vacancies, which become mobile at high temperature. As illustrated in Figure 1, transport rates are governed not only by local energetics of “site-hopping”, but also long-range energetic defect interactions. The tendency for vacancies in complex oxides to order, and thus prevent all oxygen vacancies from having equal mobility, also presents a challenge. Theories used to rationalize these materials must consider these long and short-range energetics.

Of particular utility are experimental techniques that can separate local ki-

netics and energetic interactions from long-range forces and macroscopic transport. In this article, we summarize some of our success in using high-temperature oxygen-17 spin-lattice relaxation and lineshape measurements to accomplish this deconvolution.

Figure 1: Schematic of the vacancy mechanism for oxygen transport. Bulk transport is accomplished by exchange of oxygen anions and oxygen-ion vacancies. In the lower left we show how vacancies may be trapped by thermodynamic ordering of the vacancies; on the right we show how trapping may occur because of Coulombic interactions between (charged) vacancies and charged point defects.



NMR Relaxation: Simulation and Theory

In a few cases, workers have successfully predicted macroscopic ion-transport based on NMR kinetics, for example BaF_2 [3]. Such success has invited similar investigations of yttria-doped ceria [4,5,6]. Results with ceria, however, have been less successful for two reasons. First, quadrupolar nuclei, such as ^{17}O , have more complex relaxation behavior than spin- $\frac{1}{2}$ nuclei such as ^{19}F . Thus vacancy

hopping kinetics are more difficult to extract unambiguously from ^{17}O NMR data [4,5]. Second, even if NMR provides reliable kinetics for atomic motion, attractive interactions between vacancies and defects in ceria influence conductivity [6]. These interactions preclude straightforward analysis using simple defect models, as in BaF_2 [3].

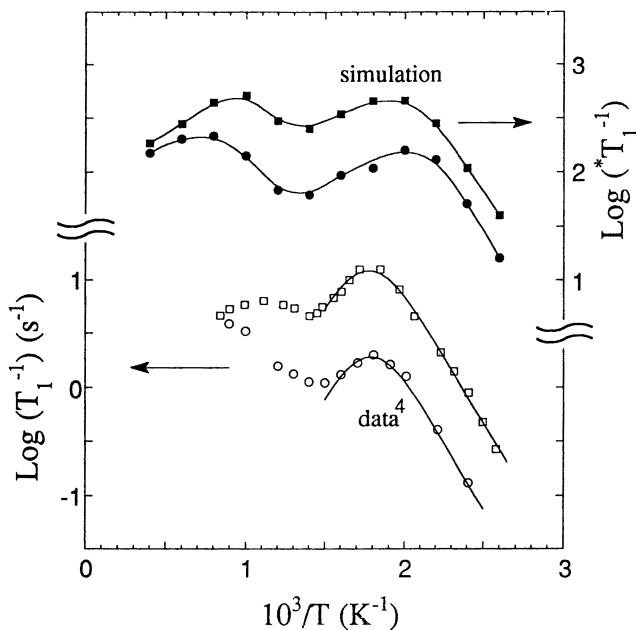
In order to overcome both these challenges, we have developed a dynamic Monte Carlo simulation of vacancy motion in yttria-doped ceria. This method [7-11] has allowed us to better extract vacancy hopping kinetics from complex ^{17}O -NMR data, and to explore the role of long range forces in influencing macroscopic oxygen transport.

The simulation depicts ceria as a fluorite lattice, $11 \times 11 \times 11$ unit cells in size, with periodic boundary conditions. Defects and vacancies are positioned in the lattice initially at random. The vacancies are then allowed to move by switching places with adjacent oxygen atoms according to activated kinetics. Once the system reaches thermodynamic equilibrium, statistics are accumulated for calculating the spin-lattice relaxation rate (electric field-gradient fluctuations) [11], and the ionic conductivity (vacancy self-diffusion) [10]. We take the activation energy to be that of defect-free ceria, modified locally by inter-ionic forces among vacancies and defects. Interactions are modeled as Coulombic potentials in a dielectric medium of pure ceria. Vacancy hopping kinetics for pure ceria are considered adjustable parameters that we hope to extract from NMR data. Further details regarding these calculations may be found in references [10] and [11].

Figure 2 compares our simulation results with published data [4,5] for oxygen-17 spin-lattice relaxation in yttria-doped ceria. Both data and simulation show that relaxation rate increases with dopant concentration and exhibits two local maxima. The temperature of the first maximum (250-300C) is approximately independent of dopant concentration, and is associated directly with vacancy hopping (fast)[11]. The second temperature maximum (>600C) depends strongly on dopant concentration, and appears to be associated indirectly with vacancy motion via (slow) movement of ^{17}O atoms relative to stationary charged defects[11]. Thus a single relaxation mechanism associated with one motional process can produce multiple T_1^{-1} maxima. This observation appears to be significant for the interpretation of relaxation data, and had not been reported before. In our case detailed analysis confirms previously determined kinetics: an activation energy and pre-exponential factor of 0.49 eV and 2.78×10^{12} Hz, respectively [4,5].

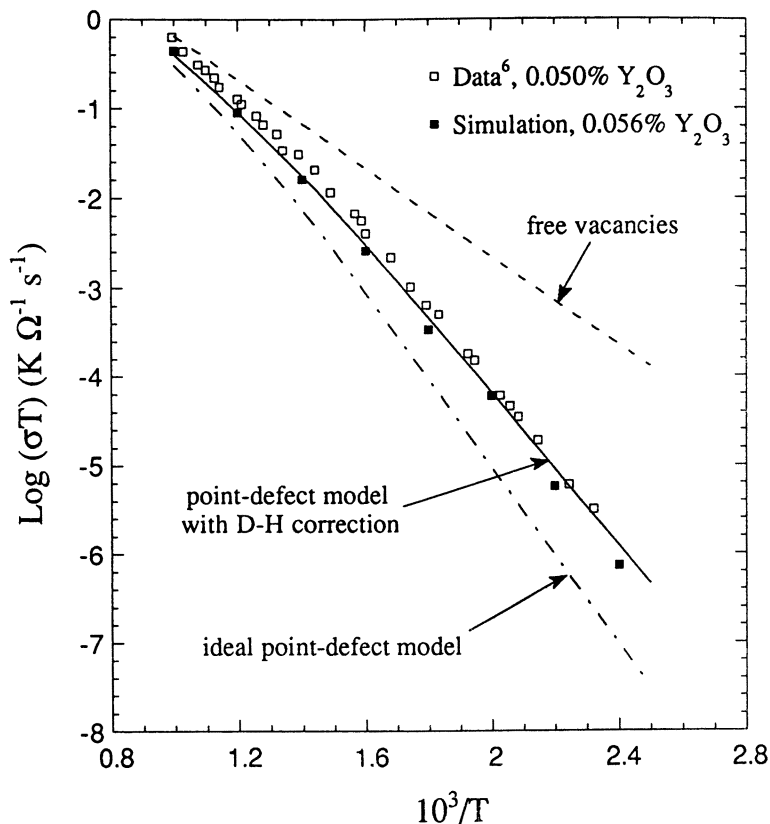
With these local hopping parameters extracted from NMR, we can also simulate ionic conductivity. Figure 3 shows a comparison between our simulation and published transport data [6]. The excellent agreement suggests that inter-ionic forces play a significant role in determining ion transport properties. Effects of attractive forces are apparent in both simulation results and conductivity data, appearing as a higher activation slope than the bulk vacancy-hopping activation energy obtained from NMR.

Figure 2: Simulated [11] and measured [4] spin lattice relaxation of oxygen-17 in yttria-doped ceria as a function of temperature and dopant concentration. Closed symbols indicate simulation points while open symbols indicate data. Concentrations are quoted in mole% Y_2O_3 in CeO_2 : squares, 0.06% and circles, 0.02%. Although the simulation results reported here are non-dimensional, $*T_1^{-1}$ can be related quantitatively to T_1^{-1} with an appropriate value for the Sternheimer factor [11]. For these simulations, the activation energy and attempt rate for vacancy hops in bulk ceria are specified to be 0.5 eV and $2.8 \times 10^{12} \text{ s}^{-1}$, respectively. Each simulation point represents an ensemble average over $\sim 10^4$ ^{17}O nuclei, and 250 runs with different random defect configurations, requiring ~ 60 CPU minutes on a Cray XM-P/28. Lines through the simulation points are to aid the eye; lines through the data are theoretical fits assuming a single activated process for relaxation [4]. The data are from Fuda et al [4,5].



One model for treating this association is to assume that vacancies and defects react chemically to form a third species [6]. This “ideal point-defect” model predicts that as the temperature decreases, the Arrhenius slope should approach the sum of the vacancy-hopping activation energy and the vacancy-defect association enthalpy [6]. As shown elsewhere, however, this model over-predicts the effects of association, and fails to explain the concentration dependence of the ionic conductivity at low temperature [10]. The failure of this model in light of the agreement between data and simulation demonstrates that long-range forces provide an additional energetic term to the association.

Figure 3: Simulated and measure ionic conductivity of 0.06% yttria in ceria. Closed squares indicate simulation points; open squares indicate data. The dashed line is a prediction of ionic conductivity based on kinetics from NMR assuming free vacancies (no vacancy-defect association). The dash-dot line is the same prediction assuming vacancy-defect association given by an ideal point-defect model [10]. The solid line is the prediction assuming a point-defect model that includes a Debye-Hückel correction [10]. Data are from Wang et al [6].



Although our simulation includes these forces, we prefer an analytical theory which predicts their effect more conveniently. Thus let us consider a modification of the ideal point-defect model that includes a Debye-Hückel activity coefficient correction [13]. This approach for handling the effect of coulombic forces on transport is well established [14], and has been used previously to treat NaCl [15]. This method simply adds a composition dependent activity coefficient correction to the mass-action law governing ideal point-defect equilibria [10]. The solid line in Figure 3 shows the theoretical prediction of this analytical theory for the ionic conductivity based on kinetic parameters from the NMR. The theory,

simulation and data all agree well over a range of temperature and dilute dopant concentrations [10]. It is important to note that the solid line in Figure 3 is not a fit to the data. We determine microscopic rates of motion independently from NMR, and predict macroscopic transport using an analytical theory that considers properly the effect of Coulombic interactions in a dielectric solid.

Structural Heterogeneity as Determined by High Temperature NMR

In the absence of Coulombic effects, vacancies are often assumed to be “freely available” for transport. In part, this has motivated study of undoped single-phase materials with crystallographically identical oxygen sites, presumably containing large numbers of thermodynamically stable, and freely mobile, oxygen anion vacancies. In these cases, one expects the activation energy for oxygen-17 spin lattice relaxation to be identical to that measured for bulk transport.

Optimization of vacancy concentration and/or local hopping kinetics may not be sufficient, however, to maximize ion transport. Thermodynamic considerations, especially structural phase transitions and vacancy ordering, can obfuscate a clear relationship between microscopic kinetics, as determined by NMR relaxation parameters, and macroscopic transport. The relatively simple brownmillerite material $\text{Ba}_2\text{In}_2\text{O}_5$ is an example of the former situation, and the non-stoichiometric perovskites form an example of the latter.

Figure 4 shows various relaxation parameters for ^{17}O in $\text{Ba}_2\text{In}_2\text{O}_5$. The extraordinarily sharp discontinuity in NMR parameters at approximately 925C has been interpreted, with thermal analysis and x-ray diffraction data [16], as an order-disorder transition within the oxygen sub-lattice (note that structural phenomena involving only the oxygen sub-lattice are not detectable with x-ray methods). Such an order-disorder transition can be explained in terms of a model in which only one of the oxygen sites participates in long length-scale, cooperative, fluctuations of octahedral tilt inversions. Not until temperatures in excess of 1075C do all the oxygen sites participate in vacancy diffusion.

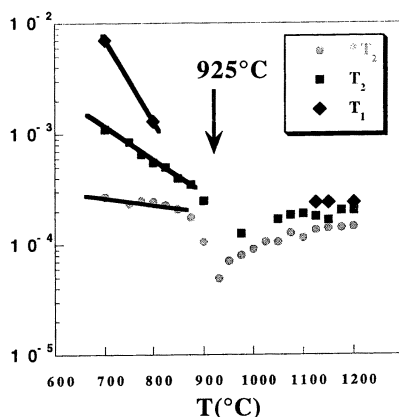
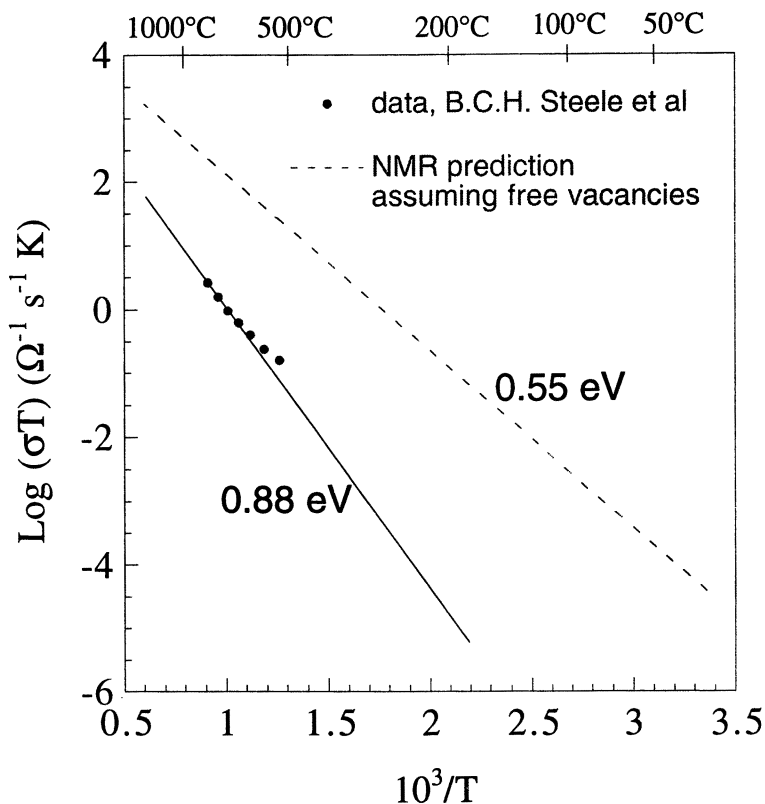


Figure 4: Relaxation times (seconds) from various experiments on ^{17}O in $\text{Ba}_2\text{In}_2\text{O}_5$. Adapted from reference [16].

More complex non-stoichiometric oxides show no structural phase transitions in the temperature ranges relevant to oxygen ion conduction, yet still have local kinetics that seem to differ bulk measurements. Figure 5 shows a comparison of ionic conductivity in $\text{BaIn}_{\frac{2}{3}}\text{Zr}_{\frac{1}{3}}\text{O}_{\frac{8}{3}}$ as determined by macroscopic methods and the predicted conductivity based upon our own ^{17}O NMR data. Disagreement is substantial.

Figure 5: Comparison of measured ionic conductivity of $\text{Ba}(\text{In}_{\frac{2}{3}}\text{Zr}_{\frac{1}{3}})\text{O}_y$ (data points, from reference [19]) with that predicted from NMR spin-lattice relaxation kinetics assuming free (unassociated) vacancies (dashed line).

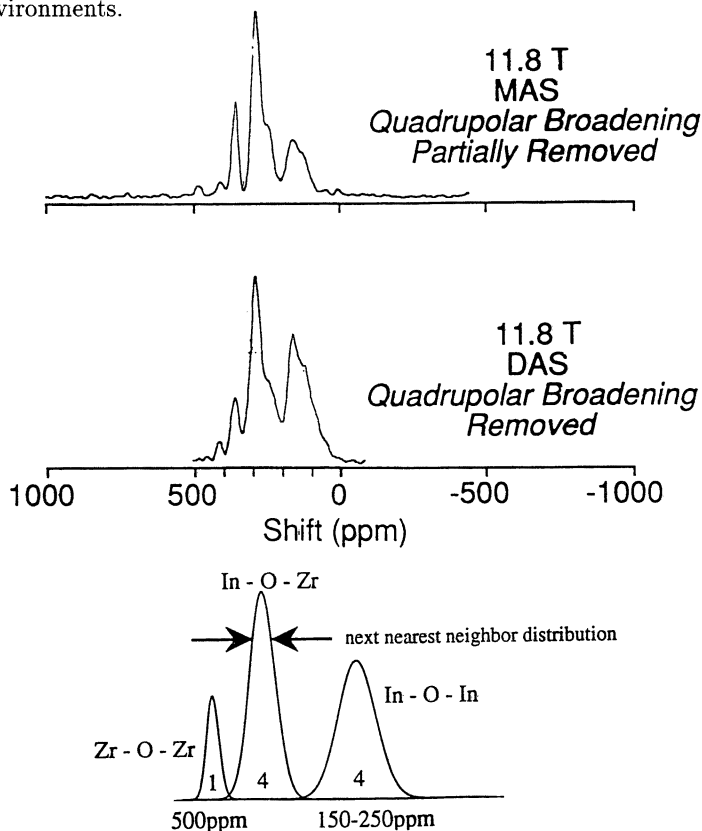


As suggested in Figure 1, parts of the oxygen sub-lattice may be unavailable for vacancy occupancy. What is needed, therefore, is a site-selective probe of the relative mobility of oxygen atoms. As shown in Figure 6, MAS, DOR, (and, by extrapolation, DAS and MQMAS) methods may be used to spectroscopically discriminate the different oxygen sites in many mixed oxides. Figure 6 compares the DAS and MAS spectra of BaInZrO with a calculated spectrum based upon

the known ^{17}O chemical shifts of pure oxides and the known stoichiometry of $\text{BaIn}_2\text{Zr}_3\text{O}_9$; the comparison is semi-quantitatively correct for both experiments [16]. In static samples, as the temperature is increased, a spin-echo measurement may then probe the *relative* mobility of the three peaks making up the high resolution spectra.

As shown in Figure 7, the right-hand side of the static spectra, associated with In-O-In sites by comparison with the high resolution spectra, clearly has a different relaxation time than the middle and right-hand portion of the spectrum. This result qualitatively establishes that vacancies do not visit all of the oxygen sub-lattice with equal probability.

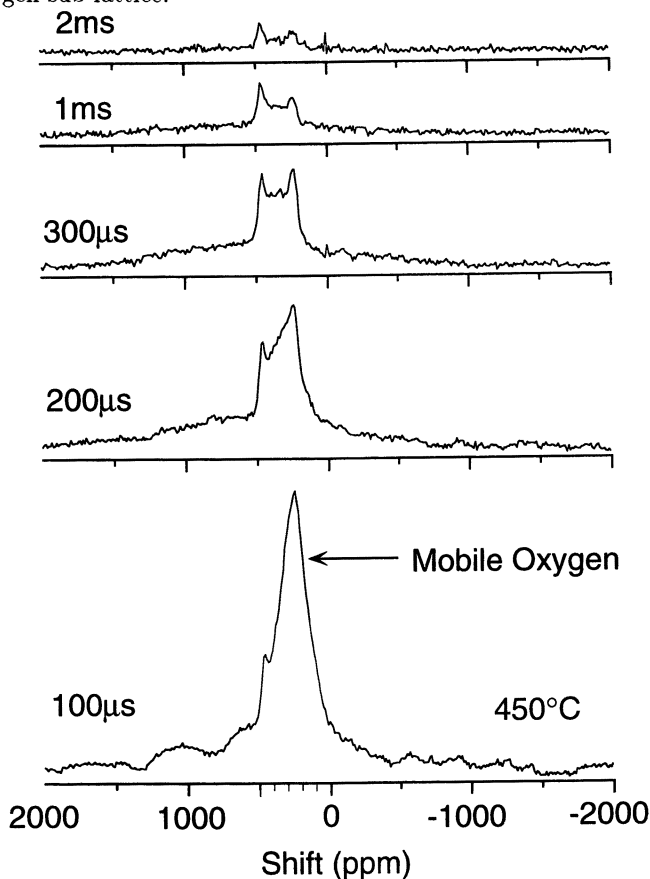
Figure 6: A comparison of MAS, DAS, and simulated ^{17}O NMR lineshapes for $\text{Ba}(\text{In}_2\text{Zr}_3)\text{O}_9$. The MAS and DAS spectra are adapted from reference 17. The simulated lineshapes are estimated from bond stoichiometry and literature values for ^{17}O chemical shifts. Note that the *right* hand side of the spectrum is associated with In-O-In oxygen bonding environments.



High resolution TEM, as well as electron and neutron diffraction results [16, 17] shown quite clearly that the vacancies can order in these structures, thereby

leading to an structurally inhomogeneous material with a “patchwork” ordering [17]. Furthermore, high-temperature ^{17}O NMR studies [18] of electronic structure also reflect this inhomogeneity: the observed shift in $(\text{La}_{0.6}\text{Sr}_{0.4})(\text{Co}_{0.8}\text{Cu}_{0.2})\text{O}_y$ and $(\text{La}_{0.5}\text{Ba}_{0.5})(\text{Co}_{0.7}\text{Cu}_{0.3})\text{O}_y$ can be deconvoluted into a temperature independent Knight shift and a temperature-dependent Curie-Weiss contact shift (Figure 8). This inhomogeneous electronic structure is consistent with the presence of layered microdomains observed previously within these materials.

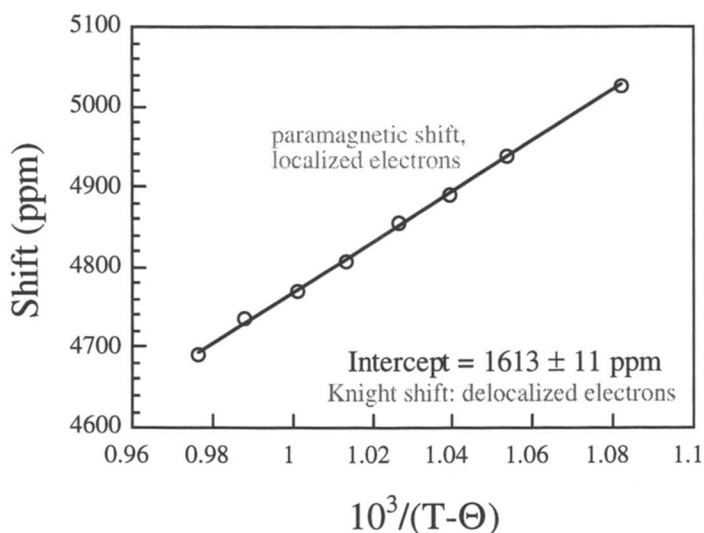
Figure 7: ^{17}O Hahn-echo spectra of $\text{Ba}(\text{In}_{\frac{2}{3}}\text{Zr}_{\frac{1}{3}})\text{O}_y$. Times indicated are the delays between pulses. Note that the right portion of the spectra decays much faster than the left portion, indicating anisotropic mobility in the oxygen sub-lattice.



These observations led us to a viewpoint in which vacancies order in two dimensional planes. Any prediction of bulk transport rates, therefore, must independently account for the energetics of vacancy motion between planes, as well as trapping of vacancies within ordered MO_6 octahedra, as shown in Figure 9. We have achieved such measurements [17,18] in both $(\text{La}_{0.6}\text{Sr}_{0.4})(\text{Co}_{0.8}\text{Cu}_{0.2})\text{O}_y$

and $(\text{La}_{0.5}\text{Ba}_{0.5})(\text{Co}_{0.7}\text{Cu}_{0.3})\text{O}_y$. In these materials only mobile oxygen contributes to the spectra due to paramagnetic broadening; thus a measure of the ^{17}O signal intensity as a function of inverse temperature yields an activation energy for vacancy trapping. Likewise, an Arrhenius plot for the linewidth yields the activation for motion between planes. The bulk conductivity of oxygen is then expected to be a product of mobility and concentration, both of which are governed by Arrhenius behavior. The sum of the activation energies is 1.1eV, within experimental error of the measured value in the literature [17].

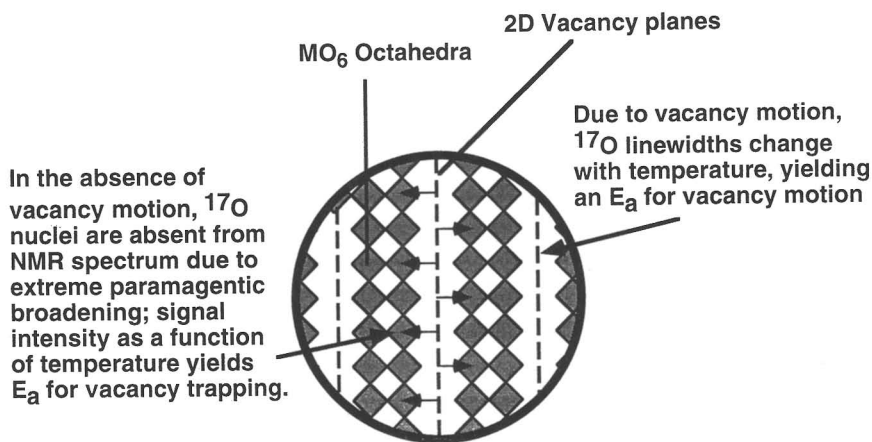
Figure 8: The shift of the oxygen-17 resonance in ppm of $(\text{La}_{0.6}\text{Sr}_{0.4})(\text{Co}_{0.8}\text{Cu}_{0.2})\text{O}_y$ vs. $\frac{1000}{(T-\Theta)}$, where $\Theta = 199\text{K}$. The intercept at $T = \infty$ corresponds to a shift of 1613 ± 11 ppm. Measurements of high-temperature oxygen-17 NMR were made at 36.2 MHz, using a home built spectrometer and a water-cooled high-temperature probe described elsewhere[16]. NMR spectra were found to contain all 5 nuclear-spin transitions, and were obtained using single $\frac{\pi}{2}$ pulses of $12\mu\text{s}$. The measurements were made between 25C and just below the decomposition temperature of the samples, and were performed under room air using a special static line to ensure $P_{\text{O}_2} = 0.21\text{atm}$ at all times and no loss of ^{17}O enrichment.



Conclusions

NMR is a powerful and widely-used tool for studies of atomic motion in solids. Here we have shown several examples of how local kinetic and structural information obtained from oxygen-17 NMR can be used to bridge the gap between atomic dynamics and macroscopic transport phenomena. Although our results have been very exciting, they have also generated many questions.

Figure 9: Schematic of two-dimensional vacancy planes, bounded by MO_6 octahedra. ^{17}O linewidth as a function of temperature yields an activation energy for mobility; signal intensity as a function of temperature yields an activation energy for oxygen ion concentration.



We found that a fairly simple thermodynamic theory (Debye-Hückel) is able to describe the effect of long-range defect interactions in doped ceria, even at relatively high dopant concentrations. How far can point-defect theory go in describing the thermodynamic and kinetic properties of solids? Certainly in the case of BaInO and BaInZrO we found strong evidence that this approach breaks down. Is there an approach that allows us to address the transition between these extremes?

Our NMR studies of more complex materials, including an ostensibly “defect-free” ternary oxide of known structure (BaInO), clearly show that vacancy thermodynamics and ordering into two-dimensional structures can affect the relationship between microscopic hopping kinetics and bulk transport. Is the “patchwork” ordering in highly defective perovskites (like BaInZrO) an equilibrium phenomenon as in BaInO ? What thermodynamic forces are present to stabilize these structures? Can these forces be rationalized and generalized?

In addition to complex atomic structure, our measurements also show strong evidence for complex electronic structure. Perhaps measurement of NMR at high temperature can be exploited to probe, simultaneously, the properties of both localized and itinerant electrons. Is inhomogeneous atomic structures related to inhomogeneous electronic structure? What roles can these measurements play in testing new theoretical models [20] for these materials? Can the gap between band structure and point-defect theory be bridged to create a deeper understanding of properties in highly defective materials?

References

1. Kofstad, P., *Nonstoichiometry, Diffusion, and Electrical Conductivity in Binary Metal Oxides*, (Robert E. Krieger Publ. Co., Malibar, Fla, 1983).
2. B. C. H. Steele, "Oxygen Ion Conductors" in *High Conductivity Solid Ion Conductors*, edited by T. Takahashi. (World Scientific Publ., 1989).
3. R. Figuera, A. V. Chadwick, J. H. Strange, *J. Phys. C:Solid State Phys.*, **11**, 55 (1978).
4. K. Fuda et al, *J. Phys. Chem. Solids* 45(11,12), 1253 (1984).
5. K. Fuda et al, *J. Phys. Chem. Solids* 46(10), 1141 (1985).
6. D. Y. Wang et al, *Solid State Ionics* 2, 95 (1981).
7. A. F. Voter and J. D. Doll, *J. Chem. Phys.* 82(1), 80 (1985).
8. H. C. Kang and W. H. Weinberg, *J. Chem. Phys.* 90(5), 2824 (1989).
9. R. L. June, A. T. Bell, and D. N. Theodorou, *J. Phys. Chem.* 95(22), 8866 (1991).
10. Stuart B. Adler and Jacob W. Smith, *Jour Chem Soc-Faraday*, 1993 **89** N16:3123.
11. Stuart B. Adler, Jacob W. Smith, Jeffrey A. Reimer, *Journal of Chemical Physics* **98** 7613 (1993).
12. D. Wolf, *Spin-temperature and Nuclear-spin Relaxation in Matter*, Basic Principles and Applications (Clarendon Press, Oxford, 1979).
13. J. S. Newman, *Electrochemical Systems*, 2nd ed. (Prentice Hall, 1991).
14. L. Onsager, *Prix Nobel*, 169-82 (1968).
15. A. B. Lidiard, *Phys. Rev.* 94(1), 29 (1954).
16. Stuart B. Adler, Jeffrey A. Reimer, Jay Baltisberger, and Ulrike Werner, *Journal of the American Chemical Society* **116** 675 (1994).
17. Stuart B. Adler, Steven Russek, Jeffrey A. Reimer, Mark Fendorf, Angelica Stacy, Qingzhen Huang, Antonio Santoro, Jeffrey Lynn, Jay Baltisberger, Ulrike Werner, *Solid State Ionics* **68** 193 (1994).
18. Stuart B. Adler and Jeffrey A. Reimer, *Solid State Ionics*, 1996, V91, 175.
19. B.C.H. Steele, *Mater. Sci. Eng. B* 1992, **B13** 79.
20. M.H.R. Lankhorst, H.J.M. Bouwmeester, H. Verweij, *Phys. Rev. Lett.* 1996, **77** 2989.

Chapter 4

The Study of Fluoridated Hydroxyapatite by ^{31}P - ^{19}F Rotational-Echo, Double-Resonance NMR

Yong Pan

Miami Valley Laboratories, The Proctor & Gamble Company, P.O. Box 538707,
Cincinnati, OH 45253-8707

This work demonstrates the use of ^{31}P - ^{19}F Rotational-Echo, Double-Resonance (REDOR) NMR to investigate fluoride in apatitic matrices. For fluorapatite, ^{19}F -observed ^{31}P - ^{19}F REDOR NMR of fluorapatite revealed the ^{31}P - ^{19}F connectivities. ^{31}P -observed ^{31}P - ^{19}F REDOR NMR determined the nearest ^{31}P - ^{19}F distance. For F^- -treated hydroxyapatite and 25% F^- -substituted fluorohydroxyapatite, the ratios of REDOR difference to full-echo intensity with various dephasing times were measured and then compared to the simulated values for models with various fluoridation depths and orientations. The simulation involved calculating the dephasing of multiple ^{31}P 's by multiple ^{19}F 's and then summing over all the P-F spin clusters, weighted by the occurring probabilities. The data showed that the OH ions in the first unit cell on the (001) surface were replaced by F ions. This result suggested the fluoridation was via the ion-exchange process rather than by the diffusion or the dissolution and remineralization pathway.

Hydroxyapatite (HAP), $\text{Ca}_{10}(\text{OH})_2(\text{PO}_4)_6$, is one of the major inorganic constituents of dental enamel and cortical bone. Incorporation of fluoride into HAP has been proven effective in preventing dental caries (1). The effects of fluoride on the mechanical properties of bone remain extremely controversial as exemplified by the contradictions in the literature (2, 3). The interaction between F^- and HAP is complicated by its dependence on fluoride concentration, pH, reaction time, and the type of HAP. The proposed pathways include ion exchange (specific adsorption) of $\text{F}^-_{(\text{aq})}$ with $\text{OH}^-_{(\text{lattice})}$; dissolution of enamel crystallites followed by reprecipitation of fluorohydroxyapatite (FHAP); and the diffusion of F^- into an apatite lattice (4, 5). Several analytical techniques have been used to address the amount of F^-

incorporated into HAP and the reaction products of fluoride with HAP, i.e., FHAP, CaF_2 , or nonspecifically adsorbed fluoride (6, 7). However, none of these techniques can provide information on the spatial distribution of F^- in HAP. The question is, then, are F^- ions uniformly distributed throughout apatite crystals or are they concentrated on the surface? On which crystal plane is the fluoridation preferred? Here we report our recent development of the use of P-F REDOR NMR to investigate the spatial distribution of F^- in apatite, which can provide detailed information on the history and mechanism of fluoride and HAP interactions.

The crystal structure of hexagonal ($\text{P6}_3/m$) apatite has been determined and refined by X-ray diffraction (8, 9). Fig. 1 shows the arrangement of F and P nuclei in fluorapatite (FAP). The F ions lie on [001] hexads separated by 9.37 Å, whereas the nearest neighbor distance for F^- along the six-fold axis is only 3.44 Å. Associated with each F ion are three PO_4^{3-} groups located in the plane perpendicular to the F^- axis. The PO_4^{3-} groups of each layer are rotated by 60° with respect to the layer below. The nearest P-F distance is 3.62 Å. Depending on the mechanism, the incorporation of F^- in apatite could be different in both depth and orientation. Several models of F^- incorporation will be discussed in section 3.2.

Rotational-Echo, Double-Resonance (REDOR) NMR, a technique for retrieving information on weak heteronuclear dipolar coupling interactions, has been applied to observe the interface in polymer blends (10) and to measure heteronuclear distances and connectivities in various biological systems (11-14). For a pair of isolated spins, the REDOR difference signal can be easily measured and translated into internuclear distances. For systems where an observed nucleus is dephased by more than one heteronucleus, the calculation requires the knowledge of the relative geometry of the nuclei (15). The calculated values for various dephasing cycles can be compared with experimental data. P-F REDOR NMR does not require isotopic labeling. For fluoridated hydroxyapatite, a proton dilute system, high-power proton decoupling is not required. Therefore, a two-channel NMR spectrometer is adequate to perform the REDOR experiment (16).

Experimental

^{31}P - ^{19}F REDOR NMR. The pulse sequence for ^{31}P -observed ^{31}P - ^{19}F REDOR is shown in Fig. 2. The ^{31}P magnetization is created by a single 90° pulse. A ^{31}P 180° pulse in the center of the REDOR dephasing period refocuses all isotropic chemical shifts at the start of data acquisition and produces a rotational spin echo. The ^{19}F 180° pulses inserted at each half-rotor period prevent the rotational spin echo from reaching full intensity. For a single spin pair, the reduced signal intensity, s , can be calculated according to the equation:

$$s = s_0 \cos[\Delta\Phi(\alpha, \beta, \lambda_D)] \quad (2.1)$$

where s_0 is the signal intensity without the application of ^{19}F 180° pulses; α is the azimuthal angle and β is the polar angle defined by the internuclear vector in a coordinate system with z axis parallel to the rotor axis; λ_D is the product of the number of rotor cycles (N_c), the dipolar coupling constant (D), and the rotor period

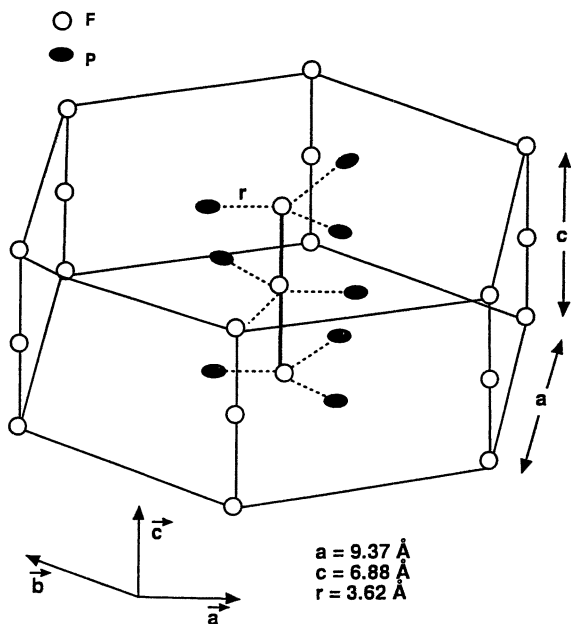


Figure 1. The crystal structure and coordinates of F and P nuclei in fluorapatite.

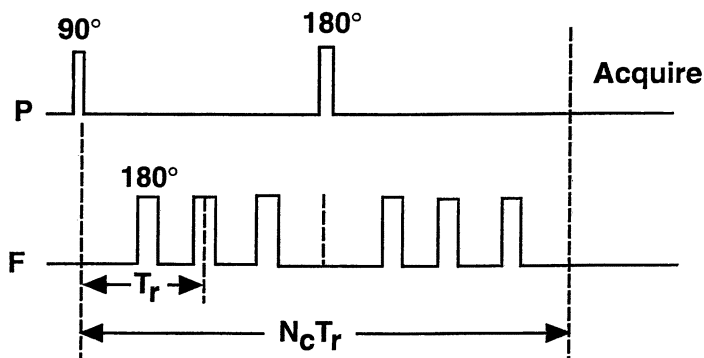


Figure 2. Pulse sequence for ^{31}P -observed ^{31}P - ^{19}F REDOR NMR. Two equally spaced ^{19}F 180° pulses per rotor period result in the dephasing of transverse ^{31}P magnetization produced by a ^{31}P 90° pulse. Phosphorus-fluorine dipolar coupling determines the extent of dephasing. A ^{31}P 180° pulse in the middle of the dephasing period refocuses the isotropic ^{31}P chemical shift difference at the beginning of data acquisition.

(T_r); and the amount of dephasing, $\Delta\Phi$, is a function of Euler angles α and β as well as λ_D . For a powder sample, $\cos[\Delta\Phi(\alpha, \beta, \lambda_D)]$ can be averaged over all orientations of spin pairs. The averaged $(s_o - s)/s_o$, known as $\Delta S/S_o$, is calculated and plotted as a function of λ_D as shown in Fig. 3 (17). The curve is universal. For an isolated spin pair, an experimental determination of $\Delta S/S_o$ can be readily translated into a dipolar coupling constant D and, therefore, an internuclear distance r since

$$D = \gamma_P \gamma_F \hbar / 2\pi r^3$$

where γ_P and γ_F are ^{31}P and ^{19}F gyromagnetic ratios and \hbar is Planck's constant.

When an observed nucleus is dephased by more than one heteronucleus, the dephasing is normally dominated by the nearest heteronucleus since the dipolar coupling is inversely proportional to the cube of the distance. However, when the neighboring heteronuclear distances are comparable, the dephasing from multiple heteronuclei will be accumulated (18):

$$s = s_o \cos\left[\sum_j \Delta\Phi_j(\alpha, \beta, \lambda_D)\right] \quad (2.2)$$

For spin-1/2 interactions, such as between ^{19}F and ^{31}P , the dephasing with plus and minus signs occurs with equal probability; therefore, the spin average can be obtained by averaging the two possible dephasing values, $\Delta\Phi_j(\alpha, \beta, \lambda_D) = \pm |\Delta\Phi_j(\alpha, \beta, \lambda_D)|$, as shown here:

$$\begin{aligned} s &= s_o \text{Re}\langle \exp(i \sum_j \Delta\Phi_j) \rangle_{spin} \\ &= s_o \text{Re}\langle \prod_j \exp(i \Delta\Phi_j) \rangle_{spin} \\ &= s_o \text{Re} \prod_j \langle \cos \Delta\Phi_j + i \sin \Delta\Phi_j \rangle_{spin} \quad (2.3) \\ &= s_o \text{Re} \prod_j [1/2 \cos(|\Delta\Phi_j|) + 1/2 \cos(-|\Delta\Phi_j|) \\ &\quad + i/2 \sin(|\Delta\Phi_j|) + i/2 \sin(-|\Delta\Phi_j|)] \\ &= s_o \prod_j \cos(|\Delta\Phi_j|) \\ &= s_o \prod_j \cos \Delta\Phi_j \end{aligned}$$

To calculate the powder average, we cannot average over α and β for each spin independently because they are fixed in a rigid lattice. Instead, we must (a) express both α and β in terms of the Euler angles that reference to a coordinate system fixed in the lattice and then (b) average over α and β . If we know the relative geometry of all the spins, the averaging is straightforward (15, 18). This calculation assumes that the homonuclear interactions are relatively small and are effectively averaged by magic-angle spinning.

Experimental Conditions.

NMR Spectroscopy. NMR spectra were obtained on a Bruker MSL-300 spectrometer operating at 121.46 and 282.29 MHz for ^{31}P and ^{19}F , respectively. For this work, a ^{19}F /multinuclear double-tuned probe with Vespel housing was used for optimized ^{19}F observation (Doty Scientific, Inc.). A PC-based spin-rate controller allowed a 5-mm silicon nitride rotor with Vespel end caps to spin up to 14 kHz with a fluctuation within ± 2 Hz. The 90° pulse width was $3\ \mu\text{s}$ for ^{31}P and $2.5\ \mu\text{s}$ for ^{19}F . For ^{31}P -observed REDOR, ^{19}F 180° pulses had alternate xy phases and irradiation was on resonance. The buffer acquisition mode was used so that the FID's with dephasing pulses were recorded on the even-numbered scans and the FID's without dephasing pulses were recorded on the odd-numbered scans. The difference signal could be reliably obtained because the operating conditions of the observation channel did not change from scan to scan.

Fluoride-Selective Electrode Analysis. The fluoride-selective electrode analysis was performed with an Orion combination fluoride electrode (Model 960900). Typically, about 1.5 mg of HAP was dissolved in 1.0 ml of 1N HCl. A 0.15 ml aliquot of the solution was then diluted to a total volume of 2.0 ml with a 50/50 mixture of water/TISAB (Total Ionic Strength Adjustment Buffer from Orion Research Inc.). The calibration curve was generated by using NaF as a standard. Three preparations were analyzed and the average value was taken for each sample.

Samples.

FAP and FHAP. FHAP and FAP samples were synthesized according to the method of McCann (19). Specifically, an aqueous solution of $\text{Ca}(\text{NO}_3)_2$ and KH_2PO_4 was slowly added with stirring to a dilute (0.1 mM) KF solution buffered with potassium acetate to pH 4.7. The amount of KF was varied to generate FHAP's with various substitutions. The precipitated FHAP powder was collected, washed with fluorine-free distilled water, and dried at 85°C for 8 hours. The apatite structure was confirmed by powder X-ray diffraction. The F^- substitution level was determined by fluoride-selective electrode analysis. A 100% F^- -substituted sample (FAP) and a 25% F^- -substituted sample (25% F^- -substituted FHAP) were used in this study.

F^- -treated HAP. In the study of the fluoridation of hydroxyapatite, HAP was prepared by aqueous precipitation at pH 9 and 37°C (19). The surface area was determined to be $128\ \text{m}^2/\text{g}$ using the gas (N_2) adsorption/desorption technique. 0.15 g HAP was stirred in 20 ml of nanopure H_2O . The pH was adjusted and controlled to be between 7.1 and 7.3, and then 0.725 ml of NaF solution (14 mg/ml) was added. After five minutes of stirring, the precipitate was filtered and dried at 95°C . The F content was determined by fluoride-selective electrode analysis to be 0.93% by weight, which is equivalent to 25% of the OH^- being substituted by F^- on average.

Results

REDOR NMR on Fluorapatite. The ^{19}F -observed ^{31}P - ^{19}F REDOR NMR spectra of FAP are shown in Fig. 4a with the experimental conditions as specified in the caption. After eight-rotor-cycle dephasing, the fluorine signal is almost completely dephased. A strong difference signal is observed (Fig. 4a, top). This result is expected since each ^{19}F in FAP has three nearest ^{31}P neighbors at a distance of 3.60 Å (Fig. 1). The ^{19}F -observed REDOR NMR spectra of CaF_2 are shown in Fig. 4b for comparison. Under the same experimental conditions, no F signal is dephased and the difference signal is null.

It is not straightforward to determine the P-F distance by ^{19}F -observed REDOR due to multiple- ^{31}P dephasing in this system. However, the P-F distance can be determined by ^{31}P -observed ^{31}P - ^{19}F REDOR. Fig. 5 shows the spectra of ^{31}P -observed REDOR of FAP. The amount of dephasing is small after two- and four-rotor-cycle dephasing, and it is dominated by the nearest ^{19}F neighbor. The experimental ratios of the REDOR difference signal to full echo signal are 0.038 and 0.20 after two- and four-rotor-cycle dephasing, respectively, which correspond to P-F dipolar coupling constants of 875 and 1025 Hz (12, 17). These constants translate to P-F distances of 3.65 Å and 3.50 Å, compared to 3.60 Å from X-ray data (8). This minor disparity is due to the additional dephasing by the two next nearest ^{19}F neighbors, which are 4.9 Å away (8). In FAP, phosphorus-phosphorus homonuclear dipolar couplings are on the order of a few hundred Hz, which are sufficiently averaged by the 9 kHz magic-angle spinning. Therefore, quantification of ^{31}P -observed ^{31}P - ^{19}F REDOR is not affected by these couplings.

^{31}P - ^{19}F REDOR NMR on 25% F^- -substituted FHAP and F^- -treated Hydroxyapatite. ^{19}F -observed ^{31}P - ^{19}F REDOR spectra of FAP and F^- -treated HAP are illustrated in Fig. 6a and 6b, respectively. The ratios of the difference signal to the full-echo signal with various dephasing rotor cycles for the F^- -treated sample match those for FAP (Fig. 7), indicating that the F^- in the F^- -treated sample has been incorporated into the apatitic matrix as FAP or FHAP.

^{31}P -observed ^{31}P - ^{19}F REDOR spectra of F^- -treated HAP and 25% F^- -substituted FHAP are illustrated in Fig. 8a and 8b, respectively. Due to the difference in F^- distribution, differences in the REDOR difference signal intensities were observed between these two samples. For comparison, the experimental $(\Delta S/S_0)$'s with various dephasing cycles for these two samples are plotted in Fig. 9i and 9h.

REDOR Dephasing for F^- Distribution Models. The dephasing for ^{31}P -observed ^{31}P - ^{19}F REDOR of the F^- -treated HAP can be calculated using

$$\Delta S / S_0 = \sum_i (\Delta S / S_0)_i P_i \quad (3.1)$$

where $(\Delta S/S_0)_i$ is the dephasing for the i th kind of ^{31}P - ^{19}F cluster calculated from Eq. 2.3, P_i is the probability of finding a ^{31}P in the i th kind of ^{31}P - ^{19}F cluster, and the sum over i counts every possible ^{31}P - ^{19}F cluster. The dephasing for several

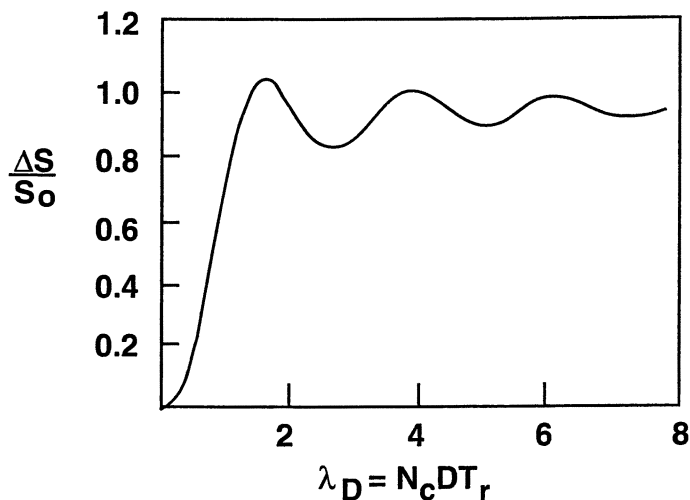


Figure 3. Calculated ratio of REDOR difference to full-echo intensity for an isolated spin pair as a function of λ_D , the product of the number of rotor cycles (N_c), the P-F dipolar coupling constant (D), and the rotor period (T_r).

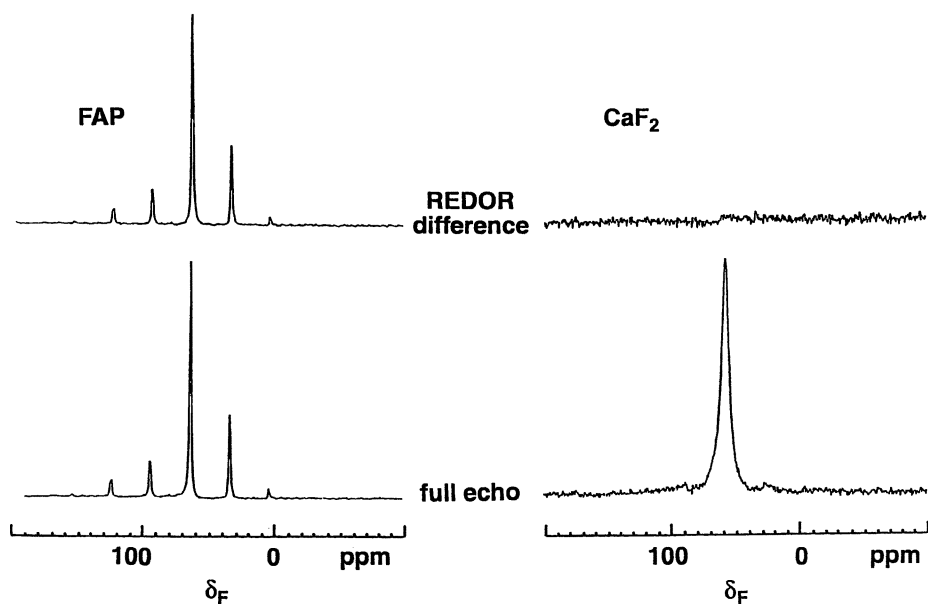


Figure 4. ^{19}F -observed ^{31}P - ^{19}F REDOR NMR spectra obtained from 150 mg of fluorapatite (a) and 130 mg of calcium fluoride (b). The pulse sequence of Figure 1 was used over eight rotor cycles with magic-angle spinning at 9 kHz. The recycle delay was 30 sec. The REDOR difference spectrum (top) is the difference between rotational spin echo ^{19}F NMR with and without the ^{31}P pulses. The difference signal arises only from those ^{19}F 's coupled to ^{31}P 's.

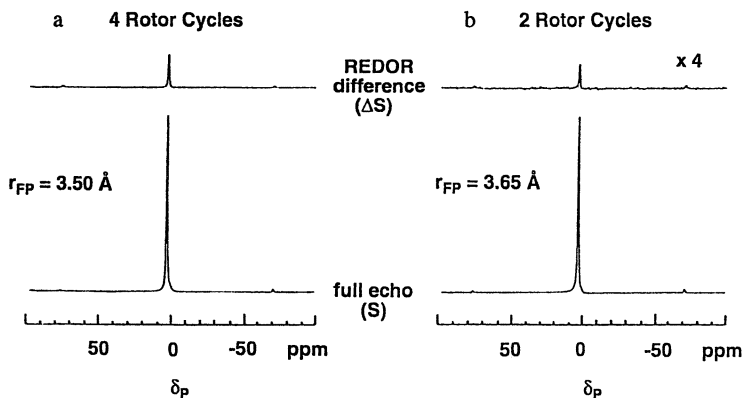


Figure 5. ^{31}P -observed ^{31}P - ^{19}F REDOR NMR spectra of fluorapatite obtained with four-(a) and two- (b) rotor-cycle dephasing. The recycle delay was 20 sec and magic-angle spinning was at 9 kHz. The REDOR difference spectrum (top) is the difference between rotational spin echo ^{31}P NMR with and without the ^{19}F 180° pulses. The experimental ratios of the REDOR difference signal to the full echo signal are 0.038 and 0.20 after two- and four-rotor-cycle dephasing, respectively. These ratios correspond to a distance of 3.65 Å and 3.50 Å for the nearest P-F pair, compared to 3.60 Å from X-ray data.

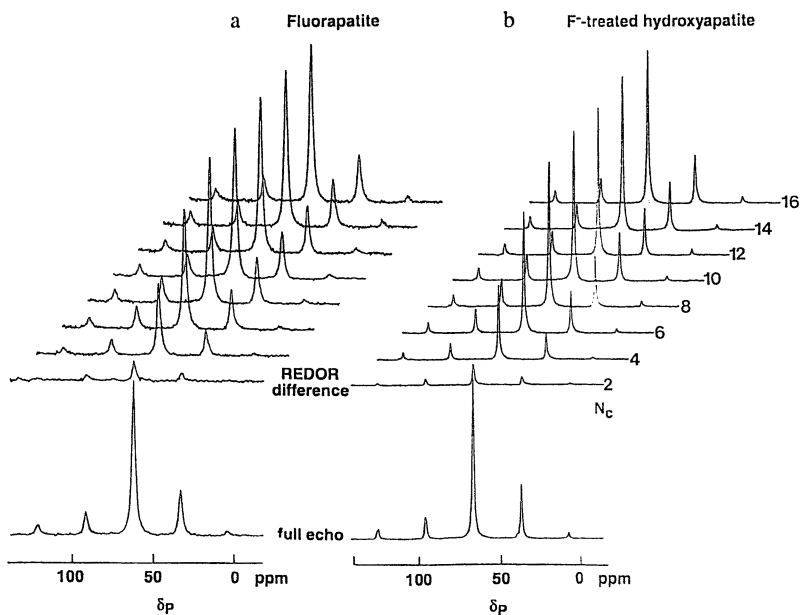


Figure 6. ^{19}F -observed ^{31}P - ^{19}F REDOR NMR spectra of 150 mg of fluoroapatite (a) and 160 mg of F-treated hydroxyapatite (b). The recycle delay was 30 sec and magic-angle spinning rate was 9 kHz. The REDOR difference spectra (top) are the difference between rotational spin echo ^{19}F NMR with and without the ^{31}P pulses. 48 averages were collected for each spectrum of the F-treated hydroxyapatite.

^{19}F - Observed REDOR NMR of FAP and F^- -treated HAP

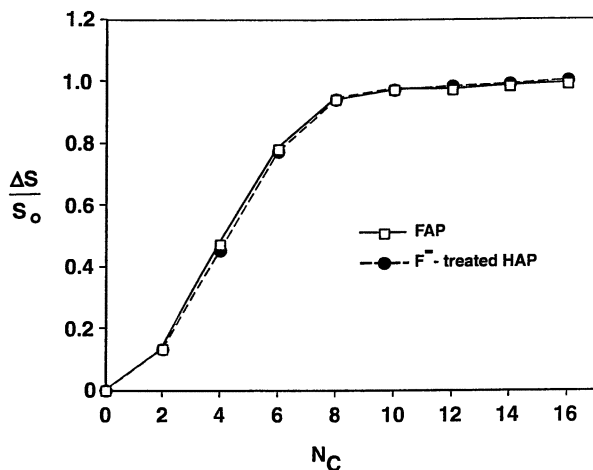


Figure 7. The ratios of difference signal to full-echo signal with various dephasing rotor cycles for F^- -treated HAP and for FAP.

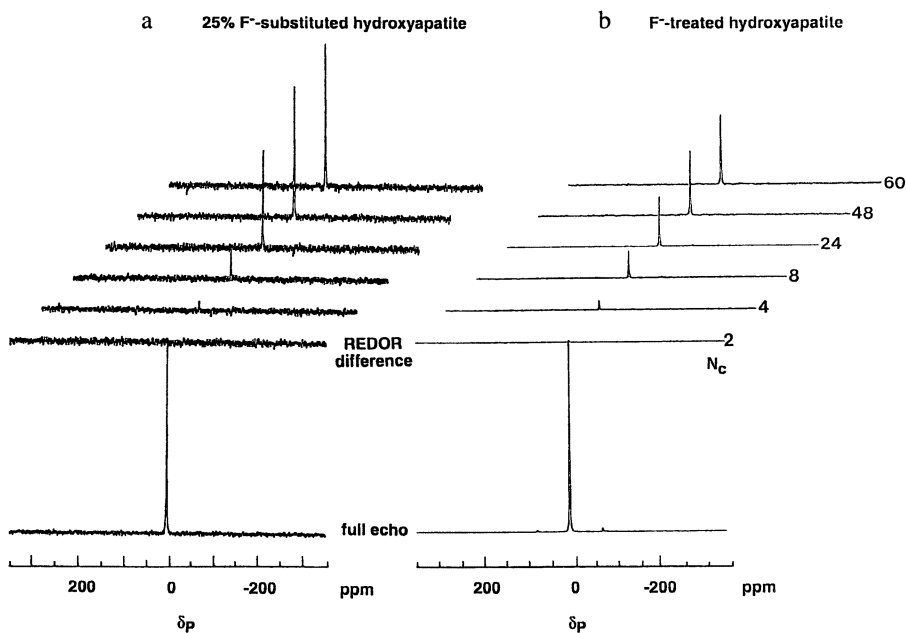


Figure 8. ^{31}P -observed ^{31}P - ^{19}F REDOR NMR spectra of 25% F^- -substituted FHAP (a) and F^- -treated HAP (b) obtained with 2 to 60 rotor cycles. The recycle delay was 20 sec and magic-angle spinning rate was 9 kHz. The REDOR difference spectra (top) are the difference between rotational spin echo ^{31}P NMR with and without the ^{19}F 180° pulses. Up to 1000 scans were collected for each spectrum of the F^- -treated HAP.

31P-OBSERVED REDOR NMR

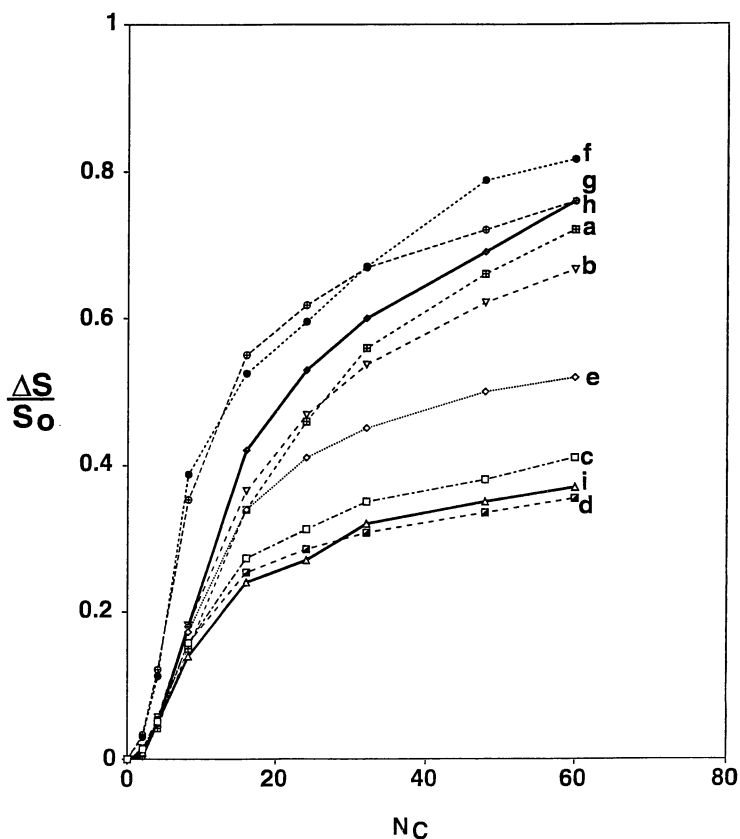


Figure 9. Ratios of REDOR difference signal to full-echo signal with various rotor cycles for the following models: (a) random distribution, (b) the first layer of OH ions in the (001) plane is replaced by F ions, (c) the first two layers of OH ions in the (001) plane are replaced by F ions, (d) the first three layers of OH ions in the (001) plane are replaced by F ions, (e) the first and the third layers of OH ions in the (001) plane are replaced by F ions, (f) the first layer of OH ions in the (100) plane is replaced by F ions, (g) the first two layers of OH ions in the (100) plane are replaced by F ions, (h) experimental data for 25% F⁻-substituted FHAP, and (i) experimental data for F-treated HAP.

simple models which are important to understanding the fluoridation mechanism was calculated as follows:

Random Distribution. If F ions are randomly distributed throughout the sample (Fig. 10a), each ^{31}P has 20 possible sites for ^{19}F 's within a distance of 12 Å. The probability of finding the nearest ^{19}F at the i th-nearest site, P_i , is $0.25(1 - 0.25)^{i-1}$ considering that, on average, 25% of the OH ions in the sample are replaced by F ions, based on the results of the fluoride-selective electrode analysis. Because the dephasing is dominated by the nearest ^{19}F and the F-P distances are known from the FAP crystal data, $(\Delta S/S_o)_i$, the REDOR dephasing by a ^{19}F at the i th site, can be taken directly from the REDOR universal curve (Fig. 3). The REDOR dephasings were then summed over i from 1 to 20 using Eq. 3.1 for various dephasing rotor cycles; these are plotted in Fig 10a.

OH Ions of the First Layer of the Unit Cell Along the (001) Plane are Replaced by F Ions. In this model, all ^{19}F 's are concentrated in the first layer (Fig. 10b). Since F^- substitution level is 25%, the model implies that the crystallites are eight-unit cells thick with a fluorine-containing layer on the surfaces. Based on the crystal structure (Fig. 1), every ^{31}P in the same layer has the same relative geometry to ^{19}F 's. For example, the ^{31}P at (0, 0, 0) in the first layer has 4 ^{19}F 's at (-7.837, 3.26, 0), (-3.121, -4.908, 0), (6.311, -4.908, 0), and (1.595, 3.26, 0) within 12 Å. $(\Delta S/S_o)_1$ can be calculated using Eq. 2.3 and the coordinates. Similarly, $(\Delta S/S_o)_2$ --dephasing for the ^{31}P 's in the second layer--and $(\Delta S/S_o)_3$ --dephasing for the ^{31}P 's in the third layer--can also be calculated. ^{31}P 's in further layers are at least 12 Å distant; the dephasings are negligible. The probability of finding a ^{31}P in the first, the second, or the third layer is 0.25 since the F^- substitution is 25% on average. The total dephasing, $(\Delta S/S_o)$, was then calculated, based on Eq. 3.1, and plotted for various N_c (Fig. 9b). Note, in the calculation, only the average F^- substitution level (25%) and the coordinates of F and P nuclei in the crystal unit are used. The data on crystal size and surface area were not needed.

Other Models. In the same manner, we calculated REDOR dephasing for the following models: The OH ions of the first two layers of the unit cells along the (001) surface are replaced by F ions (Fig. 10c); the OH ions of the first three layers of the unit cells along the (001) surface are replaced by F ions (Fig. 10d); the OH ions of the first and the third layers of the unit cells along the (001) surface are replaced by F ions (Fig. 10e); the OH ions in the first layer of the unit cells along the (100) surface are replaced by F ions (Fig. 10f); and the OH ions in the first two layers of the unit cells along the (100) surface are replaced by F ions (Fig. 10g). The results of these calculations are plotted in Fig. 9.

Discussion

The experimental data for the 25% F^- -substituted FHAP (Fig. 9a) match the calculated values for the random distribution model (Fig. 9h). The data for the F^- -treated sample (Fig. 9i) fit best with models c and d, in which the OH ions in the

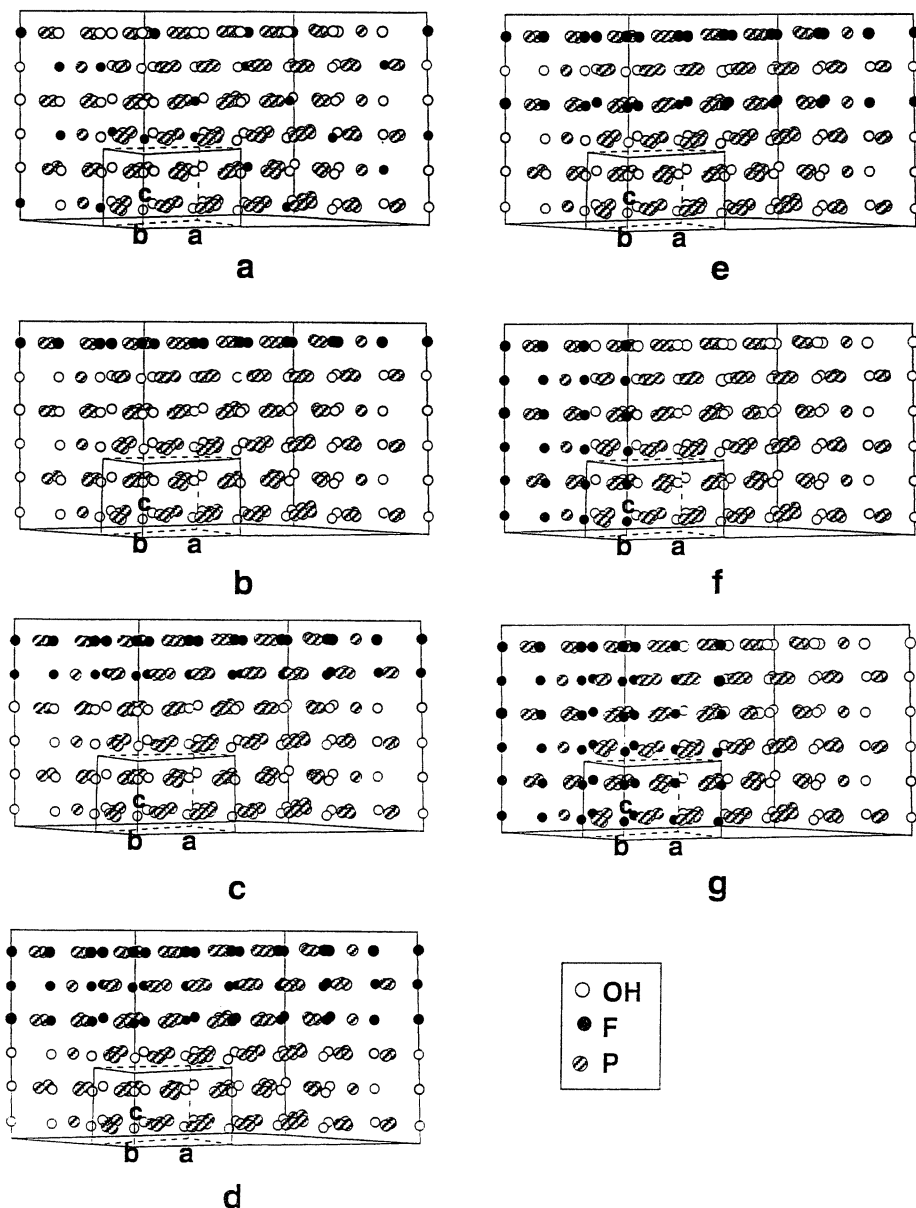


Figure 10. The models for F^- distribution in an apatitic lattice. (a) Random distribution, (b) the OH ions of the first layer of the unit cell along the (001) surface are replaced by F ions, (c) the OH ions of the first two layers of the unit cells along the (001) surface are replaced by F ions, (d) the OH ions of the first three layers of the unit cells along the (001) surface are replaced by F ions, (e) the OH ions of the first and the third layers of the unit cells along the (001) surface are replaced by F ions, (f) the OH ions in the first layer of the unit cells along the (100) surface are replaced by F ions, and (g) the OH ions in the first two layers of the unit cells along the (100) surface are replaced by F ions.

In Solid-State NMR Spectroscopy of Inorganic Materials; Fitzgerald, J.; ACS Symposium Series; American Chemical Society: Washington, DC, 1999.

first two or three layers of the unit cells along the (001) plane are substituted by F ions.

For models c and d, the fluoridation depth is 6.9 and 10.4 Å, respectively. These values are reasonable when compared with the 6.1 Å average fluoridation depth obtained from the calculation based on the surface area (128 m²/g) and the average F⁻ substitution (25%), since the calculation assumes the fluoridation is isotropic in orientation. While it is true that needle-like crystallites are common in biological apatite, for synthetic HAP, when CO₃²⁻ content is less than 0.01%, the crystals formed are less structured or have hexagonal faces of {1,0,-1,0} with pyramidal faces of {1,0,-1,1} at both ends (20). Examination of the HAP by high-magnification light microscopy showed the majority of the HAP samples in our study were in a less-structured, non-needle crystal habit.

The depth of the F⁻ incorporation suggested that the fluoridation occurred via the ion-exchange process rather than by the diffusion or the dissolution and remineralization pathway (4). In our study, the five-minute treatment was too short for F ions to penetrate deeply into the crystal lattice. The ion exchange occurred preferentially on the (001) plane. This result is expected since F⁻ channels are exposed along the (001) surface. The exchange through the (100) or the (010) planes is hindered by Ca²⁺ and PO₄³⁻ ions. This conclusion can also be related to the dissolution study by Arends, et al. (21) of a single HAP needle-like crystal with hexagonal basal faces in acid, in which the acid attack or penetration starts with one etch pit in the (001) face and then forms a longitudinal hole parallel to the c-axis.

Acknowledgments

The author would like to thank Chris Klug (Stanford University) for sharing his program for REDOR calculation, Ed Cox and Nicole Black (Procter and Gamble) for fluoride-selective electrode analysis and assistance in preparing the figures, and Drs. Jake Schaefer and Jon Goetz (Washington University), James Yesinowski (Naval Research Lab), Don White and Fred Wireko (Procter and Gamble) for helpful discussions.

References

1. Brown, W. E.; Konig, K. G. *Caries Res.*, **1977**, *11*, 1.
2. Lees, S; Hanson, D. B. *Cal. Tiss. Int.*, **1992**, *50*, 88.
3. Lundy, M. W.; Wergedal, J. E.; Teubneer, E.; Burnell, J.; Aherrard D.; Baylink, D. J. *Bone*, **1989**, *10*, 321.
4. Arends, J.; Nelson, D. G. A.; Dijkman, A. G.; Jongbloed, W. L. in *Cariology Today*; Guggenheim, B.; Ed.; Karger: Basel, **1984**, 245.
5. Featherstone, J. D. B.; Glana, R.; Shariati, M.; Shields, C. P. *J. Dent. Res.*, **1990**, *69*, 620.
6. White, D. W.; Bowman, W. D.; Faller, R. V.; Mobley, M. J.; Wolfgang, R. A.; Yesinowski, J. P. *Acta Odontol. Scand.*, **1988**, *46*, 375.
7. Kreinbrink, A. T.; Sazavsky, C. D.; Pyrz, J. W.; Nelson, D. G. A.; Honkonen, R. S. *J. Magn. Reson.*, **1990**, *88*, 267.

8. Kay, M. I.; Young, R. A.; Posner, A. S. *Nature*, **1964**, *204*, 1050.
9. Posner, A. S.; Perloff, A.; Diorio, A. F. *Acta Cryst.*, **1958**, *11*, 308.
10. Tong, G.; Pan, Y.; Afeworki, M.; Poliks, M. D.; Schaefer, J. *Macromolecules*, **1995**, *28*, 1719.
11. Marshall, G. R.; Beusen, D. D.; Kociolek, K.; Redlinski, A. S.; Leplawy, M. T.; Pan, Y.; Schaefer, J. *J. Am. Chem. Soc.*, **1990**, *112*, 963.
12. Pan, Y.; Gullion, T.; Schaefer, J. *J. Magn. Reson.*, **1990**, *90*, 330.
13. Forrest, T. M.; Wilson, G. E.; Pan, Y.; Schaefer, J. *J. Biol. Chem.*, **1991**, *266*, 4485.
14. McDowell, L. M.; Holl, S. M.; Qian, S.; Li, E.; Schaefer, J. *Biochem.*, **1993**, *32*, 4560.
15. McDowell, L. M.; Klug, C. A.; Beusen, D. D.; Schaefer, J. *Biochem.* submitted.
16. Pan, Y. *Solid State Nucl. Magn. Reson.*, **1995**, *5*, 263.
17. Gullion T.; Schaefer, J. in *Advances in Magnetic Resonance*; Warren, W. S. Ed.; Academic Press: San Diego, **1989**, *Vol. 13*; 57.
18. Bocey, J. B. Thesis, University of Illinois, Urbana-Champaign, **1972**, 28.
19. McCann, H. G. *Arch. Oral Biol.*, **1968**, *13*, 987.
20. Arends, J.; Schuthof, J.; Van Der Linden, W. H.; Bennema, P.; Van Den Berg, P. *J. Crystal Growth*, **1979**, *46*, 213.
21. Arends, J.; Jongebloed, W. L. *J. Dent. Res.* **1979**, *special issue 8*, 58, 837.

Chapter 5

Solid-State ^1H , ^{17}O , and ^{27}Al NMR Studies of the Surface Chemistry of Alumina Materials

John J. Fitzgerald

Department of Chemistry and Biochemistry, South Dakota State University,
Brookings, SD 57007

Recent high-resolution solid-state MAS and CP/MAS ^{17}O and ^{27}Al NMR and ^1H CRAMPS studies of alumina-based materials of importance to understanding the surface and internal (bulk) structural chemistry of transition aluminas are reviewed. MAS and CP/MAS ^{17}O and ^{27}Al NMR studies of model $\alpha\text{-Al}_2\text{O}_3$, $\text{AlO}(\text{OH})$ and $\text{Al}(\text{OH})_3$ materials, and transition aluminas that have provided atomic-level information about the structure and behavior of both internal and surface Lewis acid and Brønsted acid sites are described. CP/MAS ^{27}Al NMR has been particularly useful to directly observe both 4- and 6-coordinate Al-OH Brønsted sites, and 4-, 5- and 6-coordinate AlO_x Lewis acid sites on transition aluminas. ^1H CRAMPS and dipolar dephasing studies of proton sites in model aluminum hydroxides and oxyhydroxides containing structurally well-understood Al_2OH and Al_3OH groups with different hydrogen bonding details, and the protons of two surface and internal (bulk) Al-OH groups and "physisorbed" water associated with a high surface-area ($230\text{ m}^2/\text{g}$) pseudo-boehmite ($\text{Al}_2\text{O}_3 \cdot 2.05\text{H}_2\text{O}$), are also discussed. Concurrent ^{27}Al MAS NMR spectra obtained at 14 T for transition aluminas formed from pseudo-boehmite following dehydroxylation from $300\text{ }^\circ\text{C}$ to $1100\text{ }^\circ\text{C}$ have provided new structural understanding about the 4-, 5- and 6-coordinate aluminum-containing γ - or δ -aluminas formed by condensation of the Al_2OH or AlOH groups at $350\text{ }^\circ\text{C}$ to $500\text{ }^\circ\text{C}$. Based on the ^1H and ^{27}Al NMR, three mechanisms are proposed for the condensation of the Brønsted Al-OH groups in pseudo-boehmite using crystalline boehmite as a structural model.

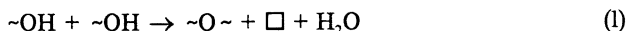
The Surface Chemistry of Alumina

Alumina-Based Materials. Alumina-based materials such as anhydrous and hydrous aluminum oxides and hydroxides, and a wide range of calcined aluminum

oxides such as corundum or α -alumina (α -Al₂O₃), γ -alumina and transitional aluminas are widely used as industrial catalysts, catalyst supports, adsorbents, coatings, ceramics and soft abrasives (1-3). The state of hydration of a specific alumina material is related to its stoichiometry and structure. While the hydroxides, gibbsite and bayerite, have related crystal structures (1-3) consisting of double layers of hexagonal closely-packed arrays of hydroxyl ions with each aluminum being coordinated to six anions that form edge-shared octahedral Al(OH)₆ structural units, the aluminum oxyhydroxides [AlO(OH)] occur in two distinct forms, boehmite and diaspore, that exist in hexagonal closed-packed arrangements of hydrogen-bonded oxides built up of edge-sharing AlO₄(OH)₂ or AlO₃(OH)₃ octahedral units (4). The Al³⁺ ion exists in a distorted, edge-sharing octahedral array of oxide ions that form a double layer, the resulting double layers being connected by zigzag chains of hydrogen bonds (4). Pseudoboehmite is a poorly crystallized aluminum oxyhydroxide with a water content of 1.5 - 2.5 moles (5). The x-ray diffraction pattern of pseudo-boehmite shows broad lines that coincide with the XRD lines of boehmite (1).

The transitional aluminas, χ -Al₂O₃, η -Al₂O₃, γ -Al₂O₃, κ -Al₂O₃ and θ -Al₂O₃, are formed from oxyhydroxides and hydroxides under a range of dehydration or dehydroxylation conditions as shown in Figure 1. The two terms are used here to represent the formal loss of water by desorption of "physisorbed" water or by condensation of hydroxyl groups, respectively (1,3,4). The materials, γ -Al₂O₃ and η -Al₂O₃, are known to crystallize in a defect spinel structure as observed for MgAl₂O₄. The strong one-dimensional disorder found in η -Al₂O₃ makes it a more effective acidic catalyst than γ -Al₂O₃ for olefin isomerization reactions (4).

Hydration and Dehydration of Aluminas. Strongly dried aluminas such as γ -Al₂O₃ and η -Al₂O₃ chemisorb at least a monolayer of water when exposed to moisture at room temperature (5). According to De Boer *et al.* (6) the hydration surface of γ -alumina retains 13 molecules of water/100 Å² of surface after evacuation at 25 °C for 100 hrs, while after drying at 120 °C, γ -Al₂O₃ still retains 8.25 molecules of water/100 Å² (6). Peri and Hannan (7) found that γ -alumina adsorbs water at room temperature and after calcination at 600 °C and reexposure to moist air. The surface water was postulated to include both "physisorbed" water and surface hydroxyl groups. During lower temperature heating, desorbed water molecules react to form "surface" hydroxyl groups (11,13); at higher temperatures, the adjacent surface hydroxyls condense to form water molecules, that are subsequently removed by evacuation according to the dehydration reaction:



where \square represents an oxygen vacancy formed and \sim represents an Al-O bond (8). This vacancy may be a vacant oxygen site of a five-coordinated aluminum (AlO₅) originating from a 6-coordinate AlO₆ precursor site.

Surface Lewis and Brønsted Acid Sites on Aluminas. Based on infrared studies, Peri (5,7,9,12) postulated a surface model for γ -alumina that includes five different surface hydroxyl sites to explain the five observable infrared spectral bands. This model was later refined by Knozinger and Ratnasamy (10) to include the (111)

and (110) planes and includes the different Type I, II and III sites as shown in Figure 2. These five sites can be distinguished on the basis of their structural arrangements (including hydrogen bonding) and the coordination numbers of the associated aluminum and oxygen atoms. This model of Knozinger and Ratnasamy (10) provides a framework for discussing and describing the various hydrogen, oxygen and aluminum chemical environments associated with various Al-OH sites. According to

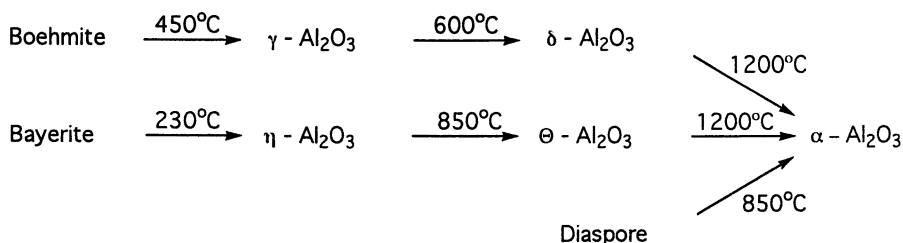


Figure 1. Thermal conversions of aluminum oxyhydroxides and hydroxides

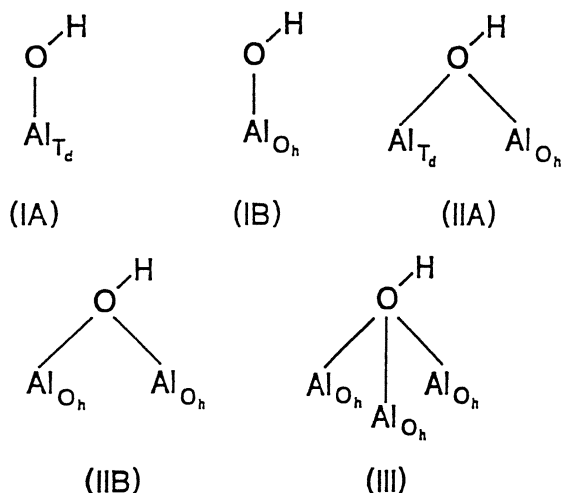


Figure 2. Types of surface hydroxyl groups of γ -alumina, as proposed by Peri (9).

this model, aluminum hydroxides, oxyhydroxides and transitional aluminas contain at least one of these five distinct types of Brønsted Al-OH hydroxyl sites. The Type III site is the most acidic site, whereas the Type IA and IB sites are the most basic. The relative contribution of specific crystal faces ultimately determines the occurrence and number of each Al-OH group (5).

The surface chemistry of aluminum oxide systems such as transition aluminas are among the most complex of metal oxide catalysts due to the presence of not only surface Brønsted acid sites due to these Al-OH moieties, but also Lewis acid sites due to coordinately unsaturated AlO_x sites, where $x = 3, 4$ or 5 . Evidence for these Brønsted acid sites, and to some extent, the Lewis acid sites, have been principally derived from FTIR studies (14-18). The catalytic activity of Brønsted Al-OH sites is not due to the acidic nature of the oxygen-proton bond but is likely due to differences in the energetically favorable hydrogen bonding interactions between surface Al-OH groups and adsorbed substrate molecules. The primary hydrogen bonding differences between various Al-OH surface groups are related to the coordination number of the oxygens of these surface groups. Al-OH groups may have oxygens with from one to three neighbor aluminums (Type I, II and III sites of Peri (5)) that contain either four-, five- or six-coordinated aluminums, respectively. Recent diffuse reflectance FTIR studies (18) of transition aluminas suggest the presence of Al-OH sites of Type I containing 4-coordinate (I_4) and six-coordinate (I_6) aluminum-containing groups, Al-OH sites of Type I containing $\text{Al}_6\text{-OH-Al}_6$ (II_{66}) and $\text{Al}_6\text{-OH-Al}_4$ (II_{64}) groups, and Al-OH sites of Type III with a combination of three associated four- and six-coordinate aluminums (III_{666} or III_{664}) as observed in the Al_3OH group (See Figure 2).

Lewis acidity is produced on the surface and within transition alumina materials as a result of the thermally-induced dehydroxylation of various aluminum hydroxides, oxyhydroxides and lower-temperature transition aluminas to form materials with coordinately unsaturated AlO_x sites and cation vacancies. The surface Lewis acid sites of aluminas are postulated to be of reduced aluminum coordination numbers of three, four and five (18). Solid-state NMR spectroscopic evidence (18-22) for 4- and 5-coordinate sites has been obtained; however, no evidence has yet been obtained for three-coordinate sites, although these latter sites have been postulated based on FTIR studies (14-18). The 4- and 5-coordinate Lewis sites originate from dehydroxylation of adjacent 6-coordinate AlOH and Al_2OH groups in precursor alumina materials, with the occurrence of both new sites (due to dehydroxylation) and "old" 4- and 5-coordinate aluminum sites that previously existed prior to dehydroxylation of these materials. The complexity of the catalytic acidity of alumina materials is likely the result of the spatial and chemical interrelationship between adjacent Lewis acid and Brønsted acid sites. In fact, recent FTIR studies (18) suggest that Lewis acid sites that are in close proximity to Brønsted acid sites of Type I_6 are the most acidic regions on the surfaces of transition aluminas.

Solid-State ^{17}O AND ^{27}Al NMR Studies of Alumina Materials

Solid-state NMR techniques provide unique capabilities to obtain information about both the structural nature and chemical dynamics of the surface chemistry of alumina

materials. The potential of solid-state NMR spectroscopy to provide considerably more detailed structural, dynamical and proximity information about both Brønsted acid and Lewis acid sites on the surface and within the internal (bulk) structure of transition aluminas is evident from recent investigations (19-22). The use of MAS ^{17}O and ^{27}Al (both $I = 5/2$ quadrupole nuclides) NMR is complicated by the residual second-order quadrupole line broadening contributions to their observed NMR resonances, that are not completely averaged by MAS even at higher magnetic fields (23,24,26-31). The presence of observable lower symmetry ^{27}Al sites, and to a lesser extent ^{17}O sites, makes spectral interpretations difficult for substances like transition aluminas that also contain a range of different aluminum and oxygen sites. Even recent advances such as multiple quantum (MQ) MAS techniques (32,33), that have been shown to provide more detailed chemical information from MAS ^{27}Al NMR spectra by eliminating the residual second-order quadrupole line broadening effects observed for resonances from such materials, have significant limitations due to its lack of sensitivity and use for quantitation purposes.

The study of surface sites by selective enhancement of the MAS ^{17}O and ^{27}Al NMR by cross-polarization (CP) has been especially informative for ^{27}Al (19-22,24,34,35); however, the understanding of the CP dynamics of the spin magnetization transfer process between ^1H and quadrupole nuclides like ^{17}O and ^{27}Al is still not fully understood (35-37). CP/MAS ^{17}O NMR (36) is, however, likely to provide important new insights into the surface structures and dynamics of aluminas in the future.

MAS and CP/MAS ^{27}Al NMR Studies. Morris and Ellis (19) have used solid-state CP/MAS ^{27}Al NMR to study the surface sites of α -alumina, γ -alumina, and pretreated γ -aluminas. The SP/MAS ^{27}Al NMR spectra of γ -alumina shows two peaks at 65 ppm and 3 ppm due to internal tetrahedral and octahedral aluminums, respectively, whereas the CP/MAS ^{27}Al NMR spectrum of γ -alumina shows two peaks at 6.0 ppm and 55 ppm due to octahedral and tetrahedral surface sites containing Al-OH moieties (Figure 3). Calcination of a γ -alumina to different degrees of dehydroxylation was shown to broaden the CP/MAS ^{27}Al NMR signal at 6 ppm, while heating γ -alumina to 350 °C for 8 hrs (partially dehydroxylated alumina, PDA) decreased the intensity of the signal due to the surface octahedral Al-OH sites. Continued heating of γ -alumina from 510 °C to 550 °C (intermediately dehydroxylated alumina, IDA) was shown by CP/MAS ^{27}Al NMR to further decrease the intensities of both the octahedral and tetrahedral CP ^{27}Al NMR peaks. The peak line broadening observed was due to both chemical shift dispersion (due to observed aluminums with a range of different chemical shifts) and due to quadrupole line broadening effects for aluminums with a range of different quadrupole coupling constants. Further heating of γ -alumina to 815 °C *in vacuo* (extremely dehydroxylated alumina, EDA) was shown to result in a complete loss of the ^{27}Al NMR signal as a consequence of the removal of surface protons from the hydroxyl groups (19).

The CP/MAS ^{27}Al NMR spectrum of PDA γ -alumina (350 °C) shows two peaks at 62 ppm and 0 ppm assigned to surface aluminums associated with 4-coordinate (Type Ia) and 6-coordinate aluminum-containing Brønsted acid sites of

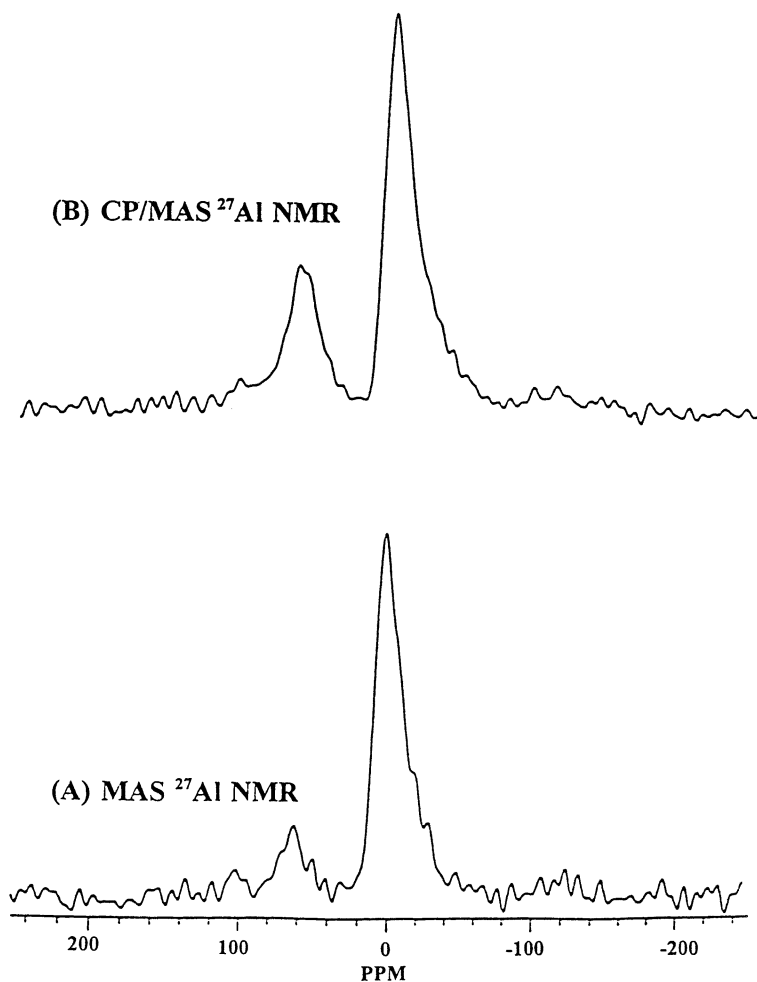


Figure 3. MAS ^{27}Al NMR of γ -alumina by Morris and Ellis (19): A) ^1H - ^{27}Al CP/MAS spectrum, and B) ^1H -decoupled MAS ^{27}Al spectrum.

Type IIB and III, respectively (12). These two Brønsted sites were proposed to represent 4-coordinate aluminum Al-OH sites of Type Ia and 6-coordinate aluminum Al-OH sites of Type IIB and III (see Figure 4). The observed decrease in the ^1H - ^{27}Al CP signal enhancement was interpreted as due to unique spin relaxation dynamics effects for the tetrahedral Al-OH Brønsted acid sites by Morris and Ellis (19), although recent studies of the CP/MAS spin relaxation dynamics for gibbsite and several Al-OH containing materials by Mortuga *et. al* (35) and reexamination of γ -alumina by Maciel and Ellis (22) suggest that both octahedral and tetrahedral Al-OH sites undergo similar ^1H - ^{27}Al CP magnetization transfer behavior.

CP/MAS ^{27}Al NMR measurements by Morris and Ellis (19) also involved studies of PDA-alumina following deuteration with D_2O to replace the protons of the surface Al-OH groups. The adsorption of the Lewis base, pyridine, was then used to provide the nearby protons for CP magnetization transfer to the aluminums. These workers observed two ^{27}Al NMR signals at 35 ppm and 7 ppm as shown in Figure 4 following adsorption of pyridine to Lewis acid sites on PDA γ -alumina, a 35 ppm signal due to the formation of five-coordinate AlO_4 -pyridine Lewis acid/base adducts (formally AlO_4 surface sites), and a 7 ppm signal due to the formation of octahedral AlO_5 -pyridine Lewis acid/base adducts (formally AlO_5 surface sites). An additional broad ^{27}Al NMR component spanning 7 to -27 ppm was also observed and tentatively assigned to even lower symmetry 6-coordinate AlO_6 Lewis acid/base adduct sites formed following complexation with pyridine. These later experiments were consistent with previous ^{15}N NMR studies of Lewis acid-pyridine adduct formation on transition alumina surfaces by Majors and Ellis (20). In these latter studies, two ^{15}N NMR peaks were observed due to ^{15}N -pyridine adsorbed on 4- and 6-coordinate aluminum-containing Lewis acid surface sites. This work was consistent with earlier MAS ^{15}N NMR studies by Ripmeester (47) that reported the existence of two distinguishable Brønsted acid Al-OH sites of Type I and II on transition aluminas. The lability of these sites with regard to water loss following dehydration was presented as evidence for the formation of two discernable Lewis acid sites from these latter ^{15}N NMR measurements.

Huggins and Ellis (21) also carried out variable-temperature ^{27}Al MAS NMR studies to examine the surfaces of α - Al_2O_3 and transition aluminas. Their work examined several issues raised by O'Reilly (60) who explained the observed loss of the ^{27}Al NMR signal intensity for high surface-area aluminas as due to the formation of surface aluminum sites with large electric field gradients as a result of structural surface site distortions following dehydroxylation. In the work of Huggins and Ellis (21), the ^{27}Al NMR signal intensities of variable surface-area transition aluminas was measured using α -alumina as a spin counting standard. At room temperature, only 55% of the aluminum in γ -alumina was observable using static NMR measurements, whereas at 90 K, incomplete recovery of all the Al signal intensity was noted. These results suggested that the non-observable aluminum at RT was due to either proton spin and/or chemical dynamics behavior. "Proton hopping" between adjacent surface aluminums was proposed to provide an efficient quadrupolar relaxation pathway for the ^{27}Al nuclide. At lower temperatures, the proton dynamics was slower permitting ^{27}Al signal detection, although several relaxation regimes are likely to exist. These

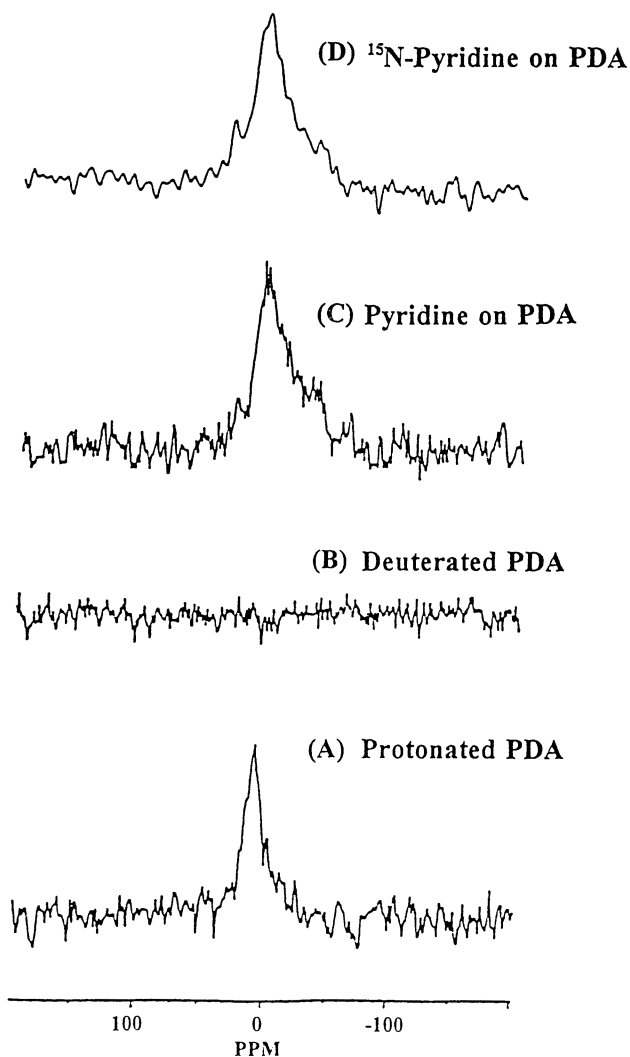


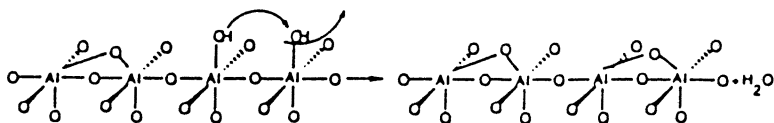
Figure 4. ^1H - ^{27}Al CP/MAS spectra of A) protonated PDA γ -alumina, B) deuterated PDA γ -alumina, C) 25% monolayer coverage of pyridine on PDA γ -alumina, and D) 25% monolayer coverage of ^{15}N -pyridine on PDA γ -alumina. (Morris and Ellis (19)).

workers proposed an alumina surface chemistry model in which three mechanisms of surface proton and oxygen dynamics (Figure 5) are involved to account for the ^{27}Al NMR behavior: Scheme A) two neighboring hydroxyl groups condense, with the formation of molecular water that may either move or "hop" across the surface, leave the surface, reassociate to form two adjacent hydroxyls or cap a Lewis acid site (AlO_5); Scheme B) surface hydrogens move causing rearrangement of hydroxyl groups to new positions, and Scheme C) the Lewis acid sites migrate and the hydroxyl groups move. The first mechanism was proposed to occur on untreated aluminas, where the concentration of hydroxyl groups is large, whereas the second and third mechanisms were proposed to occur on alumina surfaces that are with or without "physisorbed" water.

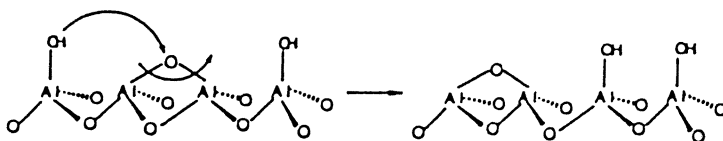
Coster, Blumenfeld and Fripiat (34) recently used ^1H - ^{27}Al CP/MAS NMR to examine the Lewis acidity for a γ -alumina and two different transition aluminas with high contents of 5-coordinate AlO_5 groups (Super 5) as shown in Figure 6. Isotopically enriched $^{15}\text{NH}_3$ was used to probe the Lewis acid surface sites, thus allowing magnetization transfer to surface aluminums from the protons of ammonia. The work of Coster *et al.* (34) showed that dehydrated γ -alumina with or without adsorbed ammonia shows four CP/MAS ^{27}Al resonances due to two four-coordinate Lewis acid sites, one five-coordinate Lewis acid site and one six-coordinate Lewis acid site. Table I summarizes the C_q values, isotropic chemical shifts and % distributions determined for these four sites on γ -alumina and related sites for one of the high 5-coordinate aluminum content (Super 5) transition aluminas. Both single-pulse and CP/MAS ^{27}Al NMR measurements of the γ -alumina following rehydration showed three peaks, with the four-coordinate ^{27}Al peak at 59 ppm disappearing. In addition, the CP/MAS ^{27}Al NMR spectra showed changes in the relative peak intensities of these Lewis acid sites. Two types of surface Lewis acid sites were also observed for γ -alumina following chemisorption of ammonia, a 4-coordinate site (58 ppm) and a 5-coordinate site (40 ppm). Chemisorption of water by rehydration was shown to convert these two sites to new 5-coordinate and 6-coordinate aluminum sites, respectively. This water readsorption process was proposed to be accompanied by a surface reconstruction process involving rearrangement of significantly distorted aluminum-oxygen sites following the dissociative chemisorption of water. The mechanism of CP/MAS magnetization transfer in these experiments was postulated to occur directly from protons on the rehydrated surface or from the protons of adsorbed NH_3 to the surface aluminums or by a "proximity" mechanism from adjacent Brönsted Al-OH neighbor protons to the aluminums.

MQMAS ^{27}Al NMR of Transition Aluminas. The study of the structural nature of the 4-, 5- and 6-coordinate internal and surface sites of transition aluminas by MAS ^{27}Al NMR remains a formidable challenge that has to date been hampered by two significant complications that limit spectral resolution, quantitation and measurements of the local site quadrupolar parameters that are needed to describe the aluminum sites in such materials. First, while MAS averages the dipolar, chemical shift anisotropy of ^{27}Al , and the first-order quadrupolar contributions for the observed central $1/2 \leftrightarrow -1/2$ transition, the second-order quadrupolar contributions are not

Scheme A



Scheme B



Scheme C

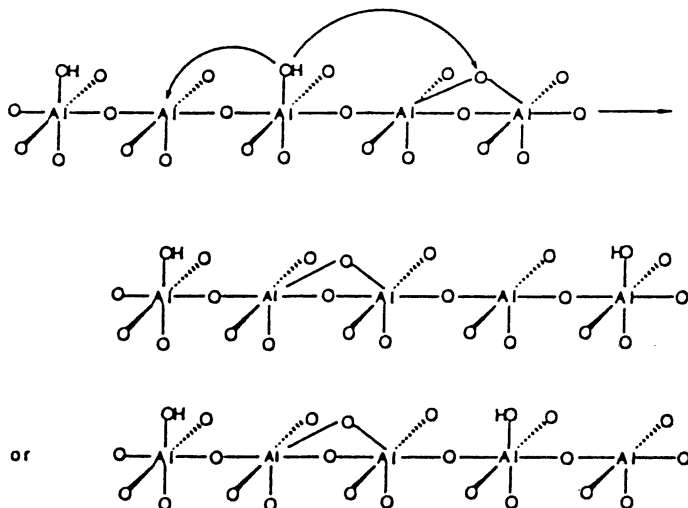


Figure 5. Proposed mechanisms for Brønsted and/or Lewis acid mobility of protons and oxygens on the surface of a transition alumina (Huggins and Ellis (21)).

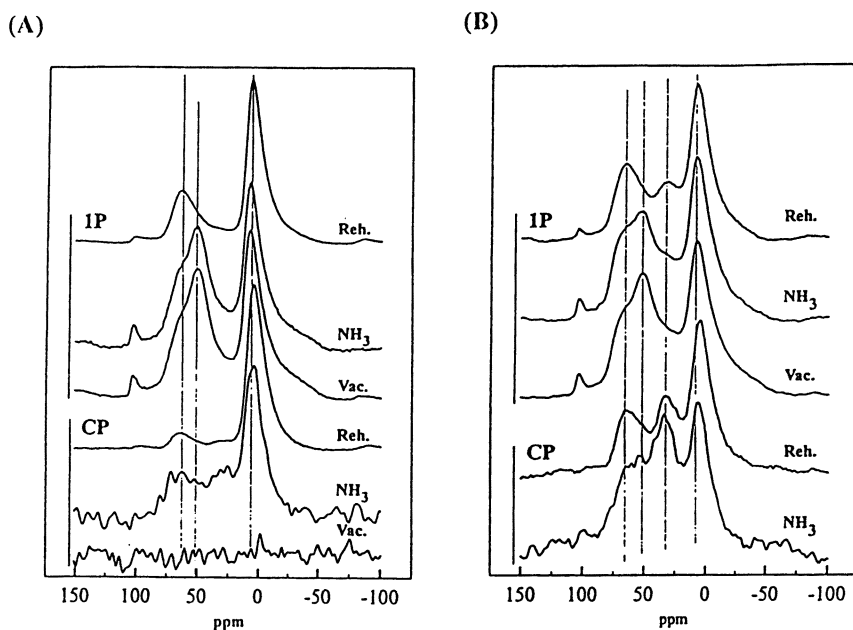


Figure 6. MAS ^{27}Al NMR spectra of A) γ -alumina, and B) Super5 transition alumina (2). Definitions according to Coster, Blumenfeld and Fripiat (34): the notation IP equals single-pulse for rehydrated (reh.), NH_3 adsorbed on sample (NH_3), evacuated (vac.); CP equals ^1H - ^{27}Al cross-polarization for rehydrated (reh.) and NH_3 adsorbed on sample (NH_3).

Table I

²⁷Al NMR Spectral Parameters for Various Aluminas Based on Spectral Deconvolution/Simulation.

NMR Experiment	Sample Treatment	$\delta_{\text{iso}}(^{27}\text{Al})$, ppm	C_Q , MHz	% Content
γ -Aluminas				
SP/MAS	Dehydrated	72.5	5.1	27
		58.0	4.9	24
		43.0	5.1	6
		11.5	3.5	43
SP/MAS	Rehydrated (OH)	71.5	5.1	32
		44.0	5.1	2
		10.0	3.55	66
CP/MAS	Rehydrated (OH)	72.5	5.1	11
		38.5	3.5	2
		10.0	3.5	87
CP/MAS	NH ₃ Adsorption at 1150C	71.5	5.5	33
		35.0	5.5	23
		8.5	3.5	44
Super 5 (1)				
SP/MAS	Dehydrated	72.5	6.1	30
		57.5	6.1	30
		39.0	5.7	21
		12.5	3.8	19
SP/MAS	Rehydrated (OH)	73.0	6.75	44
		39.5	5.45	34
		11.5	4.5	22
CP/MAS	Rehydrated (OH)	72.5	6.75	48
		39.0	4.9	35
		9.5	3.8	17
CP/MAS	NH ₃ Adsorption at 1150C	66.5	6.6	54
		42.5	5.5	34
		8.5	3.8	12

Details of deconvolution procedure given in Coster, Blumenfeld and J.J. Fripiat (34).

completely averaged. This latter effect results in the observation of different, overlapping powder patterns of varying shape that are magnetic field dependent for each aluminum resonance. Complete averaging of the second-order quadrupolar contributions is not obtained even for ^{27}Al nuclei with moderate quadrupole coupling constants (3-5 MHz) at very high fields and fast spinning speeds. In the case of transition aluminas, that are composed of multiple aluminum sites with coordination numbers from four to six, local oxygen environment distortions around the ^{27}Al nuclei in both the internal and surface sites have been proposed by Huggins and Ellis (21) to cause significant line broadening that make many of these sites with even larger quadrupolar coupling constants unobservable even at high field and room temperature. Theoretical calculations have been presented by Huggins and Ellis (21) for many different model surface site clusters that contain from two to four adjacent 4-, 5- and 6-coordinate aluminum sites having calculated coupling constants from 1.0 MHz to as high as 24 MHz. The problem of deconvolution and simulation of these overlapping ^{27}Al resonances with this range of C_q values is thus significant.

The second important problem associated with MAS ^{27}Al NMR spectra of transition aluminas is that these materials have a high degree of amorphous character and possibly contain domain regions of different degrees of order/disorder for the multiple local aluminum sites having different coordination numbers and symmetry. The occurrence of a range of different local sites leads to increases in the observed line broadening of the resonances in the 4-, 5- and 6-coordinate number AlO_x spectral regions. The effects of chemical shift dispersion for the broadened resonances due to the 4-, 5- and 6-coordinate aluminum site populations in ^{27}Al NMR, are also extremely difficult to estimate in the presence of the second-order quadrupolar line broadening effects.

Significant progress to separate and quantify the contributions due to the residual second-order quadrupolar effects for different sites and the accompanying chemical shift dispersion effects has been recently approached using multiple-quantum (MQ) MAS ^{27}Al NMR measurements (25,32), and to some extent, nutation (32) and satellite transition (SATRAS) NMR. (33). In the case of MQMAS ^{27}Al NMR and nutation spectroscopy, a recent report by Kentgens *et. al* (32) has described the application of these techniques to γ -alumina and γ -alumina impregnated with various P/Mo, Al/P and Al/Mo catalytic materials. The MAS ^{27}Al NMR results (Figure 7A) for γ -alumina show two resonances at 9 ppm and 67 ppm assigned to octahedral and tetrahedral aluminums with an O_h/T_d content of 0.68/0.32, that may be contrasted with the 0.75/0.25 value reported by John *et. al* (59) for γ -alumina. The calculated average C_q and η values from off-resonance ^{27}Al nutation studies were ca. 5.0 MHz and 0.5, respectively, for the octahedral resonance and 4.5 MHz and ca. 0, respectively, for the tetrahedral resonance (Figure 7B and 7C). Evidence for a large distribution of both isotropic chemical shifts (due to a distribution of 4- and 6-coordinate populations) and quadrupolar line broadening effects (due to different C_q values for Al sites in each of the 4- and 6-coordinate Al populations) was obtained by MQMAS ^{27}Al NMR (Figure 7D). For γ -alumina, the triple-quantum 3QMAS ^{27}Al spectrum shows that both the 4- and 6-coordinate resonance regions run parallel to the isotropic shift (σ_{iso}) axis at low-field, and strongly bend away from the quadrupolar induced shift (QIS) axis at

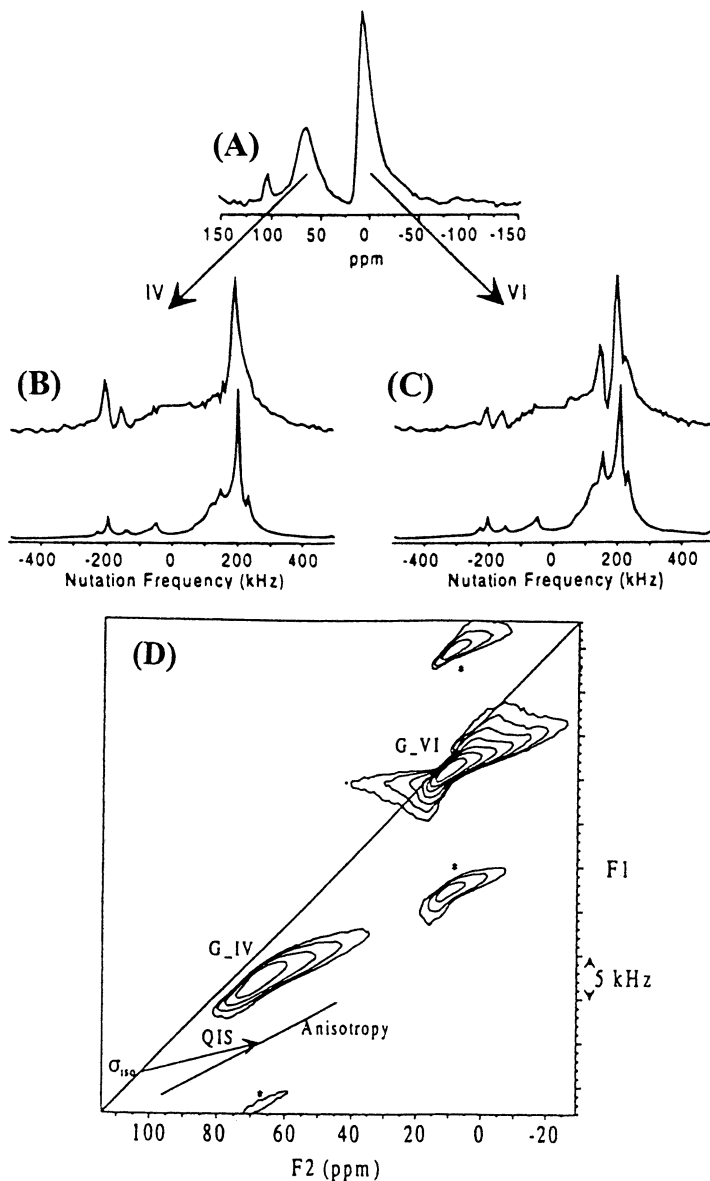


Figure 7. Top: MAS ^{27}Al NMR spectra of A) γ -alumina showing 4-coordinate (67 ppm) and 6-coordinate (9 ppm) resonances. B/C) Off-resonance nutation ^{27}Al NMR spectra of 4-coordinate and 6-coordinate peak region. Note simulations below each. Bottom: D) Triple-quantum 3QMAS ^{27}Al NMR spectrum of γ -alumina showing the F1 and F2 dimension for the 4-coordinate and 6-coordinate region. Note the range for the F2 dimension in terms of isotropic chemical shifts along the σ_{iso} axis, and the bending along the QIS axis of the F1 dimension indicating a distribution of quadrupolar interactions (32).

high-fields. The former observation supports the premise that the resonances reflect a range of distributions in chemical shift and the latter is indicative of a range of C_q values. These important experiments suggest the potential of MQMAS techniques to explore some of the significant questions regarding transition aluminas, including distinctions between both surface and internal aluminum site distributions in these materials using CP/MQMAS ^{27}Al NMR techniques.

Besides these MQMAS ^{27}Al NMR studies, a recent report using satellite transition spectroscopy (SATRAS) should be noted since this work likely has bearing on the generally measured average C_q values for 4-, 5- and 6-coordinate aluminum regions calculated from the observed MAS and MQMAS ^{27}Al NMR results. In studies of a χ -alumina prepared by dehydration of gibbsite, Smith *et. al* (33) reported the use of SATRAS to improve the resolution and extract quadrupolar parameters from the observed 4-, 5- and 6-coordinate Al resonances in amorphous χ -alumina. These workers showed that while the average C_q values for the 4-, 5- and 6-coordinate aluminum sites were in the range 2.7 to 5.0 MHz, three somewhat featureless resonances in the MAS ^{27}Al NMR spectra (Figure 8A-E) due to 4-, 5- and 6-coordinate aluminums were resolved in the satellite transition region (Figure 8F-J) with the following parameters: (AlO_6 , 70.0 \pm 2%, $Q_c = 680\pm 35$ kHz, $\eta = 0.3$, $\delta_{\text{iso}} = 11.5\pm 0.5$; AlO_5 , 7.5 \pm 1%, $Q_c = 400\pm 40$ kHz, $\eta = 0.3$, $\delta_{\text{iso}} = 38.0\pm 1.0$; and AlO_4 , 22.5 \pm 1.5%, $Q_c = 750\pm 55$ kHz, $\eta = 0.3$, $\delta_{\text{iso}} = 71.5\pm 1.0$). These results, like those from the recent MQMAS ^{27}Al NMR studies, suggest the importance of more advanced approaches to obtain significantly new information regarding both the internal (bulk) aluminum sites in these materials, as well as the surface aluminum site distributions of importance to the catalytic activity and catalytic support properties of transition alumina materials.

MAS and CP/MAS ^{17}O NMR Studies. Walter and Oldfield (24) have reported MAS and CP/MAS ^{17}O NMR studies of the internal (bulk) and surface sites in aluminum oxides and hydroxides, and transition aluminas. The ^{17}O MAS NMR of α -alumina showed one signal associated with bulk OAl_4 units containing 4-coordinate oxygen. The spectrum of bayerite shows a single peak due to the Al_2OH site of Type IIB that contains three-coordinate oxygen. The ^{17}O NMR of ^{17}O -enriched crystalline boehmite revealed two peaks assigned to structurally related OAl_4 and Al_2OH sites. The use of ^1H - ^{17}O cross polarization (38) permitted the selective enhancement of the weak Al_2OH signal for boehmite and bayerite. Both these sites represent model Brønsted acid surface sites for γ -alumina containing Al-OH groups of Type IIB. Transition aluminas, on the other hand, were found to contain two types of bulk oxygen sites: tetrahedral four-coordinate OAl_4 oxygens, and to a lesser extent, trigonal 3-coordinate OAl_3 oxygen sites, as shown in Figure 9. The range of bond angles and bond distances associated with the trigonal sites was suggested to cause a wider range of chemical shifts and larger quadrupole coupling constants. The ^1H - ^{17}O CP/MAS NMR spectrum of a γ -alumina as shown in Figure 10 also showed evidence for surface hydroxyl groups that accounted for nearly all of the calculated 13% of the surface OH moieties on γ -alumina. A summary of the ^{17}O chemical shifts, C_Q values and asymmetry parameters for the various oxygen sites in these alumina systems are

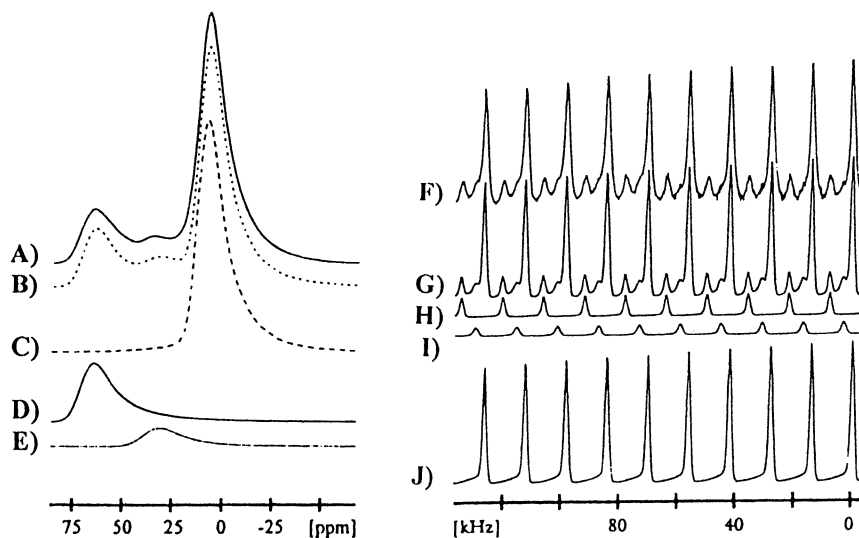


Figure 8. Satellite transition spectroscopy (SATRAS) for ^{27}Al NMR of the transition alumina, χ -alumina, showing 4-, 5- and 6-coordinate aluminum sites. Left: A) Experimental MAS ^{27}Al NMR, B) simulated NMR, and C/D/E) various AlO_6 , AlO_4 and AlO_5 components. Right: F) Experimental MAS ^{27}Al NMR spectra, showing satellite transitions, G) simulated spectra, and H/I/J) various AlO_4 , AlO_5 and AlO_6 components (33).

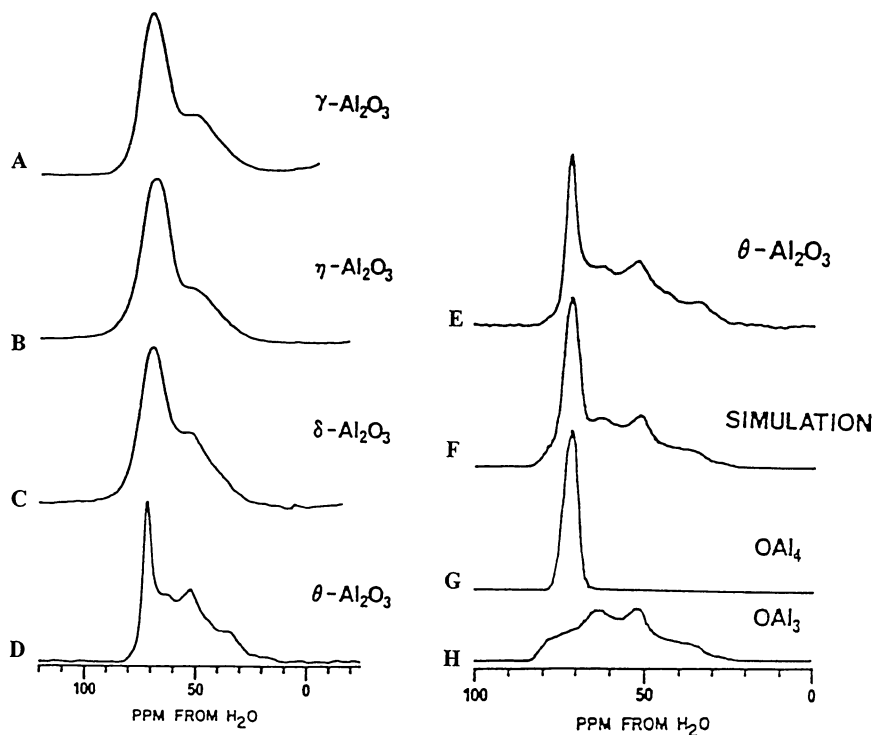


Figure 9. MAS ^{17}O NMR spectra of various transition aluminas (Walter and Oldfield (24)): A) γ -alumina, B) η -alumina, C) δ -alumina, D) θ -alumina, E) experimental spectra for θ -alumina, F) simulated spectra for θ -alumina, G) and H) simulation of two components of spectra for θ -alumina.

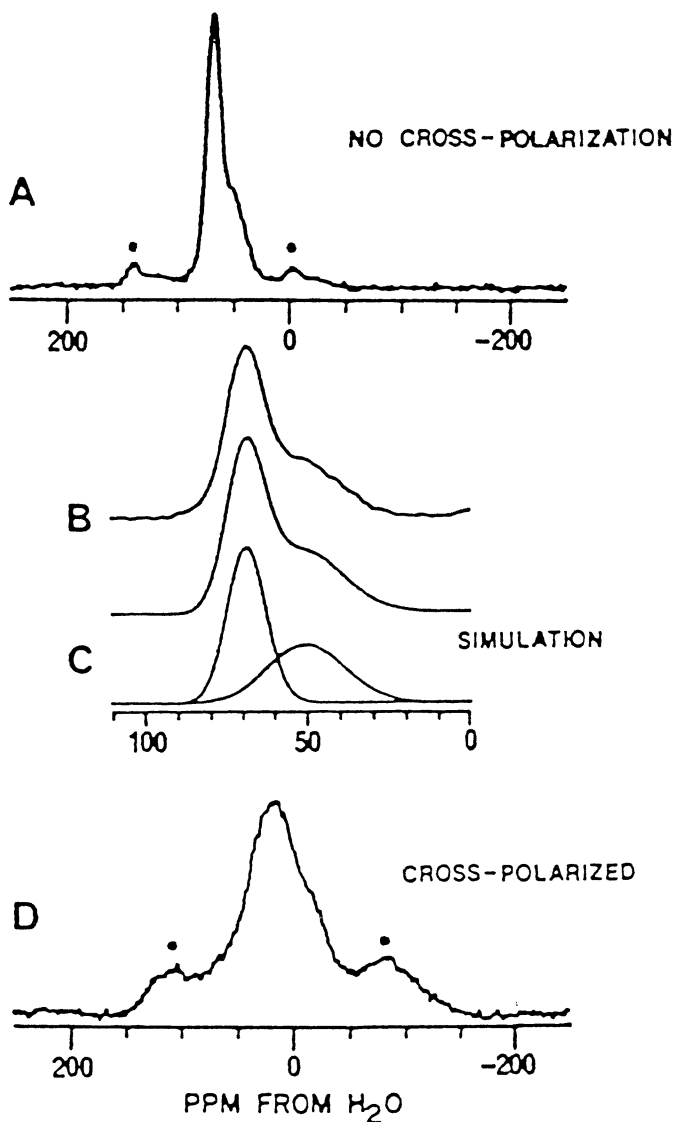


Figure 10. MAS ^{17}O NMR spectra of γ -alumina at 68 MHz: A) MAS spectrum with proton decoupling, B) expanded spectrum, C) simulated spectrum with two components, D) CP/MAS spectrum with proton decoupling (Walter and Oldfield (24)).

given in Table II. While these important initial investigations did not contribute significantly to our detailed understanding of alumina surface chemistry, more detailed knowledge of the surface Brønsted acid and Lewis acid sites on alumina materials by ^1H - ^{17}O CP/MAS NMR is likely following further developments in understanding the role of spin-locking and spinning speed on the ^1H - ^{17}O CP spin dynamics and relaxation processes (36-38).

Solid-State ^1H CRAMPS NMR Studies of Alumina Materials

MAS ^1H NMR and, in particular, ^1H CRAMPS (combined rotation and multiple pulse spectroscopy) techniques (22,39-43) have recently provided important means to directly examine the proton populations of Brønsted acid Al-OH groups of importance to alumina surface chemistry as discussed herein and elsewhere (44-46). The presence of strong ^1H - ^1H dipolar interactions (that cause large linewidths), in particular, are amendable to significant reduction by multiple-pulse techniques via CRAMPS; however, strong ^1H - ^{27}Al interactions and ^1H chemical shift dispersion effects observed for the ^1H NMR resonances of high-surface area alumina materials still limit this approach (44-46).

Recently, ^1H CRAMPS investigations by Fitzgerald, Maciel and co-workers (44-46) have contributed significantly to our understanding of the surface chemistry of protons on alumina materials. These investigations have studied the proton populations associated with model aluminum oxyhydroxides and hydroxides, and the hydroxyl groups and "physisorbed" water moieties associated with a high surface-area (230 m^2/g) pseudo-boehmite ($\text{Al}_2\text{O}_3 \cdot 2.05\text{H}_2\text{O}$) following dehydration/dehydroxylation (44,46). The relationship between the interpretation of the ^1H CRAMPS spectral assignments of this high surface-area material and its experimental weight-loss profiles, following lower temperature dehydration (50 $^\circ\text{C}$ - 110 $^\circ\text{C}$) and higher temperature dehydroxylation (300 $^\circ\text{C}$ - 1100 $^\circ\text{C}$) under both ambient pressure and *in vacuo* conditions are summarized here. In addition, the concurrent use of ^{27}Al NMR and ^1H CRAMPS measurements to obtain NMR evidence for local structural changes occurring for both the aluminum and hydrogen atoms in these materials during various dehydration/dehydroxylation conditions are also described for pseudo-boehmite materials dehydrated from 100 $^\circ\text{C}$ to 1100 $^\circ\text{C}$.

Weight-Loss Profiles For Dehydration/Dehydroxylation of Pseudo-Boehmite. Two processes have been postulated (5) to occur during the dehydration of a variety of hydrated alumina materials: 1) the loss of water molecules by desorption of physically adsorbed or bulk molecular water, and 2) the condensation of adjacent surface or internal hydroxyl groups. Both processes can be identified by experimental measurements of the weight-loss profiles observed upon heating hydrated alumina materials. The desorption of "physisorbed" water occurs at lower temperatures (100 $^\circ\text{C}$ to 120 $^\circ\text{C}$)(6), while the condensation by dehydroxylation of hydroxyl groups occurs above 110 $^\circ\text{C}$. Removal of hydroxyl groups under various higher temperature dehydration/dehydroxylation conditions has been postulated to give rise to strained Al-O-Al linkages on the alumina surface, imparting catalytic properties

Table II

Oxygen-17 NMR Parameters, Including Quadrupole Coupling Constants, Asymmetry Parameters and Isotropic Chemical Shifts for Various Aluminas.

Compound	Site Description	C_Q , MHz	η	δ_{iso} (ppm)
α - Al_2O_3	OAl_4	2.17	0.55	75
AlO(OH) Boehmite	OAl_4	1.20	0.1	70
	Al_2OH	5.0	0.5	40
Al(OH) ₃ Bayerite	Al_2OH	6.0	0.3	40
γ - Al_2O_3	OAl_4	1.8	--	73
η - Al_2O_3	OAl_4	1.6	--	73
δ - Al_2O_3	OAl_4	1.6	--	72
θ - Al_2O_3	OAl_4	1.2	0.6	72
	OAl_3	4.0		79

Derived from simulations at 67.8 MHz MAS spectra.
See details in Walter and Oldfield (24).

to the alumina materials. Since pseudo-boehmite is composed exclusively of octahedral AlO_6 sites (Figure 11A), it is likely that the oxygen vacancies produced during the condensation of hydroxyl groups reduce the aluminum coordination number to four and five, thereby forming Lewis acid AlO_4 and AlO_5 structural moieties.

The average gravimetric weight losses of solution-equilibrated (Curve A) and "as received" solid samples (Curve B) of a pseudo-boehmite material (Norton, $\text{Al}_2\text{O}_3 \cdot 2.05 \text{H}_2\text{O}$) heated from 50 °C to 1100 °C are given in Figure 9 (44). Weight-loss data obtained from a TGA thermogram obtained in ambient atmosphere is also included in Figure 11 (Curve C) for comparison. The weight-loss profiles (44), plotted as moles H_2O /moles Al (maximum of 2.05 $\text{H}_2\text{O}/\text{Al}$) versus dehydration/dehydroxylation temperature, for these alumina materials (Curve A) show three distinguishable regions: 1) an initial region of weight loss from 50 °C to 200 °C corresponding to a dehydration process that can be related to the removal of "physisorbed" and/or bulk molecular water prior to the condensation of hydroxyl groups, 2) a temperature region from 200 °C to 350 °C, in which significant weight-loss is observed that is associated with the first stage of dehydration by condensation of Al-OH groups, and 3) a final region of weight-loss from 350 °C to 1100 °C that is attributed to a second stage of dehydration by condensation of hydroxyl groups. Differences in the three weight-loss profiles for the different conditions of sample heating as shown in Figure 11 have been previously described (44) and are due to vapor pressure effects occurring during water desorption and resorption under these different weight-loss measurement conditions.

^1H CRAMPS Spectra of Pseudo-Boehmite Materials. The ^1H CRAMPS spectra obtained at 187 MHz and 360 MHz on the high surface-area pseudo-boehmite sample equilibrated at pH 6.5, then heated at 110 °C, and then evacuated at 6.5 mtorr for 24 hours, is shown in Figure 12. The two resonances at ca. 3.0 ppm and 8.2 ppm have been assigned to two distinguishable structural Al-OH moieties, an octahedral aluminum-containing AlOH site and an octahedral aluminum-containing Al_2OH site, respectively, as depicted in Figure 13A. These two six-coordinate aluminum sites of pseudo-boehmite are similar to the Type IB and Type IIB sites of the surface model proposed by Peri (5,12) for γ -alumina as shown in Figure 2. These two types of Al-OH sites likely exist in pseudoboehmite in an approximately equal ratio as depicted in Figure 13A. In crystalline boehmite, by contrast, the two major aluminum sites are the protonated Al_2OH sites and the non-protonated Al_3O sites (47-51), with a minimal content of AlOH sites except for those located on the external surfaces of the crystalline particles for this layered structure.

The ^1H CRAMPS results at 4.39 T and 8.45 T show increasing resolution of the proton peaks at higher field, probably because of a narrowing of the observed resonances as a result of decreased quadrupole interference with the MAS averaging of the ^1H - ^{27}Al dipolar interactions (52). The presence of the two aluminums close by the protons of the Al_2OH sites leads to increased ^1H line broadening in comparison with the proton peak of the Al-OH group; however, chemical shift dispersion due to a wide range of different proton environments for both of the AlOH and Al_2OH sites is probably the dominant line broadening influence at higher fields, e.g., 360 MHz.

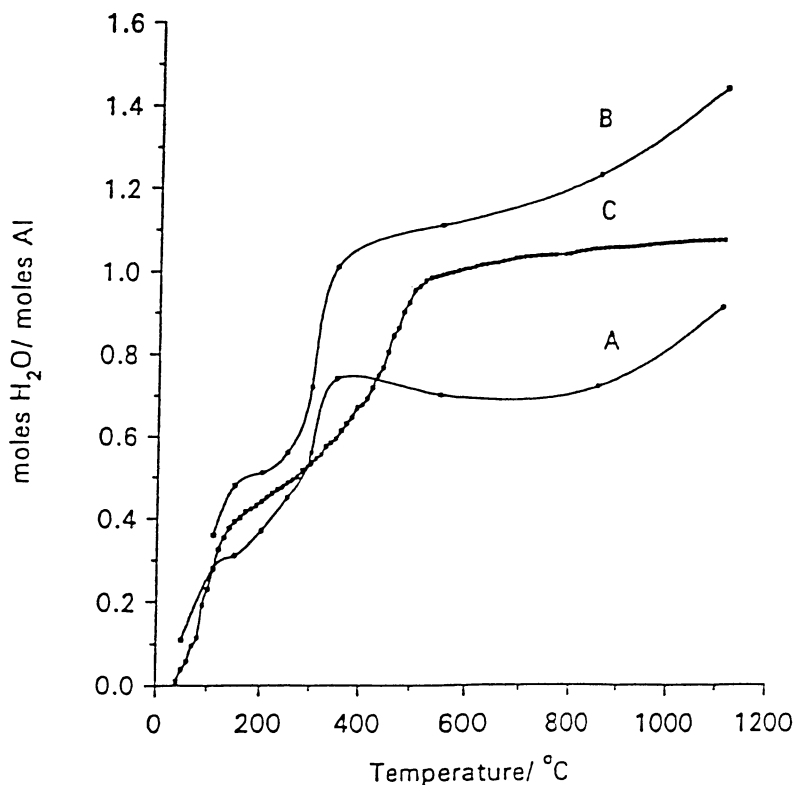


Figure 11. Weight-loss profiles for the high-surface area pseudo-boehmite ($\text{Al}_2\text{O}_3 \cdot 2.05\text{H}_2\text{O}$) material: A) gravimetric analysis of samples equilibrated in aqueous suspensions over the pH range 3-12 (Curve A). B) gravimetric analysis of "as received" samples (Curve B). C) thermogravimetric (TGA) analysis of an "as received" sample in ambient atmosphere at $20\text{ }^\circ\text{C}/\text{min}$ (Curve C) (Fitzgerald *et. al* (44)).

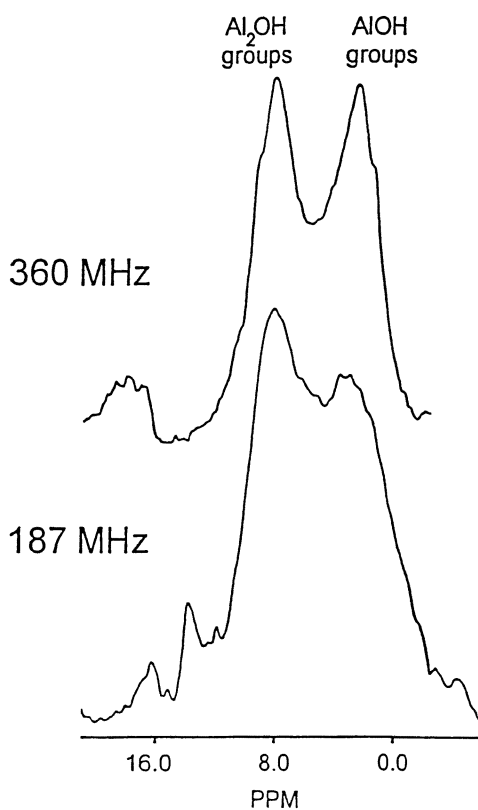


Figure 12. 187 MHz and 360 MHz ^1H CRAMPS NMR spectra of a pseudo-boehmite ($\text{Al}_2\text{O}_3 \cdot 2.05\text{H}_2\text{O}$) material equilibrated in an aqueous suspension at pH 6.5, filtered, heated at 110 °C for 5 hr, and evacuated for 24 hr at 6.5 mtorr (Fitzgerald *et. al* (44)).

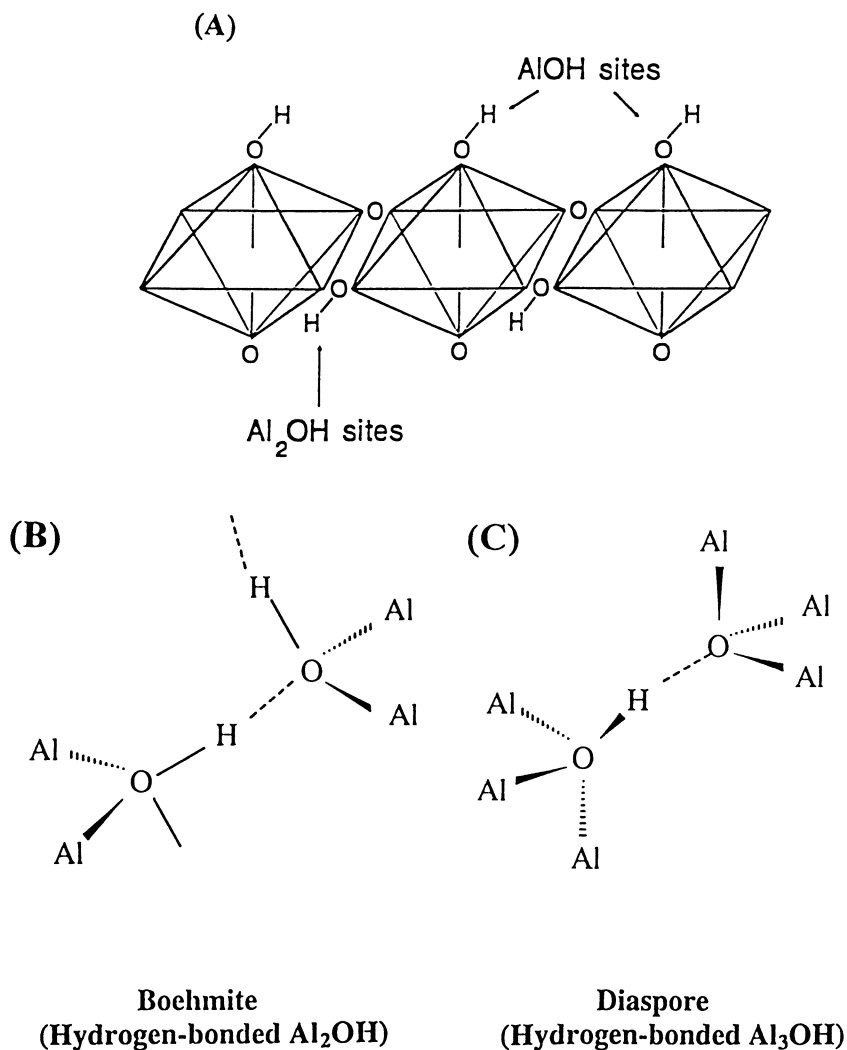


Figure 13. Structural diagrams of aluminum hydroxides: A) two types of structural surface hydroxyl sites for pseudoboehmite, and hydrogen bonding differences in B) boehmite and C) diaspoire.

^1H - ^1H dipolar dephasing experiments described previously by Bronnimann *et al.* (39) for silicas have been used to qualitatively determine the relative strengths of the ^1H - ^1H dipolar coupling between protons of the two types of Al-OH groups. The ^1H CRAMPS dipolar dephasing results previously reported (39) showed that the Al_2OH resonance at 8.2 ppm is dephased beyond observation after 20 μs , whereas the AlOH peak at 3.0 ppm requires 80 μs of dephasing to completely disappear. Dipolar dephasing preferentially attenuates the transverse magnetization of protons involved in stronger dipolar interactions with other protons (39). The rapid disappearance of the proton signal of the Al_2OH groups at a smaller dephasing time indicates that these protons are involved in stronger ^1H - ^1H dipolar coupling, probably due to differences in hydrogen bonding, than for the protons of the AlOH groups. Based on this behavior, the 8.2 ppm resonance for pseudo-boehmite is assigned to closely associated, "clustered" hydroxyls, while the signal at 3.0 ppm is assigned to "isolated" hydroxyls. From the internuclear distances implied from Figure 13A, the former ^1H resonance is assigned to the protons of Al_2OH groups, and the latter resonance to protons of the AlOH groups (44).

^1H CRAMPS Spectra of Model Aluminum Hydroxides and Oxyhydroxides.

The ^1H CRAMPS spectra for several crystalline aluminum oxyhydroxide and hydroxides have also been previously reported (46) as shown in Figure 14. These alumina materials represent important models for Brønsted Al-OH sites due to the detailed structural information available from x-ray and neutron diffraction studies of these materials (47-51, 53-58). A summary of the various types of Al-OH sites, their ^1H chemical shifts, and their observed dipolar dephasing times for each resonance for these model compounds is given in Table III. The ^1H CRAMPS spectrum of crystalline boehmite (Figure 14A) shows a single peak at 8.8 ppm due to the protons associated with the six-coordinate aluminum Al_2OH sites (Figure 13B), similar to the Type IIB sites of γ -alumina as proposed by Peri (5,9). Similar dipolar dephasing experiments for boehmite show that the protons associated with these Al_2OH sites dephase beyond observation after 20 μs dephasing periods, similar to the results obtained for the Al_2OH sites of the high surface-area pseudo-boehmite (44). The ^1H CRAMPS spectrum for crystalline diaspore as shown in Figure 14B depicts a single peak centered at 10.8 ppm assigned to the protons associated with the Al_3OH sites (Figure 13C) that are similar to the Type III hydroxyl groups of γ -alumina as proposed by Peri (5,9). The inductive effect caused by the three second nearest-neighbor aluminum ions causes the Al_3OH protons to be more acidic than the protons associated with the Al_2OH groups in boehmite (see Figure 13B); therefore, the lower shielding experienced by the Al_3OH protons leads to a lower field chemical shift. The 10.8 ppm peak for diaspore is observed to disappear after 40 μs of dephasing period, showing weaker ^1H - ^1H dipolar couplings than the protons of the Al_2OH groups of boehmite. The H...H distances in boehmite and diaspore are approximately 1.9 Å and 2.7 Å, respectively (48-51); therefore, it is expected that the protons in boehmite are coupled more strongly than the corresponding hydrogen-bonded protons in diaspore (see Figure 13B and 13C).

The ^1H CRAMPS spectrum of gibbsite shown in Figure 14C depicts three

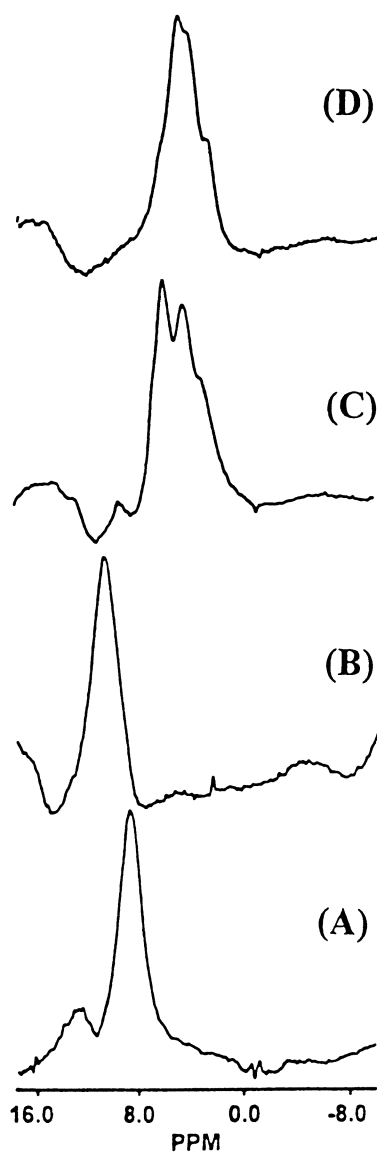


Figure 14. ^1H CRAMPS NMR spectra obtained at 360 MHz for aluminum oxyhydroxide and hydroxide materials evacuated at 6.5 mtorr for 24 hours: A) boehmite, B) diaspore, C) gibbsite, and D) bayerite (Piedra *et. al* (46)).

Table III

¹H CRAMPS Spectral Assignments for Various Al-OH Groups in Alumina Materials

Type of Site (Peri)	Compound	δ (¹ H), ppm	Dipolar Dephasing Time
Al ₂ OH (II B)	Boehmite AlO(OH)	8.8	20 μ
Al ₃ OH (III)	Diaspore AlO(OH)	10.8	40 μ
Al ₂ OH (II B)	Gibbsite Al(OH) ₃	5.8	20 μ
Al ₂ OH (II B)		4.3	20 μ
Al ₂ OH (II B)		2.9	20 μ
Al ₂ OH (II B)	Bayerite Al(OH) ₃	5.0	20 μ
Al ₂ OH (II B)		4.3	20 μ
Al ₂ OH (II B)		2.9	20 μ
Al ₂ OH (II B)	Pseudo-Boehmite Al ₂ O ₃ • 2.05 H ₂ O (230 m ² /g)	8.2	20 μ
AlOH (I B)		3.0	80 μ
H ₂ O physisorbed		4.0	40-60 μ

Results based on 360 MHz ¹H CRAMPS by Fitzgerald *et. al* (44).

distinguishable peaks at 5.8 ppm, 4.3 ppm and 2.9 ppm in an approximate 3:2:1 ratio. Six geometrically distinct protons exist in gibbsite (56,57) with three of these hydrogen atoms [H(1), H(2) and H(4)] forming intralayer hydrogen bonds, and three hydrogens [H(3), H(5) and H(6)] forming interlayer hydrogen bonds with hydroxyl groups of the adjacent layer. The ^1H CRAMPS peak at 5.8 ppm is assigned to the protons of the three interlayer OH...O pairs O(6)H(6)...O(2), O(3)H(3)...O(4) and O(5)H(5)...O(1). Based on the differences in the structural environments of the three intralayer hydrogens [H(1), H(2) and H(4)], the ^1H NMR peak at 2.9 ppm is assigned to hydrogen H(2), and the 4.3 ppm resonance is assigned to hydrogens H(1) and H(4). The Al_2OH protons associated with all three peaks dephase in 20 μs indicating similar ^1H - ^1H dipolar coupling to the protons in boehmite.

The ^1H CRAMPS spectrum of bayerite shown in Figure 14D also exhibits three peaks at 5.0 ppm, 4.3 ppm and 2.9 ppm. Based upon the average hydrogen-bond distances, the 5.0 ppm resonance is assigned to the three different Al_2OH protons involved in the interlayer hydrogen bonding: O(1)H(1)...O(4), O(2)H(2)...O(6), and O(3)H(3)...O(5). Hydrogens H(4) and H(6) form hydrogen bonds with oxygen O(2) of layer B and are assigned to the 4.3 ppm signal, whereas hydrogen H(5) that is hydrogen-bonded to oxygens O(1) and O(3) in the same layer B, is assigned to the 2.9 ppm signal (58). The dipolar dephasing results indicate that all six types of protons in bayerite dephase in a very similar fashion to the protons of the Al_2OH groups in boehmite and gibbsite.

^1H CRAMPS Studies of the Dehydration of Pseudo-Boehmite at Low Temperature (< 300°C). Dehydration of hydrated alumina materials such as gibbsite, bayerite, boehmite and pseudo-boehmite at low temperatures have been associated with processes involving desorption and readsorption of surface water. Pseudo-boehmite and related materials are widely used as precursors for the preparation of transition aluminas under a variety of pretreatment conditions. The ^1H CRAMPS spectra of four different high surface-area pseudo-boehmite samples dehydrated at room temperature: one desiccated over Drierite, one heated at 110 °C at atmospheric pressure (725 torr) for 5 hours, one heated at 110 °C at atmospheric pressure (725 torr) for 5 hours followed by evacuation at 6.5 mtorr for 24 hours, and one heated at 110 °C under vacuum (8 mtorr) for 24 hours, are shown in Figure 15 (44). The ^1H CRAMPS spectra of the desiccated sample (Figure 15A) and the sample heated at 110 °C under ambient pressure (Figure 15B) exhibit a broad peak at 4.0 ppm due to "physisorbed" water, and a less intense shoulder at 8.2 ppm due to the Al_2OH sites; the 3.0 ppm resonance due to AlOH sites is absent. The ^1H CRAMPS spectrum of the sample heated at 110 °C in ambient pressure, followed by evacuation at 8 mtorr for 5 hours (Figure 15C) shows a decrease in intensity for the water peak (4.0 ppm) compared to the proton peak of the Al_2OH group, indicating that partial removal of "physisorbed" water may be achieved by simply heating the pseudo-boehmite solid at 110 °C. The proton signal for "physisorbed" water apparently masks the AlOH peak at 3.0 ppm, possibly because of proton chemical exchange between the protons of the AlOH groups and the protons of "physisorbed" water; this could occur in a fashion similar to the mechanism depicted in Scheme A of the Huggins and Ellis

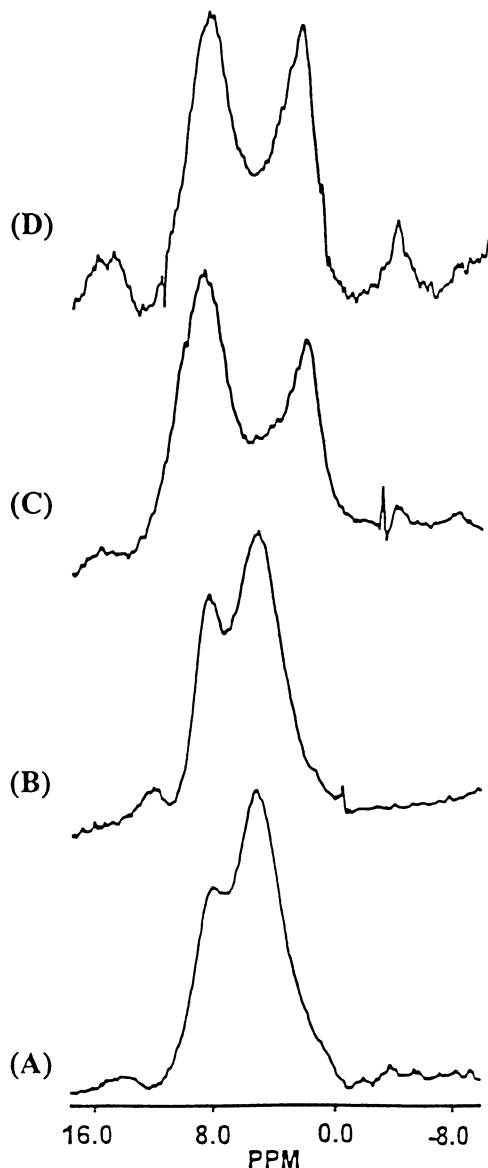


Figure 15. 360 MHz ^1H CRAMPS spectra of pseudoboehmite ($\text{Al}_2\text{O}_3 \cdot 2.05\text{H}_2\text{O}$) materials prepared following various dehydration procedures: A) dessication over Drierite at ambient pressure (725 torr) for 72 hr, B) heating at 110°C (in ambient pressure) for 5 hr, C) heating at 110°C (in ambient pressure) for 5 hr, followed by evacuation at 6.5 mtorr for 24 hrs, and D) heating at 110°C under vacuum (8mtorr) for 24 hrs (Fitzgerald *et. al* (44)).

model for aluminas (21). The protons of "physisorbed" water molecules may also experience spin-spin flip-flop exchange with the AlOH protons on the surface, rendering the spin equilibration between the AlOH protons and "physisorbed" water protons fast, at least on the relevant time scale of these experiments.

Further water removal (disappearance of 4.0 ppm peak) is accomplished by heating pseudo-boehmite at 110 °C and 725 torr, followed by evacuation at 6.5 mtorr for 24 hours, thus allowing observation of the 3.0 ppm peak associated with AlOH sites. A low intensity "physisorbed" water peak is now observed between the ^1H NMR signals at 3.0 and 8.2 ppm (Figure 15C) as a result of some traces of water on or within the pseudo-boehmite material [N.B. The pseudo-boehmite material utilized is a porous material that likely contains some internal, trapped water as well as "physisorbed" surface water: in addition, both internal and external structural Al_2OH and AlOH groups are present.] The ^1H CRAMPS spectrum (Figure 15D) for a pseudo-boehmite solid heated *in vacuo* at 110 °C depicts only the two ^1H NMR peaks at 8.0 ppm and 3.0 ppm associated with the surface and/or interior Al_2OH and AlOH sites, respectively, in a nearly 1:1 ratio, indicating complete removal of all the "physisorbed" water protons.

^1H CRAMPS Studies of the Dehydration of Pseudo-Boehmite at High Temperature (> 300°C). A series of ^1H CRAMPS spectra of pseudo-boehmite samples equilibrated at pH 6.5, heated from 110 °C to 1100 °C, and then evacuated at 6.5 mtorr for 24 hours, is given in Figure 16 (44). Such heating/evacuation procedures with dehydration temperatures up to 350 °C remove nearly all the "physisorbed" water protons. At temperatures up to 300 °C, the peaks for both the Al_2OH and AlOH sites are observed for the interior and/or surface hydroxyl groups of transition alumina-like materials. In the 300 °C to 350 °C region, the proton peak at 8.2 ppm due to Al_2OH groups shows a drastic reduction in its peak intensity due to a dehydration process as a result of condensation of adjacent, "clustered" Al_2OH surface hydroxyls. For the sample heated at 350 °C, a sharp artifact peak at about 12 ppm is also observed due to a rotor line. Heating at temperatures above 350 °C results in a gradual reduction in the intensity of the 3.0 ppm signal as a consequence of further loss of hydroxyl groups due to condensation of the "isolated" AlOH groups. However, the broad, low-intensity proton peak in the ^1H CRAMPS spectra of the 550 °C and 1100 °C samples indicates that complete removal of all the Al-OH protons does not occur even after heating at 1100 °C, followed by evacuation at 6.5 mtorr for 24 hours. A broad distribution of different types of residual Al-OH protons is still observed.

Mechanisms of Dehydroxylation Of Internal/Surface Protons of Pseudo-Boehmite.

The assignment of the ^1H CRAMPS resonances to the Al_2OH and AlOH sites are based on the assumption that these groups exist on the surface (external) and within (internal) the pseudo-boehmite material and are structurally similar to the primary Al_2OH and minor surface AlOH sites of crystalline boehmite (47-51). According to this model, the pseudo-boehmite structure consists of three different types of Al-OH

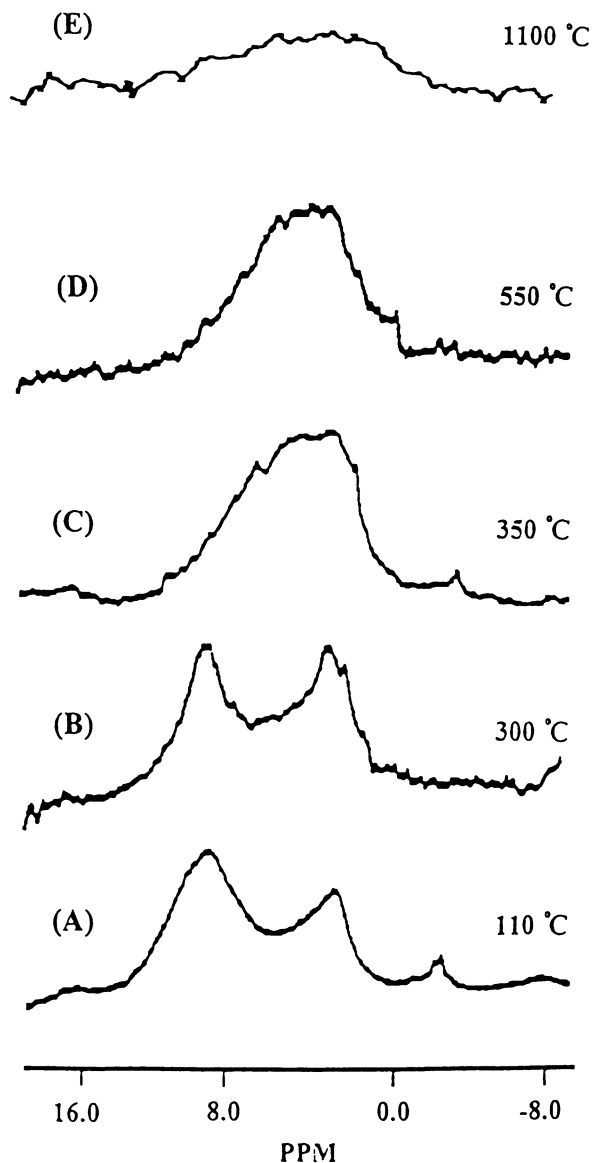
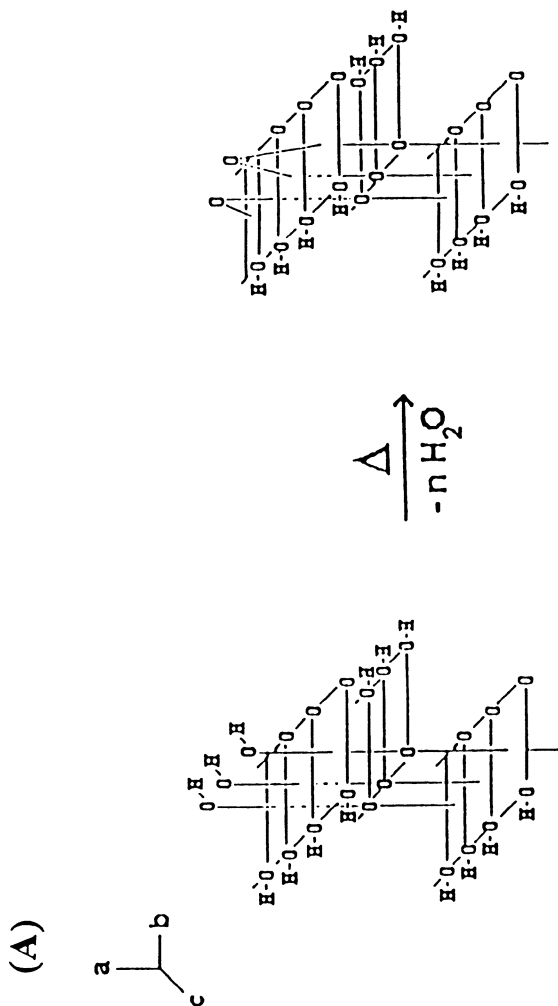


Figure 16. 360 MHz ^1H CRAMPS spectra of pseudo-boehmite ($\text{Al}_2\text{O}_3 \cdot 2.05\text{H}_2\text{O}$) material equilibrated in aqueous suspension at pH 6.5, filtered, heated in the 100–1100 °C temperature range (as specified in the figure), followed by evacuation at 6.5 mtorr for 24 hours (Fitzgerald *et al.* (44)).

groups: a) interlayer Al_2OH sites, b) surface and/or internal "clustered" Al_2OH sites, and c) surface and/or internal "isolated" AlOH sites (see Figure 17). Interlayer and "clustered" Al_2OH sites differ in the nature of their hydrogen bonding. Interlayer Al_2OH sites have hydrogen bonding between the oxygen of one layer and the hydrogen of an adjacent layer, whereas "clustered" Al_2OH groups have hydrogen bonding between an oxygen atom and a hydrogen atom coordinated to an adjacent oxygen in the same layer. The dipolar dephasing results suggest that the stronger ^1H - ^1H dipolar interactions of the Al_2OH protons are due to stronger hydrogen bonding; however, the dipolar dephasing data do not provide enough evidence to make a clear distinction between the two types of Al_2OH sites. In the AlOH groups, the oxygen is only two-coordinate, with available electron pairs that might be utilized in the formation of hydrogen bonds with neighboring water molecules, thus accounting for the proton exchange process between AlOH groups and water molecules.

Mechanisms of Condensation of Al_2OH and AlOH Groups. There are three possible combinations of hydroxyl sites by which condensation might occur: a) by the combination of pairs of Al_2OH sites, b) by the combination of pairs of AlOH sites, and c) by combination of Al_2OH sites with AlOH sites. The proposed schemes that depict these three modes of condensation are given in Figure 17. The reported internuclear O-O distance between pairs of octahedral, edge-sharing Al_2OH sites in crystalline boehmite is 2.535 Å, the same as the O-O distance between a pair of AlOH sites; the corresponding O-O distance between a Al_2OH - AlOH pair is 2.558 Å, whereas the distance between the interlayered Al_2OH - Al_2OH pair is 2.709 Å (4, 47-51). Based on these parameters, Al_2OH - Al_2OH condensation and AlOH - AlOH condensation between octahedral sites is expected to be favored over the condensation of Al_2OH - AlOH pairs, and should definitively be preferred over the condensation of interlayer Al_2OH pairs. Figure 17A depicts a proposed scheme by which the condensation of axially-distributed surface/internal AlOH groups (oriented along the a axis) may occur. The condensation of such axial AlOH groups would result in the formation of some highly distorted, "external", six-coordinate $\text{AlO}_4(\text{OH})_2$ sites and "internal", six-coordinate $\text{AlO}_4(\text{OH})_2$ sites. The condensation of equatorial Al_2OH sites (located on the b-c plane) would give rise to some "external", five-coordinate AlO_4OH sites and "internal", five-coordinate AlO_5 sites as shown in Figure 17B. Condensation of the interlayer Al_2OH groups results in crosslinking of adjacent layers with concomitant formation of channels or pores throughout the material, as depicted in Figure 17C, where highly-distorted, six-coordinate AlO_6 sites are generated. The simultaneous condensation of AlOH and Al_2OH groups, which would occur by a simultaneous combination of the schemes described in Figures 17A and 17B, would also generate highly-distorted, four-coordinate AlO_4 sites (not shown here).

Based on this description of the condensation of the two different types of structural Al-OH sites (both internal and external), the formation of the less-distorted five-coordinated AlO_4OH sites should be favored over the formation of the more distorted six-coordinated $\text{AlO}_4(\text{OH})_2$ sites. Hence, it is proposed that the condensation of equatorial, "clustered" Al_2OH sites will be energetically more favorable than the condensation of axially-distributed, "isolated" AlOH hydroxyl groups, followed by the interlayer Al_2OH sites.



(B)

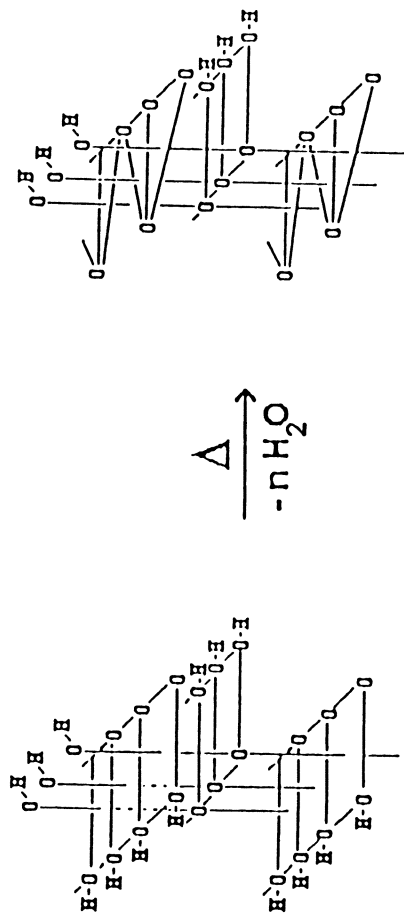
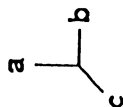


Figure 17. Proposed schemes for the condensation of structural hydroxyl groups of pseudo-boehmite: A) condensation of "isolated" AlOH groups, B) condensation of "clustered" Al₂OH groups, and C) condensation of interlayered Al₂OH groups. Some of the Al-O bonds were deliberately omitted in the figure for clarity (Fitzgerald *et. al* (44)).

Continued on next page.

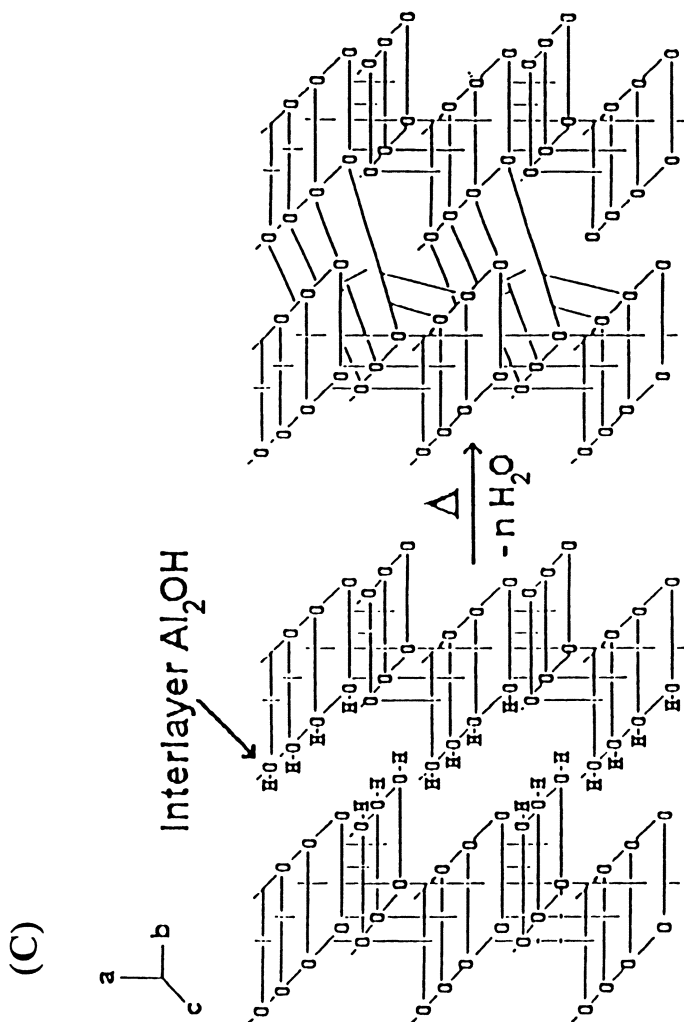


Figure 17. Continued.

MAS ^{27}Al NMR Studies of Dehydration of (HSA) Pseudo-Boehmite.

MAS ^{27}Al NMR studies of various aluminum hydroxides, oxyhydroxides and transition aluminas formed by the dehydroxylation of boehmite and bayerite in the 100 °C to 1000 °C region have been previously reported by John, Alma and Hays (59) at the lower magnetic fields of 7.0 T and 11.4 T. These studies showed that ^{27}Al NMR may be used to obtain in a semiquantitative fashion the relative ratios of octahedral aluminum to tetrahedral aluminum for the various transition aluminas formed from boehmite and bayerite. However, the ^{27}Al NMR observation of only 80% of the aluminum present (at 11 Tesla only) in the various transition aluminas formed in the systems studied by John *et. al* (59) precluded an accurate quantitative determination of the ratio of the octahedral aluminum to tetrahedral aluminum for these materials due to the experimental NMR pulse lengths, pulses sequences and magnetic field strengths used by these workers.

MAS ^{27}Al NMR Studies at 14 Tesla of the Dehydroxylation of Pseudo-Boehmite. MAS ^{27}Al NMR studies at high magnetic field (14 T) for transitional aluminas formed by heating of pseudo-boehmite from 110 °C to 1100 °C have been recently reported (44). These studies provided detailed structural information regarding changes in the coordination environments of the aluminum sites following dehydroxylation of pseudo-boehmite materials. A series of MAS ^{27}Al NMR spectra taken at 156.38 MHz for dehydrated pseudo-boehmite solids obtained by calcination from 110 °C to 1100 °C, followed by evacuation at 6.5 mtorr for 24 hours, is given in Figure 18, together with various reference spectra of $\alpha\text{-Al}_2\text{O}_3$, $\gamma\text{-Al}_2\text{O}_3$ and $\gamma\text{-Al}_2\text{O}_3$ dehydrated at 1280 °C, followed by evacuation. The ^{27}Al NMR spectrum (Figure 18A) of pseudo-boehmite dehydrated at 110 °C exhibits a sharp peak at 8.8 ppm assigned to AlO_6 sites, similar to crystalline boehmite and diaspore (spectra not shown). At 300 °C dehydration, the ^{27}Al NMR spectrum (Figure 18B) shows a low intensity peak at 69 ppm due to newly formed four-coordinate AlO_4 sites, in addition to the six-coordinate peak at 8.8 ppm. Following dehydration at 350 °C, the sample shows an ^{27}Al NMR spectrum (Figure 18C) that exhibits three peaks, a more intense four-coordinate peak at 67.8 ppm, a broad, but intense peak at 9.0 ppm due to six-coordinate aluminum, and a weak but discernable NMR signal at 37.0 ppm that is assigned to five-coordinate aluminum sites. The ^{27}Al NMR spectrum of the 350 °C sample is similar to that of a commercial γ -alumina sample (Figure 18E, peaks at 9.0 and 68.8 ppm), indicating that the pseudo-boehmite is dehydrated to a transition alumina.

The spectrum (Figure 18D) of the 550 °C dehydrated sample is very similar to that of the sample dehydrated at 350 °C, showing three resonances at 9.0, 36.5 and 68.4 ppm. The spectra for the samples dehydrated at 300 °C, 350 °C and 550 °C all show this 36-37 ppm aluminum peak which is assigned to five-coordinate AlO_5 sites, consistent with similar assignments of five-coordinate AlO_5 sites observed in barium

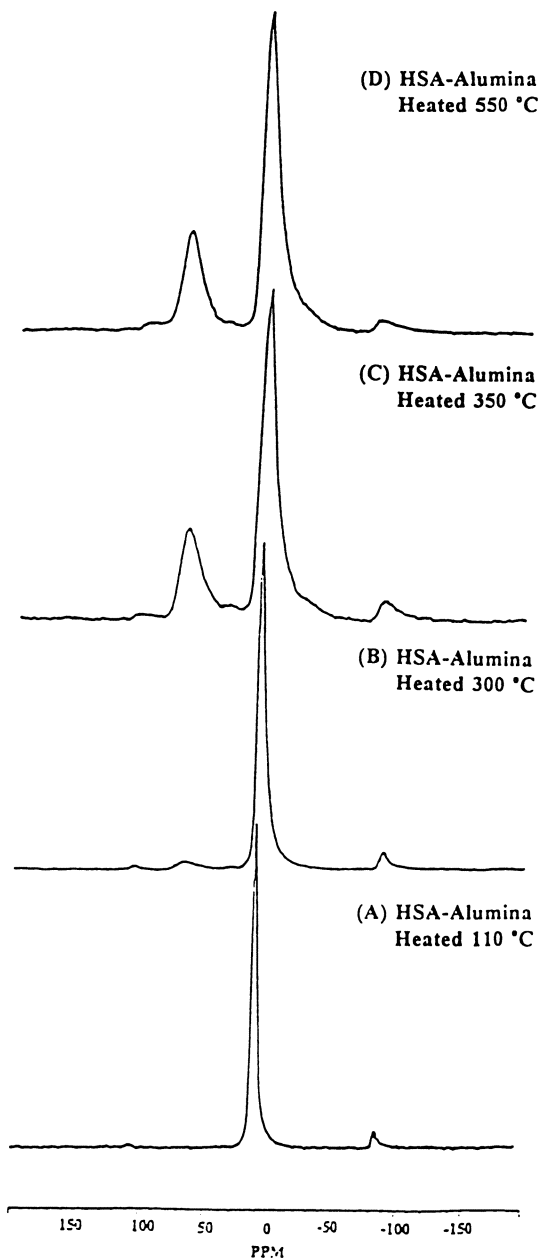
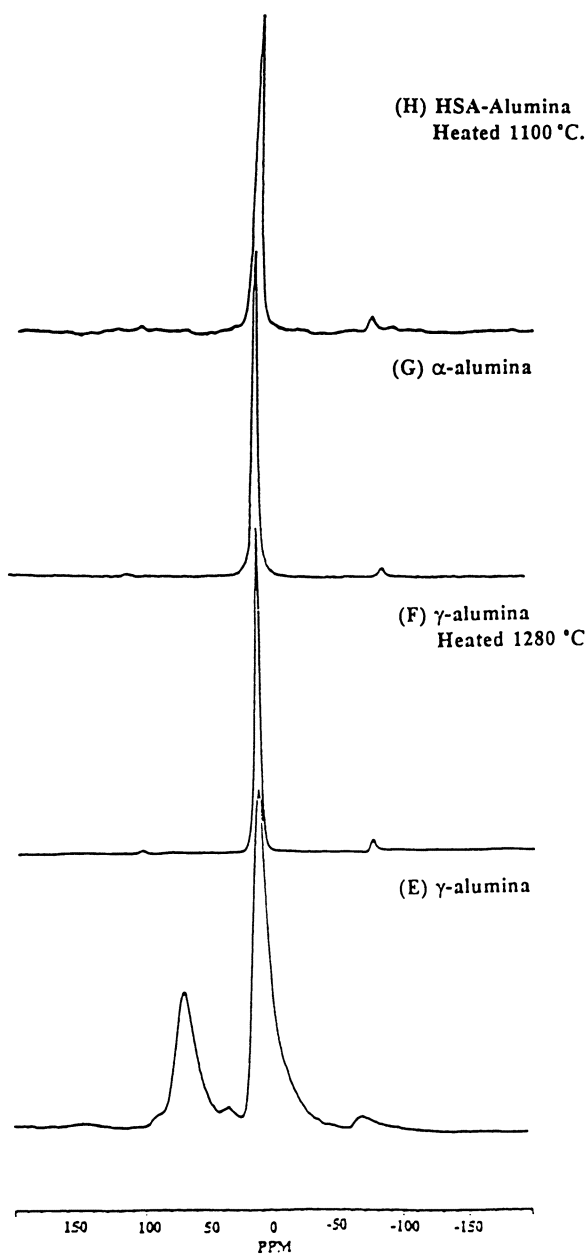


Figure 18. ^{27}Al MAS NMR spectra obtained at 14 T for various aluminum oxide materials: A) pseudo-boehmite heated at 110 °C, B) pseudo-boehmite heated at 100 °C, C) pseudo-boehmite heated at 350 °C, D) pseudo-boehmite heated at 550 °C, E) γ -alumina, F) γ -alumina, heated 3 hours at 1280 °C, G) α -alumina, H) pseudo-boehmite heated 1100 °C (Fitzgerald *et. al* (44)).

Figure 18. *Continued.*

aluminum glycolate, andalusite, pyrophyllite dehydroxylate, dehydrated kaolinite (metakaolinite), selected silica-alumina solids (26-31), and commercial γ -alumina (Figure 18E).

At a higher degree of dehydration, 1100 °C, the ^{27}Al NMR spectrum of the dehydrated pseudo-boehmite material shows only a single 6-coordinate AlO_6 resonance at 14.3 ppm (Figure 18H), similar to α -alumina (Figure 18G, 13.9 ppm) and the γ -alumina sample (Figure 18F, 14.1 ppm) heated at 1280 °C. These results provide conclusive evidence that the transition aluminas produced from pseudo-boehmite that is heated from 300 °C to 350 °C undergo a solid-state thermal conversion to α -alumina at 1100 °C, similar to the α - to γ -alumina conversion observed for commercial γ - Al_2O_3 (59).

Quantitation of ^{27}Al NMR Spectra. A fundamental question regarding the ^{27}Al NMR spectra is whether these spectra show intensities that properly represent the amounts of aluminum in the dehydrated samples. This is particularly true for ^{27}Al NMR signals associated with aluminum sites with very low symmetry, and consequently very large electric field gradients that produce broad NMR resonances. The question of "invisible aluminum" has been a common problem noted in recent solid-state ^{27}Al NMR studies of minerals such as andalusite, dehydrated clays such as pyrophyllite dehydroxylate and metakaolin (28-31), as well as surface aluminum sites on transition aluminums with reduced coordination numbers (20,21,59-63,66). Spin counting experiments were therefore carried out on the pseudo-boehmite material and its dehydration products formed over the temperature range 300 °C to 1280 °C. A plot of the integrated ^{27}Al NMR centerband intensity for pseudo-boehmite and its dehydrated products, as a function of pulse length (0.10 to 1.0 usec) shows a complex relationship (related to the relative size of the quadrupolar interactions and the RF field strength) (61-63). Comparison to the integrated signal for the centerband of an authentic sample of kaolin (containing a known number of ^{27}Al spins) gave the NMR-detectable aluminum content for each of the dehydrated materials. The integrated intensities after a 0.10 usec pulse (the shortest achievable) were found to correlate with the TGA results. Comparison of the aluminum content determined by ^{27}Al NMR spin counting to the values obtained from TGA analysis indicated that (to within experimental uncertainty) all of the aluminum nuclei in the dehydrated materials are being observed at very short pulse lengths at a magnetic field strength of 14 Tesla. Therefore, the major changes in the ^{27}Al NMR spectra of the dehydrated transition aluminas obtained by calcination of pseudo-boehmite shown here indicate that all of the aluminums are NMR observable, and that the integrated peak intensities accurately reflect the 4-, 5- and 6-coordinate aluminum contents in these samples. These results may be contrasted with the only work reported on the relative contents of 4- and 6-coordinate aluminas in transition aluminas by John *et. al.*, (59), where not all the aluminum is observable at lower magnetic fields. [N.B. The surface area of the pseudo-boehmite calcined between 500°C and 550°C may be estimated to vary from 150 to 180 m^2/g (See Huggins and Ellis (21), Figure 1). Based on the plot of O'Reilly (60), ca. 70% of the aluminum should be observable based on a comparable surface area from his measurements of a similar surface area transition alumina. This

value may be compared to the 95% to 98% observable aluminum values obtained for the NMR observable aluminum in the samples reported here and measured at a higher magnetic field strength of 14 Tesla.]

Relationship Between ^1H and ^{27}Al NMR Results For Pseudo-Boehmite.

The major changes in the aluminum coordination environment obtained from the ^{27}Al NMR spectra of the dehydration products of the HSA pseudo-boehmite may be interpreted in relation to information obtained on the proton populations from the ^1H CRAMPS results. In the sample dehydrated at 110 °C, the ^{27}Al NMR shows a single 6-coordinate peak at 8.8 ppm due to $\text{Al}(\text{OH})_6$ sites, while the ^1H CRAMPS spectrum of a sample heated at 110 °C under vacuum (6.5 mtorr) for 24 hours show two resonances due to the "isolated" AlOH (2.3 ppm) and "clustered" Al_2OH (8.2 ppm) groups. Heating pseudo-boehmite to 300 °C gives an ^{27}Al NMR spectrum showing a single, intense 8.8 ppm resonance, with the appearance of very low signal intensity in the 4- and 5-coordinate Al chemical shift region (30-70 ppm), due to the initial stages of the condensation of Al-OH groups. The ^1H CRAMPS spectrum shows no changes in resonances due to the two AlOH and Al_2OH proton populations, except for the low-intensity, broad signal between these two peaks (Figure 15B) due to residual "physisorbed" water protons. The ^1H CRAMPS spectrum of the sample dehydrated at 300 °C, and the subsequent changes in the spectra of samples dehydrated at 350 °C and 550 °C described below indicate that these early stages of condensation of aluminum-coordinated hydroxyl groups probably occur in the absence of "physisorbed" water. The loss of water at 300 °C is due to the initiation of condensation of adjacent hydroxyl groups of the "clustered" Al_2OH groups.

The ^{27}Al NMR spectra (Figure 18C and 18D) of the samples dehydrated at 350 °C and 550 °C show 4-, 5- and 6-coordinate peaks with fractional areas of 0.23, 0.03 and 0.74, respectively. The fractional peak areas for the 4-, 5- and 6-coordinate aluminum peaks in the spectrum of γ -alumina (Figure 18E) are 0.27, 0.04 and 0.69. These results reported here from ^{27}Al NMR at 14 T may be compared to the extensive results reported by John, Alma and Hays (59) for the fractional octahedral and tetrahedral aluminum contents determined for the various dehydrated transitional aluminas obtained from bayerite and boehmite over the temperature range of 100 °C to 1000 °C as shown in Figure 19. These results of John, Alma and Hays (59) obtained from ^{27}Al NMR spectra at 7.0 T and 11.4 T show that the various transition aluminas have the following fractional peak areas for the 4-coordinate aluminums: γ (0.25), δ (0.25), θ (0.00) and η (0.35), with the remaining peak areas being due to 6-coordinate aluminums. The work of John *et al.* (59) and Lippens (3,54) have also shown that crystalline boehmite undergoes dehydration to γ -alumina (0.27 T_d) at 450 °C, then to δ -alumina (0.25 T_d) at 750 °C, then to a mixture of α - + θ -alumina (both 0.00 T_d) at 1000 °C, and finally to α -alumina (0.00 T_d) at 1200 °C. The ^{27}Al NMR results obtained here for pseudo-boehmite corroborate the interpretation that the formation of either γ - or δ -alumina begins initially at 300 °C, and is essentially complete from an ^{27}Al NMR viewpoint in the 350 °C to 550 °C temperature range (900 °C for δ -alumina), where a fractional 4-coordinate aluminum composition in the range 0.25-0.27 is observed for γ - and η -alumina.

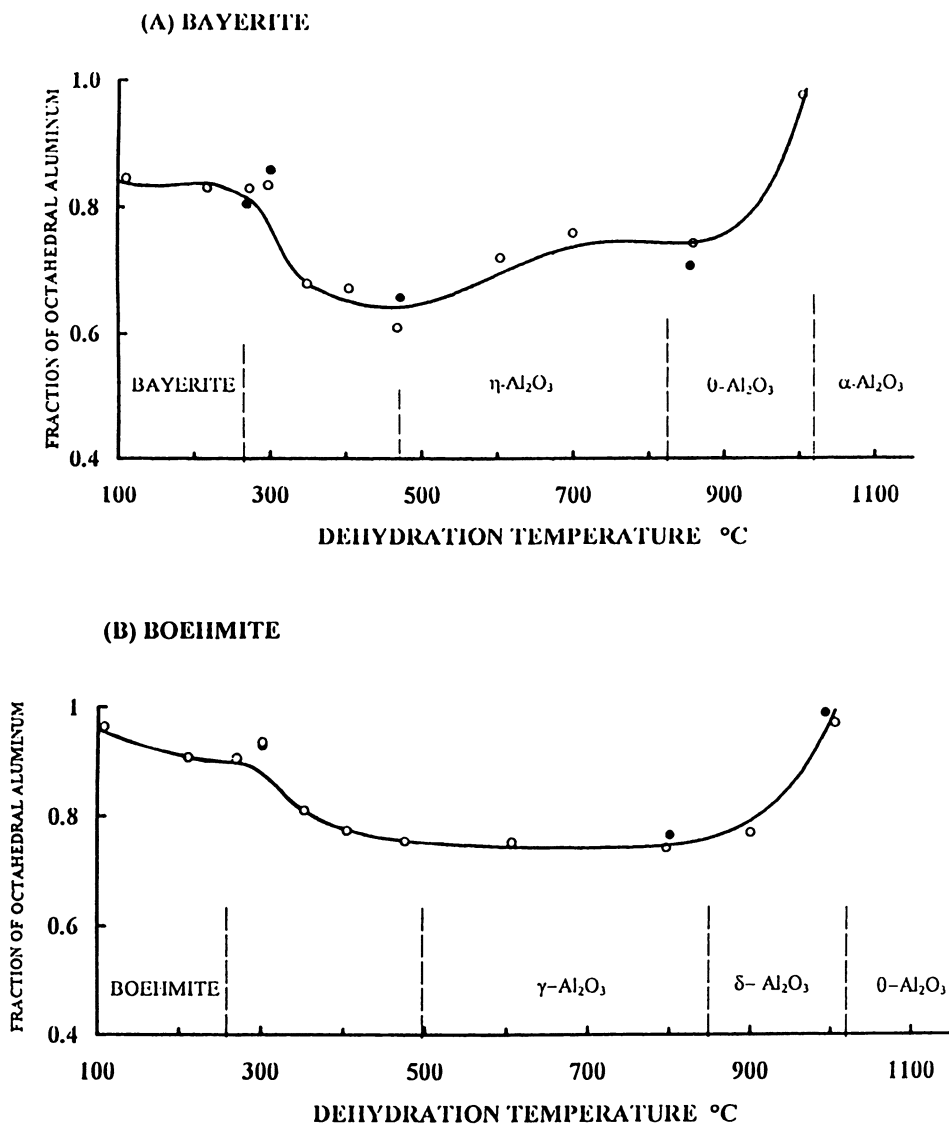


Figure 19. Plot of fractional octahedral aluminum determined by ^{27}Al NMR for various transitional alumina materials formed by dehydroxylation of: A) bayerite and B) boehmite, at various heating temperatures from 100 °C to 1000 °C (modified from John, Alma and Hays (59)).

The ^1H CRAMPS results provide additional insight into the formation of transition alumina (either γ - or δ -) in the 350 °C to 550 °C region from the pseudo-boehmite. The formation of principally 4-coordinate and 6-coordinate aluminums, in addition to a minor population of 5-coordinate aluminums, occurs by condensation of both the "clustered" Al_2OH and "isolated" AlOH groups at 350 °C to 550 °C. The rate of condensation of the "clustered" Al_2OH groups is greater than for the "isolated" AlOH groups and occurs at lower temperature, as evidenced by the more significant changes in the ^1H NMR peak at 8.2 ppm for the lower temperature (350 °C) sample compared with the 550 °C sample (Figure 16). The various schemes for the condensation of the AlOH groups shown in Figure 17 indicate that the adjacent "clustered" Al_2OH groups may condense to 5-coordinate aluminums, with the formation of distorted 6-coordinate sites as well. Simultaneous condensation of Al_2OH and AlOH groups would lead to the formation of appreciable amounts of distorted, 4-coordinate aluminums, as is observed from the ^{27}Al NMR spectra of the 350 °C and 550 °C dehydrated samples. A low population of 5-coordinate aluminums in these spectra suggest that the AlO_5 species may be intermediate Lewis acid sites formed prior to the more abundant 4-coordinate aluminum sites.

In the samples dehydrated at 550 °C to 1100 °C, the ^1H CRAMPS spectra show a very broad resonance extending over a 10 ppm chemical shift range due to residual protons. However, the relative proton populations of the sample dehydrated at 1100 °C is markedly reduced relative to the spectrum of the 550 °C sample, as evidenced by the decrease in the signal-to-noise ratio of the ^1H CRAMPS signal for the sample dehydrated at 1100 °C. The observed broad proton peak in the spectra of these samples dehydrated at 550 °C and 1100 °C is due to a wide range of chemically different proton-bearing AlO_4 and AlO_6 aluminum polyhedra in the 550 °C sample, and a similar wide distribution of AlO_6 octahedra in the 1100 °C sample. Another possible contribution to the broad ^1H CRAMPS resonances is the occurrence of "proton hopping", as proposed by Huggins and Ellis (21) from their variable temperature ^{27}Al NMR studies of dehydrated transition aluminas.

Conclusions

The use of solid-state multinuclear MAS ^1H , ^{17}O and ^{27}Al NMR techniques to examine the surface and internal (bulk) structure and dynamics associated with alumina materials of widespread catalytic utility has made significant progress over the last decade. Information about the chemical environments of hydrogen, oxygen and aluminum atoms in Al-O and Al-OH structural units associated with the Brønsted acid and Lewis acid sites on and within model aluminum-oxygen systems and important transition aluminas has been particularly successful. The continued application of ^1H - ^{17}O and ^1H - ^{27}Al CP/MAS techniques for ^{17}O and ^{27}Al NMR measurements, including variable temperature studies, are still necessary to sort out the details of both the chemical dynamics and spin dynamics behavior relevant to the surface chemistry of important high surface-area aluminas. In addition, recent advances in MQMAS ^{17}O and ^{27}Al NMR will undoubtedly contribute to a more thorough understanding of the magnitude and range of distortions around the oxygen and aluminum atoms in these

systems from relevant NMR studies of relevant systems containing these Brønsted acid and Lewis acid surface sites. Recent REDOR and TEDOR techniques (67,68) also show additional promise for the extraction of internuclear distance information related to the proximity of the proton-, oxygen- and aluminum-containing surface sites and various adsorbed substrates. Further studies of the surface chemistry of additional alumina materials by ^1H CRAMPS are necessary, including variable temperature studies, to obtain more detailed information regarding the NMR behavior of the Brønsted Al-OH protons on additional alumina materials. The ability to reduce the ^1H - ^{27}Al dipolar interactions by ^{27}Al decoupling approaches may also lead to increasingly narrower resonances for the ^1H NMR spectra of these systems, thereby permitting improved resolution of peaks due to different types of Brønsted acid sites of relevance to alumina surface/substrate interactions at the atomic-level. Of particular importance is the use of more sophisticated solid-state NMR approaches to begin exploring the role of both structural factors and chemical/spin dynamics behavior related to the spatial and chemical interrelations between the Lewis acid and Brønsted acid surface sites for transition alumina catalysts and alumina-supported catalysts of varying surface areas and porosities.

Acknowledgements

The author gratefully acknowledges support from National Science Foundation Grants No. RII-8902066, OSR-9108773 and CHE-9021003 and the Office of the President, South Dakota State University. The author is especially indebted to Professor Gary E. Maciel, a longtime collaborator and mentor, for his many contributions and significant ideas related to the work described herein on ^1H CRAMPS studies of the pseudo-boehmite materials.

References

- (1) Wefers, K.; Misra, C. *Oxides and Hydroxides of Aluminum*; Alcoa Technical Paper No. 19, Alcoa Laboratories, 1987.
- (2) Gitzen, W. H. *Alumina as a Ceramic Material*; The American Ceramic Society: Columbus, 1970, pp 15.
- (3) Lippens, B. C.; Steggerda, J. J. In *Physical and Chemical Aspects of Adsorbents and Catalysts*; Linsen, B. G.; Fortuin, J. M. H.; Okkerse, C., Steggerda, J. J., Eds.; Academic Press: New York, 1970.
- (4) Cocke, D. L.; Johnson, E. D.; Merrill, R. P. *Catal. Rev.-Sci. Eng.* **1984**, *26*, 163-231.
- (5) Peri, J. B. *J. Phys. Chem.* **1965**, *69*, 211-219.
- (6) DeBoer, J. H.; Fortuin, J. M. H.; Lippens, B. C.; Meijs, W. H. *J. Catalysis* **1963**, *2*, 1-7.
- (7) Peri, J. B.; Hannan, R. B. *J. Phys. Chem.* **1960**, *64*, 1526-1530.
- (8) Gates, B. C.; Katzer, J. R.; Schuit, G. C. A. *Chemistry of Catalytic Processes*; McGraw-Hill: New York, 1979, pp 249-260.
- (9) Peri, J. B. *J. Phys. Chem.* **1965**, *69*, 220-230.

- (10) Knozinger, H.; Ratnasamy, P. *Catal. Rev.-Sci. Eng.* **1978**, *17*, 31-70.
- (11) Parkyns, N. D. *J. Phys. Chem.* **1971**, *75*, 526-531.
- (12) Peri, J. B. *J. Phys. Chem.* **1965**, *69*, 231-239.
- (13) Schreiber, L.B.; Vaughan, R.W. *J. Catal.* **1975**, *40*, 226-235.
- (14) Morterra, C.; Magnacca, G. *Catal. Today* **1996**, *27*, 497.
- (15) Tsyganenko, A.A.; Madilovich, P.P. *J. Chem Soc., Faraday Trans.*, **1996**, *92*, 4843.
- (16) Morterra, C.; Chiorino, A.; Ghiotti, G.; Garrone, E. *J. Chem. Soc., Faraday Trans.* **1979**, *75*, 271.
- (17) Busca, G.; Lorenzelli, V.; Sanchez, E.; Guidetti, R. *J. Catal.*, **1991**, *131*, 167.
- (18) Liu, X.; Truitt, R., unpublished results, 1997
- (19) Morris, H. D.; Ellis, P. D. *J. Am. Chem. Soc.* **1989**, *111*, 6045-6049.
- (20) Majors, P.D.; Ellis, P.D. *J. Am. Chem. Soc.* **1987**, *109*, 1648-1653.
- (21) Huggins, B. A.; Ellis, P. D. *J. Am. Chem. Soc.* **1992**, *114*, 2098-2108.
- (22) Maciel, G.E.; Ellis, P.D. "NMR Characterization of Silica and Alumina Surfaces", in *NMR Techniques in Catalysis*, A.T. Bell and A. Pines, Eds., Marcel Dekker, Inc., NY 1994.
- (23) Alemany, L.B. *Appl. Magn. Reson.* **1993**, *4*, 179-20.
- (24) Walter, T. H.; Oldfield, E. *J. Phys. Chem.* **1989**, *93*, 6744-6752.
- (25) Frydman, L.; Harwood, J.S. *J. Am. Chem. Soc.* **1995**, *117*, 5367.
- (26) Fitzgerald, J.J.; Dec, S.F.; Hamza, A.I. *Am. Mineral.* **1989**, *74*, 1405-1408.
- (27) Lambert, S.F.; Millman, W.S.; Fripiat, J. *J. Am. Chem. Soc.* **1989**, *111*, 3517-3522.
- (28) Cruickshank, M.C.; Dent Glasser, L.S.; Barri, A.I.; Poplett, I.J.F. *J. Chem. Soc., Chem. Commun.* **1986**, 23-24; Alemany, L.B.; Kirker, G.W. *J. Am. Chem. Soc.* **1986**, *108*, 6158-6162.
- (29) Dec, S.F.; Fitzgerald, J.J.; Frye, J.S.; Shatlock, M.P.; Maciel, G.E. *J. Magn. Reson.* **1991**, *93*, 403-406.
- (30) Gilson, J.-P.; Edwards, G.C.; Peters, A.W.; Rajagopalan, K.; Wormsbecker, R.F.; Roberie, T.G.; Shatlock, M.P. *J. Chem. Soc., Chem. Commun.* **1987**, 91-92.
- (31) Dec, S.F.; Maciel, G.E.; Fitzgerald, J.J. *J. Am. Chem. Soc.* **1990**, *112*, 9069-9077.
- (32) Kraus, H.; Prins, R.; Kentgens, A.P.M. *J. Phys. Chem.* **1996**, *100*, 16336.
- (33) Kunath-Fandrei, G.; Bastow, T.J.; Hall, J.S.; Jager, C.; Smith, G.E. *J. Phys. Chem.*, **1995**, *99*, 15138.
- (34) Coster, D.; Blumenfeld, A.L.; Fripiat, J.J. *J. Phys. Chem.* **1994**, *98*, 6201-6211.
- (35) Mortuza, M.G.; Dupree, R.; Kohn, S.C. *Appl. Magn. Reson.* **1993**, *4*, 89-100.
- (36) Vega, A.J. *J. Magn. Reson.* **1992**, *96*, 50.
- (37) Vega, A.J. *Solid-State NMR* **1992**, *1*, 17.
- (38) Walter, T.H.; Turner, G.L.; Oldfield, E. *J. Magn. Reson.* **1988**, *76*, 106-120.
- (39) Bronnimann, C. E.; Chuang, I.; Hawkins, B. L.; Maciel, G. E. *J. Am. Chem. Soc.* **1987**, *109*, 1562-1564.

- (40) Maciel, G.E.; Bronnimann, C.E.; Hawkins, B.L.; "High-Resolution ^1H Nuclear Magnetic Resonance in Solids by CRAMPS", in *Adv. in Magn. Reson.*, The Waugh Symposium, 14, S. Warren, ed., Academic Press, San Diego, CA, 1990, pp. 125-150.
- (41) Bronnimann, C.E.; Hawkins, B.L.; Zhang, M.; Maciel, G.E. *Anal. Chem.*, **1988**, *60*, 1743-1750.
- (42) Pfeifer, H. "Applications of NMR Spectroscopy to Surfaces and Catalysts: Acidic Sites and Absorbed Species", in *Nuclear Magnetic Resonance in Modern Technology*, G. E. Maciel, ed., NATO ASI Series, Vol. 447, Kluwer Academic Publishers, Dordrecht, Netherlands, 1994, p. 504.
- (43) Burum, D. P.; Rhim, W. K. *J. Phys. Chem.* **1979**, *71*, 944-956.
- (44) Fitzgerald, J. J.; Piedra, G.; Dec, S. F.; Maciel, G. E. *J. Am. Chem. Soc.* **1997**, *119*(33) 7832-7842.
- (45) Piedra, G.; Fitzgerald, J.J.; Ridenour, C.F.; Maciel, G.E. *Langmuir* **1996** *12*(8), 1958-1966.
- (46) Piedra, G.; Fitzgerald, J.J.; Dando, N.; Dec, S.F.; Maciel, G.E. *Inorg. Chem.* **1996**, *35*(12), 3474-3478.
- (47) Ripmeester, J.A. *J. Am. Chem. Soc.* **1983**, *105*, 2925-2927.
- (48) Christoph, G. G.; Corbató, C. E.; Hofmann, D. A.; Tettenhorst, R. T. *Clay and Clay Minerals* **1979**, *27*, 81-86.
- (49) Hill, R.J. *Clay and Clay Minerals* **1981**, *29*, 435-445.
- (50) Christensen, A. N.; Lehman, M. S.; Convert, P. *Acta Chem. Scand.* **1982**, *A36*, 303-308.
- (51) Corbató, C. E.; Tettenhorst, R. T.; Christoph, G. G. *Clay and Clay Minerals* **1985**, *33*, 71-75.
- (52) Haase, J.; Freude, D.; Freulich, T.; Himpel, G.; Kerbe, F.; Lippmaa, E.; Pfeifer, H.; Sarv, P.; Schaefer, H.; Seiffert, B. *Chem. P. Lett.* **1989**, *156*, 328-332.
- (53) Ewing, F. J. *J. Phys. Chem.* **1935**, *3*, 203.
- (54) Lippens, B.C.; de Boer, J.H. *Acta Cryst.* **1964**, *17*, 1312-1321.
- (55) Busing, W. R.; Levy, H. A. *Acta Cryst.* **1958**, *11*, 798.
- (56) Saafeld, H.; Wedde, M. *Z. Kristallogr.* **1974**, *139*, 129; Perrotta, A.; Minnick, R. *U.S. Patent* 5,334,366, Aug. 2, 1994.
- (57) Giese, R. F. *Acta Cryst.* **1976**, *B32*, 1719.
- (58) Zigan, F.; Joswig, W.; Burger, N. *Z. Kristallogr.* **1978**, *148*, 255; Fricke, R.; Wullhorst, B. *Z. Anorg. Chem.* **1972**, *205*, 127.
- (59) John, C.S.; Alma, N.C.; Hays, G.R. *Appl. Catal.* **1982**, *6*, 341-346.
- (60) O'Reilly, D.E. *Adv. Catal.* **1960**, *12*, 31.
- (61) Pearson, R. M.; Schramm, C. M. *Colloids and Surfaces* **1990**, *45*, 323-334, and references therein.
- (62) Haase, J.; Oldfield, E. *J. Magn. Reson. A*, **1993**, *104*, 1-9.
- (63) Schmitt, K.D.; Haase, J.; Oldfield, E. *Zeolites* **1994**, *14*, 89-100.
- (64) Pearson, R.M.; *J. Catal.* **1971**, *23*, 388-394.
- (65) Fitzgerald, J.J.; Kohl, S.D.; Piedra, G.; Dec, S.F.; Maciel, G.E. *Chem. Mater.* **1994**, *6*(11), 1915-1917.
- (66) Smith, M.E.; *Appl. Magn. Reson.* **1993**, *4*, 1-64.
- (67) Gullion, T.N.; Schaefer, J. *J. Magn. Reson.* **1989**, *81*(1), 196-200.
- (68) Blumenfeld, A.L.; Coster, D.J.; Fripiat, J.J. *Chem. Phys. Lett.* **1994**, *231*, 491.

Chapter 6

An Overview of Solid-State NMR Correlation Experiments in Phosphate Glass Systems

R. M. Wenslow, K. Fiske, and K. T. Mueller

Department of Chemistry, The Pennsylvania State University,
University Park, PA 16802

Methods for high-resolution heteronuclear correlation solid-state nuclear magnetic resonance are presented for the study of structure in phosphate and aluminophosphate glass systems. Combinations of magic-angle spinning, cross-polarization, transferred-echo double resonance, dynamic-angle spinning, and variable-contact-time cross-polarization methods are used as a powerful array of tools for probing local microstructure, especially the next-nearest neighbor coordination sphere, in these systems.

The structural characterization of solid materials can be hampered by compositional inhomogeneity, amorphous character, or the presence of impurities. In many cases, structural studies of these materials via diffraction methods yield results averaged over an entire sample which may lack long-range ordering or a homogeneous composition. An atomistic (or molecular-level) structural interpretation is then impossible, and little understanding is obtained relating the microstructural environments of the atoms to the observed physical properties of a complex material. Solid-state nuclear magnetic resonance (NMR) spectroscopy is a powerful tool for the determination of local structure in complex inorganic materials, even those that lack long-range order or compositional homogeneity (1,2). As such, solid-state NMR is now widely used for characterization of structure and chemistry in complex systems (3).

In NMR spectra of polycrystalline or amorphous solids, resonances usually appear broad and featureless due to the lack of molecular motion on the time scale of the NMR experiments. The technique of magic-angle spinning (MAS) NMR provides an averaging of anisotropic interactions through mechanical spinning of a sample about an axis aligned at the magic angle ($\theta_m = 54.74^\circ$) with respect to the magnetic field (4,5). Often combined with high-power proton decoupling and cross-polarization (CP) of magnetization from abundant ^1H nuclei, solid-state MAS NMR of spin-1/2 nuclei such as ^{13}C , ^{29}Si , and ^{31}P has entered the world of high resolution, becoming a useful tool for the elucidation of structure. Further methods are now available to narrow resonances from quadrupolar nuclei (such as ^{11}B , ^{17}O , ^{23}Na , and ^{27}Al), and these methods involve more complicated sample reorientation (6-8), or multiple-quantum excitation and evolution schemes (9). A necessary condition for structural studies of complex solids is the resolution of spectral resonances, either

directly in an experimentally-obtained spectrum or through an analysis aimed at deconvoluting overlapping and unresolved features in the spectrum. Overall, the array of solid-state NMR techniques available to researchers now provide reliable experimental approaches in studies of a growing number of complex materials.

The study of nuclear "connectivity" or proximity is approachable with NMR by at least two routes. The first uses well-studied relationships of isotropic chemical shift values to assign nearest or next-nearest-neighbor coordination spheres to the nuclei contributing to the observed, and often quantifiable, resonances. Extensions of this methodology expand upon a more detailed knowledge of the chemical shift anisotropy tensor to form a clearer understanding of local electromagnetic environments. In all such studies, comparisons to results from well-characterized materials are helpful, or even essential, for understanding the local structure.

The mechanism by which nuclear polarization is transferred in cross-polarization (and other) NMR experiments provides a second route to local microstructural information. In the absence of spin diffusion between like target spins, the only way that resonances can be produced in a CP experiment arises due to the action of the distance-dependent dipolar coupling between heteronuclei. Therefore, if a signal appears in the CP spectrum obtained by transferring polarization from one spin species to a second, the nuclei contributing to the observed resonances must be proximal to the source nuclei. While this method ultimately fails in investigations employing very abundant and highly-polarized ^1H nuclei, reliable connectivity information can be obtained in more dilute or less-polarized spin systems in a straightforward manner.

The use of conventional CP methods to produce *quantitative* internuclear distances is complicated, and a number of new MAS NMR methods have also been developed in recent years to accurately determine the homonuclear and heteronuclear distances in disordered solids (10). In particular, rotational-echo double-resonance (REDOR) and transferred-echo double-resonance (TEDOR) experiments are utilized to measure heteronuclear distances up to 10 Å (11-13). Interatomic distances are calculated in REDOR and TEDOR experiments by measurement of the internuclear dipole-dipole coupling. The magnitude of this coupling is simply related to the distance between nuclei, but these experiments also allow *qualitative* connectivity or proximity studies since the direct dipole coupling is a through-space interaction that diminishes quickly with distance. Applications of these techniques have primarily addressed the measurement of internuclear distances in biomolecular systems, but they have recently been exploited in studies of a number of inorganic materials to separate "connected" resonances from those with no proximity to heterospins in double-resonance experiments (14-20).

In many inorganic systems containing quadrupolar spin species, it is advantageous to utilize the polarization of quickly-relaxing quadrupolar spins to increase the sensitivity or speed of accumulation of signals from coupled spins with very long spin-lattice relaxation times. Difficulties, however, arise due to the increased complexity of the spin energy levels for nuclei with spin greater than one-half (21,22), but these may be reduced, eliminated, or even favorably utilized with a proper choice of experiments.

The work presented here outlines strategies for the application of solid-state heteronuclear correlation NMR in studies of phosphate and aluminophosphate glass systems. Although only results from CP studies are shown, we also discuss the TEDOR experiment as it is useful in many of the same circumstances. One-dimensional CPMAS NMR experiments involving quadrupolar nuclei are particularly sensitive to local order in inorganic systems, revealing resonances only between nuclei that are close enough in space to have a substantial dipolar coupling. The dynamics of the heteronuclear cross-polarization processes is another important measure of the local microstructure near to backbone phosphorus atoms. Further, the use of two-dimensional CP (or TEDOR) heteronuclear correlation experiments

provides an opportunity for spectral editing, enhancing our studies of local structures. Finally, we describe a two-dimensional method employing dynamic-angle spinning (DAS) NMR for quadrupolar nuclei coupled with CP to spin-1/2 nuclei, achieving for the first time true high resolution for both the quadrupolar and non-quadrupolar spins (23). Initial applications of this experiment to amorphous systems are discussed.

Experimental Methods

The NMR radiofrequency (RF) pulse sequences for one-dimensional CP and TEDOR NMR experiments are shown in Figure 1. In the CP experiment, a preliminary 90° pulse on the I channel is followed by simultaneous irradiation of both I and S spins during a contact time (typically lasting between 0.1 msec and 20 msec). The RF field intensities are varied to match a modified Hartmann-Hahn match condition obtained when considering the use of quadrupolar nuclei in the weak field regime and under MAS conditions. The modified match condition is (22):

$$(I+1/2) \gamma_I B_{1,I} = (S+1/2) \gamma_S B_{1,S} \pm n\nu_r \quad n = 1 \text{ or } 2 \quad (1)$$

where I and S in this equation are the spin magnetic quantum numbers for the I and S nuclei (for example, in $^{23}\text{Na} \rightarrow ^{31}\text{P}$ CPMAS experiments $I = 3/2$ and $S = 1/2$). The quantities γ_X (with $X = I$ or S) are the gyromagnetic ratios of the nuclei, and $B_{1,X}$ is the strength of the RF field for the X nuclei. The rotor frequency is ν_r , and the offset of the best match conditions by one or two rotor cycles has been predicted theoretically and observed experimentally (16). After the simultaneous RF pulses, a one-dimensional free-induction decay is obtained on the S channel of the spectrometer. In practice, one of the RF channels is fixed in strength and the other is varied until an optimal match is found. A useful beginning point is to choose a spinning frequency, experimentally determine the nutation frequency of one spin species, and then set the 90° time for the second set of spins so as to approximately match the conditions of equation 1.

A one-dimensional TEDOR experiment likewise transfers coherence from one set of nuclei to the other, in this case via simultaneous 90° pulses applied after the buildup of unobservable anti-phase magnetization. After an initial 90° pulse on the I spins, rotor-synchronized 180° pulses are applied to either spin manifold at least twice per rotor cycle. After the coherence transfer, additional dephasing is required to convert the coherences to observable signal. In both the CPMAS and TEDOR experiments, the resulting signals derive only from those S spins that are coupled to I spins via the dipolar coupling. Hence, these "connectivity" experiments provide at least qualitative information regarding the proximity in space of the nuclei, while at best they report on the distribution in distances and positions of the nearby spins.

Two-dimensional versions of the CP and TEDOR experiments are shown in Figure 2. In each, a preliminary evolution period (t_1) is provided after the initial 90° pulses while the normal data acquisition defines the second time period (t_2). Due to the coherent nature of the spin magnetization as it evolves from one time period to the next, two-dimensional Fourier analysis provides a correlation map of resonances from proximal nuclei. Time-proportional phase incrementation (TPPI) acquisition schemes are normally used to provide pure absorption phase data sets.

A further modification of the one-dimensional CP experiment is also useful for studying amorphous systems. Variation of the contact time during which both RF fields are turned on results in an initial growth, and ultimate decay, of the observed CP signal intensities. Based on simple spin thermodynamic models (24), three time constants are used to model the growth and decay of the signal. Two of them, the $T_{1\rho}$ values for the two nuclear spin systems, describe the ability to "lock" the magnetization during the experiment and therefore contribute most to the decay of the

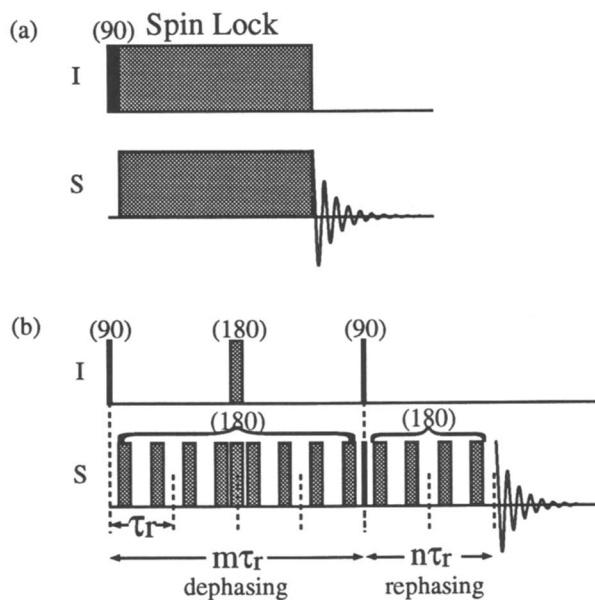


Figure 1. The RF pulse sequences shown are for one-dimensional (a) CP and (b) TEDOR solid-state NMR experiments.

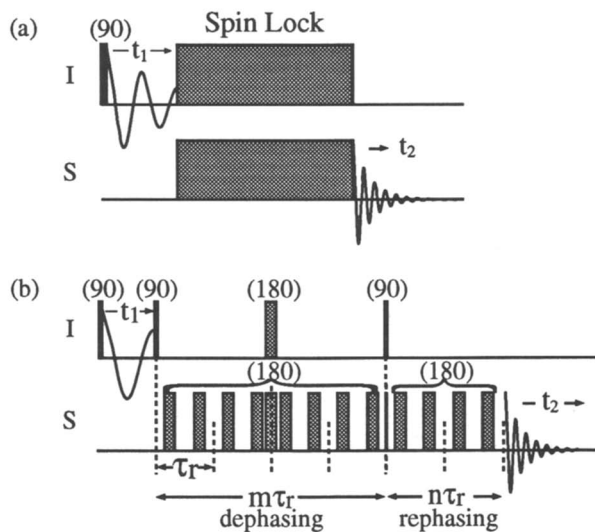


Figure 2. The RF pulse sequences shown are for two-dimensional (a) CP and (b) TEDOR solid-state NMR experiments.

intensity. The third, the CP time constant (T_{CP}), reveals the rate of magnetization buildup, and hence reflects the strength of the dipolar coupling. Stronger overall dipolar couplings are obtained from a combination of smaller internuclear distances and more neighboring spins contributing to the dipolar interaction. Through careful studies, we have begun to unravel the relative contributions of these effects in glass systems.

Spectroscopic Results

Conventional one-dimensional MAS spectra from ^{23}Na , ^{27}Al , and ^{31}P nuclei in a selection of glasses are shown in Figure 3. Important features to note include the characteristic isotropic chemical shift values of the resolved ^{31}P resonances, the broad nature of the ^{23}Na spectra, and the broad, yet resolved features of the ^{27}Al resonances. In the sodium phosphate glass, ^{31}P resonances are observed that may be assigned quite confidently to Q_2 - and Q_1 -type ^{31}P sites, where Q_n denotes a phosphate tetrahedron with n bridging oxygens to next-nearest neighbors (and therefore $4 - n$ non-bridging oxygens which terminate the three-dimensional network). Also, the ^{31}P spectra reveal a wide sideband pattern due to the large chemical shift anisotropy present. In our analyses, all sidebands for a particular resonance are either integrated to ensure proper quantification, or numerically folded into the centerband(s) for simplified viewing.

A one-dimensional CP spectrum (Figure 4) from the sodium to phosphorus spins in a sodium phosphate glass ($\text{Na/P} = 1.3$) provides evidence that the sodium nuclei are in the next-nearest-neighbor coordination sphere for both the Q_2 (-16.7 ppm) and Q_1 (1.8 ppm) ^{31}P sites in this glass. As the CP contact time is varied to a much larger value (8 msec), the relative intensity of the Q_2 site increases compared to the Q_1 site. Our studies show that in this particular system the spin-lattice relaxation times in the rotating frame ($T_{1\rho}$) for the ^{31}P spins does not vary much between different Q_n sites (here measured as 58 msec for both the Q_1 and Q_2 species). The sodium spin-locking, while complicated, also appears uniform across the sample. Therefore we attribute this qualitative variation in CP signal as a function of contact time to a difference in CP rate constant (T_{CP}) between the different sodium/phosphorus pairs at Q_1 and Q_2 sites.

As stated earlier, the magnitude of T_{CP} depends on both the distance between spins and the number of spins contributing to the CP process. Our observations are consistent with the reorganization theory of Van Wazer, which states that network depolymerization takes place as modifiers are added to the P_2O_5 glass system (25), and that non-bridging oxygen sites are coordinating the metal cations. The Q_2 site should have a smaller number of non-bridging oxygen sites with negatively-charged oxygen species near to positively-charged sodium cations. Hence, the cross-polarization buildup for this site should in theory be slower. The possibility of smaller Na-P internuclear distances associated with the faster-polarizing Q_1 site is discounted in these systems, since the average P-O bond length should be longer at a Q_1 site than at a Q_2 site due to the equilibration of electron density in the non-bridging P-O bonds. If all other parameters describing the CP process are then approximately equal, this results in a later maximum of CP intensity for the Q_2 site as a function of contact time. Full studies of the CP signal intensities as a function of contact time, coupled with modeling of the CP dynamics with a spin-thermodynamic model, corroborate these observations and provide a quantitative rate constant to compare to measured values in other glasses.

One-dimensional CP studies have also been performed on sodium aluminophosphate glasses with a range of compositions. Both one-dimensional $^{23}\text{Na} \rightarrow ^{31}\text{P}$ and $^{27}\text{Al} \rightarrow ^{31}\text{P}$ CPMAS spectra were obtained to study the local structure of the phosphate units. Examples of the spectra obtained are shown in Figure 5 for a glass prepared with a composition of 50% Na_2O , 8% Al_2O_3 , and 42% P_2O_5 (or 50-8-

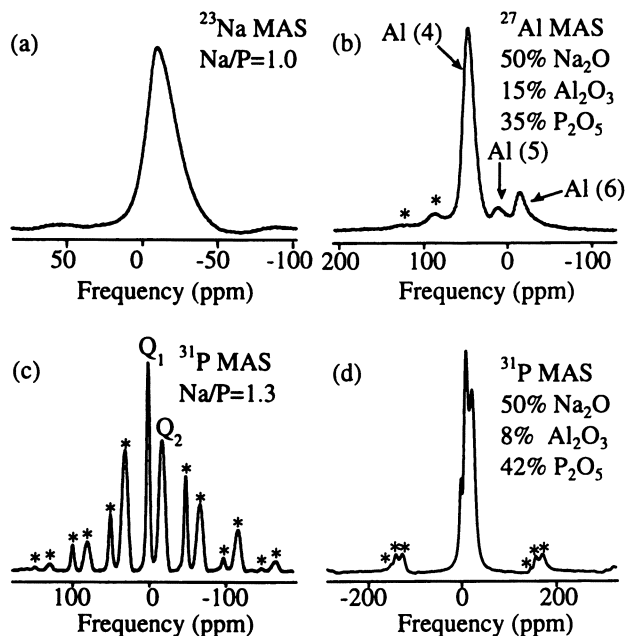


Figure 3. The magic-angle spinning spectra from ^{23}Na , ^{27}Al , and ^{31}P nuclei in a number of phosphate and aluminophosphate glasses demonstrate both the complexity of the glass structures and the information content present in the NMR spectra.

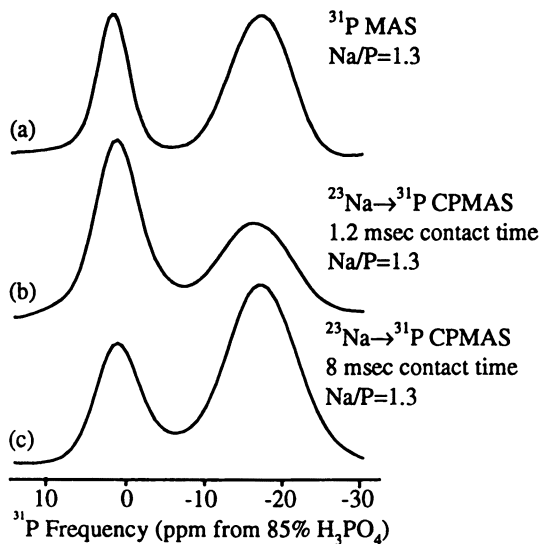


Figure 4. ^{31}P MAS and $^{23}\text{Na} \rightarrow ^{31}\text{P}$ CPMAS spectra from a sodium phosphate glass with $\text{Na/P} = 1.32$ demonstrate the spectral resolution of Q_1 and Q_2 phosphate sites, as well as the variation of CP signal intensity as a function of contact time.

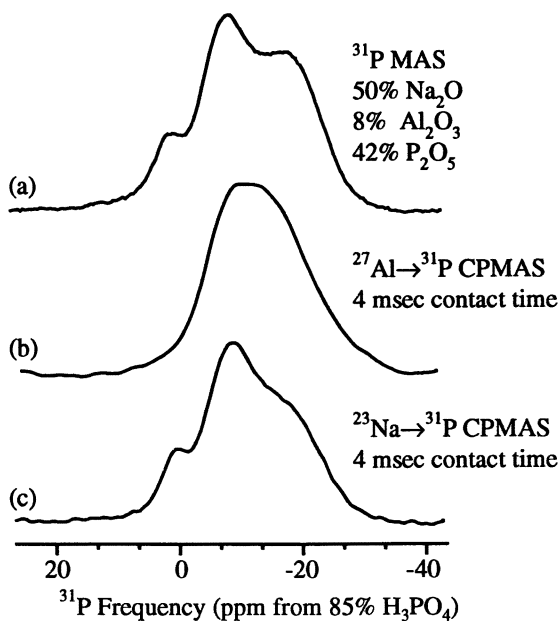


Figure 5. ^{31}P MAS, $^{23}\text{Na} \rightarrow ^{31}\text{P}$ CPMAS, and $^{27}\text{Al} \rightarrow ^{31}\text{P}$ CPMAS spectra from a sodium aluminophosphate glass (50-8-42) indicate which ^{31}P resonances arise from phosphorus nuclei with ^{23}Na or ^{27}Al in their next-nearest-neighbor coordination spheres.

42). The aluminum in these glasses is assumed to enter the backbone, while the role of the sodium atoms is somewhat unclear. The CP spectra in Figure 5 were obtained near the maxima in the overall CP intensities as a function of contact time. The top spectrum is a conventional ^{31}P MAS spectrum from this glass, while the lower spectra are $^{23}\text{Na} \rightarrow ^{31}\text{P}$ and $^{27}\text{Al} \rightarrow ^{31}\text{P}$ CPMAS spectra. The MAS spectrum reveals three primary phosphate resonances representing at least three tetrahedrally-coordinated phosphate units with different next-nearest-neighbor coordination spheres. The $^{23}\text{Na} \rightarrow ^{31}\text{P}$ CPMAS experiment displays significant intensity for all three phosphorus sites, indicating the presence of sodium in the second coordination sphere of all backbone atoms. The one-dimensional $^{27}\text{Al} \rightarrow ^{31}\text{P}$ CPMAS spectrum displays intensity for only two of the three phosphate resonances. The phosphorus resonance at +3 ppm can therefore be assigned to a phosphate tetrahedron with no aluminum atoms in its second coordination sphere due to the lack of intensity for this resonance in the $^{27}\text{Al} \rightarrow ^{31}\text{P}$ CPMAS experiment. This study, coupled with examination of the time-dependent build-up of the CP signal in these and other model phosphate glass systems, leads to an improved view of the local structure of the glass-forming atoms from the point-of-view of both the backbone and modifier atoms. However, at this point the full role of the sodium cations is still unclear.

Two-dimensional CP and TEDOR spectra correlate the resonances from one species (in our experiments, the quadrupolar ^{23}Na or ^{27}Al spins) with resonances from another set of nuclei (*e.g.*, spin-1/2 ^{31}P or ^{29}Si). We illustrate these experiments with two CP examples from the same glass system. The system is a sodium aluminophosphate glass with a 50-15-35 composition. The first two-dimensional spectrum, shown in Figure 6, is a $^{23}\text{Na} \rightarrow ^{31}\text{P}$ heteronuclear CPMAS correlation spectrum, where all Na/P correlated resonances are observed. The one-dimensional ^{31}P MAS spectrum displays resonances at -1.2 and 8.7 ppm, as well as a shoulder near to -10 ppm. One-dimensional cuts along the ^{31}P dimension and through the full two-dimensional spectrum reveal strong $^{23}\text{Na}/^{31}\text{P}$ correlation in the peaks at -1.2 and 8.7 ppm. A correlation to the shoulder at -10 ppm is also partially present, indicating that some of the intensity of the shoulder in the MAS spectrum arises from ^{31}P nuclei coupled to ^{23}Na spins.

An $^{27}\text{Al} \rightarrow ^{31}\text{P}$ two-dimensional CPMAS heteronuclear correlation spectrum from the same sodium aluminophosphate glass (50-15-35 composition) is shown in Figure 7. Here, the two-dimensional spectrum changes dramatically with respect to the ^{31}P resonances. Three slices (labeled (a), (b), and (c)) are taken at the isotropic shift values for the four-, five-, and six-coordinate ^{27}Al sites in the glass. The peak at +8.7 ppm in the ^{31}P spectrum has clearly disappeared in all of these subspectra. As seen in the earlier one-dimensional studies of a glass with a 50-8-42 composition, this indicates that the downfield ^{31}P resonance comes from sites that have no aluminum atoms in their next-nearest-neighbor coordination spheres. Each of these subspectra also shows varying amounts of "connectivity" from different ^{27}Al sites to ^{31}P resonances at -2 to -4 ppm (actually shifted with respect to one another). Other regions of ^{31}P resonances for sites connected to ^{27}Al sites with different coordinations are seen further upfield. These results reveal both the complex nature of ^{31}P MAS spectra in these systems, as well as the power of two-dimensional heteronuclear correlation experiments for probing these complex internuclear connectivities.

The solid-state NMR spectra of quadrupolar nuclei, those with spin greater than one-half, are complicated due to broadening of resonances caused by the interactions of these non-spherical nuclei with local changes in the electric field strength. A high-resolution two-dimensional NMR experiment was developed in our laboratory to correlate resonances between quadrupolar and spin-1/2 nuclei in polycrystalline and other disordered materials (23). True high-resolution is achieved by correlating the dynamic-angle spinning NMR spectrum of quadrupolar nuclei in one dimension with the magic-angle spinning spectrum of nearby spin-1/2 nuclei in the second dimension.

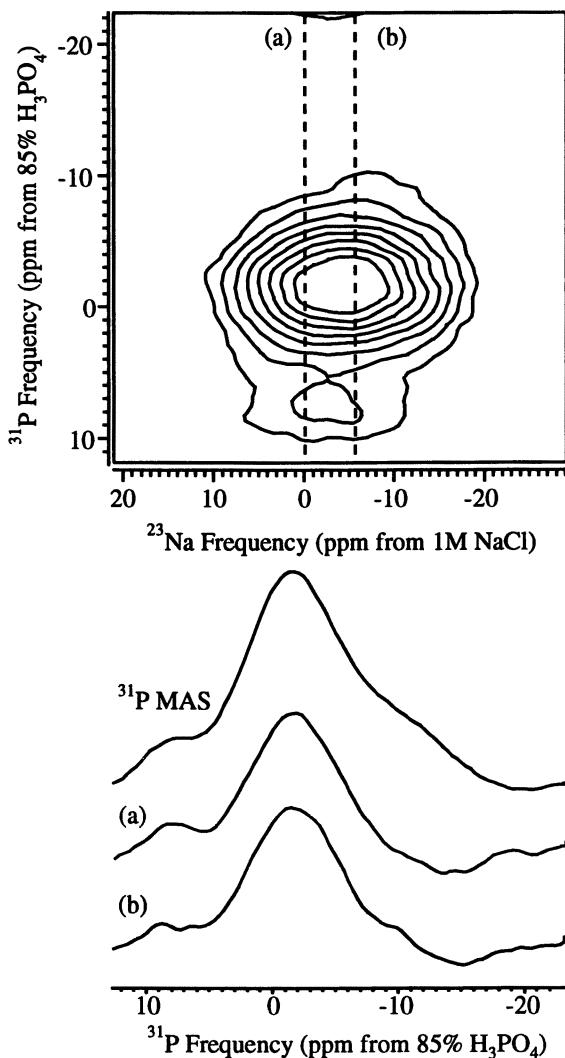


Figure 6. The two-dimensional $^{23}\text{Na} \rightarrow ^{31}\text{P}$ CPMAS spectrum from an aluminophosphate glass demonstrates the correlation of ^{23}Na and ^{31}P resonances in this glass. Two ^{31}P slices through different parts of the ^{23}Na spectrum are compared to the ^{31}P MAS spectrum.

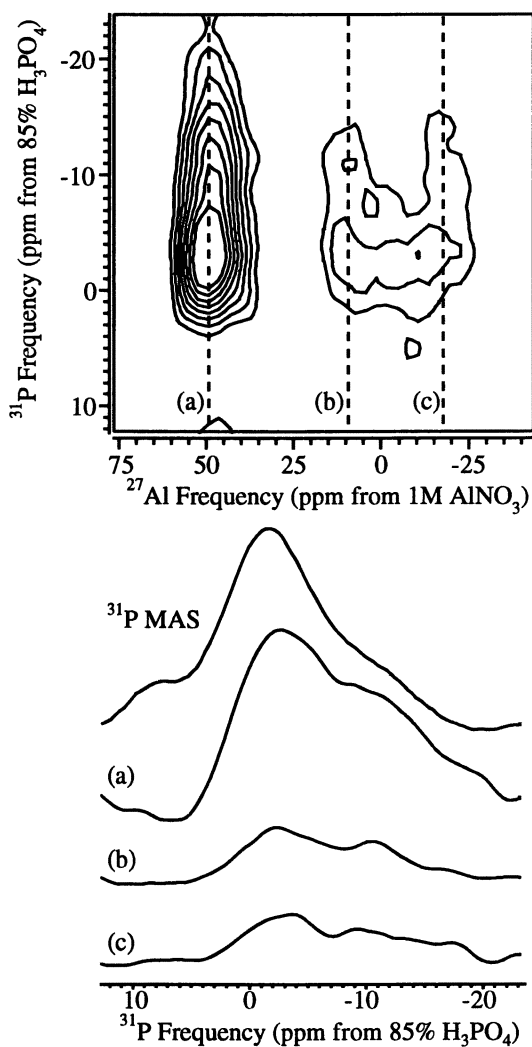


Figure 7. The two-dimensional $^{27}\text{Al} \rightarrow ^{31}\text{P}$ CPMAS spectrum from an aluminophosphate glass demonstrates the correlation of ^{27}Al and ^{31}P resonances in this glass. Three slices through different parts of the ^{27}Al spectrum, corresponding to aluminum with different coordinations, are compared to the ^{31}P MAS spectrum.

The DAS technique narrows the resonances from half-integer spin quadrupolar nuclei (like ^{23}Na and ^{17}O) using a "flip" of the NMR rotor axis during the experiment (8). A CP sequence then transfers spin coherence from the quadrupolar spins to nearby spin-1/2 nuclei. High-resolution signals from the spin-1/2 nuclei are then detected after a final flip to the conventional magic angle. One useful pulse sequence and rotor-orientation timing is sketched in Figure 8. Rather than a straightforward use of two-spinning angles for the DAS experiment, followed directly by a CP sequence, we utilize an "equal time" DAS experiment with the DAS pair ($\theta_1 = 79.19^\circ$, $\theta_2 = 37.38^\circ$) with a subsequent hop to 0° for the CP. This is easily accomplished in our fixed-coil design DAS probe (26). This particular version of the experiment was chosen based on experimental trials of many permutations of the angles used for the DAS and the CP sections of the experiment, this one providing the most efficient signal acquisition.

It is well-known that spinning a sample can complicate the CP dynamics through a time-dependent modulation of the dipolar coupling frequencies (27). In addition, MAS affects the quadrupolar species, providing a time-dependent modulation of the first-order quadrupolar frequencies that can lead to a loss of central ($+1/2 \leftrightarrow -1/2$) transition magnetization under spin-locking conditions. This modulation and signal loss can be controlled, to some extent, by a variation of spinning speed and RF field strength relative to the quadrupolar frequencies. This is quantified via the adiabatic-passage parameter:

$$\alpha = \frac{\omega_1^2}{\omega_Q \omega_r} \quad (2)$$

where ω_1 is the RF field strength (scaled by $I + 1/2$ in the limit that quadrupolar coupling strength is much greater than the RF field strength), ω_Q is the quadrupolar frequency (as defined by Vega), and ω_r is the rotational frequency (21,22). Here, all frequencies are defined in units of rad/sec, but α is an overall dimensionless parameter so that the choice of units must simply be consistent. Three different regimes are identified, those with $\alpha \gg 1$ (the adiabatic regime), $\alpha \ll 1$ (sudden passage), and the intermediate regime. It is found that being in the intermediate regime is in fact the worst possible case for spin-locking of quadrupolar central transition magnetization. In all of the experiments described here we attempt to work in the sudden-passage regime, maintaining low RF field strengths (with 15-20 μsec 90° pulses for the central transitions of the quadrupolar spins) and moderate to high spinning speeds.

Experimentally, we have noted exceptional gains in CP intensity and efficiency when performing CP at 0° (28). The large gain in CP signal intensity arises predominantly from the removal of the time dependence from the first-order quadrupolar interaction when spinning at 0° . In this situation, the sodium spin-locking is quite superior when spinning parallel to the field. In many $^{23}\text{Na} \rightarrow ^{31}\text{P}$ one- and two-dimensional CP experiments, signal acquisition times become prohibitively long while transferring magnetization under MAS conditions, while acquisition after CP at 0° yields reasonable signal in a much shorter time. The quick spin-lattice relaxation times of the quadrupolar nuclei also allow much faster repetition of the experiment performing CP at either spinning angle, while the longer relaxation times of nuclei such as ^{31}P and ^{29}Si allow time for coherent reorientation of the rotor to the conventional magic angle prior to high-resolution signal accumulation. All of these factors must be taken into consideration when designing experiments to yield high-resolution correlations between quadrupolar and spin-1/2 nuclei. High-resolution multiple-quantum MAS experiments (MQMAS) can be effectively applied to ^{23}Na nuclei, negating the need for complicated sample hopping as in a DAS experiment. Resolution is increased in a MQMAS experiment due to the

reduction of the homonuclear dipolar coupling under high-speed MAS conditions. The MQMAS experiment may then be extended into a two-dimensional experiment in the same manner as the DAS/CP/MAS experiment, but the ability to carry out CP at 0° is then lost. The additional degree of freedom available for controlling and regulating the CP dynamics via hopping the sample spinning axis has been found necessary in a number of situations in our laboratory.

The DAS/CP/MAS technique was first demonstrated with a correlation experiment between the ^{23}Na and ^{31}P nuclei in polycrystalline sodium trimetaphosphate (23), and a representative DAS/CP/MAS spectrum is shown in Figure 9. The resolution obtained in this new experiment allows qualification, and possibly quantification, of the amount of correlation or "connectivity" between pairs of nuclear sites in solids.

DAS NMR experiments have known limitations when applied to sodium nuclei in polycrystalline materials and glasses. In polycrystalline solids, homonuclear sodium-sodium interactions are not refocused in the DAS experiment and some residual line broadening occurs (typically on the order of 500 to 700 Hz). The resonances in spectra of sodium trimetaphosphate are separated by frequencies greater than the residual broadening: the isotropic peaks occur in the DAS spectrum with a difference of approximately 1700 Hz in a 9.4 T magnetic field, so that resolved resonances are observed. ^{23}Na DAS spectra from glasses generally display a single broad resonance due to additional line broadening arising from a distribution of bond angles and distances in the glass. In sodium tellurite glasses, Tagg and coworkers probed sodium sites with DAS NMR, extracting average values as well as ranges of isotropic chemical shifts and quadrupolar parameters (29). The broad lines present in the spectrum could not be fully narrowed with DAS, but this was due to the disorder broadening. Their data showed that a probable change in sodium coordination occurs in these systems as the modifier concentration increases.

The disorder broadening found in NMR spectra from glasses cannot be removed by any NMR experiment. However, different sodium environments in a glass may also arise due to "connectivities" or association of the cations with different types of phosphate units. To investigate this possibility, it is necessary to combine the high resolution capability of DAS for quadrupolar nuclei with the connectivity discrimination of two-dimensional heteronuclear cross-polarization. As shown above, the powerful "spectral editing" afforded by the two-dimensional DAS/CP/MAS experiment allows for separation of distinct sodium resonances connected to distinct phosphate units. Preliminary DAS/CP/MAS studies of mixed alkali phosphate glasses are encouraging, and results showing spectral resolution of different sodium sites connected to different phosphate tetrahedral units are currently being analyzed and expanded.

Conclusion

In conclusion, we have demonstrated applications of one- and two-dimensional heteronuclear correlation NMR experiments to glass systems. Using quadrupolar nuclei such as ^{23}Na and ^{27}Al , we can perform correlation experiments to ^{31}P nuclei, mapping out the internuclear "connectivities" in these systems using the dipolar interaction. The use of other experiments such as REDOR, TEDOR, and TRAPDOR (17,30,31) are possible in many of these systems as well. The TEDOR experiment is especially attractive since it also results in transfer of spin coherence from a source to a target set of atoms, and should be quite insensitive to spin diffusion of the magnetization of the target nuclei. We have also outlined new methodology that shows promise for enhanced resolution in these systems using quadrupolar narrowing experiments as parts of heteronuclear correlation NMR methods, and full results will soon be reported. Ultimately this complete methodology should aid in advancing the understanding of structure/property relationships in glasses.

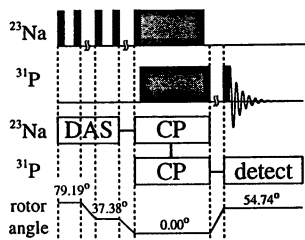


Figure 8. The RF pulse sequence and rotor orientation scheme used for DAS/CP/MAS experiments.

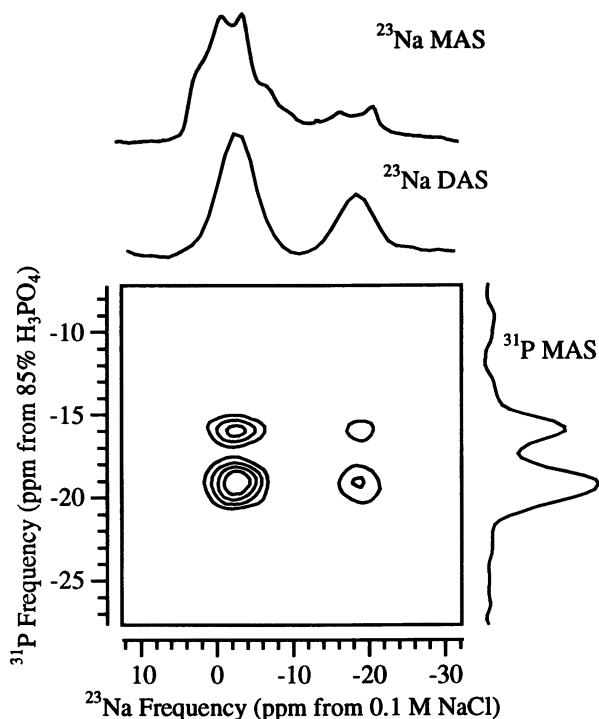


Figure 9. For polycrystalline $\text{Na}_3\text{P}_3\text{O}_9$, the one-dimensional ^{23}Na MAS spectrum (top) is broad and overlapping. The DAS spectrum (middle) reveals resolved resonances. The two-dimensional DAS/CP/MAS spectrum (bottom) shows clearly resolved cross peaks from "connected" ^{23}Na and ^{31}P resonances.

Literature Cited

1. Eckert, H. *Prog. NMR Spectros.* **1992**, *24*, 159-293.
2. Eckert, H. in *NMR. Basic Principles and Progress* Springer-Verlag: Berlin, Heidelberg, 1994; Vol. 33; pp 125-197.
3. Fyfe, C. A. *Solid State NMR for Chemists*; C.F.C. Press: Guelph, Ontario, 1983.
4. Andrew, E. R.; Bradbury, A.; Eades, R. G. *Nature* **1959**, *183*, 1802-1803.
5. Lowe, I. J. *Phys. Rev. Lett.* **1959**, *2*, 285-287.
6. Chmelka, B. F.; Mueller, K. T.; Pines, A.; Stebbins, J.; Wu, Y.; Zwanziger, J. W. *Nature (London)* **1989**, *339*, 42-43.
7. Chmelka, B. F.; Zwanziger, J. W. in *NMR. Basic Principles and Progress* Springer-Verlag: Berlin, Heidelberg, 1994; Vol. 33; pp 79-124.
8. Mueller, K. T.; Sun, B. Q.; Chingas, G. C.; Zwanziger, J. W.; Terao, T.; Pines, A. *J. Magn. Reson.* **1990**, *86*, 470-487.
9. Frydman, L.; Harwood, J. *J. Am. Chem. Soc.* **1995**, *117*, 5367-5368.
10. Griffiths, J. M.; Griffin, R. G. *Analytica Chimica Acta* **1993**, *283*, 1081-1101.
11. Gullion, T.; Schaefer, J. *J. Magn. Reson.* **1989**, *81*, 196-200.
12. Hing, A. W.; Vega, S.; Schaefer, J. *J. Magn. Reson.* **1992**, *96*, 205-209.
13. Gullion, T.; Schaefer, J. *Advances in Magnetic Resonance* **1989**, *13*, 57-83.
14. Fyfe, C. A.; Grondey, H.; Mueller, K. T.; Wong-Moon, K. C.; Markus, T. *J. Am. Chem. Soc.* **1992**, *114*, 5876-5878.
15. Fyfe, C. A.; Mueller, K. T.; Grondey, H.; Wong-Moon, K. C. *Chem. Phys. Lett.* **1992**, *199*, 198-204.
16. Fyfe, C. A.; Mueller, K. T.; Grondey, H.; Wong-Moon, K. C. *J. Phys. Chem.* **1993**, *97*, 13484-13495.
17. van Eck, E. R. H.; Janssen, R.; Maas, W. E. J. R.; Veeman, W. S. *Chem. Phys. Lett.* **1990**, *174*, 428-432.
18. van Eck, E. R. H.; Veeman, W. S. *J. Am. Chem. Soc.* **1993**, *115*, 1168-1169.
19. Fyfe, C. A.; Wong-Moon, K. C.; Huang, Y.; Grondey, H.; Mueller, K. T. *J. Phys. Chem.* **1995**, *99*, 8707-8716.
20. van Wüllen, L.; Züchner, L.; Müller-Warmuth, W.; Eckert, H. *Sol. State NMR* **1996**, *6*, 203-212.
21. Vega, A. J. *J. Magn. Reson.* **1992**, *96*, 50-68.
22. Vega, A. J. *Sol. State NMR* **1992**, *1*, 17-32.
23. Jarvie, T. P.; Wenslow, R. M.; Mueller, K. T. *J. Am. Chem. Soc.* **1995**, *117*, 570-571.
24. Mehring, M. *Principles of High-Resolution NMR in Solids*; 2nd ed.; Springer-Verlag: Berlin, 1983.
25. Van Wazer, J. R. *Phosphorous and its Compounds*; Interscience Publishing Inc.: New York, 1958; Vol. 1, pp 722-769.
26. Mueller, K. T.; Chingas, G. C.; Pines, A. *Rev. Sci. Instrum.* **1991**, *62*, 1445-1452.
27. Sardashti, M.; Maciel, G. E. *J. Magn. Reson.* **1987**, *72*, 467-474.
28. Fyfe, C. A.; Wong-Moon, K. C.; Grondey, H.; Mueller, K. T. *J. Phys. Chem.* **1994**, *98*, 2139-2142.
29. Tagg, S. L.; Youngmann, R. E.; Zwanziger, J. W. *J. Phys. Chem.* **1995**, *99*, 5111-5116.
30. Grey, C. P.; Eijkelenboom, A. P. A. M.; Veeman, W. S. *Sol. State NMR* **1995**, *4*, 113-120.
31. Grey, C. P.; Vega, A. J. *J. Am. Chem. Soc.* **1995**, *117*, 8232-8242.

Borate Glass Structure Probed with Dynamic Angle Spinning NMR

J. W. Zwanziger, R. E. Youngman¹, and M. Braun²

Department of Chemistry, Indiana University, Bloomington, IN 47405

Dynamic Angle Spinning NMR is used to probe the short and intermediate range order of boron oxide glass and potassium borate glasses. Through comparison with crystalline potassium borates of known structure, the boron resonances are assigned to various structures, including four-fold coordinate species, and three-fold coordinate boron in three-membered rings and in less ordered environments. The primary conclusions reached are: (1) that about 70% of the boron in boron oxide glass is bound in three-membered boroxol rings; (2) that the clustering of these rings gives rise to intermediate range order in this material; and (3) that upon alkali oxide modification both ring and non-ring boron are modified, with a propensity for further ring closure leading to an excess of rings that contain four-fold coordinate boron.

Boron oxide is an essential component of many industrial glasses, in part because of its exceptionally good glass forming ability. This tendency is exemplified by pure boron oxide itself, which does not crystallize from the liquid at ambient pressure [1]. Crystals have been grown only by application of pressure (20 kbar) to the melt. The resulting crystals consist of BO_3 units, sharing oxygen at the corners and forming extended chains. There is a variety of evidence indicating that boron oxide glass consists of the same BO_3 groups, a significant fraction of which are linked in six-membered boroxol rings (B_3O_3).

¹Present address: Department of Materials Science and Engineering, University of Illinois, 105 South Goodwin Avenue, Urbana, IL 61801.

²Present address: Institute of Optics and Quantum Electronics, Friedrich Schiller University, Jena, Germany.

This evidence includes Raman spectroscopy [2], neutron scattering [3,4], NQR [5], and NMR [6-8]. However, no crystalline form of boron oxide has been prepared that contains these rings, and indeed modeling studies of boron oxide glass have typically suggested that there is not a large fraction of rings, in contrast to the interpretations of the many experimental studies [9,10].

Additives such as alkali oxides are known to cause conversion of three-fold coordinate boron in BO_3 groups to BO_4^- units, in which the boron is four-fold coordinate. Crystal structures of many such compounds are known, and contain three- and four-fold coordinate boron in both ring and chain structures.

In both modified borate glasses and pure boron oxide glass the local structure around the boron atoms is quite ordered, with bonding geometries similar to what is seen in borate crystals. This means that the BO_3 groups are nearly planar, and the BO_4^- groups nearly tetrahedral. Because of this ordering, NMR has been an exceptionally successful probe of structure in these materials. Bray and his group, in fact, established NMR as a key tool in glass science primarily through application to borates [11,12]. They were able to show that the fraction of three-fold to four-fold coordinate boron could be determined from the ^{11}B NMR spectrum, and also pioneered studies of ^{17}O and ^{10}B in these materials [6]. Because these experiments were performed with CW NMR and static sample techniques, the achievable resolution was not sufficient to resolve boron in similar three-fold sites, for example boron in boroxol rings and in non-ring BO_3 units. Therefore, while these studies demonstrated beyond doubt what the basic building blocks of borate glasses are, they could not reveal as much about how these units are linked in the pure glass and modified borate glasses.

Because both boron nuclei (^{11}B and ^{10}B) have substantial electric quadrupole moments, conventional high-resolution solid-state NMR methods like magic angle spinning (MAS) do not yield resolution enhancements comparable to what can be obtained on spin- $\frac{1}{2}$ nuclei like ^{13}C and ^{31}P . Recent advances in NMR methodology, however, have provided the necessary tools to obtain the several orders of magnitude improvement in resolution necessary to probe the next level of structure in borate glasses, namely the linkages between the basic units [13-16]. The purpose of this contribution is to describe the application of several of these new experiments to both boron oxide and alkali oxide borate glasses. Our primary results are: (1) a direct assignment of resonances in glassy boron oxide to ring and non-ring BO_3 units, thereby quantifying these two units; (2) the inference of intermediate range order due to ring-ring binding in glassy boron oxide, through interpretation of boron and oxygen NMR data; and (3) a new model of the modification process, which includes modification at both the boroxol ring and non-ring boron sites.

In the next section of the paper we detail the experimental methods used in these studies. Then we present results, followed by discussion and interpretation. We close with conclusions and an outline of planned future work.

Experimental Methods

Sample Preparation Glasses enriched to 90% in boron-10 were made by fusing together appropriate quantities of boric acid (Strem, 99.9995%), boric acid enriched to 97% in ^{10}B (Aldrich) and potassium carbonate (Strem, 99.8%) at 1000°C . Depletion of the ^{11}B isotope was necessary to alleviate spin diffusion in the DAS NMR experiments [7]. The melts were held at this temperature for one hour and quenched by removing the platinum crucible from the furnace and cooling in a dry nitrogen atmosphere. The clear, colorless glasses were broken into small pieces and stored under nitrogen to minimize absorption of water. After obtaining Raman data on the bulk samples, the glasses were powdered for NMR analysis. X-ray powder diffraction was used to verify the amorphous character of these samples. Final compositions were checked by weight loss measurements.

Potassium borate glasses, enriched in oxygen-17, were prepared by fusing together appropriate amounts of ^{17}O -enriched boron oxide and potassium carbonate. The synthesis of ^{17}O -enriched B_2O_3 is described elsewhere [8]. After thoroughly mixing these two materials, they were melted at 1000°C for 15 minutes. The melts were quenched by cooling in a dry nitrogen environment.

NMR Spectroscopy ^{11}B NMR spectra were acquired at both 115.6 MHz and 64.2 MHz, using a home-built spectrometer. Sample-spinning experiments were carried out with a commercial DAS probe (Doty Scientific), under the control of the spectrometer. Typical sample rotation frequencies were 6-7 kHz.

The DAS experiment was designed to remove anisotropic broadenings and yield high resolution NMR spectra of quadrupolar nuclei like ^{11}B and ^{17}O [13-16]. For these nuclei, at the magnetic field strengths used here, anisotropic terms of both first and second order are important. Conventional Magic Angle Spinning (MAS) removes the first order terms, but not the second order. Because the anisotropies depend on both $P_2(\cos\theta)$ and $P_4(\cos\theta)$, where P_l is a Legendre polynomial and θ is the angle between the rotor axis and the magnetic field, there is no single angle θ about which sample spinning removes both sources of broadening. DAS exploits the fact that there are *pairs* of angles such that

$$P_2(\cos\theta_1) = -kP_2(\cos\theta_2), \quad P_4(\cos\theta_1) = -kP_4(\cos\theta_2). \quad (1)$$

The experiment is executed with two time evolution periods, the first with the sample spinning about θ_1 , and the second about θ_2 . Because of the sign change in the anisotropy, a spin echo is formed in which all first and second order broadening is canceled out. Using this experiment, sites with 20 kHz line widths under static conditions and 5 kHz line widths under MAS yield spectra with 200 Hz-wide lines.

For the DAS experiments discussed here, the rotor orientation angles used were $\theta_1 = 37.38^\circ$ and $\theta_2 = 79.19^\circ$, with $k = 1$. The time to reorient the probe and re-establish stable spinning between these angles was 40 msec. For the glass samples, the shifted-echo DAS sequence with hypercomplex data acquisition was used, while for the

crystalline samples only shifted-echo DAS was employed [15]. Each data set consisted of typically 64-128 scans (256 complex points) at each of 80 t_i points, with 15-60 seconds (for glasses) and 600 seconds (crystals) between scans to allow for full relaxation of all sites. Each such series of data was zero-filled to 512 x 512 before transformation. No smoothing was used in either dimension. The time necessary to acquire each spectrum varied from about 24 hours for glass samples in the higher field, to as much as several weeks for the crystalline samples at the low field. The major difference is that the relaxation times in the glasses are typically an order of magnitude shorter than in corresponding crystals.

Raman Spectroscopy Raman spectra were obtained on a commercial Raman spectrometer (Spectra-Code) at the Purdue University Chemistry Department Laser Facility. The excitation source was the 632.8 nm line of a 30 mW helium-neon laser and the spectral resolution was 3 cm^{-1} . The instrument uses integral holographic filtering and a liquid-nitrogen-cooled CCD detector. Data was obtained using large pieces of glassy sample, sealed in a quartz sample cuvette. The scattering intensity was integrated over 600 s of detector exposure time. Spectra were acquired under ambient pressure and temperature conditions.

Results

Figure 1 shows a typical two-dimensional DAS spectrum of a potassium borate glass. The powder patterns obtained at different isotropic shifts are shown on the right side of this figure; the total powder pattern is projected at the top of the contour plot. At left is the high resolution dimension. Figure 2 shows a series of high-resolution spectra as a function of potassium oxide content.

Raman spectra (not shown) of the potassium borate glasses show the same behavior seen in previous studies [2,17-21]. The dominant feature is a sharp, strong peak at 808 cm^{-1} in pure B_2O_3 glass, which decreases in intensity with added modifier. In addition, a somewhat broader peak grows in at about 770 cm^{-1} . By a modifier level of 33%, the 808 cm^{-1} has vanished. Additionally, broad weak features in the 300-800 cm^{-1} region were seen, which at low modifier content have been assigned to motions of the loose BO_3 units [22].

Discussion

NMR Evidence for the Existence of Boroxol Rings While as noted in the introduction a considerable amount of experimental evidence has been interpreted as showing the existence of boroxol rings in boron oxide glass, the precision by which the fraction of boron in such groups can be determined has been questioned. In particular, Raman cross sections (the main source of evidence for rings) are quite difficult to quantify, and diffraction measurements (both neutron and x-ray) can be interpreted with models that show good agreement with the structure factors but differ greatly in the number of rings they contain. Here we present assignments of our NMR data which argue strongly for the existence of a large fraction of boron in boroxol rings, in accord with the conventional view of this system.

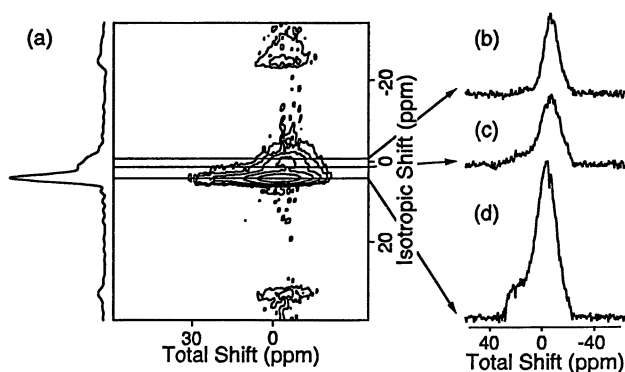


Figure 1. (a) Two-dimensional DAS spectrum of ^{11}B in $(\text{K}_2\text{O})_{20}(\text{B}_2\text{O}_3)_{80}$ glass. The projection at left is the high-resolution dimension. Shifts are in ppm referenced to $\text{Et}_2\text{O}\cdot\text{BF}_3$. Slices through the data at three key isotropic shifts are shown to the right: (b) -0.3 ppm, four-fold coordinate boron; (c) 1.0 ppm, loose BO_3 units; (d) 4.7 ppm, BO_3 units in rings. (Reproduced with permission from ref. 24. Copyright 1996 American Chemical Society.)

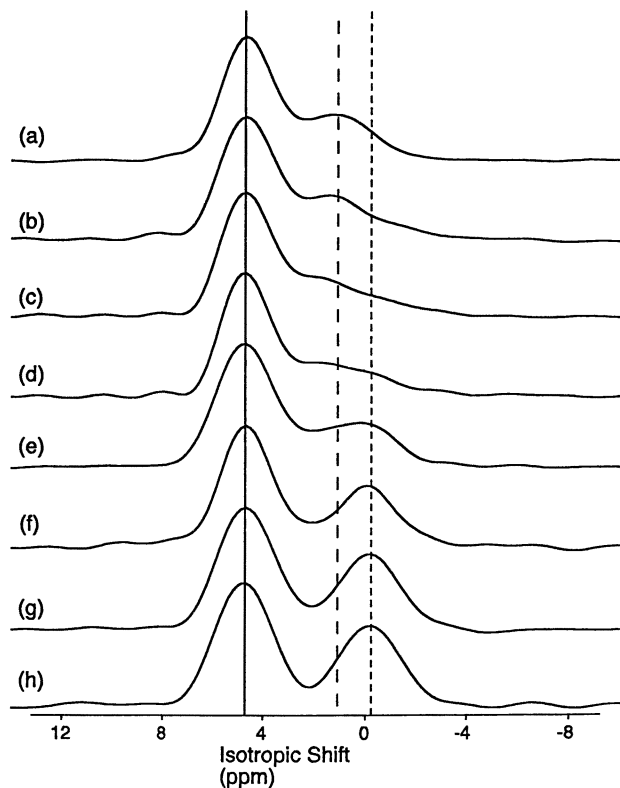


Figure 2. Isotropic shift spectra of ^{11}B in $(\text{K}_2\text{O})_x(\text{B}_2\text{O}_3)_{1-x}$ glasses, from DAS NMR. (a) $x=0.0$ (B_2O_3); (b) $x=0.08$; (c) $x=0.13$; (d) $x=0.18$; (e) $x=0.23$; (f) $x=0.28$; (g) $x=0.33$; and (h) $x=0.38$. The vertical lines are drawn at the isotropic shifts of the three sites. Solid line: 4.7 ppm, the ring three-coordinate boron shift; long dashed line: 1 ppm, boron in loose BO_3 units; short dashed line: -0.3 ppm, four-coordinate boron. (Reproduced with permission from ref. 24. Copyright 1996 American Chemical Society.)

The two ^{11}B resonances in boron oxide glass have isotropic shifts of 4.7 ppm and 1.0 ppm at 8.4 Tesla; these shifts are the sum of the isotropic chemical shift and the second order quadrupole shift. The contributions can be separated by performing the experiment at a different field; we have done this, and find the parameters given in Table I [7]. Based on the intensities (0.7 and 0.3) we assigned the down-field resonance to boroxol ring boron, and the up-field resonance to non-ring BO_3 units, in agreement with earlier work which suggested that between 60% and 80% of the boron are in boroxol rings. The chemical shifts as assigned in Table I are in agreement with *ab initio* results of Tossell [23].

Table I. Parameters of ^{11}B Resonances in B_2O_3 Glass

<i>Site Intensity</i>	<i>Isotropic Shift (8.4 T)^a</i>	<i>Isotropic Chemical Shift^a</i>	<i>Quadrupole Product^b</i>
0.7	4.7 ppm	18.0 ppm	2.7 MHZ
0.3	1.0 ppm	13.0 ppm	2.6 MHZ

^aShifts are relative to $\text{Et}_2\text{O}\cdot\text{BF}_3$.

^bThe quadrupole product is given by $(e^2Qq/h)\sqrt{1+\eta^2/3}$, with e^2Qq/h the quadrupole coupling and η the asymmetry.

SOURCE: Adapted from ref. 7.

In alkali oxide-modified glasses, as we will discuss in more detail below, resonances with isotropic shifts of 4.7 ppm and 1.0 ppm are again observed at 8.4 Tesla, with a third resonance at -0.3 ppm appearing as the alkali oxide concentration is increased. Here we wish to discuss the results obtained from the NMR spectra of potassium borate crystals [24]. The crystal structures of the compounds studied are all known, and so the boron resonances can be assigned unambiguously from their intensities. The assignments are shown in Table II. The first point to note is that boron in the metaborate ring, $\text{B}_3\text{O}_6^{3-}$, has an isotropic shift of 4.9 ppm, almost identical to the 4.7 ppm shift seen in the glass. The metaborate ring is a planar boroxol ring capped by non-bridging oxygen. Next, in the crystals, non-ring BO_3 groups are found in the range 1.0-2.3 ppm, with the down-field shift arising from a BO_3 group with two BO_4^- neighbors. BO_3 groups in modified boroxol rings have isotropic shifts within a ppm of the metaborate shift, never farther upfield than 3.8 ppm. These results on crystalline compounds are, in our opinion, only consistent with assignment of the 4.7 ppm shift in the glass to boroxol rings, and the 1.0 ppm shift to non-ring BO_3 groups. This assignment leads to 70% of the boron in boroxol rings, and 30% in non-ring units, in agreement with numerous previous estimates.

Intermediate Range Order of Pure B_2O_3 Given that the building blocks of boron oxide glass are planar BO_3 units, the intermediate range order is generated by how these units

Table II. Sites and ^{11}B Isotropic Shifts from Potassium Borate Crystals

<i>Structural Unit</i>	<i>Isotropic Shift^a</i>
nonring BO_3	1.0-2.3 ppm
BO_4^-	-0.3 ppm
BO_3 : metaborate	4.9 ppm
BO_3 : pentaborate	3.7 ppm
BO_3 : triborate	3.8 ppm
BO_3 : di-triborate	5.4 ppm
BO_3 : diborate	5.4 ppm

^aIsotropic shifts at 8.4 Tesla, relative to $\text{Et}_2\text{O}\cdot\text{BF}_3$.

SOURCE: Adapted from ref. 24.

are linked together. The short-range intermediate range order results from the boroxol rings, and since some 70% of the boron are in these units, it is clear that ordering on this length scale is extensive. The way in which these rings, and the non-ring BO_3 units, are linked give rise to longer range intermediate range order. Since these bridges are made through oxygen, ^{17}O NMR suggests itself as a suitable probe of the types of linking oxygen. The first results of such experiments were obtained by Bray and co-workers, who showed the presence of multiple oxygen sites, again within and outside of boroxol rings [6].

Recently we obtained very high-resolution ^{17}O NMR spectra, using the Double Rotation (DOR) NMR experiment, which showed three resolved oxygen sites [8]. This experiment removes both first and second-order quadrupole broadening, as does DAS. A difficulty in using this experiment, as compared to DAS and MAS, is the comparatively low spinning rates achievable (< 1 kHz). This gives rise to spectra with a great many spinning sidebands, making accurate intensity determination problematic. To circumvent this problem we performed time-dependent simulations of the spectra, which account for the sidebands, and used the interaction parameters and intensities to simulate MAS spectra, which we could record with excellent signal to noise and little interference from sidebands. The results of these consistency checks were that the spectra arise from three sites with relative populations 0.5 ± 0.1 , 0.3 ± 0.1 , and 0.2 ± 0.1 . The interaction parameters (chemical shift and quadrupole coupling) of the three sites are similar and all indicate oxygen in bridging configurations.

To assign these sites we constructed a model based on the assumption that four resolvable oxygen sites could be present: oxygen in boroxol rings, oxygen bridging boroxol rings, oxygen bridging rings and non-ring BO_3 , and finally oxygen bridging two non-ring BO_3 units. Two facts were used to constrain the concentrations of these four units: the ratio of oxygen to boron in the glass (3/2) and the fraction of boron present in rings (0.7, based on our NMR data on these samples) [7,8]. This is sufficient to

constrain the oxygen site populations leaving only a single degree of freedom. For example, consider the ring oxygen. Call the number of ring boron atoms R ; then there are also R ring oxygen atoms, since the ring composition is B_3O_3 . The fraction of ring oxygen is then R/N , where N is the total number of oxygen atoms. But $N/M = 3/2$, where M is the total number of boron atoms. Therefore $R/N = 2R/3M = 0.7 \times 2/3 = 0.47$, since for the fraction of boron in rings $R/M = 0.7$. We thus assign the experimentally observed resonance with intensity 0.5 as the ring oxygen site (note that there are no adjustable parameters in this assignment). For the other three oxygen sites two independent equations may be derived, following reasoning similar to the above. The solutions of these equations may be found in terms of one of the three unknowns, and they show that there is only one region of solution space that corresponds to the observed intensities of 0.5, 0.3, and 0.2: when the population of ring to non-ring bridging oxygen is small.

A small concentration of ring to non-ring connections suggests that the glass consists of regions rich in boroxol rings, and regions poor in rings. From the size of rings and the assumption that each ring on the surface of a ring-rich region makes a single connection to non-ring BO_3 units, we estimated the size of the ring-rich regions to be about 20–40 Å. Interestingly, recent light-scattering measurements at the glass transition in B_2O_3 [25,26] are consistent with structural inhomogeneities on this length scale. Indeed, intermediate-range order is conjectured to be universal in glass formation. Our data suggests its structural origin in this particular material.

Modification by Conversion from Three-fold to Four-fold Coordination As stated in the introduction, there is considerable evidence showing that as modifiers are added to borate glass, the initial structural change is the conversion of three-fold coordinate boron to four-fold coordination. Because of the presence of both boroxol rings and non-ring BO_3 units in the pure glass and melt [22], this modification could happen at either site or both. Considerable work using Raman spectroscopy indicates that the pure boroxol rings are modified in some way, as the sharp 808 cm^{-1} peak indicative of the boroxol rings diminishes in intensity and is replaced by a broader feature at about 770 cm^{-1} . This pattern is observed also in the present study, as mentioned above in Section 3.

The DAS NMR data presented in Figure 2 also provides a way to follow the structural changes upon modification. In this Figure it is clear that as more modifier is added, the less intense peak at 1.0 ppm decreases in intensity, while a new feature grows in at -0.3 ppm. The strong feature at 4.7 ppm decreases slightly. These three resonances are all well-fit by Gaussian lineshapes, and from such fits the relative intensities of the three resonances can be extracted. To make such a determination we fixed the isotropic shift of each resonance at its observed value in the 0% modification sample (for the 4.7 ppm and 1.0 ppm features) or the 30% modification (the -0.3 ppm feature). Then, the intensities and widths were allowed to vary freely in fitting the spectra for different modifier content. The results for the relative intensities are shown in Figure 3. The widths do not change significantly with added modifier.

We verified that the DAS NMR experiment gives reliable relative intensities for this system by recording spectra of crystalline potassium borates, and comparing the

boron site intensities against the populations derived from the crystal structures. This is a significant check because the three-fold and four-fold boron have quite different quadrupole interaction parameters, and hence different NMR nutation behavior. We found that by working at high pulse powers both the three-fold and four-fold site intensities are correctly reproduced. This strategy was used to acquire all the glass data presented here.

At 0% modifier (pure B_2O_3 glass) the features in the NMR spectra have been assigned previously as boroxol ring boron (4.7 ppm) and non-ring BO_3 units (1.0 ppm) [7]. [Note that these are isotropic shifts, not chemical shifts, and as such include both isotropic chemical shift and second-order quadrupole effects. The latter are field-dependent, so these shifts are specific to 8.4 Tesla, the field at which the measurements were made.] This assignment is based on intensities, but agrees with recent *ab initio* calculations [23]. The feature at -0.3 ppm is due to four-coordinate boron. We studied this feature in detail with ^{10}B NMR (chosen, due to its integer spin and lower gyromagnetic ratio, to accentuate quadrupole effects as much as possible) and found it to be remarkably insensitive not only to the modifier content in the glass, but even to the chemical nature of the modifier (K_2O , Rb_2O , Na_2O etc.) and the physical structure (glass or crystal). The four-fold coordinate sites thus have a very robust structure and NMR shift signature. The three-fold sites are more difficult to assign in the modified glasses, and we turn to this problem in the next section.

A Unified Model for Borate Modification Chemistry As noted above, Raman spectra strongly indicate that the symmetric boroxol ring is modified, presumably being converted to triborate (two three-fold and one four-fold coordinate boron in a ring) and more complex ring structures. Earlier work from our laboratory, using DAS NMR, indicated that substantial modification happens as well at the non-ring BO_3 sites, which we observed in rubidium borate glasses to decrease markedly in intensity as modifier was added [27]. Moreover, the NMR resonance initially assigned to the boroxol ring boron in B_2O_3 decreased only slightly in intensity with added modifier. These observations together suggested an interpretation in contradiction with Raman studies, namely that the ring sites are not modified to any great extent, while the non-ring BO_3 groups are preferentially converted to BO_4^- .

Here we use our more complete data set, which includes both NMR and Raman spectra, to describe a unified model of modification [24]. First, our NMR results (Figure 3) show that the resonance assigned to loose BO_3 units decreases strongly with R ; a fit to the data yields

$$L^3 = 0.35 - 0.75R, \quad (2)$$

where L^3 is the fraction of boron in loose BO_3 units. Likewise, the fraction of boron in all four-fold coordinate sites can be taken as

$$L^4 + Rg^4 = R, \quad (3)$$

where L^4 and Rg^4 are the fractions of boron in loose and ring-bound four-fold sites, respectively. This estimation assumes that each modifier ion produces a single BO_4^- unit, and hence that no non-bridging oxygen are formed. At the modifier concentrations considered here this is a reasonably accurate assumption. Finally, the fraction of three-fold boron in rings of all kinds, Rg^3 , follows from normalization, as

$$Rg^3 = 1 - L^3 - L^4 - Rg^4 = 0.65 - 0.25R. \quad (4)$$

Lines corresponding to the above model are plotted on Figure 3, along with the data, and show reasonable agreement. We assume in this plot that all three-fold coordinate boron in rings have equivalent isotropic shifts, and thus overlap in the resonance at 4.7 ppm. To check this assumption we have examined a variety of crystalline potassium borates, of known structure, and found that the three-fold ring sites are always within 1 ppm of the 4.7 ppm boroxol ring shift.

The above equations give a general model in agreement with our NMR data on the partitioning of the three-coordinate boron between rings and loose units. Our NMR data do not resolve individual modified ring structures, so there are a variety of ways to realize this model. We proceed by assuming that the modified rings include tetraborate and diborate groups, in accord with earlier analyses of alkali borate glasses. Then the glasses are taken to consist of 5 basic units: boroxol rings, tetraborate and diborate units, and loose BO_3 and BO_4^- . To estimate the fractions of these building blocks we need 5 independent constraints. One is provided by normalization, and Eqs. 2 and 3 provide two more. Our Raman data give an estimate of the fraction of boroxol rings. In this data we see the 808 cm^{-1} band decreasing roughly linearly, and vanishing by roughly the composition $R = 0.5$ (this is in reasonable agreement with earlier ^{10}B NMR studies [28,29]). From the NMR data on B_2O_3 we find B^3 , the fraction of boron in boroxol rings, to be 0.65, and so the fraction of boroxol rings themselves is 0.38. The boroxol ring fraction in the modified glass is thus taken as $0.38 - 0.76R$, that is, a linear function that vanishes at $R = 0.5$. Finally, the diborate concentration is taken from Jellison and Bray's results [28], who found that the ratio of boron in diborate groups to boron in rings is roughly zero for $R < 0.1$, and then increases approximately linearly to about 0.68 by $R = 0.5$.

From Eqs. 2, 3, normalization, and the concentrations of boroxol rings and diborate rings, an estimate of the various units in the glasses can be made as a function of composition. Figure 4 shows the results, expressed in terms of the fraction of boron present in each type of site. The relative concentrations of boroxol, tetraborate, and diborate rings are quite similar to earlier determinations [28,29]. Here, however, account is taken explicitly of the loose units, so the concentrations of the ring species are reduced in absolute terms.

The agreement between the ring fractions exhibited in Figure 4 and those obtained in earlier works [28,29] is encouraging because here the only ingredient taken from those works is the diborate concentration. The boroxol ring fraction is set by our Raman results, and the loose 3- and 4-fold fractions by the DAS NMR results. Figure 4 thus represents a model that is consistent with our present high-resolution NMR results on

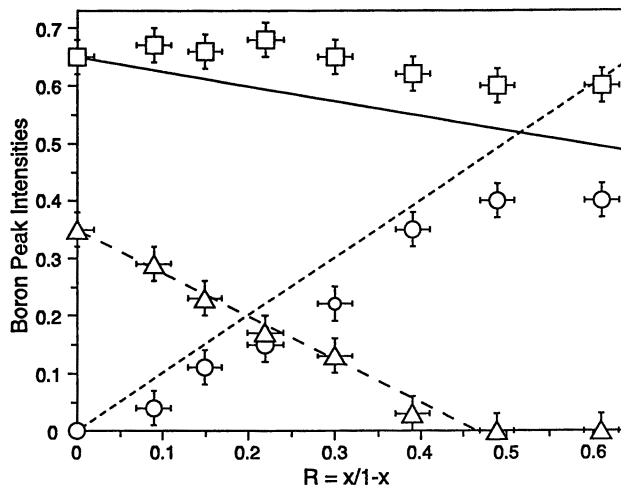


Figure 3. Intensities, obtained from spectral fits, of the three main features in the DAS NMR spectra of ^{11}B in $(\text{K}_2\text{O})_x(\text{B}_2\text{O}_3)_{1-x}$ glasses as a function of $R = x/1-x$, the ratio of modifier to boron oxide concentration. Squares: 4.7 ppm peak. Triangles: 1.0 ppm peak. Circles: -0.3 ppm peak. Solid lines are from the model of Eqs. 2-4. (Reproduced with permission from ref. 24. Copyright 1996 American Chemical Society.)

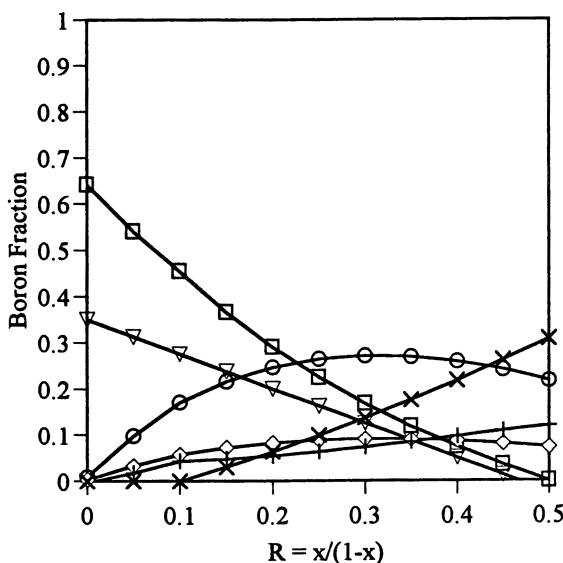


Figure 4. Fraction of boron in each type of site for the model outlined in the text. \square : boroxol rings (B^3); ∇ : loose BO_3 groups (L^3); \circ : 3-coordinate boron in tetraborate groups (T^3); \diamond : 4-coordinate boron in tetraborate (T^4); \times : three- and four-coordinate boron in diborate (D^3 , D^4); $+$: loose BO_4 groups (L^4).

the loose units, Raman spectra of the boroxol rings, and earlier ^{10}B wide-line NMR results on the modified ring fractions.

Conclusions

We have presented results of several studies on borate glass structure, made primarily with high-resolution and multidimensional NMR methods. In pure B_2O_3 glass we have used Double Rotation NMR to probe the oxygen environments, and found that three independent sites could be resolved. We constructed a model to interpret these sites, which suggests that the boroxol rings have a tendency to aggregate in the glass. This would explain the intermediate range order observed in scattering studies in this material.

In potassium borate glasses we were able to follow the modification using two-dimensional Dynamic Angle Spinning NMR. These experiments resolve three sites, assigned to ring, loose BO_3 , and four-fold coordinate boron. The partitioning of the boron among these sites can be modeled in a simple way that is in reasonable agreement with the data. Then, by combining the intensities of these sites with Raman spectra and earlier estimations of the diborate concentration, a full model is developed which gives the concentrations of five structural units as a function of modifier: boroxol rings, tetraborate and diborate groups, and loose BO_3 and BO_4^- groups. The model is consistent with the present DAS NMR data, Raman spectra, and the earlier studies of the modified rings. We believe it to be a significant result in this field, because for the first time the loose units are explicitly included in a structural model. While the majority of boron atoms are present in rings, at low modifier concentrations the majority of structural units are loose BO_3 . Thus taking them into account is important. Finally, the model provides a unified treatment of a variety of different experiments, each capable of probing different elements of the glass structure.

Acknowledgments

This research was supported by the National Science Foundation under Grants DMR-9115787 and DMR-9508625.

Literature Cited

- [1] Uhlmann, D.; Hays, J.; Turnbull, D. *Phys. Chem. Glasses* **1967**, *8*, 1.
- [2] Bril, T. *Philips Res. Rep. Suppl.* **1976**, *2*, 1.
- [3] Hannon, A.; Wright, A.; Blackman, J.; Sinclair, R. *J. Non-Cryst. Solids* **1995**, *182*, 78.
- [4] Hannon, A.; Grimley, D.; Hulme, R.; Wright, A.; Sinclair, R. *J. Non-Cryst. Solids* **1994**, *177*, 299.
- [5] Gravina, S.; Bray, P. J. *J. Magn. Reson.* **1990**, *89*, 515.
- [6] Jellison, Jr., G. E.; Panek, L. E.; Bray, P. J.; Rouse, Jr., G. B. *J. Chem. Phys.* **1977**, *66*, 802.
- [7] Youngman, R. E.; Zwanziger, J. W. *J. Non-Cryst. Solids* **1994**, *168*, 293.
- [8] Youngman, R. E.; Haubrich, S.; Zwanziger, J. W.; Janicke, M.; Chmelka, B. *Science* **1995**, *269*, 1416.

- [9] Soules, T. *J. Chem. Phys.* **1980**, *73*, 4032.
- [10] Soppe, W.; van der Marel, C.; van Gunsteren, W.; den Hartog, H. *J. Non-Cryst. Solids* **1988**, *103*, 201.
- [11] Silver, A.; Bray, P. J. *J. Chem. Phys.* **1958**, *29*, 984.
- [12] Bray, P. J. *J. Non-Cryst. Solids* **1987**, *95 & 96*, 45.
- [13] Chmelka, B. F.; Mueller, K. T.; Pines, A.; Stebbins, J.; Wu, Y.; Zwanziger, J. W. *Nature* **1989**, *339*, 42.
- [14] Mueller, K. T.; Sun, B.; Chingas, G. C.; Zwanziger, J. W.; Terao, T.; Pines, A. *J. Magn. Reson.* **1990**, *86*, 470.
- [15] Grandinetti, P.; Baltisberger, J.; Llor, A.; Lee, Y.; Werner, U.; Eastman, M.; Pines, A. *J. Magn. Reson. A* **1993**, *103*, 72.
- [16] Chmelka, B. F.; Zwanziger, J. W. In *Solid State NMR III*; Blümich, B.; Kosfeld, R., Ed.; NMR Basic Principles and Progress 33; Springer: Berlin, 1994; pp 79-124.
- [17] Meera, B.; Ramakrishna, J. *J. Non-Cryst. Solids* **1993**, *159* (1993), 1.
- [18] Konijnendijk, W.; Stevels, J. *J. Non-Cryst. Solids* **1975**, *18*, 307.
- [19] Kamitsos, E.; Karakassides, M.; Chryssikos, G. *Phys. Chem. Glasses* **1989**, *30*, 229.
- [20] Chryssikos, G.; Kamitsos, E.; Karakassides, M. *Phys. Chem. Glasses* **1990**, *31*, 109.
- [21] Kamitsos, E.; Chryssikos, G.; Karakassides, M. *J. Non-Cryst. Solids* **1990**, *123*, 283.
- [22] Walrafen, G. E.; Samanta, S. R.; Krishnan, P. N. *J. Chem. Phys.* **1980**, *72*, 113.
- [23] Tossell, J. A. *J. Non-Cryst. Solids* **1995**, *183*, 307.
- [24] Youngman, R. E.; Zwanziger, J. W. *J. Phys. Chem.* **1996**, *100*, 16720.
- [25] Bokov, N. A. *J. Non-Cryst. Solids* **1994**, *177*, 74.
- [26] Moynihan, C. T.; Schroeder, J. *J. Non-Cryst. Solids* **1993**, *160*, 52.
- [27] Youngman, R. E.; Zwanziger, J. W. *J. Am. Chem. Soc.* **1995**, *117*, 1397.
- [28] Jellison, Jr., G.; Bray, P. *J. Non-Cryst. Solids* **1978**, *29*, 187.
- [29] Feller, S.; Dell, W.; Bray, P. *J. Non-Cryst. Solids* **1982**, *51*, 21.

Chapter 8

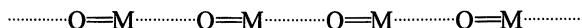
A ^{17}O Solid State NMR Study of the Lead Zirconium Titanate System ($\text{PbZr}_x\text{Ti}_{1-x}\text{O}_3$)

Walter G. Klemperer and David L. Richard

Beckman Institute for Advanced Science and Technology, Frederick Seitz Materials Research Laboratory and Department of Chemistry, University of Illinois at Urbana-Champaign, Urbana, IL 61801

Oxygen-17 NMR spectra of four different lead zirconium titanate (PZT) phases $\text{PbZr}_x\text{Ti}_{1-x}\text{O}_3$ were measured at ambient temperature. Resonances observed for these mixed-metal perovskites appear in distinct chemical shift regions assigned to OTi_2 , OTiZr , and OZr_2 oxygen atoms. Spectra of the orthorhombic and rhombohedral materials are consistent with structural data derived from X-ray diffraction studies in that oxygen centers in markedly different bonding environments display very different chemical shifts. Only one type of bonding environment was observed in the tetragonal materials, in apparent contradiction to X-ray diffraction studies, and this observation is tentatively interpreted in terms of a fluxional (dynamic) structure for the tetragonal phases.

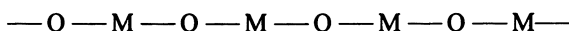
A large family of early transition metal mixed metal oxides having the perovskite structure are polar materials having remarkable electrical, mechanical, and optical properties, and much effort has been devoted to understanding the microscopic origin of their ferroelectric, ferroelastic, and electrooptic behavior (1,2). These materials are cubic and hence nonpolar at elevated temperatures, but undergo a phase transition at the Curie temperature, T_C , to a polar phase, and since the phase transition is associated with the generation of polarity, the nature of this phase transition has been studied exhaustively (3-6). The polarity observed in the low temperature phases arises principally from linear or approximately linear transition-metal-oxygen chains of the type shown in **a**, where short, strong metal-oxygen



a

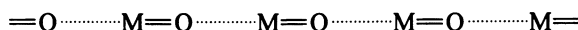
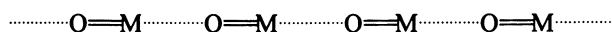
multiple bonds alternate with longer, weaker metal-oxygen bonds. The transition at T_C is observed to proceed with conservation of this metal-oxygen connectivity, and two models have been proposed for the mechanism of this phase transition, a displacive model and an order-disorder model. In the displacive model, the transition metal centers are displaced from their unsymmetric positions in the polar structure **a** to symmetric positions as shown in **b**, and since the chains become

centrosymmetric in this process, the net polarity of the entire array is also lost. In the order-disorder model, the unsymmetrical environments assumed by the transition metal centers and oxygen centers in the low temperature polar phase are retained in the high temperature nonpolar phase, but the structure is fluxional, with the transition metal centers hopping rapidly between equivalent, unsymmetric



b

environments as shown in c. In the dynamic model, the effect of the phase transition on materials properties is the same as with the static displacive model



c

in that the permanent dipole associated with the low temperature phase is eliminated. The dynamic model implies quite different local properties in the high temperature phase, however, in that the unsymmetric bonding environment observed in the low temperature polar phase (see a) is preserved in the high temperature phase (see c).

The preliminary study reported here was undertaken to determine whether solid state ^{17}O NMR spectroscopy might be capable of distinguishing between static and fluxional metal oxide frameworks in early transition metal perovskites. Oxygen-17 NMR chemical shifts are known to be very sensitive to local bonding environments in transition metal oxide compounds (7), and the chemical shifts observed for oxygen nuclei in environments a and b might therefore be quite different. If so, NMR spectra of early transition metal perovskites would allow fluxional structures (see c), to be distinguished from static structures (see b). Such a distinction would in turn allow the phase transitions involved to be identified as displacive transitions or order-disorder transitions. Magnetic resonance spectroscopy has been utilized in a similar fashion to characterize potassium dihydrogen phosphate and structurally-related ferroic materials (8). In this case, the issue of concern is not symmetric vs. unsymmetric oxygen bonding as in a and b but instead, symmetric ($\text{O}\cdots\text{H}\cdots\text{O}$) vs. unsymmetric ($\text{O}\text{---}\text{H}\cdots\text{O}$) hydrogen bonding.

The technologically important lead zirconium titanate (PZT) phases $\text{PbZr}_x\text{Ti}_{1-x}\text{O}_3$ were selected for study for two reasons. First, proven sol-gel procedures are available in the literature that can be adapted for the preparation of PZT samples in ^{17}O -enriched form, a necessary prerequisite for obtaining good ^{17}O NMR signal-to-noise ratios with the low field instrumentation available (9). Second, four different ambient-temperature PZT phases can be prepared by varying the Zr/Ti mole ratio. Phase transformations can therefore be studied at constant temperature by varying only the Zr/Ti mole ratio, thus eliminating the need to separate temperature effects from structural effects. In this sense, the present study complements the temperature-dependent ^{17}O NMR study of BaTiO_3 reported by Spearing and Stebbins (10).

Experimental Section

Lead zirconium titanates $\text{PbZr}_x\text{Ti}_{1-x}\text{O}_3$ were prepared in ^{17}O -enriched form using a modified version of a procedure described by Budd, Dey, and Payne (11-13). In each case, a stock solution 1 M in total titanium plus zirconium concentration was hydrolyzed with an equal volume of a 2-methoxyethanol solution containing 10 atom % ^{17}O -enriched water (2 M) and saturated aqueous ammonia (0.1 M NH_3). The hydrolyzed solutions were allowed to age for 3 days, yielding gels for samples with $x = 0.00 - 0.50$ and sols for $x = 0.53 - 1.00$. Volatiles were then removed *in vacuo*, and the resulting solid materials were dried at 150°C for 10 hours and ground to powders in an agate mortar. Crystalline products were obtained by heat treating these powders in a closed circulating system (14) under 10 atom % ^{17}O -enriched oxygen gas at 650°C for 15 minutes.

All samples were characterized by X-ray powder diffraction using a Rigaku D-max IIIA diffractometer with $\text{CuK}\alpha$ radiation operated at 40kV and 20mA. The powder diffraction data obtained were in good agreement with reported literature values (12,15,16). Oxygen-17 MAS NMR spectra were collected at 40.7 MHz on a General Electric 300 MHz widebore spectrometer using an Otsuka Electronics MAS solid state probe with spinning rates of 5 - 15 KHz.

Results and Discussion

The specific phases examined were $\text{PbZr}_x\text{Ti}_{1-x}\text{O}_3$, $x = 0.00, 0.25, 0.50, 0.53, 0.60, 0.75,$ and 1.00 , phases abbreviated below as PZT(0,100), PZT(25,75), PZT(50,50), PZT(53,47), PZT(60,40), PZT(75,25), and PZT(100,0). Oxygen-17 MAS NMR spectra of the five mixed-metal PZT samples and the two end members of the series, lead titanate and lead zirconate, are shown in Figure 1; ^{17}O NMR chemical shifts are listed in Table I. Each of the compounds studied has the perovskite structure in which every oxygen atom is bonded to two and only two octahedrally coordinated transition metal centers. Three types of oxygen atoms are therefore possible in the mixed-metal phases: OTi_2 oxygen atoms bonded to two titanium atoms, OTiZr oxygen atoms bonded to one titanium atom and one zirconium atom, and OZr_2 oxygen atoms bonded to two zirconium atoms. Comparison of the ^{17}O NMR spectrum of PbTiO_3 with the spectra of the mixed metal PZT phases implies assignment of resonances observed in the 430 to 450 ppm region to OTi_2 oxygen atoms. Since ^{17}O resonances observed for mixed-metal PZT samples in the 360 to 370 ppm region increase in intensity relative to the intensities of the OTi_2 resonances with increasing zirconium content, these resonances are assigned to OZr_2 oxygen atoms. Peaks or shoulders that appear in the intermediate 400 to 415 ppm chemical shift region in the ^{17}O NMR spectra of mixed-metal PZT samples are assigned to OTiZr oxygen atoms. As would be expected for approximately statistical distributions of titanium and zirconium metal centers in the perovskite framework, the intensity of the OTiZr resonance reaches a maximum relative to the intensities of the OTi_2 and OZr_2 resonances at the PZT(50,50) composition where the OTi_2 and OZr_2 resonances have the same intensity. The ^{17}O NMR spectrum of the PbZrO_3 end member differs from the spectra of the other PZT samples examined in that it displays several peaks even though it contains only OZr_2 and no OTi_2 or OTiZr oxygen centers. These resonances are distributed in a reasonably symmetric fashion around the 360 to 370 ppm OZr_2 chemical shift region observed for the mixed metal PZT samples. Note that the ^{17}O chemical shifts observed for OTi_2 and OZr_2 oxygen atoms are in good agreement with those reported for the same types of oxygen atoms in calcium, strontium, and barium zirconates and titanates (10,17). Note also that the samples studied here were crystallized at a relatively low temperature, 650°C . Spectra of materials crystallized at higher temperatures may yield significantly different ^{17}O MAS NMR spectra, a possibility currently under investigation.

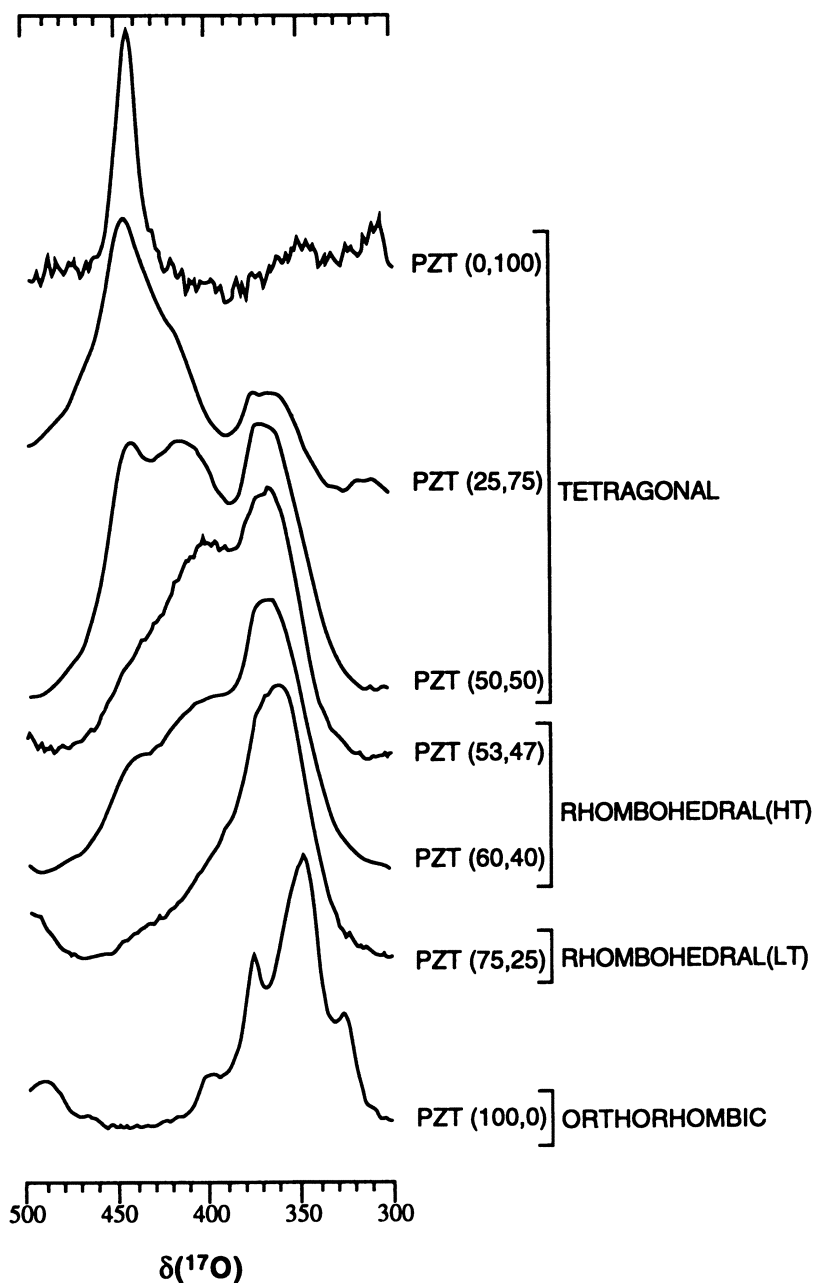


Figure 1. 40.7-MHz ^{17}O MAS NMR spectra of $\text{PbZr}_x\text{Ti}_{1-x}\text{O}_3$, $x = 0.00, 0.25, 0.50, 0.53, 0.60, 0.75,$ and 1.00 . See Table I for chemical shift data.

Four PZT phases have been identified at ambient temperature using X-ray diffraction techniques (18-21), and the phase observed for each of the compositions studied is indicated in Figure 1 and Table I. The bonding environments of the oxygen atoms in each of the four PZT phase domains at ambient temperature are shown in Figure 2 in terms of transition metal to oxygen bond lengths and bond angles at the oxygen centers. These bond lengths and bond angles were obtained using X-ray diffraction techniques, and the distances and angles shown in Figure 2 for the mixed-metal PZT(58,42) and PZT(90,10) phases are average values averaged over the crystallographically disordered zirconium and titanium metal centers. In the two rhombohedral phases, the so-called low temperature (LT) and high temperature (HT) rhombohedral phases, all of the oxygen atoms are crystallographically equivalent, and the ^{17}O NMR spectra of rhombohedral PZT samples shown in Figure 1 each display only three resonances: one OTi_2 , one OTiZr , and one OZr_2 resonance. The chemical shifts observed for each type of oxygen are quite insensitive to changes in composition and are very similar in the rhombohedral HT and LT phases. The unsymmetric oxygen bonding environments in the LT and HT rhombohedral phases are very similar (see Figure 2), and the differences are easily accounted for in terms of a lattice expansion associated with higher zirconium content, given that the atomic radius of zirconium is larger than that of titanium. Turning to the orthorhombic lead zirconate phase, the five different oxygen bonding environments identified in Figure 2d imply five resonances in the ^{17}O NMR spectrum of PZT(100,0). Only four ^{17}O resonances are observed in the PZT(100, 0) spectrum, but the *ca.* 70 ppm range in the chemical shift values

Table I. ^{17}O NMR Chemical Shifts for Lead Zirconium Titanates^a

Composition	Phase	Chemical Shifts ^b		
		OTi_2	OTiZr	OZr_2
PZT(0,100)	Tetragonal	445		
PZT(25,75)	Tetragonal	446	— ^c	368
PZT(50,50)	Tetragonal	443	412	368
PZT(53,47)	Rhombohedral (HT)	— ^c	402	367
PZT(60,40)	Rhombohedral (HT)	434	406	366
PZT(75,25)	Rhombohedral (LT)	— ^c	— ^c	362
PZT(100,0)	Orthorhombic			400 376 349 327

^a Data obtained from the spectra shown in Figure 1. ^b Chemical shifts are given in ppm downfield from water at 25 °C. ^c shoulder.

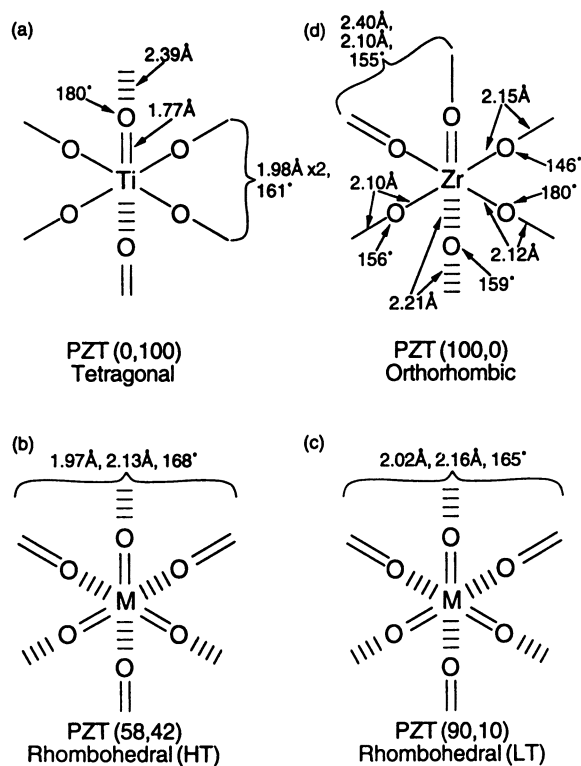


Figure 2. Bond lengths and bond angles at oxygen centers in the transition metal oxide framework of (a) tetragonal PbTiO_3 (17), (b) rhombohedral (HT) $\text{PbZr}_{0.58}\text{Ti}_{0.42}\text{O}_3$ (18), (c) rhombohedral (LT) $\text{PbZr}_{0.90}\text{Ti}_{0.10}\text{O}_3$ (19), and (d) orthorhombic PbZrO_3 (20). Symmetry-equivalent oxygen centers are spanned by braces.

listed in Table I shows that ^{17}O NMR chemical shifts are quite sensitive to differences in oxygen bonding environment. Quite the opposite effect is observed in the case of the other end member of the PZT family, lead titanate, where ^{17}O chemical shifts appear to be relatively insensitive to oxygen bonding environment. In the tetragonal PZT(0,100) structure, one-third of the oxygen atoms are very unsymmetrically bonded to titanium atoms and two-thirds of the oxygen atoms are symmetrically bonded to titanium atoms (see Figure 2a). By analogy with the orthorhombic lead zirconate case, two ^{17}O resonances are anticipated, yet only one relatively sharp resonance is observed (see Figure 1). The same situation prevails for the other tetragonal PZT phases: the ^{17}O NMR spectra of PZT(25,75) and PZT(50,50) shown in Figure 1 display only one OTi₂ resonance, one OTiZr resonance, and one OZr₂ resonance. Moreover, the three resonances observed in the spectra of the tetragonal materials have chemical shifts that are very similar to those observed for the corresponding types of oxygen centers in spectra of the rhombohedral phases (see Table I). The simplest interpretation of this apparent inconsistency is a fluxional metal-oxygen framework for the tetragonal PZT phases (see above). The oxygen bonding environment defined X-ray crystallographically for the symmetrically bonded oxygen centers in the tetragonal PZT(0,100) phase (see Figure 2a) is under these circumstances a time-averaged environment (see c). As a result, the ^{17}O NMR chemical shifts observed for "symmetrically bonded" oxygen atoms *should* be very similar to the ^{17}O NMR chemical shifts observed for the unsymmetrically bonded oxygen atoms in the tetragonal PZT samples. The ^{17}O NMR chemical shifts for both types of OTi₂ oxygen centers in the tetragonal PZT phases are similar and differ only slightly from the ^{17}O NMR chemical shifts of the unsymmetrically bonded OTi₂ oxygen centers in the rhombohedral (HT) and rhombohedral (LT) phases. The same holds true for the ^{17}O NMR chemical shifts of OTiZr and OZr₂ resonances in the tetragonal and rhombohedral phases.

Conclusions

Oxygen-17 MAS NMR spectra of mixed-metal lead zirconium titanates display three resonances at ambient temperature that appear in distinct chemical shift regions associated with doubly-bridging OTi₂, OTiZr, and OZr₂ oxygen centers. Chemical shift arguments based on X-ray crystallographic structural data suggest a fluxional structure for the tetragonal phase and static structures for the rhombohedral and orthorhombic phases. In terms of the phase transitions involved, this interpretation implies an order-disorder model for the rhombohedral/tetragonal phase transition and a displacive model for the rhombohedral/orthorhombic phase transition if the dynamic and static nature of the tetragonal and orthorhombic phases respectively is maintained up to the relevant phase boundaries. These preliminary conclusions are tentative since they are based on chemical shift arguments, and they must be reexamined after a much larger number of different PZT samples have been studied. In this context, we note that the phase behavior of lead zirconium titanates is known to be more complex than the phase diagram based on X-ray diffraction data alone, particularly in the regions near phase boundaries (22,23). Given its ability to resolve chemically and structurally distinct oxygen centers in lead zirconium titanates, ^{17}O NMR spectroscopy promises to be a powerful tool for investigation of local stoichiometry, local structure, metal ordering, lattice dynamics, and phase transitions in these materials and other mixed-metal perovskites.

Acknowledgments

The authors gratefully acknowledge helpful discussions with Professors Dwight Viehland and David Payne. Support was provided by the United States Department of Energy, Division of Materials Science, under contract DEFG02-96ER45439.

Literature Cited

1. Lines, M. E.; Glass, A. M. *Principles and Applications of Ferroelectrics and Related Materials*; Oxford University: Oxford, 1977.
2. Jona, F.; Shirane, G. *Ferroelectric Crystals*; Dover: New York, 1993.
3. Fatuzzo, E.; Merz, W. J. *Ferroelectricity*; Wiley: New York, 1967.
4. Blinc, R.; Zeks, B. *Soft Modes in Ferroelectrics and Antiferroelectrics*; North-Holland: Amsterdam, 1974.
5. Cohen, R. E. *Nature*, **1992**, *358*, 136-138, and references cited therein.
6. Dougherty, T. P.; Wiederrecht, G. P.; Nelson, K. A.; Garrett, M. H.; Jensen, H. P.; Warde, C. *Science*, **1992**, *258*, 770-774, and references cited therein.
7. Day, V. W.; Klemperer, W. G. *Science*, **1985**, *228*, 533-541.
8. Reference 4, Chapter 9, and references cited therein.
9. Melnick, B. M.; Cuchiaro, J. D.; McMillian, L. D.; Paz de Araujo, C. A.; Scott, J. F. *Ferroelectrics*, **1990**, *112*, 329-351.
10. Spearing, D. R.; Stebbins, J. F. *J. Am. Ceram. Soc.*, **1994**, *77*, 3263-3266.
11. Budd, K. D.; Dey, S. K.; Payne, D. A. *Brit. Ceram. Proc.*, **1985**, *36*, 107-121.
12. Lakeman, C. D. E.; Payne, D. A. *J. Am. Ceram. Soc.*, **1992**, *75*, 3091-3096.
13. Li, J.-F.; Viehland, D.; Lakeman, C. D. E.; Payne, D. A. *J. Mater. Res.*, **1995**, *10*, 1435-1440.
14. Kallo, D.; Preszler, I.; Payer, K. *J. Sci. Instrum.*, **1964**, *41*, 338-340.
15. Kakegawa, K.; Mohri, J.; Takahashi, T.; Yamamura, H.; Shirasaki, S. *Solid State Commun.*, **1977**, *24*, 769-772.
16. Lin, C. T.; Scanlan, B. W.; McNeill, J. D.; Webb, J. S.; Li, L.; Lipeles, R. A.; Adams, P. M.; Leung, M. S. *J. Mater. Res.*, **1992**, *7*, 2546-2554.
17. Bastow, T. J.; Dirken, P. J.; Smith, M. E.; Whitfield, H. J. *J. Phys. Chem.*, **1996**, *100*, 18539-18545.
18. Nelmes, R. J.; Kuhs, W. F. *Solid State Commun.*, **1985**, *54*, 721-723.
19. Michel, C.; Moreau, J.-M.; Achenbach, G. D.; Gerson, R.; James, W. J. *Solid State Commun.*, **1969**, *7*, 865-868.
20. Ito, H.; Shiozaki, Y.; Sawaguchi, E. *J. Phys. Soc. Japan*, **1983**, *52*, 913-919.
21. Glazer, A. M.; Roleder, K.; Dec, J. *Acta Crystallogr., Sect. B*, **1993**, *49*, 846-852.
22. Dai, X.; Xu, Z.; Viehland, D. *J. Am. Ceram. Soc.*, **1995**, *78*, 2815-2827.
23. Viehland, D. *Phys. Rev. B*, **1995**, *52*, 778-791.

Chapter 9

Multinuclear NMR Study of Host–Guest Interactions in Sodalites

G. Engelhardt

Institute of Chemical Technology I, University of Stuttgart, D-70550
Stuttgart, Germany

The framework of sodalites consists of a perfectly periodic array of all-space filling $[4^66^8]$ polyhedra (sodalite or β -cages) formed by a network of corner-sharing TO_4 tetrahedra ($T = \text{Si}$ and/or Al). The cages may accommodate a large variety of guest species such as cations, anions, water, or organic molecules. The interactions of the guests with the host framework in aluminosilicate ($T = \text{Si}, \text{Al}$), and silica sodalites ($T = \text{Si}$) are studied by multinuclear solid-state NMR spectroscopy. ^{29}Si and ^{27}Al NMR provide information on the framework structure, and ^{23}Na , ^1H , and ^{13}C NMR is applied to characterise the cage fillings. Structural phase transitions of the host framework and the dynamics of the guest species are studied by variable temperature NMR. The potential of NMR in providing detailed information on the sodalite structure which complements the results of diffraction techniques is demonstrated by selected sodalite compositions containing various cations and anions, water, organic molecules, or paramagnetic Na_4^{3+} clusters as guest species.

The host structure of sodalites consists of a three-dimensional, four-connected tetrahedral framework formed by corner-sharing TO_4 tetrahedra. While sodalite-type frameworks are known for a large variety of T-atoms (e.g., Be, Zn, B, Ga, Ge, P, As, Si, Al), in the present study only *aluminosilicate sodalites* ($T = \text{Si}, \text{Al}$), and *silica sodalites* ($T = \text{Si}$) are considered. Figure 1a shows the basic polyhedral building unit of sodalites known as sodalite cage or β -cage. The T-atoms form $[4^66^8]$ polyhedra (truncated octahedra) which belong to the five Fedorov solids and can be connected to a space-filling array as shown in Figure 1b. The cages may enclathrate a vast variety of cationic, anionic and/or neutral guest species as depicted in one of the cages in Figure 1b by a central anion tetrahedrally surrounded by four cations. Depending on the type and distribution of guest species, sodalites may exhibit unique optical, electronic, magnetic and other interesting properties rendering this class of compounds attractive, e.g., as matrices for metal and semiconductor clusters in the

quantum size regime ("nanocomposites"). Such clusters and other guest species may be formed by selective chemical reactions inside the β -cages and the related "intracage chemistry" has recently found considerable interest.

It is obvious that the specific structure and properties of a certain sodalite composition are strongly affected by the interaction between the host framework and the enclathrated guests. The steric and coordination requirements of the guest species together with Coulomb and Van der Waals interactions or hydrogen bonds are important factors determining the resulting structure. A number of powerful techniques are available to investigate host-guest interactions in sodalites which include x-ray and neutron diffraction, elastic and inelastic neutron scattering, IR and Raman spectroscopy, EXAFS and XANES, and others. A valuable complement to these techniques is solid-state NMR spectroscopy which provides detailed information on the local structure around the respective NMR nucleus (1). The sodalite framework can be studied by ^{29}Si and ^{27}Al NMR, and even ^{17}O NMR may be applied but ^{17}O isotopic enriched materials have to be used rendering this technique expensive and impracticable for routine use. A number of other nuclei are suitable to investigate the guest species, e.g., ^{23}Na for the Na^+ cations, ^1H for H_2O , OH^- and other proton containing species, and ^{13}C for organic molecules. In this paper, solid-state NMR spectroscopy is applied to study selected sodalite compositions comprising *aluminosilicate sodalites* (T = Si, Al) containing mainly Na^+ cations, mono- as well as divalent anions, and paramagnetic Na_4^{3+} clusters, and *silica sodalites* (T = Si only) enclathrating various organic guest species. The work presented here has been carried out in close cooperation with a number of scientists from different laboratories. Their names and locations are given at the beginning of each subchapter.

Aluminosilicate sodalites with diamagnetic guest species

(J.Felsche, P.Sieger, Konstanz, Germany)

The majority of aluminosilicate sodalites have a 1:1 ratio of strictly alternating silicon and aluminum atoms in the framework and possess a cubic structure. The negative charges introduced by the $(\text{AlO}_4)_2^-$ tetrahedra and, if present, by additional guest anions in the sodalite cages are balanced by alkali metal cations, preferably by Na^+ . The general unit cell composition is given by $[\text{Na}_4\text{A}]_2[\text{SiAlO}_4]_6$ for monovalent anions A, and $[\text{Na}_4\text{A}'][\text{Na}_4][\text{SiAlO}_4]_6$ for divalent anions A'. In this notation, the first brackets contain the cage fillings, while the last brackets describe the sodalite framework. Aluminosilicate sodalites can be prepared with a single type of anion or with different anions in the cages (see below). Furthermore, the β -cage can also contain hydroxy groups and/or water molecules according to the general composition $[\text{Na}_{3+n}(\text{OH})_n(\text{H}_2\text{O})_m]_2[\text{SiAlO}_4]_6$ (2).

^{29}Si NMR of the aluminosilicate framework. The ^{29}Si MAS NMR spectra of cubic aluminosilicate sodalites with uniform cage fillings consist of a single narrow line (typical linewidth 0.5 - 2 ppm), indicating the crystallographic equivalence of all Si atoms in the framework. The position of this line, i.e. the ^{29}Si chemical shift, $\delta(\text{Si})$, depends sensitively on the type of guest species within the cages. It has been shown already in earlier work (3) that this dependency is related to changes in the SiOAl bond angles due to expansion or contraction of the β -cages induced by the different space requirements of the cage contents.

Figure 2 presents a plot of $\delta(\text{Si})$ versus the SiOAl bond angle, α , for 33

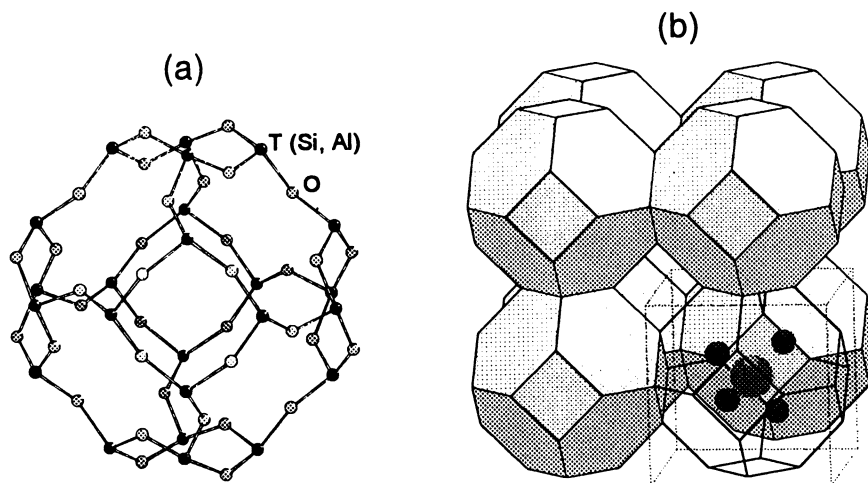


Figure 1. The structure of sodalites. (a) Single sodalite cage, (b) space filling array of sodalite cages (oxygen atoms omitted).

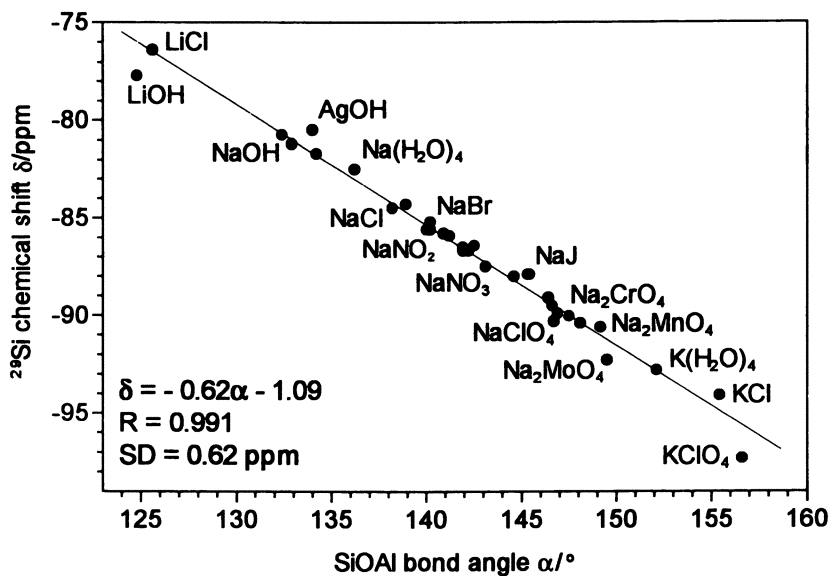


Figure 2. Plot of ^{29}Si chemical shifts versus SiOAl bond angles of aluminosilicate sodalites with different cage contents. The guest species in the β -cages are indicated for selected compositions.

sodalite compositions taken from our own work and from the literature (3, 4, 5, 6). The shift range extends from -76.4 ppm for lithium chloride sodalite to -97.3 ppm for potassium perchlorate sodalite (5), corresponding to a range of α from 125.6° to 156.6°, respectively. The linear correlation between $\delta(\text{Si})$ and α observed previously for a smaller set of data (3) is clearly confirmed: linear regression yields $\delta(\text{Si}) = -0.62\alpha - 1.09$ with a correlation coefficient of 0.991 and a standard deviation of 0.62 ppm. Since, in cubic structures, α is related to the lattice parameter, a_0 , a similar correlation between $\delta(\text{Si})$ and a_0 can be established (3). Both correlations may be used to determine the SiOAl bond angle and the lattice parameter, respectively, from the ^{29}Si chemical shift of any cubic sodalite composition. Applying established geometrical models of the sodalite structure (7), the atomic coordinates of the framework, cation-anion and cation-oxygen distances and other interesting details of the crystal structure of sodalites can be calculated from α and a_0 . Thus, in the unique case of cubic sodalites, the full crystal structure can be determined from a single routine ^{29}Si NMR experiment. Moreover, even for non-cubic sodalites with crystallographic inequivalent Si sites the mean SiOAl bond angle for each of the distinct $\text{Si}(\text{OAl})_4$ environments can be obtained from $\delta(\text{Si})$ of the corresponding lines in the ^{29}Si NMR spectrum.

Similar correlations have been established between the ^{27}Al chemical shift, $\delta(\text{Al})$, of the framework aluminum atoms and the AlOSi bond angles (β). However, since ^{27}Al is a quadrupolar nucleus ($I = 5/2$), $\delta(\text{Al})$ must be carefully corrected for quadrupolar shift contributions.

Sodalites with mixed cage contents. For sodalite compositions with two different types of guest anions the latter may be distributed evenly among the β -cages over the whole structure (forming a "solid solution") or the distinct anions may be separated in two segregated phase domains, each formed by equally filled cages. The former situation generally applies if the size of the different anions is similar and the cage dimensions (and thus the SiOAl bond angles) can adopt an average value satisfying the steric requirements of all guests. In this case, the ^{29}Si MAS NMR spectrum exhibits a single resonance at the average (composition-weighted) chemical shift of the pure sodalite compositions. On the other hand, segregated domains of differently filled β -cages are formed if the two guest anions differ considerably in size and can thus not be accommodated in β -cages of the same dimension. Therefore, two phase domains consisting of cages of different size appear which are characterised by different SiOAl bond angles, and two resonances are to be expected in the ^{29}Si MAS NMR spectrum.

Both situations are exemplified in Figures 3a and 3b by the ^{29}Si MAS NMR spectra of two sodalites of general composition $[\text{Na}_4\text{A}]_{2-x}[\text{Na}_4\text{B}]_x[\text{SiAlO}_4]_6$, with $\text{B} = \text{H}_3\text{O}_2^-$ (the hydrogen dihydroxide anion $[\text{H}-\text{O}-\text{H}-\text{O}-\text{H}]^-$ (8)) for both, and $\text{A} = \text{Br}^-$ (Figure 3a) or ClO_4^- (Figure 3b). The spectra show that the Br^- and H_3O_2^- guest anions are evenly distributed over a single sodalite phase in the former case (single line shifting from $\delta(\text{Si}) = -84.3$ ppm for $x = 2$ to -85.3 ppm for $x = 0.3$, a shift of -85.8 is observed for $x = 0$), while segregated phases of the two sodalites containing either ClO_4^- or H_3O_2^- are formed in the latter case (two resonances of changing intensity, at -84.3 ppm for the H_3O_2^- and at -90.3 ppm for the ClO_4^- sodalite) (4). The differences in $\delta(\text{Si})$ of the pure compositions ($x = 0$ and $x = 2$) corresponds to a similar difference in the lattice parameters which is small ($\Delta a_0 = 0.047$ Å) for the $\text{Br}^-/\text{H}_3\text{O}_2^-$ sodalites

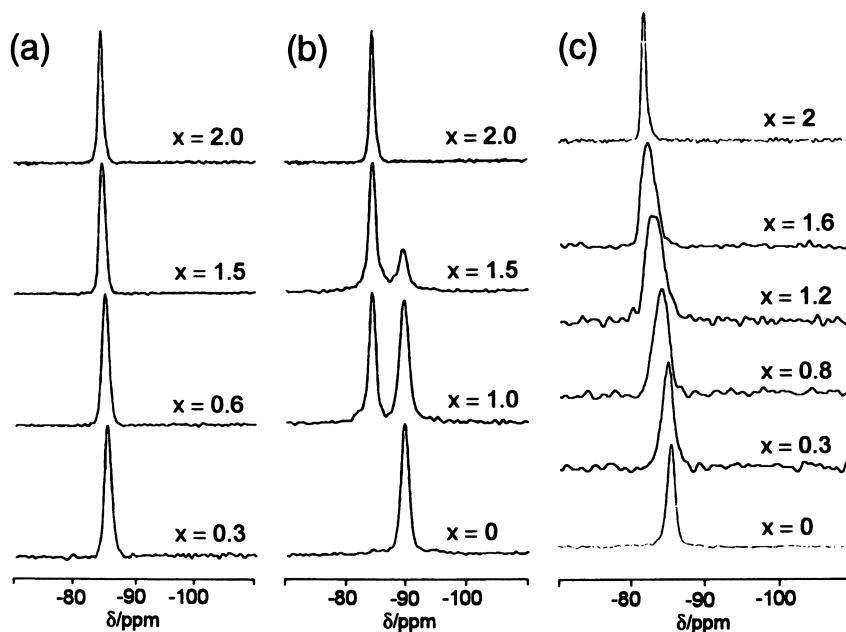


Figure 3. ^{29}Si MAS NMR spectra (79.4 MHz) of sodalites of general composition $[\text{Na}_4\text{A}]_{2-x}[\text{Na}_4\text{B}]_x[\text{SiAlO}_4]_6$ with $x = 0 - 2$. (a) $\text{A} = \text{Br}^-$, $\text{B} = \text{H}_3\text{O}_2^-$, (b) $\text{A} = \text{ClO}_4^-$, $\text{B} = \text{H}_3\text{O}_2^-$, (c) $\text{A} = \text{NO}_2^-$ and $\text{B} = \text{OH}^-$.

but large ($\Delta a_o = 0.192 \text{ \AA}$) for the $\text{ClO}_4^-/\text{H}_3\text{O}_2^-$ sodalites, indicating the considerable expansion of the ClO_4^- containing β -cage which can no longer match the dimensions of the smaller H_3O_2^- filled cages in a single average structure.

The ^{29}Si MAS NMR spectra of another mixed sodalite composition which has $A = \text{NO}_2^-$ and $B = \text{OH}^-$ is shown in Figure 3c. Although in this case the cage dimensions of the pure compositions are rather different ($\Delta\delta(\text{Si}) = 4.2 \text{ ppm}$, $\Delta a_o = 0.178 \text{ \AA}$), a single resonance is observed over the whole composition range which is markedly broadened for the intermediate compositions, i.e., a single but obviously distorted sodalite phase is formed. The reason for this observation is that the mixed $\text{NO}_2^-/\text{OH}^-$ sodalites were prepared by dehydration of the corresponding $\text{NO}_2^-/\text{H}_3\text{O}_2^-$ sodalites in which an even distribution of the distinct cage filling exists ($\Delta\delta(\text{Si}) = 1.3 \text{ ppm}$, $\Delta a_o = 0.040 \text{ \AA}$) and a single narrow ^{29}Si MAS NMR line is observed for all compositions (not shown). Since a redistribution of the guest anions during the dehydration process cannot occur, the original distribution remains and a strained and distorted framework is formed with a distribution of SiOAl bond angles leading to the observed broadening of the ^{29}Si NMR resonances. Applying the above correlation between $\delta(\text{Si})$ and the SiOAl bond angle, the range of the latter in the intermediate compositions can be estimated from the line width and amounts to about 4.5° for the sample with $x = 1.2$.

^{23}Na NMR of the Na^+ cations. ^{23}Na is a quadrupolar nucleus ($I = 3/2$) and thus the quadrupole interaction plays an important role in the ^{23}Na NMR spectra of sodalites. The quadrupole interactions are determined by the charge distribution around the sodium ions, i.e. preferably by the effective charge and geometrical arrangement of the atoms in the first coordination sphere of the sodium cation (9). In sodium aluminosilicate sodalites, the Na^+ ions are located in a tetrahedral arrangement above the center of four of the six-rings of the β -cages (see Figure 1b) and are coordinated to the oxygen atoms of these rings. Further coordinative bonds may be formed to distinct coordination sites of the anions or H_2O molecules in the cages. The specific coordination of the Na^+ ions determines the quadrupole interaction and thus valuable information on the cation location in the β -cages may be derived from the ^{23}Na NMR spectra.

Figure 4 displays two examples with different sodium coordinations. Figure 4a shows the environment of one out of the four Na^+ ions per β -cage in sodium hydroxy sodalite, $[\text{Na}_4\text{OH}]_2[\text{SiAlO}_4]_6$. In this case, Na^+ has four nearest oxygen neighbours with similar Na-O distances, three of the six-ring ($d_{\text{Na-O}} = 2.36 \text{ \AA}$) and another one of the OH⁻ group ($d_{\text{Na-O}} = 2.41 \text{ \AA}$), forming a slightly distorted NaO_4 tetrahedron (10). While for an ideal tetrahedral arrangement the quadrupole interaction vanishes, the symmetry distortion gives rise to a weak interaction, and a second order quadrupole pattern characterised by a quadrupole coupling constant, QCC, of 2.0 MHz appears in the ^{23}Na MAS NMR spectrum. In the anhydrous sodium sodalite, $[\text{Na}_3]_2[\text{SiAlO}_4]_6$, shown in Figure 4b, the sodium environment is very different (11). Since the cage doesn't contain an anion, electrostatic repulsion shifts the Na^+ ions near to the six-ring plane resulting in an almost planar hexagonal NaO_6 coordination with the six oxygen atoms of the six-ring. The strong quadrupole interaction of this planar coordination (9) is clearly reflected by the very broad quadrupole pattern in the ^{23}Na MAS NMR spectrum and the large QCC of 5.9 MHz determined from the spectrum by computer simulation.

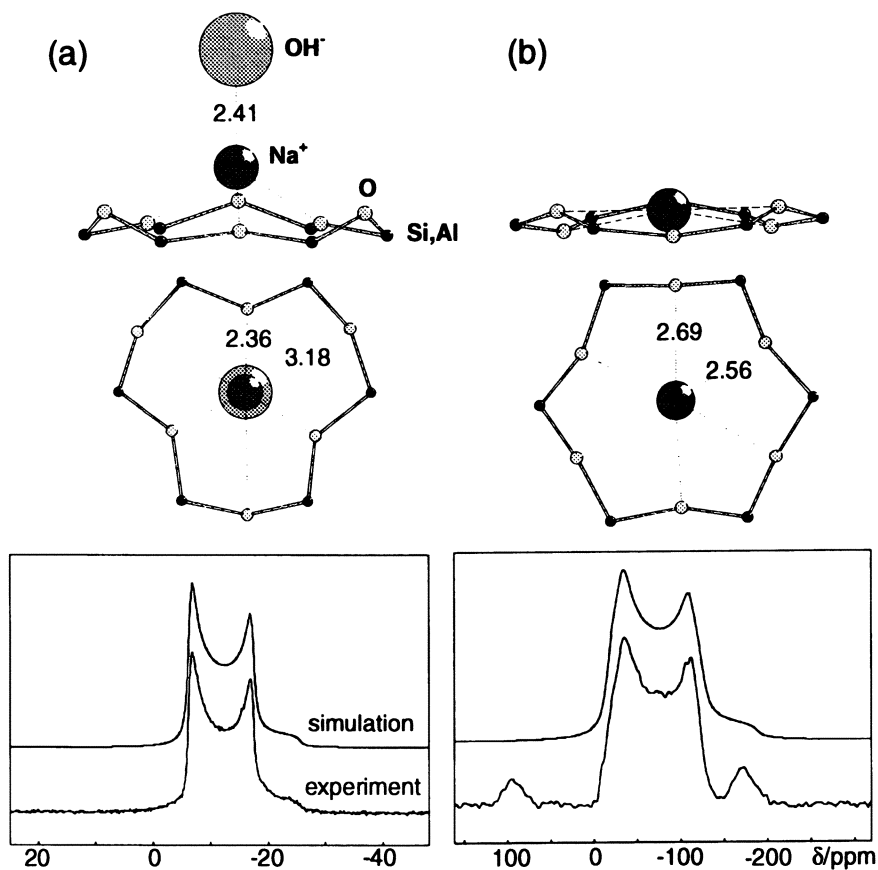


Figure 4. Structural presentation of sodium-oxygen coordinations near the six-ring windows of the β -cages (the Na-O distances are given in Å), and the corresponding experimental and simulated ^{23}Na MAS NMR spectra (105.8 MHz). (a) Sodium hydroxo sodalite, $[\text{Na}_4\text{OH}]_2[\text{SiAlO}_4]_6$, (b) anhydrous sodium sodalite $[\text{Na}_3]_2[\text{SiAlO}_4]_6$.

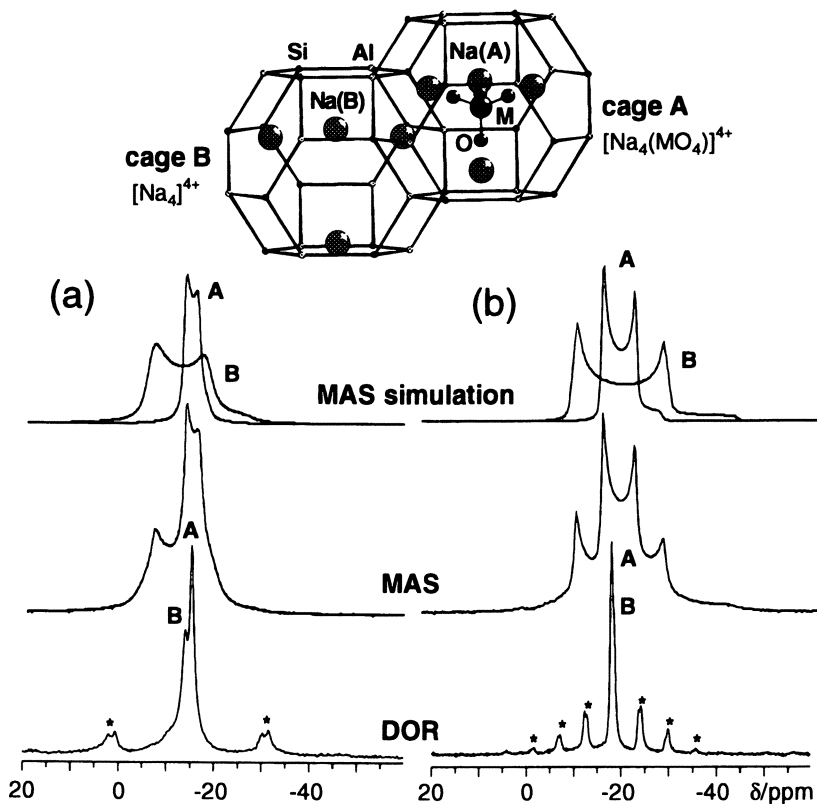


Figure 5. Structural presentation of the two distinct cage contents in sodalites of general composition $[\text{Na}_4(\text{MO}_4)][\text{Na}_4][\text{SiAlO}_4]_6$ with divalent MO_4^{2-} anions, and the ^{23}Na MAS, DOR and simulated spectra (105.8 MHz) of (a) sodium sulphate sodalite ($M = \text{S}$) and (b) sodium chromate sodalite ($M = \text{Cr}$). Asterisks indicate spinning side bands.

A number of other sodium sodalites containing different types of monovalent anions (e.g., Cl^- , Br^- , J^- , NO_2^- , NO_3^- , ClO_4^- , H_3O_2^- , CN^- , SCN^- , HCOO^- , CH_3COO^- , and $\text{B}(\text{OH})_4^-$) have been studied by ^{23}Na NMR, and interesting information on the coordination symmetry of the Na^+ ions could be derived (4). Moreover, in some compositions even dynamic reorientation processes of the guest anions could be characterised by its influence on the quadrupole interaction of the sodium cations measured by ^{23}Na NMR experiments at variable temperature. An interesting case is the sodium borate sodalite, $[\text{Na}_4\text{B}(\text{OH})_4]_2[\text{SiAlO}_4]_6$ (12) which shows a single narrow resonance in the ^{23}Na MAS NMR spectrum above 295 K due to averaging of the quadrupole interaction by fast rotation of the $\text{B}(\text{OH})_4^-$ anion, but exhibits a complex quadrupolar broadened line shape below 290 K where the anion dynamics are frozen. In the DOR (double rotation) spectrum the broad resonance decomposes into four sharp lines of equal intensity indicating the presence of four crystallographically inequivalent sodium sites in agreement with the space group $\text{P}4_2\text{1c}$ suggested for this structure (4, 13).

Sodalites with divalent anions. The structure of sodium aluminosilicate sodalites with divalent MO_4^{2-} anions of general composition $[\text{Na}_4(\text{MO}_4)]_2[\text{Na}_4][\text{SiAlO}_4]_6$, ($\text{M} = \text{S}, \text{Cr}$) contains two alternating types of differently filled β -cages, one type (A) containing the anion and four Na^+ ions, and the another type (B) containing four Na^+ ions only (see Figure 5). Each of the four sodium cations in A-type cages are coordinated to three framework oxygen atoms and to the oxygen atoms of the MO_4^{2-} anion, while the cations in B-type cages interact merely with the framework oxygens, similar to the anhydrous sodalite $[\text{Na}_3]_2[\text{SiAlO}_4]_6$ shown in Figure 4b. According to the discussion in the preceding paragraphs, the ^{23}Na quadrupole interactions should be stronger in the B-type than in the A-type cage. This is clearly visible from the ^{23}Na MAS NMR spectra of sodium sulphate sodalite and sodium chromate sodalite displayed in Figure 5a and 5b, respectively. Two quadrupolar powder pattern appear in each spectrum, one with a strong quadrupole interaction for Na^+ in the B-type cages (QCC = 2.1 MHz for the SO_4^{2-} and 2.6 MHz for the CrO_4^{2-} -sodalite) and the other one with a smaller QCC for Na^+ in the A-type cages (QCC = 1.0 and 1.6 MHz, resp.) (4, 13). In full agreement with this interpretation, the corresponding DOR NMR spectra (shown in Figure 5 below the MAS spectra) exhibit two partially overlapping narrow lines at the centers of gravity of the MAS lines.

Aluminosilicate sodalites with paramagnetic Na_4^{3+} clusters.

(V.I.Srdanov, P.Sieger, G.Stucky, Santa Barbara, USA; M.Feuerstein, O.Groeger, Stuttgart, Germany, D.Markgraber, Graz, Austria)

When anhydrous sodalite of composition $[\text{Na}_3]_2[\text{SiAlO}_4]_6$ is exposed to sodium vapour, each sodalite cage can absorb an additional sodium atom which is spontaneously ionised and shares its electron with the three Na^+ ions already present in the cage, thus forming a paramagnetic $(\text{Na}^+)_4e^- \equiv \text{Na}_4^{3+}$ cluster (14). In these structures, the unpaired electron replaces the negative anion in the cages and the name *sodium electro sodalite* (SES) is adopted for the composition $[\text{Na}_4]_2[\text{SiAlO}_4]_6$, in accordance with the common nomenclature. If all cages are filled with Na_4^{3+} clusters, a highly regular bcc lattice of unpaired electrons (akin to F-centers in ionic solids) is formed with an electron-electron distance of 7.69 Å and an electron spin density as

high as 3×10^{21} spins/cm³. The latter value is much higher than the F-center concentration reached so far in ionic solids and is close to the Mott criterion for the insulator-metal transition (15). Materials of this kind are of high interest due to their structural, optical, electronic, and magnetic properties and are subject of intense theoretical and experimental investigations (16).

The ²⁷Al and ²⁹Si MAS NMR spectra of an almost fully loaded (96%) and a partially doped (76%) SES are displayed in Figure 6. These spectra differ strikingly from those of the sodalites with diamagnetic guests in that additional resonances appear in the δ -range between 70 and 140 ppm for ²⁷Al and between -77 and -13 ppm for ²⁹Si (17). Lines in this range have never been observed before for any sodalite or other aluminosilicate and are caused by paramagnetic shifts due to the interaction of the ²⁷Al and ²⁹Si nuclei with the unpaired electrons associated with the Na₄³⁺ clusters. The size of the paramagnetic shift depends on the number of β -cages containing paramagnetic Na₄³⁺ (designated A-type cages) and diamagnetic Na₃³⁺ units (B-type cages) surrounding the respective T-atom. Since in the sodalite structure each T-atom is part of four β -cages, up to five different nearest T-environments of type [nA(4-n)B] with n = 0-4 can appear. Due to the high concentration of Na₄³⁺ filled A-cages in the 96% loaded sample, the strong resonance at lowest field (line 4) has to be attributed to the [4A0B] environment, and the very weak resonance at highest field ($\delta(\text{Al}) = 62$ ppm, $\delta(\text{Si}) = -87$ ppm) originates from residual [0A4B] environments (line 0). Due to the lower sodium loading, three additional lines can be identified in the 73% loaded sample (17) which are attributed to T-atoms in [3A1B] (line 3), [2A2B] (line 2), and [1A3B] environments (line 1), respectively. The weak lines at high field are assumed to originate from T-atoms in [0A4B] surroundings with one (line 0') or two (line 0'') second-nearest A-type cages. Table I summarises the paramagnetic ²⁷Al and ²⁹Si shifts, $\Delta\delta = \delta(n) - \delta(0)$, of the seven lines observed in the 73% loaded sample.

Table I. Paramagnetic shifts, $\Delta\delta$, Fermi contact coupling constants, A_N , and unpaired electron spin densities, $|\Psi(0)|^2$, of Al and Si atoms in 73% sodium loaded SES

No. (type)	²⁷ Al			²⁹ Si		
	$\Delta\delta/\text{ppm}$	A_N/MHz	$ \Psi(0) ^2 \cdot 10^4/\text{a.u.}$	$\Delta\delta/\text{ppm}$	A_N/MHz	$ \Psi(0) ^2 \cdot 10^4/\text{a.u.}$
0 (0A4B)	0	0	0	0	0	0
0' (0A4B)'	7	0.084	0.72	5	0.046	0.52
0'' (0A4B)''	14	0.187	1.61	12	0.122	1.38
1 (1A3B)	32	0.445	3.83	30	0.320	3.60
2 (2A2B)	53	0.764	6.57	49	0.538	6.07
3 (3A1B)	66	1.070	9.22	61	0.756	8.51
4 (4A0B)	74	1.290	11.10	69	0.919	10.35

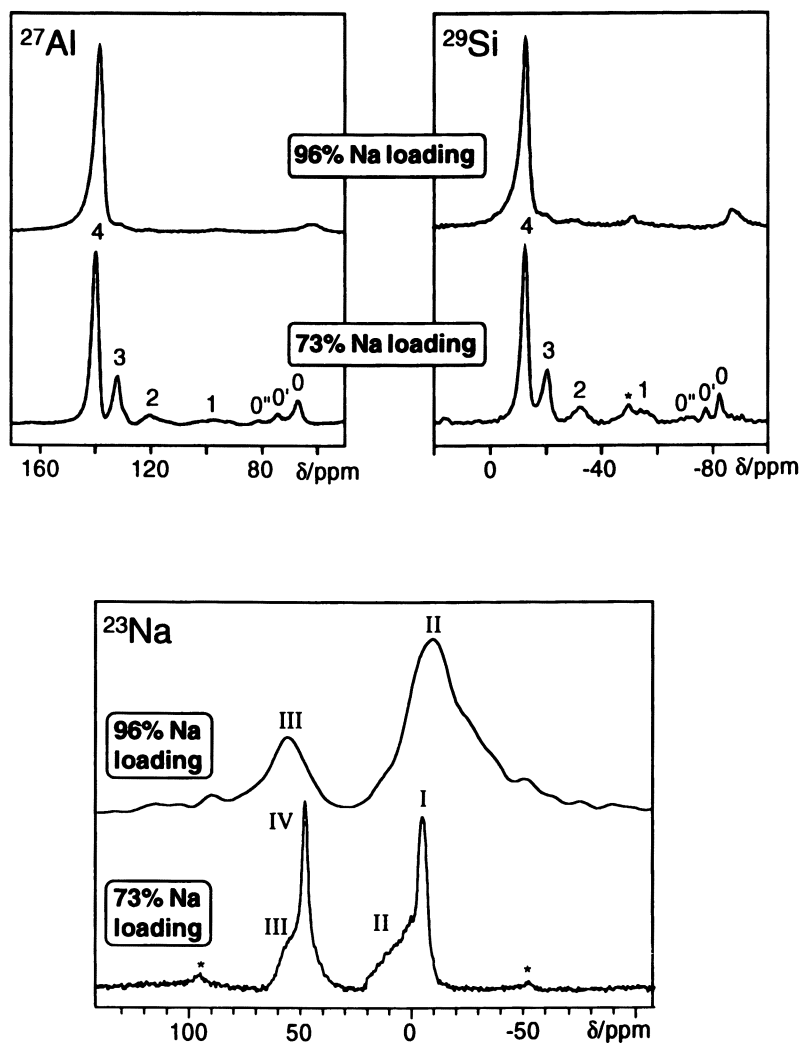


Figure 6. ^{27}Al (104.3 MHz), ^{29}Si (79.5 MHz), and ^{23}Na (105.8 MHz) MAS NMR spectra of sodium electro sodalites with different degree of sodium loading. The designations of the lines are explained in the text.

From the relative integrated line intensities, I_n , the percentage of A-type cages, i.e. the degree of sodium loading, can be estimated according to $\%A = 100 \sum 0.25 n I_n / \sum I_n$. As to be expected for paramagnetic shifts, variable temperature ^{27}Al MAS NMR experiments in the region between 100 K and 360 K reveal a pronounced temperature dependence of the line positions which is maximum for line 4 ($\delta(\text{Al}) = 191$ ppm at 100 K), decreases from line 3 to line 0', and vanishes for line 0. The temperature dependence follows the Curie-Weiss law (with a anomalously large negative Weiss-temperature of about -200 K for line 4 which gradually decreases for the other lines) indicating mutual exchange interactions of the unpaired electron spins.

It is well known that paramagnetic NMR shifts may be due to isotropic Fermi contact interactions and/or dipolar pseudocontact interactions. There are strong arguments to conclude that the Fermi contact interaction predominates in the SES materials (e.g., isotropic electronic g-factors from ESR (18), weak spinning side bands in the MAS NMR spectra, temperature independent NMR line widths). For a given temperature, the Fermi contact shift is proportional to the hyperfine coupling constant, A_N , which is usually obtained from ESR experiments. However, due to exchange narrowing, the ESR spectra of highly doped SES samples show only a single narrow line which renders the direct determination of A_N impossible. It seems thus important that this parameter can be calculated from the paramagnetic NMR shifts. The magnitude of A_N estimated from the shifts of the various resonances in the ^{27}Al and ^{29}Si NMR spectra of SES increases from line 0' to line 4 and is collected in Table I. Moreover, since A_N is related to the unpaired electron density at the interacting nucleus, $|\Psi(0)|^2$, this quantity can also be estimated from the NMR spectra and increases from about $4 \cdot 10^{-4}$ a.u. for T-atoms in [1A3B] environments to about 10^{-3} a.u. for the [4A0B] environments (see Table I).

In the ^{23}Na MAS NMR spectra of the partially and fully loaded SES samples, the resonance of the sodium in the Na_4^{3+} cluster could not be observed, obviously due to excessive paramagnetic broadening. However, as shown in the lower part of Figure 6, several other resonances appear in the ^{23}Na MAS NMR spectra which are attributed to Na^+ in undoped domains (line I), Na^+ in B-cages surrounded by other nearest B-cages but second- nearest A-cages (line II), and Na^+ in B-cages adjacent to A-cages (line III). The latter two resonances are broad and shift downfield with lowering the temperature, similar to the ^{27}Al resonances. In addition, a narrow line at about 50 ppm (line IV) is observed in the 73% loaded sample which is temperature independent and disappears after brief exposure of the sample to air. This resonance is assumed to originate from some diamagnetic surface sodium species. In the fully loaded sample a further resonance appears at 1123 ppm (not shown), typical of the Knight shift of excess metallic sodium at the crystallite surface.

Silica sodalites.

(P.Behrens, G.van de Goor, C.Braunbarth, Konstanz, Germany)

Different from the aluminosilicate sodalites considered in the preceding chapter, the framework of silica sodalites is electroneutral and hydrophobic, i.e. no guest cations for charge compensation or water molecules are present in the cages. It has been shown, however, that a number of neutral organic molecules which act as structure directing agents in the synthesis of silica sodalites can be enclathrated in the β -cages. So far five silica sodalites with different guest molecules have been prepared which

are ethylene glycol silica sodalite (EGSS) (19), ethanol amine silica sodalite (EASS), ethylene diamine silica sodalite (EDSS) (20), 1,3,5-trioxane silica sodalite (TRSS) (21), and 1,3-dioxolane silica sodalite (DISS) (22). The interactions between the neutral guest molecules and the sodalite framework are generally weak and restricted to dipole-dipole interactions, weak hydrogen bonds, and Van der Waals contacts. Nevertheless, these interactions are strong enough to induce specific changes in the geometry and symmetry of the host framework and may influence the conformations and dynamics of the guest molecules. Again, ^{29}Si MAS NMR has considerable potential to characterize subtle changes in the framework structure, while ^{13}C and ^1H MAS NMR are the suitable techniques to study the structural properties of the guest molecules.

At 300 K a single sharp line (typical linewidth 0.2 - 0.5 ppm) is observed in the ^{29}Si MAS NMR spectra for each of the five silica sodalites mentioned above, indicating that all framework Si atoms are crystallographically equivalent. This is in agreement with the cubic symmetry derived from XRD. The chemical shifts, $\delta(\text{Si})$, are collected in Table II, they show characteristic differences reflecting different SiOSi bond angles, α . The latter can be calculated by applying the previously established correlation between $\delta(\text{Si})$ and α of silica frameworks (23) and are also given in Table II, together with the maximum bond angle (24) and chemical shift to be expected for a fully expanded sodalite framework.

Table II. ^{29}Si chemical shifts, $\delta(\text{Si})$, and calculated SiOSi bond angles, α , of silica sodalites (20)

	TRSS	DISS	EGSS	EASS	EDSS	<i>fully exp.</i>
δ/ppm	-116.3	-117.9	-116.8	-118.0	-118.4	-117.8
$\alpha/^\circ$	157.1	161.0	158.3	161.3	162.4	160.5

It follows from the data of Table II that the frameworks of DISS, EASS and EDSS are fully expanded (α close to α_{max}), while those of TRSS and EGSS are partially collapsed (α smaller than α_{max}). It is of interest, that the partially collapsed structure of EGSS could not be derived from single crystal XRD data (25) since the distinction between the related space groups $\text{Im}\bar{3}\text{m}$ for the fully expanded and $\text{I}\bar{4}3\text{m}$ for the partially collapsed structures (24) turned out to be impossible due to dynamic disorder of the framework oxygen atoms.

At lower temperature the ^{29}Si MAS NMR spectra of TRSS and DISS exhibit only some small shifts and broadenings of the single lines, whereas the spectra of EGSS, EASS and EDSS change dramatically. As shown in Figure 7, the single lines observed at 300 K split reversibly into two or three resonances at lower temperatures, which indicates the presence of crystallographically inequivalent Si-sites, i.e. structural phase transitions from cubic to lower crystallographic symmetry. Reversible temperature dependent phase transitions were also detected by DSC and variable temperature XRD measurements (20) of EGSS, EASS and EDSS, and the transition temperatures are in the same range as those of the pronounced changes observed in

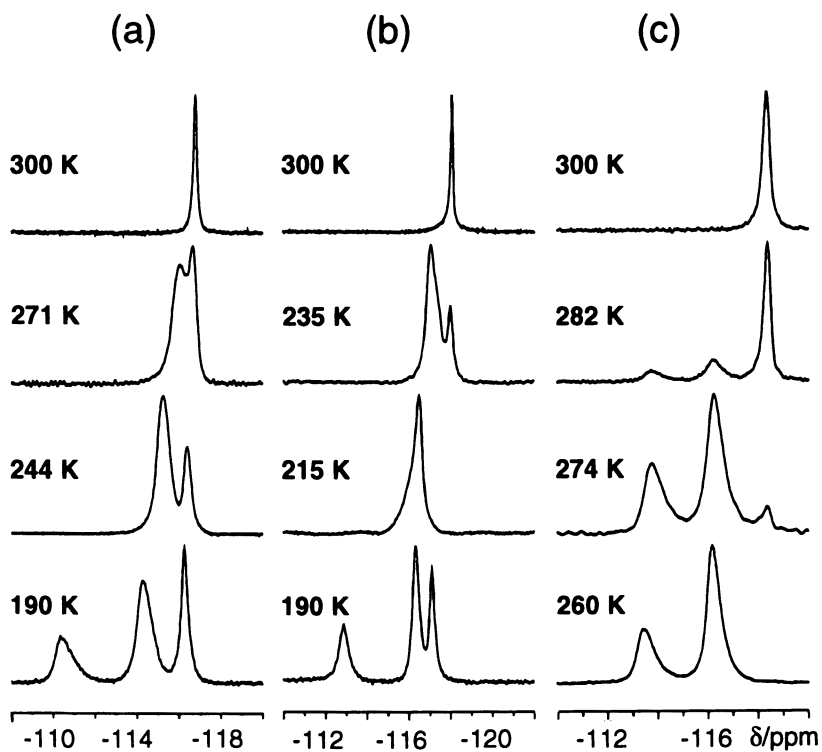


Figure 7. ^{29}Si MAS NMR spectra (79.5 MHz) at variable temperature of silica sodalites containing (a) ethylene glycol, (b) ethanol amine, and (c) ethylene diamine as guest molecules.

the ^{29}Si MAS NMR spectra. The DSC peaks appear at 276, 223 and 187 K for EGSS, 256, 223 and 195 K for EASS, and 269, 135 and 122 K for EDSS, the latter two being outside the temperatures applied in the MAS NMR experiments. These transition temperatures were related by XRD to symmetry changes from cubic to monoclinic to triclinic for EGSS, and from cubic to tetragonal for EDSS (at 269 K). In the case of EASS, XRD indicates a transition from cubic to lower symmetry below 256 K but, surprisingly, cubic symmetry is restored in the range of 223 K to 195 K, while below 195 K the symmetry changes again to non-cubic (20). This observation is clearly confirmed by the ^{29}Si MAS NMR spectra of EASS which show two respectively three lines (non-cubic structures) at 235 K and 190 K but a single line (cubic structure) at 300 K and 215 K. For further XRD structure refinements of the various non-cubic phases it may be important that ^{29}Si MAS NMR provides quantitative information on the number (equal to the number of lines) and relative populations (from line intensities) of inequivalent Si-sites as well as their mean Si-O-Si bond angles (from chemical shifts).

^1H and ^{13}C MAS NMR studies have proved that the organic guest species are enclathrated in the β -cages of silica sodalites as intact molecules over the whole temperature range (20, 22). In general, the spectra are very similar to those measured for the corresponding compounds in solution which indicates fast dynamic reorientation of the guest species. Small and temperature dependent line shifts are often observed due to Van der Waals interactions with the surrounding framework walls or weak hydrogen bonds to framework oxygen atoms. At low temperatures the mobility of the guest molecules may be restricted resulting in characteristic shifts and broadenings of the ^1H and ^{13}C resonances. In certain cases, detailed information on the molecular dynamics can be derived from the temperature dependent changes of the spectra. As an example, Figure 8 shows the ^1H MAS NMR spectra of the trioxane molecule in TRSS at various temperatures. At 307 K a single narrow line is observed at 5.1 ppm indicating fast ring inversion of the trioxane molecule in the NMR time scale. With decreasing temperature the line becomes broader and splits below about 280 K into two lines for the axial and equatorial protons, a clear indication that the inversion process is frozen at low temperature. From an Arrhenius plot the activation energy for the inversion is estimated to $55 \pm 5 \text{ kJmol}^{-1}$ which is about 10 kJmol^{-1} larger than that measured for the trioxane molecule in solution (26). This increase in the conformational stability of the trioxane molecule if occluded in the β -cage may be explained by weak hydrogen bonds between the equatorial hydrogen atoms and the framework oxygen atoms which follow from a recent Rietveld refinement of the powder neutron diffraction data (25).

Conclusions

The results presented above demonstrate that multinuclear solid-state NMR provides important and detailed information on the local structure and host-guest interactions of sodalites. Because NMR spectroscopy is an element-selective technique, the atoms of the sodalite host framework (Si, Al) and those of the guest species, e.g., charge compensating cations (Na^+) or organic guest molecules (C, H), can be studied separately. NMR measurements at variable temperature yield additional information on structural phase transformations and dynamic processes of the guest molecules. Thus, solid-state NMR is a valuable complement to diffraction techniques probing the

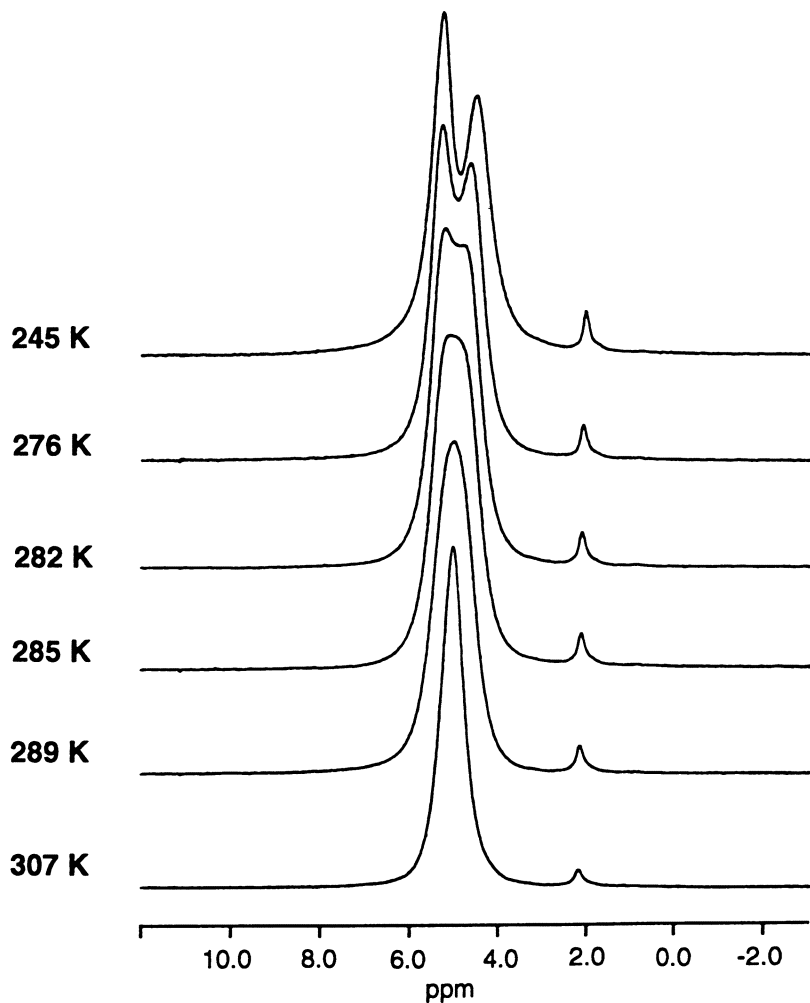


Figure 8. ^1H MAS NMR spectra (400.13 MHz) at variable temperature of trioxane silica sodalite. The weak line at about 2 ppm originates from an impurity.

periodical long-range structure. The examples considered in this study show clearly that the combination of both the local (from NMR) and long-range (from XRD) structural information is a prerequisite for the detailed and thorough analysis of the complex structural properties of sodalites and other host-guest systems.

References

1. Engelhardt, G.; Michel, D. *High-Resolution Solid-State NMR of Silicates and Zeolites*; John Wiley & Sons: Chichester, U.K., 1987
2. Engelhardt, G.; Felsche, J.; Sieger, P. *J. Am. Chem. Soc.* **1992**, *114*, 1173.
3. Engelhardt, G.; Luger, S.; Buhl, J. Ch.; Felsche, J. *Zeolites* **1989**, *9*, 182.
4. Engelhardt, G.; Sieger, P.; Felsche, J. *Anal. Chim. Acta* **1993**, *283*, 967.
5. Brenchley, M. E.; Weller, M. T. *Zeolites* **1994**, *14*, 682.
6. Jacobsen, H. S.; Norby, H.; Bildsoe, H.; Jakobsen, H. J. *Zeolites* **1989**, *9* 491.
7. Hassan, I.; Grundy, H.D. *Acta Cryst.* **1984**, *B40*, 6.
8. Wiebcke, M.; Engelhardt, G.; Felsche, J.; Kempa, B. P.; Sieger, P.; Schefer, J.; Fischer, P. *J. Phys. Chem.* **1992**, *96*, 392.
9. Koller, H.; Engelhardt, G.; Kentgens, A.; Sauer, J. *J. Phys. Chem.* **1994**, *98*, 1544
10. Luger, S.; Felsche, J.; Fischer, P. *Acta Cryst.* **1987**, *C43*, 1.
11. Felsche, J.; Luger, S.; Baerlocher, Ch. *Zeolites* **1986**, *6*, 367.
12. Buhl, J.C.; Engelhardt, G.; Felsche, J. *Zeolites* **1989**, *9*, 40.
13. Engelhardt, G.; Koller, H.; Sieger, P.; Depmeier, W.; Samoson, A. *Solid State Nucl. Magn. Reson.* **1992**, *1*, 127.
14. Barrer, R. M.; Cole, J. F. *J. Phys. Chem. Solids* **1968**, *29*, 1755.
15. Mott, F. N. *Metal-Insulator Transition*; Taylor & Francis: London, 1990.
16. Srdanov, V. I.; Blake, N. P.; Markgraber, D.; Metiu, H.; Stucky, G. D. *Stud. Surf. Sci. Catal.* **1992**, *85*, 115.
17. Engelhardt, G.; Feuerstein, M.; Sieger, P.; Markgraber, D.; Stucky, G. D.; Srdanov, V. I. *J. Chem. Soc. Chem. Commun.* **1996**, 729
18. Breuer, R. E. H.; de Boer, E.; Geismar, G. *Zeolites* **1989**, *9*, 336.
19. Bibby, D. M.; Dale, M. P. *Nature* **1985**, *317*, 157.
20. Braunbarth, C. M.; Behrens, P.; Felsche, J.; van de Goor, G.; Wildermuth, G.; Engelhardt, G. *Zeolites* **1996**, *16*, 207.
21. Keijsper, J.; den Ouden, C.; Post, M. *Stud. Surf. Sci. Catal.* **1989**, *48B*, 237
22. van de Goor, G.; Behrens, P.; Felsche, J. *Microporous Mater.* **1994**, *2*, 493
23. Engelhardt, G. *Stud. Surf. Sci. Catal.* **1989**, *52*, 151.
24. Depmeier, W. *Acta Cryst.* **1984**, *B40*, 6.
25. van de Goor, G. *PhD Thesis*, University of Konstanz, Germany, **1995**.
26. Pedersen, B. *Acta Chem. Scand.* **1968**, *22*, 1705.

Chapter 10

Investigation of the Host–Guest Structures of Molecular Sieves by One- and Two-Dimensional Solid-State NMR Techniques

C. A. Fyfe, A. C. Diaz, A. R. Lewis, J. M. Chézeau, H. Grondey,
and G. T. Kokotailo

Department of Chemistry, University of British Columbia, Vancouver, British
Columbia V6T 1Z1, Canada

One of the most important characteristics of molecular sieve systems is the size and shape selectivity they display towards organic molecules. Unfortunately, it is very difficult to obtain detailed, reliable structures for these host/guest systems to properly understand the details of the interactions because of the lack of large enough single crystals for single crystal diffraction experiments. In this lecture we will outline the development of a protocol to use one and two dimensional NMR experiments to determine these structures which should be of general applicability.

A most important characteristic of molecular sieve systems which is common to their applications as catalysts, sorbents and in gas separations is the size and shape selectivity toward adsorbed organic molecules conferred by the molecular dimensions of their channel and cage systems (1-4). Because of their small crystallite dimensions, powder rather than single-crystal XRD techniques must be used for structure determinations. While it is possible to define framework topologies and structures with powder X-ray diffraction, particularly if Rietveld analysis and synchrotron radiation are used (5,6), it is very difficult to reliably determine the structures of organic sorbate/framework complexes which would yield important information on the detailed nature of the interactions. Important exceptions in this regard are the single crystal XRD studies of van Koningsveld and co-workers who determined detailed high-quality structures of the high-loaded forms of p-xylene and p-dichlorobenzene in zeolite ZSM-5 (7,8). These are the most reliable zeolite/sorbate structures to date.

In recent years high resolution solid state NMR has emerged as an important technique complementary to XRD in the investigation of zeolite structures, being particularly sensitive to short to medium range geometries and orderings (9). For some time we have worked to develop new approaches to the investigation of zeolite

structures by combining solid-state NMR techniques and XRD studies with the aim of ultimately being able to determine the 3-D structures of their complexes with sorbed organic molecules by NMR. In this paper, we outline the development of these techniques and their current standing.

Results and Discussion

In high-resolution solid state NMR, the widths of the signals from dilute spin-1/2 nuclei are determined by the degree of crystallinity and the perfection of the local ordering. This can be achieved in the case of zeolites by investigating high-quality, completely siliceous systems where there is only the Si(4Si) local environment present. As illustrated in Figure 1 for (a) ZSM-12 (10) and (b) ZSM-5 (11), sharp resonances are now observed whose numbers and relative intensities reflect the number and occupancy of the crystallographically inequivalent T-sites in the unit cell. In the case of AlPO_4 materials, there is exact alternation of Al and P giving completely and perfectly ordered frameworks in the as-synthesized materials. This effect is quite general for perfectly crystalline and ordered solids.

These spectra may be used to monitor various structural transformations, for example, those induced by temperature as in the case of ZSM-5 (12,13), or in the case of AlPO_4 materials by the hydration/dehydration of octahedral Al sites. Of particular importance, they yield information on the interaction of organic sorbates with the molecular sieve framework. For example, Figure 2c shows the ^{29}Si spectrum of ZSM-5 with p-xylene present at a loading of two molecules per unit cell (u.c.). Comparison with Figure 1b shows that the number of T-sites has decreased from 24 to 12 indicating a change in symmetry from monoclinic to orthorhombic induced by the absorption of the organic molecules. Further, the similarities between the spectra of ZSM-5 in the presence of p-xylene and p-dichlorobenzene and p-chlorotoluene (Figure 2) indicate that the interactions, at least in this case, are based on the size and shape of the organic molecule since the CH_3 and Cl substituents have the same steric factors but the molecules differ in most other aspects (14). The difficulty in using these spectra further is that the assignment of the resonances to the different T-sites is generally not known, although there may be some information from the intensities if the site occupancies are different. In the case of ZSM-12 and ZSM-5, all of the site occupancies are the same and no assignments are possible.

This problem can be solved by using two dimensional homonuclear correlation experiments, such as COSY and INADEQUATE, to establish the three-dimensional (Si-O-Si) connectivity pattern within the framework when the topology is known (15). Figure 3 shows such an experiment on ZSM-12 (10). These experiments yield the assignments of the resonances shown in Figure 3. The above experiments are based on the scalar $^{29}\text{Si}/^{29}\text{Si}$ J-coupling which operates through the bonding network. Knowledge of the assignments may now be used to gain additional information on the details of the structures and the various changes which they can undergo.

The last step in the extension of these solid state NMR techniques is to apply them to the investigation of the three dimensional structures of zeolite-sorbate

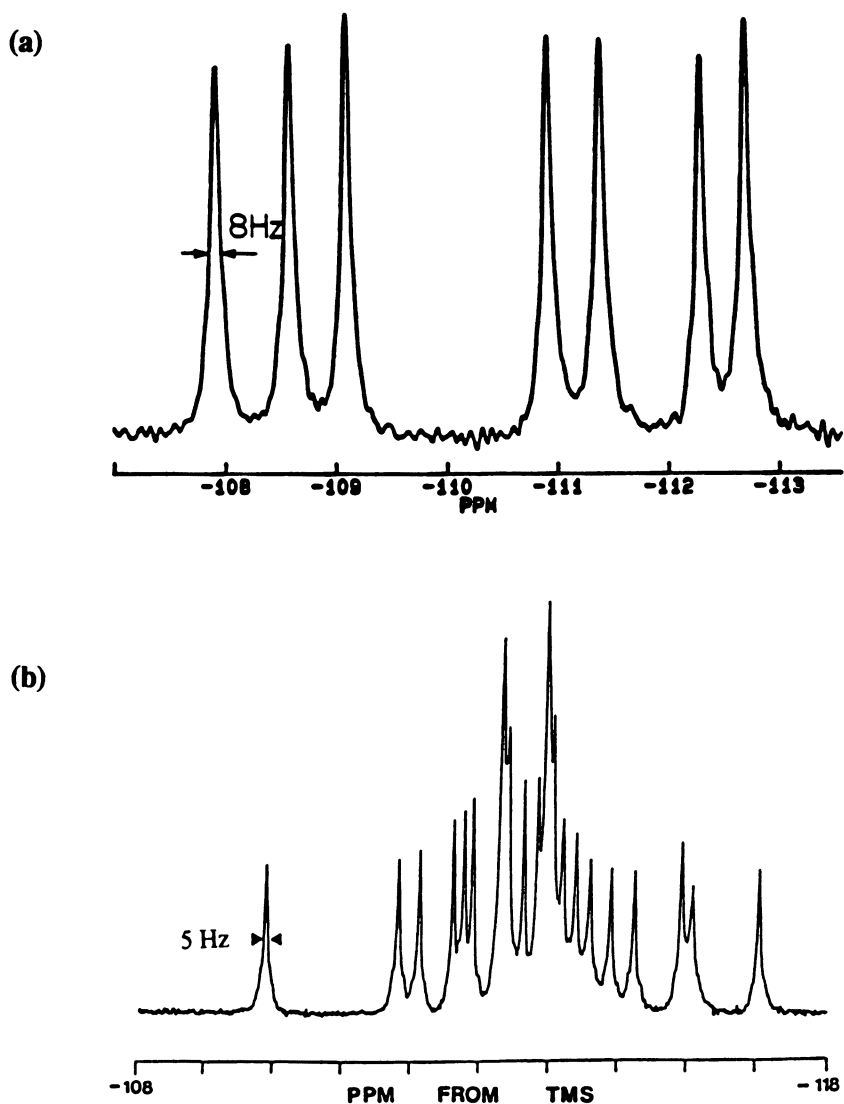


Figure 1. (a) ^{29}Si MAS NMR spectrum of ZSM-12. Reproduced with permission from ref. 10. Copyright 1990 American Chemical Society. (b) ^{29}Si MAS NMR spectrum of ZSM-5. Reproduced with permission from ref. 11. Copyright 1988 American Chemical Society.

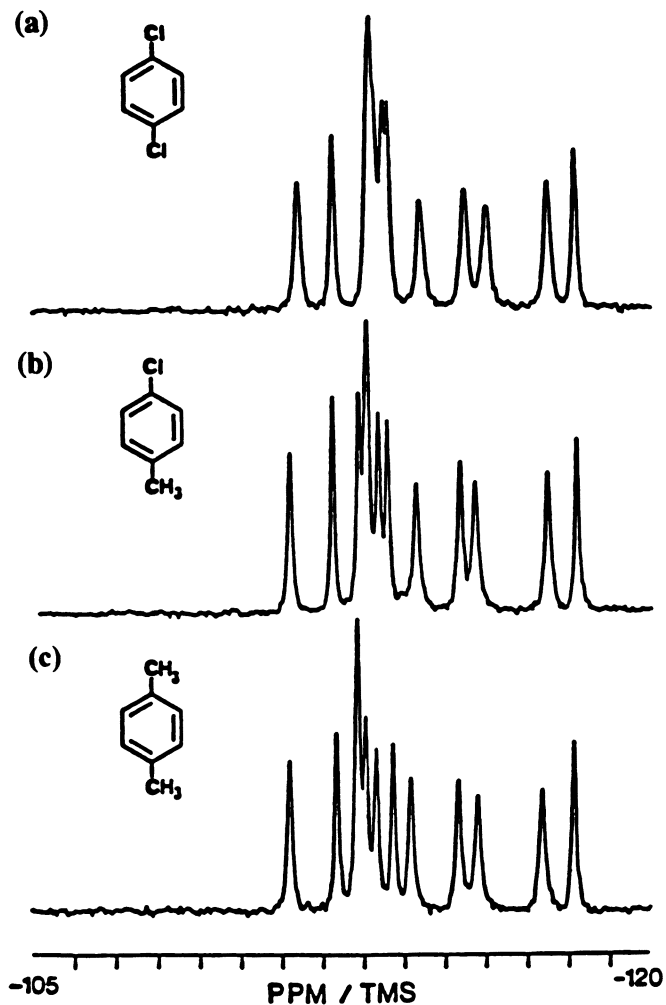


Figure 2. ^{29}Si MAS NMR spectra of ZSM-5 loaded with 2 molecules per u.c. of (a) p-dichlorobenzene, (b) p-chlorotoluene, and (c) p-xylene. Adapted from ref. 15.

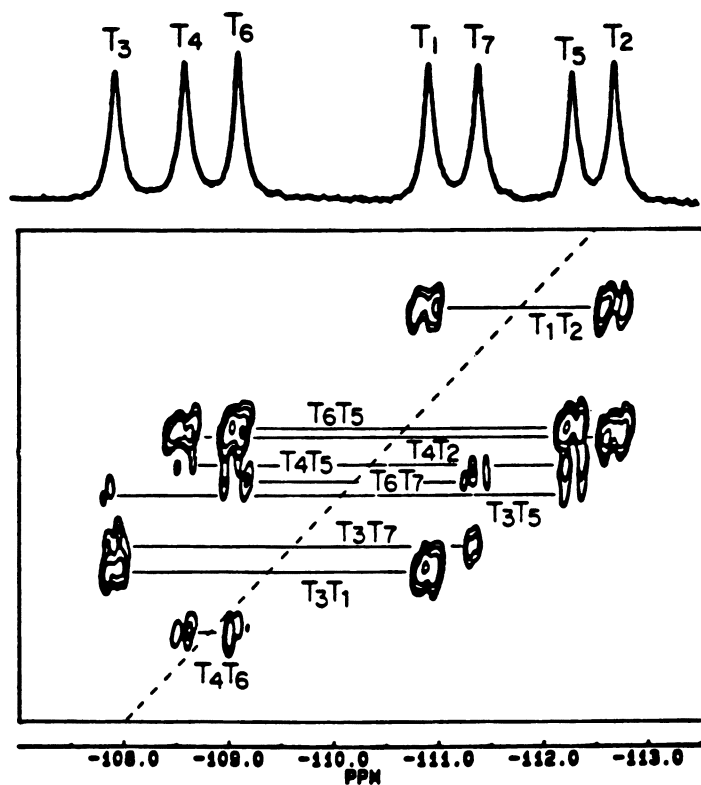
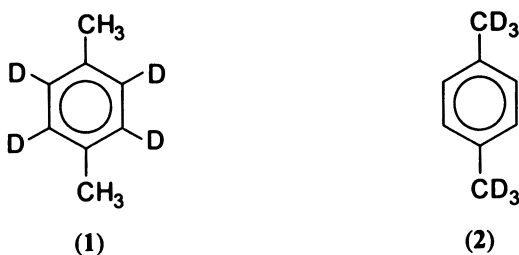


Figure 3. ^{29}Si INADEQUATE experiment on ZSM-12. Reproduced with permission from ref. 10. Copyright 1990 American Chemical Society.

complexes. This can be done by using experiments such as cross-polarization (CP), REDOR and TEDOR, which are based on the through-space dipolar interaction. Because of the strong distance dependence, the distances between the T-sites in the framework (whose identities are now known) and nuclei on suitably isotopically substituted substrates may be determined, yielding the 3-D structure of the zeolite-sorbate complex. To test the validity of this approach we have investigated a number of such experiments applied to the high-loaded form of zeolite ZSM-5 containing p-xylene where the answer is known from the high-quality single crystal structure of van Koningsveld and co-workers (7).

The simplest experiment is the CP technique with protons as the source nuclei. In order to localize the polarization source as much as possible, experiments were carried out with the two specifically deuterated p-xylenes (1) and (2).



Since the CP process is greatly dependent on molecular motions, these must be well understood for the system being studied. In the present work, these motions were investigated by wide line deuterium NMR of the sorbed organics. It was found that at 6-8 molecules/u.c., the methyl groups in the organic substrate rotate rapidly while the aromatic rings are essentially rigid but a proportion show some low frequency "ring-flips" around the 1,4-axis. However, care must be taken that no motions occur during the very long evolution times (100 ms) of these experiments (see on). It was established from ^{13}C spin diffusion experiments (not shown) that no such motions occur when the experiments are carried out 0 °C.

The effect of the distance dependence can be seen qualitatively from a comparison of the CP spectra with that from a simple one-pulse experiment as shown in Figure 4. The structure is orthorhombic with 24 T-sites of equal occupancy and the assignments of the resonances come as previously from 2-D INADEQUATE experiments (16-18). In the CP spectrum some signals are obviously enhanced compared to the others. The resonances due to the T-sites 1, 2, 10, 12 and 16 are quite well resolved and these were used in the study.

The spin-dynamics of the cross-polarization process from I to S nuclei as a function of time is described by equation 1 (19).

$$S(t) = S_{\max} \left(1 - \frac{T_{\text{CP}}}{T_{\text{Ip(H)}}} \right)^{-1} \left(\exp\left(-\frac{t}{T_{\text{Ip(H)}}}\right) - \exp\left(-\frac{t}{T_{\text{CP}}}\right) \right) \quad (1)$$

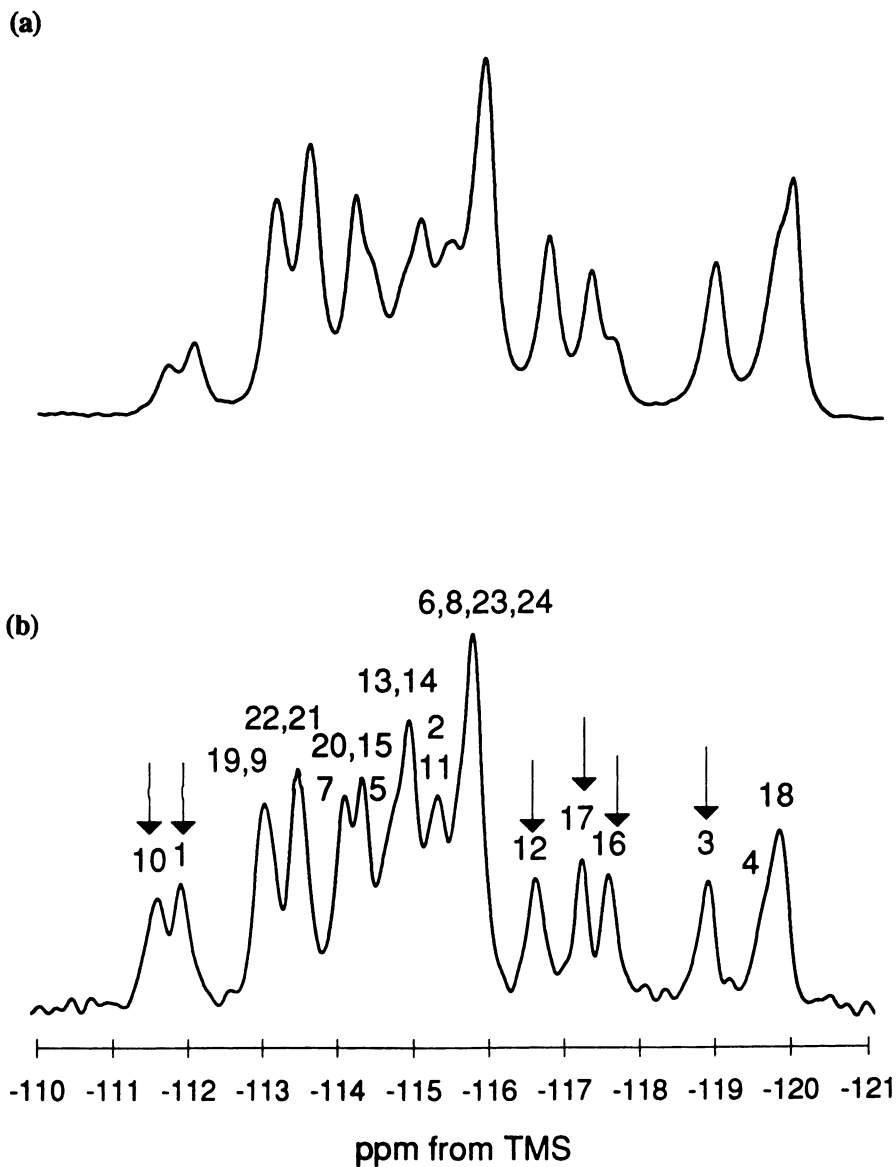


Figure 4. ^{29}Si NMR spectra of ZSM-5 loaded with 8 molecules per u.c. of p-xylene (2). (a) CP/MAS with 5ms contact time and a recycle delay of 5s. (b) Quantitative ^{29}Si MAS (recycle delay 350 s). The numbers indicate T-sites.

S_{\max} represents the theoretical maximum signal intensity obtainable from the polarization transfer, $T_{1\rho(H)}$ the proton $T_{1\rho}$ value and T_{CP} the cross-polarization time constant. Thus the S signal intensity as a function of time should consist of an exponential growth controlled by the cross polarization transfer and an exponential decay due the $T_{1\rho}$ process. Of particular interest, T_{CP} can be related to the second moment of the IS dipolar interaction ($\Delta\omega_{IS}^2$) as in equation 2 and is proportional to r_{IS}^6 as in equation 3 (20).

$$1/T_{CP} = \frac{C_{IS} (\Delta\omega_{IS}^2)}{(\Delta\omega_{II}^2)^{1/2}} \quad (2)$$

$$1/T_{CP} \propto (\Delta\omega_{IS})^2 \propto \frac{\gamma_I^2 \gamma_S^2}{\sum r_{IS}^6} \quad (3)$$

Using these equations, the cross-polarization results can be related to the sorbate-lattice internuclear distances.

Figure 5 shows the experimental CP curves for the well-resolved resonances indicated with arrows in Figure 4 for complexes of p-xylenes (1) and (2) (21). Qualitatively, it can be seen that silicons 10, 1, 17 and 3 are much more efficiently polarized and hence closer to the methyl protons than 16 and 12 (Figure 5a), and that silicons 12, 3 and 17 are closer to the ring protons than silicons 16, 10 and 1 (Figure 5b).

More quantitatively, the data can be compared directly with the XRD data. The structure is found to have two sites, one at the channel intersections and one in the zig-zag channels (Figure 6), and the lattice sorbate distances and related second moments can be calculated. The CP curves in Figure 5 can be fitted by deriving the $T_{1\rho(H)}$ values from the clearest decays and using these data to deduce the T_{CP} values. Figure 7 shows plots of the $1/T_{CP}$ values determined vs. the second moments calculated for the different T-sites, validating the general approach used.

As a final demonstration of the correctness of the structure, Figure 8 shows comparisons of the complete CP spectra predicted from the correlations of Figure 7. In both cases the agreement is excellent even though the fit was derived from only a few resolved resonances and the two spectra show quite different relative intensities.

Thus, in this case where the structure is well described, the CP technique yields a result in good agreement with the known structure. Similar results have been obtained using the REDOR (22,23) technique. It is thus felt that with proper precautions and with particular attention to the motions of different parts of the organic guest molecules, cross polarization will be a viable technique for the determination of the structures of zeolite/sorbate complexes. This has been verified for the low-loaded form of p-xylene in ZSM-5 (3 molecules/u.c.) where the structure is not known from single crystal diffraction.

Where the dipolar interaction is between isolated pairs of spins, a much more direct approach can be taken and the internuclear distances determined directly.

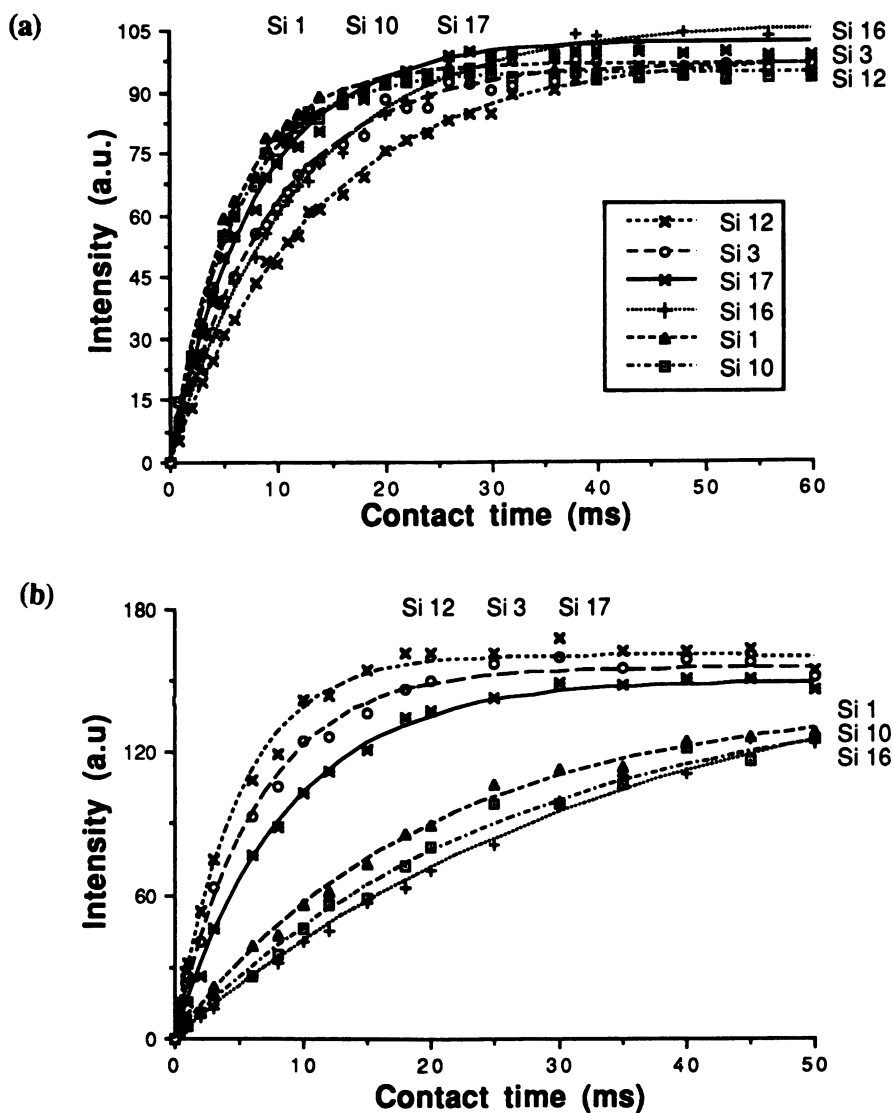
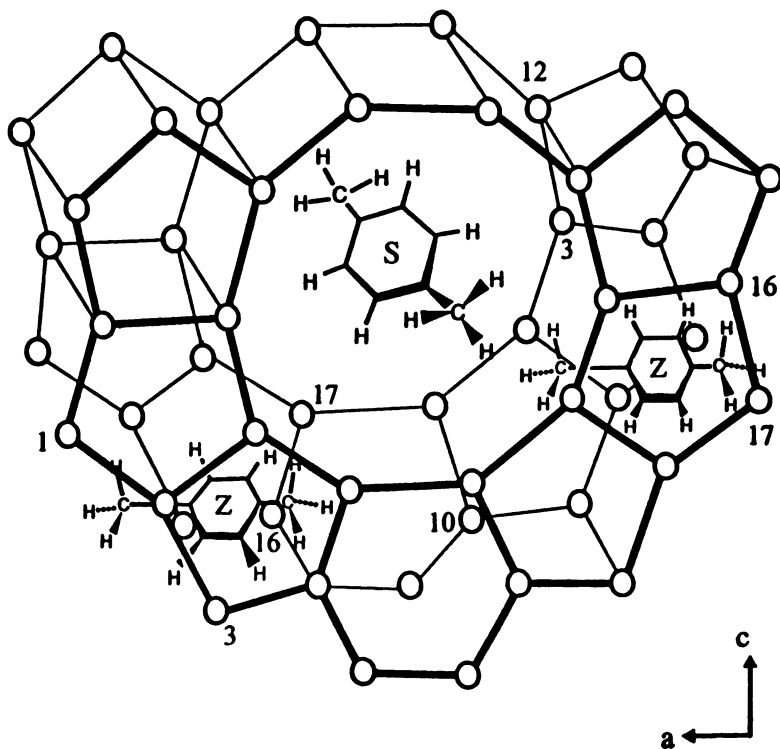


Figure 5. Variation of the intensity as a function of the contact time for complexes of ZSM-5 and (a) p-xylene (1), and (b) p-xylene (2). Spectra were recorded at 0 °C, and the loading was 8 molecules per u.c.



S: p-xylene in the straight channels

Z: p-xylene in the zig-zag channels

Figure 6. View along the straight channel of ZSM-5 showing the location of p-xylene molecules (loading of 8 molecules per u.c.) as determined from the single crystal structure (7). Oxygen atoms have been omitted for clarity.

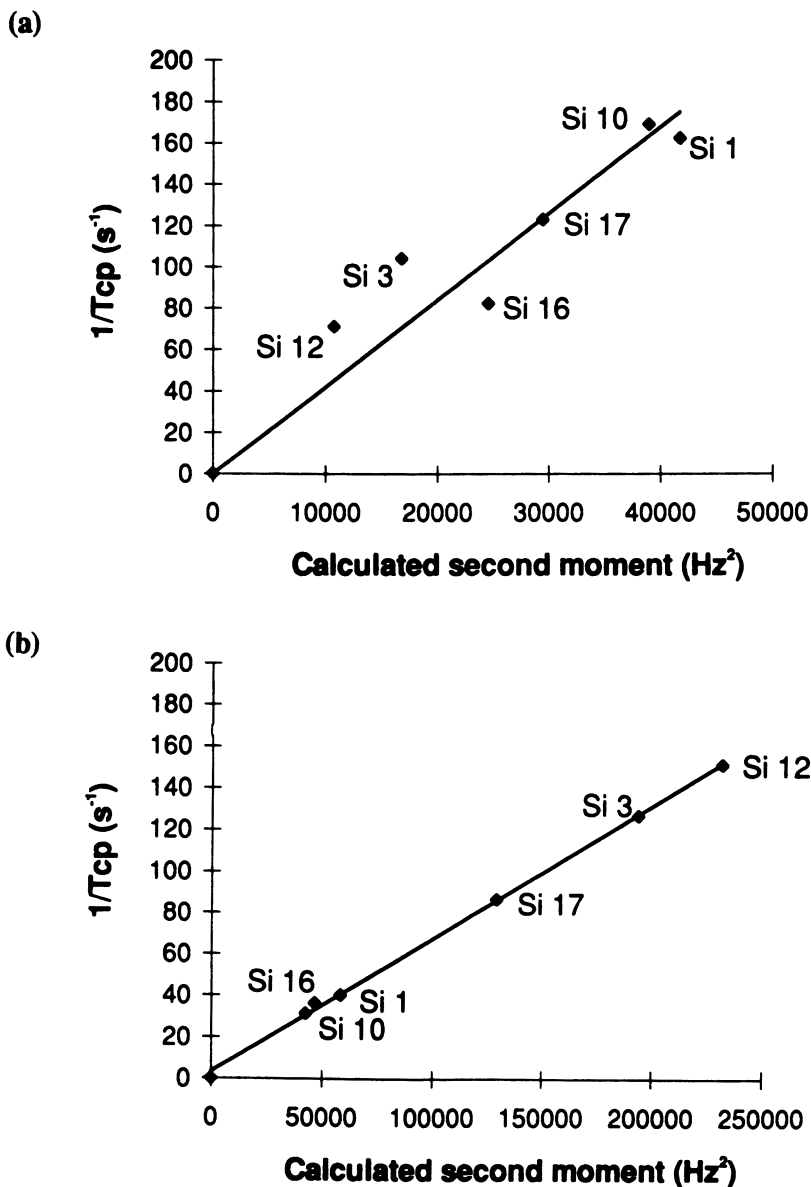


Figure 7. Plot of experimental T_{CP} values versus the calculated second moment ($\Delta\omega_{IS}^2$) values for ZSM-5 loaded with 8 molecules per u.c of (a) p-xylene (1), and (b) p-xylene (2).

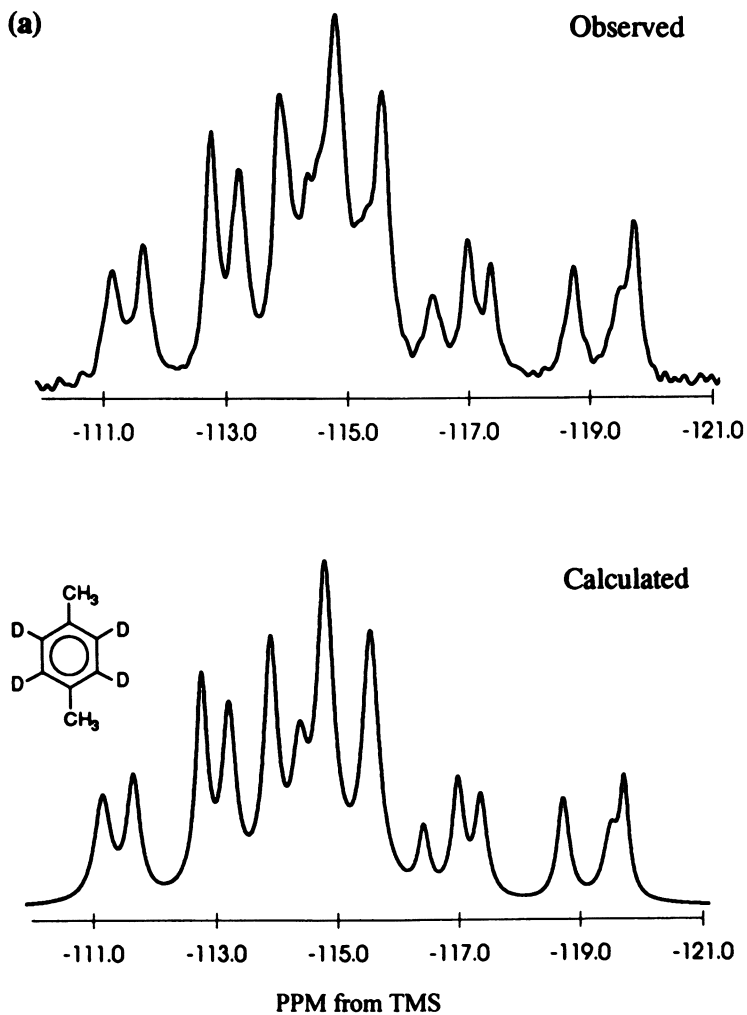
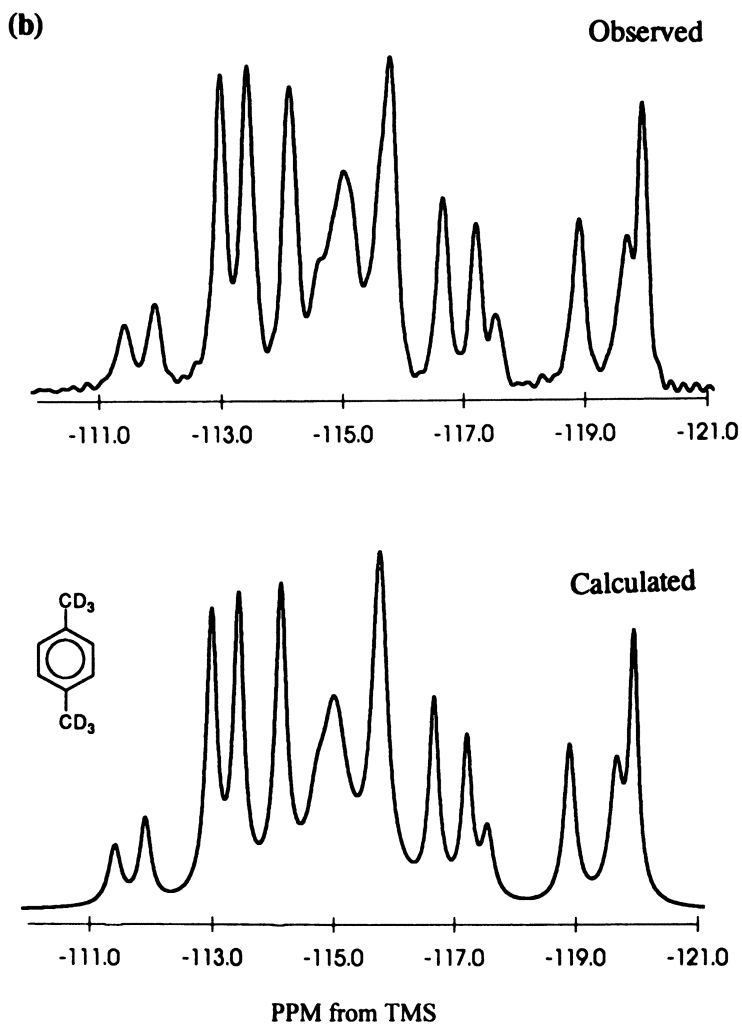


Figure 8. Comparisons of the observed ^{29}Si CP/MAS NMR spectra with those calculated from the second moment / T_{CP} correlations for ZSM-5 loaded with 8 molecules per u.c. of (a) p-xylene (1), and (b) p-xylene (2).

Figure 8. *Continued.*

Such a situation exists for octadecasil, the purely siliceous analogue of $\text{AlPO}_4\text{-16}$, prepared from fluoride-ion containing media (24). The structure, as shown in Figure 9a contains fluoride ions in the D4R units and has two silicon sites T_1 and T_2 in the ratio of 4:1 (24). Figure 9b illustrates the $^{29}\text{Si}/^{19}\text{F}$ interactions. The T-1 silicons interact with the fluoride ions as isolated spin pairs due to the low (4.6%) natural abundance of ^{29}Si . The more distant T-2 silicons each interact with a tetrahedron of fluoride ions. From the crystal structure, the $^{29}\text{Si}/^{19}\text{F}$ distances are 2.63 and 5.69 Å, corresponding to dipolar couplings of 1234 and 122 Hz respectively. Knowing the structure makes this system an ideal test of the techniques.

The basic pulse sequences for the REDOR (22,23) and TEDOR (25,26) experiments are shown in Figure 10. In both cases, the averaging of the dipolar interaction to zero over a rotor cycle by MAS is prevented by the application of 180° pulses which reverse its sign at specific points in the cycle. In this way, the final spectrum will reflect the magnitude of the dipolar interaction and the time over which it has evolved.

In the REDOR experiment shown in Figure 10a, presaturation and fixed relaxation delay were used prior to application of the ^{29}Si 90° pulse to ensure quantitative reliability of successive pulses because the ^{29}Si nuclei have long relaxation times. The 180° pulses on ^{29}Si are applied at exactly one half and full rotor cycles as indicated and a single 180° pulse is applied to the ^{19}F nuclei at the exact mid-point of the sequence. The sequence produces an echo, the second half of which is recorded. Two separate experiments are carried out, one with the I nucleus dephasing pulse on-resonance (S_f signal) and one with the pulse 5 MHz off-resonance (S_o signal) and the REDOR difference signal is the normalized function $(S_o - S_f)/S_o$. The experiments are carried out with the system evolving for different numbers of rotor periods and the resulting plot of $(S_o - S_f)/S_o$ is the REDOR curve (23).

For the case of two isolated spins, the REDOR difference signal intensity grows as in equation 4 (23), where n is the number of rotor periods and the averaging is over all possible orientations of the internuclear vector. The factor $\Delta\Phi_{R,n}$ gives the dipolar dephasing of the signal by the IS dipolar interaction over n rotor periods and includes the dipolar coupling. τ_r is the time for one complete rotor cycle.

$$\frac{(S_o - S_f)}{S_o} = 1 - \frac{1}{4\pi} \int_0^{2\pi} \int_0^\pi \cos(\Delta\Phi_{R,n}) \sin\beta \, d\beta \, d\alpha \quad (4)$$

$$\Delta\Phi_{R,n} = 4\sqrt{2} n D \tau_r \sin\alpha \sin\beta \cos\beta \quad (5)$$

The signal variation as a function of n is a curve growing to a relative intensity of 1 with a non-periodic oscillatory behaviour from which the dipolar coupling may be determined.

Figure 11a shows the experimental data for the T-1 silicon site in octadecasil together with the best fit theoretical curve corresponding to $D = 1180$ Hz (27). This yields an internuclear distance of 2.67 Å, in good agreement with the value of 2.63

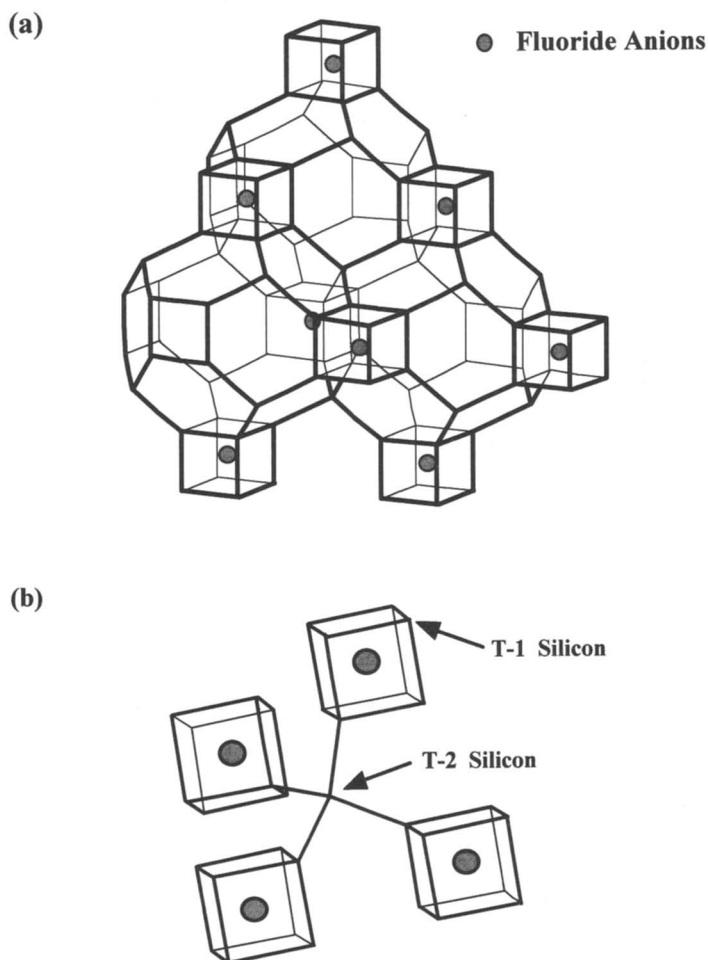


Figure 9. (a) Representation of the framework structure of octadecasil showing the location of the fluoride anions in the double 4-ring units. (b) Portion of the structure indicating the two different types of T-sites.

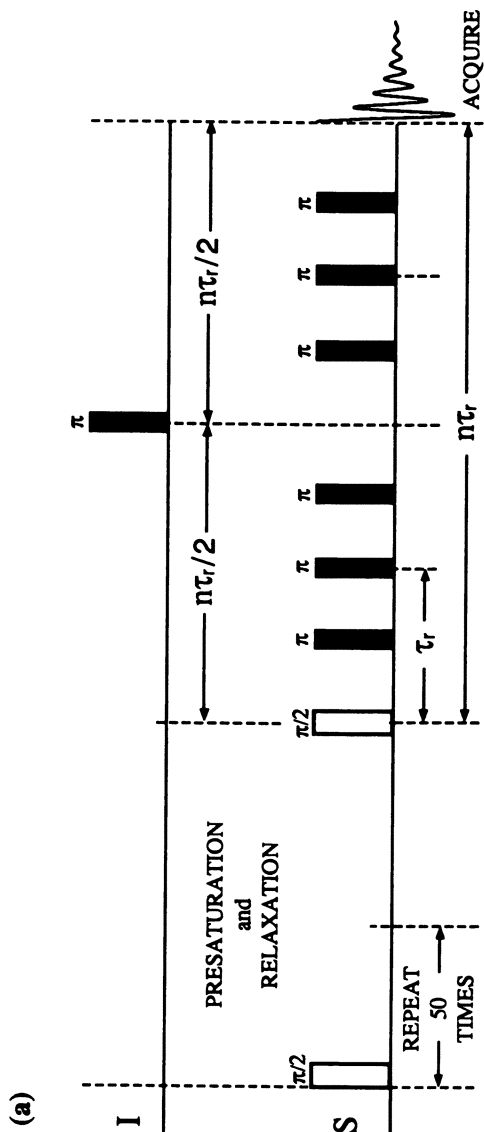
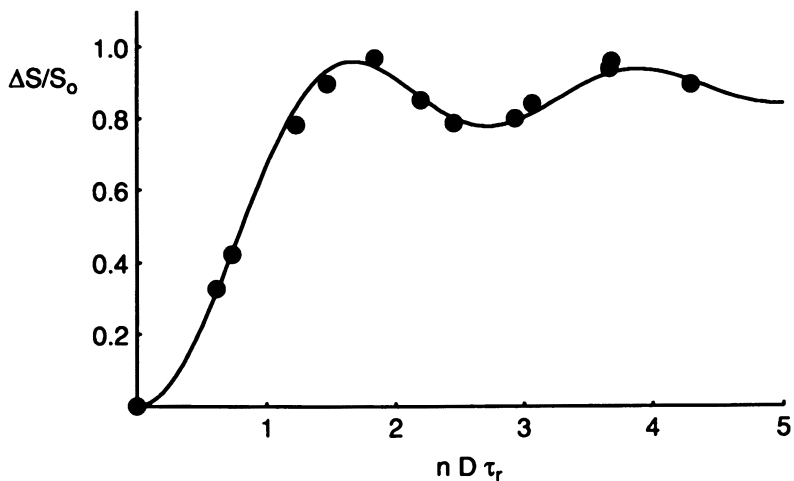


Figure 10. (a) REDOR pulse sequence with initial presaturation and a single dephasing pulse on the observed nuclei. (b) TEDOR pulse sequence with dephasing pulses on the observed nuclei before the coherence transfer, and on the unobserved nuclei after.

(a)



(b)

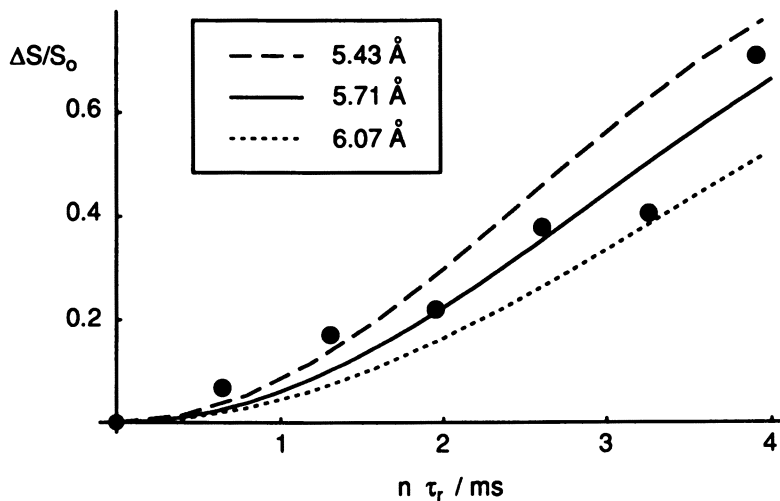


Figure 11. REDOR data and fits for the two types of T-sites in octadecasil. (a) T-1 silicons with curve calculated assuming an isolated ^{29}Si - ^{19}F spin-pair with an internuclear distance of 2.67 Å. (b) T-2 silicons and theoretical curves determined for a tetrahedral arrangement of four fluoride ions about a central silicon with different distances.

Å from the X-ray structure. The data does not reach a value of 1 because of the incomplete (*ca.* 90%) occupancy of the double 4-ring units by fluoride ions (24). The REDOR curve can also be calculated for the T-2 site but since the spins are no longer in a simple pair, the geometric relationship between them must be known (or postulated) and the calculation is more complex (28-30). Figure 11b shows the observed data for the T-2 site and curves calculated for a tetrahedral arrangement of spins with different $^{29}\text{Si}/^{19}\text{F}$ distances. Again, there is excellent agreement between the internuclear distance of 5.7 Å from the NMR data and the diffraction derived value of 5.69 Å. It is of interest to note that a structure could probably have been postulated from these distances and the ratio of the T-1 and T-2 sites obtained by NMR.

In the TEDOR experiment (25,26), the initial excitation is of the *I* nucleus (^{19}F), followed by a 180° pulse after $n/2$ rotor periods. During each rotor period, 180° pulses are applied to the *S* nuclei (^{29}Si) at the 1/4 and 3/4 points in the rotation. These again prevent the dipolar interactions from being averaged to zero and antiphase magnetization builds up on the *I* spins. At the echo point, the simultaneous application of 90° pulses on both channels gives a coherence transfer from the *I* to the *S* spins. This subsequently evolves into observable *I* magnetization during the second half of the sequence which is carried out for *m* rotor periods. The TEDOR signal is thus a function of both *n* and *m* and both can be varied. Because of the coherence transfer, the observed spectrum directly reflects the evolution of the dipolar interaction and only a single experiment is carried out. An additional advantage is that two-dimensional experiments may be carried out if there are several *I* resonances.

Quantitatively, the dipolar dephasing is described by equation 6 with the dephasing during the first evolution period consisting of *n* rotor periods given by equation 7 and a similar dephasing during the *m* rotor periods after the coherence transfer (26). The $\Delta\Phi_{T,n}$ and $\Delta\Phi_{T,m}$ functions contain the dipolar coupling, *D*, which can therefore be obtained from the experiment.

$$S_T = \frac{1}{4\pi} \int_0^{2\pi} \int_0^\pi \sin(\Delta\Phi_{T,n}) \sin(\Delta\Phi_{T,m}) \sin\beta \, d\beta \, d\alpha \quad (6)$$

$$\Delta\Phi_{T,n} = 4\sqrt{2} \, n \, D \, \tau_r \, \cos\alpha \, \sin\beta \, \cos\beta \quad (7)$$

Qualitatively, the signal grows to a maximum and then falls to a negative value and oscillates around zero, modulated by the dipolar coupling. Figure 12 shows the experimental TEDOR data for the T-1 site in octadecasil for an experiment where *n* was fixed at two rotor periods and *m* varied, and vice versa. The theoretical curves calculated for different values of *D* demonstrate the sensitivity of the experiment. The best fit (*D* = 1200 Hz) yields a $^{29}\text{Si}/^{19}\text{F}$ distance of 2.65 Å, again in excellent agreement with the X-ray determined value.

The success of the experiments presented here demonstrates that it will be possible to use the dipolar-based CP, REDOR and TEDOR experiments to determine the structures of molecular sieve/sorbate complexes; information which in

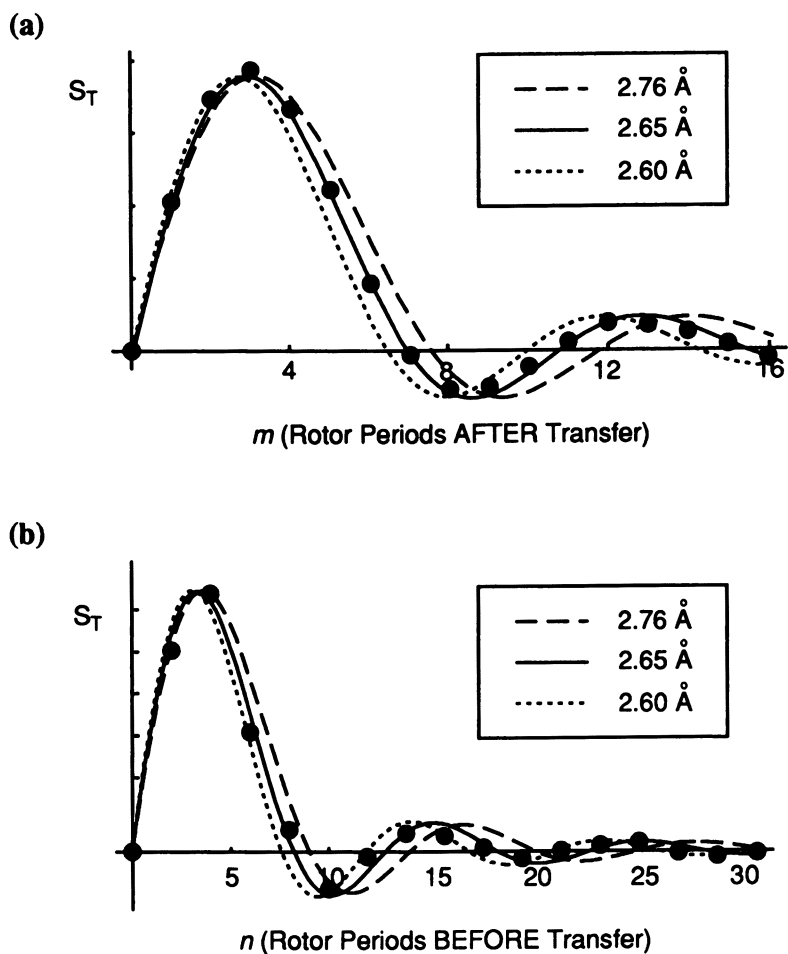


Figure 12. TEDOR data and fits for the T-1 silicon obtained with (a) $n = 2$, m varied, and (b) n varied, $m = 2$. The theoretical curves were calculated for the Si-F distances indicated.

general will not easily be obtained from diffraction measurements. In addition to the systems described in the present work we have also carried out successful experiments using $^{19}\text{F}/^{31}\text{P}$ and $^{13}\text{C}/^{29}\text{Si}$ interactions on other molecular sieve systems, indicating that the approach may be of quite general applicability.

Acknowledgments

C.A.F. acknowledges the support of the NSERC, Canada in the form of operating and equipment grants. A.C.D. thanks INTEVEP S.A. for a Postgraduate Scholarship.

Literature Cited

- (1) Meier, W. M. In *Molecular Sieves*. *Soc. Chem. Ind.* London, p. 10, 1968.
- (2) Breck, D.W. *Zeolite Molecular Sieves*; Wiley Interscience: New York, 1974.
- (3) Smith, J.V. *Zeolite Chemistry and Catalysis*; Rabo, J.A., Ed. ACS Monograph Series 171, American Chemical Society: Washington, DC, 1976.
- (4) Barrer, R.M. *Zeolites and Clay Minerals as Sorbents and Molecular Sieves*; Academic Press: London, 1978.
- (5) W.I.F.; Harrison, W.T.A.; Johnson, M.W. In *High Resolution Powder Diffraction. Materials Science Forum*; Catlow, C.R.A., Ed.; Trans Tech. Publication: Aermannsdorf, Switzerland, 1986; Vol. 9 pp. 89-101.
- (6) Eisenberger, P.; Newsam, J.B.; Leonowicz, M.E.; Vaughn, D.E.W. *Nature*, **1984**, *309*, 45.
- (7) van Koningsveld, H.; Tuinstra, F.; van Bekkum, H.; Jansen, J.C. *Acta Cryst.*, **1989**, *B45*, 423.
- (8) van Koningsveld, H.; Jansen, J.C., van Bekkum, H. *Acta Cryst.*, **1996**, *B52*, 140.
- (9) Fyfe, C.A.; Gobbi, G.C.; Murphy, W.J.; Ozubko, R.S.; Slack, D.A. *J. Am. Chem. Soc.*, **1984**, *106*, 4435.
- (10) Fyfe, C.A.; Feng, Y.; Gies, H.; Grondy, H.; Kokotailo, G.T. *J. Am. Chem. Soc.*, **1990**, *112*, 3264.
- (11) Fyfe, C.A.; Strobl, H.; Kokotailo, G.T.; Kennedy, G.J.; Barlow, G.E. *J. Am. Chem. Soc.*, **1988**, *110*, 3373.
- (12) Fyfe, C.A.; Kennedy, G.J.; Kokotailo, G.T.; Lyerla, J.R.; Fleming, W.W. *J. Chem. Soc., Chem. Commun.*, **1985**, 740.
- (13) Hay, D.G.; Jaeger, H.; West, G.W. *J. Phys. Chem.*, **1985**, *89*, 1070.
- (14) Fyfe, C.A.; Strobl, H.; Gies, H.; Kokotailo, G.T. *Can. J. Chem.*, **1988**, *66*, 1942.
- (15) Fyfe, C.A.; Feng, Y.; Grondy, H.; Kokotailo, G.T.; Gies, H. *Chem. Rev.*, **1991**, *91*, 1525.
- (16) Fyfe, C.A.; Grondy, H.; Feng, Y.; Kokotailo, G.T. *J. Am. Chem. Soc.* **1990**, *112*, 8812.
- (17) Fyfe, C.A.; Grondy, H.; Feng, Y.; Kokotailo, G.T. *Chem. Phys. Lett.*, **1990**, *173*, 211.

- (18) Fyfe, C.A.; Feng, Y.; Grondey, H.; Kokotailo, G.T. *J. Chem. Soc., Chem. Commun.*, **1990**, 1224.
- (19) Mehring, M. *Principles of High Resolution NMR in Solids*. Second edition, 1983, Springer, Berlin.
- (20) Pines, A.; Gibby, M.G.; Waugh, J.S. *J. Chem. Phys.*, **1973**, *59*, 569.
- (21) Fyfe, C.A.; Diaz, A.; Grondey, H.; Fahie, B. To be published.
- (22) Gullion, T.; Schaefer, J. *J. Magn. Reson.*, **1989**, *81*, 196.
- (23) Gullion, T.; Schaefer, J. *Adv. Magn. Reson.*, **1989**, *13*, 55.
- (24) Caillet, P.; Guth, J.L.; Hazm, J.M.; Gies, H. *Eur. J. Solid State Inorg. Chem.*, **1991**, *28*, 345.
- (25) Hing, A.W.; Vega, S.; Schaefer, J. *J. Magn. Reson.*, **1992**, *96*, 205.
- (26) Hing, A.W.; Vega, S.; Schaefer, J. *J. Magn. Reson. Ser. A*, **1993**, *103*, 51.
- (27) Fyfe, C.A.; Lewis, A.R.; Chézeau, J.M.; Grondey, H. Submitted to *J. Am. Chem. Soc.*
- (28) Naito, A.; Nishimura, K.; Tuzi, S.; Saitô, H. *Chem. Phys. Lett.*, **1994**, *229*, 506.
- (29) McDowell, L.M.; Klug, C.A.; Beusen, D.D.; Schaefer, J. *Biochemistry*, **1996**, *35*, 5395.
- (30) Goetz, J.; Schaefer, J. Presented at 38th Rocky Mountain Conference, Denver, Colorado, July 21-25, 1996.

Chapter 11

Double-Resonance and Two-Dimensional Silicon-29 NMR Spectroscopy of Minerals

Jay S. Shore¹, Susan M. DePaul^{2,4}, Matthias Ernst^{2,5}, and Brian L. Phillips³

¹Department of Chemistry and Biochemistry, South Dakota State University, Brookings, SD 57007

²Materials Sciences Division, E. O. Lawrence Berkeley National Laboratory and Department of Chemistry, University of California, Berkeley, CA 94720

³Department of Chemical Engineering and Materials Science, University of California, Davis, CA 95616

Results of novel double-resonance and two-dimensional ²⁹Si NMR measurements, including ²⁷Al-to-²⁹Si and ²³Na-to-²⁹Si cross-polarization, ²⁹Si isotropic/anisotropic correlation, and ¹H/²⁹Si heteronuclear correlation experiments are reported. ²⁷Al-to-²⁹Si and ²³Na-to-²⁹Si cross-polarization were used to improve sensitivity, making two-dimensional ²⁹Si NMR techniques more feasible. ²⁹Si two-dimensional isotropic/anisotropic correlation spectra of the minerals albite, sepiolite, and gyrolite were measured and the principal components of the chemical-shift tensor for each site determined. A modified version of the TOSS-reTOSS pulse sequence was used and is shown to yield pure-phase isotropic/anisotropic correlation spectra. ¹H/²⁹Si heteronuclear correlation spectra of gyrolite and sepiolite were measured and used to assign ²⁹Si resonances to distinct crystallographic sites, to determine the proximity between silicon and hydrogen atoms, and to study ¹H-to-²⁹Si cross-polarization dynamics.

Approximately 95% of the earth is composed of silicate minerals. Many silicates, particularly aluminosilicates such as clays and feldspars, have considerable short-range disorder not easily studied by traditional diffraction techniques. Nuclear magnetic resonance (NMR) spectroscopy is sensitive to interactions that occur within 10 angstroms of the observed nucleus, making NMR an excellent probe of an

⁴Current address: Max-Planck-Institut für Polymerforschung, Postfach 3148, D-55021 Mainz, Germany.

⁵Current address: Laboratory for Physical Chemistry, University of Nijmegen, Toernooiveld, NL-6525 ED Nijmegen, Netherlands.

atom's local electronic environment, amenable to samples with little or no long-range order, and often complementary to diffraction techniques.

One-dimensional ^{29}Si NMR has successfully and routinely been used to study the structural chemistry of minerals, due in part to the typically high resolution of ^{29}Si NMR, the sensitivity of the ^{29}Si isotropic chemical shift to the local electronic environment, and empirical correlations between ^{29}Si isotropic chemical shift and structural parameters, such as bond angles and bond lengths. Over the past fifteen years, one-dimensional ^{29}Si NMR spectroscopy has been used to answer many questions pertaining to silicate structure and chemistry.

By comparison, multi-dimensional NMR techniques have been used only sparingly due to the low sensitivity of ^{29}Si NMR and the fact that many silicates lack abundant hydrogen from which to cross-polarize. The natural abundance of ^{29}Si is only 4.7% and ^{29}Si often has long relaxation times. For minerals and glasses, ^{29}Si longitudinal relaxation times can be thousands of seconds long. The few reported solid-state two-dimensional ^{29}Si NMR experiments suggest considerable promise for these techniques and include: homonuclear correlation experiments (COSY, J-scaled COSY, INADEQUATE) on ^{29}Si -isotopically enriched (1,2) and natural abundance samples (3-17), $^1\text{H}/^{29}\text{Si}$ heteronuclear correlation experiments (18-22), $^{27}\text{Al}/^{29}\text{Si}$ dipolar-dephasing experiments (23), ^{29}Si isotropic/anisotropic correlation experiments (24,25), and ^{29}Si exchange experiments (26).

In this work, the utility of ^{23}Na -to- ^{29}Si and ^{27}Al -to- ^{29}Si cross-polarization techniques to overcome the low sensitivity of ^{29}Si NMR and thus increase the feasibility of two-dimensional NMR experiments is discussed. Two-dimensional isotropic/anisotropic correlation experiments, for example, enable the separation of anisotropic powder lineshapes based on a site's isotropic chemical shift. Silicon-29 anisotropic chemical shift parameters have been determined for a limited number of compounds (27,28) due to the frequent overlap of resonances in one-dimensional NMR spectra. With isotropic/anisotropic correlation techniques anisotropic lineshapes can be measured more readily, and correlations between structure and anisotropic chemical shift parameters can be determined. Recently, Grandinetti et al. (25) have used ^{29}Si isotropic/anisotropic correlation spectroscopy to determine the relative populations of silicon with different numbers of Si-O-Si linkages in ^{29}Si -isotopically enriched CaSiO_3 glass with greater accuracy than is achievable using one-dimensional NMR techniques.

Heteronuclear correlation spectroscopy has been used to determine the relative proximity of chemical species and assign resonances to specific chemical sites. Zumbulyadis (22) used $^1\text{H}/^{29}\text{Si}$ heteronuclear correlation spectroscopy to assign proton resonances to specific environments in amorphous hydrogenated silicon, α -Si:H. Vega (21) used $^1\text{H}/^{29}\text{Si}$ heteronuclear correlation spectroscopy to characterize resonances in conventional proton magic-angle spinning (MAS) spectra of surface species sorbed on silica and zeolites. Fyfe et al. (20) studied methyl functionalized silica gels using $^1\text{H}/^{29}\text{Si}$ heteronuclear correlation spectroscopy. Harris et al. used $^1\text{H}/^{29}\text{Si}$ heteronuclear correlation spectroscopy to study magadiite (19) and octosilicate (18). The low proton concentration typical of silica, aluminosilicates, and zeolites results in weak ^1H homonuclear dipolar coupling. Hence, well resolved ^1H MAS NMR spectra can be obtained without the use of multiple-pulse techniques (21). $^1\text{H}/^{29}\text{Si}$ heteronuclear correlation spectra can be used to measure the proximity of silicon sites to water and hydroxyl protons, assign ^{29}Si resonances to specific

crystallographic sites, study cross-polarization dynamics, and acquire ^{29}Si -detected ^1H NMR spectra free of signals from probe background and hydrous impurity phases.

Experimental

To determine the feasibility of, and understand ^{27}Al -to- ^{29}Si and ^{23}Na -to- ^{29}Si cross-polarization dynamics, crystalline albite in its low temperature form, from Cazadero, CA was studied (29). This form of albite (low albite) is highly ordered with respect to Si and Al distribution of tetrahedral sites (30). Its structure has been thoroughly studied (29,30), and it has a single aluminum, single sodium, and three silicon sites. To determine the utility of double-resonance and two-dimensional ^{29}Si NMR techniques on structurally more complex silicate minerals, sepiolite and gyrolite were also studied. Both sepiolite (31,32) and gyrolite (33) have low iron content, multiple silicon sites, and poorly understood structures. Sepiolite has been the subject of many ^{29}Si NMR studies (34-39); there has been some disagreement on the assignment of the ^{29}Si resonances to specific crystallographic sites. A sample of sepiolite (SepSp-1) was purchased from the University of Missouri-Columbia, Source Clay Minerals Repository (Columbia, MO); the sample of gyrolite (approximately, $\text{Ca}_4\text{Si}_6\text{O}_{15}(\text{OH})_2 \cdot 4\text{H}_2\text{O}$, with some Na and Al substitution) is from Pune, India.

The ^{29}Si NMR spectra of albite were measured at 11.7 T (^{29}Si : 99.34 MHz, ^{27}Al : 130.31 MHz, ^{23}Na : 132.28 MHz), using a Chemagnetics CMX-500 spectrometer, a home-built double-resonance MAS NMR probe, and a 14 mm rotor purchased from Chemagnetics. All ^{29}Si NMR spectra of albite are referenced to tetramethylsilane (TMS) using an external standard.

The ^{29}Si and ^1H NMR spectra of gyrolite and sepiolite were measured at 9.4 T (^{29}Si : 79.5 MHz, ^1H : 400.1 MHz) with a Bruker ASX-400 spectrometer. CPMAS probes that use 4mm and 7mm rotors were used for the $^1\text{H}/^{29}\text{Si}$ heteronuclear correlation and isotropic/anisotropic correlation experiments, respectively. All ^{29}Si NMR spectra of gyrolite and sepiolite are referenced to tetramethylsilane (TMS) using diopside as an external secondary standard (-84.2 ppm).

The spinning axes of the MAS probes were initially set to 54.74° using the ^{81}Br NMR signal of KBr. All two-dimensional NMR spectra measured are pure-phase and were obtained using the method of States et al. (40) or whole-echo acquisition (41,42). All spectra were processed using the computer program RMN (43), and were fit to simulated lineshapes using either a Power Macintosh 7100/80 and a program written in C/C++ or a Silicon Graphics Indigo workstation and a program written in FORTRAN (44). Both fitting programs were based on the Herzfeld-Berger analysis of spinning sideband patterns (45).

^{27}Al -to- ^{29}Si and ^{23}Na -to- ^{29}Si Cross-polarization

Cross-polarization between spin-half nuclei during magic-angle spinning (MAS) is a well established technique to increase the sensitivity of low-abundant and low-sensitive isotopes (46-48). However, cross-polarization involving quadrupolar nuclei

is not as well-understood and only recently has begun to be exploited, mostly for assigning peaks or determining connectivities rather than enhancing sensitivity. Most of the difficulties of ^{27}Al -to- ^{29}Si and ^{23}Na -to- ^{29}Si cross-polarization arise from the quadrupolar nature of aluminum and sodium nuclei. Additional technical difficulties arise from the small differences in ^{29}Si and ^{27}Al or ^{23}Na NMR frequencies (at 11.7 T, ^{29}Si : 99.34 MHz, ^{27}Al : 130.31 MHz, ^{23}Na : 132.28 MHz).

The most common method of transferring magnetization from one nuclear spin species to another is to spin-lock both using rf-fields with amplitudes consistent with the Hartmann-Hahn condition (48). For the transfer of magnetization between spin-half nuclei (I) and the central transition of quadrupolar nuclei (S), while spinning the sample about the magic angle at a rate faster than the homonuclear dipolar coupling, the Hartmann-Hahn condition becomes,

$$\omega_{\text{II}} = \left(S + \frac{1}{2}\right)\omega_{\text{IS}} + n\omega_r, \quad (1)$$

where n is an integer; ω_{II} and ω_{IS} are the rf-field strengths applied to the spin-half and quadrupolar nuclei, respectively. The angular frequency of the rotor is ω_r and S is the spin-quantum number of the quadrupolar nuclei. Along with satisfying the Hartmann-Hahn condition, both spin species have to be spin-locked long enough for magnetization to be transferred. Cross-polarization to or from quadrupolar nuclei is complicated by the complex behavior of quadrupolar nuclei during a spin-lock and MAS. Vega (49,50) was first to report a theoretical description of the behavior of quadrupolar nuclei during a spin-lock and MAS, considering the quadrupolar interaction to first-order. To better understand the complex behavior, a detailed analysis of ^{27}Al -to- ^{29}Si cross-polarization and of the dependence of the ^{27}Al spin-lock efficiency on the spinning speed (ω_r) and rf-field strength (ω_{IS}) for low rf-field strengths during MAS was undertaken and has been published elsewhere (51); relevant aspects of that work are summarized below.

Quadrupolar nuclei have $(2S+1)$ eigenstates with energy levels that depend on the orientation of the crystallite relative to the static magnetic field. During MAS, as the crystallite is rotated and a spin-locking field is applied, the energy levels are time-dependent. Depending on the orientation of the crystallite relative to the rotor, the quadrupolar interaction passes through zero 2 or 4 times during a full rotation of the rotor. It is these zero-crossings that affect the spin-lock efficiency of quadrupolar nuclei. The population of the spin states after a zero-crossing depends on the rate of change of the quadrupolar interaction at the zero-crossing. As shown by Vega (49,50), the adiabaticity of the transition is a function of the spinning rate (ω_r), rf-field strength (ω_{IS}), and quadrupolar frequency (ω_Q , $\omega_Q = (3e^2qQ)/(2S(2S-1)\hbar)$), and can be described using an adiabaticity parameter (α),

$$\alpha = \frac{\omega_{\text{IS}}^2}{\omega_Q \omega_r}. \quad (2)$$

The crystallite orientations can be included explicitly in the adiabaticity parameter (52), but are not necessary for a qualitative description of the observed experimental

behavior. For $\omega_Q \gg \omega_{IS}$, there are three regimes of spin-lock behavior. If the passage through the zero-crossing is sufficiently slow to be adiabatic ($\alpha > 1$) then the populations are transferred from the original eigenstates to new eigenstates and magnetization can be locked throughout the rotor cycle. If the passage is fast enough to be categorized as sudden ($\alpha \ll 1$), there are no changes in the states of the spin system and the magnetization remains locked. In the intermediate regime ($\alpha \approx 1$), there is a rapid decay of the spin-locked magnetization. Due to the large rotor used for our experiments, the spinning speed was limited to less than 2.5 kHz, ω_{IS} to less than 5.0 kHz, and hence α to less than 0.02 (sudden-passage regime). The quadrupolar frequencies ($\omega_Q/2\pi$) for aluminum and sodium in low albite are 0.493 and 1.29 MHz, respectively (53).

Even in the sudden-passage regime ($\alpha \ll 1$), it is not always possible to spin-lock the central transition of quadrupolar nuclei in a powder. For some combinations of ω_{IS} and ω_r , the total magnetization decays within the first few rotor cycles, despite the spin-lock, due to destructive interference between magnetization from crystallites with different orientations in the rotor. When the quadrupolar interaction is small enough that it is sufficient to consider it only to first-order, destructive interference occurs when the following condition is satisfied,

$$\omega_{IS} = \frac{2N}{S + \frac{1}{2}} \omega_r, \quad (3)$$

where N is an integer. When the quadrupolar interaction has to be considered to second-order, or if the rf-field is applied off-resonance by more than a few hundred Hertz, the spin-lock is inefficient when

$$\omega_{IS} = \frac{N}{S + \frac{1}{2}} \omega_r. \quad (4)$$

Both experimental measurements and numerical simulations of the spin-lock behavior of aluminum in albite show distinct dips in the spin-lock efficiency when Equation 4 is satisfied (51,54). Numerical simulations for crystallites with different orientations relative to the rotor show that if neither equations 3 nor 4 are satisfied, then the spin-lock efficiency is maximum and there are only small orientation dependent oscillations of the spin-locked magnetization (51,54). A theoretical treatment of some of these interference effects has been given in the literature (49,50,52,55).

To setup ^{27}Al -to- ^{29}Si cross-polarization the optimal ^{27}Al locking field is first determined by measuring the signal intensity as a function of rf-field strength at a constant spinning speed. The ^{29}Si locking field strength is then adjusted to match the Hartmann-Hahn condition (Equation 1). It is important that the spinning speed is stable during all experiments. In Figure 1 are ^{29}Si MAS NMR spectra obtained with ^{27}Al -to- ^{29}Si and ^{23}Na -to- ^{29}Si cross-polarization and single-pulse excitation. The parameters for all experiments were optimized for signal-to-noise. The three spectra were acquired in the same amount of time and have been normalized by scaling with the square-root of the number of scans, making the intensity of the noise equivalent.

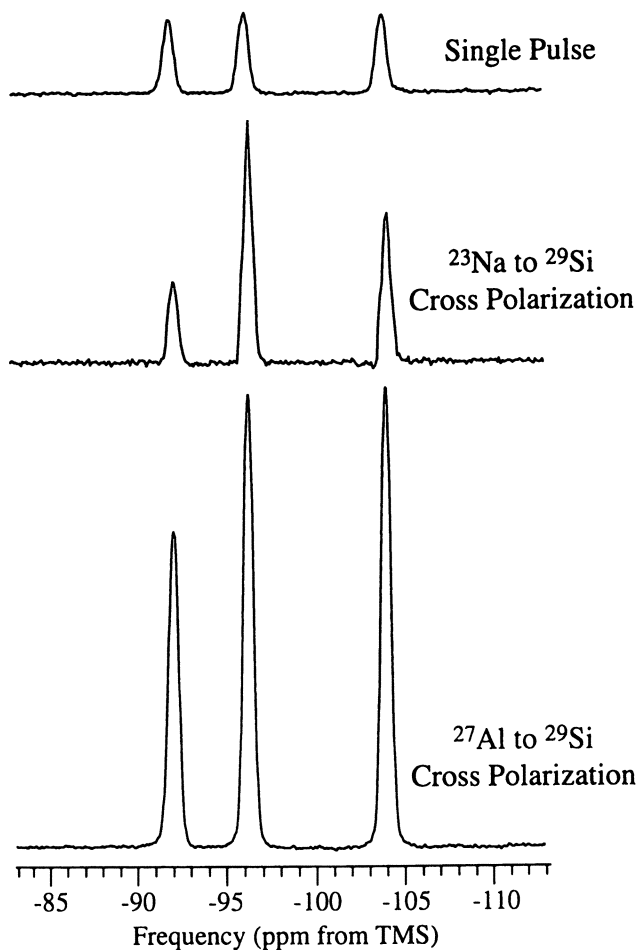


Figure 1. ^{29}Si MAS NMR spectra of crystalline albite acquired with single-pulse excitation, ^{23}Na -to- ^{29}Si and ^{27}Al -to- ^{29}Si cross-polarization at 11.7 T. The parameters for each experiment were optimized for signal-to-noise. The spectra were measured in the same amount of time (8000 s) and have been normalized by scaling with the square-root of the number of scans, making the intensity of the noise equivalent.

A factor of five signal-to-noise enhancement per unit time was achieved using ^{27}Al -to- ^{29}Si cross-polarization, corresponding to a factor of twenty-five reduction in time. The signal enhancement is due to the aluminum having a shorter recycle delay than the silicon, by a factor of 400. In the spectrum acquired with single-pulse excitation, the intensities of the three silicon resonances are equivalent, reflecting the equal populations of the three crystallographic sites. For the spectrum acquired using ^{27}Al -to- ^{29}Si cross-polarization, the two silicon resonances for the silicon with single next-nearest neighbor aluminum (-96.1 and -103.9 ppm) have equal intensities while the silicon resonance for the silicon with two next-nearest neighbor aluminum (-91.8 ppm) has considerably lower intensity. The ^{27}Al -to- ^{29}Si cross-polarization dynamics appear unique for the silicon site with the unique aluminum next-nearest neighbor environment. The three ^{29}Si resonances of albite have been assigned to distinct crystallographic sites based on correlations of the chemical shift with the T-O-Si angle (56), the mean Si-O bond length (57) and the bond strengths (28).

The spin-lattice relaxation time in the rotating frame ($T_{1\rho}$) of the three silicon sites were measured using three separate on-resonance experiments and were determined to be 5.8, 12.8, and 11.5 s for the silicon peaks at -91.8, -96.1, and -103.9 ppm, respectively. The contact-time dependence was fit to a simple model based on the thermodynamic description of cross-polarization (58) using the measured $T_{1\rho}$ values; the cross-polarization time constants (T_{cp}) were determined to be 0.36, 0.45, and 0.42 s for the silicon peaks at -91.8, -96.1, and -103.9 ppm, respectively. The intensity differences in the spectra measured using ^{27}Al -to- ^{29}Si cross-polarization appear to be related to the spin-lattice relaxation time in the rotating frame and the cross-polarization rate. Both rates correlate with the second moment of the ^{27}Al - ^{29}Si dipolar broadening (59) calculated from the crystal structure (30).

The difference in intensities of the ^{29}Si resonances in the spectrum acquired with ^{23}Na -to- ^{29}Si cross-polarization (Figure 1) is probably due to the shorter $T_{1\rho}$ of the -91.8 ppm ^{29}Si resonance and the larger quadrupolar frequency of ^{23}Na . The larger linewidth of the ^{23}Na resonance is more difficult to spin-lock uniformly than the ^{27}Al resonance.

Our results show that both ^{27}Al -to- ^{29}Si and ^{23}Na -to- ^{29}Si cross-polarization can be used to enhance the ^{29}Si NMR signal-to-noise ratio and make two-dimensional ^{29}Si NMR techniques more practical for silicates that do not contain abundant hydrogen.

^{29}Si Isotropic/Anisotropic Correlation Spectroscopy

Most of the structural information obtained using ^{29}Si NMR has relied on the isotropic chemical shift and empirical relationships between the ^{29}Si isotropic chemical shift and structural features, such as aluminum occupancy of next-nearest neighbor positions, total cation-oxygen bond strength, Si-O-T bond angles, and Si-O bond lengths. More detailed correlations between the structure and the anisotropic chemical shift parameters are expected due to the larger information content of the anisotropic chemical shift parameters.

The chemical shift interaction is strongly dependent on the local electronic environment and has an isotropic (orientationally independent) and an anisotropic

(orientationally dependent) component. The isotropic chemical shift (δ_{iso}) is a measure of the isotropic component and the anisotropic chemical shift (δ_{aniso}), and asymmetry parameter (η) characterizes the anisotropic component. The chemical shift parameters can be defined as follows:

$$\delta_{\text{iso}} = \frac{\delta_{xx} + \delta_{yy} + \delta_{zz}}{3} \quad (5)$$

$$\delta_{\text{aniso}} = \delta_{zz} - \delta_{\text{iso}}, \quad \eta = \frac{\delta_{xx} - \delta_{yy}}{\delta_{zz} - \delta_{\text{iso}}} \quad (6)$$

$$|\delta_{zz} - \delta_{\text{iso}}| \geq |\delta_{yy} - \delta_{\text{iso}}| \geq |\delta_{xx} - \delta_{\text{iso}}|, \quad (7)$$

where δ_{zz} , δ_{yy} , and δ_{xx} are the principal components of the chemical shift tensor. For a single crystal, the complete chemical shift tensor can be determined by measuring the resonance frequencies in one-dimensional NMR spectra as a function of the orientation of the crystal about two axes relative to the magnetic field (59). A more efficient technique involves the sudden reorientation of the crystal relative to the magnetic field during a two-dimensional experiment (60). For powders, the principal components of the chemical shift tensor can be determined from NMR spectra of static or (slowly) rotating samples. However, for samples with multiple crystallographic sites, the NMR resonances often overlap, precluding the determination of the chemical shift parameters from one-dimensional spectra. The problem of spectral overlap can be overcome by using two-dimensional NMR techniques that combine the higher resolution of an isotropic dimension with the high information content but lower resolution of an anisotropic dimension. With two-dimensional isotropic/anisotropic correlation techniques, anisotropic powder patterns or spinning sideband manifolds of different chemical sites can be separated by their isotropic shifts and the principal components of the chemical shift tensor for each crystallographic site can be determined. The interpretation of the anisotropic chemical shift parameters from spectra may be complicated by motion or magnetic impurities that affect the NMR lineshapes.

Many two-dimensional techniques with isotropic and anisotropic dimensions have been developed and include: switched-angle spinning (SAS) (61), variable-angle correlation spectroscopy (VACS) (62,63), magic-angle hopping (MAH) (64,65), magic-angle turning (MAT) (66), TOSS-reTOSS (67), and variations of the above (68,69). Of these, magic-angle turning and TOSS-reTOSS require only conventional MAS equipment.

TOSS was developed by Dixon et al. (70,71) to remove spinning sidebands. Kolbert and Griffin (67) developed TOSS-reTOSS, a two-dimensional isotropic/anisotropic correlation experiment by adding the TOSS sequence in reverse order as shown in Figure 2a. The original TOSS-reTOSS pulse sequence does not yield pure-phase spectra. However, by combining whole-echo acquisition (41,42) with the TOSS-reTOSS pulse sequence (Figure 2b) pure-phase isotropic/anisotropic

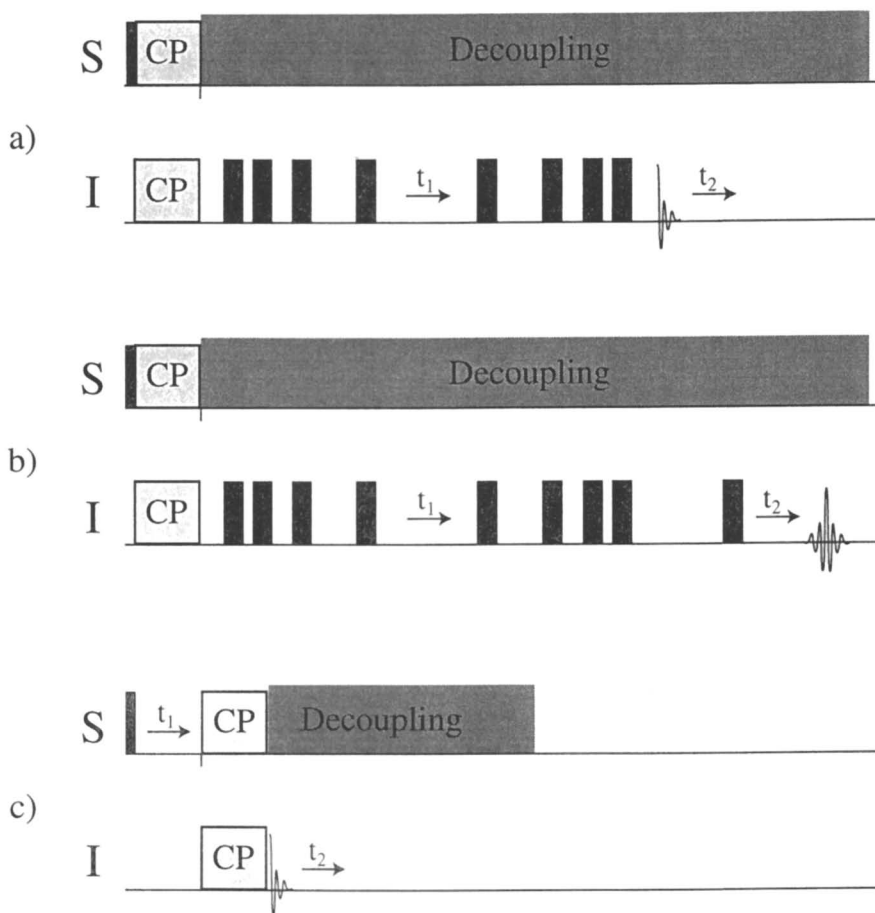


Figure 2. (a) The Original TOSS-reTOSS pulse sequence (67) for measuring isotropic/anisotropic correlation spectra. (b) The TOSS-reTOSS pulse sequence combined with whole-echo acquisition for obtaining pure-phase isotropic/anisotropic correlation spectra. (c) The pulse sequence used to measure the $^1\text{H}/^{29}\text{Si}$ heteronuclear correlation spectra. In all pulse sequences, 90° and 180° pulses are represented by narrow and wide black bars, respectively.

correlation spectra can be measured. While the TOSS-reTOSS pulse sequence is sensitive to large frequency offsets, due to the small chemical shift range and relatively small chemical shift anisotropies typical of ^{29}Si , no artifacts were observed nor expected.

In Figure 3 is a ^{29}Si isotropic/anisotropic correlation spectrum of albite measured using ^{27}Al -to- ^{29}Si cross-polarization and the TOSS-reTOSS pulse sequence with whole-echo acquisition. By fitting the one-dimensional slices from the anisotropic dimension to simulated lineshapes, the chemical shift parameters given in Table I were determined (51,54). Similar isotropic/anisotropic correlation spectra were acquired using three different versions of the magic-angle turning sequence (data not shown) (54). The silicon site with two aluminum next-nearest neighbors ($\delta_{\text{iso}} = -91.6$ ppm) clearly has a larger absolute anisotropic chemical shift ($\delta_{\text{aniso}} = -35$ ppm) than those that have a single next-nearest neighbor aluminum ($\delta_{\text{aniso}} = -22$ and -26 ppm).

In Figure 4 is a ^{29}Si isotropic/anisotropic correlation spectrum of sepiolite measured using ^1H -to- ^{29}Si cross-polarization and the TOSS-reTOSS pulse sequence with whole-echo acquisition. From the width of the peaks in the anisotropic dimension, the homogeneous linewidth is less than 50 Hz, much smaller than the peaks in the isotropic dimension. Slices from the anisotropic dimension were fit to simulated lineshapes, as shown in Figure 5, to determine the chemical shift parameters (Table I). Table I also includes the chemical shift parameters of gyrolite, also determined by fitting anisotropic slices of an isotropic/anisotropic correlation spectrum measured using ^1H -to- ^{29}Si cross-polarization and the TOSS-reTOSS pulse sequence with whole-echo acquisition.

Correlations between anisotropic chemical shift parameters and the number of Si-O-Si linkages have been reported for a series of silicon sites (25,27,28). Silicon with no next-nearest neighbor silicon, $Q^{(0)}$, and those with four, $Q^{(4)}(\text{OAl})$, have negligible anisotropic chemical shifts and asymmetry parameters; sites with a single next-nearest neighbor silicon, $Q^{(1)}(\text{OAl})$, or three, $Q^{(3)}(\text{OAl})$, have large anisotropic chemical shifts opposite in sign, and asymmetry parameters close to zero; sites with two next-nearest neighbor silicon, $Q^{(2)}(\text{OAl})$, have large anisotropic chemical shifts and intermediate asymmetry parameters. For the $Q^{(n)}(\text{mAl})$ notation, n indicates the number of next-nearest neighbor tetrahedral sites (Si or Al) and m denotes how many of these tetrahedral sites are aluminum.

In Table I the isotropic chemical shift (δ_{iso}), the anisotropic chemical shift (δ_{aniso}), the asymmetry parameter (η), and the Q notation of the silicon sites of albite, sepiolite, and gyrolite are given. Two of the silicon sites of albite are $Q^{(4)}(\text{1Al})$ while the third is $Q^{(4)}(\text{2Al})$; all have significant anisotropic chemical shifts suggesting that next-nearest neighbor aluminum atoms affect the size of anisotropic chemical shifts and asymmetry parameters.

Sepiolite (31,32) and gyrolite (33) have been reported to have complex structures with essentially only $Q^{(3)}(\text{OAl})$ silicon; the large range of anisotropic chemical shifts and asymmetry parameters indicate that structural/chemical features other than the number and identity of next-nearest neighbor tetrahedral sites affect these parameters. Our data indicates that isotropic/anisotropic correlation spectroscopy may become an important technique for measuring anisotropic

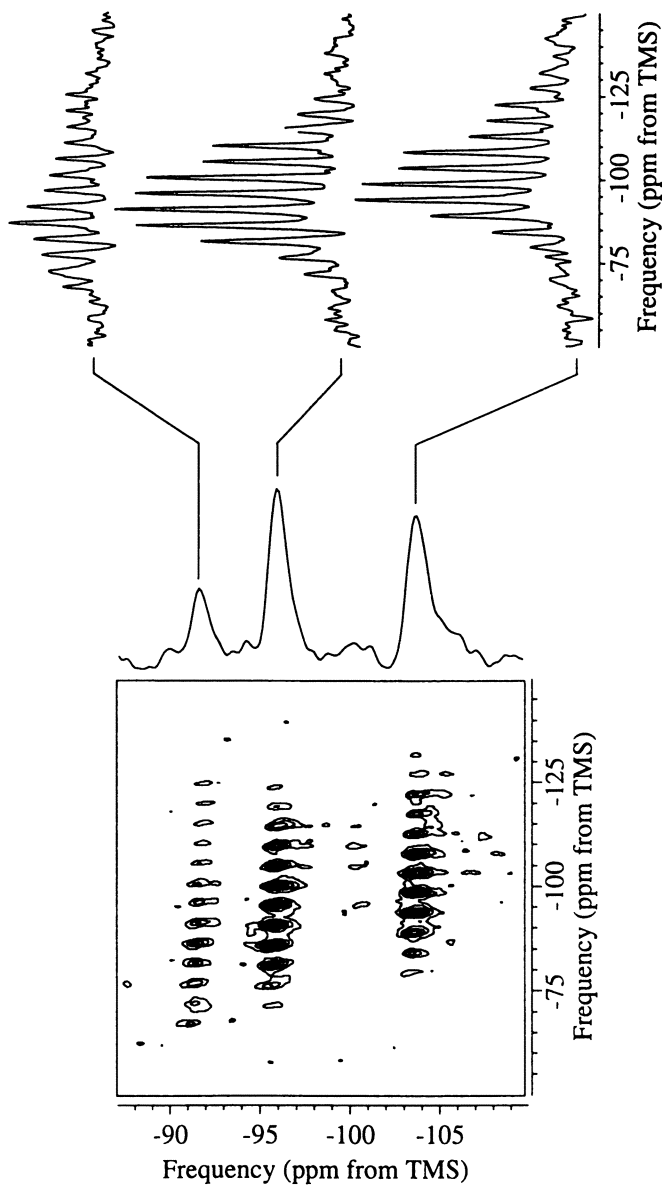


Figure 3. A ^{29}Si NMR isotropic/anisotropic correlation spectrum of albite. To the left a two-dimensional contour plot is shown with contour levels from 10 to 100% in increments of 10%. In the center the projection of the isotropic dimension is shown. To the right three anisotropic spectra extracted from the two-dimensional spectrum are shown. This isotropic/anisotropic correlation spectrum was measured at 11.7 T, with a spinning speed of 470 Hz and using the TOSS-reTOSS pulse sequence with whole-echo acquisition and using ^{27}Al -to- ^{29}Si cross-polarization.

Table I. ^{29}Si Chemical shift Parameters

	$Q^{(n)}(\text{mAl})$	δ_{iso} (ppm)	δ_{aniso} (ppm)	η
Albite	$Q^{(4)}(2\text{Al})$	-91.8	-35	0.8
	$Q^{(4)}(1\text{Al})$	-96.1	-22	0.8
	$Q^{(4)}(1\text{Al})$	-103.9	-26	0.6
Sepiolite	$Q^{(3)}(0\text{Al})$	-92.0	-15	0.9
	$Q^{(3)}(0\text{Al})$	-94.5	-10	0.8
	$Q^{(3)}(0\text{Al})$	-98.2	-38	0.3
Gyrolite	$Q^{(3)}(0\text{Al})$	-91.8	-27	0.3
	$Q^{(3)}(0\text{Al})$	-93.6	-46	0.3
	$Q^{(3)}(0\text{Al})$	-98.9	-25	0.6

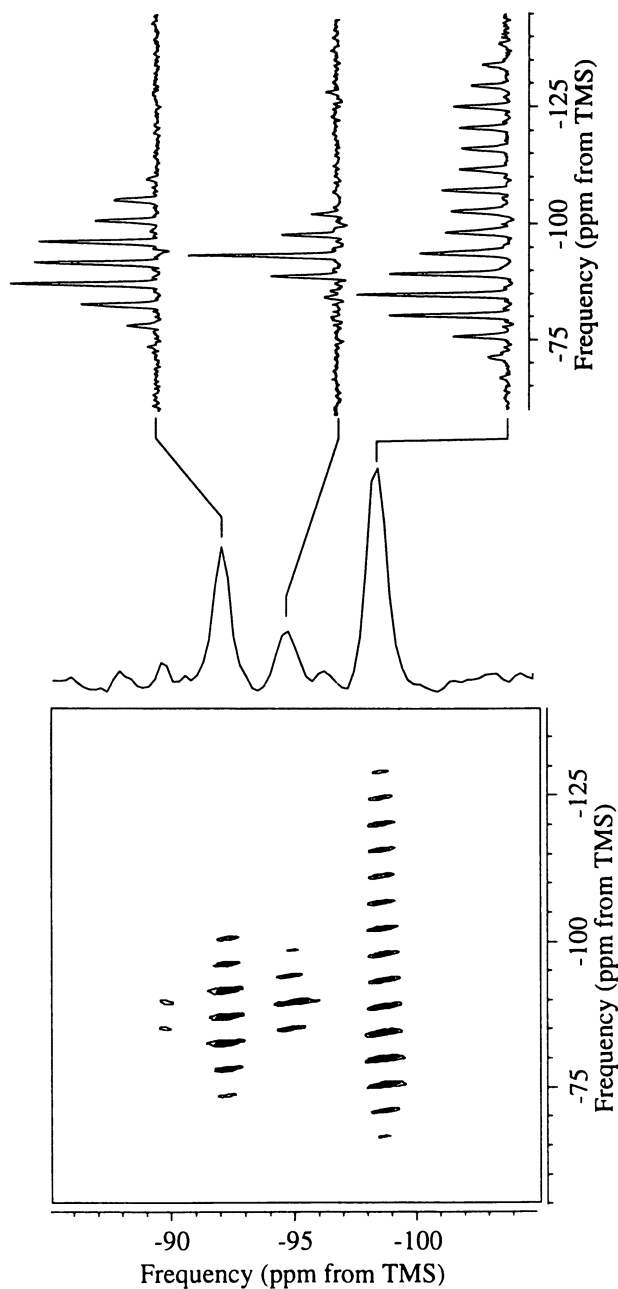


Figure 4. A ^{29}Si NMR isotropic/anisotropic correlation spectrum of sepiolite. To the left a two-dimensional contour plot is shown with contour levels from 5 to 100% in increments of 5%. In the center the projection of the isotropic dimension is shown. To the right three anisotropic spectra extracted from the two-dimensional spectrum are shown. This isotropic/anisotropic correlation spectrum was measured at 9.4 T, using the TOSS-reTOSS pulse sequence with whole-echo acquisition (Figure 2b) and using ^1H -to- ^{29}Si cross-polarization with a contact time of 8 ms and a spinning speed of 356 Hz.

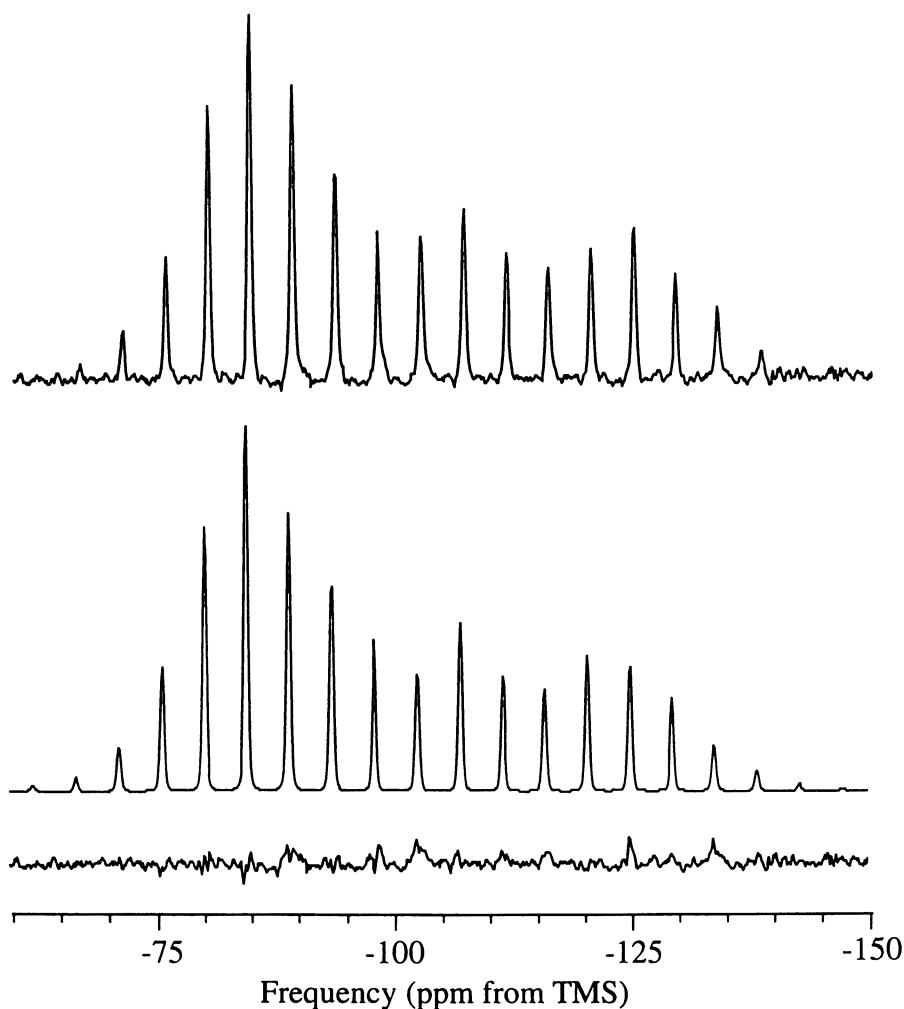


Figure 5. Experimental (top), simulated (center), and difference (bottom) spectra of the -98.2 ppm silicon site of sepiolite extracted from the two-dimensional isotropic/anisotropic correlation spectrum (Figure 4). The experimental spectrum was fit using the Herzfeld-Berger analysis of the spinning sidebands (54); the following parameters were obtained: isotropic chemical shift (δ_{iso}) of -98.2 ppm, anisotropic chemical shift (δ_{aniso}) of -38 ppm, and asymmetry parameter (η) of 0.3.

chemical shift parameters, assigning ^{29}Si resonances, and studying the structural chemistry of silicates.

$^1\text{H}/^{29}\text{Si}$ Heteronuclear Correlation Spectroscopy

Diffraction techniques are the methods of choice for the structural determination of materials with long-range order. However, short-range distributions of Si and Al at tetrahedral sites, positions of hydrogen atoms, and molecular motion are difficult to measure with diffraction techniques. NMR spectroscopy is dominated by interactions that occur within 10 angstroms of the nucleus and can be used to provide complimentary structural information. In particular, $^1\text{H}/^{29}\text{Si}$ heteronuclear correlation spectroscopy can be used to determine the relative proximity of silicon and hydrogen atoms and to assign resonances to specific crystallographic sites and hence is a promising technique for studying structures of hydrogen-containing silicates.

$^1\text{H}/^{29}\text{Si}$ heteronuclear correlation spectroscopy is simple to implement with standard CPMAS instrumentation; due to the relatively low proton concentration of most silicates, multiple-pulse ^1H homonuclear decoupling is typically not needed to obtain a high resolution ^1H MAS NMR dimension. In addition, with this technique ^{29}Si -detected ^1H NMR spectra, free of signals from probe background and hydrous impurity phases can be measured.

In Figure 6 is a $^1\text{H}/^{29}\text{Si}$ heteronuclear correlation spectrum of sepiolite acquired with a contact time of 10 ms. This spectrum has intensities consistent with a spectrum acquired with a contact time of 2 ms (data not shown) indicating that spin diffusion is probably not effecting the relative intensities. The peaks at roughly 5 and 0.8 ppm in the proton dimension are due to water and hydroxyl protons, respectively. From the contour plot, it is apparent that magnetization was transferred from water protons to all silicon sites and most efficiently to those that correspond to the -85, -92.0, and -98.2 ppm resonances; magnetization was also transferred from hydroxyl protons to silicon sites that correspond to the -92.0, -94.5, and -98.2 ppm resonances, but not to that at -85 ppm. That no magnetization is transferred from hydroxyl protons to the -85 ppm site indicates that this site is not a terminal Si-OH, but may be a $\text{Q}^3(1\text{Al})$ site as has been proposed (38). The different efficiencies of the magnetization transfer between the sites reflect their relative proximity. The ratios of the magnetization transferred from hydroxyl and water protons to the -92.0, -94.5, and -98.2 ppm silicon resonances are consistent with the site assignments of Barron and Frost (35). The -94.5 ppm resonance is assigned to the silicon site closest to the hydroxyl protons and farthest from water, denoted by Fripiat et al. (37) as the center site. The resonance at -98.2 ppm is assigned to the silicon site closest to the water and farthest from the hydroxyl groups, the edge site. The resonance at -92.0 ppm is assigned to the near-edge site.

In general, magnetization transfer from water is expected to be less efficient than from hydroxyl protons due to motion of the water molecules reducing the ^1H - ^{29}Si dipolar coupling. Intensities of the ^{29}Si -detected protons of water may also be reduced due to strong homonuclear dipolar coupling resulting in short $T_{1\rho}$ and T_2 values of the protons of water. These affects are illustrated by comparing the projections of the ^1H dimension of the $^1\text{H}/^{29}\text{Si}$ heteronuclear correlation spectra with

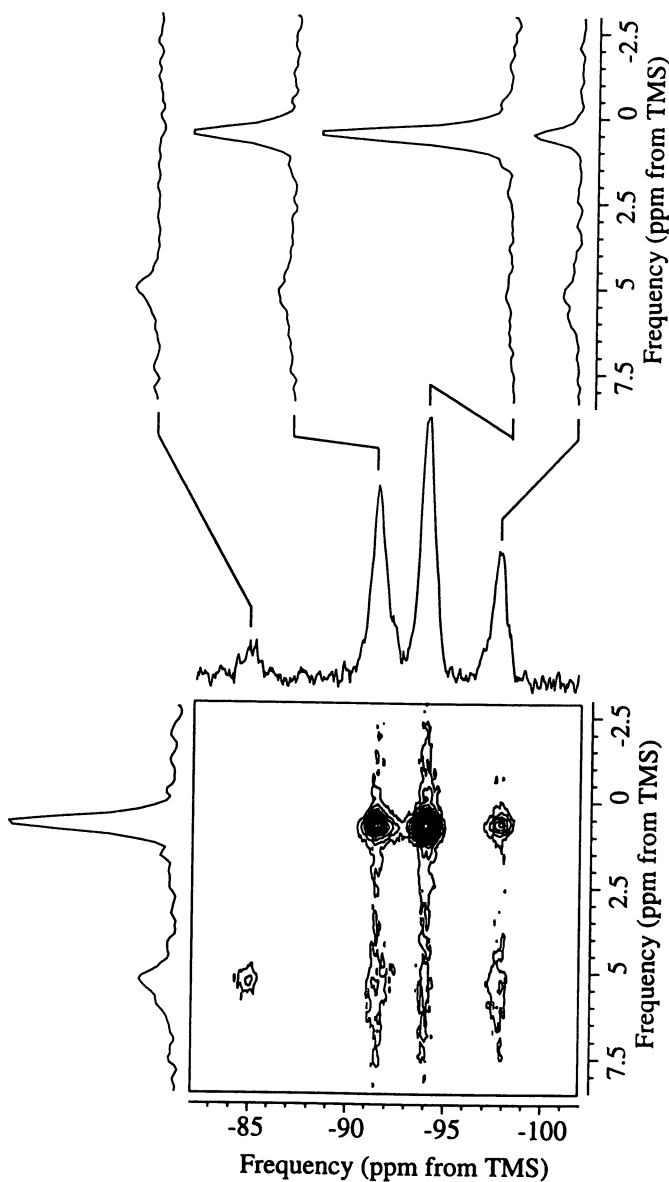


Figure 6. $^{29}\text{Si}/^1\text{H}$ heteronuclear correlation spectrum of sepiolite. To the left a two-dimensional contour plot is shown with contour levels from 10 to 100% in increments of 10%. In the center the projection of the ^{29}Si dimension is shown. To the right the ^1H NMR spectra extracted from the two-dimensional $^{29}\text{Si}/^1\text{H}$ heteronuclear correlation spectrum is shown. This $^{29}\text{Si}/^1\text{H}$ heteronuclear correlation spectrum was measured at 9.4 T using the pulse sequence shown in Figure 2c with a contact time of 10 ms and a spinning speed of 11 kHz. The method of States et al. was used to obtain pure-phase spectra.

standard ^1H MAS spectra (Figure 7). In the projection of the ^1H dimension of the heteronuclear correlation spectrum of sepiolite, the intensity of the hydroxyl protons is considerably larger than the intensity of the water protons. In a one-dimensional ^1H MAS NMR spectrum acquired independently, the intensity of the water protons is much larger, indicating that magnetization is transferred much more efficiently to the silicon from the hydroxyl protons. In a $^1\text{H}/^{29}\text{Si}$ heteronuclear correlation spectrum of gyrolite magnetization is transferred selectively from two different types of hydroxyl protons (Figure 7a); no magnetization transfer from water protons was observed. $^1\text{H}/^{29}\text{Si}$ heteronuclear correlation spectroscopy is useful for establishing connectivities. However, the intensities must be interpreted carefully as for any CPMAS experiment.

Conclusion

One-dimensional ^{29}Si NMR has been highly useful and routinely used for studying the structural chemistry of silicates. Double-resonance and two-dimensional ^{29}Si NMR can potentially provide more detailed information. For minerals that do not contain hydrogen, cross-polarization from ^{23}Na or ^{27}Al to ^{29}Si can be used to increase the sensitivity of ^{29}Si NMR making two-dimensional experiments more feasible. For example, by using ^{27}Al -to- ^{29}Si cross-polarization, two-dimensional ^{29}Si NMR spectra of albite were measured in two days instead of fifty. However, care must be taken whenever cross-polarizing to or from quadrupolar nuclei due to their complex spin-lock behavior. The efficiency of a spin-lock on quadrupolar nuclei is strongly dependent on spinning speed, rf-power levels, and quadrupolar coupling constants and is more complex when off-resonance or second-order quadrupolar terms have to be considered.

Isotropic/anisotropic correlation and $^1\text{H}/^{29}\text{Si}$ heteronuclear correlation spectroscopy are particularly well-suited for studying silicate minerals. Isotropic/anisotropic correlation spectroscopy is useful in obtaining the anisotropic chemical shift and asymmetry parameters for chemical systems with multiple crystallographic sites. By combining whole-echo acquisition with the TOSS-reTOSS pulse sequence pure-phase isotropic/anisotropic correlation spectra can be measured. $^1\text{H}/^{29}\text{Si}$ heteronuclear correlation spectroscopy is useful in assigning ^{29}Si NMR resonances to specific crystallographic sites and measuring the relative cross-polarization efficiency from different protons. It was shown that cross-polarization from water protons is much less efficient than from the protons of hydroxyl groups in sepiolite and gyrolite.

Acknowledgments

This work was partially supported by the Director, Office of Energy Research, Office of Basic Energy Sciences, Materials Sciences Division, U.S. Department of Energy, under contract DE-AC03-76SF00098, by the National Science Foundation under grant #OSR-9452894 and by the South Dakota Future Fund. S.M.D. thanks the National Science Foundation for a graduate fellowship. Assistance from Mr.

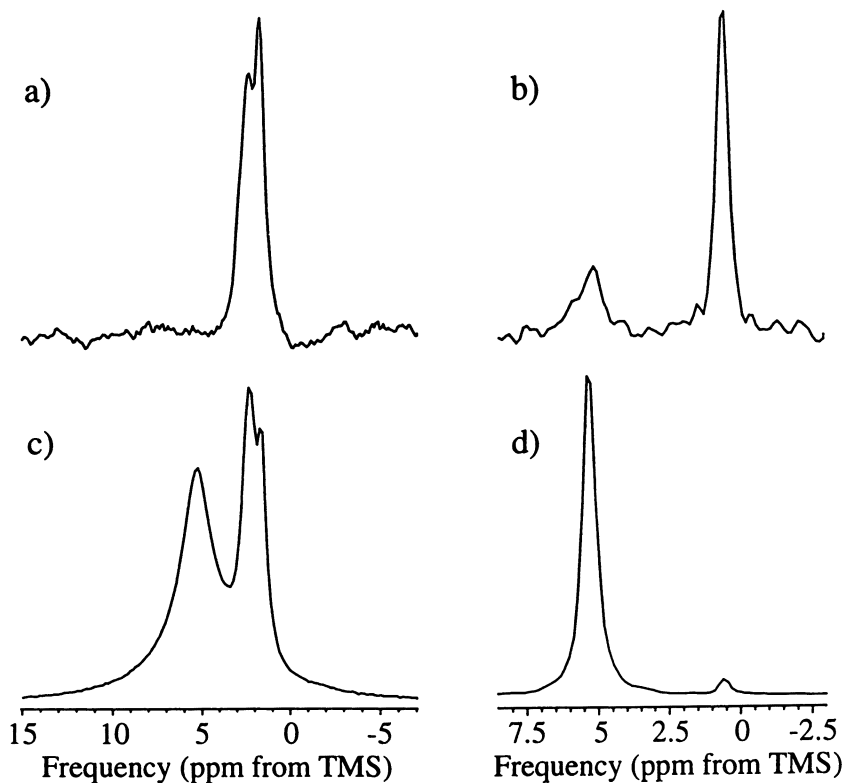


Figure 7. Projections of the ^1H dimension of $^{29}\text{Si}/^1\text{H}$ heteronuclear correlation spectra of (a) gyrolite and (b) sepiolite (Figure 6) and ^1H MAS NMR spectra of (c) gyrolite and (d) sepiolite measured independently

Brian Vollmer, Professor John J. Fitzgerald, Professor Alexander Pines and Professor Jonathan F. Stebbins is gratefully acknowledged.

Literature Cited

- 1) Knight, C. T. G.; Kirkpatrick, R. J.; Oldfield, E. *J. Non.-Cryst. Solids* **1990**, *116*, 140-144.
- 2) Fyfe, C. A.; Gies, H.; Feng, Y. *J. Am. Chem. Soc.* **1989**, *111*, 7702-7707.
- 3) Fyfe, C. A.; Gies, H.; Feng, Y.; Kokotailo, G. T. *Nature* **1989**, *341*(6239), 223-5.
- 4) Fyfe, C. A.; Grondey, H.; Feng, Y.; Kokotailo, G. T. *J. Am. Chem. Soc.* **1990**, *112*, 8812-8820.
- 5) Fyfe, C. A.; Feng, Y.; Gies, H.; Grondey, H.; Kokotailo, G. T. *J. Am. Chem. Soc.* **1990**, *112*, 3264-3270.
- 6) Fyfe, C. A.; Gies, H.; Feng, Y.; Grondey, H. *Zeolites* **1990**, *10*, 278-282.
- 7) Fyfe, C. A.; Grondey, H.; Feng, Y.; Kokotailo, G. T. *J. Am. Chem. Soc.* **1990**, *112*, 8812-20.
- 8) Fyfe, C. A.; Gies, H.; Feng, Y.; Grondey, H. *Zeolites* **1990**, *10*, 278-82.
- 9) Fyfe, C. A.; Feng, Y.; Gies, H.; Grondey, H.; Kokotailo, G. T. *J. Am. Chem. Soc.* **1990**, *112*, 3264-70.
- 10) Fyfe, C. A.; Feng, Y.; Grondey, H.; Kokotailo, G. T.; Mar, A. *J. Phys. Chem.* **1991**, *95*, 3747-3751.
- 11) Fyfe, C. A.; Feng, Y.; Grondey, H.; Kokotailo, G. T.; Gies, H. *Chem. Rev.* **1991**, *91*, 1525-43.
- 12) Fyfe, C. A.; Feng, Y.; Grondey, H.; Kokotailo, G. T.; Mar, A. *J. Phys. Chem.* **1991**, *95*, 3747-51.
- 13) Fyfe, C. A.; Grondey, H.; Feng, Y.; Kokotailo, G. T.; Ernst, S.; Weitkamp, J. *Zeolites* **1992**, *12*, 50-53.
- 14) Fyfe, C. A.; Grondey, H.; Feng, Y.; Kokotailo, G. T.; Ernst, S.; Weitkamp, J. *Zeolites* **1992**, *12*, 50-3.
- 15) Fyfe, C. A.; Mueller, K. T.; Kokotailo, G. T. In *NMR Techniques in Catalysis*; Bell, A. T.; Pines A., Eds.; Marcel Dekker, Inc.: New York, 1994, pp 11-67.
- 16) Benn, R.; Grondey, H.; Brevard, C.; Pagelot, A. *J. Chem. Soc., Chem. Commun.* **1988**, 102-3.
- 17) Kolodziejewski, W.; Barrie, P. J.; He, H.; Klinowski, J. *J. Chem. Soc., Chem. Commun.* **1991**, 961-2.
- 18) Almond, G. G.; Harris, R. K.; Franklin, K. R. *Solid State Nucl. Magn. Reson.* **1996**, *6*, 31-38.
- 19) Almond, G. G.; Harris, R. K.; Graham, P. *J. Chem. Soc., Chem. Commun.* **1994**, 851-852.
- 20) Fyfe, C. A.; Zhang, Y.; Aroca, P. *J. Am. Chem. Soc.* **1992**, *114*, 3252-3255.
- 21) Vega, A. J. *J. Am. Chem. Soc.* **1988**, *110*, 1049-54.
- 22) Zumbulyadis, N. *Phys. Rev. B* **1986**, *33*, 6495-6496.
- 23) Fyfe, C. A.; Wong-Moon, K. C.; Huang, Y.; Grondey, H.; Mueller, K. T. *J. Phys. Chem.* **1995**, *99*, 8707-16.
- 24) Zhang, P. Z.; Dunlap, C.; Florian, P.; Grandinetti, P. J.; Farnan, I.; Stebbins, J. F. *J. Non.-Cryst. Solids* **1996**, *204*, 294-300.

- 25) Zhang, P. Z.; Grandinetti, P. J.; Stebbins, J. F. *J. Phys. Chem. B* **1997**, *101*, 4004-4008.
- 26) Farnan, I.; Stebbins, J. F. *J. Non-Cryst. Solids* **1990**, *124*, 207-215.
- 27) Stebbins, J. F. In *A Handbook of Physical Constants: Mineral Physics and Crystallography*; Ahrens, T. J. Ed.; AGU Reference Shelf Series, vol. 2; American Geophysical Union: Washington, D.C., 1994, pp 303-331.
- 28) Smith, K. A.; Kirkpatrick, R. J.; Oldfield, E.; Henderson, D. M. *Am. Mineral.* **1983**, *68*, 1206-15.
- 29) George, A. M.; Stebbins, J. F. *Am. Mineral.* **1995**, *80*, 878-884.
- 30) Harlow, G. E.; Brown, G. E. *Am. Mineral.* **1980**, *65*, 986-995.
- 31) Brauner, K.; Preisinger, A. *Miner. Petrogr. Mitt.* **1956**, *6*, 120-140.
- 32) Caillere, S.; Henin, S. In *The X-ray Identification and Crystal Structures of Clay Minerals*; Brown, G., Ed.; Mineralogical Society: London, 1961, pp 325-342.
- 33) Merlino, S. *Mineral. Mag.* **1988**, *52*, 377-387.
- 34) Aramendia, M. A.; Borau, V.; Jimenez, C.; Marinas, J. M.; Ruiz, J. R. *Solid State Nucl. Magn. Reson.* **1997**, *8*, 251-256.
- 35) Barron, P. F.; Frost, R. L. *Am. Mineral.* **1985**, *70*, 758-66.
- 36) Barron, P. F.; Slade, P.; Frost, R. L. *J. Phys. Chem.* **1985**, *89*, 3305-10.
- 37) D'Espinose de la Caillerie, J. B.; Fripiat, J. J. *Clay Miner.* **1994**, *29*, 313-18.
- 38) Komarneni, S.; Fyfe, C. A.; Kennedy, G. J. *Clays Clay Miner.* **1986**, *34*, 99-102.
- 39) Komarneni, S. *Clays Clay Miner.* **1989**, *37*, 469-473.
- 40) States, D. J.; Haberkorn, R. A.; Ruben, D. J. *J. Magn. Reson.* **1982**, *48*, 286-292.
- 41) Bax, A.; Mehlkopf, A. F.; Smidt, J. *J. Magn. Reson.* **1979**, *35*, 373-377.
- 42) Grandinetti, P. J.; Baltisberger, J. H.; Llor, A.; Lee, Y. K.; Werner, U.; Eastman, M. A.; Pines, A. *J. Magn. Reson., Ser. A* **1993**, *103*, 72-81.
- 43) Grandinetti, P. J. *RMN*; Department of Chemistry, Ohio State University: Columbus, OH 43210-1173, 1996.
- 44) Degroot, H. J. M.; Smith, S. O.; Kolbert, A. C.; Courtin, J. M. L.; Winkel, C.; Lugtenburg, J.; Herzfeld, J.; Griffin, R. G. *J. Magn. Reson.* **1991**, *91*, 30-38.
- 45) Herzfeld, J.; Berger, A. E. *J. Chem. Phys.* **1980**, *73*, 6021-6030.
- 46) Schaefer, J.; Stejskal, E. O. *J. Am. Chem. Soc.* **1976**, *98*, 1031.
- 47) Pines, A.; Gibby, M. G.; Waugh, J. S. *J. Chem. Phys.* **1973**, *59*, 569-590.
- 48) Hartmann, S. R.; Hahn, E. L. *Phys. Rev.* **1962**, *128*, 2042-2053.
- 49) Vega, A. J. *J. Magn. Reson.* **1992**, *96*, 50-68.
- 50) Vega, A. J. *Solid State Nucl. Magn. Reson.* **1992**, *1*, 17-32.
- 51) DePaul, S. M.; Ernst, M.; Shore, J. S.; Stebbins, J. F.; Pines, A. *J. Phys. Chem. B* **1997**, *101*, 3240-3249.
- 52) Baltisberger, J. H.; Gann, S. L.; Grandinetti, P. J.; Pines, A. *Mol. Phys.* **1994**, *81*, 1109-1124.
- 53) Kirkpatrick, R. J.; Kinsey, R. A.; Smith, K. A.; Henderson, D. M.; Oldfield, E. *Am. Mineral.* **1985**, *70*, 106-23.
- 54) DePaul, S. M. *Solid-State Nuclear Magnetic Resonance Studies of Cross Polarization from Quadrupolar Nuclei*; University of California, Berkeley: Berkeley, CA, 1997.
- 55) Sun, W.; Stephen, J. T.; Potter, L. D.; Wu, Y. *J. Magn. Reson., Ser. A* **1995**, *116*, 181-8.

- 56) Woessner, D. E.; Trewella, J. C. *J. Magn. Reson.* **1984**, *59*, 352-6.
- 57) Higgins, J. B.; Woessner, D. E. *Trans. Am. Geophys. Union (EOS)* **1982**, *63*, 1139.
- 58) Mehring, M. *Principles of High-Resolution NMR in Solids*; 2nd ed.; Springer-Verlag: Berlin, Germany, 1976; Vol. 11.
- 59) Abragam, A. *Principles of Nuclear Magnetism*; Clarendon Press: Oxford, England, 1961.
- 60) Alderman, D. W.; Sherwood, M. H.; Grant, D. M. *J. Magn. Reson.* **1990**, *86*, 60-69.
- 61) Bax, A.; Szeverenyi, N. M.; Maciel, G. E. *J. Magn. Reson.* **1983**, *55*, 494-7.
- 62) Frydman, L.; Chingas, G. C.; Lee, Y. K.; Grandinetti, P. J.; Eastman, M. A.; Barrall, G. A.; Pines, A. *J. Chem. Phys.* **1992**, *97*, 4800-4808.
- 63) Frydman, L.; Chingas, G. C.; Lee, Y. K.; Grandinetti, P. J.; Eastman, M. A.; Barrall, G. A.; Pines, A. *Isr. J. Chem.* **1992**, *32*, 161-164.
- 64) Szeverenyi, N. M.; Bax, A.; Maciel, G. E. *J. Magn. Reson.* **1985**, *61*, 440-447.
- 65) Bax, A.; Szeverenyi, N. M.; Maciel, G. E. *J. Magn. Reson.* **1983**, *52*, 147-52.
- 66) Gan, Z. *J. Am. Chem. Soc.* **1992**, *114*, 8307-9.
- 67) Kolbert, A. C.; Griffin, R. G. *Chem. Phys. Lett.* **1990**, *166*, 87-91.
- 68) Gann, S. L.; Baltisberger, J. H.; Pines, A. *Chem. Phys. Lett.* **1993**, *210*, 405-410.
- 69) Hu, J. Z.; Alderman, D. W.; Ye, C. H.; Pugmire, R. J.; Grant, D. M. *J. Magn. Reson., Ser. A* **1993**, *105*, 82-87.
- 70) Dixon, W. T.; Schaefer, J.; Sefcik, M. D.; Stejskal, E. O.; McKay, R. A. *J. Magn. Reson.* **1982**, *49*, 341.
- 71) Dixon, W. T. *J. Chem. Phys.* **1982**, *77*, 1800.

Chapter 12

Siloxane-Based Solid Networks, from Silicas to Silicones

Gary E. Maciel

Department of Chemistry, Colorado State University, Fort Collins, CO 80523

The ^{29}Si MAS NMR spectra of samples that contain the siloxane (Si-O-Si) linkage reflect the wide range of materials that are substantially held together by siloxane-based networks. These materials include naturally occurring silicas, clays and zeolites, as well as such synthetic materials as functionalized polysiloxanes and silicone polymers, and display in ^{29}Si line widths a wide range of local and/or extended structural order or homogeneity. ^{29}Si NMR spectra distinguish readily between Q_2 , Q_3 , and Q_4 sites, the first two being emphasized by $^1\text{H} \rightarrow ^{29}\text{Si}$ cross polarization (CP). ^1H NMR spectra, obtained with either fast MAS-only or CRAMPS, provide useful information on the hydrogen bonding states of surface hydroxyls of silica, and can identify a variety of pendant groups incorporated by derivatization of a silica surface or via inclusion of appropriate reagents in a sol-gel synthesis. Specific planes of a β -cristobalite surface can serve as useful models of segments of the silica surface. For derivatized silicas and functionalized polysiloxanes, ^{13}C and ^1H NMR, and when appropriate ^{15}N or ^{31}P NMR, are useful for establishing (or confirming) the structures of pendant functionalized moieties. Relaxation experiments are useful for elucidating local mobility and domain homogeneity/heterogeneity.

The Si-O bond, with a bond energy of about 432 kJ mol^{-1} , or $103 \text{ kcal mol}^{-1}$, is the basis of the *siloxane* linkage, Si-O-Si, which forms the framework of *polysiloxane* solids ranging from silicas, clays, zeolites and silicates to silicone

polymers. Silica (SiO_2), which is enormously abundant in nature [1, 2], has a non-surface structure in which each silicon atom is connected to four others via siloxane linkages, i.e., $\text{Si}(-\text{O}-\text{Si})_4$; each such silicon site is often referred to as a Q_4 site. Silica surfaces (*vide infra*) also consist of Q_3 sites, $\text{HOSi}(-\text{O}-\text{Si})_3$, and Q_2 sites, $(\text{HO})_2\text{Si}(-\text{OSi})_2$, in which silanol groups (SiOH) terminate the three-dimensional structure. Silica can be either crystalline, e.g., quartz or β -cristobalite, or amorphous, e.g., fumed silica (formed from the reaction of SiCl_4 , H_2 and O_2 in a flame) or precipitated silica or silica gel (formed via a sol gel process). Polymeric solids can also be formed in which one (or two) of the bonds to each silicon atom is (are) directed to an organic moiety; the most common example is polydimethylsiloxane (PDMS), $(\text{Me}_2\text{SiO})_n$, commonly referred to as *silicone*. The silicon-attach organic moiety can accommodate a variety of functional groups, which imparts certain desired chemical properties into the suitably tailored polysiloxane. Silicones [3] and functionalized polysiloxanes can be formed via a sol-gel process [4] involving a hydrolysis/condensation mechanism, from a starting mixture of appropriate "monomers." Industrially, PDMS is commonly formed from D_4 , a cyclic tetramer of $-\text{Si}(\text{Me})_2-\text{O}-$ groups, via a catalyzed rearrangement/condensation process. Functionalized polysiloxanes are commonly formed from reaction mixtures containing a combination of $\text{Si}(\text{OR})_4$ and $\text{RSi}(\text{OR})_3$, where R' is Me or Et and R is the organo-functional moiety.

The polysiloxane solids referred to above, as a class, are remarkably stable materials, although subject to hydrolysis in strong acidic or basic conditions. They include both highly uniform materials (e.g., crystalline: quartz, β -cristobalite, tridymite) and structurally heterogeneous materials, e.g., especially the functionalized polysiloxanes. This range in structural homogeneity is reflected in linewidths of ^{29}Si NMR spectra, obtained with magic angle spinning (MAS) [5], as seen in Figure 1. These ^{29}Si MAS spectra were obtained either with $^1\text{H} \rightarrow ^{29}\text{Si}$ cross polarization (CP-MAS) [6, 7] or with direct polarization (DP-MAS), i.e., based on generating observable ^{29}Si magnetization directly via ^{29}Si spin-lattice relaxation (no CP).

Although the major peak of each ^{29}Si DP-MAS spectrum shown in Figure 1 is centered in the -100 to -110 ppm region characteristic of a $\text{Si}(-\text{O}-\text{Si})_4$ local structure, there are substantial differences among the spectra [8]. The four spectra obtained via direct polarization (DP) show a range of linewidths spanning from about 0.3 ppm for crystalline quartz to about 13 ppm for silica glass. This range of linewidths represents a corresponding range or order, or crystallinity, as has been reported previously [9, 10-15] and as discussed in more detail below. The occurrence of shoulders at about -90 ppm and about -100 ppm in the spectra of silica gel and fumed silica (Figs. 1B-E) is due to the fact that the surface areas of these two samples are large, so the populations of $(\text{Si}-\text{O}-)_3\text{SiOH}$ (or Q_3) sites and

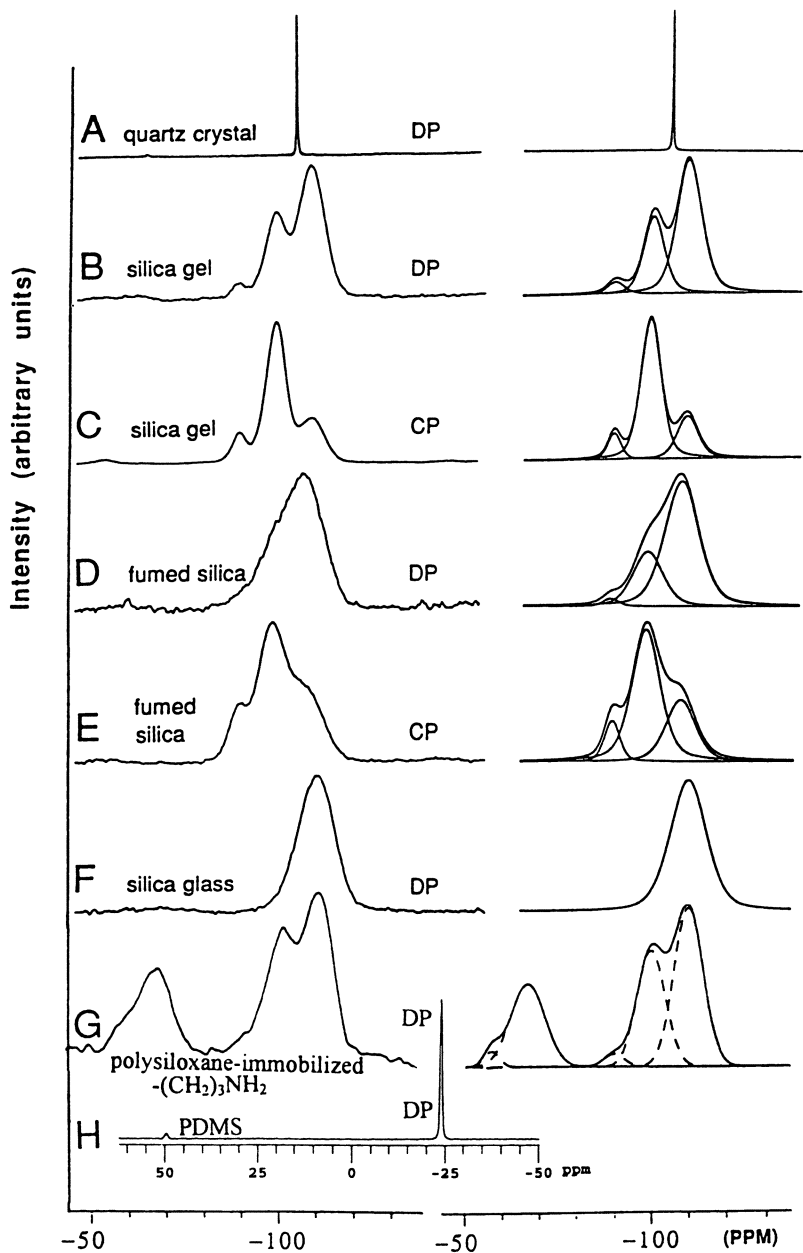


Figure 1. ^{29}Si MAS spectra of polysiloxanes, based on direct polarization (DP) or cross polarization (CP). A) Quartz crystal, B) and C) silica gel, D) and E) fumed silica, F) silica glass, G) polysiloxane-immobilized $-(\text{CH}_2)_3\text{NH}_2$, H) polydimethylsiloxane (PDMS) rubber. Left side, experimental spectra. Right side, computer-deconvoluted spectra. Taken in part from ref. 8.

$(\geq\text{Si-O})_2\text{Si}(\text{OH})_2$ (or Q_2) sites are accordingly substantial in relation to the dominant $(\geq\text{Si-O})_4\text{Si}$ (or Q_4) sites. The dramatically increased relative intensities of the Q_2 and Q_3 peaks, relative to the Q_4 peak, in the CP-MAS spectra of silica gel (Fig. 1C) and fumed silica (Fig. 1E), in comparison to relative peak intensities in the corresponding DP-MAS spectra (Figures 1B and D), reflect the selection of surface sites by the $^1\text{H} \rightarrow ^{29}\text{Si}$ CP process [16].

As indicated above, the varying linewidths seen in the ^{29}Si MAS NMR spectra of the various types of silica shown in Figure 1 reflect varying degrees of structural order, or crystallinity, in the samples. In our view, a "pure crystal" is at one end of the "order spectrum," having perfect short-range and perfect long-range order. A "partially crystalline" solid is usually considered to be a material with a high degree of short-range order (the identities and geometrical arrangements of nearest and next-nearest neighbor atoms or moieties), but the structural order is attenuated rapidly with distance. An amorphous material is one with a substantial degree of short-range order, but essentially no long-range order. A glassy material typically has only limited short-range order (with uniformity in only the *identities* of nearest and next-nearest neighbor atoms or moieties), with substantial variations in local geometry (e.g., bond angles and lengths with respect to nearest and next-nearest neighbor atoms). Recently, some investigations have started to reveal that even silica glass and vitreous silica glass possess medium range order resembling cristobalite and/or tridymite [17-19]. This entire spectrum of structural order is spanned by silica, as is amply reflected in the ^{29}Si MAS NMR spectra presented in Figure 1 of various kinds of SiO_2 samples. One sees the very narrow ^{29}Si NMR peaks (linewidth < 1 ppm) observed for the Q_4 silicon sites seen in Figure 1A for quartz (or for β -cristobalite [9, 10-13]), reflecting the high degree of order, i.e., a homogeneous structural situation, as is characteristic of true crystals. The other end of the "order spectrum" in silicas is represented by the very broad ^{29}Si Q_4 peak of a glassy SiO_2 , as seen in Fig. 1F (linewidth ~ 12 ppm). One sees from the intermediate Q_4 linewidths in Figure 1 for silica gel (~ 6 ppm) and fumed silica (~ 9 ppm) that these materials are intermediate between a highly amorphous (glassy) and a completely crystalline material. The fact that medium-range order is more extensive in silica gel than in fumed silica (with its wider distribution of bond angles and distances resulting from its formation at much higher temperatures) is manifested in the fact that the Q_4 peak of silica gel is appreciably narrower than that of fumed silica. Indeed, the relatively rapid formation processes for silica gels and fumed silicas (especially the latter), may preclude the dominance of certain thermodynamic factors that can otherwise determine the characteristics of crystal surfaces. We believe that the amorphous materials, silica gel and even fumed silica, are properly represented as having some characteristics in common with glasses and some characteristics in common with crystalline materials. In particular, we believe that the *surfaces* of these amorphous high-surface-area materials can be modeled in terms of crystal faces of β -cristobalite [8]. No doubt some other characteristics may

be modeled in terms of glassy silica, but we don't focus on such properties in this instance. Burneau et al. have indicated that various experimental results suggest some local order on the silica surface even with an amorphous bulk network [20].

The spectrum (Fig. 1G) of a functionalized polysiloxane in Figure 1 represents a polysiloxane in which pendant $-\text{CH}_2\text{CH}_2\text{CH}_2\text{NH}_2$ groups are attached to the polysiloxane framework, replacing one siloxane linkage on some of the silicon atoms. The Q_4 peak in this spectrum has a linewidth of about 8 ppm, comparable to those in the amorphous silicas (Figs. 1B-1E), and substantially less than that of silica glass. This implies that the distribution of local bond angles and bond lengths at silicon atoms is narrower for the functionalized polysiloxanes (of which the example with pendant $-\text{CH}_2\text{CH}_2\text{CH}_2\text{NH}_2$ groups is representative) than for the silica glass, in which one expects a substantial amount of strain that is "locked-in" as the fused silica is cooled to form a glass.

Our research group has synthesized and structurally characterized a substantial series of functionalized polysiloxanes [21-25], including the following pendant groups (in some cases, in binary combinations): $-\text{CH}_2\text{CH}_2\text{CH}_2\text{NH}_2$, $-\text{CH}_2\text{CH}_2\text{CH}_2\text{Cl}$, $-\text{CH}_2\text{CH}_2\text{CH}_2\text{SH}$, $-\text{CH}_2\text{CH}_2\text{CH}_2\text{PPh}_2$, $-\text{CH}_2\text{CH}_2\text{PPh}_2$, $-\text{CH}_2\text{CH}_2\text{CH}_2\text{NHCH}_2\text{CH}_2\text{NH}_2$, $-\text{CH}_2\text{CH}_2\text{CH}_2\text{NHCH}_2\text{CH}_2\text{NHCH}_2\text{CH}_2\text{NH}_2$, $-\text{CH}_2\text{CH}_2\text{CH}_2\text{N}^+(\text{CH}_3)_3$, $-\text{CH}_2\text{CH}_2\text{CH}_2\text{NHCH}_2\text{CO}_2\text{CH}_3$, $-\text{CH}_2\text{CH}_2\text{CH}_2\text{SCH}_2\text{CO}_2\text{CH}_3$, $-\text{CH}_2\text{CH}_2\text{CH}_2\text{NEt}_2$, $-\text{CH}_2\text{CH}_2\text{CH}_2\text{O}_2\text{CCH}_2\text{NH}_2$, $-\text{CH}_2\text{CH}_2\text{CH}_2\text{O}_2\text{CCH}_2\text{NHCH}_2\text{CO}_2$; and $-\text{CH}_2\text{CH}_2\text{CH}_2\text{O}_2\text{CH}_3$. Functionalized polysiloxanes with two different pendant groups were prepared by the sol-gel method with a starting reaction mixture consisting of a combination of $\text{RSi}(\text{OR}')_3$, $\text{R}''\text{Si}(\text{OR}')_3$, and $\text{Si}(\text{OR}')_4$, where $\text{R}' = \text{Me}$ or Et . This work has recently been reviewed in detail [25]. A few highlights are summarized below.

The NMR characterization of functionalized polysiloxanes, based on ^{29}Si NMR spectra of the type shown in Figure 1G, were especially useful in establishing the nature of the three-dimensional polysiloxane framework, e.g., in establishing the populations of $\text{RSi}(\text{O}-\text{Si})_3$, $\text{RSi}(\text{OSi})_2\text{OR}$, Q_3 , and Q_4 sites. To avoid the need to characterize CP spin dynamics that would be needed to quantitate $^1\text{H} \rightarrow ^{29}\text{Si}$ CP-MAS results, some DP-MAS experiments were carried out with suitably long repetition delay periods [22]; on the basis of deconvoluted DP-MAS ^{29}Si spectra of this type (e.g., Fig. 1G), in combination with associated ^{13}C NMR results, it is possible to generate a hypothetical structure of a functionalized polysiloxane. Figures 2 and 3 show two examples of such structures.

^{13}C CP-MAS NMR is useful in determining, or confirming the structures of pendant groups, in estimating the amounts of residual (unhydrolyzed/uncondensed) methoxy and ethoxy groups of starting materials, in estimating the ratios of two different types of pendant groups, when two are present, and in establishing qualitatively the local mobilities (via dipolar-dephasing or ^{13}C -detected T_1^H

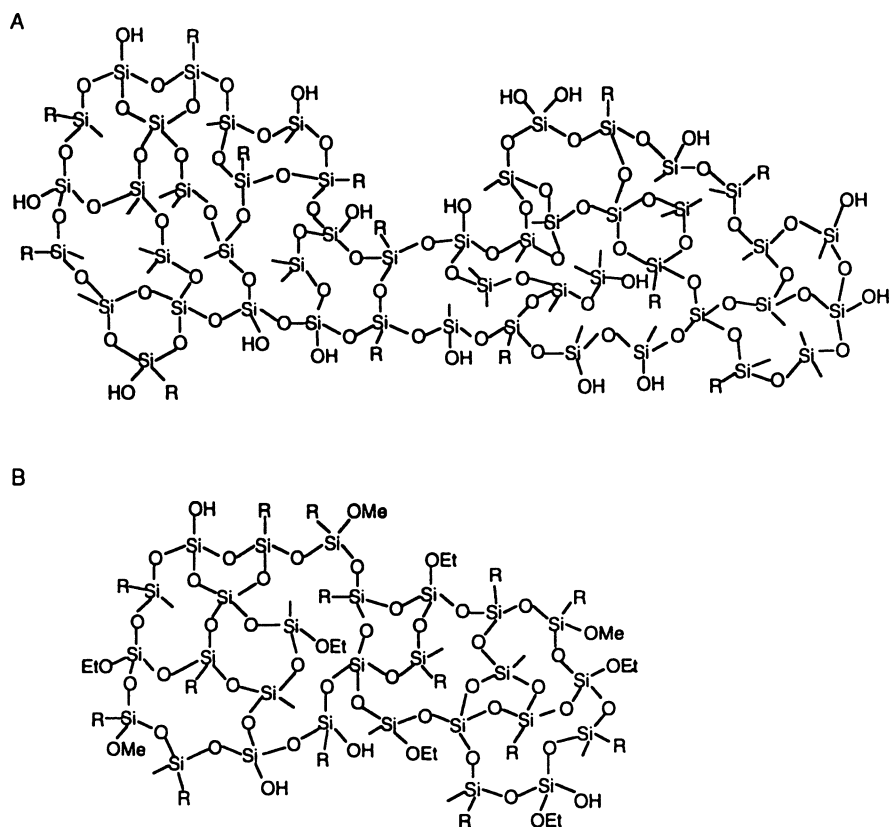


Figure 2. Representative (hypothetical) structures of polysiloxane-immobilized systems based on ^{29}Si DP-MAS spectra (e.g., Fig. 1G). A) Polysiloxane-immobilized $-\text{CH}_2\text{CH}_2\text{CH}_2\text{NH}_2$, B) polysiloxane-immobilized $-\text{CH}_2\text{CH}_2\text{CH}_2\text{Cl}$. Ref. 21.

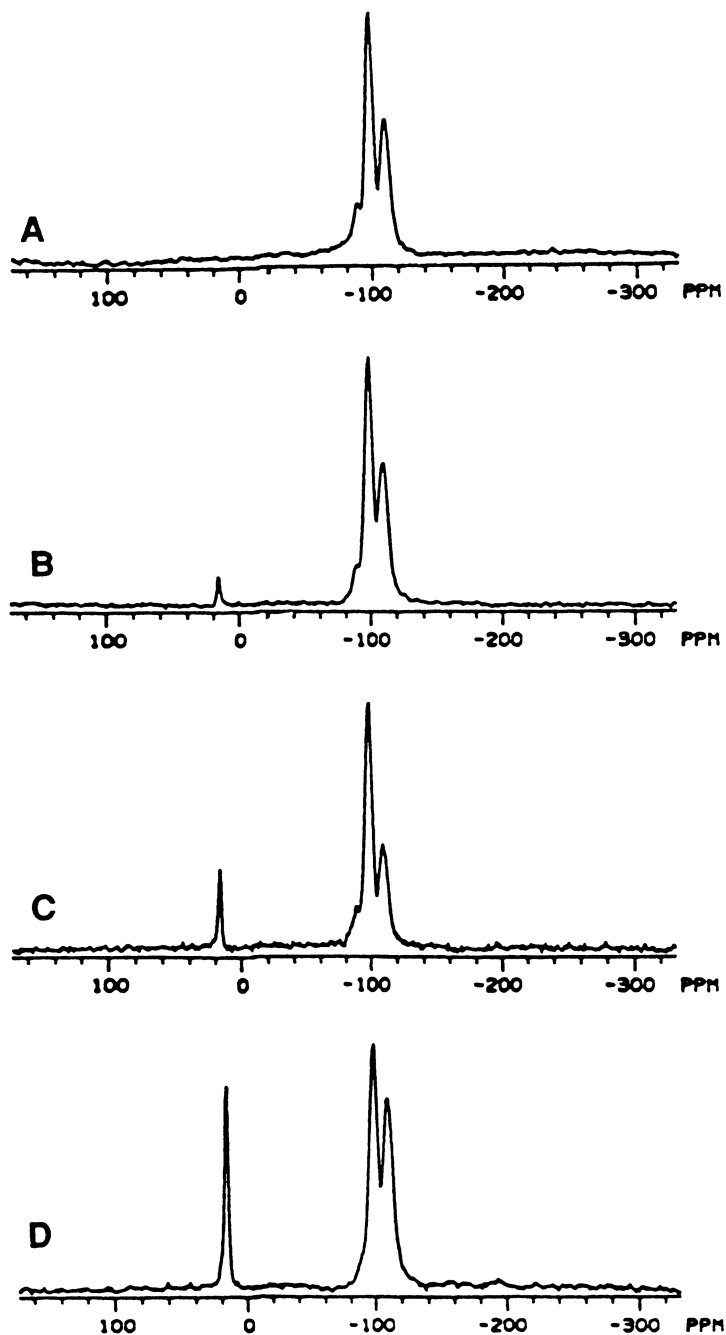


Figure 3. ^{29}Si CP-MAS spectra of silica (Whatman Partisil) silylated with $\text{CH}_3(\text{CH}_2)_{17}\text{Si}(\text{CH}_3)_2\text{Cl}$. A) Unsilylated, B) - D) increasing degree of silylation.

experiments) of the various structural segments of a functionalized polysiloxane structure. As is ^{15}N NMR, the ^{13}C NMR peak of C-2 in amine-functionalized polysiloxanes is useful in elucidating the hydrogen-bonding and/or proton-transfer status of the system [22, 23]. Using large-volume ($\sim 2.5\text{ cm}^3$) samples and ^1H - ^{15}N cross polarization, ^{15}N CP-MAS spectra have readily been obtained on amine-functionalized polysiloxanes [22, 23]. For phosphine-functionalized polysiloxanes, the strong, convenient ^{31}P spectra are valuable for assessing what fraction of the $-\text{PPh}_2$ moieties are converted to $-\text{P}(\text{O})\text{Ph}_2$ groups by inadvertent oxidation (presumably by O_2) [24].

One of the most useful features of $^1\text{H} \rightarrow \text{X}$ CP-MAS experiments on functionalized polysiloxanes is the ability to measure ^1H spin-lattice relaxation times of the protons responsible for generating magnetization in each X site observed in the X-detected $^1\text{H} \rightarrow \text{X}$ CP-MAS spectra (where in these cases $\text{X} = ^{13}\text{C}$, ^{29}Si or ^{31}P) obtained with inversion of ^1H magnetization prior to $^1\text{H} \rightarrow \text{X}$ CP. T_1^{H} values are not only useful for estimating local mobilities, but also for interrogating domain homogeneity/heterogeneity [25].

The proton spin-lattice relaxation time, T_1^{H} , in a diamagnetic sample is typically dominated by the dipole-dipole interactions and the resulting communication among the protons, and is particularly sensitive to molecular motions; therefore, T_1^{H} values have been used widely to derive information not only on molecular motion, but also about domain uniformity or phase separation in solids. In single-phase solids with an abundance of protons, the protons are usually so strongly coupled by homonuclear dipolar interactions that possible differences in proton spin-lattice relaxation are averaged out by spin diffusion, and a single T_1^{H} would be observed in this case. In heterogeneous samples, different values can be observed for different phases.

The T_1^{H} approach based on ^{13}C detection is particularly suitable for examining the phase distribution of the organic pendant groups in the polysiloxane network of the polysiloxane-immobilized system, and, if they are present, unhydrolyzed ethoxy groups and methoxy groups [21, 25]. Unhydrolyzed ethoxy groups and/or methoxy groups come from the non-ligand-bearing starting material, $\text{Si}(\text{OEt})_4$, and ligand-bearing starting material, e.g., $(\text{MeO})_3\text{SiCH}_2\text{CH}_2\text{CH}_2\text{SH}$, and could *a priori* represent spatially different regions or phases in an inhomogeneous material (i.e., if they are not largely homogeneous). The examination of T_1^{H} values measured from the ^{13}C signals of ethoxy groups, methoxy groups and pendant (ligand) groups provides information on the distribution of the ligand groups in the sample: if the ligand groups in a particular sample are uniformly distributed in the polysiloxane network, then the same value would be expected for T_1^{H} measured via the ^{13}C signals of the ethoxy, methoxy and ligand groups. Further information can be obtained by comparing these ^{13}C -detected T_1^{H} values with the results of analogous measurements based on ^{29}Si signals of SiOH groups. In the case of

polysiloxane-immobilized -PPh₂ systems, ³¹P-derived T₁^H values are useful for addressing the domain(s) containing the organophosphine moieties [24].

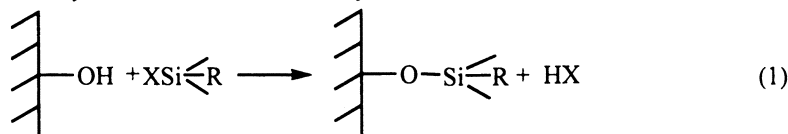
The protons of organic ligand groups are expected to be mainly responsible for the T₁^H values of the pendant ligand groups detected via ¹³C resonances. They may represent different regions of the material from those regions in which are concentrated SiOH groups, which are at least substantially (if not totally) responsible for ²⁹Si-detected T₁^H values. Therefore, comparison between the ²⁹Si-detected T₁^H values and ¹³C-detected T₁^H values should provide information about domain uniformity or phase separation. In each case, for a specific sample examined at a specific magnetic field strength, only one T₁^H value (within experimental error) was obtained, irrespective of which ¹³C, ²⁹Si or ³¹P peak was detected for determining T₁^H. Furthermore, when more than one type of pendant group was present in a given sample (e.g., -CH₂CH₂CH₂SH and -CH₂CH₂CH₂NH₂), only *one* ¹³C-derived T₁^H value was observed. These results imply that the two types of ligand groups (e.g., thiol and monoamine) are uniformly mixed in the polysiloxane network; they are not phase separated. The fact that the ¹³C-detected T₁^H value and the ²⁹Si-detected T₁^H values for the silicon sites of the -60 ppm region and the -100 ppm region are all the same for a given sample, within experimental error, suggests that the organofunctionalities in each of these two samples are in the same phase as the silica-like network [25].

Silicones, such as polydimethylsiloxane (PDMS), [-Si(Me)₂O-]_n, have only two siloxane linkages at each silicon atom in the repeat unit [3]. In their simplest forms, silicones are linear or cyclic polymers or oligomers, commercial products being based mainly on linear polymers. PDMS can be produced as liquids with a range of viscosities, gels, gums or elastomers; the detailed state and properties depend mainly on molecular weight and the degree of cross linking. In PDMS, cross linking is commonly achieved via the carbon-based structure (e.g., coupling between -CH₂ groups generated from methyl groups, or from reaction between >Si-H and >Si-CH=CH_2 moieties that replace a small fraction of the >Si-CH_3 groups) or by including a coupling agent of the form SiX₄ or CH₃SiX₃ in the reaction mixture. Figure 1H shows the ²⁹Si DP-MAS spectrum of a PDMS rubber. The sharp (6 ppm) single peak reflects the simple, relatively homogeneous chemical structure of the repeat unit. -Si(Me)₂O-, as well as motional averaging (narrowing) of what instantaneous differences may exist among the bond angles and bond lengths of individual -Si(Me)₂O- units.

Among the various kinds of siloxane-based systems identified above, silicas, including derivatized silicas, are the ones on which our research group has focused most strongly on a long-term basis [8, 16, 21-55]. The silicon atom sites in the interior of each silica particle are of the Si(OSi<sub>4) or Q₄ type, with four siloxane linkages oriented at tetrahedral angles with respect to each other, attached to each

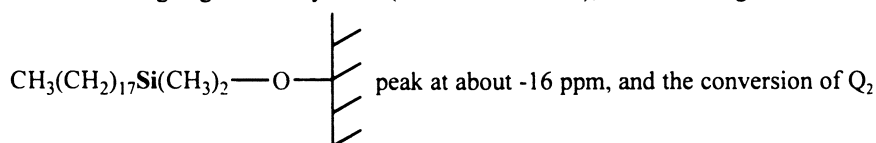
silicon atom. The surface sites of an underivatized silica consists primarily of Q_4 sites, along with $\text{HOSi}(\text{OSi}\leq)_3$ (Q_3) sites and $(\text{HO})_2\text{Si}(\text{OSi}\leq)_2$ (Q_2) sites; these *silanol* (SiOH) moieties seem to dominate the surface properties.

The *silylation* of silica surfaces, by reactions of the type,



(where $\begin{array}{c} \diagup \\ | \\ \diagdown \end{array}$ represents the silica surface) can produce a variety of surface-derivatized

silicas in which a desired chemical functionality (part of R) is immobilized on silica particles. Figure 3 shows ^{29}Si CP-MAS spectra of a silica sample at various stages of silylation with $\text{CH}_3(\text{CH}_2)_{17}\text{Si}(\text{CH}_3)_2\text{Cl}$. The spectrum of the underivatized silica (Fig. 3A) shows the Q_2 , Q_3 and Q_4 peaks mentioned above at -89, -99 and -109 ppm. With increasing degrees of silylation ($A \rightarrow B \rightarrow C \rightarrow D$), one sees the growth of the



intensity into Q_4 intensity (actually the result of $Q_2 \rightarrow Q_3$ and $Q_3 \rightarrow Q_4$) as silanol groups are silylated.

In the case represented by Figure 3, there is only one labile group (Cl) on the silylating agent, so the nature of the attachment of the $\text{CH}_3(\text{CH}_2)_{17}\text{Si}(\text{CH}_3)_2\text{—}$ moiety to the silica surface is rather obvious. However, many silylating agents have two or three leaving groups. An important example is the case in which $(\text{EtO})_3\text{SiCH}_2\text{CH}_2\text{CH}_2\text{NH}_2$ is the silylating agent, with three ethoxy groups available for reactions to form siloxane bridges to the silica surface and/or to other $\text{SiCH}_2\text{CH}_2\text{CH}_2\text{NH}_2$ silicon atoms [38, 41]. Figure 4 shows some of the various structures that one might expect for the silylated silica surface; missing from this picture of a hypothetical derivatized surface structure are any unreacted ethoxyl groups, the presence or absence of which can be determined (*vide infra*) from ^{13}C NMR spectra (peaks at about 17 and 58 ppm for the CH_3 and CH_2 group, respectively).

Figure 5 shows ^{29}Si CP-MAS spectra obtained in a detailed study of the effect of reaction conditions on the silylation of silica gel by the “coupling” agent, $(\text{EtO})_3\text{SiCH}_2\text{CH}_2\text{CH}_2\text{NH}_2$ [41]. Four different pre-silylation drying temperatures of the silica gel were explored (200 °C, 110 °C, RT = 25 °C and AQ = no drying, aqueous reaction conditions), as well as five post-reaction “curing” temperatures

Silica Gel Derivatized with $(\text{CH}_3\text{CH}_2\text{O})_3\text{SiCH}_2\text{CH}_2\text{CH}_2\text{NH}_2$

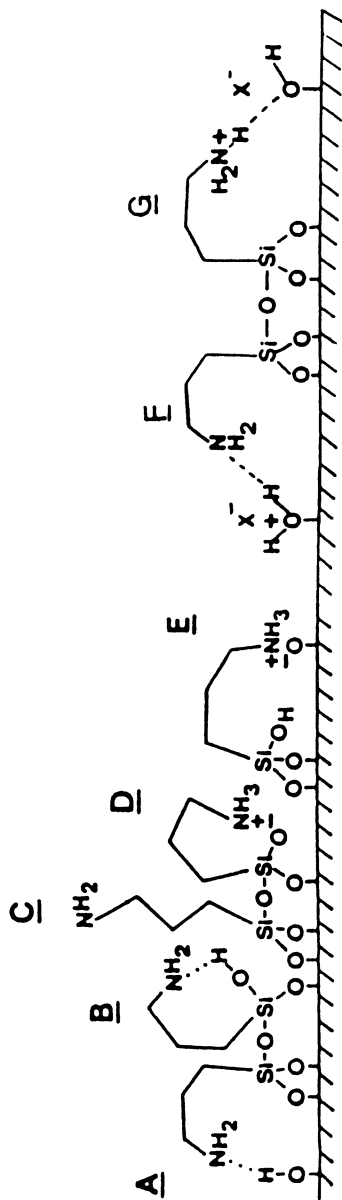


Figure 4. Hypothetical, possible surface structures of silica silylated with $(\text{EtO})_3\text{SiCH}_2\text{CH}_2\text{CH}_2\text{NH}_2$, showing a variety of attachments to the surface and a variety of hydrogen-bonding and acid-base situations. Ref. 41.

(200 °C, 150 °C, 110 °C, 65 °C and RT = 25 °C). In Figure 5 one sees that, by increasing the amount of water present in the reaction mixture (decreasing pre-silylation temperature or employing aqueous reaction conditions) or by increasing the post-reaction curing temperature, one can shift the populations of surface-attached $(-\text{O}-)_3\text{SiCH}_2\text{CH}_2\text{CH}_2\text{NH}_2$ groups from those that have only one siloxane attachment (about -49 ppm) to those with two (about -58 ppm) or even three (about -66 ppm) siloxane attachments to the surface and/or other $(-\text{O}-)_3\text{SiCH}_2\text{CH}_2\text{CH}_2\text{NH}_2$ moieties. Corresponding ^{13}C CP-MAS spectra (an example shown in Figure 6) of such samples show the sensitivity of the C-2 (or β) carbon chemical shift to the acid/base state and the ability to detect residual ethoxy groups (unusually prominent in the example shown in Figure 6). As reflected in the ^{29}Si and ^{13}C NMR spectra, there is a close structural analogy between the surface-derivatized samples represented in Figures 4-6 and the polysiloxane-immobilized $-\text{CH}_2\text{CH}_2\text{CH}_2\text{NH}_2$ sample represented in Figure 1G, prepared by a sol-gel process from a mixture of $\text{Si}(\text{OEt})_4$ and $(\text{EtO})_3\text{SiCH}_2\text{CH}_2\text{CH}_2\text{NH}_2$.

The ^1H CRAMPS spectra [56, 57] shown in Figure 7, for a $(\text{CH}_3)_3\text{SiCl}$ -silylated silica gel, a polysiloxane-immobilized $-\text{CH}_2\text{CH}_2\text{CH}_2\text{Cl}$ sample and a silica sample derivatized by $(\text{EtO})_3\text{SiCH}_2\text{CH}_2\text{CH}_2\text{NH}_2$, demonstrate that the ^1H CRAMPS technique is also useful in characterizing the various kinds of polysiloxane systems discussed above. The spectra of samples containing large populations of pendant $-\text{CH}_2\text{CH}_2\text{CH}_2\text{Cl}$ groups (Fig. 7B) and $-\text{CH}_2\text{CH}_2\text{CH}_2\text{NH}_2$ groups (Fig. 7C, D) are dominated by peaks from those groups, while in the spectrum of a very lightly-silylated sample prepared by silylating silica gel with $(\text{CH}_3)_3\text{SiCl}$, the $(\text{CH}_3)_3\text{Si}$ -peak does not obscure the peaks due to unsilylated portions of the silica surface.

Various forms of underivatized silica itself have also been studied productively and extensively by ^1H NMR and ^{29}Si NMR. As seen above (Fig. 1A-F), ^{29}Si CP-MAS NMR provides surface-emphasized spectra in which one can readily distinguish peaks (or clearly defined shoulders) due to $(\text{HO})_2\text{Si}(\text{OSi}\leftarrow)_2$ (Q_2), $\text{HOSi}(\text{OSi}\leftarrow)_3$ (Q_3) and $\text{Si}(\text{OSi}\leftarrow)_4$ (Q_4) sites, primarily at the surface. Such spectra obtained on silica gel or fumed silica samples that have been treated under vacuum at a temperature of 500 °C or above show that the only silanols remaining are Q_3 silanols. ^{29}Si CP-MAS experiments on silica samples that have been "equilibrated" with deuterated water show that a small fraction of the silanols are not readily accessible to D_2O exchange, even in boiling samples; such "trapped" silanols have been characterized via time-domain ^{29}Si CP-MAS studies to be primarily non-hydrogen-bonded Q_3 silanols [48, 55]. Figure 8 shows ^{29}Si CP-MAS spectra of a silica gel that had been equilibrated with D_2O at 25 °C (Fig. 8A) and then exposed to air for various periods of time, until eventually (essentially 90 minutes) the original, unexchanged sample is recovered (Fig. 8B). One sees that the Q_2 (geminal) silanol peak is essentially gone with the D_2O -exchanged sample, although a Q_3 signal is certainly present; after only 90s of exposure to air, both the Q_2 and Q_3 signals are seen to be growing in.

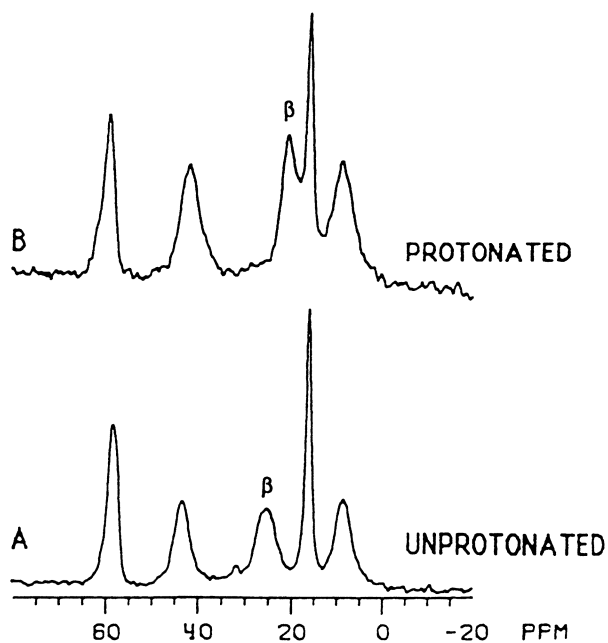


Figure 6. ^{13}C CP-MAS spectra of silica gel silylated with $(\text{EtO})_3\text{SiCH}_2\text{CH}_2\text{CH}_2\text{NH}_2$. A) Unprotonated, B) protonated by HCl treatment.

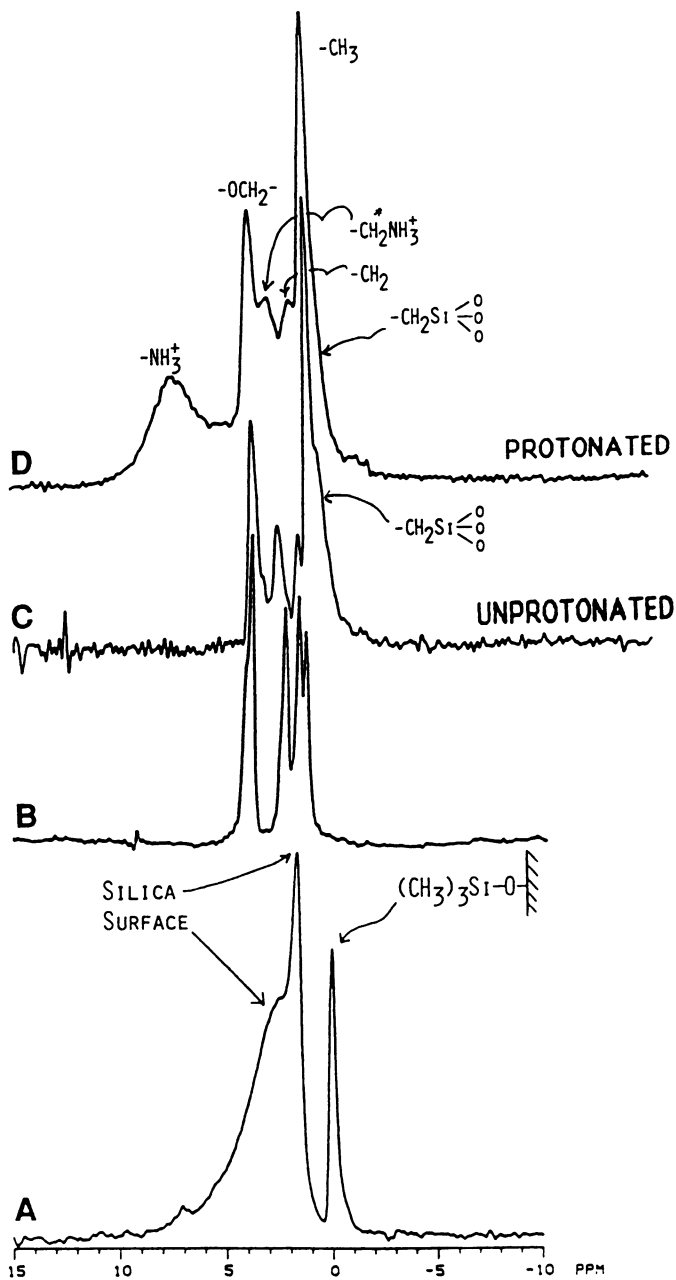


Figure 7. ^1H CRAMPS spectra of $(\text{CH}_3)_3\text{SiCl}$ -derivatized silica gel (A); polysiloxane-immobilized $-\text{CH}_2\text{CH}_2\text{CH}_2\text{Cl}$ (B); silica gel silylated with $(\text{EtO})_3\text{SiCH}_2\text{CH}_2\text{CH}_2\text{NH}_2$, unprotonated (C) and protonated by HCl (D).

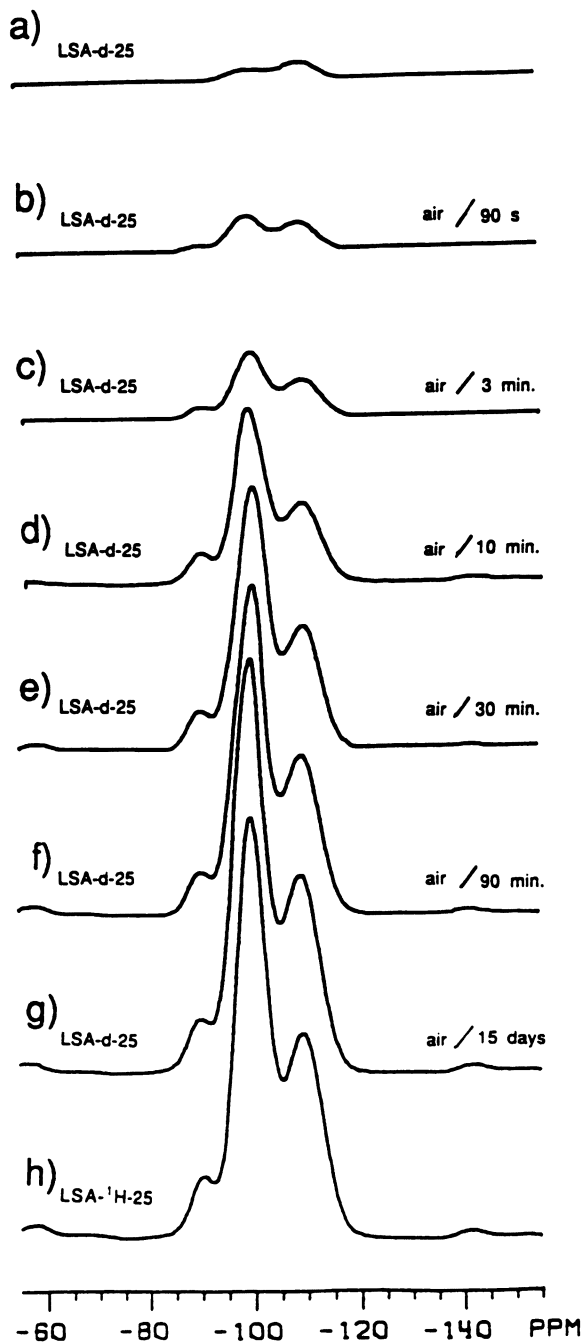


Figure 8. ^{29}Si CP-MAS spectra of a silica gel sample that has been D_2O -exchanged at 25 °C (Fig. 8a) and then exposed to air for the indicated periods of time, h) spectrum of the un-exchanged (initial) silica. Ref. 47.

^1H NMR studies, based on either the CRAMPS (combined rotation and multiple-pulse spectroscopy) or fast-MAS techniques, are useful for studying the hydrogen-bonding states of hydroxyl protons (of silanols and water) on the silica surface. Figure 9 shows the ^1H CRAMPS spectra of a silica gel with various stages of hydration/dehydration [40]. One sees that of the three features (Fig. 9A") identified in the spectrum of untreated (but not very wet) silica gel (Fig. 9A), the relatively sharp peak at about 3 ppm is removed by evacuation at 25 °C (Fig. 9B) and is easily identified as "excess" physisorbed water. The broad feature identified as hydrogen bonded silanols (with some contribution from water that is strongly influenced via hydrogen bonding by and to the silica surface) is still present after evacuation at 200 °C (Fig. 9C), but is absent in the spectrum of the sample that has been evacuated at 500 °C (Fig. 9D, which consists only of a sharp peak at about 2 ppm due to isolated (non-hydrogen-bonded) silanols. Figure 10 shows analogous ^1H CRAMPS results on a fumed silica [55].

Identification of the broad feature in the ^1H CRAMPS spectra of silica samples that have been evacuated at moderate temperatures (roughly < 500 °C) with hydroxyl groups (mainly silanols) that are strongly hydrogen bonded (and relatively immobile) at the silica surface, its strengthened by the ^1H - ^1H dipolar-dephasing results (obtained by inserting a dephasing period between the initial pulse that generates transverse magnetization and the multiple-pulse detection period). An example is shown in Figure 11, which displays ^1H CRAMPS dipolar-dephasing results on silica samples at three stages of dehydration (untreated, 2.6% dehydration weight loss, 500 °C evacuation) [40, 46, 47, 55]. One sees that the physisorbed water peak (~3 ppm) and the isolated-silanol shoulder (~2 ppm) substantially survive even a 1 ms dephasing period, because of weak ^1H - ^1H dipolar interactions due to the absence of hydrogen bonding (2 ppm peak) or rapid motional averaging (3 ppm peak); the broad peak due to relatively immobile hydrogen-bonded hydroxyls is dramatically dephased within 50 μs .

Figure 12 shows that CRAMPS-like spectra, but with the broad signal due to hydrogen-bonded silanols (and relatively immobile water at the surface) not as well defined as in CRAMPS spectra, can be obtained by fast-MAS (12 KHz), without the multiple-pulse sequence [55]. However, as seen in Figure 13, even the slow spinning used in the CRAMPS experiments (~2 KHz) is sufficient to bring about dehydration of fumed silica over time, unless the sample is extremely well sealed (e.g., glass fusion by torch); this effect is, of course, more dramatic at higher MAS speeds.

With the ability of ^{29}Si NMR to identify Q_2 , Q_3 and Q_4 sites on the silica surface, and with ^1H NMR able to identify the extent (or mobility) of hydrogen bonding, it is useful to correlate these two types of information. *A priori*, it would seem that a ^1H - ^{29}Si HetCor approach would best provide this kind of correlation; and

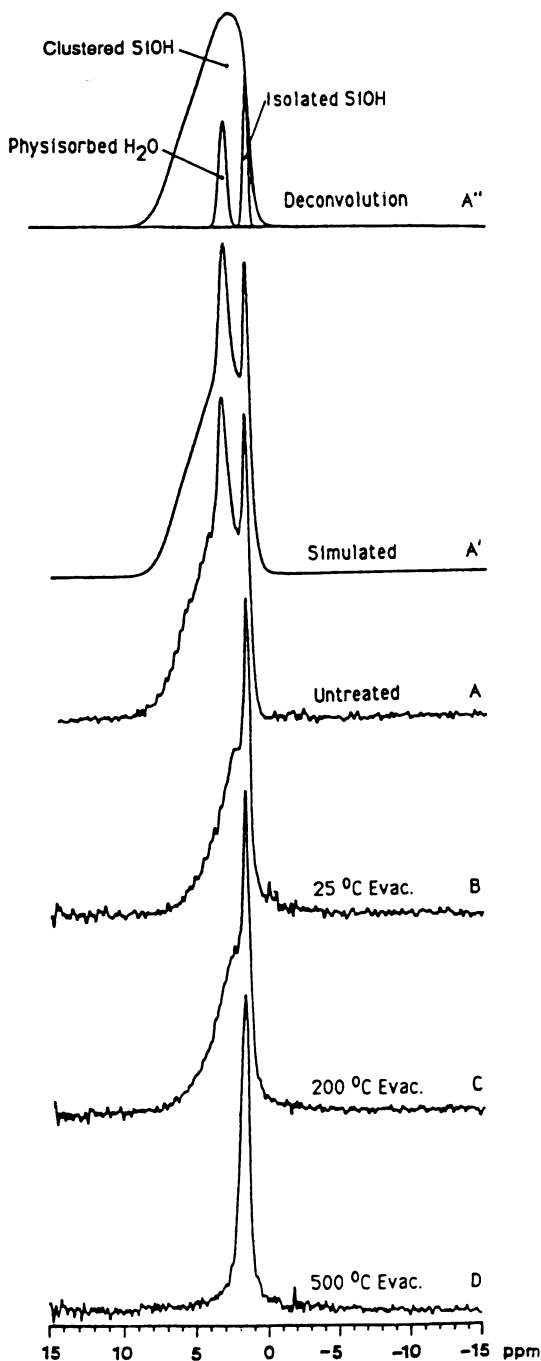


Figure 9. ^1H CRAMPS spectra of silica gel at various stages of dehydration (A - D), and a computer simulation (A', A''). Ref. 40.

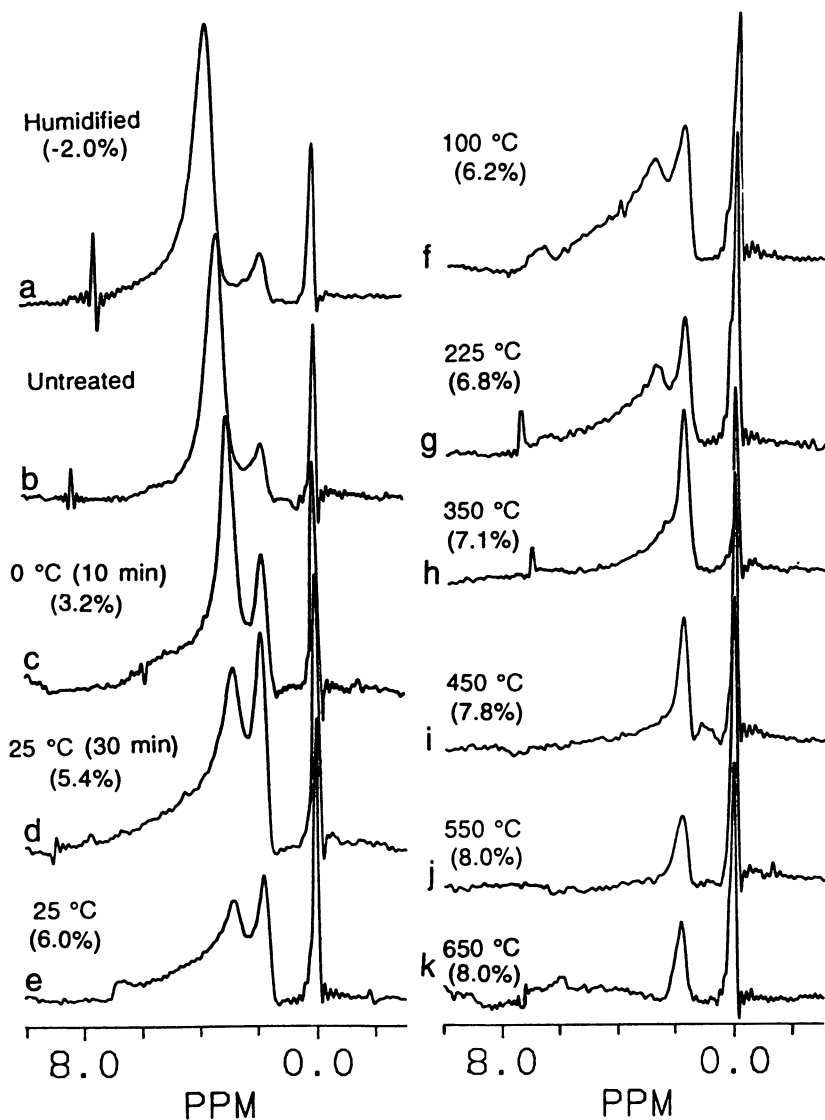


Figure 10. ^1H CRAMPS spectra of Cab-O-Sil fumed silica as a function of hydration/dehydration state (weight loss due to drying shown in parentheses). Sharp peak at 1.0 ppm due to a PDMS reference. Ref. 55.

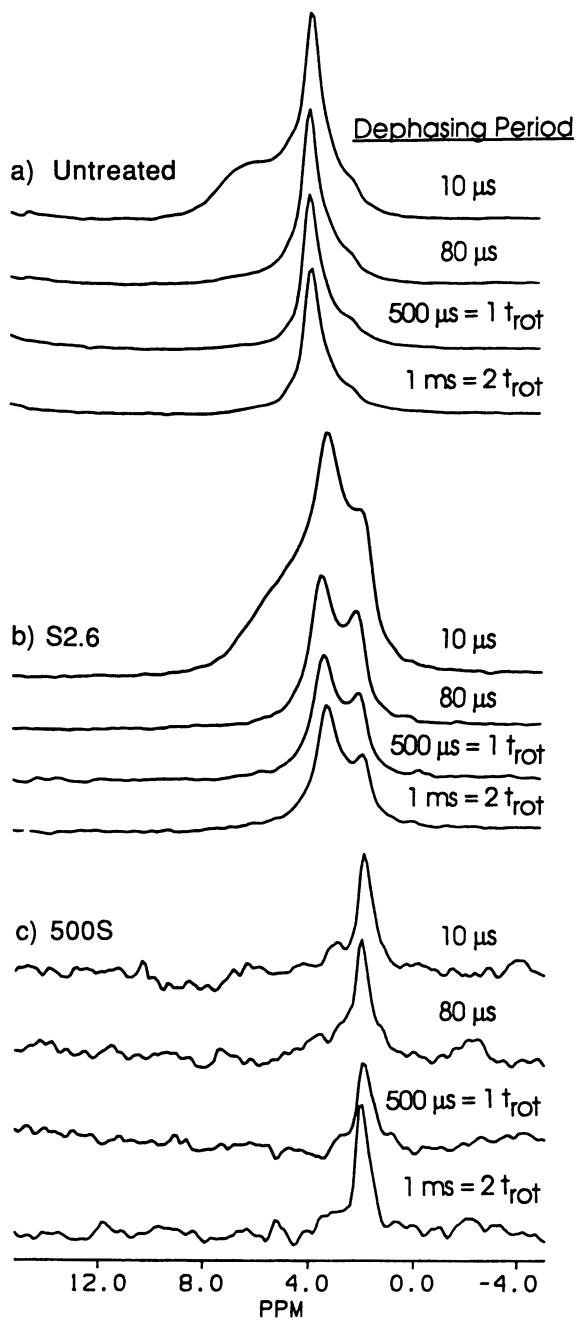


Figure 11. ^1H CRAMPS dipolar-dephasing spectra obtained on a silica gel at three stages of dehydration. A) Untreated, B) dehydrated with 2.6% weight loss, and C) evacuated at 500 °C. Ref. 47.

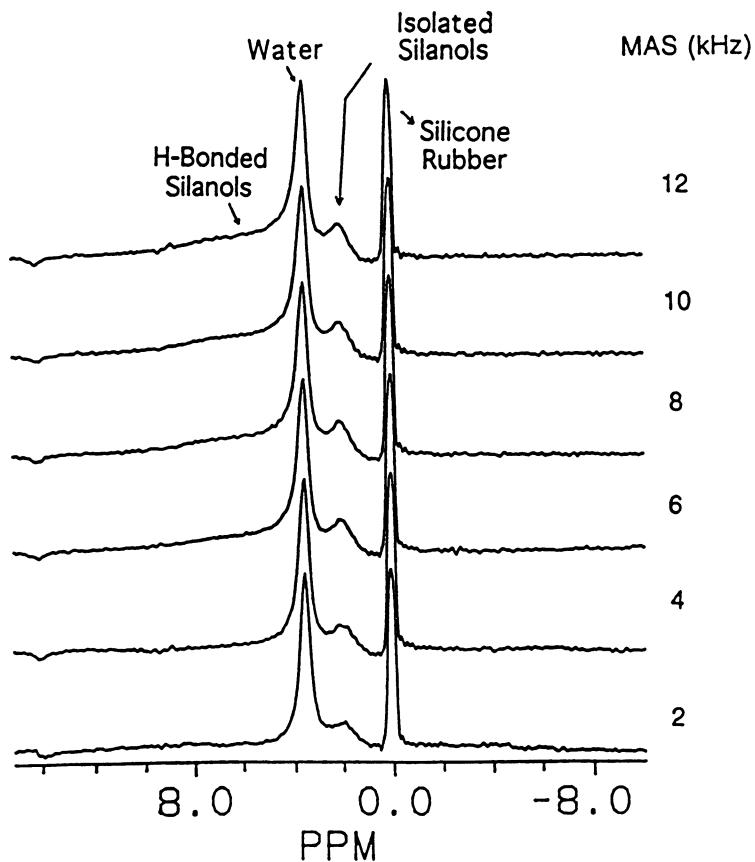


Figure 12. ^1H MAS-only spectra of a Cab-O-Sil fumed silica as a function of MAS speed, with a silicone rubber (PDMS) signal as a reference. Ref. 55.

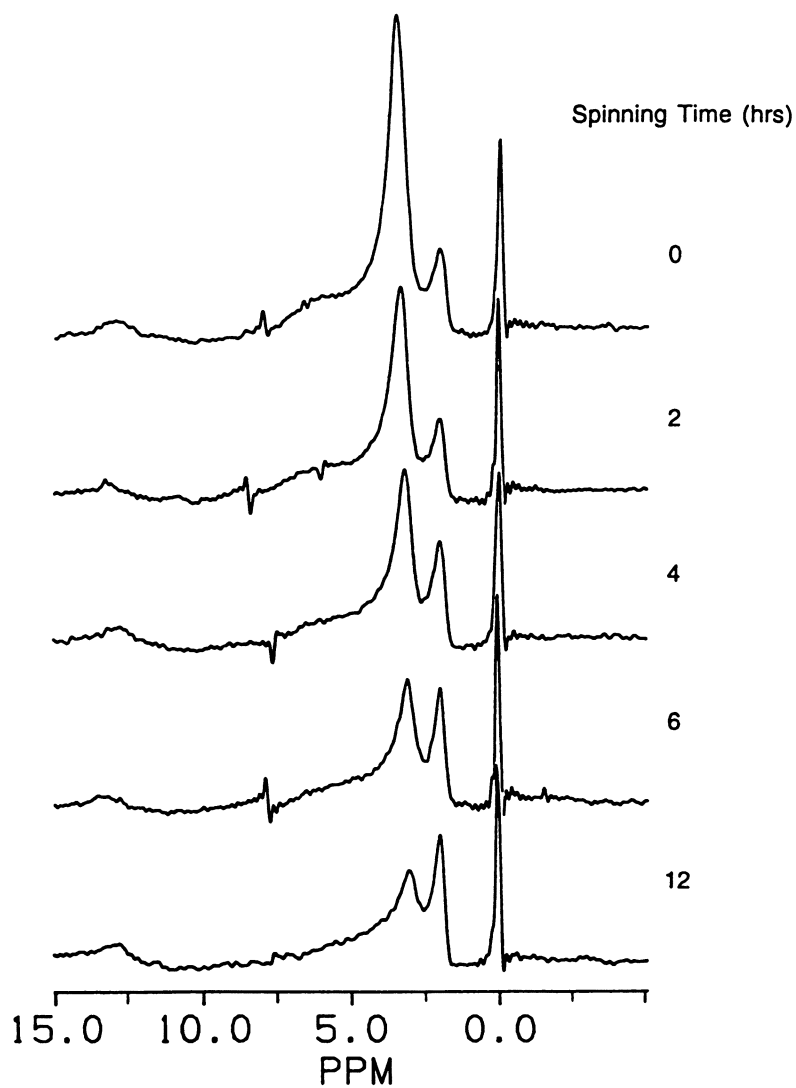


Figure 13. Effect of measurement time on ^1H CRAMPS spectra of a Cab-O-Sil fumed silica. Ref. 55.

it is possible that this will turn out to be the case. However, it is a more difficult task than in the typical ^1H - ^{13}C HetCor experiment, where there are stronger ^1H -X dipolar interactions due to directly bonded nuclei; there are no direct ^1H - ^{29}Si bonds in silica. As an alternative strategy, a variety of ^1H - ^{29}Si CP-MAS experiments have been carried out in which the behavior of proton magnetization during one segment of the sequence identifies the hydrogen-bonding state, and this is projected onto ^{29}Si magnetization during detection [46, 55]. This approach can take such simple forms as turning off the ^1H decoupler during: a) detection (where MAS averages ^1H - ^{29}Si dipolar interactions best for those protons that are not strongly coupled with other protons), b) a period between the CP generation of ^{29}Si magnetization and ^{29}Si detection (^1H - ^{29}Si dipolar dephasing, which is most efficient for the strongest ^{29}Si dipolar couplings to protons that are strongly coupled with other protons) or c) a period prior to $^1\text{H} \rightarrow ^{29}\text{Si}$ CP (where the magnetization of protons that are strongly coupled with other protons is attenuated by dephasing and hence less available for polarization transfer to ^{29}Si during the CP period). Figures 14-16 show examples of these three strategies. In each case, one sees that the protons most responsible for generating geminal (Q_2) silanol magnetization via CP are the hydrogen-bonded silanols, while non-hydrogen-bonded protons (with weaker ^1H - ^1H dipolar interactions) are more heavily involved in CP transfer to single (Q_3) silanols.

From data of the type represented in Figures 14-16 (especially Fig. 15) and from corresponding variable-contact-time ^1H - ^{29}Si CP curves, it is possible to derive the fraction of each type of silanol (Q_2 and Q_3) that is hydrogen bonded and the fraction that is not. It has also been demonstrated, as implied in the discussion of Figures 9 and 10, that dehydration/dehydroxylation of the silica surface proceeds in the following order as the dehydration/ dehydroxylation temperature is increased: physisorbed water, hydrogen-bonded silanols, non-hydrogen bonded silanols.

There have been, of course, numerous other ^{29}Si and/or ^1H NMR studies of silicas by other research groups. Perhaps most notable among these have been the studies of Brinker and co-workers [4, 58, 59] and of Legrand and co-workers [60-64].

The accumulated ^1H and ^{29}Si NMR data on silicas, as outlined briefly above, are consistent with a model of the silica surface in which it is composed primarily of small segments having structures corresponding to 100-type and 111-type faces of β -cristobalite (with terminal Si-O-moieties in the form of silanols) [8]. Recognizing that such materials as silica gel and fumed silica are indeed *amorphous*, one knows that they do *not* manifest long-range order, so these β -cristobalite-like surface segments probably do not extend beyond dimensions of a few nm.

Figure 17 shows "side views," looking onto such a 100 face (harboring geminal, or Q_2 , silanols) and a 111 face (with single, or Q_3 , silanols). One can see that the geminal silanols of such a 100 face are well situated geometrically for inter-

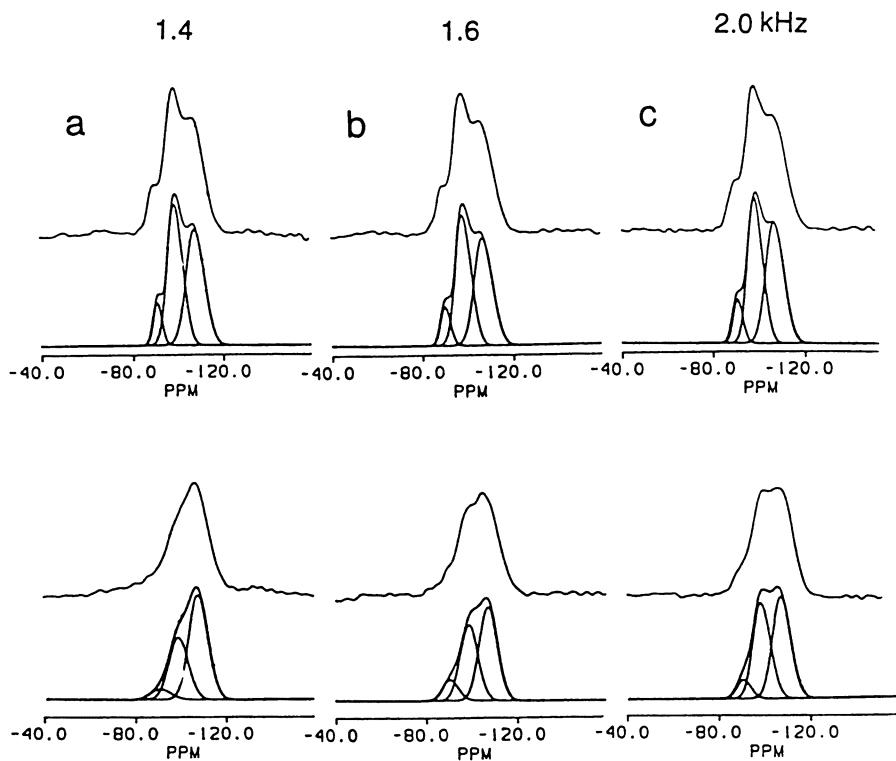


Figure 14. ^1H -decoupled (top spectrum of each set) and ^1H -coupled (bottom spectrum of each set) ^{29}Si CP-MAS spectra of untreated Cab-O-Sil fumed silica at three different MAS speeds, as indicated. Computer-simulated spectrum and individual deconvoluted contributions shown below each experimental spectrum. Ref. 55.

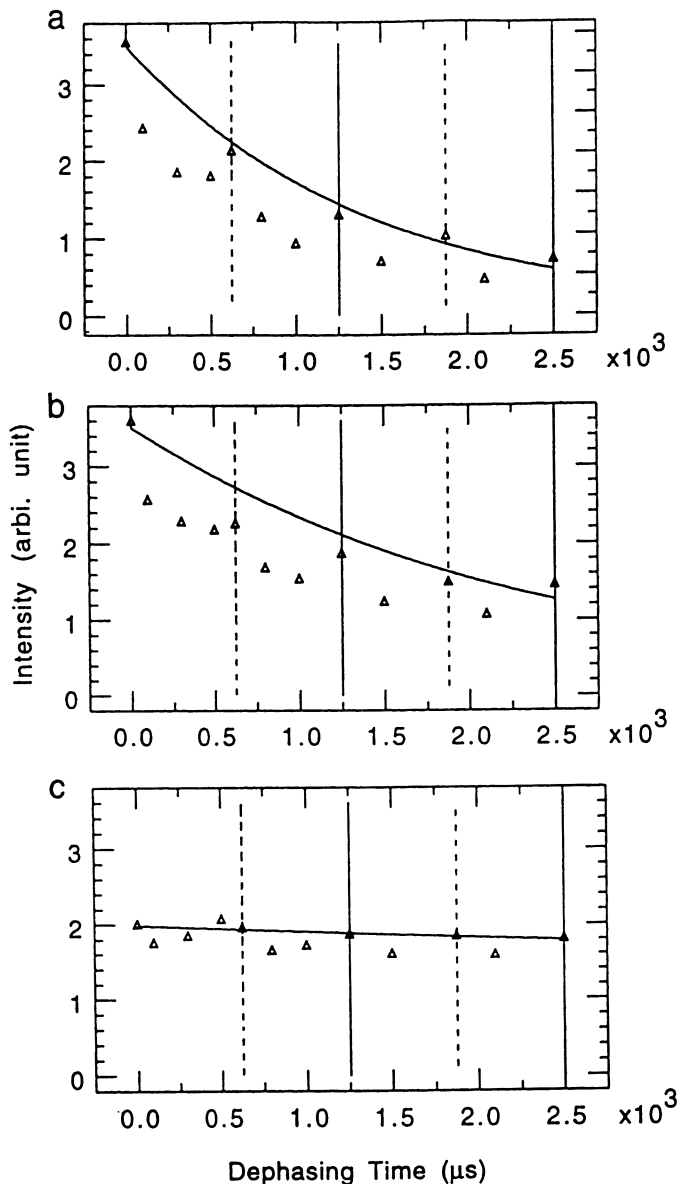


Figure 15. Plots of the deconvoluted peak intensities of the ^{29}Si CP-MAS NMR spectra of untreated Cab-O-Sil fumed silica vs. ^1H - ^{29}Si dipolar-dephasing time, up to four rotor periods. CP contact time, 5 ms; MAS speed, 1.6 kHz. Vertical dashed lines show odd numbers of rotor periods and vertical solid lines show even numbers of rotor periods. A) geminal silanols, B) single silanols and C) Q_4 silicons. The fitting curves represent the best fits, from which T_2' was derived. Ref. 55.

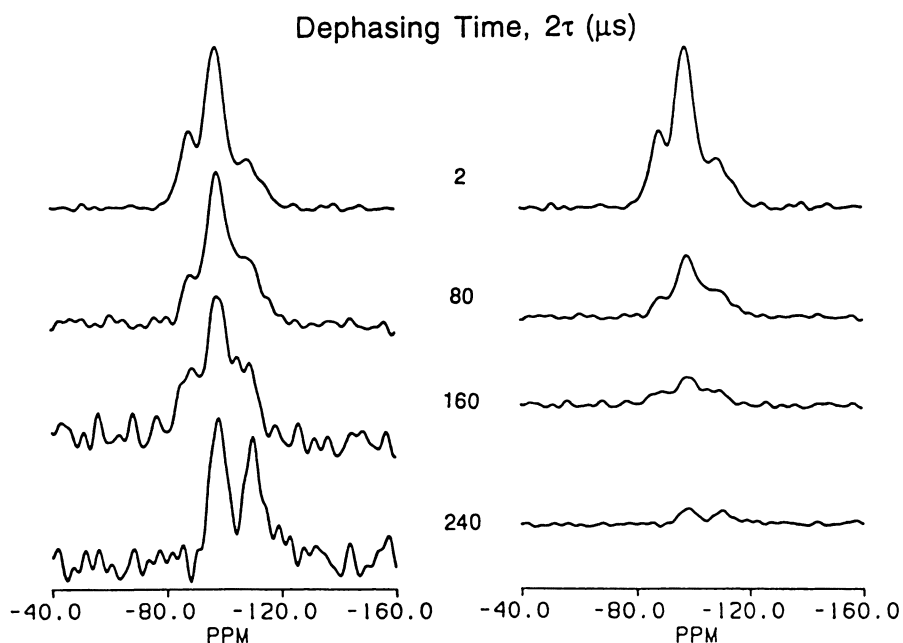


Figure 16. ^{29}Si CP-MAS spectra of Cab-O-Sil fumed silica obtained with four different ^1H - ^1H dipolar-dephasing times (as indicated) prior to $100\ \mu\text{s}$ CP period. Spectra on the left scaled to a common height of the $-99\ \text{ppm}$ peak; and spectra on the right plotted on a common absolute intensity scale. Ref. 55.

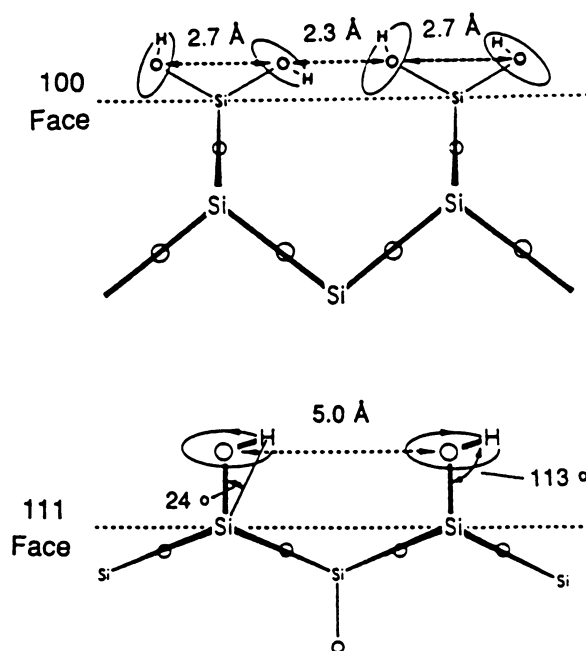


Figure 17. Side views of the 100 β -cristobalite face with geminal silanols, and the 111 β -cristobalite face, with single silanols. Ref. 8.

silanol hydrogen bonding, while the Q₃ silanols of the 111 face are too far apart for hydrogen bonding. This clear distinction between hydrogen-bonded Q₂ silanols and non-hydrogen-bonding Q₃ silanols is altered in predictable ways at intersections between 100 and 111 faces. Invoking such intersections also makes it possible to generate models of pores [8].

Acknowledgments

The author gratefully acknowledges the central roles played by several students and postdoctorals, especially Drs. I-Ssuer Chuang, Charles H. Bronnimann, and Dean Sindorf, and that much of the material described in this paper was supported by NSF Grant No. CHE-9021003.

Literature Cited

1. Iler, R.K., *The Chemistry of Silica*; Wiley, NY, 1979.
2. *The Colloid Chemistry of Silica*, H.E. Bergna (ed), Advances in Chemistry Series 234; American Chemical Society: Washington, D.C. (1994).
3. Koerner, G., *Silicones, Chemistry and Technology*, Goldschmidt Th., Schulze, M. and Weis, J. (eds), CRC Press, Boca Raton (FL), 1991.
4. Brinker, C.J. and Scherer, G.W. *Sol-Gel Science: The Physics and Chemistry of Sol-Gel Processing*; Academic Press: New York, 1990.
5. Andrew, E.R., *Prog. Nucl. Magn. Reson.*, 1972, 1.
6. Pines, A.; Gibby, M.G; and Waugh, J.S., *J. Chem. Phys.*, 1973, 59, 569.
7. Schaefer, J. and Stejskal, E.O., *J. Am. Chem. Soc.*, 1976, 98, 1031.
8. Chuang, I-S. and Maciel, G. E. *J. Phys. Chem.*, 1997, 101, 3052.
9. Devreux, F.; Boilot, J.P.; Chaput, F.; and Sapoval, B. *Phys. Rev. Lett.*, 1990, 65, 614.
10. Smith, J.V. and Blackwell, C.S. *Nature*, 1983, 303, 223.
11. Engelhardt, G. and Radeaglia, R. *Chem. Phys. Lett.*, 1984, 108, 271.
12. Phillips, B.L.; Thomson, J.C.; Xiao, Y.; and Kirkpatrick, R.J. *Phys. Chem. Minerals*, 1993, 20, 341.
13. Spearing, D.R.; Farnan, I.; and Stebbins, J.F. *Phys. Chem. Minerals*, 1992, 19, 307.
14. Pettifer, R.F.; Dupree, R.; Farnan, I.; and Stornberg, U. *J. Non-Cryst. Solids*, 1988, 106, 408.
15. Xiao, Y.; Kirkpatrick, R.J.; and Kim, Y.J. *Phys. Chem. Minerals*, 1995, 22, 30.
16. Maciel, G.E. and Sindorf, D.W. *J. Am. Chem. Soc.*, 1980, 102, 7606.
17. Henderson, G.S., Fleet, M.E. and Bancroft, G.M. *J. Non-Cryst. Solids*, 1984, 68, 333.
18. Gerber, T. and Himmel, B. *J. Non-Cryst. Solids*, 1986, 3, 324.
19. Himmel, B.; Gerber, T.; Heyer, W.; and Blau, W. *J. Mater. Sci.*, 1987, 22, 1374.

20. Burneau, A.; Humbert, B.; Barres, O.; Gallas, J.P.; and Lavalley, J.C. in Ref. [2], p. 199.
21. El-Nahhal, I. M.; Yang, J. J.; Chuang, I.; and Maciel, G.E. *J. Non-Cryst. Solids*, **1996**, *208*, 105.
22. Yang, J. J.; El-Nahhal, I. M.; and Maciel, G. E., *J. Non-Cryst. Solids*, **1996**, *204*, 105.
23. Yang, J. J.; El-Nahhal, I. M.; Chuang, I.; and Maciel, G. E. *J. Non-Cryst. Solids*, **1997**, *209*, 19.
24. Yang, J. J.; El-Nahhal, I. M.; Chuang, I.; and Maciel, G. E., *J. Non. Cryst. Solids*, **1996**, *212*, 281.
25. Maciel, G. E., "NMR Characterization of Functionalized Polysiloxanes," Solid State NMR of Polymers, I. Ando, ed., Elsevier Science, Amsterdam, submitted.
26. Maciel, G. E.; Sindorf, D. W.; and Bartuska, V. J., *J. Chromatogr.*, **1981**, *205*, 438.
27. Sindorf, D. W. and Maciel, G. E. *J. Am. Chem. Soc.*, **1981**, *103*, 4263.
28. Fischer, A. B.; Bruce, J. A.; McKay, D. R.; Maciel, G. E.; and Wrighton, M.S. *Inorg. Chem.*, **1982**, *21*, 1766.
29. Sindorf, D. W. and Maciel, G. E. *J. Phys. Chem.*, **1982**, *86*, 5208.
30. Sindorf, D. W. and Maciel, G. E. *J. Am. Chem. Soc.*, **1983**, *105*, 1487.
31. Sindorf, D. W. and Maciel, G. E. *J. Am. Chem. Soc.*, **1983**, *105*, 1848.
32. Sindorf, D. W. and Maciel, G. E. *J. Am. Chem. Soc.*, **1983**, *105*, 3767.
33. Sindorf, D. W. and Maciel, G. E. *J. Phys. Chem.*, **1983**, *87*, 5516.
34. Linton, R.W.; Miller, M.L.; Maciel, G.E.; and Hawkins, B.L., *Surface and Interface Anal.*, **1985**, *7*, 196.
35. Miller, M.L.; Linton, R.W.; Maciel, G.E.; and Hawkins, B.L. *J. Chromatogr.*, **1985**, *319*, 9.
36. Rudzinski, W. E.; Montgomery, T. L.; Frye, J. E.; Hawkins, B. L.; and Maciel, G. E. *J. Chromatogr.*, **1985**, *323*, 281.
37. Rudzinski, W. E.; Montgomery, T. L.; Frye, J. E.; Hawkins, B. L.; and Maciel, G. E. *J. Catalysis*, **1986**, *98*, 444.
38. Caravajal, G.S.; Leyden, D.E.; and Maciel, G.E. in *Chemically Modified Surfaces. Volume 1: Silanes, Surfaces and Interfaces*, Leyden, D. E. (ed.), Gordon and Breach Science Publishers, New York, **1986**, 283-303.
39. Maciel, G.E.; Ziegler, R.C.; and Taft, R.K. in *Chemically Modified Surfaces. Volume 1: Silanes, Surfaces and Interfaces*, Leyden, D. E. (ed.), Gordon and Breach Science Publishers, New York, **1986**, 413-429.
40. Bronnimann, C. E.; Ziegler, R. C.; and Maciel, G. E. *J. Am. Chem. Soc.*, **1988**, *110*, 2023.
41. Caravajal, G. S.; Leyden, D. E.; Quinting, G. R.; and Maciel, G. E. *Anal. Chem.*, **1988**, *60*, 1776.
42. Bronnimann, C.E.; Zeigler, R.C.; and Maciel, G.E. in *Chemically Modified Surfaces. Volume 2: Chemically Modified Surfaces in Science and Industry*, Leyden, D.E. and Collins, W.T. (eds.), Gordon and Breach Science Publishers: NY, 1988, pp. 305-318.

43. Zeigler, R.C. and Maciel, G.E. in *Chemically Modified Surfaces*. Volume 2: Chemically Modified Surfaces in Science and Industry, Leyden, D.E. and Collins, W.T. (eds.), Gordon and Breach Science Publishers: NY, 1988, pp. 319-336.
44. Zeigler, R. C. and Maciel, G. E. *J. Am. Chem. Soc.*, **1991**, *113*, 6349.
45. Zeigler, R. C. and Maciel, G. E. *J. Phys. Chem.*, **1991**, *95*, 7345.
46. Chuang, I-S.; Kinney, D. R.; Bronnimann, C. E.; Zeigler, R. C.; and Maciel, G.E. *J. Phys. Chem.*, **1992**, *96*, 4027.
47. Kinney, D. R.; Chuang, I-S.; and Maciel, G. E. *J. Am. Chem. Soc.*, **1993**, *115*, 6786.
48. Chuang, I-S.; Kinney; D. R.; and Maciel, G. E. *J. Am. Chem. Soc.*, **1993**, *115*, 8695.
49. Maciel, G. E.; Bronnimann, C. E.; Zeigler, R. C.; Chuang, I-S.; Kinney, D. R.; and Keiter, E. A. in *Advances in The Colloid Chemistry of Silica Chemistry*, Horacio Bergna (ed.), American Chemical Society, Washington, D.C., **1994**, *234*, 269-282.
50. Maciel, G. E.; and Ellis, P. D. *NMR Characterization of Silica and Alumina Surfaces* in *NMR Techniques in Catalysis*, Alex Pines and Alexis Bell (eds.), Marcel Dekker, Inc.: NY, **1994**, 231-310.
51. Maciel, G. E. *Structures of Silica Surfaces*, Grant, D. M.; Harris, R. K.; and Gerstein, B. C., (eds.), in *Encyclopedia of Nuclear Magnetic Resonance*, John Wiley & Sons, Ltd., Sussex, England, in press (1996).
52. Maciel, Gary E. *NMR in the Study of Surfaces. ¹H CRAMPS and ²⁹Si CP-MAS Studies of Silica*, Maciel, G. E., ed., in *Nuclear Magnetic Resonance in Modern Technology*, Kluwer, Dordrecht, Netherlands, 1994, pp. 401.
53. Sato, S.; and Maciel, G. E. *J. Molec. Catal. A*, **1995**, *101*, 153.
54. Chuang, I-S.; and Maciel, G. E. *J. Am. Chem. Soc.*, **1996**, *118*, 401.
55. Liu, C.; and Maciel, G. E. *J. Am. Chem. Soc.*, **1996**, *68*, 1401.
56. Bronnimann, C. E.; Hawkins, B. L.; Zhang, M.; and Maciel, G. E. *Anal. Chem.*, **1988**, *60*, 1743.
57. Maciel, G. E.; Bronnimann, C. E.; and Hawkins, B. L. *High-Resolution ¹H Nuclear Magnetic Resonance in Solids via CRAMPS*, Warren, S. (ed.) in *Advances in Magnetic Resonance: The Waugh Symposium*, Academic Press, Inc., San Diego, CA, 1990, Vol. 14, pp. 125-150.
58. Brinker, C. J.; Kirkpatrick, R. J.; Tallant, D. R.; Bunker, B. C.; and Montez, B. *J. Non-Cryst. Solids*, **1988**, *99*, 418.
59. Brinker, C. J.; Brow, R. K.; Tallant, D. R.; and Kirkpatrick, R. J. *J. Non-Cryst. Solids*, **1990**, *120*, 26.
60. Legrand, A. P.; Hommel, H.; Tuel, A.; Vidal, A.; Balard, H.; Papirer, E.; Levitz, P.; Czernichowski, M.; Erre, R.; Van Damme, H.; Gallas, J. P.; Hemidy, J. F.; Lavalley, J. C.; Barres, O.; Burneau, A.; and Grillet, Y. *Adv. Colloid Interface Sci.*, **1990**, *33*, 91.
61. Tuel, A.; Hommel, H.; Legrand, A. P.; and Kovats, E. *Langmuir*, **1990**, *6*, 770.

62. Tuel, A.; Hommel, H.; Legrand, A. P.; Chevallier, Y.; and Morawski, J. C. *Colloids Surf.*, **1990**, *45*, 413.
63. Leonardelli, S.; Facchini, L.; Fretigny, C.; Tougne, P.; and Legrand, A. P. *J. Am. Chem. Soc.*, **1992**, *114*, 6412.
64. Legrand, A.P.; Taibi, H.; Hommel, H.; Tougne, P.; and Leonardelli, S. *J. Non-Cryst. Solids* , **1993**, *155* , 122.

Chapter 13

Wide-Line ^{14}N NMR in Solids

James P. Yesinowski and Edward A. Hill¹

Code 6120, Naval Research Laboratory, Washington, DC 20375-5342

Static NMR powder patterns of the quadrupolar ^{14}N nucleus ($I=1$) typically extend over several MHz. Techniques that enable the observation of such patterns will be described and illustrated with spectra of inorganic nitrates and nitrides. A fictitious spin-1/2 behavior is evoked by the irradiation of only a very small portion of the entire powder pattern at any one time. Several new techniques depend upon the concept of a Reorientation-Induced Redistribution of Isochromats. In the first of these, when the sample is slowly turned about an axis perpendicular to the external magnetic field significant gains in detection sensitivity can be achieved. In the second, very large anisotropic interactions that inhomogeneously broaden NMR spectra, such as the ^{14}N nuclear quadrupole coupling constant, can be measured at a single frequency by observing modulations in the amplitude of a spin-echo under slow turning conditions. Finally, results for hexamethylenetetramine demonstrate how transition-selective ^{14}N NMR can be used to quantitatively study slow molecular motions.

The past 15 years or so have witnessed a dramatic increase in the number of NMR studies of quadrupolar nuclei, i.e. those with nuclear spin $I > 1/2$. The so-called half-integral nuclei ($I=n/2$, where n is an odd integer) are well-represented across the entire Periodic Table, and together with the ^2H nucleus ($I=1$) have been the focus of the majority of such studies. Many other papers in this Symposium demonstrate this continued interest in half-integral quadrupolar nuclei both in the development of new experimental approaches to extracting as much information as possible and in the applications of various techniques to chemically-significant problems. The spatial averaging of the anisotropic quadrupolar interactions by rapid sample spinning, at either the magic-angle (MAS) or other combinations of angles (DAS and DOR) has provided much opportunity for increasing the resolution and information content of spectra.

¹NRC/NRL postdoctoral fellow.

The development of NMR techniques for quadrupolar nuclei having integral spin has been quite different. The nuclei that qualify are few although important: only $I=1$ (^2H , ^6Li , ^{14}N) and $I=3$ (^{10}B). The NMR techniques themselves differ in fundamental ways from those used for half-integral quadrupolar nuclei because of the differing structure of the Zeeman energy levels in the two cases. Specifically, for half-integral nuclei the central $\frac{1}{2} \leftrightarrow -\frac{1}{2}$ transition is often observed, since to first order its frequency is independent of the nuclear quadrupole coupling constant.¹ In contrast, all allowed transitions for integral spin nuclei depend in first order upon the nuclear quadrupole coupling constant (NQCC), resulting in much broader lines under equivalent conditions.¹ Line-narrowing techniques such as MAS have proven useful only in cases where the NQCC is rather small (e.g. < 200 kHz), restricting the technique in most cases to the ^2H nucleus. Therefore, the NMR spectroscopy of integral spin nuclei is essentially wide-line in character, unless single-crystals or ordered phases (e.g. liquid crystals) are used. The use of a quadrupolar-spin echo to obtain wide-line spectra from ^2H has proven exceedingly successful,² and many such studies have been reported. However, for ^{14}N this approach is of little use due to the difficulty of obtaining the required non-selective excitation over a wide frequency range (often exceeding 1 MHz).

We will show how some of these difficulties presented by the ^{14}N nucleus can be overcome, with examples drawn from inorganic powders such as potassium nitrate, silicon nitride, and nitric acid trihydrate. All of the approaches discussed will involve the observation of only a small fraction of the entire powder pattern at any one time. This peculiarity gives rise to a number of unusual features in NMR experiments that we have been able to exploit.

In the next section we will discuss some basic selective-excitation techniques useful for the detection of ^{14}N NMR wide-line spectra. The subsequent three sections will deal with three very different consequences of what we refer to as the Reorientation-Induced Redistribution of Isochromats (or $(\text{RI})^2$). In the RotIsseRle experiment, a very slow sample rotation about an axis perpendicular to the magnetic field offers a simple but very useful means of improving the sensitivity of wide-line spectra through the $(\text{RI})^2$ effect. The method should also be applicable to observing central transitions of half-integral quadrupolar nuclei that are so severely broadened by second-order interactions that the entire pattern cannot be excited and observed at one time. We then describe a novel approach to obtaining information about the width of extremely broad powder patterns from measurements *at a single frequency* that can be carried out with the same slow-rotation apparatus, but which relies on a different $(\text{RI})^2$ effect. These STEAMER (Slow Turning Echo Amplitude Modulation and Echo Reduction) experiments have interesting extensions to other problems involving the measurement of very large anisotropic interactions in inhomogeneously-broadened NMR spectra, and permit one to distinguish two separate sources of broadening in powder spectra: inhomogeneous anisotropic interactions and a distribution of isotropic interactions. In the final section we will show that $(\text{RI})^2$ effects manifest themselves not only when the sample undergoes coherent mechanical rotation, but also when random (incoherent) molecular motions occur in the sample itself. Using hexamethylenetetramine as a test case, we demonstrate several variants of hole-burning experiments that can be used to quantitatively study such molecular dynamics at one single NMR carrier frequency.

Selective-excitation Techniques for ^{14}N Wide-Line NMR Spectra

The basic problem encountered by the solid-state NMR spectroscopist who wishes to study the 100% naturally-abundant ^{14}N nucleus in one of its many interesting and relevant chemical forms arises from its large NQCC in all but the most symmetrical of environments. The NQCC is the product of the ^{14}N nuclear electric quadrupole moment (a constant) and the electric field gradient (EFG), which is a second-rank tensor quantity characterizing the anisotropy of the electronic distribution about the nucleus. The large range of EFG's possible in various bonding environments is clearly illustrated by the histogram in Figure 1 depicting the distribution of reported ^{14}N NQCC values, which fall over the frequency range 0-8 MHz. The median ^{14}N NQCC value is 3-4 MHz, which although substantial, is still smaller than the ^{14}N Larmor frequency due to the Zeeman interaction in typical superconducting NMR magnets. In particular, all of the ^{14}N NMR experiments reported here were performed at the relatively modest field strength of 7.05 T, corresponding to a ^{14}N Larmor frequency of 21.6 MHz (and a proton frequency of 300 MHz). It is therefore appropriate to treat the quadrupolar interaction as a perturbation in the high-field ^{14}N NMR experiment.

The energy-level diagram in Figure 2 depicts the three Zeeman levels of the ^{14}N nucleus being shifted by a first-order quadrupolar interaction (in the present experiments it will not be necessary to consider second-order effects, which are well-understood). The two allowed fundamental transitions $0 \rightleftharpoons +1$ and $0 \rightleftharpoons -1$ are depicted by arrows. For a given specific orientation of the EFG tensor, these two transitions form a doublet centered about the central Zeeman frequency (including the chemical shift term) with a splitting proportional to the quadrupolar interaction for that particular orientation. However, for a randomly-order powder sample consisting of crystallites each with its own EFG tensor orientation, the theoretical result is a broad powder pattern of the type familiar from ^2H NMR spectroscopy. Unlike the ^2H case, however, it is generally not experimentally feasible to excite and observe the entire ^{14}N NMR powder pattern at one time, due to both limitations on the rf power available in a pulsed experiment and the finite bandwidth of resonant NMR probes.

As a result, the ^{14}N NMR experiments described here have a bandwidth considerably narrower than the frequency range of the entire powder pattern, and either the $0 \rightleftharpoons +1$ or $0 \rightleftharpoons -1$ transition (but not both) is irradiated for a given EFG orientation. Therefore, the excitation employed is *transition-selective* (irradiating only one of the two allowed transitions) as well as *frequency-selective* (irradiating only a subset of all possible EFG orientations that form the powder pattern). The effects of selective excitation on two energy levels in a three-level spin system such as shown in Figure 2 can be analyzed within an operator subspace describing the rotations of a fictitious $I=1/2$ nucleus.³ The selective $\pi/2$ pulse time in this subspace turns out to be $1/\sqrt{2}$ times the non-selective $\pi/2$ pulse time. Another important consequence of the fictitious spin-1/2 behavior of selective irradiation is that a Hahn spin-echo [$(\pi/2)_x - \tau - (\pi)_{x \text{ or } y} - \tau$ - observe] is the appropriate sequence to use to overcome the loss of the rapidly-decaying Free-Induction-Decay (FID) signal within the unobservable dead-time of the NMR probe. This is in contrast to the non-selective excitation of ^2H NMR spectra via a "quadrupolar-echo" sequence [$(\pi/2)_x - \tau - (\pi/2)_x - \tau$ - observe].

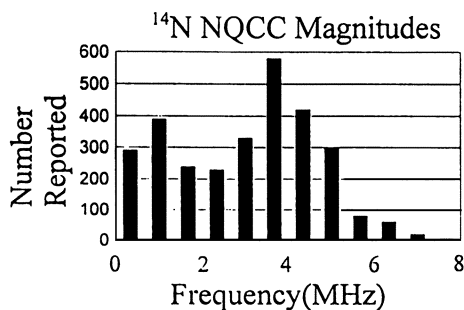


Figure 1: Histogram of ^{14}N NQCC values (magnitude) reported in a database¹⁹ of ~10,000 compounds (including compounds not containing nitrogen).

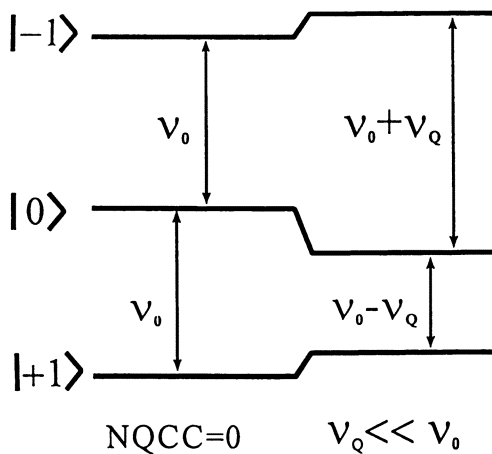


Figure 2: Energy level diagram for ^{14}N ($I=1$) in a large magnetic field showing the splitting of the central Larmor frequency transition at ν_0 by the first-order nuclear quadrupolar interaction ν_Q . In a powder sample, a range of values for ν_Q broadens the spectrum.

An experimental example of the above approach is shown in the ^{14}N NMR partial spectrum of KNO_3 in Figure 3. A τ value of 500 μs was used to avoid probe ringdown. Note that the width of the region observed is only about 40 kHz, whereas the entire theoretical powder pattern (dashed line) extends over 1.5 MHz. In order to obtain the entire powder pattern, the frequency must be stepped and separate acquisitions stored, retuning the probe and transmitter as necessary. Although a stepped-frequency approach to obtaining a spectrum point-by-point is not uncommon in wide-line NMR spectroscopy in general, improved frequency resolution can be obtained by a method recently discussed in detail.⁴ In this approach a sufficiently small frequency increment (step-size) is used and the sub-spectra are co-added in the frequency domain. An example of this "high-resolution wide-line" approach is the ^{14}N NMR powder pattern spectrum of KNO_3 we have recently reported.⁵ The observed spectrum agreed well with a theoretical spectrum calculated from the NQCC parameters of $\chi = 751$ kHz and $\eta = 0.022$ obtained from a single-crystal NMR study.⁶

A significant sensitivity gain was obtained for this stepped-frequency spectrum of KNO_3 by coadding 512 echoes in a Carr-Purcell-Meiboom-Gill train of pulses $(\pi/2)_x - \tau - [(\pi)_y - 2\tau]_n$, with τ set to 1 ms. Even though we measured a ^{14}N T_2 at the horn of 20 ms with a simple two-pulse Hahn spin-echo sequence, the decay time in the CPMG experiment is greatly prolonged such that substantial signal is present even after 1 second. This behavior we attribute to a type of pulsed spin-locking effect involving the two fictitious spin-1/2 levels that has originally been observed for spin-1/2 nuclei with pulse angles Θ , in the train less than π ,⁷ and for CPMG trains in other cases.⁸ The coaddition of echoes produces a substantial signal:noise advantage, approximately $\sqrt{512} \approx 22$ in the present situation (this estimate ignores any decay during the pulse-train).

One of our original motivations to investigate ^{14}N NMR was to be able to obtain structural and dynamical information about nitric acid hydrates and their surfaces. These materials are believed to be important constituents of Polar Stratospheric Clouds (PSC's) that heterogeneously catalyze reactions ultimately leading to ozone destruction above the poles.⁹ As a first preliminary example of the potential utility of ^{14}N NMR in this area, Figure 4 shows a portion of the spectrum obtained from nitric acid trihydrate (NAT, $\text{HNO}_3 \cdot 3\text{H}_2\text{O}$) at -30°C . The sample was prepared by freezing an aqueous solution of the same composition outside the magnet; the solution supercools to about -55°C , but can be observed to melt around -19°C . A CPMG train of 16 coadded echoes was necessary to see any signal at all, which even then is rather weak due to a long spin-lattice relaxation time. Nevertheless, no proton decoupling (or deuteration) was needed to obtain this spectrum, and it should be possible to eventually map out the entire spectrum and obtain the first ^{14}N NQCC information for solid nitric acid or its hydrates (NAT is believed to contain a nitrate group and an oxonium ion based on X-ray diffraction¹⁰).

Sensitivity Gains from Slow Sample Rotation (RotIsseRIe)

One of the frustrations of doing ^{14}N NMR experiments as we have described is their inefficiency: all we are ever observing is some small fraction of the crystallites in a sample. This limitation is depicted in Figure 5, which depicts the spectrum arising from an axially-symmetric CSA tensor that can be viewed as representing one branch (e.g. the

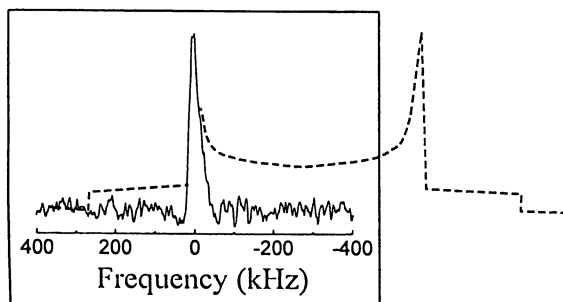


Figure 3: Selectively-excited Hahn spin-echo ^{14}N NMR spectrum of KNO_3 , obtained at the perpendicular edge. The schematic powder pattern for the nearly-axially-symmetric NQCC tensor is shown as a dashed line.

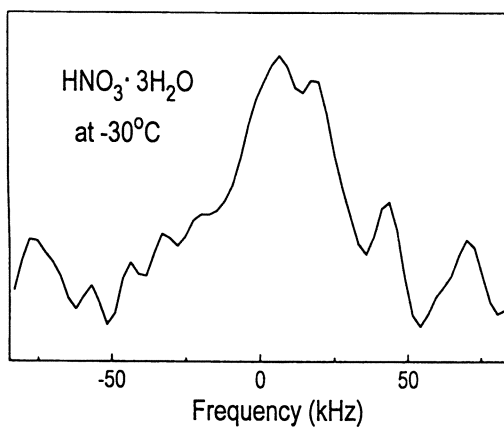


Figure 4: ^{14}N NMR spectrum of nitric acid trihydrate obtained +250 kHz from the center NH_4Cl peak using co-added echoes in a CPMG train.

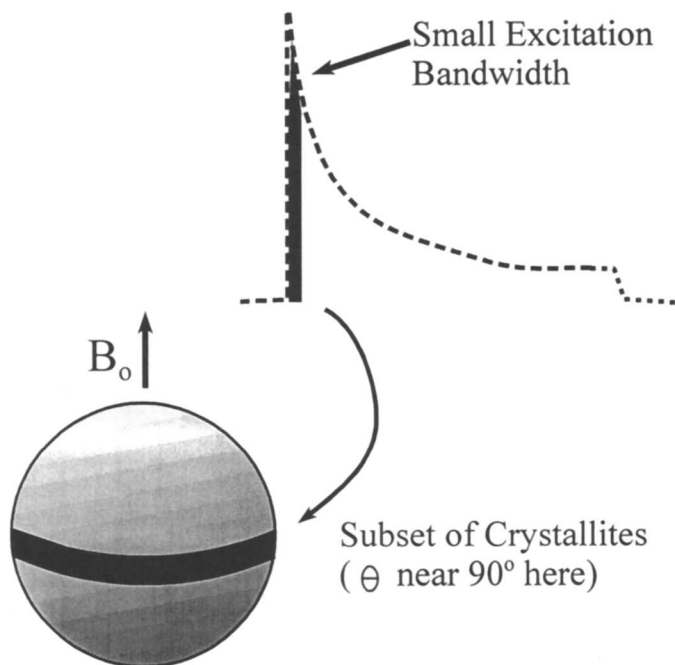


Figure 5: Equatorial band of orientations of an axially-symmetric second-rank tensor corresponding to selective excitation of the perpendicular edge of the powder pattern. Only one branch of the ^{14}N quadrupolar powder pattern is depicted.

0 \Rightarrow +1 one) of the powder pattern. The signal observed in this spectrum at the perpendicular edge (horn) only arises from a narrow band of EFG orientations at the equator. The repetition rate of the experiment is limited by the need to allow sufficient time for significant spin-lattice relaxation to take place. If, however, we were to reorient the powdered sample about an axis *perpendicular* to the external magnetic field, as shown in Figure 6, a new belt of spins that are for the most part unsaturated would be brought into the equatorial region. This simple picture suggests how very slow sample rotation about a perpendicular axis will improve the sensitivity of the experiment, by permitting faster pulsing (shorter recycle delays) without overheating the spins. For this reason, and also recalling that this sensitivity gain results from (RI)² effects, we call the experiment RotIsseRIe. Figure 6 also schematically depicts the bevelled-gear arrangement used to carry out slow rotation via a drive shaft connected to a 1 rpm synchronous motor at the base of the magnet.

The usefulness of the RotIsseRIe experiment is illustrated in Figure 7 by the ¹⁴N NMR stepped-frequency spectrum of silicon nitride. The axially-symmetric ¹⁴N NQCC in this important ceramic material had previously been determined to have a magnitude of 2.1 MHz both from splittings observed in the ²⁹Si MAS-NMR spectrum¹¹ as well as from ¹⁴N pure NQR (Yesinowski, J.P., unpublished results). The 30 mm diameter vial containing the sample resulted in a ¹⁴N selective $\pi/2$ pulse width of about 70 μ s and a correspondingly narrow bandwidth of excitation, so that the stepped frequency spectrum was only obtained at discrete points. A $\pi/2$ - π spin-echo rather than a CPMG echo train was used to obtain the signal because the 1 rpm rotation would be expected to affect the CPMG behavior due to the continuous frequency change. By the simple expedient of using a stepper motor to provide stepped rather than continuous rotation, however, it would be possible to obtain sensitivity gains from both the RotIsseRIe experiment and the use of coadded echoes as discussed above. The apparent static spin-lattice relaxation time is estimated to be about 2 minutes. The spectrum in Figure 7 is consistent with an axially-symmetric NQCC of 2.1 MHz (a detailed fit has not yet been carried out, because of the need to incorporate second-order quadrupolar effects as well as the isotropic chemical shift; deducing the latter would require measuring the low-frequency perpendicular edge and neglecting any chemical shift anisotropy).

We have numerically modelled the sensitivity gain to be anticipated from RotIsseRIe for the case of an axially-symmetric tensor (Hill, E.A.; Yesinowski, J.P. to be published). The approach requires one to consider the frequency history of each isochromat. Figure 8 depicts this history for a set of isochromats that are resonant with the rf carrier at the point in time ("the present") outlined by the square box. The NMR frequency at this point corresponds to an orientation of the EFG tensor with respect to the magnetic field having a polar angle at the time of pulsing/detection of $\theta_0 = 70^\circ$. Shown are six different values of the azimuthal angle α_0 of the EFG tensor at the time of pulsing/detection. Because of the rotation, each different α_0 has its own frequency history. The quantitative simulation of the RotIsseRIe experiment considers all α_0 values, and determines in which *prior* pulse they were saturated, and the extent to which they recover by spin-lattice relaxation. The experimental results for KNO₃ agree well with the predictions, and the maximum signal:noise gain in that case obtained by optimizing the recycle delay is 2.5. For the silicon nitride spectrum, the sensitivity advantage is even

Reorientation-Induced Redistribution of Isochromats

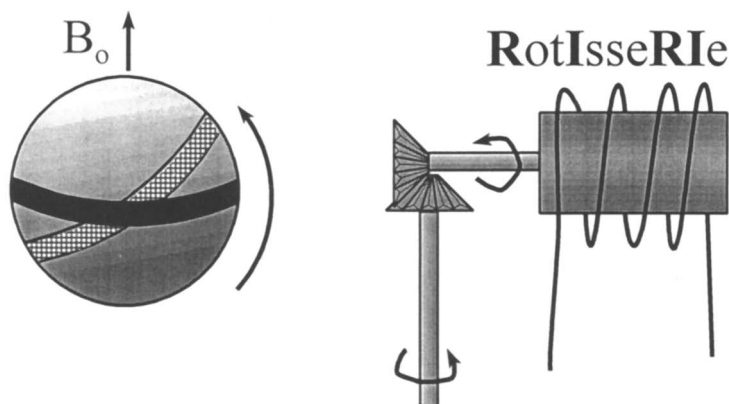


Figure 6: Reorientation of the equatorial band in Figure 5 induced by rotation about an axis perpendicular to the magnetic field. The experimental apparatus used for this RotIsseRIe experiment is shown schematically at right.

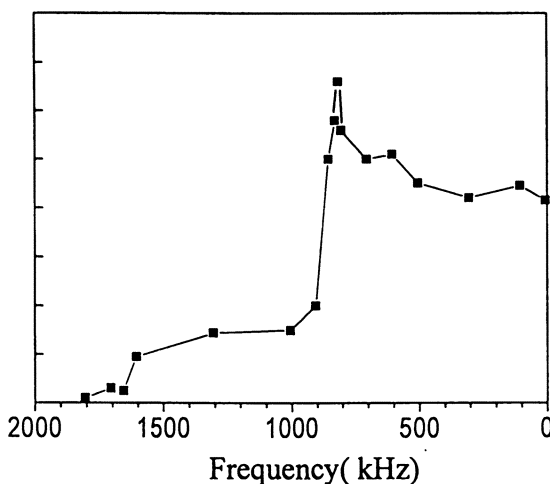


Figure 7: Stepped-frequency selective-excitation spin-echo ^{14}N NMR spectrum of Si_3N_4 , corresponding to half of an axially-symmetric powder pattern with NQCC of 2.1 MHz. The spectrum was acquired under RotIsseRIe conditions of 1 rpm. Despite the ^{14}N T_1 of several minutes, a recycle delay of 5.4s could be used.

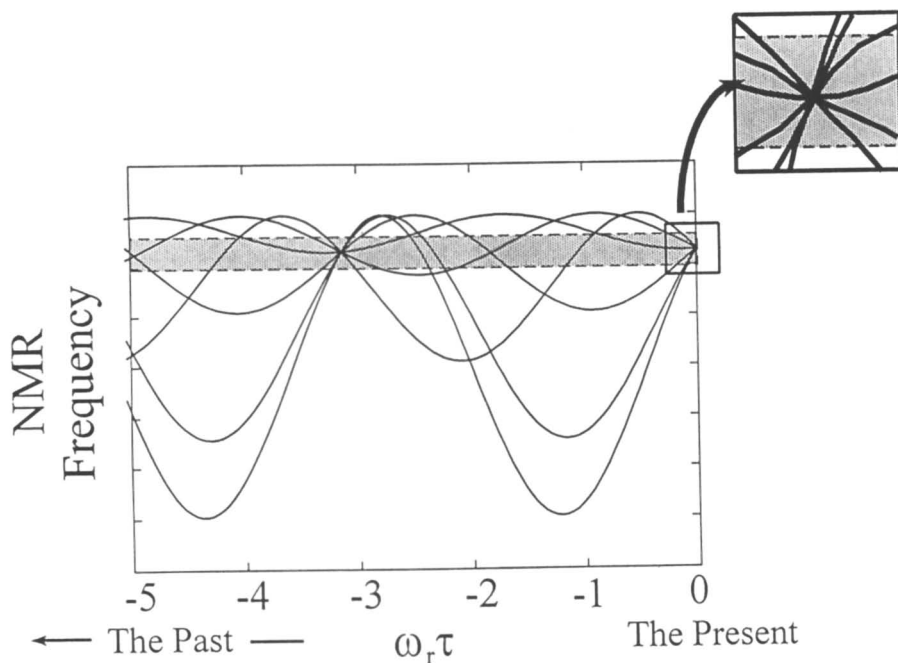


Figure 8: Frequency history of a set of six ^{14}N isochromats arising from an axially-symmetric NQCC tensor undergoing rotation about an axis perpendicular to the magnetic field with an angular velocity ω_r . The horizontal grey region corresponds to the frequency range excited/detected at time $t=0$ (square box and inset). The NQCC tensor has a polar angle $\theta = 70^\circ$ in this figure, but a range of azimuthal angles α_0 that lead to differing time developments.

more considerable: since the NQCC value is considerably larger, a smaller fraction of the entire signal is observed in any one acquisition. We estimate that there is an approximately 4.5-fold gain in sensitivity, or a 20-fold reduction in the experiment time required, for the silicon nitride spectrum in Figure 7. Since the data in Figure 7 took 12 hours to acquire, about 10 days would have been needed to obtain an equivalent spectrum in the absence of RotIsseRIe.

Measuring Large Anisotropies in Inhomogeneously-broadened NMR Spectra with STEAMER

The description of the RotIsseRIe experiment in terms of the frequency history of isochromats as depicted in Figure 8 has made one assumption: that the excitation and detection of the set of spins whose frequencies reside within the grey band is not directly affected by the change in each isochromat's frequency during the excitation/detection process itself (schematically indicated by the small square region and inset). For the experiments described above, this was a reasonable assumption, since the frequency variation during the 200 μs echo interval could be neglected. Under other conditions, e.g. faster rotation, longer intervals, or larger NQCC values, this may not be the case. Consider the situation in which a two-pulse Hahn spin-echo is used to excite and detect the isochromats shown in the expanded inset in Figure 8. The continuous change in resonance frequencies of the initially-excited isochromats during the spin-echo interval leads to varying degrees of phase accumulation for these same isochromats, since they have differing frequency developments induced by rotation about a second axis. We will make the assumption, reasonable in the present case, that the same isochromats experience perfect 90° and 180° rotations by the pulses. In other words, *no* isochromat excited by the first ($\pi/2$) pulse will change its frequency sufficiently due to rotation to move outside the region of excitation of the second (π) pulse. The varying phase accumulations then show up as both a loss in echo intensity and changes in the sign of the echo compared to the normal T_2 decay signal, and lead us to refer to the experiment as STEAMER (Slow Turning for Echo Amplitude Modulation and Echo Reduction).

The full quantitative description of the experiment for an axially-symmetric tensor is given elsewhere.¹² We will now simply sketch the derivations and state some of the principal results. We need merely to consider each branch of the powder pattern separately as arising from an interaction having the form of a chemical-shielding anisotropy; the two branches then appear as the \pm terms in the expressions below, due to their mirror symmetry. The time dependence of the nuclear resonance frequency $\nu(t)$ due to rotation can be expressed by:

$$\nu(t) = \nu_0 \pm \frac{3}{8} \chi (3 \cos^2[\theta(t)] - 1) \quad (1)$$

where ν_0 is the nuclear Zeeman frequency in Hz, the \pm symbol refers to the two possible interlevel transitions, χ is the NQCC value in Hz, and θ is the polar angle of the EFG tensor principal axis relative to the magnetic field (z) axis, which is made time-dependent

by sample rotation about the x axis. Since $\theta(t)$ is not explicitly known, we make a coordinate transformation to describe $v(t)$ more naturally in a frame where two angles describe the orientation of the tensor with respect to the slow-rotation axis. One of these angles contains $\omega_r t$ in its argument to take care of the time-dependence, where ω_r is the angular rotation frequency. We then make the reverse transformation to obtain $v(t)$ explicitly as a function of time, which appears as $\omega_r t$:

$$v(t) = v_0 \pm \frac{9}{8} \chi \{ \sin^2(\theta_0) \sin^2(\omega_r t) \sin^2(\alpha_0) + \cos^2(\theta_0) \cos^2(\omega_r t) + 2 \sin(\theta_0) \cos(\theta_0) \sin(\omega_r t) \cos(\omega_r t) \sin(\alpha_0) - \frac{1}{3} \} \quad (2)$$

Note that θ_0 and α_0 in this expression are the spherical angles describing the tensor at time $t=0$ in the lab frame, and that for a non-rotating tensor the frequency would not depend upon the azimuthal angle α_0 . For convenience we refer to a set of nuclei having the same resonance frequency at time $t=0$ as "isochromats;" the range of α_0 coordinates causes these nuclei to have frequencies which spread across the frequency domain for time $t>0$.

The phase angle (relative to an axis in a reference frame rotating at the rf carrier frequency) accumulated by isochromats during the course of the Hahn spin-echo sequence is:

$$\Delta\Phi(\tau, \tau') = \int_0^{\tau} [v(t) - v_r] dt - \int_{\tau}^{\tau'} [v(t) - v_r] dt \quad (3)$$

where τ is the delay between the $\pi/2$ pulse at $t=0$ and the π pulse, v_r is the rf carrier frequency, and $\Delta\Phi$ is the accumulated phase in units of cycles at time τ' ($\geq \tau$). Inserting Eq. 2 into Eq. 3 yields the final result that can be directly employed in simulations:

$$\begin{aligned} \Delta\Phi(\tau, \tau') = & \{ v_0 \pm \frac{3}{8} \chi [3 \cos^2(\theta_0) - 1] - v_r \} (2\tau - \tau') \\ & \pm \frac{9}{32} \frac{\chi}{\omega_r} \{ 2\omega_r [\sin^2(\theta_0) \sin^2(\alpha_0) - \cos^2(\theta_0)] (2\tau - \tau') \\ & - \sin(2\theta_0) \sin(\alpha_0) [2 \cos(2\omega_r \tau) - \cos(2\omega_r \tau') - 1] \\ & - [\sin^2(\theta_0) \sin^2(\alpha_0) - \cos^2(\theta_0)] [2 \sin(2\omega_r \tau) - \sin(2\omega_r \tau')] \} \end{aligned} \quad (4)$$

A further simplification can be achieved under conditions meeting a "short-time approximation," i.e. when $\omega_r \tau \leq \omega_r \tau' \ll |\sin(2\theta_0) \sin(\alpha_0)|$, by an expansion in powers of time. The leading (quadratic) term, which can be quite useful for describing the STEAMER behavior of frequency regions not unreasonably close to the perpendicular or parallel edges of the powder pattern, is particularly informative:

$$\begin{aligned} \Delta\Phi_q(\tau, \tau') = & \{ v_0 \pm \frac{3}{8} \chi [3 \cos^2(\theta_0) - 1] - v_r \} (2\tau - \tau') \\ & \pm \frac{9}{16} \chi \omega_r \sin(2\theta_0) \sin(\alpha_0) (2\tau^2 - \tau'^2) \end{aligned} \quad (5)$$

We see that the accumulated phase angle, which leads to a loss in the magnitude of the

echo, is linearly proportional to the quadrupole coupling constant χ (in general unknown) and the known rotation rate ω_r . It is also proportional to the square of the echo interval τ . In terms of the expanded inset in Figure 8, the quadratic expression refers to the time interval during which the *frequency* evolution is linear with time.

Applying Eq. 5 to a simulation still requires integration over all possible α_0 values for a fixed θ_0 . It is possible to do this analytically and obtain the following expression for the detected echo signal:

$$S_q(\tau, 2\tau) \propto J_0\left[\frac{2}{4}\pi\chi\omega_r \sin(2\theta_0)\tau^2\right] \quad (6)$$

where J_0 is the Bessel function of order zero. This function has its first node (zero-crossing) at an argument of 2.41, and has ever-more-rapid oscillations (reflecting the quadratic time dependence of the phase angle discussed above). Thus, within the short-time approximation one can use STEAMER data and Eq. 6 to obtain an unknown axially-symmetric χ by a simple converging iterative process (i.e. recalculating θ_0 for each assumed χ). A graphical solution is also feasible, assuming that one branch of the powder pattern dominates the behavior.

An example of STEAMER behavior is shown in Figure 9 for silicon nitride, Si_3N_4 . The static T_2 decay has been fit to a single-exponential with a time constant of 11.3 ms (dashed line). Note that these static measurements suffer from a poor signal:noise ratio due to the absence of a RotIsseRle effect. The decay of the spin-echo signal under slow-rotation (solid squares) is considerably more rapid, and agrees reasonably well with a STEAMER simulation using Eq. 4 above and weighting the calculated behavior with a T_2 decay (solid curve). Note that *no adjustable parameters were used in this simulation*, since the value of χ is known to be 2.1 MHz (see above). In this particular experiment, we did not observe negative-going echoes or clear evidence of oscillations, both of which we have subsequently seen for KNO_3 .¹² We believe that this may be due to a considerable degree of jerkiness in the rotation of the large (30 mm O.D.) sample vial, that would result in variations of the rotation rate ω_r from scan to scan, and which would therefore tend to average out the oscillatory behavior.

It might seem desirable to avoid having to measure T_2 in a separate experiment by obtaining STEAMER data employing a constant τ value and varying ω_r instead. This approach is indeed feasible, but requires that two precautions be taken. One, the RotIsseRle sensitivity enhancement will vary with rotation speed, and cannot be made identical simply by changing the pulse repetition interval. Thus, longer recycle delays will be required to obtain quantitative echo intensities as a function of ω_r . Two, if RotIsseRle enhancements are sought, perhaps in a qualitative search for nodes in the oscillatory behavior, then one must be careful not to set the recycle delay to some integer fraction of *half* the rotation period. For example, for a 1 r.p.m. rotation, a recycle delay of 7.5 s = 30s/4 would be undesirable since it would reduce the RotIsseRle enhancement due to coherent interference (E.A. Hill; J.P. Yesinowski to be published).

Besides the obvious extensions of the STEAMER experiment to the case of a non-zero asymmetry parameter, the use of other types of echoes (stimulated or quadrupolar)

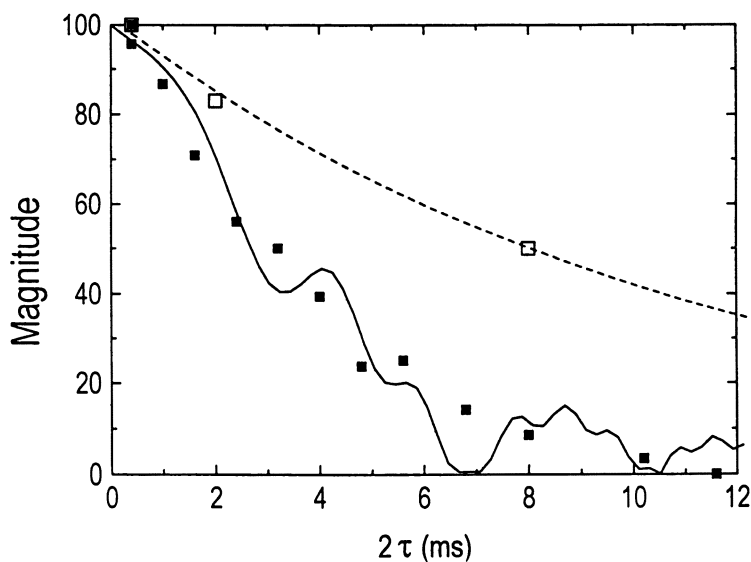


Figure 9: ^{14}N NMR selective-excitation spin-echo signals as a function of the pulse interval τ for Si_3N_4 at +806 kHz from the central NH_4Cl resonance (near the perpendicular edge). The open squares are for a static sample, and correspond to a T_2 decay constant of 11.3 ms. The solid squares represent the STEAMER experiment data, with sample rotation at 1 rpm. The solid curve is the STEAMER theoretical simulation with no adjustable parameters for a 2.1 MHz NQCC.

may offer advantages. The experiment is inherently two-dimensional, since there is also information about the echo intensity as a function of frequency from the carrier and from different carrier frequencies. It is also worth emphasizing that this slow rotation experiment, unlike coherent averaging techniques employing spinning, does not require that the anisotropic interactions be describable by tensors or simple combinations of tensors of any rank. Rather, it is sufficient that the angular dependence of the anisotropy be known. Thus, STEAMER may also prove useful in investigating extremely broad second-order powder patterns of half-integral nuclei, as discussed in the introduction.

¹⁴N NMR Techniques for Studying Slow Molecular Motions

The preceding sections have dealt with consequences of the Reorientation-Induced Redistribution of Isochromats in samples undergoing a coherent mechanical rotation. The RotIsseRle effect involves "moving" the frequencies of the isochromats excited and detected outside of the range of excitation/detection for the next repetition of the pulse sequence. The STEAMER experiment does not necessarily require doing this, since it is concerned with the accumulated phase of an isochromat whose frequency is varying due to the rotation. Both experiments have assumed a rigid sample, more precisely, that the EFG tensor is fixed and unvarying in the frame of the crystallite, which undergoes a rigid rotation as part of a tightly-packed powder sample. If this is not the case due to molecular motions, other types of experiments can be used to obtain quantitative information about such motions.

In particular, hole-burning experiments have been used in the past to obtain dynamical information.¹³ The peculiarity of applying them to selective ¹⁴N NMR is that the desired information must and can be extracted from only a small portion of the entire powder pattern. As an example of how quantitative information can be obtained from ¹⁴N NMR experiments at a single frequency, without having to step through the entire powder pattern, we will show results for the tetrahedral-jump process in hexamethylenetetramine (HMT), (CH₂)₆N₄. The HMT molecule (see Figure 10) has the same tetrahedral symmetry as adamantane, and like adamantane undergoes tetrahedral jumps among equivalent sites near room temperature, albeit at a slower rate. This motion has been studied by a variety of magnetic resonance techniques, making it a good test case for the present experiments.

The four ¹⁴N EFG tensors in each HMT molecule are directed along the four 3-fold symmetry axes, and the result is an axially-symmetric NQCC tensor ($\chi = 4.414$ MHz, $\eta = 0$).^{14,15} We chose to look at the horn of the powder pattern (ca. 1.7 MHz above the center ¹⁴N Larmor frequency) simply because of its high relative signal intensity. The sequence used to obtain the data shown in Figure 11 consists of DANTE¹⁶ pulse trains that saturate or "burn a hole" in the observed region of the inhomogeneously-broadened powder pattern. The DANTE trains consist of fifty 0.75 μ s tipping pulses separated by 25 μ s delay intervals; these values were chosen to result in zero (but not inverted) on-resonance magnetization. Note that the nominal on-resonance flip-angle is considerably greater than that expected from the measured 8.3 μ s selective $\pi/2$ pulse time, due to the pulse risetimes. The width of the hole is approximately 4 kHz, larger than the homogenous linewidth of 0.7 kHz calculated from the T₂ measured from a Hahn spin-echo experiment (460 μ s). The difference presumably is due to the DANTE train length

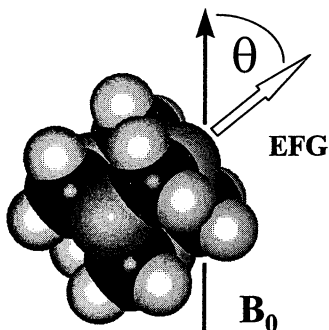


Figure 10: Model of a molecule of hexamethylenetetramine [$N_4(CH_2)_6$] with N (gray), C (black), and H (white). The arrow indicates the principal axis of one of the four axially symmetric ^{14}N EFG tensors, oriented along one of the four 3-fold axes of the regular tetrahedron formed by the nitrogen atoms. Here θ is the polar angle of this principal axis relative to the external magnetic field B_0 .

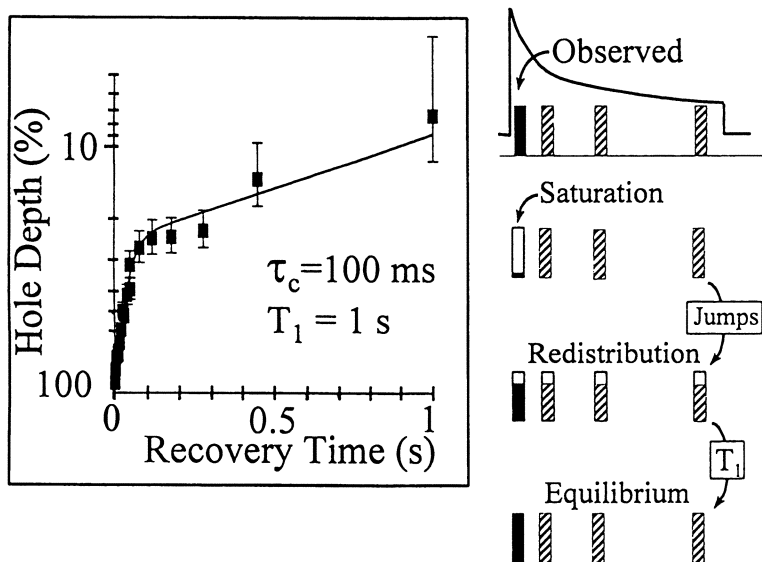


Figure 11: ^{14}N NMR single DANTE-train hole-burning experiment to study slow motions in hexamethylenetetramine (HMT). The hole depth is plotted versus the recovery time. The right side depicts schematically the two dynamic processes occurring: tetrahedral jumps with a correlation time τ_c and spin-lattice relaxation.

of $1.25 \text{ ms} = (0.8 \text{ kHz})^{-1}$ and the apodization used of 1 kHz. After a recovery period of varying duration, a Hahn spin-echo sequence with a delay time of $90 \mu\text{s}$ is used to detect the signal, and the sequence is repeated with a recycle delay of 4 s. The experimental results in Figure 11 are analyzed with a 4-site exchange model. At the start of the experiment saturation will label a group of nuclei in the HMT powder sample having $\theta = 90^\circ$, for example (θ being the angle between the EFG tensor and the external field). Each individual nucleus thus labelled will jump eventually to three other well-defined θ orientations, but considered as a group there will be a continuum of destination θ orientations determined by the tetrahedral geometry of the molecule. However, we need only to define four "bins" of ^{14}N nuclear magnetization, independent of the specific EFG orientations or frequencies of the ^{14}N nuclei. These bins exchange magnetization with one another because of the tetrahedral jump process, and each bin's magnetization is independently driven towards its equilibrium value by spin-lattice relaxation processes. The right side of Figure 11 schematically depicts this process: (1) the DANTE sequence saturates the magnetization of one bin (the observed bin); (2) exchange due to HMT molecular reorientation causes this saturation to spread relatively rapidly to all four bins (one observed, three unobserved), resulting in a relatively quick recovery of the observed bin's magnetization to about 75% of its original value; (3) after the magnetization in the different bins has nearly equalized (reaching a quasi-equilibrium) due to the jumps, spin-lattice relaxation mediates the recovery of all four bins to full equilibrium at a slower rate. Thus, the differing time scales of molecular reorientation and spin-lattice relaxation give rise to the clear break in the hole recovery data seen in Figure 11.

The mathematical details and assumptions of the 4-site exchange model are presented elsewhere.¹⁷ We simply note that the two-parameter fit of the hole-recovery data in Figure 11 to this model yields a correlation time for the tetrahedral jump process τ_c at room temperature of $103 \pm 6 \text{ ms}$ and a spin-lattice relaxation time constant of $0.96 \pm 0.23 \text{ s}$. The former is in close agreement with the value previously determined by ^2H NMR of 104 ms.

Two additional experiments offer some improvements and cross-checks on the single-DANTE saturation experiment above. Multiple-DANTE saturation pulses can be used, separated by intervals that are comparable to the jump times but significantly shorter than spin-lattice relaxation. This SINK (Saturation Inter-Nuclear Kinetics) sequence was first used in ^{19}F MAS-NMR experiments to study cross-relaxation between a minor and a major peak.¹⁸ Using a SINK sequence with a 100 ms delay between the 16 DANTE saturation pulses, we observe a single-exponential relaxation process with a time constant of $0.99 \pm 0.12 \text{ s}$. The agreement with the previous experiment is excellent; note the increased accuracy of the SINK determination of T_1 .

The second additional experiment that offers sensitivity advantages over the single-DANTE train saturation sequence uses a series of hard $\pi/2$ pulses to saturate one bin instead of the more narrowly frequency-selective DANTE train. Our experiments used 5 such pulses separated by $200 \mu\text{s}$ intervals. The resultant "whole"-burning data (not shown) were analyzed with a three-parameter fit to yield a jump time $\tau_c = 99 \pm 5 \text{ ms}$ and $T_1 = 0.96 \pm 0.09 \text{ s}$, again in good agreement with the previous analyses. The improved accuracy of the experiment results from detecting the recovery of a maximal amount of magnetization (i.e. the "whole" observed region is saturated, which nevertheless

represents only a limited region in the total frequency-space and θ -space). Note that the additional parameter in the fit represents the value to which the hole depth recovers, which in this experiment has the value 0.38 rather than the value of 0.25 obtained from the single DANTE-train experiment. This increase reflects a partial saturation of some of the other three bins by the less-selective $\pi/2$ saturation pulses used.

The above hole-burning and "whole"-burning experiments show that ^{14}N NMR can be used to accurately determine dynamical parameters from measurements at only one position in a wide powder pattern. Although the nature of the dynamical process in HMT was in this case known beforehand to be a tetrahedral jump, the existence of a 4-site exchange process in the general sense could have been inferred directly from the functional form of the single-train DANTE hole-burning data. Thus, other exchange processes such as n-site jumps could certainly be identified in a similar manner. These experiments also suggest a simple new method for detecting motion in nitrogen-containing samples: one measures the hole depth at a fixed recovery time while varying the number of preparatory DANTE trains, or the number of "whole"-burning saturation trains. The hole depths will be equal to one another in the absence of motion or spectral spin diffusion, the latter being generally unimportant for ^{14}N NMR.

Conclusions

We have demonstrated that wide-line ^{14}N NMR can be used to characterize inorganic materials by their ^{14}N NQCC values, even when these are several MHz in magnitude. A variety of techniques have been discussed that enable one to obtain such information with enhanced sensitivity either by stepping the frequency or by slowly rotating the sample and observing at a fixed frequency. Additional techniques based upon the concept of spectral hole-burning are shown to be capable of providing detailed quantitative information about slow molecular motions from measurements at a single frequency. With the further development of the techniques introduced here and the use of higher static magnetic field strengths to obtain better sensitivity, we expect the long-dormant field of ^{14}N NMR in solids to become an active area of research because of the important role nitrogen plays in nearly all branches of chemistry.

While the development of the techniques mentioned above was stimulated by the problems encountered in performing wide-line ^{14}N NMR experiments, they have much wider applicability. Indeed, all of the techniques discussed should be applicable to any spin-1/2 or quadrupolar nuclei whose entire spectrum cannot be observed at one carrier frequency. Furthermore, the STEAMER experiment should prove useful even in cases when the entire spectrum *can* be observed, since it distinguishes anisotropic interactions from a distribution of isotropic interactions.

Acknowledgment

We acknowledge the Office of Naval Research for the support of this work, and our colleagues Drs. Allen Garroway, Ken McGrath and Joel Miller for helpful discussions.

Literature Cited

1. Abragam, A.; *Principles of Nuclear Magnetism* (Clarendon Press, Oxford 1961).
2. Davis, J.H.; Jeffrey, K.R.; Bloom, M.; Valic, M.I.; Higgs, T.P. *Chem. Phys. Lett.* **1976**, *42*, 390-394.
3. Vega, S.; Pines, A. *J. Chem. Phys.* **1977**, *66*, 5624-5644. Wokaun, A.; Ernst, R.R. *J. Chem. Phys.* **1977**, *67*, 1752-1758.
4. Clark, W.G.; Hanson, M.E.; Lefloch, F.; Ségransan, P. *Rev. Sci. Instrum.* **1995**, *66*, 2453-2464.
5. Hill, E. A. and Yesinowski, J. P. *J. Amer. Chem. Soc.* **1996**, *118*, 6798-6799.
6. Bastow, T.J. and Stuart, S.N. *Z. Naturforsch.* **1990**, *45a*, 459-463.
7. Rhim, W.-K.; Burum, D.P.; Elleman, D.D. *Phys. Rev. Lett.* **1976**, *37*, 1764-1766.
8. Suh, B.J.; Borsa, F.; Torgeson, D.R. *J. Magn. Reson. A*, **1994**, *110*, 58-61.
9. Molina, M.J.; Zhang, R.; Wooldridge, P.J.; McMahan, J.R.; Kim, J.E.; Chang, H.Y.; Beyer, K.D. *Science* **1993**, *261*, 1418-1423.
10. Luzzati, P. V. *Acta. Cryst.* **1953**, *6*, 152-157.
11. Olivieri, A.; Hatfield, G. *J. Magn. Reson.* **1991**, *94*, 535-542.
12. Hill, E.A.; Yesinowski, J.P. *J. Chem. Phys.* **1997**, *106*, 8650-8659.
13. Kuhns, P.L.; Conradi, M.S. *J. Chem. Phys.* **1982**, *77*, 1771-1778.
14. Watkins, G.D.; Pound, R.V. *Phys. Rev.* **1952**, *85*, 1062.
15. Alexander, S.; Tzalmona, A. *Phys. Rev.* **1965**, *138*, A845-A855.
16. Bodenhausen, G.; Freeman, R.; and Morris, G.A. *J. Magn. Reson.* **1976**, *23*, 171-175.
17. Hill, E.A.; Yesinowski, J.P. *J. Chem. Phys.*, **1997**, *107*, 346-354.
18. Moran, L.B.; Yesinowski, J.P., *Solid State NMR* **1992**, *1*, 307-311.
19. Chihara, H. *J. Molec. Struct.* **1982**, *83*, 1-7.

Chapter 14

Solid-State NMR of Nitrides and Oxynitrides

M. E. Smith

Department of Physics, University of Kent, Canterbury, Kent CT2 7NR,
United Kingdom

The application of solid-state NMR to nitride and oxynitride ceramics and glasses is reviewed. The relative merits of the different nuclei and the techniques available are discussed. NMR has principally been used either for phase identification in complex crystalline/amorphous mixtures, or to identify local environments allowing the atomic ordering in such materials to be elucidated. Examples of both these areas of application are given.

Nitride and oxynitride ceramics now generate much technological interest due to their stability and chemical inertness at elevated temperatures, and in many cases their mechanical strength. Optimisation of the properties of such materials is usually regarded as in the domain of materials science and engineering. The chemical complexity of these materials and the fact that many of the properties of interest are related to the local atomic structure has required the application of advanced spectroscopic techniques. Detailed understanding of the atomic scale structure has suggested routes for more efficient synthesis (e.g. at lower temperatures) and provided improved insight into the properties of ceramic materials.

Over the last decade solid-state NMR has increasingly shown itself to be an extremely valuable spectroscopic technique as a part of a complete materials characterisation methodology. It has made an impact in the field of nitride and oxynitride ceramics in two main ways. Its first use is for phase identification or "fingerprinting". Comparison is made to NMR spectra from well-characterised, usually single phase samples, and by matching resonance peak positions one can identify phases in complex mixtures. The great advantage of solid-state NMR is that it provides short-range order information thereby permitting identification of disordered phases from the NMR spectrum. Traditional diffraction methods are often insensitive to such phases. In addition, the direct quantitative nature of NMR provides a means to experimentally determine accurately the content of the various crystalline and amorphous phases. For sintering of Si_3N_4 with Y_2O_3 , for example, the high atomic number of ^{89}Y leads to even relatively minor yttrium-containing

phases dominating the X-ray diffraction (XRD) pattern, thereby requiring careful quantitative interpretation of such powder patterns. Secondly, NMR has been used to identify local environments in various phases from which information detailed atomic scale structural models can be postulated. For such phases there are often high degrees of atomic substitution possible that in structurally ordered materials lead to atomic disorder. When this atomic disorder involves elements such as silicon/aluminium and oxygen/nitrogen, distinguishing these elements by traditional X-ray scattering techniques can be extremely difficult.

Interest in nitrides has centred around Si_3N_4 and AlN based materials which are amenable to ^{29}Si and ^{27}Al NMR. Oxynitrides offered themselves as an obvious extension of the study of structural influences on the ^{29}Si isotropic chemical shift which had initially concentrated on silicates and aluminosilicates (1). The early ^{29}Si magic angle spinning (MAS) NMR work on silicates and zeolites showed that the isotropic chemical shift was the most directly informative spectral parameter with the shift principally determined by the Q^n -species (where n is the number of bridging bonds in a particular SiO_4 unit). The isotropic ^{29}Si chemical shift is also determined by the number of aluminium next-nearest-neighbours and structural inequivalences (1). Oxynitride ceramics offer a wide range of nearest-neighbour coordinations (i.e. $\text{SiN}_x\text{O}_{4-x}$).

Tetrahedrally coordinated aluminium can also have the same range of nearest-neighbour coordinations in such materials, although significant technical complications arise in observing them since ^{27}Al is a spin (I) $-5/2$ nucleus, thus experiencing quadrupole effects that make the unambiguous identification of such species difficult. Even in pure oxygen-containing aluminosilicates, the electric field gradient ($\text{efg} = \text{eq}$) can become large at distorted sites (e.g. kyanite, andalusite (2)). The quadrupole interaction arises between the nuclear electric quadrupole moment (eQ) and the efg at the nuclear site, and is characterised by the quadrupole coupling constant ($C_Q = e^2Qq/h$) and an asymmetry parameter (η) (see ref. 3 and references therein for details). The quadrupole interaction causes substantial splitting of the non-central or satellite transitions through first-order effects that spread the intensity from these transitions over a wide frequency range, typically for ^{27}Al of ~ 1 MHz. The practical consequence of this is that most ^{27}Al MAS NMR studies usually only observe the central ($1/2 \leftrightarrow -1/2$) transition which is not perturbed by the quadrupole interaction to the first-order. In satellite transition NMR spectroscopy, the satellite transitions are narrowed into an extensive series of spinning sidebands, and although some novel information has been produced from this elegant experiment, both accumulation and analysis of the data are not straightforward (4). For the central transition the quadrupole interaction can be sufficiently large that second-order effects become important and their angular variation is only partially averaged by MAS, thereby leaving substantial residual linewidth that degrades spectral resolution compared to ^{29}Si MAS NMR (1,3). For mixed nearest-neighbour coordinations, the efg can be extremely large producing substantial second-order effects. The consequence of these effects for the early ^{27}Al MAS NMR at spinning speeds below 4 kHz was that only sites with small C_Q values were narrowed. Signals from the strongly broadened aluminium sites (that decay

rapidly in the time domain) are lost in the long preacquisition deadtime delays that were also often used. This is illustrated in Figure 1 for 15R AlN-polytypoid where the ^{27}Al MAS NMR spectrum at 3 kHz shows two relatively sharp resonances at ~ 110 and ~ 5 ppm lying on top of a broad component. Removal of the first 40-50 μs eliminates the broad underlying component from the spectrum. Spinning at 15 kHz (Fig. 1(b)) is sufficient to average the interaction at most of the sites since the broad underlying resonance is now absent but the actual linewidth of the averaged resonances is larger. This broadening can be simply understood since at MAS speeds at faster rates, the linewidths are averages for sites with larger C_Q values that have greater residual second-order widths. That there is a range of C_Q values in such materials is evidenced from the shape of the MAS resonances observed which are distinctly asymmetric, with sharp positive edges (largely located by the isotropic chemical shift) and a tail to less positive shift that results from the distribution of C_Q (4). Most early ^{27}Al MAS NMR spectra observed only the most symmetric sites and these often constituted a relatively minor fraction of the aluminium-content of the samples. By quantitative comparison with an $\alpha\text{-Al}_2\text{O}_3$ standard, as little as 10% of the aluminium seen from some silicon-aluminium-oxygen-nitrogen (sialon) ceramics (5). The problem of quantification in ^{27}Al MAS NMR spectra in general has proved a great impetus to improve NMR hardware for solids. The most significant advances have been in the use of high applied magnetic fields (up to 17.5 T), fast MAS speeds (up to 20 kHz) and the application of faster digitisation (3).

Other nuclei exist in nitride and oxynitride systems that are potentially very attractive for solid-state NMR, particularly ^{15}N ($I = 1/2$) and ^{17}O ($I = 5/2$). Both nuclei have large chemical shift ranges which makes them sensitive to even quite small structural changes. In systems that contain Si-O bonds, the quadrupole interaction for ^{17}O can be quite significant and necessitates fast MAS speeds. The major drawback of both these nuclei is the sensitivity problem that results from their low natural abundance at 0.4% for ^{15}N and 0.037% for ^{17}O . However, even modest enrichment (6,7) can lead to significant improvements in sensitivity and the unique perspective that these nuclei offer can often be crucial in understanding structure, particularly atomic ordering. An alternative nucleus is ^{14}N , but this nucleus has often been discounted since it is a spin-1 nucleus. All the ^{14}N NMR transitions experience the quadrupole interaction to first-order that usually leads to broad ^{14}N resonances. However, some recent elegant work (8) has shown that MAS can cause significant narrowing of this inhomogeneous interaction providing quite high resolution spectra. In the metal sialon systems, some of the metal nuclei can be classified in the "possible but difficult category" for solid-state NMR, namely ^{89}Y ($I = 1/2$) and ^{25}Mg ($I = 5/2$), with some examples of their application being reported here.

Experimentally, the majority of NMR studies have relied on MAS and once the optimum conditions have been worked out, accumulation of such spectra from these materials is straightforward. There are a number of points that should be noted. For ^{15}N NMR a wide range of secondary shift references are employed and results are often quoted against that secondary shift reference making correction necessary prior to comparison of spectra between different studies. A common

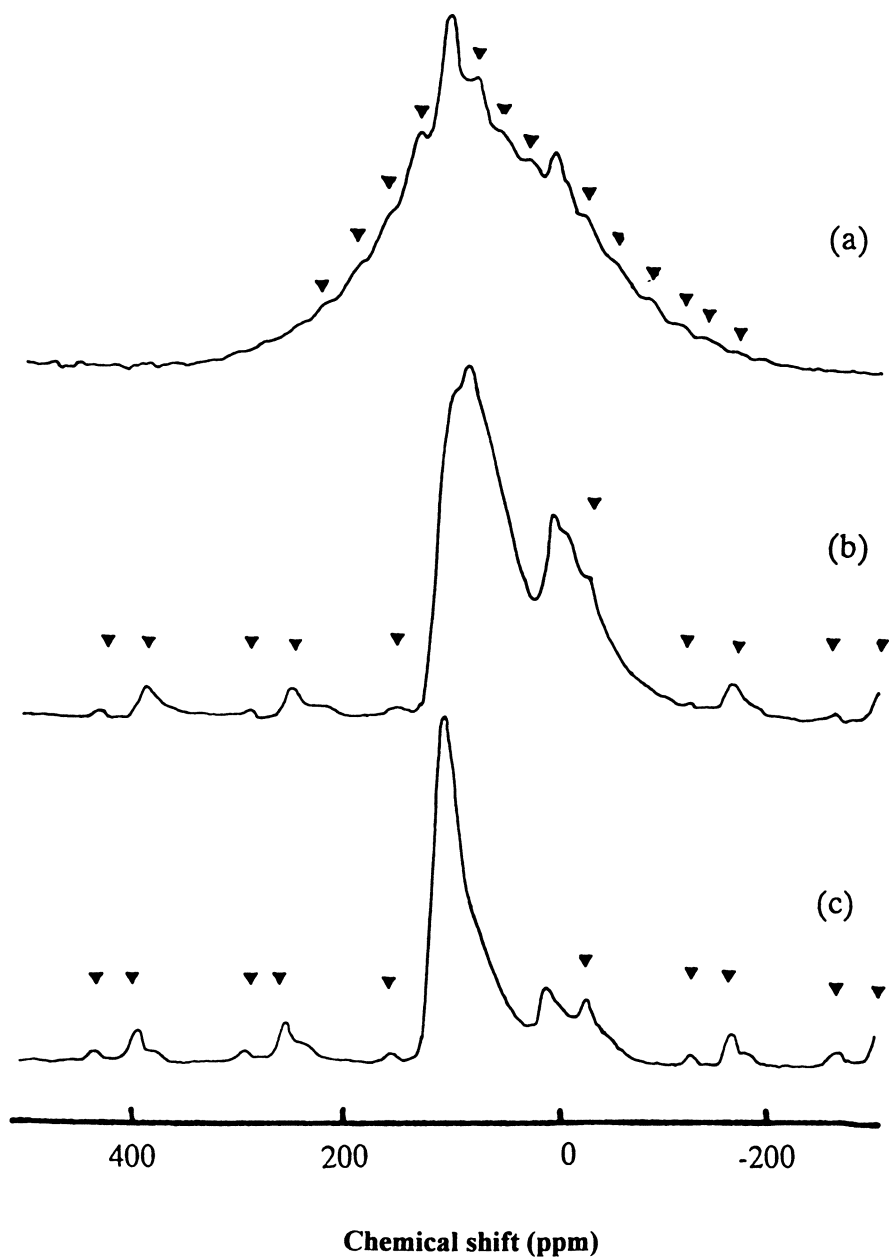


Figure 1. ^{27}Al MAS NMR spectra at 9.4 T of 15R polytypoid spinning at (a) 3 kHz and (b) 15 kHz, and (c) 21R polytypoid spinning at 15 kHz. (Taken with permission from reference 48. Copyright 1992.)

secondary standard, at least amongst those studying inorganic nitrides, is needed. The ammonium ^{15}N resonance of NH_4NO_3 would seem an obvious candidate. The major experimental difficulty of nitride systems is the very long relaxation times (T_1) encountered, especially for the spin-1/2 nuclei (^{29}Si , ^{15}N and ^{89}Y). For pure Si_3N_4 , T_1 for both ^{15}N and ^{29}Si is around 3000 s (9,10). In $\text{Y}_4\text{Si}_2\text{O}_7\text{N}_2$ T_1 for ^{29}Si was estimated to be around 10000 s (11). These long T_1 values are a reflection of the lack of impurity relaxation and the highly rigid nature of such network materials. This means the pulse angle/recycle conditions have to be very carefully chosen to obtain quantitative spectra and the experiments can be extremely time-consuming (11). The situation is often worse for ^{89}Y with its low gyromagnetic ratio. For silicates, the narrow ^{89}Y MAS NMR resonances mean that overnight with 45 minute recycle delays, sufficient signal-to-noise could be accumulated (12). ^{89}Y resonances from oxynitride ceramics have proved more elusive and it was not until paramagnetic doping was introduced that such ^{89}Y resonances could be observed. In an extensive study of this effect in yttrium sialons, the most effective lanthanide was Eu^{3+} , causing rapid relaxation but little paramagnetic broadening of the ^{89}Y resonance (13).

Silicon Nitride Based Ceramics.

Silicon nitride (Si_3N_4) forms the basis of many high temperature ceramics. It is a planar structure with planes of silicon and nitrogen stacked along the c-axis. Differences in the stacking of these planes, which are parallel to the basal plane of the hexagonal unit cell, give rise to the two polymorphs, being ABCD for $\alpha\text{-Si}_3\text{N}_4$ and ABAB for $\beta\text{-Si}_3\text{N}_4$. The $\alpha\text{-Si}_3\text{N}_4$ structure has two inequivalent silicon sites with an average bond length difference of 0.0021 nm. ^{29}Si MAS NMR spectra readily distinguish these polymorphs with $\beta\text{-Si}_3\text{N}_4$ showing a single resonance at around -49 ppm and $\alpha\text{-Si}_3\text{N}_4$ having two resonances separated by ~ 2 ppm at -47.1 and -49.0 ppm (Fig. 2, 9,10,14,15). Amorphous Si_3N_4 has a ^{29}Si NMR resonance at -47 ppm but a much greater linewidth (Fig. 2, (9)). Nitrogen occurs in NSi_3 units in silicon nitrides and for $\beta\text{-Si}_3\text{N}_4$ there are two sites in the ratio 3:1 that differ in their arrangement relative to the threefold Si_3N_4 axis. These two resonances are observed in this ratio as seen in its ^{15}N MAS NMR spectrum (Fig. 2). Four ^{15}N resonances are observed in $\alpha\text{-Si}_3\text{N}_4$ (Fig. 2, (10)). One study reported that fine structure could be detected in the ^{29}Si NMR peaks of Si_3N_4 (15) attributed to residual $^{14}\text{N}\text{-}^{29}\text{Si}$ dipolar coupling but this was disputed since the linewidth remained approximately the same in a highly ^{15}N -enriched sample (10). Recently, the theory of residual $^{29}\text{Si}\text{-}^{14}\text{N}$ dipolar coupling in MAS NMR spectra has been explored in some detail (16).

Silicon nitride is a starting material in the manufacture of a number of other phases and the purity of the initial powder is very important. Accurate phase analysis is vital and a careful NMR study has shown for a wide range of commercial Si_3N_4 powders that they are often complex mixtures of the two polymorphs, together with amorphous Si_3N_4 , $\text{Si}_2\text{N}_2\text{O}$ and an oxide phase (Fig. 3). In some cases silicon nitride is not even the major phase (9). The presence of large amounts of disordered phases makes accurate analysis by traditional XRD techniques difficult.

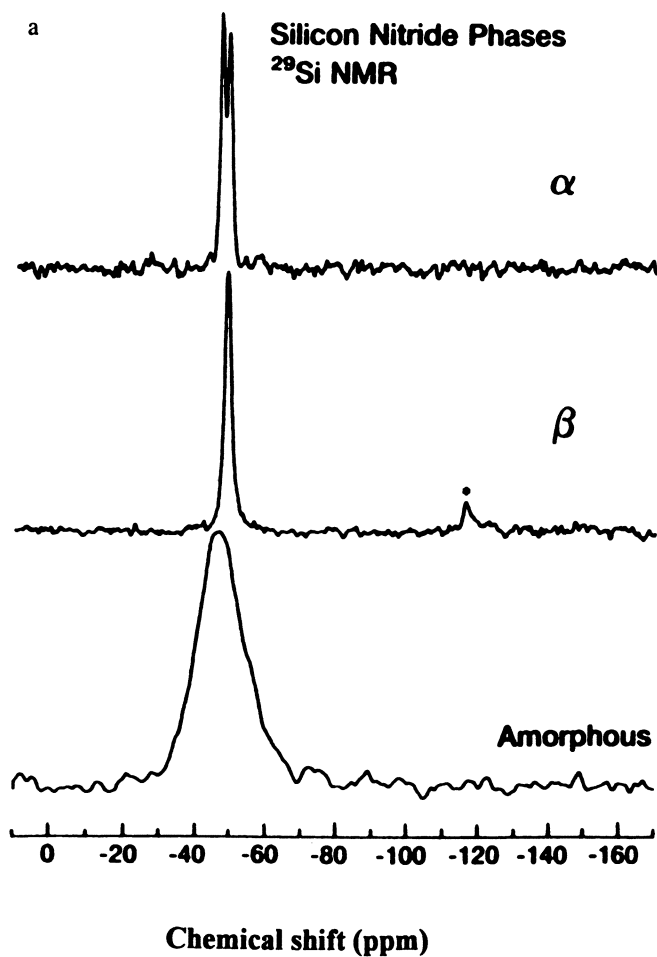


Figure 2. (a) ^{29}Si MAS NMR spectra of α -, β - and amorphous Si_3N_4 (Taken from Ref. 9 with permission) and (b) ^{15}N MAS NMR spectra of α - and β - Si_3N_4 . (Taken with permission from reference 10. Copyright 1990.)

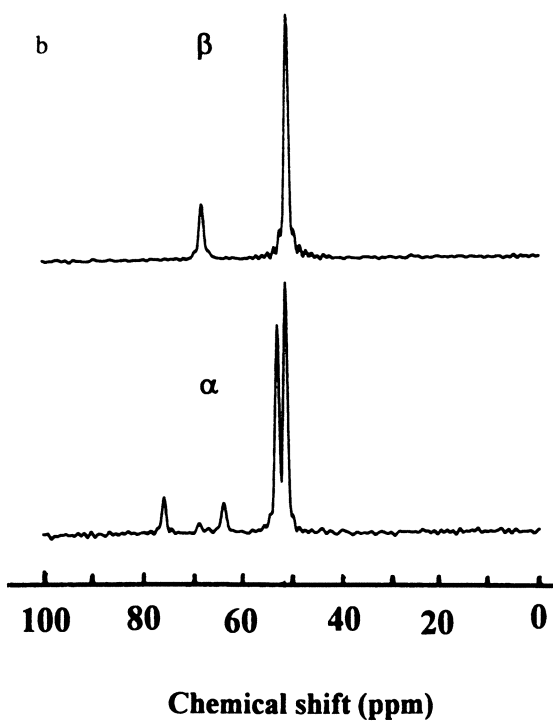


Figure 2. *Continued.*

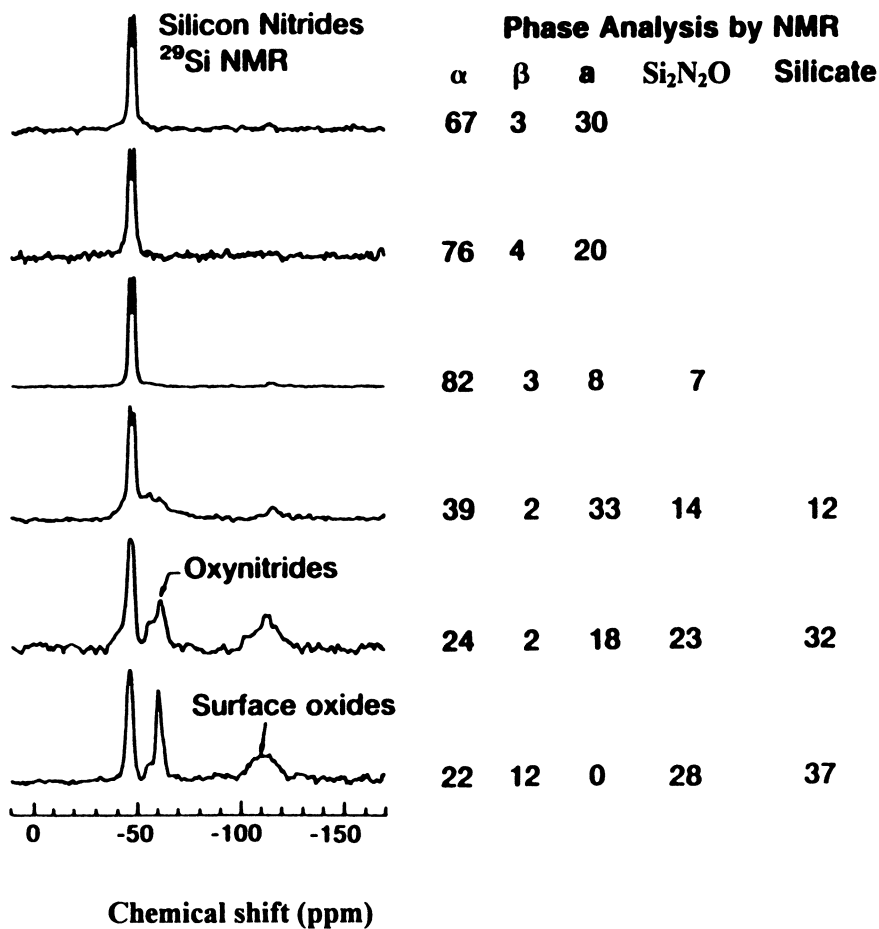


Figure 3. ²⁹Si MAS NMR analysis of commercial Si₃N₄ powders.
(Taken with permission from reference 77. Copyright 1989 Chapman and Hall.)

Nanoscale Si_3N_4 prepared by laser heating can be poorly crystalline and ^{29}Si NMR has shown the presence of Si-OH and Si-O-Si bonds (17,18). A process has also been outlined for a gas phase reaction of trichlorosilane and ammonia to produce a Si_3N_4 layer on the surface of silica particles as characterised by ^{29}Si MAS NMR (19). Rather than direct nitridation more subtle chemical routes for the production of Si_3N_4 are being investigated and solid-state NMR is playing an important role in elucidating the reaction mechanisms. Pyrolysis of polyethylsilazane within an NMR probehead to produce Si_3N_4 allowed the identification of reaction intermediates by ^{29}Si MAS NMR (20). Production of ultrafine Si_3N_4 -SiC composites has been characterised by ^{29}Si MAS NMR including from laser combustion of hexamethyldisilazane in the range temperature 1000 - 1600°C (21). From polysilazane characterisation by ^1H , ^{13}C and ^{29}Si NMR, the formation of an amorphous ceramic at 1000°C that is converted to a stable crystalline form at 2000°C was identified (22). For ultrafine SiC- Si_3N_4 particles, ^{29}Si MAS NMR showed that up to 1300°C there is not much change in the structure of the particles but at 1500°C, nitrogen dissolved in the structure is lost leaving β -SiC particles with some nitrogen at the surface as SiC_3N units (23).

In many applications Si_3N_4 is alloyed with Al_2O_3 which dissolves into the β - Si_3N_4 structure to form β' -sialon $\text{Si}_{6-z}\text{Al}_z\text{O}_z\text{N}_{8-z}$ ($0 \leq z \leq 4$). The wide solid solubility leads to some interesting atomic ordering problems. A remarkable observation across this solid solution range is that the ^{29}Si isotropic chemical shift remains quite constant at ~ -49 ppm with some linebroadening at higher z values (12,24,25). ^{15}N MAS NMR spectra show the same two peaks as for β - Si_3N_4 with little change with composition (24). ^{27}Al NMR spectra from β' -sialon have proved quite a challenge for MAS with early work showing some quite sharp peaks. Quantitative comparison has revealed that this narrow signal corresponded to as little 10% of the total aluminium-content (5). A comparison of ^{27}Al NMR 15 kHz MAS spectra at 4.7 and 11.7 T field strengths is given in Fig. 4 for a $z = 4$ β' -sialon. The NMR results at 4.7 T have very little sample-related structure that can be definitely assigned, whereas, the ^{27}Al NMR at 11.7 T shows some additional fine structure. While these spectra cannot be completely resolved, some of these peaks must correspond to mixed $\text{AlN}_x\text{O}_{4-x}$ environments. The main conclusion drawn from the ^{29}Si and ^{27}Al MAS NMR for the β' -sialon system is that there is preferential bonding of nitrogen to silicon and oxygen to aluminium. The structure of β' -sialon is independent of the method of preparation with ^{27}Al and ^{29}Si MAS NMR spectra from conventional sintering being very similar to those from a self-propagating high temperature synthesis (25). One of the important questions for the application of β' -sialon is its oxidation resistance at elevated temperatures. ^{29}Si and ^{27}Al MAS NMR have shown that at elevated temperatures initially some amorphous SiO_2 and non-crystalline mullite form, with the remaining β' -sialon having a lower z -value and a concomitant decrease in the AlO_4 -content of the sialon (26).

To make β' -sialon commercially more viable, a number of studies have investigated the possibility of lower temperature synthesis routes using a variety of starting materials. The general principle is to start with an aluminosilicate, which is reduced in a carbothermal reaction and then nitrided to β' -sialon. Specific cases

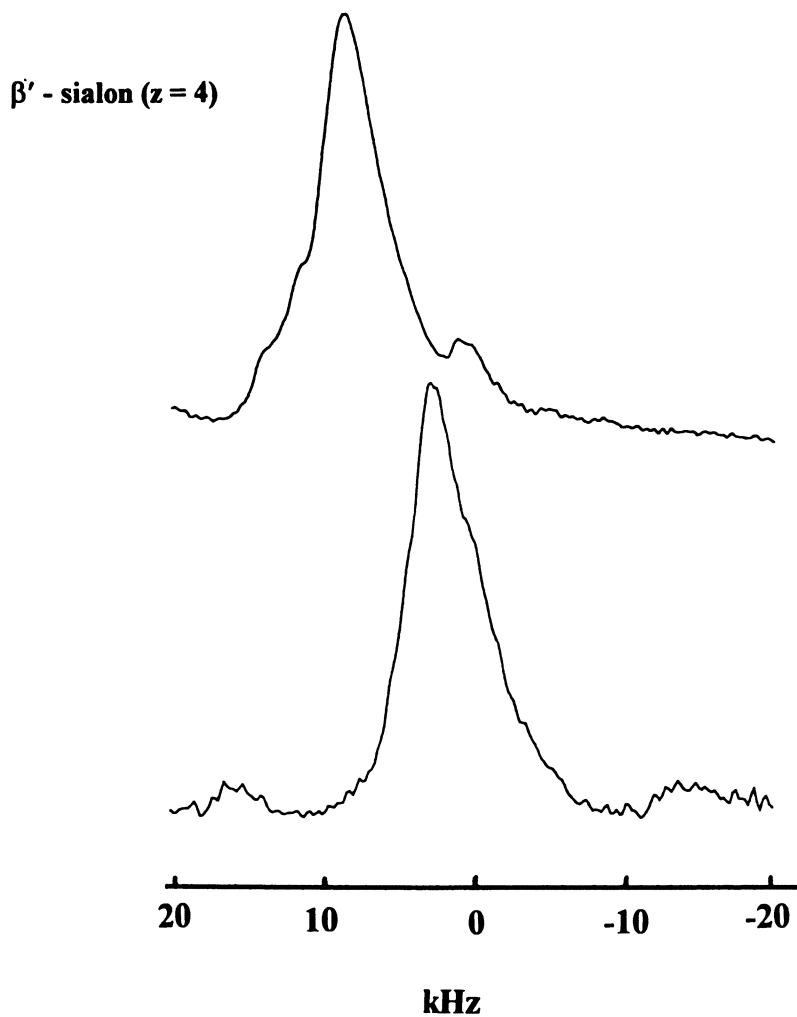


Figure 4. ^{27}Al MAS NMR spectra at 4.7 T (lower) and 11.7 T (upper) for β' -sialon ($z = 4$) spinning at 15 kHz.

have included using a montmorillonite-polyacrylonitrile composite (27) but the most commonly studied case is the use of 1:1 clay minerals related to kaolinite (28,29). The initial calcination breaks down the clay structure, with the thermal decomposition of kaolinite being one of the most studied reactions in ceramic processing (e.g. 30,31) producing a nanoscale mixture of mullite and silica. A typical set of ^{29}Si and ^{27}Al MAS NMR spectra illustrating the reaction sequence is shown in Fig. 5 for a mixture of halloysite and brown coal. Carbothermal reaction converts the silica formed in the decomposition of the clay to SiC by reaction with CO, which subsequently reacts with the silica remaining in mullite to form Si_3N_4 (see ^{29}Si MAS NMR, Fig. 5). The aluminium largely remains as a mullite phase in the early stages of the reaction. At later times, the mullite reacts with the Si_3N_4 , SiC and nitrogen from the atmosphere to give β' -sialon. The success of this reaction depends on the aluminium and silicon being intimately mixed on a nanometre scale with atomic transport occurring via the gas phase (28). This can be a problem in that significant transport must occur, changing the bulk composition. SiO is a volatile component that is thought to be transported to the cooler parts of the furnace, where it reacts and is deposited. These deposits have been collected and analysed by solid-state ^{29}Si NMR (32). The addition of Al_2O_3 , MgO and Y_2O_3 as densifying aids in the carbothermal production of β' -sialon have been investigated by multinuclear solid-state NMR (^{27}Al , ^{29}Si , ^{25}Mg and ^{89}Y) and allow clear identification of the minor secondary phases that form (33). Sialon fibres have been produced by a similar reaction using a polyaluminocarbosilane formed from polycarbosilane and a modified aluminium alkoxide. ^{29}Si MAS NMR showed that conversion of the SiC_4 peak to $\text{SiN}_x\text{O}_{4-x}$ occurred at about 1000°C. The ^{29}Si NMR peak is broad (characteristic of disorder) and crystallisation to β' -sialon occurs at 1500°C. The ^{27}Al MAS NMR spectra show that at 1000°C the aluminium is largely AlO_4 and at 1500°C there are a variety of oxygen and nitrogen nearest neighbour environments for aluminium (34).

There is much less solubility of Al_2O_3 in α - Si_3N_4 and to form a stable phase requires the addition of some other metal oxide such as MgO, CaO or Y_2O_3 . The ^{29}Si isotropic NMR chemical shift has been observed to remain constant at ~ -48 ppm (Table I). ^{27}Al MAS NMR spectra of α' -sialon show a peak characteristic of only AlO_4 units. ^{27}Al and ^{29}Si MAS NMR has been used to follow the preparation of fine-grained calcium α' -sialon (35).

Silicon oxynitride ($\text{Si}_2\text{N}_2\text{O}$) is the other aluminium-free phase in the Si-Al-O-N system. $\text{Si}_2\text{N}_2\text{O}$ contains a single silicon SiN_3O site at a shift of -63 ppm (14). Some aluminium solubility is possible in $\text{Si}_2\text{N}_2\text{O}$ to produce O' -sialon ($\text{Si}_{2-x}\text{Al}_x\text{N}_2\text{O}_{1+x}$; $0 \leq x \leq 0.4$). As aluminium is dissolved, the ^{29}Si NMR chemical shift remains quite constant with a small peak due to secondary β' -sialon seen at -48 ppm (24). ^{27}Al MAS NMR spectra show resonances at 65 ppm which correspond to AlO_4 units, and a minor peak at 2.3 ppm, the latter corresponding to a secondary phase. Formation of amorphous $\text{Si}_2\text{N}_2\text{O}$ has been studied by ^{29}Si MAS NMR. Nitridation of Aerosil with ammonia at 1100°C produces no Si_3N_4 or SiO_2 signals in the ^{29}Si MAS NMR spectrum, indicating the formation of pure $\text{Si}_2\text{N}_2\text{O}$ (36). Reaction of a high surface area sol-gel SiO_2 under a flowing atmosphere of nitrogen and ammonia

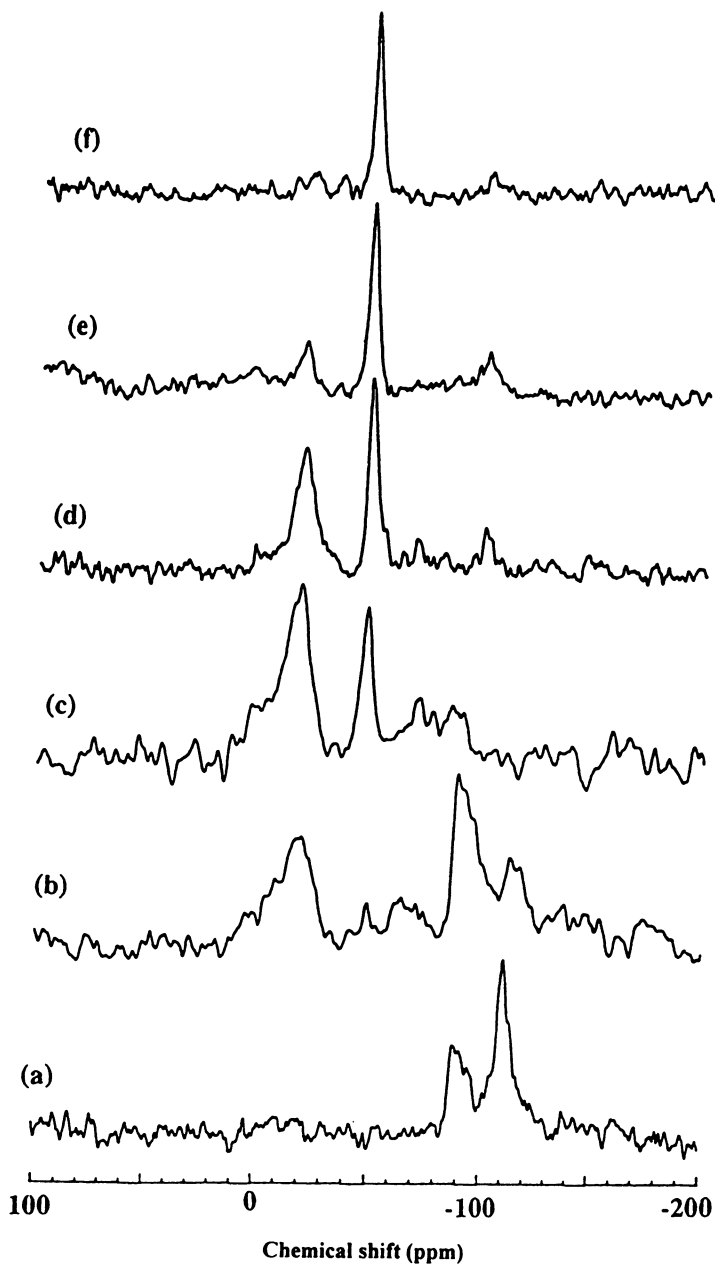


Figure 5. ^{29}Si and ^{27}Al MAS NMR spectra of reaction intermediates in the carbothermal reduction and nitridation of halloysite clay to produce β' -sialon. (Taken with permission from reference 28. Copyright 1994 Royal Society of Chemistry.)

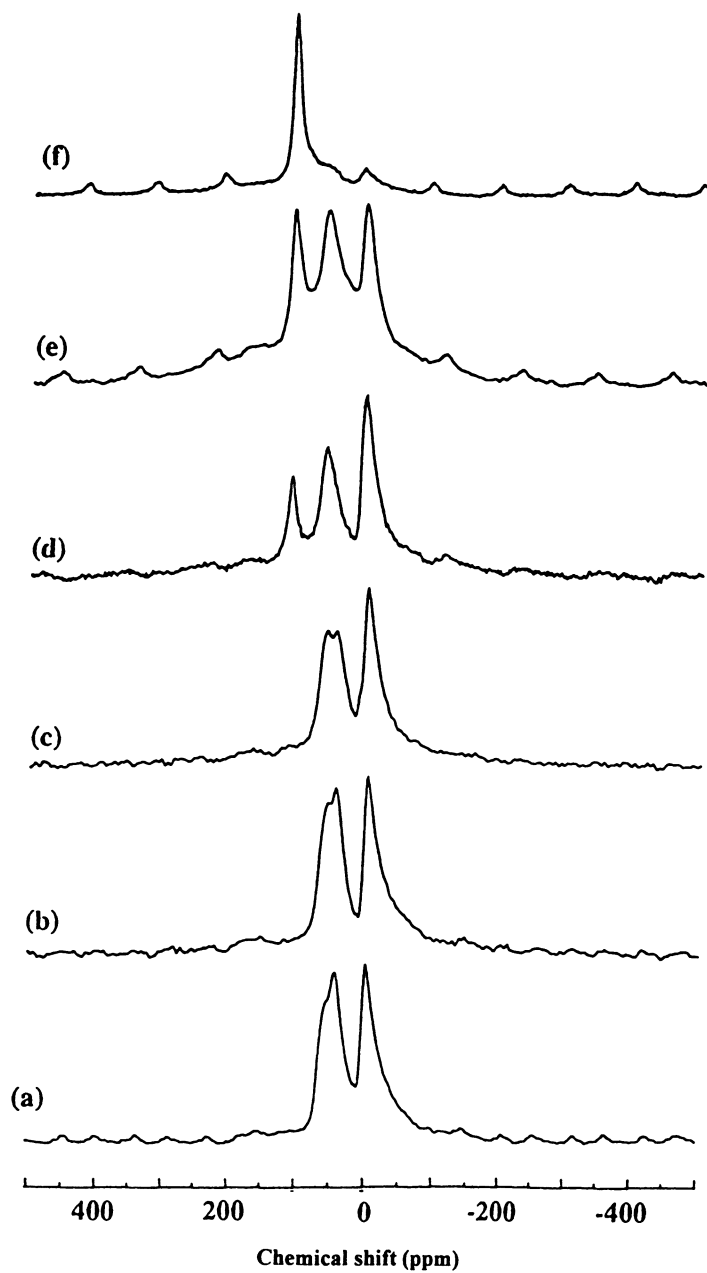


Figure 5. *Continued.*

Table I. ^{29}Si and ^{15}N isotropic chemical shifts and ^{27}Al peak positions from Si-Al-O-N ceramic phases.

Phase	^{29}Si δ_{iso} (ppm)	^{27}Al δ_p (ppm)	^{15}N δ_{iso} (ppm)	Ref.
α - Si_3N_4	-49.0, -47.1		49.0, 50.8, 61.4, 73.5	9, 10 14, 15
α' , $\text{CaSi}_9\text{Al}_3\text{O}_{15}$	-47.6			76
α' , $\text{Y}_{0.5}\text{Si}_9\text{Al}_3\text{O}_{1.5}\text{N}_{14.5}$	-47.8			76
amorphous Si_3N_4	-46.4			9
β - Si_3N_4	-48.5		51.5, 68.7	9, 10 14, 15
β' , $\text{Si}_{5.4}\text{Al}_{0.6}\text{O}_{0.8}\text{N}_{7.4}$	-48.4		52.4, 68.8	24
β' , Si_5AlON_7	-48.5	75, 89, 108		5, 14
β' , $\text{Si}_2\text{Al}_4\text{O}_4\text{N}_4$	-48.3	8, 75, 89, 108		5, 14
$\text{Si}_2\text{N}_2\text{O}$	-63.0		40.3	14, 24
O' , $\text{Si}_{1.9}\text{Al}_{0.1}\text{N}_{1.9}\text{O}_{1.1}$	-60.9		40.8, 51.6	24
O' , $\text{Si}_{1.76}\text{Al}_{0.24}\text{N}_{1.76}\text{O}_{1.24}$	-61.3	64.7		24
O' , $\text{Si}_{1.72}\text{Al}_{0.28}\text{N}_{1.72}\text{O}_{1.28}$	-60.9		41.1, 51.8, 68.8	24
AlN		114	64.4	5, 40
ALON, 35.7 mol% AlN		14.3, 66.6, 106	55	5, 42, 47
ALON, 83 mol% AlN		14, 67, 106		47
12H polytypoid	-33.4, -47.7			41
15R polytypoid	-21.0, - 34.3, -47.2	10, 93, 112		40, 41, 48
21R polytypoid	-20.0, -32.5, -46.1	10, 112		41, 48
27R polytypoid	-20.8, -31.5, -45.9			41
X-phase, $\text{Si}_3\text{Al}_6\text{O}_{12}\text{N}_2$	-56.5	2.8, 59		38, 39

gives a very complex mixture of amorphous phases after 12 hours nitridation at 1000°C. There are residual SiO₂ and silanol (Si-OH) ²⁹Si NMR peaks occurring between -40 to -80 ppm. The intensity of the ²⁹Si NMR signal in the Si₃N₄ and Si₂N₂O region increases but the sample remains a complex mixture (37).

Sialon X-phase (approximate composition Si₃Al₆O₁₂N₂) often occurs as both an intermediate in the formation of, and as a secondary phase in, some sialon ceramics. It has a structure closely related to mullite. An early study (38) reported ²⁷Al MAS NMR resonances at 66.9 and 0.8 ppm but no ²⁹Si NMR results, presumably due to a very long T₁. More recently distinct ²⁷Al NMR signals have been reported at 59 and 2.8 ppm using much faster MAS, with the ²⁹Si NMR peaks occurring at -56.5 ppm. The observed resonances are consistent with SiO₂N₂, AlO₄ and AlO₆ coordination units in the structure that is closely related to that of mullite, with nitrogen preferentially occupying the tricoordinate anion site with the nearest neighbour sites being preferentially occupied by silicon (39).

Aluminium Nitride Based Ceramics.

Aluminium nitride (AlN) is a wurtzite structure made up of AlN₄ units in a hexagonal lattice that gives a ²⁷Al MAS NMR shift of 114 ppm (5,40). Observation of the ²⁷Al satellite NMR transitions gives C_Q = 1.913 MHz and η ~ 0 (8). ¹⁵N NMR of AlN shows a major peak at 63.7 ppm with a T₁ of 600 s (41,42). ¹⁴N in AlN has a surprisingly small C_Q close to zero (8). AlN is often prepared by nitridation of elemental aluminium. The major impurities in such AlN materials are aluminium metal, and alumina that forms by reaction with moisture. Solid-state ²⁷Al NMR is extremely valuable at characterising these impurities with sensitivity to such impurities down to ~ 0.05 wt% (43). Reaction of AlN with moisture occurs to form ammonia and surface aluminium hydroxides/oxides which can be followed by ²⁷Al MAS NMR. In bulk polycrystalline AlN, a thin surface oxide layer forms that can be readily detected as an AlO₆ resonance. In an ultrafine AlN powder this reaction can transform the sample almost completely to AlO₆ coordination (44). The surface reaction of AlN particles has been studied in detail using ¹H-²⁷Al CP MAS NMR which indicates that the surface is a complex mixture of AlO(OH) and Al(OH)₃ that rapidly forms on exposure to the atmosphere (45). As for Si₃N₄ more subtle chemical routes to form AlN are being investigated with its formation by pyrolysis of polyethyliminoalane being characterised by ²⁷Al MAS NMR (46).

As oxygen is dissolved into AlN the structure transforms to a defective cubic spinel i.e. related to γ-Al₂O₃; however the presence of nitrogen stabilises this structure at temperatures where γ-Al₂O₃ would normally transform to α-Al₂O₃. Some solid solution exists but the phase region is centred on 35.7 mol% AlN, corresponding to 5AlN:9Al₂O₃. ²⁷Al MAS NMR peaks are observed corresponding to AlN₄, AlO₄ and AlO₆ units with the ¹⁵N NMR chemical shift remaining at the same position as for AlN (5,42). Considerable linebroadening of the ¹⁵N NMR indicates a range of next-nearest-neighbours (42). There was also some difficulty in accurately quantifying the ²⁷Al MAS NMR spectra of Alons due to the large efgs

that could result from the mixed local nitrogen/oxygen coordinations. At an applied magnetic fields of 14.1 T quantitative analysis indicates that most of the aluminium was observed and spectra for an extensive series are shown in Fig. 6. The higher field ^{27}Al NMR spectra allowed partial resolution of signals attributed to mixed nearest neighbour coordination units (47). There is some dispute for example as to whether a peak at 106 ppm corresponds to AlN_4 or AlN_3O , and this is likely to remain somewhat ambiguous until much better resolution is available and correlations to well known structures can be made.

The sialon polytypoids are closely related to AlN and are formed by the addition of silicon and oxygen to AlN to give a series of compounds $(\text{Si,Al})_m(\text{O,N})_{m+1}$. To accommodate the excess non-metal atoms over the 1:1 ratio of wurtzite two structural alterations occur including the incorporation of an octahedrally coordinated layer and some half-filled occupancy of the tetrahedral layers. ^{29}Si and ^{27}Al MAS NMR spectra have been obtained from various AlN -polytypoids (24,38,40,48). Several ^{29}Si NMR peaks are observed with isotropic chemical shifts in the region of ~ -35 to -49 ppm. The different ^{29}Si peaks all have been assigned to SiN_4 units in different layers on the basis of their changing intensities as a function of composition. A shift of -35 ppm is quite positive for SiN_4 units but is consistent with some tetrahedra in the polytypoid structure being edge-sharing. Early ^{27}Al MAS NMR studies showed that there were either only relatively narrow well defined resonances at ~ 110 ppm and an octahedral peak at ~ 10 ppm (38), or these resonances were present overlying a broad NMR signal (40). Faster MAS speeds have revealed a second tetrahedral resonance at ~ 90 ppm (48). The ^{27}Al MAS NMR spectra show that all the octahedra are AlO_6 . It is probable that the two tetrahedral units observed are AlN_4 and AlN_3O , since the relative intensities of these lines change with composition as expected, provided a model is chosen where only aluminium occupies the octahedral layer and aluminium in the tetrahedral layers bonds preferentially to oxygen compared to silicon (48).

Metal Silicon-Aluminium Oxynitrides.

The addition of metal oxides greatly increases the range of sialon compounds that can be formed. Solid-state NMR of ^{29}Si in particular can be used to elucidate atomic scale ordering of such compounds, which is difficult by standard diffraction methods because of the similarity of the scattering of some of the constituent elements. Also with heavy metals, phases containing these elements can dominate the diffraction pattern and subtle changes in the ordering of the other lighter elements is missed by XRD. NMR has also proved to be very useful for identifying phases in complex mixtures and has allowed reaction pathways to be followed. The first studies synthesised single phase samples containing well defined local coordinations and allowed the effect of nitrogen on the shifts of ^{29}Si and ^{27}Al to be investigated. The main systems investigated were yttrium and lanthanum silicon oxynitrides (i.e. aluminium-free) (49-53). A shift change for ^{29}Si of 10-15 ppm per nitrogen substitution for oxygen is typically observed (Table II). It is apparent that with all the other structural influences that it is often not possible to make an

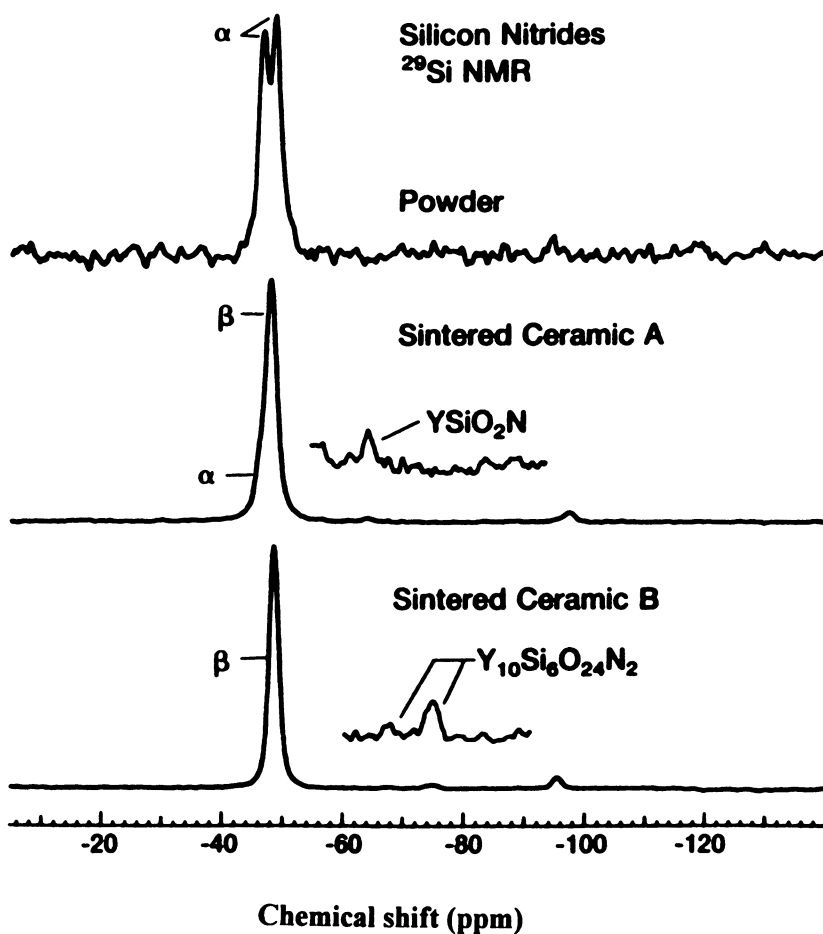


Figure 6. ^{27}Al MAS NMR spectra at 14.1 T of $\text{AlN-Al}_2\text{O}_3$ sintered mixtures of different mol% AlN. (Taken with permission from reference 47. Copyright 1994.)

Table II. ^{29}Si and ^{15}N isotropic chemical shifts from crystalline metal sialon phases.

Phase	^{29}Si δ_{iso} (ppm)	^{15}N δ_{iso} (ppm)	Ref.
$\text{Y}_5\text{Si}_3\text{O}_{12}\text{N}$	-67.5, -74.8		49, 52
$\text{La}_5\text{Si}_3\text{O}_{12}\text{N}$	-77.7		50, 51
$\text{Y}_4\text{Si}_2\text{O}_7\text{N}_2$	-74.4	226.6, 112.6	49, 52
$\text{Y}_4\text{SiAlO}_8\text{N}$	-74.8		
$\text{La}_4\text{Si}_2\text{O}_7\text{N}_2$	-84.2		50, 51
$\text{Y}_2\text{Si}_3\text{O}_3\text{N}_4$	-56.7	143.4, 126.4, 105.1	49, 52
$\text{Y}_2\text{Si}_{2.9}\text{Al}_{0.1}\text{O}_{3.1}\text{N}_{3.9}$	-57		57
$\text{Sm}_2\text{Si}_{2.8}\text{Al}_{0.2}\text{O}_{3.2}\text{N}_{3.8}$	-35		58
YSiO_2N	-65.3		49, 52
LaSiO_2N	-72.4	155	50, 51
$\text{La}_3\text{Si}_3\text{Al}_3\text{O}_{12}\text{N}_2$	-68, -77		53
$\text{La}_3\text{Si}_8\text{O}_4\text{N}_{11}$	-56.5, -68.2	120, 60	53, 7
$\text{Y}_2\text{SiAlO}_5\text{N}$	-72.2	148.5	72
$\text{Mg}_5\text{Si}_3\text{AlO}_{11}\text{N}$	-62.0, -75.1		
LiSiON	-51.0	54.4	53, 76

unambiguous assignment of the local coordination directly from the isotropic chemical shift because of the overlap of the shift ranges of the different local structural units.

The use of ^{29}Si MAS NMR to follow reactions has been well illustrated in these systems. For example, the formation of $\text{Y}_2\text{Si}_3\text{O}_3\text{N}_4$ (N-melilite) by sintering of Y_2O_3 and Si_3N_4 under nitrogen was investigated in detail (49). NMR showed that although N-melilite can be formed as a single phase eventually, unexpectedly the reaction was not direct and YSi_3N_5 formed as an intermediate phase. High temperatures are required to produce dense Si_3N_4 components making them expensive; therefore, methods have been investigated that can reduce sintering temperatures. One approach that has been examined to reduce sintering temperatures of Si_3N_4 is the addition of small amounts of metal oxides (e.g. Y_2O_3 , La_2O_3 , MgO , CaO) that form a liquid oxynitride phase at the sintering temperature, greatly aiding densification with the liquid phase effectively acting as a flux. This approach produces dense Si_3N_4 but has the disadvantage that the liquid phase solidifies at grain boundaries at the end of the reaction. It is the nature of this grain boundary phase that often determines the behaviour of the system so the identification and quantification of such phases is vital. However, the grain boundary phases constitute only a minor fraction of the total composition and thus present a challenge for the sensitivity of solid-state NMR. A very elegant experiment by Carduner examined the effect of Y_2O_3 additives on Si_3N_4 densification used solid cylinders of the samples which were machined to fit tightly in MAS rotors (52). This greatly increased the filling factor compared to a powder and allowed minor amounts of secondary phases to be detected (Fig. 7). More recently, an extensive study has examined the effect of small additions of Al_2O_3 , MgO and Y_2O_3 on Si_3N_4 densification (54). The secondary phases formed were a low- z β' -sialon for Al_2O_3 , a mixture of MgSiO_3 and an Mg-Si-O-N glass for MgO , and a mixture of phases for Y_2O_3 . ^{29}Si MAS NMR was used in conjunction with ^{25}Mg and ^{89}Y NMR to investigate this problem (54).

The ^{29}Si resonances from single phases have been used to examine the atomic ordering in metal silicon oxynitride phases. In early studies of $\text{Y}_2\text{Si}_3\text{O}_3\text{N}_4$ and $\text{Y}_4\text{Si}_2\text{O}_7\text{N}_2$ (N-YAM), single ^{29}Si NMR signals were detected, leading to the postulate of structures that had single well defined silicon environments (49). Much more recent work has reproduced the ^{29}Si MAS NMR spectra but augmented the structural information by ^{15}N MAS NMR measurements. An illustration of this is N-YAM which contains "disilicate" $\text{Si}_2\text{O}_5\text{N}_2$ units for which two possible oxygen-nitrogen orderings are possible (Fig. 8), with either only SiO_3N or equal numbers of SiO_2N_2 and SiO_3N units present. Pauling's Second Crystal Rule suggests that nitrogen occupies the bridging position. The ^{15}N MAS NMR spectrum showed two resonances at 226.6 and 112.6 ppm with the more positive shift assigned to the more ionic terminal, non-bridging position (55). The implication of this observation is that the ^{29}Si MAS NMR spectrum must be a composite of two overlapping resonances. A similar ^{15}N NMR study has been carried out for N-melilite that again showed that the single ^{29}Si MAS NMR peak should be interpreted cautiously as the ^{15}N spectrum could be decomposed into three overlapping peaks which can be

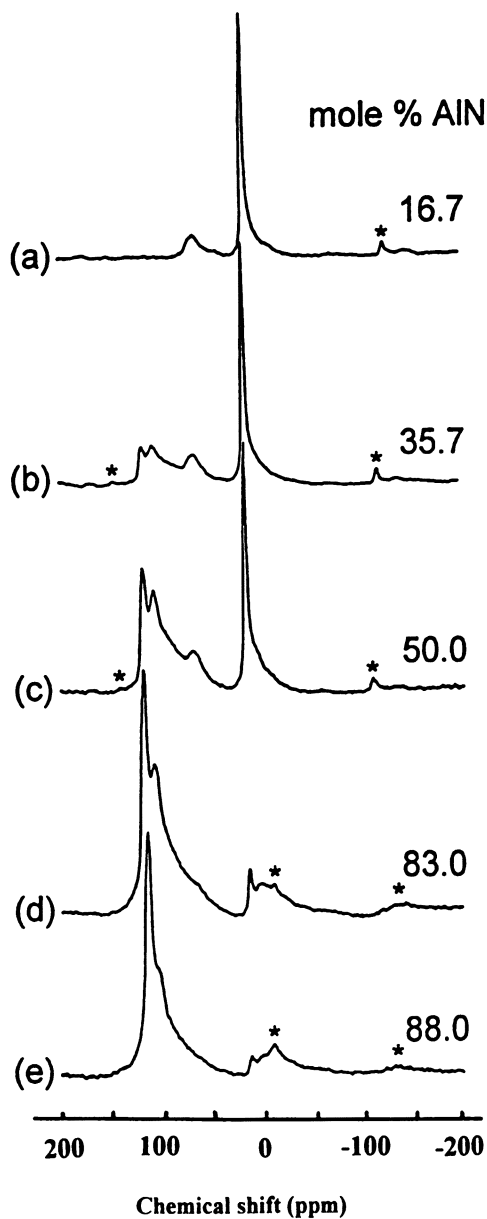


Figure 7. ^{29}Si MAS NMR detection of minor Y-Si-O-N grain boundary phases formed in Si_3N_4 using Y_2O_3 as a sintering aid. (Taken with permission from reference 77. Copyright 1989 Chapman and Hall.)

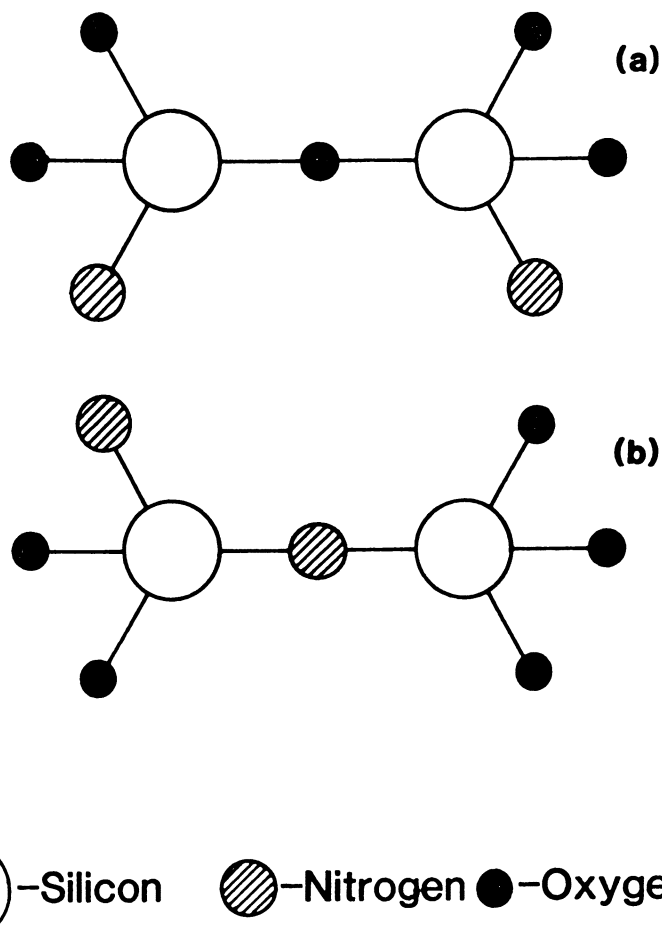


Figure 8. Possible atomic arrangements in the $\text{Si}_2\text{O}_5\text{N}_2$ unit of $\text{Y}_4\text{Si}_2\text{O}_7\text{N}_2$.

interpreted in terms of a structure with two distinct silicon coordinations (56). These ^{15}N NMR observations on N-melilite are again consistent with nitrogen favouring the bridging positions. ^{17}O NMR studies like ^{15}N NMR, also require isotopic enrichment and have been occasionally used in metal sialons (7). In lanthanum N-YAM, for example, two ^{17}O NMR peaks are observed at ~ 570 and 175 ppm, which can be readily identified, with the former an "ionic" environment associated with lanthanum only, and the other bonded to silicon. The latter ^{17}O NMR signal has a larger C_Q consistent with being associated with an Si-O bond.

Most of this work has been reported on aluminium-free materials but in some of these phases aluminium solubility is possible making ^{27}Al NMR useful for elucidating how aluminium substitutes into such materials. In yttrium N-melilite, the aluminium exists in AlO_4 units and it would appear that it favours substitution on the MgO_4 site of the parent akermanite structure (57). This would also explain the solubility limit which appears to exist when one of the three silicons is replaced. Similar observations have been seen in neodymium and samarium N-melilites and ^{29}Si and ^{27}Al MAS NMR spectra could be recorded despite the paramagnetic nature of such samples (58). In N-YAM silicon and nitrogen can be replaced by aluminium and oxygen to form a complete solid solution across the $\text{Y}_4\text{Si}_2\text{O}_7\text{N}_2\text{-Y}_4\text{Al}_2\text{O}_9$ join. The intermediate composition $\text{Y}_4\text{SiAlO}_8\text{N}$ forms a single phase and gives a ^{29}Si MAS NMR spectrum very similar to N-YAM; however, the ^{27}Al NMR spectrum is very interesting due to a peak at ~ 30 ppm in addition to a peak that corresponds to an AlO_4 site (57). This observation has yet to be explained although it has been consistently reproduced in a number of studies. $\text{Na}_3\text{AlP}_3\text{O}_9\text{N}$ and $\text{Na}_2\text{Mg}_2\text{P}_3\text{O}_9\text{N}$ contain NaO_6 and NaO_6N environments that could be resolved by ^{23}Na multiple quantum MAS NMR (59).

Related Metal Nitrides.

In metal silicon nitrides, a wide range of ^{29}Si isotropic chemical shifts are seen from -35 to -65 ppm (Table III) illustrating that overlap of the chemical shift ranges of the different local coordinations can occur. NMR has been useful in elucidating structures of such materials (e.g. LaSi_3N_5) (51,60). Nitrides in the system $\text{YN-Si}_3\text{N}_4$ have recently been synthesised by a carbothermal reduction nitridation scheme (61). The ^{29}Si MAS NMR spectra agree with the original study of these compounds (49) and were augmented with ^{89}Y MAS NMR (61). Some extremely high-resolution ^{15}N NMR spectra of MgSiN_2 have been obtained for the two nitrogen NSi_2Mg_2 environments with linewidths of only 25 Hz (7). These two sites have minor inequivalences illustrating the sensitivity of isotropic shift of ^{15}N to crystallographic changes. Other reports of NMR spectra from nitrides include BN (62), GaN (63) and TiN (64). In titanium-carbonitrides, the ^{15}N NMR chemical shift decreases from 400 to 351 ppm as the nitrogen-content decreases from 100 to 35.4% (64). ^{11}B MAS NMR at 14.1 T from BN revealed differences between cubic and hexagonal BN which have diamond-like and graphite-like structures, respectively. The two phases give ^{11}B NMR interactions of $C_Q = 0$ MHz, $\eta = 0$ and $\delta_{\text{iso}} = 1.6$ ppm and $C_Q = 2.9$ MHz, $\eta = 0$ and $\delta_{\text{iso}} = 30$ ppm for the cubic and hexagonal phases,

respectively. In turbostratic BN, a ^{11}B NMR spectrum very similar to hexagonal BN is obtained in accordance with the weak interplanar interactions and bonding, and its structure is similar to the hexagonal form of this phase (65). B-C-N compounds synthesised from organic precursors have been studied by ^{13}C and ^{11}B MAS NMR (66). The NMR spectra showed the resulting products were mixtures of amorphous boron, and turbostratically distorted hexagonal BN and graphite, rather than a single-phase compound of part of a solid solution (66). Reaction of Me_3NAlH_3 and NH_3BH_3 forms a ceramic precursor containing Al-N-B bonds. Pyrolysis under NH_3 at 1000°C was shown by ^{11}B and ^{27}Al MAS NMR to form an intimate mixture of AlN and BN (67). ^{15}N MAS and spin-echo NMR spectra showed the various nitrogen species that formed following the conversion of $[(\text{tBuCH}_2)_2\text{TaN}]_5$ with NH_3 to the cubic $\text{TaN}_{0.8}$ form (68).

Oxynitride Glasses and Glass-Ceramics.

The capability of solid-state NMR to probe the short-range order and structure of glasses is most significant despite the lack of long-range order. Nitrogen can have some profound effects on the physical properties of glasses which are attributed to the change in the effective cross-linking in the structure by the trivalent nitrogen. Comparison of a sialon glass containing up to 1 wt% nitrogen with an aluminosilicate glass of a similar composition showed more AlO_3 in the sialon glass which was attributed to the increased melt viscosity when nitrogen is present (69). Yttrium sialon glasses with constant Y:Si:Al ratio have been investigated by ^{29}Si MAS NMR. This work showed decreasing ^{29}Si chemical shifts with increasing nitrogen content indicating that nitrogen enters the structure and that a variety of local $\text{SiO}_x\text{N}_{4-x}$ units co-exist (70). The distribution of silicon amongst these units is consistent with nitrogen showing a bonding preference for silicon compared to aluminium (70). ^{27}Al MAS NMR showed that there is no Al-N bonding in such glasses and that aluminium occupies tetrahedral sites within the glass structure, although the interpretation is somewhat limited because of the fairly slow spinning speeds employed (71). ^{15}N NMR showed two peaks from NSi_2 and NSi_3 environments at 87 and 41 ppm, respectively, in an yttrium-sialon glass. However, on crystallisation, additional ^{15}N NMR peaks can be resolved due to β' -sialon, $\text{Si}_2\text{N}_2\text{O}$, metastable $\text{Y}_2\text{SiAlO}_5\text{N}$ and nitrogen substituted into $\text{Y}_3\text{Al}_5\text{O}_{12}$, the latter giving a ^{15}N resonance at 289.9 ppm (72). Similarly in Na-Si-O-N glasses, the distribution of $\text{SiN}_x\text{O}_{4-x}$ units has been elucidated by ^{29}Si MAS NMR (73,74).

Glass-ceramics are materials formed when a glass has undergone a controlled devitrification. The effect of nitrogen on glasses from the $\text{Li}_2\text{O-Al}_2\text{O}_3\text{-SiO}_2$ system close to the spodumene composition have been recently investigated. As nitrogen is added to the system as AlN, the five ^{29}Si NMR peaks of the spodumene structure that correspond to differing $\text{Q}^n(\text{mAl})$ units change their relative intensity (Fig. 9) as a function of the Si/Al ratio of the lattice. Also ill-defined intensity appears at more positive shift, suggesting that nitrogen is substituting in the glass structure. A minor ^{29}Si NMR peak at -60 ppm probably corresponds to a secondary phase. The effect of the nitrogen-content and the source

Table III. ^{29}Si and ^{15}N isotropic chemical shifts from crystalline metal silicon nitrides.

Phase	^{29}Si δ_{iso} (ppm)	^{15}N δ_{iso} (ppm)	Ref.
YSi_3N_5	-42.3, -45.5		49, 61
LaSi_3N_5	-57.3, -65.4	71.3	50, 51, 7, 59
$\text{Y}_2\text{Si}_3\text{N}_6$	-58.3, -60.8, -65.3		49, 61
$\text{Y}_6\text{Si}_3\text{N}_{10}$	-35.3, -37.7		49, 61
Mg_2SiN_2	-44.4	65.5, 76.7	54, 7
MgSiAlN_3	-42.5	45.0, 70.2	54, 7
LiSi_2N_3	-49.3		76

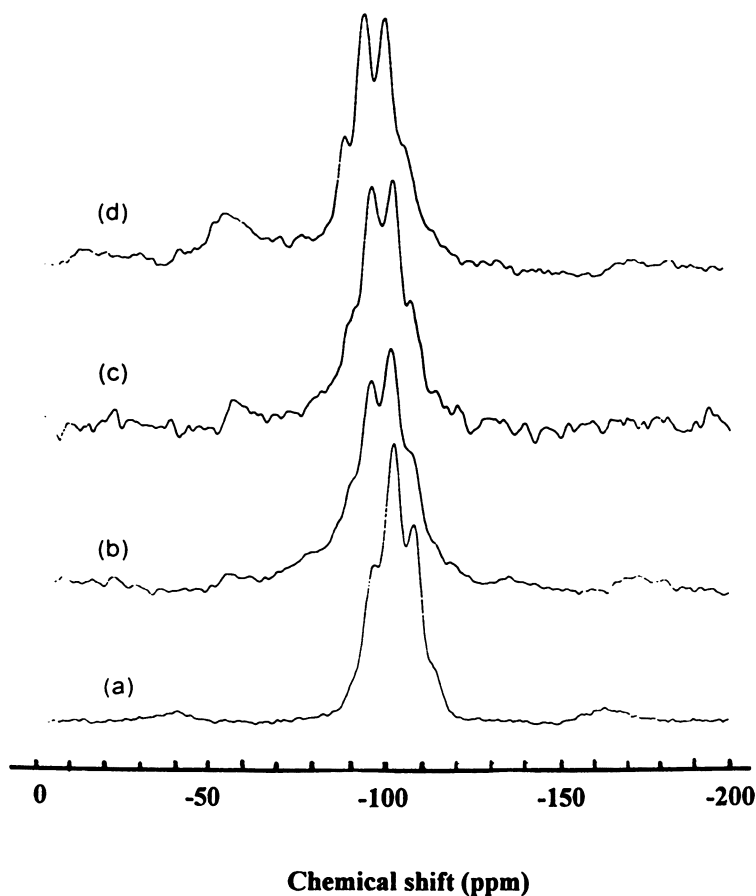


Figure 9. ^{29}Si MAS NMR spectra of various β -spodumene glass-ceramics containing 1-4 wt% ((a)-(d)) nitrogen added as AlN.

(Taken from reference 75. Copyright 1996 American Chemical Society.)

of the nitrogen (i.e. Si_3N_4 compared to AlN) on the β -quartz to β -spodumene transformation temperature have also been studied in detail (75).

Conclusion.

Solid-state NMR has already made a significant impact on the study of technologically significant inorganic nitrides and oxynitrides. Multinuclear solid-state NMR studies are extremely helpful at elucidating atomic ordering in oxynitride materials and it is the anions (i.e. oxygen and nitrogen) that will probably be increasingly used in these studies. The major application of solid-state NMR to study these ceramics is in identifying phases and intermediates in complex mixtures, particularly when some of these are amorphous. The study of oxynitrides by NMR has also called for the development of better approaches to identify mixed nearest neighbour environments of aluminium and further developments can be expected here. Most of this work to date has been carried out by specialist solid-state NMR groups but as the groundwork becomes established the technique should become a standard and widespread characterisation technique of such materials. This is already occurring to some extent as evidenced by the increasing number of papers from materials-oriented groups that turn to solid-state NMR for information.

Acknowledgments.

The author would like to thank the authors and copyright holders for giving permission to reproduce their original work and Dr T.J. Bastow (CSIRO, Melbourne) for his comments on the manuscript.

References.

1. Engelhardt, G.; Michel, D. *High Resolution Solid State NMR of Silicates and Zeolites* Wiley, Chichester 1987.
2. Alemany, L.B.; Massiot, D.; Sherriff, B.L.; Smith, M.E.; Taulelle, F. *Chem. Phys. Lett.* 1991, 177, 301.
3. Smith, M.E. *Appl. Magn. Reson.* 1993, 4, 1.
4. Jäger, C. In *NMR Basic Principles and Progress*; Blumich, B. Kosfeld, R. Eds.; Springer-Verlag: Berlin, 1994, 31, 134.
5. Dupree, R.; Lewis M.H.; Smith, M.E. *J. Appl. Crystallogr.* 1988, 21, 109.
6. Bastow, T.J.; Moodie A.F.; Smith, M.E.; Whitfield, H.J. *J. Mater. Chem.* 1993, 3, 697.
7. Harris, R.K.; Leach, M.J.; Thompson, D.P. *Chem Mater.* 1992, 4, 260.
8. Bastow, T.J.; Massiot, D.; Coutures, J.P. *Solid State NMR* (accepted for publication).
9. Carduner, K.R.; Carter, R.O.; Millberg, M.E.; Crosbie, G.M. *Anal. Chem.* 1987, 59, 2794.
10. Harris, R.K.; Leach, M.J.; Thompson, D.P. *Chem. Mater.* 1990, 2, 320.
11. Dupree, R.; Smith, M.E. *J. Magn. Reson.* 1987, 75, 153.

12. Dupree, R.; Smith, M.E. *Chem. Phys. Lett.* **1988**, *148*, 41.
13. Meinhold, R.H.; MacKenzie, K.J.D. *Solid State NMR* **1995**, *5*, 151.
14. Dupree, R.; Lewis, M.H.; Leng-Ward, G.; Williams, D.S. *J. Mater. Sci. Lett.* **1985**, *4*, 393.
15. Carduner, K.R.; Blackwell, C.S.; Hammond, W.B.; Reidinger, F.; Hatfield, G.R. *J. Am. Chem. Soc.* **1990**, *112*, 4676.
16. Olivieri, A.C. *Magn. Reson. Chem.* **1996**, *34*, 365.
17. Yue, Y.; Li, D.; Ye, C. *J. Mater. Sci. Lett.* **1996**, *15*, 691.
18. Yue, Y.; Li, D.; Ye, C. *J. Mater. Sci. Lett.* **1996**, *15*, 1079.
19. van der Voort, P.; Vansant, E.F. *Pol. J. Chem.* **1996**, *70*, 838.
20. Sigmund, W.M.; Feike, M.; Spiess, H.W.; Aldinger, F. *Mater. Res. Soc. Symp. Proc.* **1996**, *410*, 429.
21. Kortobi, Y.E.; Donanec, R.; Feldman, W.; Marchand, R.; Laurent, Y. *Inorg. Chem.* **1996**, *35*, 4957.
22. Seitz, J.; Bill, J.; Egger, N.; Aldinger, F. *J. Eur. Ceram. Soc.* **1996**, *16*, 885.
23. Suzuki, M.; Li, X.; Nakata Y.; Nagai, H.; Okuta, T. *Surf. Rev. Lett.* **1996**, *3*, 85.
24. Sjoberg, J.; Harris, R.K.; Apperley, D.C. *J. Mater. Chem.* **1992**, *2*, 433.
25. Yue, Y.; He, H.; Klinowski, J. Wu, Y.; Zhuang, H. *J. Mater. Chem.* **1996**, *6*, 1391.
26. MacKenzie, K.J.D.; Shimoda, S.; Aoki, T. *J. Mater. Chem.* **1997**, *7*, 527.
27. Bastow, T.; Hardin, S.G.; Turney, T.W. *J. Mater. Sci.* **1991**, *26*, 1443.
28. Neal, G.S.; Smith, M.E.; Trigg, M.B.; Drennan, J. *J. Mater. Chem.* **1994**, *4*, 245.
29. MacKenzie, K.J.D.; Meinhold, R.H.; White, G.V.; Sheppard C.M.; Sherriff, B.L. *J. Mater. Sci.* **1994**, *29*, 2611.
30. Fitzgerald, J.J.; Hamza, A.I.; Bronnimann, C.E.; Dec, S.F. *Solid State Ionics* **1989**, *32-33*, 378.
31. Smith, M.E.; Neal, G.S.; Trigg, M.B.; Drennan, J. *Appl. Magn. Reson.* **1993**, *4*, 157.
32. Ekstroem, T.; MacKenzie, K.J.D.; White V.V.; Brown, I.W.M.; Barris, G.C. *J. Mater. Chem.* **1996**, *6*, 1225.
33. Mackenzie, K.J.D.; Meinhold, R.H. *J. Mater. Chem.* **1996**, *6*, 821.
34. Soraru, G.D.; Mercadini, M.; Dal Maschio; Taulelle, F.; Babonneau, F. *J. Am. Ceram. Soc.* **1993**, *76*, 2595.
35. Hewitt, C.L.; Cheng, Y.-B.; Muddle, B.C. *J. Mater. Sci. Lett.* **1994**, *13*, 1612.
36. Lednor, P.W.; de Ruiter, R. *J. Chem. Soc., Chem. Commun.* **1989**, 320.
37. van Weeren, R.; Leone, E.A.; Curran, S.; Klein, L.C.; Danforth, S.C. *J. Am. Ceram. Soc.* **1994**, *77*, 2699.
38. Klinowski, J.; Thomas, J.M.; Thompson, D.P.; Korgul, P.; Jack, K.H.; Fyfe, C.A.; Gobbi, G.C. *Polyhedron* **1984**, *2*, 1267.
39. Smith, M.E. *Solid State NMR* **1994**, *3*, 111.
40. Butler, N.D.; Dupree, R.; Lewis, M.H. *J. Mater. Sci. Lett.* **1984**, *3*, 469.
41. Marshall, G.L.; Harris, R.K.; Apperley, D.; Yeung, R. *Proc. Symp. Sci. Ceram.* **1987**, *14*, 347.

42. Kruppa, D.; Dupree, R.; Lewis, M.H. private communication.
43. Haase, J.; Freude, D.; Frohlich, T.; Himpel, G.; Kerke, F.; Lippmaa, E.; Pfeifer, H.; Sarv, P.; Schaefer, H.; Sieffert, B. *Chem. Phys. Lett.* **1989**, *156*, 328.
44. Hayashi, H.; Hayamizu, K.; Yamamoto, O. *Bull. Chem. Soc. Jpn.* **1987**, *60*, 761.
45. Monie, S.A.; Aurentz, D.J.; Pantano, C.G. *Mater. Res. Soc. Symp. Proc.* **1996**, *410*, 429.
46. Koyama, S., Takeda, H.; Saito, Y.; Sugihara, Y.; Kuroda, K. *J. Mater. Chem.* **1996**, *6*, 1055.
47. Fitzgerald, J.J.; Kohl, S.D.; Piedra, G.; Dec, S.F.; Maciel, G.E. *Chem. Mater.* **1994**, *6*, 1915.
48. Smith, M.E. *J. Phys. Chem.* **1992**, *96*, 1444.
49. Dupree, R.; Lewis, M.H.; Smith, M.E. *J. Am. Chem. Soc.* **1988**, *110*, 1083.
50. Dupree, R.; Lewis, M.H.; Smith, M.E. *J. Am. Chem. Soc.* **1989**, *111*, 5125.
51. Harris, R.K.; Leach, M.J.; Thompson, D.P. *Chem Mater.* **1989**, *1*, 336.
52. Carduner, K.R.; Carter, R.O.; Rokosz, M.J.; Peters, C.; Crosbie, G.M.; Stiles, E.D. *Chem. Mater.* **1989**, *1*, 302.
53. Thompson, D.P.; Leach, M.J.; Harris, R.K. *Mater. Res. Soc. Int. Symp. Proc.* **1991**, 435.
54. MacKenzie, K.J.D.; Meinhold, R.H. *J. Mater. Chem.* **1994**, *4*, 1595.
55. Hauck, D.S.B.; Harris, R.K.; Apperley, D.C.; Thompson, D.P. *J. Mater. Chem.* **1993**, *3*, 1005.
56. Koroglu, A.; Apperley, D.C.; Harris, R.K.; Thompson, D.P. *J. Mater. Chem.* **1996**, *6*, 1031.
57. Chee, K.S.; Cheng, Y.-B.; Smith, M.E. *Chem. Mater.* **1995**, *7*, 982.
58. Chee, K.S.; Cheng, Y.-B.; Smith, M.E. *J. Eur. Ceram. Soc.* **1995**, *15*, 1213.
59. Massiot, D.; Donanec, R.; Feldman W; Marchand, R.; Laurent, Y.; *Inorg. Chem.* **1996**, *35*, 4957.
60. Hatfield, G.R.; Li, B.; Hammond, W.B.; Reidinger, F.; Yamanis, J. *J. Mater. Sci.* **1990**, *25*, 4032.
61. Ekstroem, T.C.; MacKenzie, K.J.D.; Ryan, M.J.; Brown, I.W.M.; White, G.V. *J. Mater. Chem.* **1997**, *7*, 505.
62. Connor, C. *Bull. Magn. Reson.* **1994**, *14*, 285.
63. Han, O.C.; Timken, H.K.C.; Oldfield, E. *J. Chem. Phys.* **1988**, *89*, 6046.
64. MacKenzie, K.J.D.; Meinhold, R.H.; McGavin, D.G.; Ripmeester, J.A.; Moudrakovski, I. *Solid State NMR* **1995**, *4*, 193.
65. Marchetti, P.S.; Kwon, D.; Schmidt, W.R.; Interrante, L.V.; Maciel, G.E. *Chem. Mater.* **1991**, *3*, 482.
66. Andreev, Y.G.; Lundström, T.; Harris, R.K.; Oh, S.-W.; Apperley, D.C.; Thompson, D.P. *J. Alloys Compounds* **1995**, *227*, 102.
67. Dou, D.; Ketchum, D.R.; Hamilton, E.J.M.; Florian, P.A.; Vermillion, K.E.; Grandinetti, P.J.; Sheldon, S.G. *Chem. Mater.* **1996**, *8*, 2839.
68. Holl, M.M.B.; Wolczanski, D.T.; Proserpio, D.; Bielecki, A.; Zax, D.B.; *Chem. Mater.* **1996**, *8*, 2468.

69. Sato, R.K.; Bolvin, J.; McMillan, P.F. *J. Am. Ceram. Soc.* **1990**, *73*, 2494.
70. Aujla, R.S.; Leng-Ward, G.; Lewis, M.H.; Seymour, E.F.W.; Styles, G.A.; West, G.W. *Phil. Mag. B* **1986**, *54*, L51.
71. Jin, J.; Yoko, T.; Miyaji, F.; Sakka, S.; Fukunaga, T.; Misawa, M. *Phil. Mag. A* **1994**, *70*, 191.
72. Kruppa, D.; Dupree, R.; Lewis, M.H. *Mater. Lett.* **1991**, *11*, 195.
73. Hater, W.; Mueller-Warmuth, W.; Frischat, G.H. *Glastech. Ber.* **1989**, *62*, 328.
74. Unuma, H.; Maekawa, H.; Kiyono, H.; Kawamura, K.; Maekawa, T.; Yokohama, T. *J. Ceram. Soc. Jpn.* **1992**, *100*, 1272.
75. Nordmann, A.; Cheng, Y.-B.; Smith, M.E. *Chem. Mater.* **1996**, *8*, 2516.
76. Leach, M.J.; Harris, R.K.; Thompson, D.P. *Euroceramics* Eds de With, G.; Terpstra, R.A.; Metselaar, R. Elsevier, The Hague, **1990**, 140.
77. G.R. Hatfield and K.R. Carduner, *J. Mater. Sci.*, **1989**, *24*, 4209.

Author Index

- Adler, Stuart B., 156
Braun, M., 242
Chézeau, J. M., 283
DePaul, Susan M., 2, 305
Diaz, A. C., 283
Ernst, Matthias, 305
Fiske, K., 228
Fitzgerald, John J., 2, 182
Frydman, Lucio, 136
Fyfe, C. A., 283
Grondy, H., 283
Hill, Edward A., 358
Klemperer, Walter G., 256
Kokotailo, G. T., 283
Lewis, A. R., 283
Maciel, Gary E., 326
Marinelli, Laura, 136
Medek, Ales, 136
Mueller, K. T., 228
Pan, Yong, 168
Phillips, Brian L., 305
Reimer, Jeffrey A., 156
Richard, David L., 256
Shore, Jay S., 305
Smith, M. E., 377
Wenslow, R. M., 228
Yesinowski, James P., 358
Youngman, R. E., 242
Zwanziger, J. W., 242

Subject Index

A

Albite. *See* Minerals by silicon-29 NMR spectroscopy

Alumina and alumina supports

characterizing surface chemistry of aluminas, 56, 62*f*, 63

experimental ^{27}Al NMR spectra of $\text{KAl}(\text{SO}_4)_2 \cdot 12 \text{H}_2\text{O}$ under static and MAS, 56, 57*f*

metal aluminate systems of technological significance, 65

persisting questions in alumina surface chemistry, 63, 65

relationship between solid-state NMR chemical shift δ (^{27}Al) and local chemical environment in Al–O compounds, 54, 57*f*

representative ^{27}Al MAS NMR spectra with second-order quadrupolar line broadening, 56, 58*f*, 59*f*

satellite transition spectroscopy (SATRAS) for ^{27}Al NMR of transition alumina, χ -alumina, showing 4-, 5-, and 6-coordinate aluminum sites, 63, 64*f*

two-dimensional triple quantum (2D–3Q) MAS ^{27}Al NMR spectra of AlPO-11, 56, 60*f*, 61*f*

wide range of crystalline hydrous oxides, 54, 56–65

Alumina materials surface chemistry advances with multinuclear MAS ^1H , ^{17}O , and ^{27}Al NMR, 223–224

^{27}Al MAS NMR spectra (14 T) for various aluminum oxide materials heated to various temperatures, 218*f*, 219*f*

^{27}Al NMR spectral parameters for various aluminas based on spectral

deconvolution/simulation, 190, 193*t*

alumina-based materials, 182–183

bulk oxygen site types in transition aluminas, 196, 198*f*

formation of transitional aluminas, 183

fractional octahedral aluminum by ^{27}Al NMR for transitional aluminas from dehydroxylation of bayerite and boehmite, 221, 222*f*

^1H - ^{27}Al CP/MAS NMR to examine Lewis acidity for γ -alumina and two different transition aluminas, 192*f*

^1H - ^{27}Al CP/MAS spectra of various PDA samples, 186, 188, 189*f*

^1H - ^{27}Al CP/MAS spectrum and ^1H -decoupled MAS ^{27}Al spectrum of γ -alumina, 187*f*

^1H CRAMPS NMR spectra (187 MHz and 360 MHz) of pseudo-boehmite material, 204*f*

^1H CRAMPS NMR spectra of boehmite, diaspore, gibbsite, and bayerite, 207*f*

^1H CRAMPS spectral assignments for various Al–OH groups in alumina materials, 208*t*

^1H CRAMPS spectra of model aluminum hydroxides and oxyhydroxides, 206–209

^1H CRAMPS spectra of pseudo-boehmite materials, 202, 204–206

^1H CRAMPS studies of dehydration of pseudo-boehmite at high temperature (>300 C), 211, 212*f*

^1H CRAMPS studies of dehydration of pseudo-boehmite at low temperature (<300 C), 209–211

^1H - ^{17}O CP/MAS NMR spectrum of γ -alumina, 196, 199*f*, 200

heating alumina for partially dehydroxylated alumina (PDA), 186

hydration and dehydration of aluminas, 183

MAS ^{27}Al NMR of γ -alumina showing 4- and 6-coordinate resonances, 194, 195*f*

MAS ^{27}Al NMR studies of dehydration of pseudo-boehmite, 217–223

MAS and CP/MAS ^{17}O NMR studies, 196, 198–200

MAS and CP/MAS ^{27}Al NMR studies, 186–190

mechanisms of condensation of Al_2OH and AlOH groups, 213, 214*f*, 215*f*, 216*f*

mechanisms of dehydroxylation of internal/surface protons of pseudo-boehmite, 211, 213

MQMAS ^{27}Al NMR of transition aluminas, 190, 194–196

^{17}O NMR parameters, including quadrupole coupling constants, asymmetry parameters and isotropic chemical shifts for various aluminas, 201*t*

off-resonance nutation ^{27}Al NMR spectra of 4- and 6-coordinate peak region, 194, 195*f*

proposed mechanisms for Brønsted and/or Lewis acid mobility of protons and oxygens on surface of transition alumina, 191f

satellite transition spectroscopy (SATRAS) for ^{27}Al NMR of transition alumina, χ -alumina showing 4-, 5-, and 6-coordinate aluminum sites, 196, 197f

solid-state ^{17}O and ^{27}Al NMR studies, 185–200

solid-state ^1H CRAMPS NMR studies, 200, 202–211

structural diagrams of aluminum hydroxides, 205f

surface Lewis and Brønsted acid sites on aluminas, 183–185

surface model of γ -alumina, 183–185

thermal conversions of aluminum oxyhydroxides and hydroxides, 184f

triple-quantum 3QMAS ^{27}Al NMR spectrum of γ -alumina, 194, 195f

types of surface hydroxyl groups of γ -alumina proposed by Peri, 184f

variable temperature ^{27}Al MAS NMR studies to examine α - Al_2O_3 and transition alumina surfaces, 188, 190

weight-loss profiles for dehydration/dehydroxylation of pseudo-boehmite, 200, 202

weight-loss profiles for high-surface area pseudo-boehmite, 203f

See also Pseudo-boehmite

Alumina-silica, amorphous, metal oxide type material, 65–66

Alumina-silica minerals and clays, solid-state ^{27}Al and ^{29}Si MAS NMR studies, 73–75

Aluminophosphate glass. *See* Phosphate and aluminophosphate glass systems

Aluminosilicate sodalites. *See* Sodalites, host-guest interactions

Aluminum hydroxides and oxyhydroxides. *See* Alumina materials surface chemistry

Aluminum phosphates (AIPO), unique class of molecular sieve analogs of zeolites, 75–76

Amorphous alumina-silicas, metal oxide type material, 65–66

Amorphous glasses. *See* Ceramics and glasses; Glasses, amorphous

B

Bayerite

fractional octahedral aluminum by ^{27}Al NMR for transitional aluminas from dehydroxylation of bayerite and boehmite, 221, 222f

^1H CRAMPS NMR spectra of boehmite, diaspore, gibbsite, and bayerite, 207f, 209

MAS ^{27}Al NMR studies of dehydration, 217

See also Alumina materials surface chemistry

Bioceramics and biomaterials

new areas for in-depth solid-state NMR, 102

silicon biomineralization using solid-state heteronuclear correlation techniques and ^{13}C - ^{29}Si REDOR, 102, 106

solid-state two-dimensional HETCOR NMR studies of inorganic-organic interfacial interactions in aluminosilicate, 102, 103f, 104f

Biomaterials. *See* Bioceramics and biomaterials

Boehmite

fractional octahedral aluminum by ^{27}Al NMR for transitional aluminas from dehydroxylation of bayerite and boehmite, 221, 222f

^1H CRAMPS NMR spectra of boehmite, diaspore, gibbsite, and bayerite, 206, 207f

hydrogen bonding differences from diaspore, 205f

MAS ^{27}Al NMR studies of dehydration, 217

See also Pseudo-boehmite

Bonding and structural chemical information, 46

Borate glasses

alkali oxide additives causing structure conversion, 243

dynamic angle spinning (DAS) experiment, 244–245

electric quadrupole moments for boron nuclei ^{11}B and ^{10}B , 243

evidence for boron oxide structure in glass, 242–243

experimental NMR spectroscopic methods, 244–245

- experimental Raman spectroscopic method, 245
- experimental sample preparation, 244
- fraction of boron in each type of site for model, 253*f*
- high-resolution ^{17}O NMR using double rotation (DOR) NMR showing three resolved oxygen sites, 249
- intensities from spectral fits of three main features in DAS NMR spectra of ^{11}B in $(\text{K}_2\text{O})_x(\text{B}_2\text{O}_3)_{1-x}$ glasses, 250, 253*f*
- intermediate range order of pure B_2O_3 , 248–250
- local structure about boron atoms in modified borate glasses and pure boron oxide glass, 243
- modification by conversion from three-fold to four-fold coordination, 250–251
- NMR evidence for existence of boroxol rings (B_3O_3), 245, 248
- parameters of ^{11}B resonances in B_2O_3 glass, 248*t*
- recent advances probing linkages between basic units, 243
- series of high-resolution spectra as function of potassium oxide content, 247*f*
- sites and ^{11}B isotropic shifts from potassium borate crystals, 249*t*
- typical two-dimensional DAS spectrum of potassium borate glass, 246*f*
- unified model for borate modification chemistry, 251–254
- Borides, carbides, and nitrides**
- experimental and simulated ^{23}Na MAS NMR spectra and 3Q–MAS spectra of different sodium sites in $\text{Na}_3\text{AlP}_3\text{O}_9\text{N}$ and $\text{Na}_2\text{Mg}_2\text{P}_3\text{O}_9\text{N}$, 90, 94, 95*f*
- relationship between solid-state NMR chemical shift δ (^{29}Si) and local chemical environments in (Y,Lu)SiAlON materials containing $\text{SiO}_x\text{N}_{4-x}$ ($0 < x < 4$) tetrahedra, 90, 93*f*
- ^{29}Si MAS NMR for silicon coordination environments in Si_3N_4 and silicon oxynitride, 90, 91*f*, 92*f*
- silicon carbides polytypes, ^{29}Si and ^{13}C MAS NMR spectra, 87, 88*f*
- solid-state MAS NMR in studies of formation, structure, and surface chemistry, 85, 87–94
- summary of various ^{29}Si chemical shifts ranges for silicon carbide, nitride, oxynitride, oxycarbide, and carbonitride materials, 89*t*
- Brønsted acidity**
- aluminas, 183–185
- See also* Alumina materials surface chemistry
- C**
- Carbides.** *See* Borides, carbides, and nitrides
- Carr–Purcell–Meiboom–Gill (CPMG) train of pulses, sensitivity gain for ^{14}N NMR, 362, 363*f*
- Cements and adhesives**
- application of solid-state NMR studies, 101–102
- static and MAS ^{27}Al NMR at high spinning speeds and magnetic field strengths, 101–102
- successful use of ^1H MAS NMR, ^1H CRAMPS, and ^{29}Si MAS and CP/MAS NMR, 101
- summary of ^{27}Al quadrupolar coupling constants, asymmetry parameters, and isotropic chemical shifts for synthetic calcium aluminates in cements, 102, 105*t*
- Ceramics and glasses**
- amorphous glasses, 94, 96–101
- bioceramics and biomaterials, 102–104, 106
- borides, carbides, and nitrides, 85, 87–94
- cements and adhesives, 101–102
- diverse group of technologically important inorganic materials, 76–77
- refractory metal oxides, 78–83
- six major classes of modern inorganic ceramics, 77
- three strategies in solid-state NMR studies of ceramics, 77–78
- titanium, zirconium, niobium, and tantalum oxides, 83–85, 86*f*
- See also* Nitrides and oxynitrides
- Chemical information**
- relationship between NMR parameters and chemical information, 47*t*
- types of, 46
- Chemical shift interaction**
- inorganic solids, 8, 9*f*
- powder pattern, 9*f*

- Clays. *See* Siloxane-based solid networks
- Clays and alumina-silica minerals
solid-state ^{27}Al and ^{29}Si MAS NMR studies
in clays and alumina-silicas, 73–75
static ^{17}O NMR spectra of isotopically
labeled polycrystalline talc, 74f
- Combined rotation and multiple pulse
spectroscopy (CRAMPS)
 ^1H CRAMPS spectra of model aluminum
hydroxides and oxyhydroxides, 206–209
major advances in silica surface chemistry,
49
providing insight into formation of
transition aluminas, 223
solid-state ^1H CRAMPS NMR studies of
alumina materials, 200, 202–211
spectra of silica gels of different degrees of
hydration, 19, 23f
understanding alumina surface chemistry
advanced, 56
See also Alumina materials surface
chemistry; Siloxane-based solid networks
- Composite materials, inorganic, emerging
demands for atomic-level understanding, 3
- Composites, containing inorganic
particles/fibers and matrix materials, 119
- Continuous-wave (CW) decoupling. *See*
Decoupling
- Correlation spectroscopy (COSY)
COSY results for zeolite ZSM-12, 37f
homonuclear correlation, 32, 34
recent application to complex silicate
systems, 49
summary table of silicon sites, occupancies,
and connectivities, 36f
- COSY. *See* Correlation spectroscopy
(COSY)
- CP/MAS. *See* Cross-polarization magic-angle
spinning (CP/MAS)
- CPMG. *See* Carr–Purcell–Meiboom–Gill
(CPMG) train of pulses
- CRAMPS. *See* Combined rotation and
multiple pulse spectroscopy (CRAMPS)
- Cross-polarization magic-angle spinning
(CP/MAS)
 ^{27}Al , ^{29}Si and ^{23}Na – ^{29}Si cross-polarization,
307–311
CP/MAS contact time study of ^{23}Na ($I=3/2$)
in borax, 24, 28f
CP/MAS of silica gel with different types of
surface and internal silicon sites, 24, 25f
- CP rate constant, 232
general technique in high-resolution solid-
state NMR, 19, 24–26
major advances in silica surface chemistry,
49
methods to produce quantitative internuclear
distances, 229
MAS and CP/MAS ^{17}O NMR studies of
alumina materials, 196, 198–200
MAS and CP/MAS ^{27}Al NMR studies on
alumina, 186–190
selectivity and signal enhancement
characteristics, 3
technique for transferring magnetization, 19,
24
with MAS for well-resolved spectra with
good signal-noise ratio, 24
See also Bioceramics and biomaterials;
Host–guest structures of molecular sieves;
Phosphate and aluminophosphate glass
systems
- Curie–Weiss contact shift, temperature-
dependent in oxides, 164, 165f
- ## D
- DANTE trains. *See* Wide-line ^{14}N NMR in
solids
- DAS. *See* Dynamic-angle spinning (DAS)
- Debye–Hückel theory
thermodynamic theory to describe effect of
long-range defect interactions, 166
See also Oxygen motion in oxides
- Decoupling
continuous-wave (CW) decoupling, 18
general technique for high-resolution solid-
state NMR, 18–19
 ^1H CRAMPS spectra of silica gels of
different degrees of hydration, 19, 23f
homonuclear and heteronuclear, 18
- Diaspore
 ^1H CRAMPS NMR spectra of boehmite,
diaspore, gibbsite, and bayerite, 206, 207f
hydrogen bonding differences from
boehmite, 205f
See also Alumina materials surface
chemistry
- Dipolar recovery at magic angle (DRAMA),
technique for measuring distances between
like nuclei, 39

- Direct magnetic dipolar interaction in inorganic solids, 8, 10
- Direct polarization (DP). *See* Siloxane-based solid networks
- Double Rotation (DOR)
development of technique for quadrupolar nuclei, 139
- DOR ^{27}Al NMR spectra of
aluminophosphate molecular sieves, 27, 29f
- high resolution spectra for quadrupolar nuclides, 3
- schematic diagram depicting DOR and DAS spinner systems, 27, 28f
- technique for quadrupolar nuclei, 26–27
- DP (direct polarization). *See* Siloxane-based solid networks
- DRAMA (Dipolar recovery at magic angle), technique for measuring distances between like nuclei, 39
- Dynamic-angle spinning (DAS)
development of technique for quadrupolar nuclei, 139–140
- high resolution spectra for quadrupolar nuclides, 3
- inherently two-dimensional technique, 42–43, 44f
- isotropic–anisotropic correlation of quadrupolar interaction, 42–43
- schematic diagram depicting DOR and DAS spinner systems, 27, 28f
- technique for quadrupolar nuclei, 27, 30
- two-dimensional DAS spectrum for ^{17}O in SiO_2 polymorph coesite, 43, 44f
- See also* Borate glasses; Glasses, amorphous; Phosphate and aluminophosphate glass systems; Refractory metal oxides
- E**
- Exchange spectroscopy, two dimensional (2D–EXSY)
three-pulse sequence simplest form, 43
- two-dimensional ^6Li NMR exchange spectra for Li ion diffusion in lithium orthosilicate, 43, 45f

F

- Fibers/inorganic particles and matrix materials in composites, 119
- Fluorapatite (FAP). *See* Hydroxyapatite (HAP)
- Fluoride ion incorporation. *See* Hydroxyapatite (HAP)
- Framework, open, and layered materials. *See* Open framework and layered materials
- Fundamental approaches to study inorganic solids
general techniques in high-resolution solid-state NMR, 14–26
- multidimensional NMR techniques, 31–45
- special techniques for high-resolution of quadrupolar nuclei, 26–31
- See also* Multidimensional NMR techniques

G

- Gibbsite
 ^1H CRAMPS NMR spectra of boehmite, diaspore, gibbsite, and bayerite, 206, 207f, 209
- See also* Alumina materials surface chemistry
- Glasses, amorphous
deconvolution of broad ^{17}O NMR signals by 2D DAS ^{17}O NMR measurements for series of mixed alkali silicate glasses, 97, 100f
- effect of modifier ions on silicate network structure by ^{23}Na and ^{29}Si MAS NMR, 94
- major applications, 94
- solid-state NMR for examining motion in glasses, 97
- summary of values from various ^{17}O NMR spectra of glassy and crystalline silicate systems, 97, 98t, 99r
- variable temperature NMR studies, 94, 96f, 97
- Gyrolite. *See* Minerals by silicon-29 NMR spectroscopy

H

- Half-integer quadrupolar nuclei. *See* Quadrupolar nuclei
- Hartmann–Hahn match condition
 adjusting radiofrequency (RF) field intensities to match modified Hartmann–Hahn, 230
 method for transferring magnetization from one spin species to another, 308
 rf-field amplitude determination, 19
- Heteronuclear correlation (HETCOR)
 multidimensional NMR technique, 32
 recent application to complex silicate systems, 49
 studies of calcium phosphate precursors of bone and native bone materials, 33f
See also Bioceramics and biomaterials
- High-resolution solid-state NMR
 cross polarization (CP), 19, 24–26
 decoupling, 18–19
 general techniques, 14–26
 magic-angle spinning (MAS), 15–18
See also Quadrupolar nuclei, high-resolution techniques
- Homonuclear correlation
 correlation spectroscopy (COSY), 32, 34
 COSY results for zeolite ZSM-12, 37f
 incredible natural abundance double quantum transfer experiment (INADEQUATE), 32, 34
 multidimensional NMR technique, 32, 34
- Host–guest interactions. *See* Host–guest structures of molecular sieves; Sodalites, host–guest interactions
- Host–guest structures of molecular sieves
 basic pulse sequences for REDOR and TEDOR experiments, 298f, 299f
 comparison of ^{29}Si CP/MAS NMR spectra with those calculated from second moment/ T_{CP} correlations for ZSM-5 with *p*-xylene, 290, 294f, 295f
- COSY and INADEQUATE experiments to establish three-dimensional connectivity pattern, 284, 287f
- dipolar interaction between isolated pairs of spins in octadecasil, 290, 296
- effect of distance dependence qualitatively from comparison of CP spectra with simple one-pulse experiment, 288, 289f
- experimental CP curves for well-resolved resonances for complexes of *p*-xylenes, 290, 291f
- framework structure of octadecasil with location of fluoride anions in double 4-ring (D4R) units and two silicon sites, 297f
- high resolution solid-state NMR
 complementary to X-ray diffraction methods, 283–284
- importance of size and shape selectivity, 283
- investigation of three-dimensional zeolite–sorbate structures by cross polarization (CP), REDOR, and TEDOR, 285, 288
- plots of $1/T_{\text{CP}}$ values versus second moments calculated for different T-sites, 290, 293f
- REDOR data and fits for two types of T-sites in octadecasil, 300f
- REDOR experiment conditions, 296, 301
- ^{29}Si MAS NMR spectra of zeolite ZSM-12 and ZSM-5, 285f
- ^{29}Si MAS NMR spectra of ZSM-5 loaded with 2 molecules per unit cell of *p*-dichlorobenzene, *p*-chlorotoluene, and *p*-xylene, 286f
- spectra monitoring structural transformations of zeolites, 284
- spin dynamics of CP process, 288, 290
- structure showing location of *p*-xylene molecules as determined from single crystal structure, 290, 292f
- TEDOR data and fits for T-1 silicon in octadecasil, 302f
- TEDOR experiment conditions, 301
- through-space dipolar interaction of CP technique, 288
- Hydroxyapatite (HAP)
 arrangement of F and P nuclei in fluorapatite (FAP), 169, 170f
 constituent of dental enamel and cortical bone, 168
 depth of fluoride ion incorporation, 178, 180
- experimental ^{31}P - ^{19}F REDOR NMR, 169–171
- experimental conditions for NMR spectroscopy, 172
- FAP and FHAP sample synthesis, 172
- ^{19}F -observed ^{31}P - ^{19}F REDOR NMR spectra of FAP, 173, 174f

^{19}F -observed ^{31}P - ^{19}F REDOR NMR spectra of FAP and F-treated HAP, 173, 175*f*, 176*f*
 fluoride-selective electrode analysis method, 172
 fluoride-treated HAP preparation, 172
 incorporation of fluoride, 168–169
 models of F distribution in HAP, 178, 179*f*
 ^{31}P -observed ^{31}P - ^{19}F REDOR NMR spectra of FAP, 173, 175*f*
 ^{31}P -observed ^{31}P - ^{19}F REDOR NMR spectra of F-treated HAP and 25% F-FHAP, 173, 176*f*, 177*f*
 pulse sequence for ^{31}P -observed ^{31}P - ^{19}F REDOR, 170*f*
 random distribution of F ions, 178
 REDOR dephasing for F distribution models, 173, 178
 REDOR dephasing for various models, 178, 179*f*
 replacement of OH ions by F ions on first layer of unit cell, 178
 Hyperfine coupling interaction, NMR in inorganic solids, 10

I

Incredible natural abundance double quantum transfer experiment (INADEQUATE)
 homonuclear correlation experiment, 32, 34
 recent application to complex silicate systems, 49
 Indirect dipolar-coupling mechanism, NMR in inorganic solids, 10
 INEPT. *See* Inensitive nuclei enhanced by polarization transfer (INEPT)
 Inorganic composite materials, emerging demands for atomic-level understanding, 3
 Inorganic materials, types of
 ceramics and glass materials, 76–106
 composites containing inorganic particles/fibers and matrix materials, 119
 ion conductors, 110
 metal oxides, metal oxide catalysts and supports, 48–70
 open framework and layered materials, 70–76
 semiconductors, 106–110
 superconductors, 110–119
See also Ceramics and glasses; Metal oxides

Inorganic solid materials
 composition of, 4
 development and understanding in parallel with advances in solid-state NMR methods, 3
 major categories of, 4, 5*r*
 NMR interactions in inorganic solids, 4, 8–14
 NMR studies of low and high abundance nuclides, 4, 5*r*
 properties of selected quadrupolar nuclei, 7*t*
 properties of selected spin- $\frac{1}{2}$ nuclei, 6*t*
 quadrupolar nuclei, 10–14
 relationship between NMR parameters and chemical information, 47*t*
 significant NMR challenges due to paramagnetic species present, 4
 solid-state NMR for characterization of structure and chemistry, 228–229
 spin- $\frac{1}{2}$ $\text{Ba}_2\text{In}_2\text{O}_5$ nuclei, 4, 8–10
 types of chemical information, 46
 Inensitive nuclei enhanced by polarization transfer (INEPT), polarization transfer through scalar couplings, 24, 26
 Ion conductors
 $\text{Ba}_2\text{In}_2\text{O}_5$ material exemplifying ion conducting system, 110
 narrowing broad resonances by DAS experiments, 110, 114*f*
 ^{17}O MAS NMR spectra at room temperature for $\text{Ba}_2\text{In}_2\text{O}_5$ at various magnetic fields, 113*f*
 ordering of oxygen vacancies in layers of four-coordinate indiums, 113*f*
 proposed structure of $\text{Ba}_2\text{In}_2\text{O}_5$, 113*f*
 variable temperature ^{17}O MAS NMR spectra, 110, 114*f*
 Isotropic–anisotropic correlation
 chemical shifts, 41–42
 quadrupolar interaction, 42–43

K

Knight shift
 deconvolution into temperature independent
 Knight shift in oxides, 164, 165*f*
 of NMR resonance frequency, 10
 Kyanite, experimental and simulated ^{27}Al MAS NMR spectrum, 56, 59*f*

L

Larmor frequency. *See* Quadrupolar nuclei
Layered materials. *See* Open framework and layered materials

Lead zirconium titanate system

alternating strong and weak metal–oxygen bonds, 256–257

bonding environments of oxygen atoms in each of the four lead zirconium titanate (PZT) phase domains at ambient temperature, 260, 261*f*

constant temperature study of PZT phases $\text{PbZr}_x\text{Ti}_{1-x}\text{O}_3$, 257

experimental preparation and X-ray powder diffraction identification, 258

four PZT phases at ambient temperature, 260–262

^{17}O MAS NMR spectra of five mixed-metal PZT samples, lead titanate, and lead zirconate, 258, 259*f*

^{17}O NMR chemical shifts, 260*t*

^{17}O NMR chemical shifts sensitive to local bonding environments in transition metal oxide compounds, 257

phase transition at Curie temperature, T_c , 256

resolving chemically and structurally distinct oxygen centers with ^{17}O NMR, 262

two models proposed for phase transition mechanism, 256–257

Lewis acidity

aluminas, 183–185

See also Alumina materials surface chemistry

M

Magic-angle hopping (MAH)

mechanically reorienting sample in 120° hops, 41–42

two-dimensional techniques with isotropic and anisotropic dimensions, 312

Magic-angle spinning (MAS)

effect of MAS on chemical-shielding powder pattern, 16*f*

general technique for high-resolution NMR, 15–18

line-narrowing techniques, 3

MAS and CP/MAS ^{17}O NMR studies of alumina materials, 196, 198–200

MAS and CP/MAS ^{27}Al NMR studies on alumina, 186–190

schematic diagram of kaolinite, 22*f*

Si/Al ratio determination by ^{29}Si MAS NMR, 17*f*

solid-state MAS ^{27}Al NMR spectra, 20*f*; 21*f*
technique for averaging anisotropic interactions through mechanical spinning, 228–229

See also Alumina and alumina supports; Bioceramics and biomaterials; Borides, carbides, and nitrides; Glasses, amorphous; Phosphate and aluminophosphate glass systems; Refractory metal oxides

Magic-angle turning (MAT)

similar to magic-angle hopping on conventional MAS equipment, 41–42
two-dimensional techniques with isotropic and anisotropic dimensions, 312

MAH. *See* Magic-angle hopping (MAH)

MAS. *See* Magic-angle spinning (MAS)

MAT. *See* Magic-angle turning (MAT)

Matrix materials, inorganic particles/fibers, in composites, 119

Metal oxides

alumina and alumina supports, 54, 56–65

amorphous alumina-silicas, 65–66

molybdena-containing catalysts, 70

silica materials, 48–49, 52–54

summary of various metal oxide materials, 48, 50*t*, 51*t*

vanadia-containing catalysts, 68–70

zirconium and titanium silicate and phosphate catalysts and supports, 66–68

See also Oxygen motion in oxides

Minerals by silicon-29 NMR spectroscopy

adiabaticity a function of spinning rate, rf-field strength, and quadrupolar frequency, 308–309

^{27}Al - ^{29}Si and ^{23}Na - ^{29}Si cross-polarization, 307–311

anisotropic dimension and simulated line shapes to determine chemical shift parameters, 314, 318*f*

chemical shift parameters equations, 312

complex structures of sepiolite and gyrolite, 314, 319

- experimental NMR conditions, 307
- ^1H MAS NMR spectra of gyrolite and sepiolite, 322*f*
- $^1\text{H}/^{29}\text{Si}$ heteronuclear correlation spectroscopy, 319–321
- $^1\text{H}/^{29}\text{Si}$ heteronuclear correlation spectrum of sepiolite, 320*f*
- Hartmann–Hahn condition for transferring magnetization from one spin species to another, 308
- heteronuclear correlation spectroscopy for relative proximity of chemical species and assigning resonances, 306–307
- isotropic and anisotropic components of chemical shift interaction, 311–312
- ^{23}Na - ^{29}Si and ^{27}Al - ^{29}Si cross-polarization techniques to overcome low sensitivity of ^{29}Si NMR, 306
- projections of ^1H dimension of $^{29}\text{Si}/^1\text{H}$ heteronuclear correlation spectra of gyrolite, and sepiolite, 322*f*
- ^{29}Si chemical shift parameters, 316*r*
- ^{29}Si isotropic/anisotropic correlation spectroscopy, 311–319
- ^{29}Si isotropic/anisotropic correlation spectrum of albite using ^{27}Al - ^{29}Si CP and TOSS–reTOSS pulse sequence, 314, 315*f*
- ^{29}Si isotropic/anisotropic correlation spectrum of sepiolite using ^1H - ^{29}Si CP and TOSS–reTOSS pulse sequence, 314, 317*f*
- ^{29}Si MAS NMR spectra with ^{27}Al - ^{29}Si and ^{23}Na - ^{29}Si cross-polarization and single-pulse excitation, 310*f*
- spin-lattice relaxation time in rotating frame of three silicon sites, 311
- TOSS–reTOSS pulse sequence, 313*f*
- two-dimensional techniques with isotropic and anisotropic dimensions, 312
- utility of one-dimensional and multi-dimensional ^{29}Si NMR, 306
- Molecular sieves. *See* Host–guest structures of molecular sieves
- Molybdena-containing catalysts, solid-state ^{95}Mo NMR, 70
- MQMAS. *See* Multiple-quantum magic-angle spinning (MQMAS)
- Multidimensional NMR techniques
- four stages of pulse sequences, 31
 - heteronuclear correlation (HETCOR), 32, 33*f*
 - homonuclear correlation experiments COSY and INADEQUATE, 32, 34
 - isotropic–anisotropic correlation of chemical shifts by VACSYS, MAH, and MAT, 41–42
 - isotropic–anisotropic correlation of quadrupolar interaction by DAS and MQMAS, 42–43
 - spin diffusion, 34
 - techniques for distance measurement between heteronuclei (SEDOR, REDOR, TEDOR), 34–35, 38–39
 - techniques for distance measurement between spin- $1/2$ and quadrupolar nuclei (TRAPDOR, REAPDOR), 39–41
 - two-dimensional exchange, 43
- Multilayered electronic devices, emerging demands for atomic-level understanding, 3
- Multiple-quantum magic-angle spinning (MQMAS)
- alternative processing approaches in 2D MQMAS NMR, 142, 146*f*
 - approximate nutation pulses for optimized S/N in MQMAS correlation experiments, 149*r*
 - coefficients determining peak's center of mass in sheared MQMAS spectrum in terms of isotropic chemical and quadrupolar shifts, 142, 144*r*
 - detailed descriptions of atomic sites, 3
 - effects introduced by distributions of quadrupolar and chemical shift parameters on shape of S=3/2 MQMAS resonance, 145, 147*f*
 - effects of chemical shielding anisotropy on efficiency of MQMAS, 153*f*
 - extraction of quantitative information by combination of MAS and MQMAS data, 145, 147*f*
 - isotropic–anisotropic correlation for quadrupolar interaction, 42–43
 - lack of quantitiveness, 145
 - MAS and MQMAS experiments on S=1/2, S=5/2 samples, 143*f*
 - MAS and MQMAS ^{23}Na NMR analyses of polycrystalline Na_2TeO_3 , 145, 146*f*
 - MQMAS ^{27}Al NMR of transition aluminas, 190, 194–196
 - outlook for opportunities and challenges, 150, 154

pulse sequence considerations, 145, 148–150
 series of triple-quantum excitation and conversion profiles for $S=3/2$, 148–149, 151*f*
 single-pulse excitation plots, 152*f*
 spectral features, 141–145
 technique for quadrupolar nuclei, 30
 triple-quantum ^{23}Na excitation profiles afforded by single pulse and composite pulse sequence on Na_2SO_4 sample, 151*f*
 two-pulse sequence simplest procedure capable of affording MQMAS data, 148
See also Alumina and alumina supports; Aluminum phosphates (AlPO); Quadrupolar nuclei

N

Niobium oxides

specialized electronic ceramics, 83–85, 86*f*
 static ^{93}Nb NMR spectra of low-temperature form of PhNb_2O_6 at different magnetic fields, 85, 86*f*
 summary of various titanium, zirconium, niobium, and tantalum electronic ceramics and applications, 84*t*

Nitrides. *See* Borides, carbides, and nitrides

Nitrides and oxynitrides

^{27}Al MAS NMR spectra at 14.1 T of $\text{AlN}-\text{Al}_2\text{O}_3$ sintered mixtures, 393*f*
 ^{27}Al MAS NMR spectra at 9.4 T of AlN -polytypoids spinning at 3 and 15 kHz, 379, 380*f*
 alloying Si_3N_4 with Al_2O_3 to form β -sialon, 385–387
 aluminum nitride based ceramics, 391–392
 atomic ordering in metal silicon oxynitride phases by ^{29}Si resonances, 395, 398
 glass-ceramics by controlled devitrification of glass, 399
 impact of solid-state NMR in ceramics, 377–378
 majority of NMR relying on MAS, 379, 381
 metal silicon-aluminum oxynitrides, 392, 394–398
 ^{15}N MAS NMR spectra of α - and β - Si_3N_4 , 381, 383*f*
 nitrides Si_3N_4 and AlN amenable to ^{29}Si and ^{27}Al NMR, 378

oxynitride glasses and glass-ceramics, 399–401

possible atomic arrangements in $\text{Si}_2\text{O}_5\text{N}_2$

unit of $\text{Y}_4\text{Si}_2\text{O}_7\text{N}_2$, 395, 397*f*

potentially attractive ^{15}N and ^{17}O , 379

preparation routes to AlN , 391

quadrupole coupling constant, 378

related metal nitrides, 398–399

satellite transition NMR spectroscopy

(SATRAS) not straightforward, 378

^{29}Si and ^{27}Al MAS NMR spectra of reaction

intermediates in carbothermal reduction

and nitridation of halloysite clay to form

β '-sialon, 385, 387, 388*f*, 389*f*

^{29}Si and ^{15}N isotropic chemical shifts and

^{27}Al peak positions from $\text{Si}-\text{Al}-\text{O}-\text{N}$

ceramic phases, 390*t*

^{29}Si and ^{15}N isotropic chemical shifts from

crystalline metal sialon phases, 394*t*

^{29}Si and ^{15}N isotropic chemical shifts from

crystalline metal silicon nitrides, 400*t*

^{29}Si MAS NMR analysis of commercial

Si_3N_4 powders, 381, 384*f*, 385

^{29}Si MAS NMR detection of minor $\text{Y}-\text{Si}-$

$\text{O}-\text{N}$ grain boundary phases formed in

Si_3N_4 using Y_2O_3 sintering aid, 395, 396*f*

^{29}Si MAS NMR spectra of α -, β - and

amorphous Si_3N_4 , 381, 382*f*

^{29}Si MAS NMR spectra of various β -

spodumene glass-ceramics containing 1–

4% N as AlN , 400*f*

silicon nitride based ceramics, 381–391

technical complications by nearest-neighbor

coordinations in ^{27}Al NMR, 378

use of ^{29}Si MAS NMR to follow reactions,

395

varying field strength in ^{27}Al MAS NMR

spectra for β '-sialon spinning at 15 kHz,

386*f*

yttrium sialon glasses, 399

Nitrogen-14 NMR in solids. *See* Wide-line

^{14}N NMR in solids

NMR interactions in inorganic solids

chemical shift interaction, 8, 9*f*

direct magnetic dipolar interaction, 8, 10

hyperfine coupling between nuclear

magnetic moments, 10

indirect dipolar-coupling mechanism, 10

Knight shift, 10

quadrupolar nuclei, 10–14

spin- $\frac{1}{2}$ nuclei, 4, 8–10

Zeeman interaction, 8

NMR relaxation

simulated and measured ionic conductivity of 0.06% yttria in ceria, 158, 160f

simulated and measured spin lattice relaxation of ^{17}O in yttria-doped ceria, 158, 159f

simulation and theory, 157–161

See also Oxygen motion in oxides

NMR techniques. *See* Multidimensional NMR techniques

Nuclear Quadrupole Resonance (NQR) method, 11, 14

O

Octadecasil. *See* Host–guest structures of molecular sieves

Open framework and layered materials

aluminum phosphates (AlPO), 75–76

clays and alumina-silica minerals, 73–75

zeolites, 71–73

zirconium phosphates, 76

Oxygen motion in oxides

atomic motion in solids by NMR, 165–166

comparison of measured ionic conductivity of $\text{Ba}(\text{In}_{2/3}\text{Zr}_{1/3})\text{O}_y$ with that predicted from NMR spin-lattice relaxation kinetics, 162f

deconvolution into temperature-independent

Knight shift and temperature-dependent

Curie–Weiss contact shift, 164, 165f

MAS, DOR, DAS, and MQMAS methods to discriminate between oxygen sites in mixed oxides, 162, 163f

NMR relaxation simulation and theory, 157–161

^{17}O Hahn-echo spectra of $\text{Ba}(\text{In}_{2/3}\text{Zr}_{1/3})\text{O}_y$, 163, 164f

oxygen transport sensitivity to interactions over disparate length scales, 156–157

schematic of two-dimensional vacancy planes, bounded by MO_6 octahedra, 164–165, 166f

schematic of vacancy mechanism for oxygen transport, 157f

structural heterogeneity by high temperature NMR, 161–165

various relaxation parameters for ^{17}O in $\text{Ba}_2\text{In}_2\text{O}_5$, 161f

Oxynitrides. *See* Nitrides and oxynitrides

P

Particles/fibers and matrix materials, inorganic in composites, 119

Periodic Table, nature of most abundant NMR-active isotopes, 138f

Perturbation theory, first- and second-order, quadrupolar nuclei, 11

Phosphate and aluminophosphate glass systems

application of solid-state heteronuclear correlation NMR, 229–230

correlating dynamic angle spinning (DAS) spectrum of quadrupolar nuclei with MAS of nearby spin- $\frac{1}{2}$ nuclei for true high-resolution, 235, 238

correlating resonances from two species by two-dimensional CP and TEDOR spectra, 235

DAS/CP/MAS technique for correlation of ^{23}Na and ^{31}P nuclei in polycrystalline sodium trimetaphosphate, 239, 240f

DAS technique for high resolution, 235, 238

experimental methods, 230–232

gains in CP intensity and efficiency for CP at 0° , 238

high-resolution multiple-quantum MAS (MQMAS) experiments for ^{23}Na nuclei, 238–239

limitations of DAS NMR experiments for sodium nuclei, 239

MAS spectra from ^{23}Na , ^{27}Al , and ^{31}P nuclei for selection of glasses, 233f

modified Hartmann–Hahn match condition, 230

NMR radiofrequency (RF) pulse sequences for one-dimensional CP and TEDOR NMR experiments, 231f

NMR RF pulse sequences for two-dimensional CP and TEDOR NMR experiments, 231f

one-dimensional CP spectrum from ^{23}Na to ^{31}P spins in sodium phosphate glass ($\text{Na/P} = 1.3$), 233f

^{31}P MAS, ^{23}Na - ^{31}P CP/MAS, and ^{27}Al - ^{31}P CP/MAS spectra from sodium aluminophosphate glass, 232, 234f, 235

RF pulse sequence and rotor orientation scheme for DAS/CP/MAS experiments, 240f

two-dimensional ^{23}Na - ^{31}P CPMAS spectrum from aluminophosphate glass, 236f

two-dimensional ^{27}Al - ^{31}P CPMAS spectrum from aluminophosphate glass, 237f

Polysiloxane

uniform and heterogeneous materials, 327

See also Siloxane-based solid networks

Potassium borate glass. *See* Borate glasses

Powder patterns

first-order perturbations for quadrupolar nuclei, 13f

simulated static due to various NMR interactions for spin- $\frac{1}{2}$ nucleus, 9f

Processing and synthetic effects on structure, chemical information, 46

Pseudo-boehmite

^{27}Al MAS NMR spectra (14 T) for various aluminum oxide materials heated to various temperatures, 218f, 219f

dehydration/dehydroxylation weight-loss profiles, 200, 202

^1H CRAMPS studies of dehydration at high temperature ($>300\text{ C}$), 211, 212f

^1H CRAMPS studies of dehydration at low temperature ($<300\text{ C}$), 209–211

insight into formation of transition alumina by ^1H CRAMPS results, 223

MAS ^{27}Al NMR studies at 14 T of dehydroxylation, 217–220

MAS ^{27}Al NMR studies of dehydration, 217–223

mechanisms of dehydroxylation of internal/surface protons, 211, 213

proposed scheme for condensation of "clustered" Al_2OH groups, 215f

proposed scheme for condensation of interlayered Al_2OH groups, 216f

proposed scheme for condensation of "isolated" AlOH groups, 214f

quantitation of ^{27}Al NMR spectra, 220–221

relationship between ^1H and ^{27}Al NMR results, 221–223

two types of structural surface hydroxyl sites, 205f

weight-loss profiles for high-surface area pseudo-boehmite, 203f

See also Alumina materials surface chemistry

Q

Quadrupolar nuclei

averaging out second-order quadrupolar anisotropies, 139–141

characteristic behavior upon sample reorientation, 137

development of NMR techniques, 359

distinction between first- and second-order effects, 137

energy level diagram for single crystallite of spin- $5/2$ nuclei, 12f

MAS and MQMAS experiments on $S=3/2$, $S=5/2$ samples, 143f

NMR interactions in inorganic solids, 10–14

NMR of half-integer quadrupolar spins, 136–139

orientation dependence of Legendre polynomials, 143f

perturbative description of effects by Zeeman and quadrupolar interactions on energy levels of spin- $3/2$, 137, 138f

quadrupole and Larmor frequencies, 136–137

second-order powder pattern for transition of spin- $5/2$ nucleus, 13f

sensitivity enhancement for central transition, 31

static powder pattern for spin- $5/2$ nucleus, 13f

zero-, second-, and fourth-order Legendre polynomials of cosine of spinning angle, 139

See also Multiple-quantum magic-angle spinning (MQMAS)

Quadrupolar nuclei, high-resolution techniques

double rotation (DOR), 26–27

dynamic-angle spinning (DAS), 27, 30

multiple-quantum magic-angle spinning (MQMAS), 30

satellite transition spectroscopy (SATRAS), 30–31

sensitivity enhancement for central transition, 31

R

- Rates of solid-state chemical reactions, chemical information, 46
- REAPDOR. *See* Rotational-echo adiabatic passage double resonance (REAPDOR)
- REDOR. *See* Rotational-echo double resonance (REDOR)
- Refractory metal oxides
- ^{27}Al and ^{17}O MAS NMR spectra of MgAl_2O_4 following quenching at various temperatures, 80, 81*f*
- ceramics and glasses, 78–83
- ^{25}Mg MAS NMR spectra for forsterite Mg_2SiO_4 at different temperatures, 80, 82*f*, 83
- summary of δ (^{17}O) values from ^{17}O NMR spectra of various metal oxide systems, 79*t*
- Resolution (high) techniques. *See* Quadrupolar nuclei, high-resolution techniques
- Rotational-echo adiabatic passage double resonance (REAPDOR)
- measuring distance between quadrupolar and spin- $\frac{1}{2}$ nuclei, 41
- REAPDOR experiment, 40*f*
- Rotational-echo double resonance (REDOR)
- experimental ^{31}P - ^{19}F REDOR NMR, 169–171
- heteronuclear distances by measuring dipole–dipole coupling, 229
- retrieving information on weak heteronuclear dipolar coupling interactions, 169
- technique for measuring heteronuclear distances in rotating samples, 35, 39
- version of the REDOR experiment, 38*f*
- See also* Bioceramics and biomaterials; Hydroxyapatite (HAP); Host–guest structures of molecular sieves
- Rotlsserle
- slow sample rotation for ^{14}N NMR sensitivity gains, 362, 364–368
- See also* Wide-line ^{14}N NMR in solids

S

- SAS. *See* Switched-angle spinning (SAS)
- Satellite transition spectroscopy (SATRAS)
- SATRAS for ^{27}Al NMR of transition alumina, χ -alumina showing 4-, 5-, and 6-coordinate aluminum sites, 196, 197*f*
- technique for quadrupolar nuclei, 30–31
- See also* Alumina and alumina supports
- Saturation internuclear kinetics (SINK) sequence. *See* Wide-line ^{14}N NMR in solids
- SEDOR. *See* Spin-echo double resonance (SEDOR)
- Semiconductors
- earliest NMR studies with ^{27}Al , ^{69}Ga , ^{71}Ga , ^{113}In , and ^{115}In MAS NMR, 106–107
- ^{31}P MAS NMR spectrum of $\text{Ga}_{0.5}\text{In}_{0.5}\text{P}$ under different growth conditions, 107, 108*f*
- ^{31}P MAS NMR spectrum of polycrystalline $\text{Ga}_{0.14}\text{In}_{0.86}\text{P}$ material, 107, 108*f*
- recent studies of more complex ternary and quaternary semiconductors, 107
- results of ^{31}P - ^{113}Cd SEDOR measurements for $\text{Zn}_x\text{Cd}_{1-x}\text{P}_2$ and CdGeAsP glasses, 107, 110, 111*f*
- solid-state ^{31}P and ^{113}Cd NMR spectra showing compositional variation of P and Cd sites in $\text{Zn}_x\text{Cd}_{1-x}\text{P}_2$, 107, 109*f*
- solid-state NMR studies in early stage of development, 106
- structural diagram of both ideal random and fully ordered $\text{Ga}_{0.5}\text{In}_{0.5}\text{P}$ materials, 107, 108*f*
- Sepiolite. *See* Minerals by silicon-29 NMR spectroscopy
- β^1 -Sialon. *See* Nitrides and oxynitrides
- Silanols. *See* Siloxane-based solid networks
- Silica materials
- experimental and simulated ^{23}Na MAS NMR spectra for various sodium silicate hydrates, 54, 55*f*
- known local sodium ion coordination environments, 49, 53*f*, 54
- most abundant and extensively studied metal oxide, 48–49, 52–54

- relationship between solid-state NMR chemical shift δ (^{29}Si) and local chemical environments in silicates, aluminosilicates, and zeolites, 52f
See also Siloxane-based solid networks
- Silica sodalites. *See* Sodalites, host-guest interactions
- Silicates. *See* Minerals by silicon-29 NMR spectroscopy; Siloxane-based solid networks
- Silicones. *See* Siloxane-based solid networks
- Sillimanite, ^{27}Al MAS NMR for the Si/Al mineral, 56, 58f
- Siloxane-based solid networks
 ^{13}C CP/MAS spectra of silylated silica gel, 338, 339f
 CRAMPS-like spectra with broad signal due to hydrogen-bonded silanols, 342, 346f
 distinction between hydrogen-bonded and non-hydrogen-bonded silanols, 348, 353
 effect of measurement time on ^1H CRAMPS spectra of Cab-O-Sil fumed silica and dehydration, 342, 347f
 functionalized polysiloxanes for study, 330
 ^1H CRAMPS dipolar-dephasing results on silica samples at three stages of dehydration, 342, 345f
 ^1H CRAMPS spectra of Cab-O-Sil fumed silica as function of hydration/dehydration, 342, 344f
 ^1H CRAMPS spectra of various silica and polysiloxane samples, 338, 340f
 hydrogen-bonding states of hydroxyl protons by CRAMPS or fast-MAS techniques, 342, 343f
 hypothetical surface structures of silylated silica varying attachments to surface, hydrogen-bonding, and acid-base situations, 336f
 linewidths reflecting degree of structural order or crystallinity, 329–330
 measuring ^1H spin-lattice relaxation times of protons in functionalized polysiloxanes, 333
 NMR characterization of functionalized polysiloxanes, 330–333
 polysiloxane solids by direct polarization (DP) MAS, 327–329
 potential of ^{29}Si NMR and ^1H NMR in heteronuclear correlation approach, 342, 348
 proton spin-lattice relaxation time, T_1^{H} , approach for polysiloxanes, 333–334
 representative materials, 326–327
 ^{29}Si CP-MAS spectra of D_2O -exchanged silica gel, 338, 341f
 ^{29}Si CP-MAS spectra of silica gel derivatized with coupling agent under variety of conditions, 335, 337f, 338
 ^{29}Si MAS spectra of polysiloxanes based on direct polarization (DP) or cross polarization (CP), 327, 328f, 329
 side views of 100 β -cristobalite face with geminol silanols and 111 β -cristobalite face with single silanols, 352f
 silicon atom sites in silica, 334–335
 silylation of silica surface reaction type, 335
 strategy alternative, variety of ^1H - ^{29}Si CP/MAS experiments, 348, 349f, 350f, 351f
 study of underivatized silica, 338
- SINK (saturation internuclear kinetics) sequence. *See* Wide-line ^{14}N NMR in solids
- Slow turning echo amplitude modulation and echo reduction (STEAMER)
 measuring large anisotropies in inhomogeneously-broadened NMR spectra, 368–372
See also Wide-line ^{14}N NMR in solids
- Sodalites, host-guest interactions
 ^{27}Al , ^{29}Si , and ^{23}Na MAS NMR spectra of sodium electro sodalites with varying sodium loading, 276f
 aluminosilicate and silica sodalites, 266–267
 aluminosilicate sodalites with diamagnetic guest species, 267–274
 aluminosilicate sodalites with paramagnetic Na_4^{3+} clusters, 274–277
 detail on local structure and host-guest interactions by multinuclear solid-state NMR, 280, 282
 divalent anions, 274
 ^1H and ^{13}C MAS NMR proving organic guest species enclathrated in β -cages of silica sodalites, 280
 ^1H MAS NMR spectra at variable temperature of trioxane silica sodalite, 281f
 mixed cage contents, 269–271
 ^{23}Na NMR of the Na^+ cations, 271–274

- paramagnetic shifts, Fermi contact coupling constants, and unpaired electron spin densities of Al and Si atoms, 275*t*
- plot of ^{29}Si chemical shifts versus Si–O–Al bond angles of aluminosilicate sodalites with different cage contents, 268*f*
- ^{29}Si chemical shifts and calculated Si–O–Si bond angles of silica sodalites, 278*t*
- ^{29}Si MAS NMR spectra at variable temperature of silica sodalites with different guest molecules, 279*f*
- ^{29}Si MAS NMR spectra of two sodalites of general composition and one mixed composition, 270*f*
- ^{29}Si NMR of aluminosilicate framework, 267–269
- silica sodalites, 277–280
- structure of single sodalite cage and space filling array of sodalite cages, 268*f*
- structure of sodium-oxygen coordinations near six-ring windows of β -cages and corresponding ^{23}Na MAS NMR spectra, 272*f*
- structure of two distinct cage contents with divalent MO_4^{2-} anions and ^{23}Na MAS, DOR, and simulated spectra, 273*f*
- Solid-state chemical reaction rates, chemical information, 46
- Solid-state NMR experiments, internuclear distances, 3
- Solid-state NMR of inorganic materials applications of modern inorganic materials, 3
- origins of complexity, 2–3
- Spin- $1/2$ nuclei
- NMR interactions in inorganic solids, 4, 8–10
- simulated static powder patterns due to various NMR interactions, 9*f*
- Spin diffusion
- multidimensional NMR technique, 34
- obtain qualitative structural information, 34
- Spin-echo double resonance (SEDOR)
- pulse sequence depicting "spin echo" on spin species, 38*f*
- simplest method for measuring internuclear distances, 34–35
- STEAMER. *See* Slow turning echo amplitude modulation and echo reduction (STEAMER)
- Structural and bonding information, chemical information, 46
- Study approaches for inorganic solids. *See* Fundamental approaches to study inorganic solids
- Superconductors
- ^{17}O MAS NMR at 11.7 T and 300 K of various superconductors, 112, 117*f*
- ^{17}O MAS NMR spectra at 8.45 T and 300 K of magnetically aligned $\text{YBa}_2\text{Cu}_3\text{O}_{7-x}$, 112, 115*f*
- solid-state NMR techniques, 110, 112, 119
- static spin-echo ^{17}O NMR spectra at 8.45 T of random powder of $\text{YBa}_2\text{Cu}_3\text{O}_{7-x}$ at 300 K and 77 K, 112, 115*f*
- temperature dependence of isotropic chemical shift of ^{17}O NMR resonance for conducting CuO_2 oxygen sites in $\text{Tl}_2\text{Ba}_2\text{CaCu}_2\text{O}_{8+x}$ before and after annealing, 112, 118*f*
- variable temperature ^{17}O NMR spectra of various $\text{YBa}_2\text{Cu}_3\text{O}_{7-x}$, 112, 116*f*
- ^{89}Y MAS NMR and static ^{17}O NMR on metal-substituted and related high- T_c superconductors, 112, 119
- Surface and interfacial interactions, chemical information, 46
- Surface chemistry. *See* Alumina materials surface chemistry
- Switched-angle spinning (SAS), two-dimensional techniques with isotropic and anisotropic dimensions, 312
- Synthesis and processing effects on structure, chemical information, 46
- T**
- Talc, polycrystalline, static ^{17}O NMR spectra of isotopically labeled, 74*f*
- Tantalum oxides
- specialized electronic ceramics, 83–85, 86*f*
- summary of various titanium, zirconium, niobium, and tantalum electronic ceramics and applications, 84*t*
- TEDOR. *See also* Transferred-echo double resonance (TEDOR)
- Titanium and zirconium silicate and phosphate catalysts and supports, use of NMR, 66–68

Titanium oxides
 experimental and simulated ^{47}Ti and ^{49}Ti
 MAS NMR spectra of TiO_2 polymorph
 anatase, 84*f*
 specialized electronic ceramics, 83–85, 86*f*
 summary of various titanium, zirconium,
 niobium, and tantalum electronic ceramics
 and applications, 84*t*

TOSS. *See* Total suppression of sidebands
 (TOSS)

TOSS–reTOSS

isotropic/anisotropic correlation spectra
 possible, 321
 pulse sequence, 313*f*
 two-dimensional techniques with isotropic
 and anisotropic dimensions, 312, 314

See also Minerals by silicon-29 NMR
 spectroscopy; Total suppression of
 sidebands (TOSS)

Total suppression of sidebands (TOSS),
 isotropic–anisotropic correlation
 experiment, 42

Transfer of populations in double resonance
 (TRAPDOR)

detecting dipolar couplings to quadrupolar
 nuclei, 39, 41

TRAPDOR pulse technique, 40*f*

Transferred-echo double resonance (TEDOR)

heteronuclear distances by measuring
 dipole–dipole coupling, 229

technique for measuring internuclear
 distances, 35, 39

version of TEDOR experiment, 38*f*

See also Host–guest structures of molecular
 sieves; Phosphate and aluminophosphate
 glass systems

TRAPDOR. *See* Transfer of populations in
 double resonance (TRAPDOR)

V

VACSYS. *See* Variable-angle correlation
 spectroscopy (VACSYS)

Vanadia-containing catalysts

metal oxide materials, 68–70

static ^{51}V NMR studying V(V) compounds,
 69*f*

Variable-angle correlation spectroscopy
 (VACSYS)

2D spectra to probe connectivities, 41–42

2D techniques with isotropic and anisotropic
 dimensions, 312

W

Wide-line ^{14}N NMR in solids

derivations and principal results of
 STEAMER (slow turning for echo
 amplitude modulation and echo reduction)
 experiment, 368–370

development of NMR techniques for
 quadrupolar nuclei, 358–359

distribution of reported ^{14}N NQCC values,
 361*f*

energy level diagram depicting three
 Zeeman levels of ^{14}N nucleus shifted by
 first-order quadrupolar interaction, 360,
 361*f*

example of STEAMER behavior for silicon
 nitride, 370, 371*f*

experimental apparatus for RotIsseRie
 experiment, 366*f*

experimental example of approach using ^{14}N
 NMR of KNO_3 , 362, 363*f*

extensions of STEAMER experiment and
 use of other types of echoes, 370, 372

frequency history of six ^{14}N isochromats
 resonant with the rf carrier at time
 outlined, 365, 367*f*

hole-burning and "whole"-burning
 experiments for determining dynamical
 parameters, 375

limitation in small fraction of crystallites
 observed, 362, 364*f*, 365

measuring large anisotropies in
 inhomogeneously-broadened NMR spectra
 with STEAMER, 368–372

model of hexamethylenetetramine (HMT),
 373*f*

^{14}N NMR single DANTE-train hole-burning
 experiment to study slow motions in
 HMT, 372, 373*f*, 374

^{14}N NMR techniques for studying slow
 molecular motions, 372–375

NQCC, product of ^{14}N nuclear electric
 quadrupole moment and electric field
 gradient, 360

reorientation of equatorial band by rotation
 about axis perpendicular to magnetic
 field, 365, 366*f*

saturation internuclear kinetics (SINK)
 sequence to study cross-relaxation
 between major and minor peaks, 374
 selective-excitation techniques for ^{14}N wide-
 line NMR spectra, 360–362
 sensitivity gain by coadding Carr–Purcell–
 Meiboom–Gill (CPMG) train of pulses,
 362, 363*f*
 sensitivity gains from slow sample rotation
 (RotIsseRIe), 362, 364–368
 series of hard $\pi/2$ pulses instead of
 frequency-selective DANTE train, 374–
 375
 single- and multiple-DANTE saturation
 pulses, 374
 tetrahedral-jump process in HMT, 373*f*
 transition- and frequency-selective
 excitation, 360
 usefulness of RotIsseRIe experiment shown
 in ^{14}N NMR stepped-frequency spectrum
 of silicon nitride, 365, 366*f*

Y

Yttrium. *See* Nitrides and oxynitrides; NMR
 relaxation; Superconductors

Z

Zeeman interaction
 energy level diagram for single crystallite of
 spin-5/2 nuclei, 12*f*
 quadrupolar nuclei in inorganic solids, 10–
 11
 spin- $1/2$ nuclei in inorganic solids, 8
 Zeolites
 solid-state ^{29}Si MAS NMR studies in
 zeolites, 71–73
 structural depiction of important zeolite
 materials, 72*f*
See also Host–guest structures of molecular
 sieves; Siloxane-based solid networks
 Zirconium and titanium silicate and
 phosphate catalysts and supports, use of
 NMR, 66–68
 Zirconium oxides
 specialized electronic ceramics, 83–85, 86*f*
 summary of various titanium, zirconium,
 niobium, and tantalum electronic ceramics
 and applications, 84*t*
 Zirconium phosphates, ^{31}P MAS NMR to
 obtain phosphate units, 76